Congress on Numerical Methods in Engineering 2024

Proceedings of the
Congress on Numerical Methods in Engineering 2024

September 4-6
University of Aveiro, Portugal

Edited by:

J. Alexandre Pinho-da-Cruz
Nuno Lopes
A. Gil Andrade-Campos
Juan José del Coz
David Greiner
Marino Arroyo

This page intentionally left blank

Congress on Numerical Methods in Engineering 2024

Proceedings of the
Congress on Numerical Methods in Engineering 2024

September 4-6
University of Aveiro, Portugal

A publication of:

UNIVERSIDADE DE AVEIRO
Aveiro, Portugal

Cataloging-in-Publication data

Title:	Proceedings of the Congress on Numerical Methods in Engineering 2024
Editors:	J. Alexandre Pinho-da-Cruz, Nuno Lopes, A. Gil Andrade-Campos, Juan José del Coz, David Greiner, Marino Arroyo
Edition:	Universidade de Aveiro 1st edition – July 2025
ISBN:	**978-989-9253-21-6**
DOI:	https://doi.org/10.48528/e911-zf92

Preface

This book contains the Proceedings of the Congress on Numerical Methods in Engineering 2024 (CMN 2024), which was held at the University of Aveiro, Portugal, on 4-6 September 2024.

CMN 2024 was organized jointly by the Portuguese (APMTAC) and the Spanish (SEMNI) societies of numerical methods, and by the University of Aveiro (UA). It followed the successful series of joint congresses of both societies held in Madrid (2002), Lisbon (2004), Granada (2005), Porto (2007), Barcelona (2009), Coimbra (2011), Bilbao (2013), Lisbon (2015), Valencia (2017), Guimarães (2019) and Las Palmas de Gran Canaria (2022).

CMN 2024 aimed at providing an Iberian forum for compilation and discussion of the most recent and relevant scientific and technical works in the area of numerical methods and computational mechanics, as well as their practical applications.

The following seven Keynote Lectures (KL) were held at the conference:

- KL1: "Numerical modelling of the fire behaviour of steel structures"
  Paulo Vila Real, University of Aveiro, Portugal
- KL2: "The “curse of dimensionality”. A war to be won in the composite laminates modeling"
  Xavier Oliver, Technical University of Catalonia. (UPC), Barcelona, Spain
- KL3: "Additive Manufacturing: design, production, modeling, computations"
  Ferdinando Auricchio, University of Pavia, Italy
- KL4: "Multiscale computational modelling of tissue mechanics"
  Alejandro Torres-Sánchez, European Molecular Biology Laboratory (EMBL), Barcelona, Spain
- KL5: "The revolution of material testing 2.0: how information-rich experiments and advanced numerical methods can change material testing and characterization"
  Marco Rossi, Università Politecnica delle Marche, Ancona, Italy
- KL6: “A new class of coupled phase field-based models for environmentally-assisted damage: hydrogen embrittlement and corrosion”
  Emilio Martinez-Pañeda, University of Oxford, United Kingdom
- KL7: "The collision chronicles — From sports fields to cosmic shields through simulation and modelling"
  Filipe Teixeira-Dias, The University of Edinburgh, United Kingdom

Furthermore, contributing authors were able to present their research work in sixteen proposed Thematic Sessions and two more general sessions covering the main areas of computational mechanics and computational engineering, resulting in 119 abstracts and 15 full papers accepted after scientific peer review, whose abstracts or full papers constitute this book. The sixteen Thematic Sessions (TS) held at the conference were the following:

- TS1: "Composites modelling: characterization, behaviour and structures"
  L. A. Távara, V. Mantic
- TS2: "Advances in numerical modeling of seismic structural behavior"
  H. Varum, H. Rodrigues, J. Melo
- TS3: "Computational approaches to complex fluid Systems: multiphysics perspectives"
  M. Abdollahzadeh, M. A. A. Mendes
- TS4: "Machine and deep learning techniques applied to computational mechanics"
  J. Belinha, S. M. O. Tavares
- TS5: "Computational engineering empowered by model order reduction and machine learning"
  F. Chinesta, E. Cueto, A. Huerta
- TS6: "Steel and composite structures"
  A. Espinós, N. Lopes
- TS7: "Computational methods in acoustics and vibration"
  F. D. Denia, J. Martínez-Casas
- TS8: "Optimization, metaheuristics and evolutionary algorithms in computational and civil engineering"
  D. Greiner, D. Ribeiro, V. Yepes
- TS9: "Computational models as a pre-clinical test to predict the behavior of biomechanical devices"
  A. Ramos, M. Mesnard
- TS10: "Numerical modeling of biological cell systems"
  M. Doblaré, F. J. Montáns, J. A. Sanz, J. Sarrate
- TS11: "Metal forming – material, formability, damage, fracture, and process modelling"
  J. Mendiguren, B. Erice, M.C. Oliveira, J. César de Sá, A.D. Santos
- TS12: "Optimization and inverse analysis in applied engineering"
  D. Villalba, J. Dias-de-Oliveira, J. París, A. G. Andrade-Campos, R. Valente, F. Navarrina
- TS14: "Computational modelling in mechanobiology and tissue engineering"
  P. R. Fernandes, A. P. G. Castro, J. Mora
- TS15: "Fluid mechanics applied to engineering"
  A. Santiago, H. Craveiro, L. Laím
- TS16: "Recent advances in shape and topology optimization"
  A. Ferrer, J. Martínez Frutos
- TS17: "Crashworthiness, Impact and Blast Wave Dynamics"
  A. Azevedo, T. Børvik, F. Teixeira-Dias

As previously referred, there were also two general sessions: Other topics in Numerical Methods in Engineering, Numerical applications.

The congress was attended by 145 participants from seven countries, and the editors warmly thank all the contributing authors and participants for their important role in the event's success.

The editors and conference organisers also acknowledge support towards the publication of the Proceedings and, particularly, the organisation of the Congress on Numerical Methods in Engineering 2024 to the following institutions and individuals:

- APMTAC – Associação Portuguesa de Mecânica Teórica, Aplicada e Computacional;
- SEMNI – Sociedad Española de Métodos Numéricos en Ingeniería;
- Universidade de Aveiro (UA), Portugal;
- Departamento de Engenharia Mecânica da Universidade de Aveiro;
- Departamento de Engenharia Civil da Universidade de Aveiro;
- All the Keynote Lecturers: Alejandro Torres-Sánchez, Emilio Martinez-Pañeda, Ferdinando Auricchio, Filipe Teixeira-Dias, Marco Rossi, Paulo Vila Real, Xavier Oliver;
- All the colleagues involved in the organisation, particularly to those of the Local Organising Committee: Carlos Couto, Hugo Rodrigues, Inês Meireles, João Oliveira, Pedro Antunes, Robertt Valente, Romeu Vicente;
- To all the members of the Scientific Committee, namely: Adélia Sequeira (IST/UTL), António Ferreira (FEUP), Antonio Huerta (UPC), Carlos Mota Soares (IST/UTL), Carlos Pina (LNEC), Chengxiang (Rena) Yu (UCLM), David Grei- ner (ULPGC), Dinar Camotim (IST/UTL), Elías Cueto (UNIZAR), Eugenio Oñate (UPC), Fermín Navarrina (UDC), Francisco Javier Montáns (UPM), Helder Rodrigues (IST/UTL), Ignacio Romero (UPM), Ignasi Colominas (UDC), Irene Arias (UPC), Isabel Figueiredo (UC), Ivo Dias (LNEC), João Rocha Almeida (UNL), Joan Baiges (UPC), Jorge Ambrósio (IST/UTL), José Carlos Pereira (IST/UTL), José César de Sá (FEUP), José María Goicolea (UPM), Juan José Ródenas (UPV), Luís Filipe Menezes (UC), Manuel Alves (FEUP), Manuel Tur (UPV), Miguel Cervera (UPC), Paulo B. Lourenço (UM), Paulo Oliveira (UBI), Paulo Piloto (IPB), Paulo Vila Real (UA), Pedro Camanho (FEUP), Pedro Díez (UPC), Pilar Ariza (US), Riccardo Rossi (UPC), Xavier Oliver (UPC), Xesús Nogueira (UC);
- All students that helped technically in the sessions;
- All staff of the UNAVE, particularly to Sandra Fuentes;
- Everyone that, directly or indirectly, helped in the preparation of the event or during the same.

J. Alexandre Pinho-da-Cruz, Universidade de Aveiro, Portugal
Nuno Lopes, Universidade de Aveiro, Portugal
A. Gil Andrade-Campos, Universidade de Aveiro, Portugal
Juan José del Coz, Universidad de Oviedo, Spain
David Greiner, Universidad de Las Palmas de Gran Canaria, Spain
Marino Arroyo, Universitat Politècnica de Catalunya, Spain

Aveiro, October 2024

This page intentionally left blank

Contents

List of Full Articles…...……..…….. 161

This page intentionally left blank

List of Abstracts

This page intentionally left blank

TS1: Composites modelling: characterization, behaviour and structures

This page intentionally left blank

Congress on Numerical Methods in Engineering 2024
4-6 September 2024, University of Aveiro, Portugal

Phase-field damage models via homogenization – CNM 2024

Villalta, G.[*,1], Ferrer, A.[1,2] and Otero, F.[1,3]

[1] Centre Internacional de Mètodes Numèrics a l'Enginyeria (CIMNE)
C/Gran Capitán S/N UPC Campus Nord, Edifici C1, 08034 Barcelona, Spain
web page: https://www.cimne.com

[2] Universidad Politècnica de Catalunya
Campus ESEIAAT UPC, 08222 Barcelona, Spain
web page: https://eseiaat.upc.edu/es

[3] Universidad Politècnica de Catalunya
Campus FNB UPC, 08003 Barcelona, Spain
web page: https://www.fnb.upc.edu/es

[*] e-mail: gvillalta@cimne.upc.edu

ABSTRACT

Phase-field method has become during the last two decades a powerful approach to successfully solve problems related to fracture mechanics. However, the theory still presents some limitations including unclear analytical degradation and dissipation functions and computational efficiency.

In fact, the effect of damage on the strain energy function has been habitually computed with analytical degradation functions. In this work, we propose to understand the degradation function as the homogenization of a microstructure with a void inclusion. Thus, we replace the phase field variable by microstructure parameters. Through this, we automatically obtain an orthotropic homogenized constitutive tensor which is also supported by a physical phenomenon instead of depending on ad-hoc analytical expression.

The methodology implemented consists of two stages: (1) an offline stage where the mechanical response (constitutive tensor) of the microstructure has been computed for different void parameters and (2) a second stage where the structural damage simulation is computed.

Different results have been obtained from benchmark tests to validate the formulation and the computation cost has been compared with standard phase field approach.

Congress on Numerical Methods in Engineering 2024
4-6 September 2024, University of Aveiro, Portugal

Strain-gradient-plasticity for epoxy resins in micro-scale models of fibre-reinforced composites

Igor A. Rodrigues Lopes[1], Nathan Klavzer[2], Carolina Furtado[1,3], Francisco M. Andrade Pires[1,3], Pedro P. Camanho[1,3] and Thomas Pardoen[2,4]

[1] INEGI, Universidade do Porto, Rua Dr. Roberto Frias, 400, 4200-465 Porto, Portugal, Email: ilopes@inegi.up.pt

[2] Institute of Mechanics, Materials and Civil engineering (iMMC), UCLouvain, Louvain-la-Neuve, Belgium

[3] DEMec, Faculdade de Engenharia, Universidade do Porto, Rua Dr. Roberto Frias, 4200-465 Porto, Portugal

[4] WEL Research Institute, Avenue Pasteur 6, 1300 Wavre, Belgium

ABSTRACT

Micro-mechanical simulations of advanced materials can be employed to better understand the impact of microscopic phenomena on the structural response, to design the material microstructure, or to generate data required to build surrogate macroscopic models, for instance. However, an accurate description of the micro-constituents is required.

In the case of carbon-fibre-reinforced composites, recent studies [1,2] revealed that classical elasto-plastic constitutive models are not able to capture the strain fields accurately, especially in regions of the matrix close to the fibres, where excessive strain localisation is predicted. Enriched continua like strain gradient plasticity may be adequate for a better description of the matrix deformation in these regions, as well as to capture the macroscopic strength that is often underestimated with classical models for the matrix. In this contribution, the classical pressure-sensitive elasto-plastic model proposed in [3] is enriched towards a strain-gradient plasticity formulation, where a length-scale parameter and strain-gradient-hardening parameters are included. Experimental data available from nano-scale digital image correlation [2] is employed to evaluate the suitability of this type of modelling strategy to capture the strain fields. Moreover, the impact of the additional constitutive parameters is evaluated by systematic analyses, and their values are calibrated.

This project has received funding from the European Union's Horizon Europe research and innovation programme under grant agreement No. 101056682.

REFERENCES

[1] J. Chevalier, P. P. Camanho, F. Lani and T. Pardoen. "Multi-scale characterization and modelling of the transverse compression response of unidirectional carbon fiber reinforced epoxy", *Compos. Struct.*, 209:160-176 (2019).

[2] N. Klavzer, S. F. Gayot, M. Coulombier, B. Nysten and T. Pardoen. "Nanoscale digital image correlation at elementary fibre/matrix level in polymer–based composites". *Compos. Part A Appl. Sci. Manuf.*, 168:107455 (2023).

[3] A. R. Melro, P. P. Camanho, F. M. Andrade Pires and S. T. Pinho, "Micromechanical analysis of polymer composites reinforced by unidirectional fibres: Part I – Constitutive modelling," *Int. J. Solids Struct.*, 50, 11–12: 1897–1905, (2013).

Congress on Numerical Methods in Engineering 2024
4-6 September 2024, University of Aveiro, Portugal

Nuevo elemento singular para grietas en las interfases de tipo Winkler. Aplicación a grietas de interfase en composites

Luis A. Távara, Alberto Vázquez, Mar Muñoz-Reja y Vladislav Mantič

* Grupo de Elasticidad y Resistencia de Materiales, Escuela Técnica Superior de Ingeniería, Universidad de Sevilla, Camino de los Descubrimientos s/n, 41092 Sevilla, Spain
Email: ltavara@us.es

RESUMEN

Uno de los modelos computacionales para analizar la fractura de interfases, es el denominado Modelo de Interfase Frágil Elástico Lineal (LEBIM) [1], que permite analizar la fractura de uniones adhesivas con una capa fina de adhesivo o en las diferentes interfases que pueden encontrarse en un material compuesto. El objetivo de este trabajo es aumentar la precisión de las soluciones obtenidas por el método de los elementos finitos (MEF) para grietas que se propagan en este tipo de interfases (tipo Winkler o muelles) entre adherentes elásticos lineales. El comportamiento elástico lineal en las proximidades del vértice de la grieta puede considerarse una hipótesis realista a la hora de modelar la propagación de grietas en materiales frágiles y cuasi frágiles, por ejemplo, materiales compuestos (como los reforzados con fibras largas utilizados en la industria aeronáutica).

Tomando como base la solución asintótica en este tipo grietas de interfase [2], se desarrolla un elemento finito especial triangular de 5 nodos [3]. Las funciones de forma singular singulares generadas reproducen el comportamiento radial del primer término de la solución asintótica [2]. Este elemento especial implementado en un código en un código MEF escrito en Matlab ha superado con éxito varias pruebas con condiciones de contorno tipo muelle. El nuevo elemento permite modelar grietas en interfase tipo muelle sin necesidad de utilizar mallas de elementos finitos excesivamente refinadas, que es una de las desventajas actuales en el uso del LEBIM cuando se consideran un comportamiento rígido de las interfases de los muelles.

REFERENCIAS

[1] V. Mantič, L. Távara, A. Blázquez, E. Graciani, F. París, A linear elastic - brittle interface model: Application for the onset and propagation of a fibre-matrix interface crack under biaxial transverse loads, International Journal of Fracture, Vol. 195, 15–38, 2015.
[2] S. Jiménez-Alfaro, V. Mantič, Crack tip solution for Mode III cracks in spring interfaces, Engineering Fracture Mechanics, Vol. 288, 109293, 2023.
[3] V. Mantič, A. Vázquez-Sánchez, M. Romero-Laborda, M. Muñoz-Reja, S. Jiménez-Alfaro, L. Távara, A new crack-tip element for the logarithmic stress-singularity of Mode-III cracks in spring interfaces, Computational Mechanics (in print), 2024

Embedded structures in continua

David Portillo[*], Guanfeng Zhang[†], Wenjie Xie[†], Ignacio Romero[**]

[*] Universidad Politécnica de Madrid, Spain
david.portillo@upm.es

† ANSYS Inc, US

[**] Universidad Politécnica de Madrid, Spain

ABSTRACT

Problems in which the so called reduced dimensional models, such as beams, shells or membranes, are embedded into a solid domain arise in many engineering applications or physical modelling: reinforcement bars in concrete structures, fibers in composite materials or padle rackets are some examples. We present a complete theory for modelling reduced dimensional models embedded in deformable solids. Although there are several reduced dimensional theories, each one with its own different model, in this work we deal with a general type of these reduced dimensional models which encompasses the most typical ones for beams, shells, membranes… This common description allows us to generalize the strategy for the most common structure embedded in solid problems.

The presented theory works in both small and finite strain regime. Moreover, we complete it with a numerical discretization strategy that yields convergent approximations. The ideas, based on the Arlequin method [1, 2], can be used to prove rigorously that the method is unconditionally stable for linear problems. Extending the same principles to the finite strain range we expect the resulting methods to perform well. Although no proof can be given in this case, the numerical results obtained confirm the robustness of the formulation.

REFERENCES

[1] Hachmi Ben Dhia and Guillaume Rateau. Analyse mathématique de la méthode arlequin mixte. Comptes Rendus de l'AcadÅLemie des Sciences - Series I - Mathematics, 332(7):649–654, Apr 2001.

[2] H. B. Dhia and G. Rateau. The Arlequin method as a flexible engineering design tool. International Journal for Numerical Methods in Engineering, 62(11):1442–1462, 2005.

Congress on Numerical Methods in Engineering 2024
4-6 September 2024, University of Aveiro, Portugal

Non-linear computational modeling of multilayered bending plates: The 2D+ multiscale approach

Pablo Wierna*[a], Daniel Yago[c,b], Oriol Lloberas-Valls[a,b], Alfredo Huespe[d], Javier Oliver[a,b]

[a] Escola Tècnica Superior d'Enginyers de Camins, Canals i Ports de Barcelona (ETSECCPB), Universitat Politècnica de Catalunya · BarcelonaTech (UPC), Spain
Email: oriol.lloberas@upc.edu

[b] CIMNE – Centre Internacional de Mètodes Numèrics en Enginyeria, Barcelona, Spain

[c] Escola Superior d'Enginyeries Industrial, Aeroespacial i Audiovisual de Terrassa (ESEIAAT), Universitat Politècnica de Catalunya · BarcelonaTech (UPC), Spain

[d] CIMEC-UNL-CONICET, Santa Fe, Argentina

ABSTRACT

This study introduces a novel 2D multiscale strategy, referred to as the 2D+ approach [1], employing a computational homogenization formalism tailored for modeling multilayered plates in situations dominated by bending. Such structural elements often involve advanced materials like laminated composites, characterized by a heterogeneous distribution of low-aspect-ratio layers exhibiting substantial nonlinear mechanical behavior across their thickness.

In this methodology, the macroscopic scale is represented by the 2D plate mid-plane, while the mesoscopic scale employs a 1D filament-like Representative Volume Element (RVE) orthogonal to the plate mid-plane, spanning the plate thickness. This RVE captures nonlinear mechanical behavior across the plate thickness at each integration point of the 2D plate discretization. The selected kinematics and discretization at these scales are chosen to effectively capture nonlinear mechanical behavior, achieve computational efficiency, and provide accurate stress distributions compared to high-fidelity 3D simulations.

The proposed strategy aligns with the standard first-order hierarchical multiscale framework, involving the linearization of the macro-scale displacement field along the thickness. It incorporates an additional fluctuating displacement field in the RVE to capture higher-order behavior, computed through a local 1D finite element solution of a Boundary Value Problem (BVP) at the RVE. A notable feature of the 2D+ approach is the application of the Hill-Mandel principle, establishing mechanical energy equivalence in both macro and meso scales. This weakly couples the 2D macroscopic plate and the set of 1D mesoscopic filaments, resulting in significant computational savings compared to standard 3D modeling. Solving the resulting RVE problem in terms of the fluctuating displacement field enables the enforcement of an additional condition: the fulfillment of linear momentum balance (equilibrium equations). This yields a physically meaningful 2D-like computational setting for the considered structural object (multilayered plates under bending), providing accurate stress distributions typical of full 3D models at the computational cost of 2D models.

REFERENCES

[1] P. Wierna, D. Yago, O. LloberasValls, A. E. Huespe and J. Oliver, On the efficient and accurate non-linear computational modeling of multilayered bending plates. State of the art and a novel proposal: the 2D+ multiscale approach. *Archives of Computational Methods in Engineering*, 2024, In Press.

Congress on Numerical Methods in Engineering 2024
4-6 September 2024, University of Aveiro, Portugal

MESOSCALE NUMERICAL MODELING OF LIGHTWEIGHT CONCRETE: ADVANCEMENTS AND IMPLICATIONS

J.J. del Coz-Díaz[1], M. Alonso-Martinez[1], F.P. Álvarez-Rabanal[1], F. López-Gayarre[2], Z. Fernández-Muñiz[2], M. Montes-Bayón[3] and M. Brana-Linares[1]

1: GICONSIME Research Group. EPI Gijón. University of Oviedo
C/Puig Adam s/n – 33204 Gijon
e-mail: delcoz@uniovi.es , web: http://www.giconsime.grupos.uniovi.es

2: IEMES Research Group. EPI Gijón. University of Oviedo

3: EMAB Research Group. University of Oviedo. Chemical Faculty. Av. Julián Clavería 8, 33006 Oviedo

Keywords: Numerical methods, FEM, Lightweight concrete, mesoscale models, nonlinear models, cracking and crushing.

Abstract *Lightweight concrete, distinguished by its reduced density through the use of lightweight aggregates, maintains adequate strength and durability. Notably, its reduced environmental impact is a key benefit, as it requires less energy for transportation and produces fewer greenhouse gas emissions during production compared to normal concrete. This makes lightweight concrete a sustainable choice for construction projects aiming to minimize environmental footprint while maintaining structural integrity and performance. However, exhibits complex behaviours at microscopic, mesoscopic, and macroscopic scales. This study assesses the mechanical performance of lightweight concrete (LWC) on the mesoscopic scale [1-2]. At this scale, LWC is simulated as a heterogeneous material composed by mortar, lightweight aggregates and a special interfacial transition zone [11] (s-ITZ). Numerical models, to evaluate the compressive strength of LWC, are developed using Finite Element Method (FEM). The 3-D geometry is developed using Representive Volume Elements (RVEs) in MatLab software with an own code. Several geometries are developed to include random locations, shapes and sizes of lightweight aggregate (see Figure 1). These geometries are then uploaded to the FEM analysis to simulate compressive strength tests. The advanced numerical models are meshed with FEM elements using a body fitted Cartesian algorithm [4] with an element size of 2.5 10-4 m giving more than two million nodes and elements. Furthermore, a nonlinear combined mathematical model of concrete, incorporating the Drucker-Prager material model [5-7] for compression stresses and the Willam and Warnke model [8-10] for tension stresses, is used to predict both material failure modes: cracking and crushing (see Figure 2).*

Congress on Numerical Methods in Engineering 2024
4-6 September 2024, University of Aveiro, Portugal

Linear static analysis of beam structures made of auxetic materials integrating carbon nanotubes

M.A.R. Loja *[,1,2], J. I. Barbosa [,1,2], A.R.D. Carvalho[,1,2] and I.J.C. Barbosa[,1,2]

[1] CIMOSM, Centro de Investigação em Modelação e Otimização de Sistemas Multifuncionais, ISEL/IPL, Instituto Superior de Engenharia de Lisboa, Av. Conselheiro Emídio Navarro 1, 1959-007, Lisboa, Portugal

[2] IDMEC, IST-Instituto Superior Técnico, Universidade de Lisboa, Av. Rovisco Pais, 1, 1049-001 Lisboa, Portugal

Emails: amelia.loja@isel.pt; joaquim.barbosa@isel.pt; andre.carvalho@isel.pt; ines.barbosa@isel.pt

ABSTRACT

Auxetic materials are well-known for exhibiting a negative Poisson's ratio, which particularity enables these materials to show potentially useful properties for a wide range of applications and innovative solutions [1].

This study aims to investigate beam structures made of these materials and to characterize the influence of their intrinsic geometrical parameters while considering the effects that the inclusion of carbon nanotubes [2],[3] may additionally provide to these structures.

The studies conducted, are based on the first-order shear deformation theory, implemented via the finite element method [4]. The corresponding code is verified against other solutions, when available, showing a good agreement with the results obtained by different authors.

According to the results achieved, it can be concluded that the structures' behaviour is significantly influenced by the geometrical features of these materials as well as by the integration of carbon nanotubes.

REFERENCES

[1] X. Li, W. Peng, W. Wu, J. Xiong, Y. Lu. "Auxetic mechanical metamaterials: from soft to stiff", *International Journal of Extreme Manufacturing*, 5, 042003 (2023). doi:10.1088/2631-7990/ace668

[2] S. Rathinavel, K. Priyadharshini, D. Panda. "A review on carbon nanotube: An overview of synthesis, properties, functionalization, characterization, and the application". *Materials Science and Engineering: B*, 268, 115095, (2021). doi:10.1016/j.mseb.2021.115095

[3] S. I. Yengejeh, S. A. Kazemi, A. Öchsner. "Carbon nanotubes as reinforcement in composites: A review of the analytical, numerical and experimental approaches". *Computational Materials Science*, 136, 85-101, (2017). doi:10.1016/j.commatsci.2017.04.023

[4] O.C. Zienkiewicz and R.L. Taylor, *The finite element method*, McGraw Hill, Vol. I., 1989, Vol. II, (1991).

Congress on Numerical Methods in Engineering 2024
4-6 September 2024, University of Aveiro, Portugal

Algoritmo para la predicción de la delaminación dinámica en composites utilizando el Principio de Mínima Energía Total sujeto a una condición de Tensión

Mar Muñoz-Reja[1]*, Roman Vodička[2], Vladislav Mantič[3], Luis Távara[1,3]

[1] Grupo de Elasticidad y Resistencia de Materiales, Escuela Politécnica Superior, Universidad de Sevilla, c/ Virgen de África 7, 41011 Sevilla, España.

[1] Universidad Técnica de Košice, Facultad de Ingeniería Civil, Vysokoškolská 4, Košice, 04200, Eslovaquia.

[3] Grupo de Elasticidad y Resistencia de Materiales, Escuela Técnica Superior de Ingeniería, Universidad de Sevilla, Camino de los Descubrimientos s/n, 41092 Sevilla, España
Email: mmunozreja@us.es

RESUMEN

El Criterio Acoplado de la Mecánica de Fractura Finita (CC-FFM) [1] se ha aplicado tradicionalmente minimizando la carga necesaria para satisfacer los criterios de tensión y energía con respecto al tamaño de avance de la grieta (que es una variable a priori desconocida). El objetivo de este trabajo es desarrollar una herramienta computacional general basada en el CC-FFM y el Principio de Mínima Energía Total restringido a una condición de tensión (PMTE-SC) [2]. Resultados previos han mostrado que el PMTE-SC es equivalente a la formulación original del CC-FFM [3].

Específicamente, se presenta un modelo computacional basado en el PMTE-SC para estudiar la propagación dinámica de grietas 2D en interfases cuasi frágiles sometidas a condiciones de carga dependientes del tiempo. Se utiliza un esquema escalonado de pasos de tiempo para resolver el problema de minimización de energía total por separado, en términos de desplazamientos y una variable de daño para cada paso de carga a través. Además, siguiendo a [4], se utiliza la fórmula de Crank-Nicolson en el esquema de pasos de tiempo para eliminar la atenuación numérica y tener solo la física.

Se ha implementado este algoritmo en un script de Pyhon que utiliza el código de Elementos Finitos, Abaqus®. El principal objetivo de este trabajo es comparar los resultados del código desarrollado con datos experimentales de ensayos de doble viga en voladizo (DCB).

REFERENCIAS

[1] D. Leguillon, “Strength or toughness? A criterion for crack onset at a notch.”, Eur. J. Mech. A/Solids, 21, 61-72, (2002).
[2] V. Mantic, “Prediction of initiation and growth of cracks in composites. Coupled stress and energy criterion of the finite fracture mechanics”, in: ECCM (2014).
[3] M. Muñoz-Reja, V. Mantic and L. Távara, “Comparative analytical study of the Coupled criterion and the principle of minimum total energy with stress condition applied to linear elastic interfaces”, Theor. Appl. Fract. Mech., 119, 103274, (2022).
[4] Roman Vodička, “A Computational approach of Dynamic Quasi-Brittle Fracture Using a Phase-Field Model”, Procedia Structural Integrity, 52, 242-251, (2024).

TS2: Advances in numerical modeling of seismic structural behavior

This page intentionally left blank

Congress on Numerical Methods in Engineering 2024
4-6 September 2024, University of Aveiro, Portugal

Efficiency of intensity measures for the seismic assessment of a historical stone masonry building

Daniel Caicedo*, Shaghayegh Karimzadeh*, Vasco Bernardo* and Paulo B. Lourenço*

* University of Minho, ISISE, ARISE, Department of Civil Engineering. Guimarães, Portugal
Email: dcaicedod@civil.uminho.pt

ABSTRACT

This work focuses on the identification of high-efficiency Intensity Measures (IMs) for the seismic assessment of a stone masonry historical building. The numerical model of the Holsteiner Hof building, which historical stone masonry building located in the city centre of Basel, is adopted as a case study in this research. The building is modelled through 3D macroelements that consider both the in-plane and out-of-plane response of masonry walls. A large set of accelerograms is selected and catalogued in terms of its IMs. The structure is subjected to the action of the un-scaled ground motions and the maximum responses in terms of average roof displacement and base shear (i.e., Engineering Demand Parameters, EDPs) are extracted to analyse subsequently. The coefficient of determination (R2) is adopted as an estimation of the variability in the analysis of the IM-EDP trend. Consequently, IMs providing the highest R2 values are assumed as the most efficient ones. Results reveal that the simplified methodology based on R2 from each IM-EDP set of points is suitable for the identification of highly efficient IMs for the seismic assessment of masonry buildings.

Congress on Numerical Methods in Engineering 2024
4-6 September 2024, University of Aveiro, Portugal

Modelação numérica de painéis de fachada pré-fabricados em betão armado

Liana Ostetto*, Romain Sousa† Paulo Fernandes Hugo Rodrigues***

* RISCO, Departamento de Engenharia Civil, Universidade de Aveiro, Portugal
Email: lianaostetto@ua.pt, hrodrigues@ua.pt

† RISCO, VIGOBLOCO SA, Portugal
Email: romain.sousa@gmail.com

** CERIS, Departamento de Engenharia Civil, Politécnico de Leiria, Portugal
Email: paulo.fernandes@ipleiria.pt

RESUMO

Os recentes sismos em Itália e na Turquia expuseram as principais vulnerabilidades dos edifícios pré-fabricados em betão armado (BA) [1], [2], com destaque para os problemas críticos relacionados as ligações dos painéis de fachada, causando em muitos casos o colapso desses elementos. A prática atual de projeto para edifício industriais pré-fabricados em BA geralmente negligência a contribuição dos painéis, considerando que eles não contribuem para o comportamento sísmico do edifício [1], [3]. No entanto, diversos autores constataram que os painéis podem contribuir significativamente para a resposta sísmica do edifício [1], [4], [5]. Assim, atualmente existe um grande interesse em melhorar a forma de modelação da contribuição desses elementos. Dessa forma, o presente estudo apresenta uma estratégia de modelação numérica simplificada, adaptada para estruturas pré-fabricadas, com o objetivo de simular a contribuição do sistema de revestimento convencional, com painéis e ligações associadas, na influência global da estrutura. A calibração deste modelo numérico simplificado é realizada através de resultados experimentais, no qual foram ensaiadas ligações comummente utilizadas em Portugal.

REFERÊNCIAS

[1] N. Batalha, H. Rodrigues, and H. Varum, "Seismic performance of RC precast industrial buildings—learning with the past earthquakes," *Innov. Infrastruct. Solut.*, vol. 4, no. 1, pp. 1–13, 2019, doi: 10.1007/s41062-018-0191-y.

[2] E. Del Monte, C. Falsini, S. Boschi, G. Menichini, and M. Orlando, "An innovative cladding panel connection for RC precast buildings," *Bull. Earthq. Eng.*, vol. 17, no. 2, pp. 845–865, 2019, doi: 10.1007/s10518-018-0470-1.

[3] H. Rodrigues, R. Sousa, H. Vitorino, N. Batalha, H. Varum, and P. Fernandes, "Characterisation of Portuguese RC Precast Industrial Building Stock," *Adv. Civ. Eng.*, pp. 1–19, 2020, doi: 10.1155/2020/7517205.

[4] G. Toniolo and A. Colombo, "Precast concrete structures: The lessons learned from the L'Aquila earthquake," *Struct. Concr.*, vol. 13, no. 2, pp. 73–83, 2012, doi: 10.1002/suco.201100052.

[5] G. Magliulo, M. Ercolino, and G. Manfredi, "Influence of cladding panels on the first period of one-story precast buildings," *Bull. Earthq. Eng.*, vol. 13, no. 5, pp. 1531–1555, 2015, doi: 10.1007/s10518-014-9657-2.

Congress on Numerical Methods in Engineering 2024
4-6 September 2024, University of Aveiro, Portugal

Numerical modelling and validation of the experimentally tested beam-column joint specimens

P. Sabbahfar[1], J. Melo[2], H. Varum[2], H. Rodrigues[1]

[1] RISCO, Departamento de Engenharia Civil, Universidade de Aveiro, Portugal,

[2] CONSTRUCT, Faculty of Engineering - University of Porto, Portugal, Portugal

ABSTRACT

The reinforced concrete (RC) structures built before 1970 were primarily designed to solely withstand gravity loads and the application of plain bars as poor reinforcing detailing in these structures made them significantly vulnerable to cyclic loading conditions like seismic events. One of the most critical regions in RC structures that is highly prone to failure during earthquakes is the beam-column joint panel section which affects the overall behaviour of RC frames. Several experimental investigations have explored the behaviour of the beam-column joins, built with plain or deformed bars under cyclic loadings. The corresponding results achieved from the experimental campaigns provide an insight for seismic design and detailing of the existing non-seismically conforming RC structures that have proven to exhibit weak seismic performance due to factors such as poor bond-slip reinforcement properties, which causes the damage evolution and lack of ductility in these structural components. The experimental results provide the grounds for nonlinear numerical analysis and parametric validations of the tested beam-column joint specimens. In the present work, the numerical simulation is implemented by means of generating cyclic loading on the beam-column joint model and the corresponding results include force-displacement diagrams and dissipated energy evolution. The associated experimental and numerical results are compared for assuring both results are in good agreement with respect to each other.

Congress on Numerical Methods in Engineering 2024
4-6 September 2024, University of Aveiro, Portugal

Análise numérica comparativa da resistência ao fogo após um sismo de pórticos de betão armado 2D e 3D

Hugo Vitorino*, Paulo Vila Real†, Carlos Couto‡, Hugo Rodrigues§

* RISCO, Departamento de Engenharia Civil, Universidade de Aveiro, Portugal
Email: hugo.vitorino@ua.pt
† RISCO, Departamento de Engenharia Civil, Universidade de Aveiro, Portugal
Email: pvreal@ua.pt
‡ RISCO, Departamento de Engenharia Civil, Universidade de Aveiro, Portugal
Email: ccouto@ua.pt
§ RISCO, Departamento de Engenharia Civil, Universidade de Aveiro, Portugal
Email: hrodrigues@ua.pt

RESUMO

Foram desenvolvidas várias análises numéricas com o programa SAFIR para realizar um estudo comparativo da resistência ao fogo após um sismo de pórticos de betão armado 2D e 3D. Para isso, dimensionaram-se um total de cem pórticos com três vãos e dois pisos, e cem pórticos com três vãos e seis pisos, representativos de um parque edificado, sem prescrições sísmicas. Os pórticos 3D apresentam três vãos nas direções longitudinal e transversal. Considerou-se uma redução do recobrimento nos pilares e nas vigas na região da rótula plástica para simular os danos causados pelo sismo. No caso dos pórticos 2D, tanto o dano como o incêndio são considerados nos três compartimentos do piso inferior. Quanto aos pórticos 3D, os danos são considerados nos nove compartimentos do piso inferior, e o incêndio é considerado em três compartimentos contíguos, incluindo o compartimento central. Observou-se que o dano sísmico considerado nos pórticos resulta em menor resistência ao fogo, especialmente quando se considera um dano severo, traduzido pela remoção total do recobrimento das secções dos pórticos. Em relação à comparação entre os pórticos 2D e os respetivos pórticos 3D, constatou-se que os pórticos 2D apresentam uma menor resistência ao fogo que os pórticos 3D. O desenvolvimento deste estudo sugere que a utilização de modelos 2D pode representar uma abordagem mais conservadora na análise de cenários de incêndio após um sismo. Esta abordagem pode ser adequada para certos estudos relacionados aos efeitos do fogo em estruturas de betão armado após um sismo, quando comparada com modelos 3D mais complexos.

PALAVRAS-CHAVE: Dano sísmico, Resistência ao Fogo, Sismo-Pos-fogo, Betão Armado, Análises Numéricas

TS3: Computational approaches to complex fluid systems: multiphysics perspectives

This page intentionally left blank

Congress on Numerical Methods in Engineering 2024
4-6 September 2024, University of Aveiro, Portugal

Computational investigation of the flow and geometrical configuration of an intermediate temperature solid oxide fuel cell

João Paulo C. P. de Freitas, Ana Filipa Ferreira and Pedro J. Coelho*

* IDMEC, Mechanical Engineering Department, Instituto Superior Técnico, Universidade de Lisboa, 1049-001 Lisboa, Portugal
Email: pedro.coelho@tecnico.ulisboa.pt

ABSTRACT

Fuel cells are devices that convert directly chemical energy into electrical energy by means of electrochemical reactions. Although they were discovered almost two centuries ago, only in the last few decades they have been the subject of active research from the scientific community and interest from the industry. This is due to several advantages over other power sources, namely the low or zero emissions, high efficiency, versatility, reliability and scalability. Over the last two decades, numerical simulations have been used as a cost-effective way of studying configurations and working parameters of fuel cells. The numerical simulation of a fuel cell is a challenging task, due to the multiple physical phenomena taking place in different cell components. Among the most studied ones is the intermediate temperature solid oxide fuel cell. Intermediate temperature functioning (500-700ºC) is a recurring research theme among the solid oxide fuel cell scientific literature due to benefits such as faster start-up and shutdown times and reduced thermal stresses, leading to material cost savings and selection flexibility, along with longer lifetimes. Despite lower efficiencies, intermediate temperatures permit solid oxide types to be used in applications requiring more flexibility, such as in auxiliary automobile power units. To study the flow behaviour, computational fluid dynamics is employed in this work using the ANSYS Fluent unresolved electrolyte module. A structured mesh is built, the mesh independence is verified, and the model is validated using published data for the voltage as a function of the current density. Different geometrical and flow configurations are studied to investigate the effect on the maximum temperature and efficiency of the fuel cell. The temperature, species concentration and current density field allow to explain the reasons behind the observed macro changes and the overall performance of the fuel cell.

Congress on Numerical Methods in Engineering 2024
4-6 September 2024, University of Aveiro, Portugal

Numerical methods for the simulation of the interaction between incompressible fluids and structural models

Rafael Cantón-Sánchez[†], David Portillo[+] and Ignacio Romero[+]*

† ANSYS, Madrid, Spain
Email: rafael.canton@ansys.com

[+] Escuela Técnica Superior de Ingenieros Industriales, Universidad Politécnica de Madrid, Spain
Email: david.portillo@upm.es, ignacio.romero@upm.es

ABSTRACT

Modelling the interaction between a fluid and an embedded (slender) structure is complicated because the geometry of the structure is typically reduced, and one or more of its dimensions have been removed from its description. For example, beams and shells are one- and two-dimensional bodies, respectively, and it is difficult to detect their interactions with a true continuum — like a fluid — or to transfer loads between them.

In this talk, we will describe the theory and numerical methods of a class of Arbitrary Lagrangian-Eulerian (ALE) couplings between finite element discretisations of (stabilised) incompressible flows and nonlinear structural models. The key to this approach is that each structure is accompanied by a *dragged* solid that has no independent degrees of freedom [1, 2]. These slave bodies have kinematics that are exactly determined by the motion of the structure (displacements *and* rotations) but can interact with the fluid through the standard ALE equations. As a result, the thin and slender three-dimensional representations of the structures do not add any equation to the model while being able to represent very complex motions without any concerns about element distortion.

In the talk, we will present the theory behind this coupling, details on the numerical implementation and illustrative examples involving rods and shells with nonlinear kinematics and inelastic response.

REFERENCES

[1] R. Cantón-Sánchez and I. Romero (2021) *Dimensionally reduced nonlinear solids with general loads and constitutive laws: Theory and finite element formulation for rod-like bodies*. International Journal of Solids and Structures, 210-211:273–288.

[2] R. Cantón-Sánchez, D. Portillo, and I. Romero (2023) *Dimensionally reduced, nonlinear dragged solids: Theory and finite elements for rigid and shell-like bodies*. European Journal of Mechanics - A/Solids, 100:104980.

TS4: Machine and deep learning techniques applied to computational mechanics

This page intentionally left blank

Congress on Numerical Methods in Engineering 2024
4-6 September 2024, University of Aveiro, Portugal

Machine Learning for Bone Remodeling Analysis

Ana Pais*, Jorge Lino Alves* and Jorge Belinha†

* INEGI - Institute of Science and Innovation in Mechanical and Industrial Engineering, Porto, Portugal
Email: anapais@fe.up.pt, falves@fe.up.pt

† ISEP - School of Engineering, Polytechnic of Porto, Porto, Portugal
Email: job@isep.ipp.pt

ABSTRACT

Conventional numerical techniques such as the FEM or other numerical methods can be used to model complex phenomena such as bone remodelling but require intensive computational resources due to detailed discretizations to mimic the bone's trabecular structure and the iterative nature of these time-dependent biological processes.

However, with the introduction of machine learning and deep learning is showing promising results in the field of computational mechanics for their ability to provide the same results in a fraction of the time.

In this research, a neural network was trained using data from multiple finite element analyses, incorporating details about the bone's geometry and load conditions, which are important variables in the definition of the final density distribution. This network is capable of generating a density field based on this input.

The machine learning approach results in a density field that effectively mirrors the key features of FEM analysis outcomes but with significantly reduced analysis time [1] .

REFERENCES

[1] A. Pais, J. L. Alves, and J. Belinha, “Predicting trabecular arrangement in the proximal femur: An artificial neural network approach for varied geometries and load cases,” *J. Biomech.*, vol. 161, no. November, p. 111860, 2023, doi: 10.1016/j.jbiomech.2023.111860.

Congress on Numerical Methods in Engineering 2024
4-6 September 2024, University of Aveiro, Portugal

Unit cell design for stress shielding minimization using neural networks

Ana Pais*, Jorge Lino Alves* and Jorge Belinha†

* INEGI - Institute of Science and Innovation in Mechanical and Industrial Engineering, Porto, Portugal
Email: anapais@fe.up.pt, falves@fe.up.pt

† ISEP - School of Engineering, Polytechnic of Porto, Porto, Portugal
Email: job@isep.ipp.pt

ABSTRACT

A critical focus in the design of implants is reducing stress shielding. Bone regeneration is stimulated by stress within the bone; insufficient stress due to inadequate load transfer can result in bone deterioration and subsequent complications. In scaffold design, porous structures are frequently employed to enhance cell attachment and growth. Moreover, these porous designs allow for the adjustment of mechanical properties via topological optimization.

While the mechanical properties of a unit cell can be obtained from the homogenization procedure, the reverse task of obtaining a unit cell geometry which presents the desired mechanical properties requires some optimization approach.

One of the strengths of neural networks is their ability to perform intricate, non-linear mapping between input and output data. This work focuses on training a neural network to create the ideal unit cell structure leading to a specified elastic response. The neural network is designed to map the relationship between the unit cell's configuration and its elastic properties through a process akin to reverse homogenization.

Utilizing a diverse array of geometries to compile a dataset of elastic properties and their corresponding shapes, a feed-forward neural network was developed and trained using MATLAB's deep learning toolbox. This approach enables the neural network to accurately map the interplay between unit cell designs and their mechanical characteristics.

The results obtained showed that the network could suggest new geometries whose elastic properties match with acceptable error the desired properties.

Congress on Numerical Methods in Engineering 2024
4-6 September 2024, University of Aveiro, Portugal

Application of Graph Neural Networks to snap-through problems

Pedro Martins*, Beatriz Moya†, Francisco Chinesta‡ and Elías Cueto*

* ESI Group Chair. Aragon Institute in Engineering Research. Universidad de Zaragoza. María de Luna s/n, 50018 Zaragoza, Spain.
Email: {pmartins, ecueto}@unizar.es

† CNRS@CREATE, 1 Create Way, #08-01 Create Tower, Singapore 138602
Email: beatriz.moya@cnrsatcreate.sg

‡ ESI Group chair, PIMM Lab. Arts et Metiers Institute of Technology, 151 Boulevard de l'Hôpital, 75013, Paris, France.
Email: francisco.chinesta@ensam.eu

ABSTRACT

Graph Neural Networks (GNN) [1] have been applied to a multitude of scientific problems, including to structural mechanics problems. The standard deep learning approaches do not include the physics of the problem into consideration, which poses severe limitations regarding model reliability and result interpretation. To overcome these issues, the physics of the problem can be integrated into the problem modelling using several techniques. One of such techniques is to *inform* the neural network on the thermodynamics of the problem [2] using a bias approach.

In this work a GNN based method called Thermodynamics-Informed Graph Neural Networks (TIGNN) [3] will be applied to model the snap-through phenomenon on thin shells. This nonlinear phenomenon [4] was successfully captured using TIGNN, using a training database based on FEM simulations carried out with ABAQUS. Moreover, it was possible to successfully train the model using a reduced dataset which opens the possibility of quasi-real time model inference for simulation and industrial applications.

REFERENCES

[1] M. M. Bronstein, J. Bruna, T. Cohen, and P. Veličković, *Geometric Deep Learning: Grids, Groups, Graphs, Geodesics, and Gauges*, arXiv:2104.13478, (2021).
[2] Q. Hernandez, A. Badias, F. Chinesta and E. Cueto. "Thermodynamics-informed Graph Neural Networks", *IEEE Transactions on Artificial Intelligence*, (2022).
[3] Q. Hernandez, A. Badías, D. González, F. Chinesta and E. Cueto. "Deep learning of thermodynamics-aware reduced-order models from data", *Computer Methods in Applied Mechanics and Engineering*, 379, 113763 (2021).
[4] Z. Kuang et al., "Data-driven computational framework for snap-through problems", *International Journal of Solids and Structures*, (269) 11226, (2023).

Congress on Numerical Methods in Engineering 2024
4-6 September 2024, University of Aveiro, Portugal

CFD+AI control system for room climate

Jaume Luis-Gómez‡, Noemi Negoi‡, Óscar Prades-Mateu‡, Sergio Chiva‡, Francisco Martínez†, Javier Mascarós†, Elisa Borrás†, and Raúl Martínez-Cuenca‡,*

‡ Departamento de Ingeniería Mecánica y Construcción, Universitat Jaume I, Spain
Email: raul.martinez@uji.es
† Departamento de Mantenimiento, Oceanogràfic de València, Spain

ABSTRACT

The classical approach for the design and control of room climate relies on a very simple concept: the air changes per hour. This approach is appropriate for spaces that can be considered as perfectly mixed, but it might lead to dangerous situations in spaces with flow defects (dead volumes, short-circuits, etc) or with sources of certain gases (CO_2, H_2S,…) or humidity. These spaces require mode detailed tools for the description and forecasting of fluid flow in their volume.

In this work, we present a tool for the real-time forecasting and control of climate variables in the whole volume of the facility of interest. As in [1], this tool combines Computational Fluid Dynamics (CFD) simulations and Machine Learning to provide the real-time forecasting tool. First, CFD simulations serve to train a Neural Network (NN) that can forecast the climate conditions given the current climate conditions in the facility and any possible configuration of actuators (supply/extraction fans, dehumidifiers, etc). The CFD simulations included an advanced momentum source term approach [2] to provide an accurate description of the flow coming out from the supply grilles. Then, an optimization algorithm looks for the most appropriate configuration to accomplish with the climate requirements (CO2/H2O limits, humidity and temperature ranges, …). Finally, the optimal parameters are sent to the actuators while the climate conditions are tracked. As the NN can compute about one forecast per second, the climate control can be performed in real-time (the residence time is about one hour). The feasibility of the proposed tool was demonstrated in a sector of the Oceanogràfic park in València (the figure below shows a forecast of the flow within this space as provided by the NN).

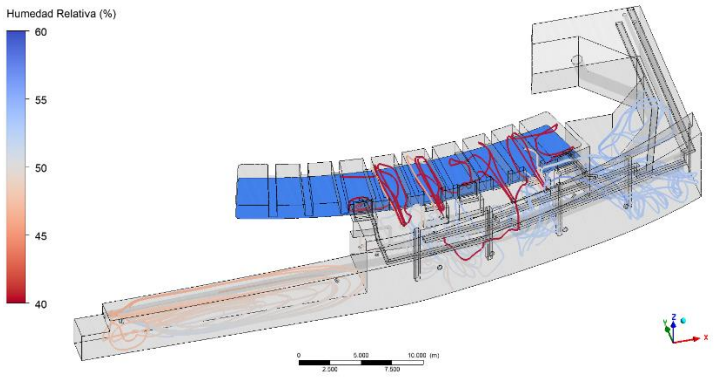

REFERENCES

[1] Iserte S., Macías A., Martínez-Cuenca R., Chiva S., Paredes R., and Quintana-Ortí E.S. Accelerating urban scale simulations leveraging local spatial 3D structure. Journal of Computational Science 62, 101741 (2022).

[2] Martínez-Cuenca R., Luis-Gómez J., Iserte S., and Chiva S. On the use of deep learning and computational fluid dynamics for the estimation of uniform momentum source components of propellers. iScience, 26 (12), 108297 (2023).

Congress on Numerical Methods in Engineering 2024
4-6 September 2024, University of Aveiro, Portugal

Implicit constitutive modelling using GRU-based RNNs and the virtual fields method

Rúben Lourenço*, Petia Georgieva† and A. Andrade-Campos*

* Department of Mechanical Engineering
TEMA - Centre for Mechanical Technology and Automation
LASI - Intelligent Systems Associate Laboratory, University of Aveiro
Aveiro, Portugal
Email: rubenl@ua.pt, gilac@ua.pt

† Dept. of Electronics, Telecommunications and Informatics
Institute of Telecommunications
Institute of Electronics and Informatics Engineering of Aveiro, University of Aveiro
Aveiro, Portugal
Email: petia@ua.pt

ABSTRACT

Constitutive models encode the stress-strain relationship of materials. Under plasticity the relationship is nonlinear and depends on the loading history. Artificial Neural Networks (ANNs) can learn these relationships directly from data without assuming a mathematical formulation. Particularly, Recurrent Neural Networks (RNNs) excel in capturing the effects of loading history for materials with path-dependent behaviour.

Implicit constitutive modelling approaches train ANNs using paired data, typically stress-strain, from numerically generated datasets. However, in real experiments, certain variables like stresses are not directly measurable, requiring indirect training using experimentally measurable variables only.

In this work, an RNN-based material model is trained using a novel indirect approach. The Virtual Fields Method (VFM) ensures local and global equilibrium conditions during the training process.

Aknowledgements

Rúben Lourenço acknowledges the Portuguese Foundation for Science and Technology (FCT) for the financial support (grant no. 2020.05279.BD), co-financed by the European Social Fund, through the Regional Operational Programme CENTRO 2020. This project has received funding from the Research Fund for Coal and Steel (grant agreement no. 888153). This project was also supported by the European Union NextGenerationEU, through the National Recovery and Resilience Plan of the Republic of Bulgaria (project no. BG-RRP-2.004-0005). This paper was also supported by the projects UIDB/00481/2020 - FCT (doi: 10.54499/UIDB/00481/2020), UIDP/00481/2020 - FCT (doi: 10.54499/UIDP/00481/2020), UIDB/50008/2020 - FCT (doi: 10.54499/UIDB/50008/2020) and UIDP/50008/2020 - FCT (doi: 10.54499/UIDP/50008/2020).

REFERENCES

[1] F. Pierron and M. Grédiac, *The Virtual Fields Method: Extracting Constitutive Mechanical Parameters from Full-field Deformation Measurements*, Springer, 2012.
[2] X. Liu et al, *Learning Nonlinear Constitutive Laws Using Neural Network Models Based on Indirectly Measurable Data*, J. Appl. Mech. Aug 87(2020) 1-8.

Congress on Numerical Methods in Engineering 2024
4-6 September 2024, University of Aveiro, Portugal

Machine Learning-Driven Approach to Contact Detection for Elliptical Shapes in $\mathbb{R}^2$

Olivier R. Gouveia[1,2], José M. Guedes[2] and Rui B. Ruben[1]

[1] CDRSP - Centre for Rapid and Sustainable Product Development, Polytechnic University of Leiria, Rua de Portugal – Zona Industrial 2430-028 – Marinha Grande, Portugal
{olivier.gouveia, rui.ruben}@ipleiria.pt

[2] IDMEC - Mechanical Engineering Institute, Instituto Superior Técnico, University of Lisbon, Av. Rovisco Pais, No.1, 1049-001, Lisbon, Portugal
jmguedes@tecnico.ulisboa.pt

ABSTRACT

Contact detection emerges as a critical bottleneck within the numerical treatment of contact problems, exerting considerable influence on speed and robustness of computational procedures [1]. As computational complexity and scale of contact problems continue growing, Machine Learning (ML) has emerged prominently in mitigating these challenges. In this evolving landscape, integrating ML into contact detection methodologies represents a forward-looking approach [2].

In this study, Artificial Neural Networks (ANN) are employed as supervised learning approach for ML-enabled contact detection. With applications in various computational fields, including granular mechanics, multibody dynamics, or accident reconstruction, elliptical shapes serve as primitive geometries of interest for this study. The ANNs process shapes' geometrical features and spatial features as input data, generating a contact flag and gap value as outputs. Tailored ANN architectures are employed based on the output type requested. For instance, a binary classification network was used for the contact query whereas a regression network was used for prediction of gap value. Random training data was generated to encompass various combinations of geometrical features generating a comprehensive range of possible contact scenarios. For optimal learning, training data was standardized by removing the mean and scaling to unit variance. The training set also included both gap values and contact statuses, serving as the ground truth for the ML models.

Predictions showed good agreement with the training and test sets, correctly predicting contact status of more than 97% of the test scenarios. Results showcased promise and potential for further application and refinement in terms of gap prediction.

REFERENCES

[1] Wang, X., Wu, W., Zhu, H., Lin, J.-S., Zhang, H. (2020). "Acceleration of contact detection between arbitrarily shaped polyhedra based on multi-cover methods in three-dimensional discontinuous deformation analysis" *Int J of Rock Mechanics and Mining Sciences*, 132, 104387.

[2] Lai, Z., Chen, Q., Huang, L. (2022) "Machine-learning-enabled discrete element method: Contact detection and resolution of irregular-shaped particles" *Int J Numer Anal Methods*, 46:113–140.

Evolutionary multi-objective optimisation of shoe sole damper geometry using surrogate models and data mining

P. Santos-Costa[1*], J. M. Nóbrega[2], C. P. Zanutto[1], M. J. Ferreira[3] and A. Gaspar-Cunha[1]

[1] Institute for Polymers and Composites, University of Minho, Guimarães, Portugal
Email: byic.mail@gmail.com, conradozanutto@dep.uminho.pt, agc@dep.uminho.pt.

[2] Department of Polymer Engineering, University of Minho, Guimarães, Portugal
Email: mnobrega@dep.uminho.pt

[3] Portuguese Footwear Research and Technology Centre, São João da Madeira, Portugal,
Email: mjose.ferreira@ctcp.pt

ABSTRACT

An important aspect to consider when designing a footwear sole is the comfort that will be provided to the user since the sole is the first interface between the floor and the person who uses it. The first issue is to evaluate the concept of comfort, which for this work is measured as the linearity of the relationship between force and displacement. The sole to be studied comprises a set of dampers with a specific geometry, which should be distributed throughout the sole, taking into consideration the force-displacement relation obtained.

This work aims to apply an optimization methodology to design comfortable shoe soles. The design variables are the set of geometrical parameters defining the damper's geometry together with the location of each damper on the foot. Simultaneously, the definition of comfort only can be quantified using multiple objectives since the linear relationship between the force applied and the displacement cannot be measured only by the minimization of the difference between the behaviour of the damper and the ideal linear behaviour because the damper behaviour is not linear. Therefore, the optimisation will be made using multi-objective evolutionary algorithms.

The calculation of the objectives will be made using a numerical modelling routine implemented in OpenFOAM computational library. However, due to the high computation times of a single case, a surrogate model using artificial neural networks was implemented to speed up the evaluation of solutions. Simultaneously, a data mining technique was used to identify the relevant decision variables and objectives [1]. The results obtained will be discussed and presented.

REFERENCES

[1] A. Gaspar-Cunha, P. Costa, F. Monaco, and A. Delbem, “Many-Objectives Optimization: A Machine Learning Approach for Reducing the Number of Objectives”, Mathematical and Computational Applications, vol. XXVIII, no. 1, p. 17 (2023), doi: 10.3390/mca28010017.

Congress on Numerical Methods in Engineering 2024
4-6 September 2024, University of Aveiro, Portugal

Artificial Intelligence Techniques in the Optimization of the Cooling Phase of Injection Moulding

T. Marques, J.B. Melo and A. Gaspar-Cunha

Institute for Polymers and Composites, University of Minho, Guimarães, Portugal
Email: pg50789@alunos.uminho.pt., pg50466@alunos.uminho.pt, agc@dep.uminho.pt.

ABSTRACT

The use of numerical modelling programs to study the injection moulding process enables the engineer to increase the speed of the development process and, simultaneously, allow the development of more efficient plastic parts, both concerning its functions and the use of less polymeric material.

However, given the large amount of data involved, which originated in the different phases of the process (plasticising, filling and cooling) and the high number of decision variables and objectives involved, more sophisticated data analysis is required since the interdependencies between decision variables and objectives and between the objectives are complex. Also, due to the computation time required by the numerical modelling routines surrogate models to replace the original evaluation of the objective function are necessary.

The objective of this work is to develop and implement data mining techniques and surrogate models based on Artificial Neural Networks (ANN) to deal with the data produced by a numerical modelling program of injection moulding, Moldex3D [1,2]. Different methodologies will be tested and the hyperparameters of the methods used will be assessed to select the best model to use.

This study was made from the point of view of the data mining and algorithm considered. The results obtained allow us to infer if the methods studied are adequate to solve the real-world problems under study, being able to capture the existing relationships between the data variables and the objectives. The results obtained show the relevance of the methodology proposed, allowing the selection of the relevant objectives to use and the optimisation of the process.

REFERENCES

[1] A. Gaspar-Cunha and A. Vieira, "A Multi-Objective Evolutionary Algorithm using Neural Networks to Approximate Fitness Evaluations," *Int. J. Comput. Syst. Signals*, 6, 18–36, (2005).

[2] A. Gaspar-Cunha, F. Monaco, J. Sikora, and A. Delbem, "Artificial intelligence in single screw polymer extrusion: Learning from computational data," *Eng. Appl. Artif. Intell.*, 116, 105397, (2022).

Congress on Numerical Methods in Engineering 2024
4-6 September 2024, University of Aveiro, Portugal

Designing conformal cooling channels for injection moulding using Moldex3D

J.B. Melo, T. Marques and A. Gaspar-Cunha†

Institute for Polymers and Composites, University of Minho, Guimarães, Portugal
Email: pg50466@alunos.uminho.pt, pg50789@alunos.uminho.pt, agc@dep.uminho.pt.

Email:

ABSTRACT

Given the complexity of some plastic parts produced by injection moulding special care must be applied when designing the moulds. If the correct design principles are not followed, defects that make the parts worthless can be obtained. Some common defects include, for example, short shot, flash, sink marks, warpage, weld lines and air traps. To avoid/minimize these defects various measures can be implemented, including optimizing process parameters, and using high-quality moulds. Proper mould design is a critical factor in reducing some of these defects.

The difficulty comes from the existing high number of design variables related to the different phases of the process, i.e., plasticising, filling, and cooling. Also, these variables are of different types: i) the operating conditions including temperatures and times; ii) the mould design, including filling channels, number of gates and cavity; and iii) the variables that depend on the machine used [1].

The objective of this work is to study the cooling phase using a numerical modelling software, Moldex3D, to get information about the influence of the design variables on the performance. Due to the complexity of the process, data mining was used to identify the relevant design variables and objectives and given the multi-objective nature of this optimization problem multi-objective evolutionary algorithms were adopted [2].

Due to the need for many runs of the modelling routine surrogate models based on the used artificial neural networks will be applied. The results obtained from the point of view of the process will show the usefulness of the methodology proposed.

REFERENCES

[1] A. Gaspar-Cunha, J.A. Covas, and J. Sikora, “Optimization of Polymer Processing: A Review (Part II-Molding Technologies),” *Materials*, 1–20, (2022).
[2] C. Fernandes, A. Pontes, J. Viana, and A. Gaspar-Cunha, “Using Multi-Objective Evolutionary Algorithms for Optimization of the Cooling System in Polymer Injection Moulding,” *Int. Polym. Process.*, 27, 213–223, (2012).

Congress on Numerical Methods in Engineering 2024
4-6 September 2024, University of Aveiro, Portugal

Integrating Numerical Models with Experimental Data for Structural Digital Twins

S.M.O. Tavares[*], J.A. Ribeiro[†], and J. Belinha[†,‡]

[*] TEMA, Departamento de Engenharia Mecânica, Universidade de Aveiro, Portugal
Email: smotavares@ua.pt

[†] FEUP, LAETA, INEGI - Institute of Science and Innovation in Mechanical and Industrial Engineering
Email: up201505717@edu.fe.up.pt

[‡] ISEP-School of Engineering, Polytechnic of Porto, job@isep.ipp.pt

ABSTRACT

Numerical simulation of structures plays a crucial role in structural design, enabling the evaluation of various phenomena and ensuring safety, even under complex loading conditions. Despite its strengths, this approach struggles to fully capture the intricacies of real-world structures. Factors such as material variations, manufacturing inconsistencies, and real-world stresses pose challenges to precise modelling. This research investigates digital twins as a solution, utilizing sensor data and machine learning to achieve a more accurate, life cycle understanding of structural behaviour. While applications in the aeronautics sector have been explored [1], this approach has potential in other sectors, such as energy.

Digital twins based on simulation models can combine external data with numerical data, as sensor readings and operational data, with information from numerical models to create a comprehensive model that can be developed with varying levels of fidelity. By combining this data with machine learning techniques like graphical neural networks (GNNs) [2], recurrent neural networks (RNNs), and physics-informed neural networks (PINNs), this research proposes new methods for updating and calibrating structural models using real-world data.

The integration of structural data with advanced updating techniques promises to revolutionize structural design and assessment. By providing valuable insights into a structure's health, safety, and reliability throughout its lifespan, digital twins can lead to more efficient and optimized structures. This includes defining operational envelopes regarding maximum loads or specific maintenance operations to reinforce the structure at critical points, thereby extending the structure's lifecycle.

REFERENCES

[1] S.M.O. Tavares, J.A. Ribeiro, B.A. Ribeiro, P.M.S.T. de Castro, “Aircraft Structural Design and Life-Cycle Assessment through Digital Twins”, *Designs*, 8(2), (2024).

[2] B.A. Ribeiro, J.A- Ribeiro, F. Ahmed, H. Penedones, J. Belinha, L. Sarmento, M.A. Bessa, S. Tavares, “SimuStruct: Simulated Structural Plate with Holes Dataset with Machine Learning Applications”. In Workshop on “Machine Learning for Materials”, The International Conference on Learning Representations (ICLR) (2023).

[3] F. Viana, M. Nabian, S. Choudhry, R. Mukund, P. Modi, R. Nascimento, Y. Yucesan, “Using hybrid physics-informed neural networks for digital twins in prognosis and health management.”, NVIDIA Developer Technical Blog, (2021).

TS5: Computational engineering empowered by model order reduction and machine learning

This page intentionally left blank

Congress on Numerical Methods in Engineering 2024
4-6 September 2024, University of Aveiro, Portugal

Thermodynamics informed Graph Neural Networks for domain dependent problems

Alicia Tierz*, Icíar Alfaro*, David González*, Francisco Chinesta†, Elías Cuerto*

* ESI Group Chair. Aragon Institute in Engineering Research (University of Zaragoza), María de Luna s/n, 50018 Zaragoza, Spain {atierz, iciar, gonzal, ecueto}@unizar.es

† ESI chair PIMM Lab Arts et Metiers Institute of Technology, 151 Boulevard d l Hôpital, 75013, Paris, France, francisco.chinesta@ensam.eu

ABSTRACT

Key Words: CFD, Geometric Deep Learning Learned simulators, Thermodynamics

In the context of modern industry, augmented reality (AR) has emerged as a promising technology that combines the physical world with virtual elements to enhance productivity and efficiency. One significant area of interest within the realm of physical scenario simulations is domain-dependent problems.

Currently, Computational Fluid Dynamics (CFD) tools offer users acc urate simulations, enabling companies to save substantial resources compared to traditional methods. However, a major drawback of this approach is the extensive CPU time required to run a single simulation. The computational cost increases significantly due to the complex physics underlying these models and the large mesh size necessary for analyzing the geometry. In an effort to reduce this high processing time, Deep Learning (DL) is being employed to address the issue, resulting in real time results with minimal loss of accuracy.

We present a DL approach for estimating different domain-dependent scenarios as a fluid sloshing in a glass or a viscoelastic beam. We propose utilizing both geometric and thermodynamic information to enhance the accuracy and generalization of the resulting integration scheme. To leverage the information provided by the Lagrangian description of movement we will apply graph neural networks (GNNs) [1] The use of geometric deep learning minimizes data consumption owing to the symmetries inherent in the problem.

The architecture is designed to learn the GENERIC (General Equation for Non-Equilibrium Reversible Irreversible Coupling) [2] structure of the problem, which is an extension of the Hamiltonian formalism used to model more general non conservative dynamics.

The employed architecture is based on Thermodynamics Informed graph neural networks [3]. A database is constructed using a CFD tool and utilized to train the graph-based architecture. The network is tested on various geometries, encompassing different filling volumes and vessel shapes containing the fluids.

REFERENCES

[1] Bronstein, M.M., Bruna J., LeCun, Y., Szlam A. and Vandergheynst, P. Geometric deep learning: going beyond euclidean data, IEEE Signal Processing Magazine (2017) 34(4): 18-42.
[2] Grmela, M. and Öttinger, H.C. Dynamics and thermodynamics of complex fluids. I. Development of a general formalism. Physical Review E, 56(6), p.6620, 1997.
[3] Hernández, Q., Badías, A., Chinesta, F., Cueto, E. (2022) (Thermodynamics informed graph neural networks. arXiv preprint arXiv:2203.01874.

Congress on Numerical Methods in Engineering 2024
4-6 September 2024, University of Aveiro, Portugal

Physics-based training-set enrichment for the POD formulation of the incompressible Navier-Stokes equations

Alba Muixí[1,*], Sergio Zlotnik[1,2], Matteo Giacomini[1,2] and Pedro Díez[1,2]

[1] Laboratori de Càlcul Numèric (LaCàN), Universitat Politècnica de Catalunya, Barcelona, Spain
*Email: alba.muixi@upc.edu

[2] International Center for Numerical Methods in Engineering (CIMNE), Barcelona, Spain

ABSTRACT

A posteriori reduced-order models, such as the proper orthogonal decomposition, play a crucial role in efficiently addressing realistic parametric problems. They rely on a training set, a family of full-order solutions (snapshots), representative of all possible outcomes of the parametric problem. Unfortunately, obtaining such a comprehensive collection of snapshots is often computationally unfeasible. To overcome this limitation, we propose a physics-based data augmentation strategy, particularly tailored for underpopulated training sets of the incompressible Navier-Stokes equations. The objective is to incorporate into the formulation features of the parametric family of solutions that were absent in the original basis, extending some of the ideas developed in [1]. The training set is enriched with artificial snapshots generated from the original ones. In this process, we exploit the incompressibility of the solutions and consider the linearised momentum balance through the solution of the Oseen equation. The strategy is tested for laminar flows in the steady-state regime. In the examples considered, this approach significantly enhances the resulting approximation, establishing itself as an effective data augmentation strategy within this framework.

REFERENCES

[1] P. Díez, A. Muixí, S. Zlotnik and A. García-González. “Nonlinear dimensionality reduction for parametric problems: a kernel Proper Orthogonal Decomposition (kPOD)”, *Int. J. Num. Meth. Engng*, 122(24), 7306-7327 (2021).

Congress on Numerical Methods in Engineering 2024
4-6 September 2024, University of Aveiro, Portugal

Thermodynamics-informed Graph Neural Networks for Flow Estimation around Arbitrary Geometries

Carlos Bermejo-Barbanoj*[,1], Alberto Badías[2], David González[1], Francisco Chinesta[3,4] and Elías Cueto[1]

[1]ESI Chair. Aragon Institute in Engineering Research (I3A)
University of Zaragoza, María de Luna s/n, 50018, Zaragoza, Spain
Email: {cbbarbanoj, gonzal, ecueto}@unizar.es

[2] School of Aeronautical and Space Engineering (ETSIAE)
Universidad Politécnica de Madrid, Pl. del Cardenal Cisneros 3, E-28040, Madrid, Spain
Email: alberto.badias@upm.es

[3] CNRS@CREATE,
1 Create Way, #08-01 Create Tower, Singapore 138602

[4] ESI Chair. PIMM Lab Arts et Métiers Institute of Technology
École Nationale Supérieure d'Arts et Métiers, 151 Boulevard de l'Hôpital, 75013, Paris, France
Email: francisco.chinesta@ensam.eu

ABSTRACT

Although computational techniques like Computational Fluid Dynamics (CFD) provide us with very accurate solutions for complex fluid mechanics simulations, they face some limitations, particularly regarding the computational cost. Traditionally, Reduced Order Models (ROM) techniques have been used to overcome this drawback, providing fast results with little accuracy loss. Nowadays, Deep Learning (DL) based models have shown their effectiveness in this field, leading to almost real-time predictions.

We propose a DL approach to estimate the dynamical evolution of a flow around two dimensional geometries, predicting the most relevant fields: velocity and pressure. To enhance solution accuracy and promote generalization, we introduce geometric and thermodynamic biases. The geometric bias is applied by using graph neural networks (GNNs) [1], while the thermodynamical bias identifies and learns the GENERIC (General Equation for Non-Equilibrium Reversible-Irreversible Coupling) [2] structure, an extension of the Hamiltonian formalism to model non-conservative systems. The combination of both biases leads to less data consumption and thermodynamically-consistent predictions. The employed architecture is based on Thermodynamics-Informed Graph Neural Networks (TIGNNs) [3]. The method is tested with different geometries and Reynolds numbers and is compared with another method that combines the use of an Autoencoder and a Structure Preserving Neural Network (SPNN) [4] to obtain a ROM that predicts the flow evolution.

REFERENCES

[1] Bronstein, M.M., Bruna , J., LeCun, Y., Szlam, A. and Vandergheynst, P. Geometric deep learning: going beyond euclidean data, *IEEE Signal Processing Magazine* 34(4): 18-42, 2017

[2] Grmela, M. and Öttinger, H.C. Dynamics and thermodynamics of complex fluids. I. Development of a general formalism. Physical Review E, 56(6), p.6620, 1997.

[3] Hernández, Q., Badías, A., Chinesta, F. and Cueto, E. Thermodynamics-informed Graph Neural Networks, *IEEE Transactions on Artificial Intelligence*, doi: 10.1109/TAI.2022.3179681, 2022

[4] Hernández, Q., Badías, A., González, D., Chinesta, F., Cueto, E. Structure-preserving neural networks. Journal of Computational Physics, vol. 426, p. 109950, 2021.

Congress on Numerical Methods in Engineering 2024
4-6 September 2024, University of Aveiro, Portugal

Recent advances in Thermodynamics-informed Graph Neural Networks

Carlos Bermejo-Barbanoj*, Alicia Tierz*, Mikel Martínez*, Pedro Martins*, Pau Urdeitx*, David González*, Francisco Chinesta†, Elías Cueto*

* ESI Group Chair. Aragon Institute in Engineering Research. Universidad de Zaragoza. María de Luna s/n, 50018 Zaragoza, Spain.
{cbbarbanoj, atierz, mikel.martinez, pmartins, purdeitx, gonzal, ecueto}@unizar.es

† ESI Group chair, PIMM Lab. Arts et Metiers Institute of Technology, 151 Boulevard de l'Hôpital, 75013, Paris, France.
francisco.chinesta@ensam.eu

ABSTRACT

Key Words: Geometric Deep Learning, learned simulators, Thermodynamics, structure-preserving neural networks.

We review some of the most recent advances in the employ of thermodynamics-informed graph neural networks for world modeling. By world modeling we mean the development of internal models of how (in general, portions) of the world work. To this end, the thus developed AI modules must be able to perceive, reason and plan about the physical phenomena occurring around them.

Our approach to this problem includes the enforcement of the laws of thermodynamics, in the absence of any other information, so as to ensure at least the fulfillment of the first and second principles (conservation of energy, non-negative entropy production).

Another challenging problem is that of self-supervised constructing (or, at least, adapting) models for objects whose geometry has not been seen before. To this end, we employ extensively graph-neural networks.

REFERENCES

[1] Grmela, M. and Öttinger, H.C. Dynamics and thermodynamics of complex fluids. I. Development of a general formalism. Physical Review E, 56(6), p.6620, 1997.
[2] Hernández, Q., Badías, A., Chinesta, F., Cueto, E. (2022) Thermodynamics informed graph neural networks. arXiv preprint arXiv:2203.01874.

Congress on Numerical Methods in Engineering 2024
4-6 September 2024, University of Aveiro, Portugal

Graph neural networks for geometric design of structures in plastic regime

Mikel Martinez*, Francisco Chinesta† and Elías Cueto*

* ESI Group Chair. Aragon Institute in Engineering Research. Universidad de Zaragoza, Maria de Luna s/n, 50018 Zaragoza, Spain
Email:{mikel.martinez, ecueto}@unizar.es
† ESI Group chair, PIMM Lab. Arts et Métiers Institute of Technology, 151 Boulevard de l'Hôpital, 75013, Paris, France.
Email: francisco.chinesta@ensam.eu

ABSTRACT

While most of the research concerning data-driven modelling of plasticity deals with the development of constitutive models[1], in this work we assume that the behaviour of the material is known. The main goal of this work is to provide the analyst with an efficient tool for the design and analysis of structures undergoing plastic strains under stringent real-time constraints.

This model employs Graph Neural Networks (GNNs)[2], effectively leveraging synthetic data generated from Finite Element Method (FEM) simulations to understand complex relationships[3]. This showcases the generalisation and robustness of our approach.

This research is motivated by the need to cut down computational costs, a crucial goal compared to the current reliance on Finite Element Method (FEM) approaches. Traditional methods, which are solely based on models, don't consider any previous knowledge in each simulation. By incorporating prior knowledge through data-driven approaches, our research speeds up predictions significantly. This can potentially boost the process design when working with plastic materials.

The parameters, such as height and length of the specimen, were fine-tuned to delineate various geometries. Subsequently, the model was tested on unseen geometries, encompassing both those within the parameter range used during training (interpolation) and those outside the range (extrapolation). The outcomes demonstrated robustness and generalisation in both scenarios.

REFERENCES

[1] Weber, P., Wagner, W. & Freitag, S. Physically enhanced training for modeling rate-independent plasticity with feedforward neural networks. *Comput Mech* **72**, 827–857 (2023). https://doi.org/10.1007/s00466-023-02316-9.

[2] Bronstein, M.M., Bruna J., Lecun, Y. Szalam A. and Vandergheynst, P. Geometric deep learning: going beyond eucliedean data, IEEE Signal Processing Magazine (2017) 34(4): 18-42.

[3] Pfaff, T., Fortunato, M., Sanchez-Gonzalez, A., & Battaglia, P. W. (2020). Learning mesh-based simulation with graph networks. *arXiv preprint arXiv:2010.03409*.

Congress on Numerical Methods in Engineering 2024
4-6 September 2024, University of Aveiro, Portugal

Preconditiong iterative solvers via reduced-order modelling for the simulation of lattice structures

R.Rubio* [1,2], A.Ferrer[1,2] and J.A.Hernandez[1,2]

[1] E.S. d'Enginyeries Industrial, Aeroespacial i Audiovisual de Terrassa, Technical University of Catalonia, C/ Colom, 11, Terrassa 08222, Spain

[2] Centre Internacional de Mètodes Numèrics en Enginyeria (CIMNE), Edifici C1, Campus Nord UPC, C/ Gran Capità, S/N 08034 Barcelona, Spain

e-mail*: raul.rubio.serrano@upc.edu

ABSTRACT

Lattice structures, present in the aerospace, automotive, or chemical industries, pose computational challenges in Finite Element Method (FEM) simulations, especially for large-scale systems. Such large-scale systems exploit the weaknesses of direct solvers, namely its high memory usage and time requirements. Consequently, a shift towards the adoption of iterative solvers and preconditioning techniques becomes indispensable in addressing these challenges.

Reduced Order Models (ROMs) offer faster solutions but come with an accuracy trade-off compared to FEM. This paper explores the use of the ROM called Empirical Interscale Finite Element Method (EIFEM) [1] as a preconditioner in a deflation strategy for the conjugate gradient method. We show some numerical examples and compare the results with the Finite Element Tearing and Interconnect (FETI) method combined with ROM techniques.

REFERENCES

[1] J.A. Hernández, A. Giuliodori, E. Soudah, Empirical Interscale Finite Element Method (EIFEM) for modeling heterogeneous structures via localized hyperreduction, Computer Methods in Applied Mechanics and Engineering, Volume 418, Part A, 2024, https://doi.org/10.1016/j.cma.2023.116492.

Congress on Numerical Methods in Engineering 2024
4-6 September 2024, University of Aveiro, Portugal

Accuracy assessment of a Reduced Order Model for the evaluation of collapse risk in metastatic vertebrae

B. Gandía-Vañó[*], F.X. García-Andres[*], E. Arana[†], E. Nadal[*], J.M. Navarro-Jiménez and J.J. Ródenas[*]

[*]Institute of Mechanical and Biomechanical Engineering (I2MB), Universitat Politècnica de València (UPV), 46022-Valencia, Spain
Email: blganva@etsid.upv.es, xagaran@upv.es, ennaso@upvnet.upv.es, jonaji@upv.es jjrodena@mcm.upv.es

[†] Dpto. Radiología. Fundación Instituto Valenciano de Oncología, 46009-Valencia, Spain.
Email: estanis.erana@uv.es

ABSTRACT

Around 40% of patients with breast or prostate cancer will develop a vertebral metastasis[1] (up to 70% in advance stages of the cancer[2]). The structural metastasis will, in some cases produce the vertebral collapse that will probably result in spinal cord lesions. This paper is part of a project that aims to develop a methodology, compatible with clinical practice, to predict the risk of this vertebral collapse.

As part of the project, we developed a methodology based on the use of the Cartesian grid Finite Element Method (cgFEM) to automatically create patient-specific FEM models from 3D medical images (computed tomography – CT scans) [3]. Then we used it to create a reduced order model (ROM) of a vertebra that allows us to predict the structural behaviour of the vertebra for any spherical tumour, of any density, placed at any point of the main body of the vertebra. In the on-line phase, this ROM is helpful for clinicians as it can instantaneously evaluate many tumour-grow scenarios. The offline phase must also be compatible with clinical practice as a ROM must be created for each vertebra and patient. In this contribution we describe a simple methodology to assess the accuracy of the ROM on the fly. This allows us to easily control the number of samples considered in the offline phase. As a result, we can create sufficiently accurate ROMs in a reduced offline time, fully compatible with clinical practice.

Acknowledgements: The authors gratefully acknowledge the financial support of the, and Universitat Politècnica de València (PAID-01-22), Generalitat Valenciana (Prometeo/2021/046) and Ministry of Science and Innovation/AEI/10.13039/501100011033/FEDER, UE (project PID2022-141512NB-I00)

REFERENCES

[1] *Las Cifras del Cáncer en España 2023.* (n.d.). Retrieved 1 10, 2024, from Sociedad Española de Oncología Médica: https://seom.org/images/Las_cifras_del_Cancer_en_Espana_2023.pdf

[2] M Eleraky, I Papanastassiou, FD Vrionis. *Management of metastatic spine disease*. Current opinion in supportive and palliative care, 182-183(2010).

[3] E Nadal, JJ Ródenas, J Albelda, M Tur. *Efficient Finite Element Methodology Based on Cartesian Grids: Application to Structural Shape Optimization*. Abstract and Applied Analysis. (2013)

Congress on Numerical Methods in Engineering 2024
4-6 September 2024, University of Aveiro, Portugal

Surrogate Models of Geometrically Parameterized Flow Systems

Matteo Giacomini[1,2], Álvaro Borrás[1,2] and Antonio Huerta[1,2,*]

[1] Laboratori de Càlcul Numèric (LaCàN), E.T.S. de Ingeniería de Caminos, Canales y Puertos, Universitat Politècnica de Catalunya, Barcelona, Spain.

[2] Centre Internacional de Mètodes Numèrics en Enginyeria (CIMNE), Barcelona, Spain.
Email: {matteo.giacomini, antonio.huerta}@upc.edu

ABSTRACT

Simulating complex flow systems with parameterized geometries in order to determine critical quantities of interest (QoI) is often prohibitively expensive due to the high dimensionality of the problem. This challenge becomes further inescapable in optimization loops where multi-querying is essential to the scheme. Additionally, simplified models usually lack the accuracy needed by physicists and engineers to provide reliable QoI estimates. This computational bottleneck poses a significant challenge for the effective conception, design, and operation of industrial systems, especially when geometric parameters are involved.

After providing a brief overview of Reduced Order Model (ROM) strategies (both *a priori* and *a posteriori*) for geometrically parametrized incompressible flows [1], optimal strokes for the push-me-pull-you (PMPY) model of a micro-swimmer are determined. Specifically, identify the cyclic parameter trajectory, which produces a given displacement of the micro-swimmer while minimizing the average power expended by it. This is done using the non-intrusive Encapsulated Proper Generalized Decomposition (PGD) to calculate separated expressions of forces and velocity that explicitly depend on the design parameters [2].

REFERENCES

[1] M. Giacomini, L. Borchini, R. Sevilla, A. Huerta, "Separated response surfaces for flows in parametrised domains: comparison of a priori and a posteriori PGD algorithms," *Finite Elements in Analysis and Design*, 196, 103530 (2021).

[2] P. Díez, S. Zlotnik, A. García-González, A. Huerta, "Encapsulated PGD Algebraic Toolbox Operating with High-Dimensional Data," *Archives of Computational Methods in Engineering*, 27(5), 1321-1336 (2020).

Congress on Numerical Methods in Engineering 2024
4-6 September 2024, University of Aveiro, Portugal

Accelerating the 2-level Topology Optimization strategy by means of a data-driven initialization strategy

A. Martínez-Martínez[1]*, O. Allix[2], F. Chinesta[3], J.J. Ródenas[1], E. Nadal[1]

[1] I2MB- Universitat Politècnica de València, Valencia, Spain. Email: {anmar29a, jjrodena, ennaso}@upv.es
[2] Université Paris-Saclay, ENS Paris-Saclay, CentraleSupélec, CNRS, LMPS. Gif-sur-Yvette, Francia. Email: olivier.allix@ens-paris-saclay.fr
[3] Laboratoire PIMM - ENS Arts et Métiers. Paris, France. Email: francisco.chinesta@ensam.eu

ABSTRACT

Automatic design tools are commonly used in the context of engineering design. Among them we can highlight the structural topology optimization (TO) , which optimizes the material distribution within specified constraints. Traditional methods, such as the SIMP method, encounter challenges in achieving high resolution structures due to strong correlations between geometric features and discretization resolution, leading to computationally intensive processes. As a result, various multi-scale techniques have emerged to reduce computational time [1]. Notably, the 2-Level TO technique proposed by [2] involves solving topological optimization in coarse discretization and subsequently addressing fine-level TO problems in each cell, preserving structural continuity between them. However, in our increasingly demanding industrial environments, and even in certain medical applications, there is a need to further reduce computational costs.

Machine learning (ML) strategies, including the one-shot approach [3], have effectively accelerated TO processes. However, these methods often encounter issues related to structural coherence, necessitating additional SIMP iterations for resolution. In response to these challenges, we introduce a data-driven framework that leverages a one-shot prediction approach within the context of 2-Level TO. Our study focuses on the critical role of defining a distance in the parameter space to minimize additional SIMP iterations. This metric serves as the foundation for defining various surrogate models and dataset creation strategies, aiming to enhance the efficiency and effectiveness of structural topology optimization

ACKNOWLEDGEMENTS

The authors gratefully acknowledge the financial support of the Ministry of Universities (FPU19 /02103), Generalitat Valenciana (Prometeo/2021/046) and Ministry of Science and Innovation/AEI/10.13039/501100011033/FEDER, UE (project PID2022-141512NB-I00)

REFERENCES

[1] [1] Ferrer, A., Oliver, J., Cante, J. C., & Lloberas-Valls, O. (2016). Vademecum-based approach to multi-scale topological material design. Advanced modeling and simulation in engineering sciences, 3, 1-22.
[2] Merli, R., Martínez-Martínez, A., Ródenas, J. J., Bosch-Galera, M., & Nadal, E. (2023). Two-level Continuous Topology Optimization in Structural Mechanics. arXiv preprint arXiv:2307.15665.
[3] Cang, R., Yao, H., & Ren, Y. (2019). One-shot generation of near-optimal topology through theory-driven machine learning. Computer-Aided Design, 109, 12-21.

Congress on Numerical Methods in Engineering 2024
4-6 September 2024, University of Aveiro, Portugal

ACBICI – A Library for the Calibration of Complex and Expensive Models

C. Schenk* and I. Romero†

* IMDEA Materials Institute, Getafe, Spain
Email: christina.schenk@imdea.org

† Universidad Politécnica de Madrid, Madrid, Spain
IMDEA Materials Institute, Getafe, Spain
Email: ignacio.romero@upm.es

ABSTRACT

Against the backdrop of continually advancing hardware capabilities, the integration of intricate and computationally expensive models, coupled with the challenges of experimental data collection, all within uncertain environments, can lead to significant expenses. Recognizing this, predictive modeling emerges as a crucial tool for conserving both time and resources in engineering applications. This is particularly relevant in industries that substantially contribute to global carbon emissions, such as steel production, responsible for approximately 20 to 25% of industrial CO2 emissions [1].

Addressing these challenges, Kennedy and O'Hagan [2] introduced a Bayesian-based approach using Gaussian processes (GP) to calibrate hybrid models under uncertainty and predict with accurate uncertainty estimates. This approach allows us to estimate the hyperparameters, model parameters, as well as underlying discrepancy and measurement errors. The versatility of this approach is particularly evident when dealing with complex models or situations with limited experimental data. The resulting novel GP-based surrogate model, created through this approach, serves as an efficient candidate for making rapid predictions. This presentation aims to showcase our novel Python library, which leverages the Bayesian-based approach introduced by Kennedy and O'Hagan, emphasizing its new features.

Furthermore, our discussion will be enriched with real-world case studies, such as the prediction of steel creep behavior or the evolution of glioblastoma cell cultures, illustrating the practical application of our methodology.

REFERENCES

[1] Clean Steel Partnership, Strategic Research and Innovation Agenda (SRIA) 2021
[2] Kennedy, M.; O'Hagan, A. Bayesian calibration of computer models. Journal of the Royal Statistical Society: Series B (Statistical Methodology), 2001, 63, 425–464.

TS6: Steel and composite structures

This page intentionally left blank

Congress on Numerical Methods in Engineering 2024
4-6 September 2024, University of Aveiro, Portugal

Evaluation of the available design codes for the sectional capacity of CFST columns considering different geometries, materials, and sectional slenderness

David Hernandez Figueirido[*,1], Vicente Albero Gabarda, Antoni Melchor Eixea, Marta Roig Flores, Ana Piquer Vicent

* Universitat Jaume I, Spain
Email: hernandd@uji.es

ABSTRACT

This study evaluates the predictive ability of different current codes to predict the sectional resistance of Concrete-Filled Steel Tubular (CFST) columns. For this, the different existing codes are briefly summarized, as well as their application ranges, in terms of materials and limits to avoid local buckling. Next, a database of experimental tests on stub columns of circular, rectangular, square and oval-elliptical section is compiled. In the experimental database there are specimens whose characteristics exceed the limits of the codes in terms of material resistance, local buckling or even in geometry. The results were analysed to see the accuracy of the models and the possibility of proposing extensions in the application ranges of the regulations. The conclusions provide valuable information for designers and researchers to assess which standard is more accurate for a certain range of characteristics of CFST columns.

Congress on Numerical Methods in Engineering 2024
4-6 September 2024, University of Aveiro, Portugal

Evaluation of stress-strain fiber models for predicting the sectional capacity of Circular CFST columns.

David Hernandez Figueirido[*,1], Vicente Albero Gabarda, Antoni Melchor Eixea, Marta Roig Flores, Ana Piquer Vicent

* Universitat Jaume I, Spain
Email: hernandd@uji.es

ABSTRACT

This research paper presents a comprehensive examination of various stress-strain fiber models applied to the sectional capacity of Circular Concrete-Filled Steel Tubular (CFST) columns. The precision of these models is corroborated through an extensive experimental database, encompassing over seven hundred columns, inclusive of noncompact and slender sections as well as high-strength materials, all of which have been meticulously compiled from existing literature. A succinct review of the fiber models considered for CFST is provided. The findings indicate that the fiber models offer a reasonable simulation of the axial compression response of CFST. An additional analysis was undertaken to ascertain the highest accuracy for each range of sectional slenderness and material resistance. The insights gleaned from this study will serve as a valuable resource for designers and researchers, enabling them to choose the most suitable modelling approaches for the design and analysis of CFST.

Congress on Numerical Methods in Engineering 2024
4-6 September 2024, University of Aveiro, Portugal

Numerical assessment of welded beam-to-column steel joints

Fernando Freire[1,*], Filip Ljubinković[1], Jorge Conde[2], Martin Vild[3] and Luís Simões da Silva[1]

[1]University of Coimbra, ISISE, ARISE, Department of Civil Engineering, Portugal.
Email: fribeiro@uc.pt, filj@uc.pt, luisss@dec.uc.pt

[2]Universidad Politécnica de Madrid, Departamento de Física y Estructuras de Edificación
Av. Juan de Herrera, 4, 28040 Madrid, Spain. ORCID: 0000-0002-5633-1170
Email: jorge.conde@upm.es

[3]Brno University of Technology, Faculty of Civil Engineering, Institute of Metal and Timber Structures, Veveri 95, 602 00, Brno, Czech Republic. ORCID: 0000-0002-2327-3162
Email: martin.vild@vutbr.cz

ABSTRACT

The Finite Element Method (FEM) is a powerful and well-consolidated numerical approach for evaluating the mechanical behaviour of structures, as long as the numerical models are properly validated against experimental tests. Welded beam-to-column joints are usually critical components in steel buildings, playing an important role in the overall integrity and stability of the structure. In Europe, the design of such joints is done following Eurocode 3 part 1-8, based upon the so-called Component Method. This paper presents a comprehensive assessment of the accuracy of design formulations in European standards for welded beam-to-column steel joints, in which the columns are welded sections. To reach this aim, a sophisticated 3-D finite element model is developed and validated with experimental tests available in the literature. Subsequently, an extensive parametric study is conducted covering different web panel slenderness, aspect ratios, joint configurations and loading conditions. The comparison of results reveals that the formulations for the initial stiffness and moment resistance in the current and forthcoming Eurocode 3 part 1-8 present a high scatter, with specific cases on the unconservative side.

Congress on Numerical Methods in Engineering 2024
4-6 September 2024, University of Aveiro, Portugal

Numerical assessment and component characterization of endplates in steel splices

Fernando Freire[1,*], Jorge Conde[2] and Luís Simões da Silva[1]

[1]University of Coimbra, ISISE, ARISE, Department of Civil Engineering, Portugal.
Email: fribeiro@uc.pt, luisss@dec.uc.pt

[2]Universidad Politécnica de Madrid, Departamento de Física y Estructuras de Edificación
Av. Juan de Herrera, 4, 28040 Madrid, Spain. ORCID: 0000-0002-5633-1170
Email: jorge.conde@upm.es

ABSTRACT

Bolted connections featuring endplates are frequently used in steel buildings as beam splices. Despite its simple geometry, this type of connection exhibits a rather complex behaviour, depending on several parameters such as bolt spacing/diameter, weld size and endplate thickness. Based on the component method, the Eurocode 3 part 1-8 provides design expressions for these joints. The main objective of this paper is to assess the Eurocode 3 formulation for endplate beam splices using a properly validated high-quality nonlinear finite element model. A comprehensive parametric study is performed including flush and extended endplates with several bolt rows subjected to bending moment. The results are evaluated based on moment-rotation curves, with focus on the main structural parameters, i.e., initial stiffness, resistance, and rotation capacity. A statistical assessment of the Eurocode expressions is performed, and relevant conclusions are offered.

Congress on Numerical Methods in Engineering 2024
4-6 September 2024, University of Aveiro, Portugal

INVESTIGAÇÃO DE VIGAS ALVEOLARES EM CONDIÇÕES DE INCÊNDIO

Luana V. Silva[1,2], Mychel Sandri[1], Nickolas Giacomitti[1,2] e Luís M. R. Mesquita[2]

1: Instituto Politécnico de Bragança
Campus Santa Apolónia, 5300-253 Bragança, Portugal
e-mail: luana.silva@ipb.pt, a46686@alunos.ipb.pt, nickolas.giacomitti@gmail.com

2: Grupo de Investigação em Construção Sustentável (GICoS)
Instituto Politécnico de Bragança
Campus Santa Apolónia, 5300-253 Bragança, Portugal
e-mail: lmesquita@ipb.pt

Palavras-chave: Vigas Alveolares de Aço, Resistência ao Fogo, Desempenho Estrutural, Ensaios experimentais; Simulações numéricas.

Resumo. *Vigas de aço alveolares são amplamente utilizadas na indústria da construção. Suas aberturas circulares na alma permitem a integração de serviços e oferecem uma solução eficaz para estruturas de grande vão. O processo de fabricação requer duas passagens de corte térmico de uma viga seção-I sólida, originando uma viga alveolar maior que sua seção original. Essas aberturas presentes nas vigas alveolares causam modos de falha local, como a encurvadura do montante da alma e o mecanismo de Vierendeel. A encurvadura do montante da alma envolve deslocamentos laterais no montante da alma com deformações de torção, enquanto o mecanismo de Vierendeel é causado pelo desenvolvimento de quatro rótulas plásticas nas seções Tê inferior e superior. A estrutura desse tipo de viga geralmente fica exposta e desprotegida, o que a torna mais vulnerável em situações de incêndio. A degradação do aço em contato com o fogo reduz sua resistência e capacidade de suporte de carga. Embora o comportamento desse tipo de viga mereça atenção devido à influência das aberturas da alma em seus modos de falha, não se dispõe de orientações para tais vigas quando sujeitas a temperaturas elevadas. Portanto, considerando a importância da verificação de segurança, este estudo analisa experimentalmente e numericamente vigas alveolares em temperaturas ambiente e elevadas. Os resultados de testes experimentais de flexão em quatro vigas alveolares com uma das extremidades encastradas são demonstrados. Não-linearidades materiais e geométricas foram consideradas no modelo de elementos finitos desenvolvido, o qual é validado com sucesso pela consistência entre os resultados numéricos e experimentais. Um estudo paramétrico com o modelo numérico é apresentado para expandir o conhecimento sobre a viga alveolar em condições de incêndio. O estudo analisa como os parâmetros geométricos da viga alveolar afetam sua resistência e as cargas de falha em diferentes condições de temperatura. Os principais modos de falha observados foram o mecanismo de Vierendeel e a encurvadura do montante da alma.*

Congress on Numerical Methods in Engineering 2024
4-6 September 2024, University of Aveiro, Portugal

Análise comparativa de critérios de colapso de estruturas porticadas em aço carbono e inoxidável em situação de incêndio

Nuno Lopes*†, João Cabral† e Paulo Vila Real†

† RISCO, Departamento de Engenharia Civil, Universidade de Aveiro, Portugal
Email: nuno.lopes@ua.pt

RESUMO

O aço inoxidável possui propriedades mecânicas a altas temperaturas superiores às do aço carbono convencional. Este melhor comportamento pode conduzir a estruturas sem necessidade de proteção ao fogo, tornando o aço inoxidável mais competitivo para uma mais ampla gama de aplicações estruturais. Este aço é caracterizado por uma relação tensão-extensão sempre não linear, normalmente aproximada por uma formulação de Ramberg-Osgood de duas fases, apresentando maiores endurecimento e ductilidade a temperaturas elevadas que o aço carbono.

A investigação sobre o comportamento mecânico de estruturas em aço inoxidável ao fogo tem-se concentrado em elementos estruturais, sendo ainda escassos os estudos sobre o comportamento global de estruturas completas. Este assunto começou recentemente a captar atenção [1], sendo o desenvolvimento de mais estudos importantes para melhor compreender o comportamento de estruturas porticadas em aço em situação de incêndio.

Com o objetivo de aumentar o conhecimento sobre o projeto de estruturas porticadas ao fogo, este trabalho aplica métodos avançados de cálculo, por meio da aplicação do método dos elementos finitos com o programa SAFIR [2], para análise e discussão dos critérios de definição de colapso estrutural. Adicionalmente, as resistências obtidas de diferentes estruturas porticadas em aço inoxidável, submetidas a diferentes cenários de incêndio, serão comparadas com casos semelhantes em aço carbono, para estudar a influência das diferentes reduções da resistência e rigidez destes aços a altas temperaturas no respetivo comportamento global. Métodos de cálculo simplificados do Eurocódigo 3 também serão considerados no estudo.

REFERÊNCIAS

[1] G. Segura, I. Arrayago, and E. Mirambell, “Plastic redistribution capacity of stainless steel frames in fire”, *Journal of Constructional Steel Research*, Volume 208, 108019 (2023).
[2] J.-M. Franssen, and T. Gernay, “Modeling structures in fire with SAFIR: theoretical background and capabilities”, *Journal of Structural Fire Engineering*, 8(3), 300–323 (2017).

Congress on Numerical Methods in Engineering 2024
4-6 September 2024, University of Aveiro, Portugal

Método da Resistência Direta na determinação da capacidade resistente de vigas de aço com aberturas na alma sujeitas a interação local-global

Flávia Gimenez Berti*, Adriano Silva Carvalho*, Carlos Humberto Martins* e Alexandre Rossi†

*Departamento de Engenharia Civil, Universidade Estadual de Maringá (UEM), Brasil.
Email: chmartins@uem.br

† Faculdade de Engenharia Civil, Universidade Federal de Uberlândia (UFU), Brasil
Email: alexandre-rossi@hotmail.com

RESUMO

As formas de colapso das vigas alveolares, são comumente estudadas e abordadas na literatura, isso pelo fato desses perfis possuírem maior suscetibilidade à flambagem, por conta das aberturas presentes na alma, que aumentam a inércia do perfil, porém reduzem a rigidez a torção da viga. A Flambagem Lateral com Torção (FLT), uma forma de colapso global muito estudada, também, para perfis de alma cheia, ocorre com maior facilidade nesses outros modelos de viga, justamente por conta das aberturas. Já a Flambagem no Montante da Alma (FMA), ocorre localizada no elemento, na região entre as aberturas da alma (montante), sendo um modo de falha exclusivo para os perfis alveolares. Individualmente, ambos modos de falha são bastante abordados na literatura, entretanto, quando se trata da interação entre eles, poucos estudos são referenciados e por isso torna-se importante a análise de vigas alveolares sob essas condições. Dessa forma, o objetivo deste trabalho será compreender a interação entre FLT e FMA, exclusivamente em vigas alveolares de aberturas circulares, caracterizadas como vigas celulares, propondo o desenvolvimento de uma curva de projeto, utilizando o Método da Resistência Direta (MRD). Desse modo, pretende-se analisar numericamente 120 modelos considerando a interação entre FLT e FMA e assim extrair uma curva normalizada pela esbeltez global-local destes perfis e determinar uma equação para o momento último de vigas celulares submetidas a esses dois modos de falha simultâneos.

Palavras-chave: Flambagem no Montante da Alma; Método da Resistência Direta; Vigas Alveolares.

REFERÊNCIAS

[1] Carvalho, A.; Oliveira, V.; Rossi,A.; Martins,C. Elastic lateral-torsional buckling behavior of steel I-beams with sinusoidal web openings. Structures. v.47, p.23-36, 2023.
[2] EUROCODE 3. EN 1993-1-1 2005 – Design of steel structures. Parte 1.1 General rules and rules for buildings. CEN - European Committee for Standardization, 2005.
[3] Sonck, D.; Belis, J. Lateral-torsional buckling resistance of cellular beams. Journal of Constructional Steel Research. v.105, p.119-128, 2015.
[4] Weidlich, C.; Sotelino, E. E Cardoso, D. An application of the direct strength method to the design of castellated beams subject to flexure. Engineering Structures. v.243, 2021.

Congress on Numerical Methods in Engineering 2024
4-6 September 2024, University of Aveiro, Portugal

Avaliação da resistência ao fogo de vigas-coluna em aço enformado a frio com secções abertas de acordo com a nova geração do Eurocódigo 3

Flávio Arrais[*,†], Nuno Lopes[*] e Paulo Vila Real[*]

[*] RISCO, Departamento de Engenharia Civil, Universidade de Aveiro, Portugal
Email: arrais.f@ua.pt

† UL-CUP, Centro Universitário do Porto, Universidade Lusófona, Porto, Portugal

RESUMO

A aplicação na construção de perfis em aço enformados a frio, que se caracterizam por possuírem secções transversais de paredes finas, está a tornar-se cada vez mais comum. As secções transversais esbeltas desses perfis proporcionam uma maior suscetibilidade à ocorrência de fenómenos de instabilidade local. Adicionalmente, a instabilidade global dos elementos e a encurvadura distorcional, relacionada com a existência de reforços na secção, são também modos de colapso muito comuns nesses perfis. Estes fenómenos de instabilidade tornam-se mais evidentes quando os perfis estão sujeitos a altas temperaturas, como as que ocorrem em caso de incêndio.

O presente estudo, que se concentra na determinação das capacidades resistentes últimas de vigas-coluna em aço enformado a frio a altas temperaturas, baseia-se em análises numéricas não lineares com imperfeições, utilizando o programa de elementos finitos SAFIR [1].

Para validação dos modelos numéricos aplicados, foram inicialmente analisados ensaios experimentais da literatura, envolvendo perfis enformados a frio à temperatura normal sujeitos a flexão composta com compressão [2] (tendo a adaptação ao fogo de modelos semelhantes sido validada previamente [3]).

Posteriormente, por meio de um estudo paramétrico que variou esbeltezas de secções, classes de aço e tipos de carregamento, as cargas últimas obtidas numericamente foram comparadas com as resistências fornecidas pelas prescrições da nova geração da parte 1-2 do Eurocódigo 3 [4]. Finalmente, com base nas observações obtidas nessas comparações, são propostas adaptações de cálculo que melhoram a previsão analítica da resistência dos diferentes elementos estruturais a altas temperaturas, com parâmetros adaptados especificamente para este tipo de perfis em aço enformado a frio de secção aberta que não se encontram diferenciados na referida norma.

REFERÊNCIAS

[1] Franssen J-M, Gernay T. “Modelling structures in fire with SAFIR®: theoretical background and capabilities.” J. Struct. Fire Eng., 8(3), 2017, 300-323.
[2] Torabian, S., Zheng, B., Schafer, B. W. “Experimental response of cold-formed steel lipped channel beam-columns”, Thin-Walled Structures, Vol. 89, pp. 152-168, 2015.
[3] Arrais, F.; Lopes, N.; Vila Real, P. “Fire design of slender cold-formed lipped channel and sigma section members with uniform temperature under compression”, Fire Safety Journal, Vol. 122, 2021, 103340.
[4] CEN, European Committee for Standardisation, *FprEN 1993-1-2:2023, Eurocode 3, Design of steel structures – Part 1-2: Structural fire design*, Belgium, 2023.

Congress on Numerical Methods in Engineering 2024
4-6 September 2024, University of Aveiro, Portugal

Human comfort assessment of steel and steel-concrete composite footbridges based on the use of design response spectra

Paula O. B. Diniz†, Jorge M. Souza†, Amanda B. Oliveira† and José Guilherme S. da Silva†*

† Postgraduate Programme in Civil Engineering (PGECIV).
State University of Rio de Janeiro (UERJ).
Rio de Janeiro/RJ, Brazil.
Email: jgss@uerj.br

ABSTRACT

The pedestrian footbridges are more and more becoming the modern landmarks of urban areas. The designers seem to continuously move the safety border, aiming to increase the pedestrian footbridges slenderness and lightness. However, more and more footbridges are carried out as light weight structures with low frequencies and low damping. These facts have generated very slender footbridges, sensitive to dynamic excitations, and consequently changed the serviceability limit states associated to the design [1-2]. In general, the current design codes and technical guides recommend the use of deterministic models to assess the dynamic structural behaviour of footbridges [3-4]. On the other hand, the effect of the uncertainties in mass, stiffness and damping of the investigated structure are relevant and lead to uncertainties on the values of the footbridges natural frequencies. Nevertheless, the human walking is a stochastic phenomenon and the dynamic force generated at each step depends of the weight, the step frequency and the step length of each pedestrian [1-2]. This way, this research work aims to contribute with the structural designers based on the development of a probabilistic approach to assess the dynamic behaviour of steel and steel-concrete composite footbridges, based on the use of design response spectra, considering the stochastic nature of the pedestrian's walking, in order to evaluating the structural response with regard to excessive vibrations that may cause human discomfort. Based on the use of probabilistic methods, it becomes possible to determine the probability of the footbridge's peak acceleration values exceeding or not the human comfort criteria. The results obtained in this research work reveal that the values of peak accelerations calculated through the deterministic methods may be overestimated in design situations.

REFERENCES

[1] J. M. Souza. *Dynamic response analysis of pedestrian footbridges considering a probabilistic modelling of the human walking*. MSc Dissertation (In Portuguese). Postgraduate Programme in Civil Engineering (PGECIV). State University of Rio de Janeiro (UERJ). Rio de Janeiro/RJ, Brazil, (2012).

[2] P. O. B. Diniz. *Human comfort assessment of footbridges based on the use of probabilistic design response spectra*. MSc Dissertation (In Portuguese / In development). Postgraduate Programme in Civil Engineering (PGECIV). State University of Rio de Janeiro (UERJ). Rio de Janeiro/RJ, Brazil, (2024).

[3] H. Bachmann and W. Ammann. *Vibrations in structures induced by man and machines*. Structural Engineering Document 3e. International Association for Bridges and Structural Engineering (IABSE), (1987).

[4] T.M. Murray, D. E. Allen, E. E. Ungar, D. B. Davis. *Steel design guide series Nbr. 11: Vibrations of steel-framed structural systems due to human activity*. American Institute of Steel Construction (AISC), 2nd Edition, Chicago, USA, (2016).

Congress on Numerical Methods in Engineering 2024
4-6 September 2024, University of Aveiro, Portugal

Dynamic structural analysis of steel towers used in power transmission lines when subjected to non-deterministic dynamic wind loadings

M. S. Rechtman† and José Guilherme S. da Silva†*

† Postgraduate Programme in Civil Engineering (PGECIV).
State University of Rio de Janeiro (UERJ).
Rio de Janeiro/RJ, Brazil.
Email: jgss@uerj.br

ABSTRACT

The lattice steel towers have been widely used as supports for power transmission lines. On the other hand, in the current design practise of steel latticed towers used to support electrical transmission lines, the structure's dynamic behaviour is not considered [1-2]. However, the main loading to be taken into account in the structural analysis of electrical transmission lines steel towers is produced by the wind loadings, which acts dynamically over the structural system composed by towers and cables [3-4]. In addition, it's not uncommon for slender towers to present disadvantageous dynamic properties, making them vulnerable to the wind action. Considering that many accidents associated to this kind of structure occur even for wind velocities below that specified in project, it's possible that most of these accidents have been produced by dynamic actions [1-2]. This way, this research work proposes an analysis methodology that can accurately simulate the coupled behaviour between the transmission line cables and the suspension structures, when subjected to wind non-deterministic loads, including in the dynamic analysis the effects of the geometric nonlinearity and the aerodynamic damping [1]. Therefore, the main objective of this research work is to develop an analysis regarding the structural behaviour of power transmission lines, when subjected to wind dynamic loadings, having in mind the assessment of the displacements and forces of the steel towers. In this work, a transmission steel tower was investigated, considering the wind non-deterministic dynamic characteristic, and the wind loads modelled by an aleatory process based on their statistical properties. The results have shown important quantitative differences associated to the displacements and forces values when the structural response of the transmission steel tower was calculated based on a static linear analysis and a dynamic geometric non-linear and non-deterministic analysis.

REFERENCES

[1] M. S. Rechtman. *Nonlinear dynamic structural modelling of transmission lines steel towers when subjected to the nondeterministic wind dynamic loads.* DSc Thesis (In Portuguese / In development). Postgraduate Programme in Civil Engineering (PGECIV). State University of Rio de Janeiro (UERJ). Rio de Janeiro/RJ, Brazil, (2024).

[2] M. I. R. Oliveira. *Structural analysis of transmission line steel towers subjected to wind dynamic effects.* MSc Dissertation (In Portuguese). Postgraduate Programme in Civil Engineering (PGECIV). State University of Rio de Janeiro (UERJ). Rio de Janeiro/RJ, Brazil, (2006).

[3] N. P. Rao, S. J. Mohan, N. Lakshmanan. A study on failure of cross arms in transmission line towers during prototype testing. *International Journal of Structural Stability and Dynamics*, vol. 5(3), 435-455, (2005).

[4] L. Kempner Jr. *Wind load methodologies for transmission line towers and conductors*. Proceedings of the Electrical Transmission and Substation Structures Conference, Texas, USA, (2009).

TS7: Computational methods in acoustics and vibration

This page intentionally left blank

Congress on Numerical Methods in Engineering 2024
4-6 September 2024, University of Aveiro, Portugal

Advanced numerical models for the evaluation of train-track-bridge interaction effects in High Speed railway bridges composed by skewed girder decks

María D. Martínez-Rodrigo*, Juan C. Sánchez-Quesada*, Emma Moliner*, Antonio Romero† and Pedro Galvín†

* Mechanical Engineering and Construction Department, Universitat Jaume I, Castellón, Spain
Email: mrodrigo@uji.es, jquesada@uji.es, molinere@uji.es

† Escuela Técnica Superior de Ingeniería, Universidad de Sevilla, Spain
Email: pedrogalvin@us.es, aro@us.es

ABSTRACT

This work is devoted to the analysis of the vertical vibratory response of High-Speed (HS) multi-track railway bridges composed by simply-supported (SS) spans and pre-stressed concrete girder decks. These bridges are relatively common in Spanish lines and, due to their cross-section low torsional stiffness and low mass, may exhibit high vertical accelerations at the platform, compromising their performance. In particular, it aims to investigate the influence of three geometrical aspects usually disregarded in numerical models used to evaluate the Serviceability Limit State of traffic safety in such structures: (i) the deck obliquity, (ii) the presence and correct execution of transverse diaphragms at the supports, and (iii) the number of successive SS spans weakly coupled through the ballast track layer. The influence of these aspects is analysed from the correlation of a detailed numerical model and experimental measurements on an in-service HS multi-track railway bridge. From the reference model, a set of variants accounting for different levels of deck obliquity and diaphragm configurations are envisaged and the maximum transverse acceleration over the platform is determined under railway excitation. The analysis is extended to bridges with an increasing number of successive spans. Special attention is paid to the location of the maximum response and to the participation of modes different from the longitudinal bending one. Finally, a numerical–experimental comparison of the bridge response under train passages is presented accounting for vehicle-bridge interaction and the models adjustment along with the actual bridge performance are assessed.

Congress on Numerical Methods in Engineering 2024
4-6 September 2024, University of Aveiro, Portugal

Dynamic characterization of a fibre-reinforced high-strength concrete pedestrian footbridge based on numerical-experimental techniques

Victor Roda-Casanova*,1, Reda Sadik El Ghoufairi, Carlos Rodrigo Villar, David Hernández-Figueirido, Joaquin L. Sancho-Bru, Maria D. Martínez-Rodrigo

* Universitat Jaume I, Spain
Email: vroda@uji.es

ABSTRACT

Pedestrian bridges are rather slender and light structures susceptible to experience important vibrations under serviceability conditions. This contribution focuses on the dynamic characterization and numerical modelling of a recently opened pedestrian bridge made of ultra-high strength concrete. Due to the mechanical characteristics of this rather new material, the footbridge is slender and its performance on the long term is not well known. Two experimental programs are conducted on the bridge to determine its main modal parameters. The first natural frequencies, modes and associated damping are identified from ambient vibration and hammer testing, applying operational and experimental modal analysis techniques. On the other hand, a detailed finite element model of the footbridge is implemented and updated from the dynamic identified properties. The vibration serviceability of the structure is assessed based on current codes. Also, from the numerical-experimental comparison, preliminary conclusions are extracted related to the general state of the footbridge and the behaviour of the boundary conditions for different amplitude levels.

Congress on Numerical Methods in Engineering 2024
4-6 September 2024, University of Aveiro, Portugal

Dynamic characterisation of a portal frame railway bridge and numerical modelling of the soil-structure interaction

J. Chordà-Monsonís[†], J.C. Sánchez-Quesada[†], E. Moliner*, M.D. Martínez-Rodrigo[†], A. Romero[#], P. Galvín[#]

*† Departamento de Ingeniería Mecánica y Construcción, Universitat Jaume I, Castelló de la Plana, Spain
Email: chordaj@uji.es, jquesada@uji.es, molinere@uji.es,

Departamento de Mecánica de Medios Continuos y Teoría de Estructuras, Universidad de Sevilla, Spain
Email: cmn2024@ua.pt

ABSTRACT

The growing demand for a more sustainable mode of transportation is driving the expansion of railway networks in various European countries. Portal frame bridges are quite common in our railway lines, which, despite having great stiffness, their dynamic behaviour is much more complex to predict due to the interaction with the soil. The inherent damping of the soil due to wave radiation along with its material damping and flexibility, may increase the natural periods identified in the bridge and reduce its vibratory response. The consideration of soil-structure interaction (SSI) could lead to more optimised designs, in the case of new structures, or to a more realistic evaluation of the Serviceability Limit States of existing bridges under new traffic scenarios. However, due to the intricate nature of this interaction, an accurate modelling of the bridge dynamics accounting for SSI is challenging and time-consuming. As a result, numerical analyses used for practical purposes often overlook SSI. Nevertheless, recent research underscores the importance of considering it to prevent discrepancies between numerical predictions and experimental measurements [1]. This study focuses on an existing portal frame railway bridge, beginning with the determination of its modal parameters from the acceleration measurements recorded during an experimental campaign performed by the authors. Subsequently, a 3D finite-element numerical model of the bridge is developed, incorporating the track, track-bridge-soil system, and employing perfectly matched layers at the model boundaries. The results obtained from this detailed model are then used to create a simplified version where the soil is replaced by a series of spring-dashpot elements. The main purpose of this simple model is the validation of a fast numerical methodology previously developed by the authors to solve the dynamic response of railway bridges under the passage of running trains with minimal computational cost [2]. After calibration of the simplified model, a comparison is carried out with the experimental measurements and numerical predictions.

REFERENCES

[1] A. Zangeneh, S. François, G. Lombaert, C. Pacoste, “Modal analysis of coupled soil-structure Systems”, *Soil Dynamics and Earthquake Engineering,* 144: 106645 (2021).

[2] P. Galvín, P, A. Romero, E. Moliner, D. P. Connolly, M. D. Martínez-Rodrigo, “Fast simulation of railway bridge dynamics accounting for soil–structure interaction”, *Bull Earthquake Eng,* 20, 3195-3213 (2022).

Congress on Numerical Methods in Engineering 2024
4-6 September 2024, University of Aveiro, Portugal

Análisis del efecto de ménsulas con péndola antiviento en la interacción dinámica entre pantógrafo y catenaria

N. H. Aldaz-Saca*†, S. Gregori†, M. Tur†, J. Gil† y F.J. Fuenmayor†

† Instituto de Ingeniería Mecánica y Biomecánica, Universitat Politècnica de Valencia, España
Email: nhaldsac@upv.es, sangreve@upv.es, matuva@upv.es, jaigiro@upv.es, ffuenmay@upv.es

RESUMEN

La eficiencia y seguridad en la operación de los trenes de alta velocidad depende en gran medida de un correcto suministro de energía, llevado a cabo mediante la interacción entre el pantógrafo, un mecanismo de barras articuladas situado en el techo de la locomotora, y la catenaria o línea aérea de contacto, un tendido de cables a lo largo de todo el trazado de la vía [1]. Este cableado está soportado regularmente por unas ménsulas que van sujetas a postes anclados al suelo.

Un componente importante de las ménsulas son los brazos de atirantado que se encargan de tirar lateralmente del hilo de contacto de la catenaria para producir una disposición en zig-zag y uniformizar así el desgaste en toda la superficie de los frotadores del pantógrafo. Para que el brazo de atirantado no entre a compresión en caso de acción del viento, se coloca un cable, conocido como péndola antiviento, entre este y el tubo de atirantado tal y como se observa en la Figura 1.

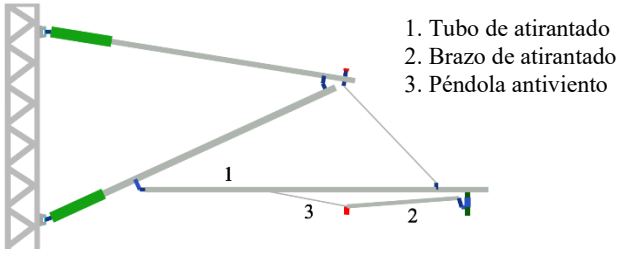

Figura 1: Imagen de una ménsula con péndola antiviento.

El presente trabajo se centra en el modelado de las péndolas antiviento, a partir de los modelos de elementos finitos de ménsula y catenaria desarrollados previamente por el grupo [2]. Se consideran cuatro posibles casos de montaje de la misma, y por medio de simulaciones se analiza el efecto que produce la incorporación de este componente en la interacción dinámica entre pantógrafo y catenaria. Los resultados muestran que, aunque el efecto no es muy significativo para el primer pantógrafo, sí que resulta importante en circulación con múltiples pantógrafos en contacto con la catenaria.

REFERENCIAS

[1] Kiessling, F., Puschmann, R., Schmieder, A. and Schneider, E., *Contact lines for electric railways: planning, design, implementation, maintenance,* John Wiley & Sons (Third edition), 2018.

[2] N. Aldaz, S. Gregori, J. Gil, M. Tur, and F.J. Fuenmayor, “Railway catenary shape-finding problem considering cantilevers and general track paths”, *Proceedings of the 7th ECCOMAS Young Investigators Conference (ECCOMAS YIC 2023)*. Zenodo, 2023.

Los autores agradecen la financiación recibida por parte de la Generalitat Valenciana (PROMETEO/ 2021/046) y la beca (PID2020-113458RB-I00) financiada por MCIN/AEI/10.13039/501100011033.

TS8: Optimization, metaheuristics and evolutionary algorithms in computational and civil engineering

This page intentionally left blank

Congress on Numerical Methods in Engineering 2024
4-6 September 2024, University of Aveiro, Portugal

Mejorando la Simulación Numérica de Implantes Cocleares mediante Algoritmos Evolutivos

D. Greiner*, M. Hernández-Gil, A. Ramos-de-Miguel, D. Benítez, J.M. Escobar

SIANI, Instituto Universitario de Sistemas Inteligentes y Aplicaciones Numéricas en Ingeniería, Universidad de Las Palmas de Gran Canaria (ULPGC), Las Palmas de Gran Canaria, España
Email: david.greiner@ulpgc.es

RESUMEN

El uso de métodos numéricos en ingeniería biomédica es cada vez más frecuente y éstos constituyen una herramienta fundamental de avance en el ámbito (ver, e.g. [1]).

En esta ponencia se emplea una simulación numérica de un implante coclear mediante elementos finitos, haciendo uso de un modelo tridimensional para la evaluación de la densidad de corriente en el interior de la cóclea. En este modelo se modifican las conductividades del medio y de la cóclea para ajustar la matriz de transimpedancia simulada a la matriz de transimpendancia medida en un paciente real.

Partiendo de antecedentes para implantes cocleares donde se combina la utilización de métodos de simulación como los elementos finitos con métodos de optimización como los algoritmos evolutivos (ver, e.g. [2][3]), en esta ponencia se propone realizar una optimización mediante algoritmos evolutivos para mejorar la focalización del implante. Como tendencia actual para mejorar la focalización se encuentra la estimulación multipolar del implante coclear, que consiste en alimentar simultáneamente varios electrodos. Con el objetivo de mejorar la estimulación multipolar estándar (conocida conmúnmente como phased array), se considera un algoritmo evolutivo donde las variables a considerar de su cromosoma, son los coeficientes de corriente de las intensidades inyectadas por cada uno de los veintidós electrodos del implante coclear. La solución óptima propuesta permite mejorar la focalización respecto de algunas de las soluciones estándar empleadas en la práctica (solución monopolar y phased array).

Se obtienen además interesantes conclusiones relativas a las características de las corrientes inyectadas que permitirían abstraer y generalizar principios de diseño en el diseño de implantes cocleares.

Agradecimientos. Este trabajo ha sido financiado por los proyectos: EIS 2021 04, Agencia Canaria de Investigación, Innovación y Sociedad de la Información del Gobierno de Canarias y Fondos Europeos FEDER; Ministerio de Ciencia, Innovación y Universidades, Gobierno de España, contrato: PID2019-110185RB-C22.

REFERENCIAS

[1] David Greiner, Irene Arias, Manuel Tur, Gil Andrade-Campos, Nuno Lopes, J Alexandre Pinho-da-Cruz, "*Proceedings of the Congress on Numerical Methods in Engineering CMN 2022*", CIMNE International Center for Numerical Methods in Engineering, ISBN: 978-84-123222-9-3, (2022).

[2] Ángel Ramos-de-Miguel, José M. Escobar, David Greiner, Ángel Ramos-Macías, “A multiobjective optimization procedure for the electrode design of cochlear implants”, *International Journal for Numerical Methods in Biomedical Engineering*, 34-8, e2992, (2018

[3] Ángel Ramos-de-Miguel, José M. Escobar, David Greiner, Domingo Benítez, Eduardo Rodríguez, Albert Oliver, Marcos Hernández, Ángel Ramos-Macías, "A phenomenological computational model of the evoked action potential fitted to human cochlear implant responses", *PLoS Computational Biology*, 18-5, e1010134, (2022).

Congress on Numerical Methods in Engineering 2024
4-6 September 2024, University of Aveiro, Portugal

COMPARACIÓN DE REDES NEURONALES Y KRIGING PARA LA OPTIMIZACIÓN ENERGÉTICA DE PUENTES Llosa PRETENSADOS

Lorena Yepes-Bellver[1], Alejandro Brun-Izquierdo[2] , Julián Alcalá[2] y Víctor Yepes[2]

1: Departamento de Mecánica de los Medios Continuos y Teoría de Estructuras
Universitat Politècnica de València
Camino de Vera, s/n, 46022 Valencia, Spain
e-mail: loyebel@alumni.upv.es

2: ICITECH. Departamento de Ingeniería de la Construcción y Proyectos de Ingeniería Civil
Universitat Politècnica de València
Camino de Vera, s/n, 46022 Valencia, Spain
e-mail: albruiz1994@gmail.com;{jualgon,vyepesp}@cst.upv.es

Palabras clave: Optimización, metamodelos Kriging, redes neuronales, metaheurísticas, puente losa postesado, sostenibilidad, energía

Resumen *El objetivo principal de este estudio es evaluar y comparar la eficacia de varios métodos de predicción espacial en una simulación aplicada para optimizar la energía incorporada durante la construcción de tableros de puentes pretensados. Se lleva a cabo una exhaustiva revisión bibliográfica para realizar un análisis transversal e identificar los parámetros de diseño cruciales. A partir de este análisis, se determinan las variables de diseño clave que pueden mejorar la eficiencia energética del forjado. Los métodos analizados son el Kriging ordinario y una red neuronal Perceptrón multicapa. Aunque el estudio de simulación indica que el rendimiento de predicción espacial de la red neuronal es algo más débil que el del método Kriging, sigue siendo un buen competidor. Para mejorar la eficiencia energética se recomiendan relaciones de esbeltez elevadas (en torno a 1/28) y emplear hormigones de 40 MPa de resistencia característica a compresión.*

TS9: Computational models as a pre-clinical test to predict the behavior of biomechanical devices

This page intentionally left blank

Congress on Numerical Methods in Engineering 2024
4-6 September 2024, University of Aveiro, Portugal

Development of computational models of biodegradable meshes for pelvic organ prolapse

F. Vaz[1*], M.E.T. Silva[1], M. Parente[2], A. A. Fernandes[2]

[1] LAETA, INEGI, Porto, Portugal

[2] LAETA, INEGI, Faculty of Engineering, University of Porto, Porto, Portugal

Email: fvaz@inegi.up.pt*; mesilva@inegi.up.pt; mparente@fe.up.pt; aaf@fe.up.pt

ABSTRACT

Pelvic organ prolapse (POP) consists of the descent of the pelvic organs and is a prevalent condition in women that can significantly affect their quality of life. This study aimed to develop biodegradable meshes as an alternative to synthetic meshes for POP repair, considering that the FDA banned mesh treatment for transvaginal prolapse due to its high risks [1]. To achieve this, computational models were created with variations in pore geometry, pore size, filament thickness, and the inclusion of filaments around specific mesh regions. One of the meshes was 3D printed to validate the simulation results, and then a uniaxial tensile test was conducted on the vaginal tissue of a sow to compare the results with the simulations. The goal was to identify meshes that exhibited behaviour similar to that of vaginal tissue. Finally, the most promising outcomes were compared with those of the uterosacral ligament and a commercially available mesh.

After a comprehensive analysis of the results, the mesh with a smaller pore diameter (1.50 mm), filaments in specific areas of the mesh, and variable filament thickness across the mesh most accurately replicated the behaviour of vaginal tissue. However, when compared with the outcomes of the uterosacral, the meshes did not exhibit similar behaviour to the ligament. The commercially available mesh also did not represent the behaviour of both the vaginal tissue and the uterosacral ligament, and thus may not be the best treatment option for POP repair.

The biocompatibility and biomechanical properties of these biodegradable meshes make them a potential solution to the drawbacks of synthetic meshes. Future research could focus on enhancing biodegradable mesh by incorporating different materials (PLA and PCL) with varying degradation periods. This enables customization based on individual patient needs and optimizes the repair process. Investigating the interplay between these materials and their impact on overall biomechanical performance may unveil innovative solutions for more effective and patient-specific POP repairs.

REFERENCES

[1] FDA, “FDA takes action to protect women’s health, orders manufacturers of surgical mesh intended for transvaginal repair of pelvic organ prolapse to stop selling all devices,” https://www.fda.gov/news-events/press-announcements/fda-takes-action-protect-womens-health-orders-manufacturers-surgical-mesh-intended-transvaginal, 2019.

Congress on Numerical Methods in Engineering 2024
4-6 September 2024, University of Aveiro, Portugal

Numerical simulation of the vaginal wall reinforcement using cog threads

N. M. Ferreira[1]*, M. E. T. Silva[2] and A. A. Fernandes[3]

[*] LAETA, INEGI, Porto, Portugal
Email: nmferreira@inegi.up.pt

[2] LAETA, INEGI, Porto, Portugal
Email: mesilva@inegi.up.pt

[3] LAETA, INEGI, Faculty of Engineering, University of Porto, Portugal
Email: aaf@fe.up.pt

ABSTRACT

Pelvic Organ Prolapse (POP) is a condition that affects women's quality of life [1]. The number of cases of genital prolapse has been on the rise each year, with one in ten women requiring at least one surgical procedure and one in four women in midlife having asymptomatic prolapse, leading to a need for innovative treatment methods. Although traditional mesh implants are commonly used, they have limitations [2]. Therefore, alternative solutions are required. This study investigates the use of biodegradable cog threads, which are typically used in facelift procedures, to reinforce and correct vaginal wall defects caused by POP.

Finite element analysis (FEA) was used to model the vaginal wall and simulate repairing defects using cog threads. The application of (FEA) to this research allows us to personalize and select suitable POP correction techniques and study the effect of alternative reinforcement techniques, pointing to areas experiencing critical levels of stress and strain. To accurately model it, we conducted uniaxial tensile tests on both the polycaprolactone (PCL) cog threads and pork vaginal tissues, which served as a human tissue analogue. This provided essential data for accurate finite element modelling. We conducted FEM simulations using Abaqus 2022. Additionally, we performed ball burst tests to investigate the interaction between cog threads and free-standing pork vaginal tissues under spherical indentation, closely mimicking in vivo conditions. By combining experimental testing with numerical simulation, we were able to comprehensively analyse the interaction between the thread and tissue.

The study results showed that cog threads have the potential to offer benefits in repairing pelvic organ prolapse (POP). This research forms a basis for further investigation into the use of cog threads for treating POP. It also highlights their advantages over traditional mesh implants in terms of shorter operative time, better recovery, and lower complication rates. Due to the nature of soft tissues, an intuitive understanding and interpretation of the parameter fittings concerning the experimental data are complex.

REFERENCES

1. Grob, A.T.M., et al., *Underestimation of pelvic organ prolapse in the supine straining position, based on magnetic resonance imaging findings.* Int Urogynecol J, 2019. **30**(11): p. 1939-1944.
2. Haylen, B.T., et al., *An International Urogynecological Association (IUGA)/International Continence Society (ICS) joint report on the terminology for female pelvic floor dysfunction.* Int Urogynecol J, 2010. **21**(1): p. 5-26.

TS10: Numerical modeling of biological cell systems

This page intentionally left blank

Congress on Numerical Methods in Engineering 2024
4-6 September 2024, University of Aveiro, Portugal

Optimal Locomotion Control of Contractile Elastic Bodies

José J. Muñoz *and Ashutosh Bijalwan†

* Universitat Politècnica de Catalunya, 08034 Barcelona, Spain
Centre Internacional de Mètodes Numèrics en Enginyeria (CIMNE), Barcelona, 08034, Spain
Email: j.munoz@upc.edu

† Centre Internacional de Mètodes Numèrics en Enginyeria (CIMNE), Barcelona, 08034, Spain
Email: abijalwan@cimne.upc.edu

ABSTRACT

Optimal locomotion in soft robotics is a prominent research field that is gaining due to recent progress in manufacturing techniques, control algorithms, and also its potential applications from autonomous vehicles, agricultural manipulators, or drug delivery [1].

For soft elastic bodies and living systems, with active contractile capabilities, the problem may be posed as minimising a time-dependent objective subjected to PDE constrains, which after FME interpolation reads [2],

$$\begin{aligned} &\min_{\mathbf{x},\mathbf{v},\mathbf{u}} \mathcal{J}(\mathbf{x},\mathbf{v},\mathbf{u}) \\ &\text{s.t. } \mathbf{v}-\dot{\mathbf{x}}=\mathbf{0} && \text{(State ODE)} \\ &\quad \boldsymbol{g}(\mathbf{x},\mathbf{v},\mathbf{u})=\mathbf{0} && \text{(Algebraic equation)} \\ &\quad \boldsymbol{c}(\mathbf{x}-\overline{\mathbf{x}},\mathbf{v}-\overline{\mathbf{v}})=\mathbf{0} && \text{(Boundary condition)} \\ &\quad \mathbf{x}(0)=\mathbf{x}_0,\mathbf{v}(0)=\mathbf{v}_0. && \text{(Initial condition)} \end{aligned}$$

with **u** the set of contractilities in each element, stemming from a deformation gradient decomposition $\mathbf{F}=\mathbf{F}_e\,\mathbf{F}_u$, with $\mathbf{F}_u=u(t)\mathbf{I}$, and $\mathbf{g}(\mathbf{x},\mathbf{v},\mathbf{u})$ the set of FE non-linear equations [2]. The optimality conditions give rise to adjoint-state ODEs, that are solved in an iterative manner [3], with special emphasis on the time-integration and type of frictional anisotropy [4].

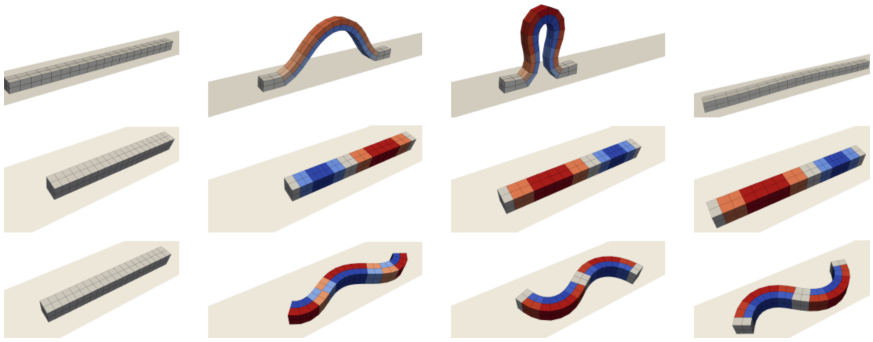

Figure 1. Optimal locomotion strategies: each row follows a different contractility pattern depending on substrate frictional conditions.

REFERENCES

[1] B.J. Nelson. Delivering drugs with microrobots, *Science* 382 (6675), 2023.
[2] A. Bijalwan, J.J. Muñoz. Adjoint-based optimal control of contractile elastic bodies. Application 3 to limbless locomotion on frictional substrates. Submitted.
[2] A. Bijalwan, J.J. Muñoz. A control Hamiltonian-preserving discretisation for optimal control. Multibody System Dynamics. 59: 19–43, 2023.
[4] S. Lenhart and J.T. Workman. Optimal control applied to biological 1150 models. Chapman and Hall/CRC, 2007.

Congress on Numerical Methods in Engineering 2024
4-6 September 2024, University of Aveiro, Portugal

A mechano-biological feedback between cancer organoids and the extra-cellular matrix initiates and sustains collective invasion

Marino Arroyo*†, Pau Blanco*†, Giancarlo Cicconofri*, Guillermo Vilanova*, Pablo Sáez*

* LaCàN, Universitat Politècnica de Catalunya, Barcelona, Spain
Email: marino.arroyo@upc.edu

† International Center for Numerical Methods in Engineering (CIMNE), Barcelona, Spain

ABSTRACT

During collective invasion, cohesive cellular strands extend into the extra-cellular matrix (ECM) and reach distant locations. At invasive protrusions, so-called leader cells organize a region with focalized adhesion, force generation, matrix alignment and proteolysis, and mechanosensing. How some cells become leaders and initiate and sustain collective invasion is not well understood. To address this question, we study monoclonal MMTV-PyMT organoids embedded in collagen matrices, where all cells at the organoid-matrix interface have invasive potential. These organoids break symmetry to develop invasive patterns with multiple thick and cohesive protrusions. By following collagen and cellular dynamics during invasion, we identify a new feedback mechanism involving fast and mechanosensitive matrix proteolysis and traction as well as the nonlinear mechanics of fibrous matrices. Using mathematical and computational modeling as well as experimental perturbations, we show that this mechanism can explain symmetry-breaking from spherical organoids, and the formation of patterns of persistent invasive collective protrusions. The computational treatment of the problem relies on non-conforming meshes for the nonlinear solid model of the ECM and an active fluid model for the cancer organoid, which are coupled with a generalized A Nitsche approach.

Congress on Numerical Methods in Engineering 2024
4-6 September 2024, University of Aveiro, Portugal

Simulating VEGF-Driven Capillary Network Formation: A Meshless Method Study

Ana Guerra*, Jorge Belinha†, Christiane Salgado¥, Fernando Jorge Monteiro¥ and Renato Natal Jorge‡

* Institute of Science and Innovation in Mechanical and Industrial Engineering (INEGI), Portugal
Email: aguerra@inegi.up.pt

† Mechanical Engineering Department, Polytechnic of Porto (ISEP), Portugal
Email: job@isep.ipp.pt

¥ Institute for Research & Innovation in Health (i3S), Portugal
Email: csalgado@ineb.up.pt; fjmont@gmail.com

‡ Mechanical Engineering Department, FEUP, Portugal
Email: rnatal@fe.up.pt

ABSTRACT

Angiogenesis, the formation of new capillaries from pre-existing ones, plays a crucial role in maintaining a functional network of blood vessels and promoting tissue homeostasis. This study focuses on simulating the development of a new capillary network in response to the chemical diffusion of vascular endothelial growth factor (VEGF), a fundamental step in angiogenesis. Given the complexity of this process, which often necessitates in vivo assays, the Radial Point Interpolation Method was employed for numerical simulation to offer a more efficient and cost-effective alternative. The model incorporated endothelial cell migration through a diffusion-reaction equation, guided by the concentration gradient of VEGF. Parameters essential for developing the numeric algorithm were derived from chick chorioallantoic membrane (CAM) bioassays, providing a basis for validating numerical results in an in vivo context.

Simulation results revealed that endothelial cells migrated accordingly to the VEGF gradient, resulting in a capillary network closely resembling experimental assays. Comparative analysis of branching number, vessel length, and branching angle between in silico and in vivo methodologies yielded statistically identical results (p-value > 0.05; n = 6). This study not only supports existing findings on VEGF-induced endothelial cell migration but also establishes the numerical model's ability to faithfully replicate observed capillary network formation. The successful validation of the model's predictions against in vivo data highlights its potential as a valuable tool for studying angiogenesis, offering a time-efficient and cost-effective alternative to traditional experimental approaches.

ACKNOWLEDGEMENTS

The authors truly acknowledge the funding provided by Ministério da Ciência, Tecnologia e Ensino Superior - Fundação para a Ciência e a Tecnologia (Portugal), under the project PTDC/EME-APL/3058/2021, DOI: 10.54499/PTDC/EME-APL/3058/2021. Additionally, the authors acknowledge the funding provided by LAETA, under project UIDB/50022/2020.

Congress on Numerical Methods in Engineering 2024
4-6 September 2024, University of Aveiro, Portugal

Staggered solution of a non-linear model for the evolution of glioblastoma cells

E. Sala-Lardies[*1], M. Pérez-Aliacar[2,3], J. Ayensa-Jiménez[2,3], M. Doblaré[2,3,4] and J. Sarrate[1]

[1] ETS d'Enginyeria de Camins, Canals i Ports de Barcelona, UPC, Spain
Email: esther.sala-lardies, jose.sarrate@upc.edu
[2] Instituto de Investigación en Ingeniería de Aragón (I3A), UZ, Spain
[3] Departmento de Ingeniería Mecánica, Escuela de Ingeniería y Arquitectura, UZ, Spain
[4] Centro de Investigación Biomédica en Red, Bioingeniería, Biomateriales y Nanomedicina (ciber-bbn), Spain
Email: marina.perez, jacoboaj, mdoblare@unizar.es

ABSTRACT

Glioblastoma (GBM) is the most common and aggressive type of brain cancer. Understanding its evolution and interaction with the tumour micro-environment is essential to develop new treatments that may improve the prognosis. To this end, microfluidic devices [1] are a useful tool that allow to perform *in vitro* experiments where some specific conditions can be reproduced or the effect of a particular test variable can be controlled. These assays can be combined with mathematical modelling to have a better understanding of each separated effect and also as a fast way to test hypotheses and propose new experiments or treatments.

A non-linear convection-diffusion-reaction model was proposed [2] to simulate the growth of GBM cells in microfluidic devices. This model permits considering as many cell phenotypes or nutrients or drugs as needed but, for the simplest case, we can consider only two cell phenotypes (live and dead tumour cells) and a single nutrient (oxygen).

The problem is solved [3] using finite elements to discretize in space and a DIRK scheme to integrate in time, leading to a large system of non-linear coupled equations to be solved at each stage. Solving this system can be computationally demanding, especially for 3D geometries that involve fine meshes. Here, we propose a staggered approach (for each phenotype and chemical specimen) to solve this non-linear system that can reduce the computational cost. Several examples are solved to illustrate the behaviour of this methodology and in which cases it is competitive compared to the monolithic approach.

REFERENCES

[1] J. M. Ayuso et al, "Development and characterization of a microfluidic model of the tumor microenvironment", *Scientific Reports*, 6, 36086 (2016).
[2] J. Ayensa-Jiménez et al, "Mathematical formulation and parametric analysis of in vitro cell models in microfluidic devices: application to different stages of glioblastoma evolution", *Scientific Reports*, 10, 1-21 (2020).
[3] A. Costa-Solé et al, "3D modeling of glioblastoma multiforme growth in microfluidic devices", *Congress on Numerical Methods in Engineering* (2022)

Congress on Numerical Methods in Engineering 2024
4-6 September 2024, University of Aveiro, Portugal

Modeling the behavior of glioblastoma multiforme cells and the evolution of the tumor micro-environment through an agent-based hybrid model.

Lucía López-de Abajo*, José María Benítez†, Luis Saucedo-Mora† and Francisco J. Montáns Leal†

* Departamento de Aeronaves y Vehículos Espaciales, Universidad Politécnica de Madrid, Spain
Email: lucia.lopezdeabajo@upm.es

† Departamento de Aeronaves y Vehículos Espaciales, Universidad Politécnica de Madrid, Spain
Emails: josemaria.benitez@upm.es, luis.saucedo@upm.es and fco.montans@upm.es

ABSTRACT

Glioblastoma multiforme (GBM) is an aggressive brain cancer characterized by neovascularization and high mitotic and infiltrative capabilities of GBM cells. The behavior of the GBM cells is conditioned by its microenvironment. For example, hypoxic conditions and/or a high cell density of tumoral cells can restrain or trigger the migration, proliferation, anoxia, or death of the cancer cells. On the other hand, hypoxic cells also trigger the sprouting of a new vasculature that will supply nutrients to the GBM cells. This makes the tumor micro-environment change and influences cell behavior. In this contribution, we show an agent-based hybrid model to simulate the biophysics underlying the GBM evolution. The model is formulated in terms of genotypic variables and it is capable of reproducing the evolution of the microenvironment conditions, the phenotypic plasticity, considering five phenotypes, and the hallmarks of the GBM.

REFERENCES

[1] J.M. Benítez, L. García-Mozos, A. P. Santos, F.J. Montáns and L. Saucedo-Mora. "A simple agent-based model to simulate 3D tumor-induced angiogenesis considering the evolution of the hypoxic conditions of the cells", *Engineering with Computers*, 38(5), 4115-4133. (2022).

[2] L. Saucedo-Mora, M.A. Sanz, F.J. Montáns and J.M. Benítez, "A simple agent-based hybrid model to simulate the biophysics of glioblastoma multiforme cells and the concomitant evolution of the oxygen field", *Computer Methods and Programs in Biomedicine*, 246, https://doi.org/10.1016/j.cmpb.2024.108046 (2024).

This page intentionally left blank

TS11: Metal forming - material, formability, damage, fracture, and process modelling

This page intentionally left blank

Congress on Numerical Methods in Engineering 2024
4-6 September 2024, University of Aveiro, Portugal

On the design of a modified Arcan test setup with strain path changes for the inverse calibration of elastoplastic constitutive models

J. Henriques[1,] *, A. Andrade-Campos[1] and J. Xavier[2]

[1]Centre for Mechanical Technology and Automation (TEMA), Intelligent Systems Associate Laboratory (LASI), Department of Mechanical Engineering, University of Aveiro, Aveiro, Portugal
Email: joaodiogofh@ua.pt, gilac@ua.pt

[2]Research and Development Unit for Mechanical and Industrial Engineering (UNIDEMI), Intelligent, Systems Associate Laboratory (LASI), Department of Mechanical and Industrial Engineering, NOVA School of Science and Technology, NOVA University Lisbon
Email: jmc.xavier@fct.unl.pt

ABSTRACT

In recent years, the manufacturing of sheet metal parts has been increasingly assisted by numerical simulation, where the calibration of the constitutive models, which determine the behaviour of the material, is required for accurate results. Moreover, the recent technological advances in optical techniques have made it possible to assess a wide range of strain states using heterogeneous test configurations and full-field measurements. The full-field kinematic data can then be combined with inverse calibration techniques to give a robust strategy for calibrating constitutive models [1]. However, the accuracy of this methodology is heavily influenced by a variety of factors, including the test configuration, the constitutive models and the selection of a suitable identification strategy. The Arcan test is an interesting test setup since it allows for the change in the loading direction in a standard uniaxial tensile testing machine, although it has been seldom used in heterogeneous test design for plastic constitutive model calibration. This work aims to design a modified Arcan test setup with strain path changes during the experimental test without the unloading of the specimen. The goal of this approach is to enhance the accuracy of the calibration of material models using a single test configuration. The designed test will be numerically validated through virtual experiments, where synthetic images are generated and further processed by digital image correlation. These results will then be used to identify the material parameters of a dual-phase steel.

ACKNOWLEDGEMENTS

J. Henriques is grateful to the Portuguese Foundation for Science and Technology (FCT) for the Ph.D. grant 2021.05692.BD. This project has received funding from the Research Fund for Coal and Steel under grant agreement No 888153. The authors gratefully acknowledge the financial support of the FCT under the project PTDC/EMEAPL/29713/2017 by UE/FEDER through the programs CENTRO 2020 and COMPETE 2020, and UID/EMS/ 00481/2013-FCT under CENTRO-01{0145-FEDER-022083. Authors also acknowledge the FCT (FCT - MCTES) for its financial support via the projects UIDB/00667/2020 (UNIDEMI).

DISCLAIMER

REFERENCES

[1] F. Pierron and M. Grédiac, “Towards Material Testing 2.0. A review of test design for identification of constitutive parameters from full-field measurements.”, *Strain*, 57, e12370 (2021).

Congress on Numerical Methods in Engineering 2024
4-6 September 2024, University of Aveiro, Portugal

Finite Element simulation of punching operations using loading rate-dependent constitutive and fracture models

David Abedul*, Lander Galdos[1], Borja Erice[1,2] and Eneko Sáenz de Argandoña[1]

[1] Mondragon Unibertsitatea, Faculty of Engineering, Department of Mechanics and Industrial Production, Loramendi 4, Arrasate-Mondragon 20500, Gipuzkoa, Spain

[2]IKERBASQUE, Basque Foundation for Science, Bilbao, Spain

[*]Corresponding author: dabedul@mondragon.edu

ABSTRACT

Blanking is a high-speed forming process that involves the separation of the material subjected to the operation. Moreover, these type of processes lead to elevated strain rates and temperatures on the sheared zone of the material.

In this study experimental punching operations carried out at varying cutting speeds (0.5, 5, 50, 500, and 5,000 mm/s) on a 5 mm thick 2205 Duplex stainless steel sheet are introduced. These operations are then replicated numerically via Finite Element simulations. The simulations employ a loading rate-dependent constitutive and fracture model, calibrated through an exhaustive material characterization campaign, to accurately capture and represent the behavior of the metal sheet.

The outcomes of the numerical simulations are compared with their experimental counterparts, evaluating force-displacement curves and sheared edge quality. This comparative analysis serves to assess the precision of the proposed numerical approach. The results highlight a great performance of the numerical punching simulations, demonstrating close agreement with the outcomes measured experimentally.

Congress on Numerical Methods in Engineering 2024
4-6 September 2024, University of Aveiro, Portugal

Finite element modelling of asymmetric rolling process – CNM 2024

H. Mouaouin*, F. Cazes*, G. Vincze† and I. Ionescu*

* LSPM, Université Sorbonne Paris Nord, Laboratoire des Sciences des Procédés et des Matériaux LSPM, CNRS, UPR 3407
Emails: Hajare.mouaouin@lspm.cnrs.fr / Fabien.cazes@lspm.cnrs.fr / Ioan.ionescu@lspm.cnrs.fr

† Centre of Mechanical Technology and Automation (TEMA), Department of Mechanical Engineering, University of Aveiro, 3810-193 Aveiro, Portugal, LASI - Intelligent Systems Associate Laboratory, Portugal
Email: gvincze@ua.pt

ABSTRACT

Rolling is a plastic deformation manufacturing process that has been in existence since the last century and is one of the most widely used processes in the industry.

In order to enhance the material's formability, asymmetric rolling can be used to optimize material properties (such as strength, elongation at rupture, and anisotropy) while improving the efficiency of the manufacturing process. To save cumbersome experiments, finite element modelling is a useful tool to virtually test and explore diverse rolling conditions, such as speeds rotations of rolls, thickness reduction or friction conditions between the sheet and the rolls.

A finite element model was developed with the Software Castem. The challenges of numerical implementation will be presented such as the choice of elements, boundary and contact conditions. For modelling, the anisotropic Hill criterion is used and combined with various hardening laws. The numerical model is validated by comparison with experimental results.

REFERENCES

[1] Kraner, J., Smolar, T. J., Volšak, D., Cvahte, P., Godec, M., & Paulin, I. (2020). A review of asymmetric rolling. *Materiali in Tehnologije*, *54*(5), 731-743.
[2] Vincze, G., Simões, F. J., & Butuc, M. C. (2020). Asymmetrical rolling of Aluminum Alloys and Steels : A review. *Metals*, *10*(9).
[3] Tamimi, S., Correia, J., Lopes, A. B., Ahzi, S., Barlat, F., & Grácio, J. (2014). Asymmetric rolling of thin AA-5182 sheets: Modelling and Experiments. *Materials Science and Engineering : A*, *603*, 150-159.

Congress on Numerical Methods in Engineering 2024
4-6 September 2024, University of Aveiro, Portugal

Using non-conforming meshes in the numerical simulation of sheet metal forming processes

Bárbara S. Curralo[†], Diogo M. Neto[†], Marta C. Oliveira[†]*, José L. Alves[†] and Luís F. Menezes[†]

† CEMMPRE, ARISE, Department of Mechanical Engineering, University of Coimbra, Portugal.
Email: barbarasafonso14@gmail.com; {marta.oliveira; diogo.neto; luis.menezes}@dem.uc.pt

† CMEMS, Microelectromechanical Systems Research Unit, University of Minho, Campus de Azurém, Guimarães, Portugal
Email: jlalves@dem.uminho.pt

ABSTRACT

The spatial discretization of deformable bodies has become an increasingly important parameter in the context of the numerical simulation with the finite element method. The accuracy of the results depends on the size of the finite elements adopted that should present good shape quality, which is not always possible, particularly when using conforming meshes. On the other hand, the use of conforming meshes that fulfil the mention requirements can lead to unaffordable computational times. These adversities can be overcome with the use of non-conforming meshes, but it is necessary to evaluate their impact on the results accuracy.

This study evaluates the performance of non-conforming meshes, composed of hexahedral trilinear finite elements, when applied to the numerical simulation of sheet metal forming processes. Three forming processes of different complexity are considered. The results are analysed for non-conforming and conforming meshes, with different levels of refinement. The zones suffering greater plastic deformation or present gradients in the distribution of local variables are subject to greater levels of refinement in the non-conforming meshes. The comparison in terms of accuracy of the results, include the evolution of global variables, such as the force applied by the tools, as well as local variables, such as the thickness distribution or the profile of the component after springback. The computational performance is evaluated based on the total number of increments, the average number of iterations per increment and the simulation time.

The implemented algorithm for mesh refinement does not allow to recover the geometric definition of curved surfaces because it only refines specific zones of the initial mesh. The study analyses the influence of the in-plane and through-thickness refinement, adopted for the critical and transition zones, in non-conforming meshes. The in-plane refinement should allow the description of the stress gradients, induced by the bending processes, to allow a correct prediction of the springback. The refinement in the thickness direction allows increasing the number of integration points, necessary for the correct description of the stress gradient through the thickness. Once these requirements are fulfilled, the results obtained with non-conforming meshes show a relative error, determined compared to the more refined conforming mesh, very small in the maximum forming force (<15%) and in the thickness variation (<5%). In the worst case, the use of a non-conforming mesh allowed a 10% reduction in computational time.

Congress on Numerical Methods in Engineering 2024
4-6 September 2024, University of Aveiro, Portugal

Comparing different remapping algorithms for adaptive mesh refinement applied to meso-scale analysis of additive manufacturing processes

Bruno M. Marques[†], Diogo M. Neto[*,†], Marta C. Oliveira[†], Luís F. Menezes[†] and José L. Alves[‡]

[†]CEMMPRE, ARISE, Department of Mechanical Engineering, University of Coimbra, Portugal
Email: bruno.marques@uc.pt; diogo.neto@dem.uc.pt; marta.oliveira@dem.uc.pt

[‡]CMEMS, University of Minho, Campus de Azurém, Guimarães, Portugal
Email: jlalves@dem.uminho.pt

ABSTRACT

Additive manufacturing is an attractive technology for producing customized and complex components, in particular the laser powder bed fusion (LPBF) process for metal parts. Several finite element modelling strategies have been developed to predict and mitigate manufacturing defects. However, the meso-scale thermo-mechanical simulations of large builds require an impractical runtime due to the wide range of length and time scales, i.e. both large number of finite elements and time increments is needed in the numerical analysis. Therefore, adaptive mesh refinement (AMR) and coarsening techniques have been used in numerical simulations to enhance the resolution in specific regions of a computational domain. This allows to reduce the total degrees of freedom while retaining the accuracy of the prediction.

Since the initial mesh is locally refined by subdividing the finite elements, some remapping procedure is required to transfer the state variables (defined at the integration points) from the old mesh to the new one, i.e. considering different levels of mesh refinement. Selecting the appropriate remapping algorithm depends on the specific requirements of the simulation and the computational resources available. The present study analyses three different remapping algorithms, namely the Inverse Isoparametric Mapping (IIM), the Dual Kriging (DK) method and the Incremental Volumetric Remapping (IVR). The IIM method uses the shape functions of the linear finite elements, while the DK method provides an explicit parametric interpolation. The IVR method is based in a volumetric approach, where the remapped state variables are obtained by means of a weighted average of the intersection volume between the meshes.

The accuracy of each remapping procedure was evaluated using a mathematical function to define the mapped state variable. Both refinement and coarsening procedures were applied to a parallelepipedal geometry defined by a non-conforming mesh composed of hexahedral finite elements. When applying the refinement procedure, some of the new integration points are generated outside of the envelope defined by the old integration points. Thus, globally the accuracy of all remapping methods was lower in the refinement procedure when compared with the coarsening one. Moreover, some remapping procedures yield values outside the range defined by the values in the initial mesh. This can be a problem in the equivalent plastic strain (non-negative) because negative values can be predicted. The IVR method does not suffer from this drawback since the mapped values are always within the range defined by the initial mesh.

Congress on Numerical Methods in Engineering 2024
4-6 September 2024, University of Aveiro, Portugal

Robust Finite Element models for the investigation of the two-stands rolling process

M. Antonicelli[1,*], G. Palumbo[1], A. Piccininni[1], S. Pantarotto[2], U. Liuzzo[2] and T. Gattamorta[2]

[1] Department of Mechanical Engineering, Mathematics & Management Engineering, Polytecnic University of Bari, via Orabona 4, 70125 Bari, Italy

[2] Marcegaglia Ravenna, via Baiona 141, 48123 Ravenna, Italy

* mattia.antonicelli@poliba.it

ABSTRACT

Rolling process is the key step during the production of steel. Within the production route of thin strips, cold rolling increases the strength due to the strain hardening but it also improves the surface finish and the dimensional quality of the product [1]. Due to the strict requirements of the rolled thin products, steel manufacturers are compelled to improve the quality and the productivity to maintain competitiveness [2]. Product quality and production economy depend on the mechanical behaviour of both the strip and the rolls. Therefore, the development of finite element (FE) models can support the process design by contributing to evaluate optimal values of the rolling parameters. The manufacturing of high-quality products is thus possible [3-4]. In this work, the two-stands rolling process (reversing cold mill, RCM) was modelled using the commercial FE code ABAQUS. On-site experimental data (strip and work rolls geometry, material properties, inward/backward tension) were acquired at the Marcegaglia plant and were used for tuning the FE model. Work-rolls were modelled as elastic deformable bodies (setting the value of the Young modulus by nanoindentation tests), while rolling forces from the RCM were used to estimate the Coefficient of Friction (CoF) at the roll-strip interface using an inverse analysis approach. The calibrated FE model was finally used to investigate the effect of main process parameters on the rolling process in order to check the effectiveness of the real working conditions.

REFERENCES

[1] J. T. Black, R. A. Kohser and E. P. DeGarmo, *Materials and processes in manufacturing*, Wiley, (2003).
[2] Z. Y. Jiang and A. K. Tieu, "Elastic–plastic finite element method simulation of thin strip with tension in cold rolling", *Journal of Materials Processing Technology*, vol. 130, pp. 511–515 (2002).
[3] K. Mori, K. Osakada and T. Oda, "Simulation of plane-strain rolling by the rigid-plastic finite element method", *International Journal of Mechanical Sciences*, vol. 24, no. 9, pp. 519–527 (1982).
[4] S. Chandra and U. S. Dixit, "A rigid-plastic finite element analysis of temper rolling process", *Journal of Materials Processing Technology*, vol. 152, no. 1, pp. 9–16 (2004).

Congress on Numerical Methods in Engineering 2024
4-6 September 2024, University of Aveiro, Portugal

Application of Long Short-Term Memory Neural Networks for the Identification of Material Hardening Parameters of Advanced High Strength Steels

Daniel J. Cruz[1], Manuel R. Barbosa[1,2], Abel D. Santos[1,2], Rui L. Amaral[1] and Jose Cesar de Sa[1,2]

[1] Institute of Science and Innovation in Mechanical and Industrial Engineering, R. Dr. Roberto Frias 400, 4200-465 Porto, Portugal; dcruz@inegi.up.pt; ramaral@inegi.up.pt;
[2] Faculty of Engineering, University of Porto, R. Dr. Roberto Frias s/n, 4200-465 Porto, Portugal; mbarbosa@fe.up.pt; abel@fe.up.pt; cesarsa@fe.up.pt

ABSTRACT

The integration of advanced metallic materials, including Advanced High-Strength Steels (AHSS), within the automotive industry has led to the development of advanced constitutive models, aiming to improve the accuracy and reliability of finite element analysis (FEA) results. The Homogeneous Anisotropic Hardening model (HAH) [1] based on distortional plasticity stands out as one of the latest and most precise models for accurately characterizing the plastic behavior of sheet metal materials, addressing phenomena such as the Bauschinger effect and permanent softening resulting from strain path changes.

This study explores the modelling capabilities of Long-Short Term Memory structures (LSTM), a type of Recurrent Neural Networks (RNN) in predicting the material hardening parameters of sheet metal materials using the results of experimental tests with reversed strain paths. Three different tests will be considered three-point bending-unbending tests, tension-compression tests with miniaturized samples, and planar reverse shear tests, are considered. RNNs are specifically designed to handle sequences over time, and their recursive architecture is particularly well-suited for modeling sequential data, such as plastic strains and back stresses in physics-based plasticity. Accordingly, the developed machine learning model uses a characteristic sequence of experimental data (e.g., punch-force displacement curve in the bending-unbending test) as input and generates the corresponding hardening parameters of the tested material as output. The data needed to design and train the network solutions was obtained from FEA, integrating the HAH model, using a user material subroutine.

The results indicate that the proposed LSTM-based approach performs comparably to traditional identification techniques in predicting material hardening parameters. This highlights the effectiveness of the developed procedure in characterizing hardening behavior under both monotonic and load reversal loadings for various materials, especially those extensively used in industrial applications, ranging from mild steels to AHSS.

REFERENCES

[1] Barlat, S.-Y. Yoon, S.-Y. Lee, M.-S. Wi, J.-H. Kim, Distortional plasticity framework with application to advanced high strength steel, International Journal of Solids and Structures, 2020, 202, 947-962.
[2] D. J. Cruz, M. R. Barbosa, A. D. Santos, R. L. Amaral, J. C. de Sa, and J. V. Fernandes, Recurrent Neural Networks and Three-Point Bending Test on the Identification of Material Hardening Parameters, Metals, 2024, 14, 8.

Congress on Numerical Methods in Engineering 2024
4-6 September 2024, University of Aveiro, Portugal

Numerical study on continuous bending under tension – CNM 2024

J. Pereira*, C. Pereira*, P. Prates*, M. Butuc* and G. Vincze*

* Centre of Mechanical Technology and Automation (TEMA), Department of Mechanical Engineering, University of Aveiro, 3810-193 Aveiro, Portugal, LASI - Intelligent Systems Associate Laboratory, Portugal
Email: joaofapereira@ua.pt, csep@ua.pt, prates@ua.pt, cbutuc@ua.pt, gvincze@ua.pt

ABSTRACT

The reduction of gas emissions is closely linked to the weight reduction of vehicles. In pursuit of lighter and safer structural components, advanced materials undergo continuous development to enhance their strength, work-hardening capability, formability, and energy absorption. The primary focus of research in metal forming is to enhance material response for improved ductility and energy absorption under crash loading conditions. In addition to the development of new alloys, innovative forming processes are being explored to meet these requirements. One such process, developed to capitalize on the advantages of incremental forming, is the continuous bending under tension (CBT) process. In this process, a bending moment is applied to a sheet metal specimen subjected to uniaxial tension. Consequently, the localized deformation offsetting the necking that usually occur in pure tension. Recent studies by Knezevic et al. and Poulin et al. [1,2] have demonstrated that this process can achieve plastic strains superior to those achieved by traditional forming processes.

The objective of the present study was to investigate the effect of the continuous bending under tension process on dual-phase steels using Abaqus commercial software. The impact of process parameters such as depth setting, distance between bending rolls, thickness, and rolls' diameter, as well as simulation-specific variables like the number of passages and friction coefficient, were analysed. Additionally, the effect of sheet thickness was also studied.

REFERENCES

[1] M. Knezevic, C. M. Poulin, X. Zheng, S. Zheng, Irene J. Beyerlein, Strengthening of alloy AA6022-T4 by continuous bending under tension. Mat. Sci. Eng. A 758, pp. 47–55, (2019)
[2] Poulin CM, Korkolis YP, Kinsey BL, Knezevic M (2019) Over five-times improved elongation-to-fracture of dual-phase 1180 steel by continuous-bending-under-tension. Material and Design 161, pp. 95–105, (2019).

Congress on Numerical Methods in Engineering 2024
4-6 September 2024, University of Aveiro, Portugal

Predicting in-situ hot cracking in metal additive manufacturing using a thermomechanical phase-field fracture model

Roya Darabi[*], Erfan Azinpour[*], Ana Reis[*] and Jose Cesar de Sa[*]

[*] Faculty of Engineering of the University of Porto (FEUP)
Rua Dr. Roberto Frias, 400, Porto, 4200-465, Portugal
e-mail: {rdarabi, azinpour, arlr, cesarsa}@fe.up.pt

ABSTRACT

Metal Additive Manufacturing (MAM) has progressed from rapid prototyping to a vital role in manufacturing. Known for its design versatility, MAM faces challenges in understanding processing parameters and detecting defects like hot cracking and porosities. We propose a thermomechanical phase-field fracture model for predicting in-situ hot cracking, grounded in thermodynamic consistency. This complex process is simulated using a hierarchical multi-application framework. Initially, adaptive mesh refinement (AMR) calculates cladding line shapes by the laser. Thermal simulation data then computes thermal strains in 3D shapes, considering cladding geometries. Phase-field fracture evaluates the effects of thermal gradients and shrinkage strains on hot cracking. Our model [1] employs staggered time schemes to manage time variations between applications, ensuring the capture of crucial phenomena. Damage is coupled with thermoelastic plasticity, incorporating heat conduction and temperature-dependent fracture properties. Implemented within the Multiphysics Object-Oriented Simulation Environment (MOOSE) framework, the model examines the influence of laser power and scanning speed on fracture properties.

Comparative evaluations with experiments illuminate thermal-induced cracking evolution during heating. This study aims to improve understanding of MAM processes, offering insights for enhancing manufacturing outcomes. Simulation results reveal key features of hot crack formation, contributing to process optimization and a deeper understanding of crack mechanisms.

REFERENCES

[1] Roya Darabi, Erfan Azinpour, Ana Reis, Jose Cesar de Sa. “Elasto-plastic phase-field analysis of thermal induced-cracking and its application towards metal additive manufacturing”, *European Journal of Mechanics - A/Solids, Vol. 107 (2024), 105369.*

This page intentionally left blank

TS12: Optimization and inverse analysis in applied engineering

This page intentionally left blank

Congress on Numerical Methods in Engineering 2024
4-6 September 2024, University of Aveiro, Portugal

Maximum stiffness versus minimum weight approaches in structural topology optimization

Diego Villalba* *†, João Dias-de-Oliveira*, José París†, António Andrade-Campos*, Robertt Valente*, and Fermín Navarrina†

* TEMA, Departamento de Engenharia Mecânica, Universidade de Aveiro, Portugal

† GMNI, Grupo de Métodos Numéricos en Ingeniería, Universidade da Coruña, España
Email: diego.villalba.rama@udc.es

ABSTRACT

Topology optimization of structures has gained wide popularity in the scientific community as a result of, among other things, the development of the additive manufacturing techniques and the 3D printing techniques. In this research, an extensive comparative analysis of the maximum stiffness [1] and the minimum weight [2] problems is developed. For this purpose, the maximum stiffness problem is formulated in its classical way, considering a volume constraint. The local stress constraints are introduced in the minimum weight problem, so that the maximum allowable stress value is not exceeded. An overweight constraint [3] is considered for the design process instead of local stress constraints. The advantages of the minimum weight problem over the maximum stiffness approaches are shown and analysed with a comparative analysis. This analysis is developed by means of the solution of some benchmark problems. Two different strategies to define the material layout in the domain are considered in the solutions of the benchmark examples: a uniform relative density per element (SIMP approach) [4] and a relative density defined with B-splines (IGA-formulation) [5]. The comparison between both approaches shows that the minimum weight formulation provides a unique solution for each problem while in the case of minimum compliance approaches solutions depend on the volume constraint. Regarding stress constraints, the results show that these have to be considered in the problem to avoid instability and structural integrity problems. The minimum weight approach, contrary to common assumption, cannot be considered equivalent in terms of attained solutions to the maximum stiffness approach, since there are important differences in terms of structural stiffness between both approaches.

REFERENCES

[1] M. P. Bendsøe and N. Kikuchi, “Generating optimal topologies in structural design using a homogenization method”, *Comput. Methods Appl Mech Engrg*, 71, 197-224 (1988).
[2] F. Navarrina, I. Muiños, I. Colominas and M. Casteleiro, “Topology optimization of structures: A minimum weight approach with stress constraints”, *Adv Eng Softw*, 36, 599-606 (2005).
[3] D. Villalba, J. París, I. Couceiro, I. Colominas and F. Navarrina, “Topology optimization of structures considering minimum weight and stress constraints by using the Overweight Approach”, *Eng. Struct.*, 273, (2022).
[4] M. P. Bendsøe and O. Sigmund, “Material interpolation schemes in topology optimization”, *Arch Appl Mech*, 36, 599-606 (2005).
[5] T. Hughes, J. Cottrell and Y. Bazilevs, “Isogeometric analysis: CAD, finite elements, NURBS, exact geometry and mesh refinement”, *Comput Methods Appl Mech Engrg*, 194, 4135-4195 (2005).

Congress on Numerical Methods in Engineering 2024
4-6 September 2024, University of Aveiro, Portugal

Design and Optimization of Steel Jackets for Offshore Wind: A Comparison Study on Three-Legged versus Four-Legged Configurations

N. Fernández-Rodríguez*, I. Couceiro, X. Nogueira and I. Colominas

Grupo de Métodos Numéricos en Ingeniería (GMNI),
E.T.S. Ingeniería de Caminos, Canales y Puertos, Universidade da Coruña, España
Email: n.fernandez2@udc.es
web page: http://caminos.udc.es/gmni/

ABSTRACT

In recent years, the use of offshore wind turbines for energy generation has grown significantly making it imperative to conduct further research on several details of their deployment. In this study, the optimization of three-legged jacket foundations is considered. Two jackets with different orientations with respect to the incoming environmental loads are modelled the g30, which has two legs facing the main incoming environmental actions and the g90, which has one of the legs facing the main incoming environmental actions. The objective is to understand the sensitivity of the modelled jackets with respect to the predominant direction of incident loads. The finite element model used is based on beam elements for every part of the offshore wind structure considering all the pieces. The structural dynamic behaviour of the fully coupled model generated is then analysed by means of a nonlinear time integration algorithm in order to incorporate, additionally the rotation of the blades.

The optimization focuses on minimizing the weight of the substructure where the design variables are the global geometry of the substructure as well as the cross-sectional dimensions of the members. The design variables controlling the overall shape of the jacket are the radii of the lower and upper bases of the circumscribed triangles. The requirements of the structure are formulated into three different sets of constraints: Ultimate Limit State, Fatigue Limit State, and natural frequencies. In order to obtain a more accurate numerical approximation, the rotational movement of the blades is included, such that a nonlinear time integration algorithm is used to update the geometry between time steps. The solution to the optimization problem proposed is based on the application of Sequential Linear Programming, reducing the nonlinear optimization problem to a series of approximated linear problems that are solved using the Simplex Method. A first-order sensitivity analysis of the objective function and constraints is obtained by analytical derivates.

For both models, the optimization algorithm has reduced the initial weight of the jacket substructure by around 40%. However, the optimal designs come with some limitations. On the one hand, the g30 jacket is mostly affected by fatigue, while the g90 jacket experiences its main restriction in compression stress in its elements. The g90 and optimal four-legged jacket design obtained in Couceiro et al. [1] exhibited a similar behaviour when facing the imposed loads. The differences observed in the optimized three-legged jackets and from their comparison to the results of the optimized four-legged jacket demonstrate the sensitivity of the response of the structure to the directionality of the loads. Therefore, for a more precise study, it will be necessary to include a variable orientation of the jacket, along with incorporating a sensitivity analysis of the structural response according to the turbine orientation and the wave and wind direction.

REFERENCES

[1] I. Couceiro, J. París, F. Navarrina, R. Guizán and I. Colominas, “Optimization of Offshore Steel Jackets: Review and Proposal of a New Formulation for Time-Dependent Constrains”, *Archives of Computational Methods in Engineering,* 27, 1049–1069 (2019).

Congress on Numerical Methods in Engineering 2024
4-6 September 2024, University of Aveiro, Portugal

Una aproximación a la optimización topológica de estructuras con restricciones en tensión y autovalores.

M. Rey*†, I. Couceiro†, J. París† y L. Ramírez†

† Grupo de Métodos Numéricos en Ingeniería-GMNI, Centro de Innovación Tecnolóxica en Edificación e Enxeñería Civil-CITEEC. Escuela de Ingeniería de Caminos, Canales y Puertos, Universidade da Coruña, Campus de Elviña, A Coruña, 15008, España.
Página web: http://caminos.udc.es/gmni, e-mail: martin.rey1@udc.es

RESUMEN

La optimización topológica de estructuras es una disciplina que basa su desarrollo en la obtención de la distribución óptima de material en un dominio dado y bajo unas cargas y condiciones de contorno concretas. Desde finales de los 80, cuando esta disciplina empezó a ganar importancia a través de los trabajos de investigadores como Bendsøe y Kikuchi [1], la formulación más implementada para la obtención del óptimo estructural ha sido la formulación de máxima rigidez con restricciones en volumen. Esto es así debido a la gran cantidad de ventajas computacionales que ofrece.

Sin embargo, diversos autores como Duysinx o París [2,3] propusieron en su momento una formulación distinta a la ya expuesta, implementando el peso como función objetivo y restricciones locales o globales en tensión. Esta metodología se ajusta más a las formas habituales utilizadas en otras ramas de la optimización estructural en ingeniería, imponiendo un control mayor sobre las tensiones y garantizando la validez del resultado final obtenido en cuanto al buen comportamiento resistente de la estructura óptima.

A mayores, es importante señalar la importancia que los problemas de inestabilidad elástica y dinámica juegan en la práctica habitual de los ingenieros estructurales. Es habitual que estos fenómenos condicionen fuertemente los diseños óptimos en tanto el pandeo y las frecuencias naturales de vibración suelen ser un limitante en estructuras esbeltas. Es por esto por lo que la cuestión de los problemas de autovalores en un medio continuo para la optimización topológica de estructuras ha sido también estudiada, pero casi en su totalidad desde el punto de vista de la formulación en máxima rigidez. Recientemente, Ferrari y Sigmund [4] publicaron un trabajo en este sentido.

En este trabajo se propone el desarrollo de una metodología de optimización topológica de estructuras con restricciones en tensión, pandeo linealizado y frecuencias naturales de vibración, imponiendo como función objetivo el mínimo peso. El objetivo principal es la obtención de óptimos estructurales en un medio continuo sobre los cuales se tenga un control efectivo de las tensiones y que cumplan con todos los criterios de estabilidad necesarios. Además, se exponen una serie de resultados numéricos acordes a problemas habituales en ingeniería civil.

REFERENCIAS

[1] Bendsøe, M. P. and Kikuchi, N. (1988). Generating optimal topologies in structural design using a homogenization method. Computer Methods in Applied Mechanics and Engineering, 71(2):197–224.
[2] Duysinx, P. and Bendsøe, M.P. (1998), Topology optimization of continuum structures with local stress constraints. Int. J. Numer. Meth. Engng., 43: 1453-1478.
[3] París, J. (2008). Restricciones en tensión y minimización del peso: Una metodología general para la optimización topológica de estructuras. PhD thesis, Universidade da Coruña, ETS de Enxeñaría de Camiños, Canais e Portos.
[4] Ferrari, F. and Sigmund, O. (2019). Revisiting topology optimization with buckling constraints. Structural and Multidisciplinary Optimization, 59(5):1401–1415.

Congress on Numerical Methods in Engineering 2024
4-6 September 2024, University of Aveiro, Portugal

PVDF-based Thin Actuator: Piezoelectric Characterization using an Inverse-FEM algorithm

António Diogo André*, Pedro Martins†

* Associated Laboratory of Energy, Transports and Aeronautics (LAETA), Biomechanic And Health Unity (UBS), Institute of Science and Innovation in Mechanical and Industrial Engineering (INEGI), Porto, Portugal
Email: a.diogo.andre@icloud.com

† Instituto de Investigación en Ingeniería de Aragón (i3A), Universidad de Zaragoza, Zaragoza, Spain
Email: palsm@fe.up.pt

ABSTRACT

Piezoelectric materials offer a wide range of applications, such as in rehabilitation scenarios, since they have the ability to function as motion sensors [1] or re-educational feedback actuators [2]. Moreover, piezoelectric materials are easy to process, which allows for the different experimental protocols found in the literature, using different fillers and solvents [3, 4].

As a result, material properties in the mechanical, chemical or piezoelectric domains are prone to significant changes which poses additional problems regarding their experimental characterization. As a consequence, and based on the mechanical behaviour of polyvinylidene fluoride (PVDF)-based thin films subjected to electrical inputs, an inverse-FEM Algorithm was developed to match the piezoelectric constants, using a software scheme combining *MathWorks Matlab* and *DS Abaqus* (Figure 1).

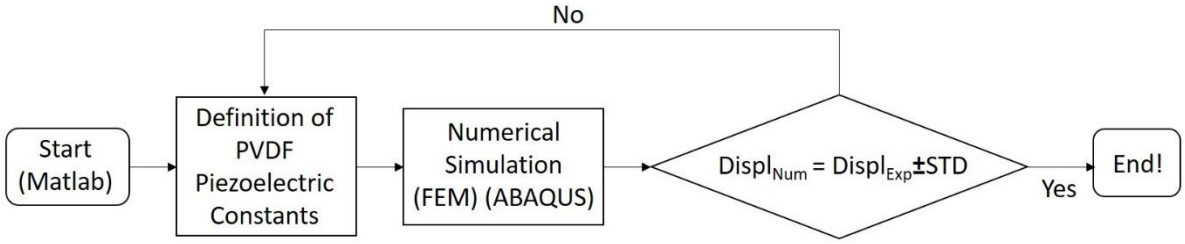

Figure 1. FEM inverse algorithm.

REFERENCES

[1] Homayounfar S. and Andrew TL, "Wearable Sensors for Monitoring Human Motion: A Review on Mechanisms, Materials, and Challenges," SLAS Technology, vol. 25, p. 9–24, February 2020.

[2] Yeh CH et al, "Application of piezoelectric actuator to simplified haptic feedback system," Sens Act Phy, vol. 303, p. 111820, March 2020.

[3] Ji W. et al "The effect of filler morphology on the dielectric performance of polyvinylidene fluoride (PVDF) based composites," Composites Part A: Applied Science and Manufacturing, vol. 118, p. 336–343, March 2019.

[4] Bottino A. et al, "Solubility parameters of poly(vinylidene fluoride)," Journal of Polymer Science Part B: Polymer Physics, vol. 26, p. 785–794, April 1988.

Automatic Identification of Macroscopic Constitutive Parameters for Polycrystalline Materials based on Computational Homogenisation

Guilherme F. Gonçalves*,[1], Rui P. Cardoso Coelho[1], Igor A. R. Lopes[2]

[1] DEMec FEUP, Departamento de Engenharia Mecânica da Faculdade de Engenharia da Universidade do Porto

[2] INEGI, Institute of Science and Innovation in Mechanical and Industrial Engineering

ABSTRACT

A numerical framework for the automatic calibration of macroscopic constitutive parameters, based on the analysis of polycrystalline RVEs with computational homogenisation, is proposed. The said framework is composed of four building blocks: i) the RVEs of a polycrystalline material, and the crystal plasticity model in [1] to define the behaviour of each of grain, ii) the macroscopic von Mises elastoplastic model, along with the Nadai-Ludwik hardening law, whose parameters are calibrated, iii) the optimisation algorithms employed to solve the inverse identification problem, and iv) a first-order homogenisation approach to link the micro- and macro-scales.

Initially, the performance of several optimisation algorithms is assessed by means of a reference identification problem. Thereafter, different calibration strategies are tested, by employing distinct loading cases, definitions of the objective function, and evaluating the impact of the sequence of determination of the elastic and plastic parameters. The accuracy of the calibrated models is assessed by comparing the results of macroscopic simulations against an FE2 model. The computing time of the FE2 simulations is 5 orders of magnitude larger than that of the macroscopic simulations, demonstrating the suitability of this framework for obtaining efficient micro-mechanics-informed constitutive models. Finally, validation against experimental data further establishes the robustness of the proposed approach.

References

[1] M. Vieira de Carvalho, D. de Bortoli, F. Andrade Pires, Consistent modeling of the coupling between crystallographic slip and martensitic phase transformation for mechanically induced loadings, International Journal for Numerical Methods in Engineering 123 (2022) 3179-3236

Congress on Numerical Methods in Engineering 2024
4-6 September 2024, University of Aveiro, Portugal

A Neural Network approach to Topology Optimization of acoustic metamaterials

D. Yago*[,♢,†], G. Sal-Anglada[♢,†], D. Roca[♢,†], J. Cante[♢,†] and J. Oliver[†,♤]

[♢] Escola Superior d'Enginyeries Industrial, Aeroespacial i Audiovisual de Terrassa (ESEIAAT), Universitat Politècnica de Catalunya · BarcelonaTech (UPC), Spain

† International Center for Numerical Methods in Engineering (CIMNE), Spain

[♤] Escola Tècnica Superior d'Enginyeria de Camins, Canals i Ports de Barcelona (ETSECCPB), Universitat Politècnica de Catalunya · BarcelonaTech (UPC), Spain

ABSTRACT

This study addresses the intricate design challenges associated with acoustic metamaterials for effective noise attenuation, with a specific focus on Multiresonant Layered Acoustic Metamaterial (MLAM) panels due to their exceptional performance in attenuating low-frequency noise below 1000 Hz [1]. These acoustic metamaterials exploit the coupling effect between two resonant frequencies, enabling these panels to achieve remarkable noise attenuation relative to their equivalent mass homogeneous counterparts.

The proposed design strategy introduces a novel two-phase approach to tackle its design: (1) a neural network-based surrogate model is integrated to efficiently assess individual effective layer properties, obtained through homogenization, and (2) a topology optimization technique is employed to maximize noise attenuation while preserving a coupled Sound Transmission Loss (STL) response. This optimization process is guided by a genetic algorithm in tandem with Deep Neural Network (DNN)-based models, resulting in configurations that surpass 20 dB of noise attenuation over 330 Hz when compared to homogeneous materials with equivalent surface density.

Notably, the use of the surrogate model significantly improves accuracy in predicting effective properties and evaluating STL response, outperforming conventional polynomial interpolation techniques. Moreover, the machine learning-based model drastically reduces the computational cost of optimizations by several orders of magnitude in contrast to direct numerical simulations. This cost-effective approach empowers the optimization of multiple objective functions and constraints [2,3].

REFERENCES

[1] D. Roca, J. Cante, O. Lloberas-Valls, T. Pàmies, and J. Oliver. "Multiresonant Layered Acoustic Metamaterial (MLAM) solution for broadband low-frequency noise attenuation through double-peak sound transmission loss response", *Extreme Mechanics Letters*, 47, 101368 (2021). DOI: 10.1016/j.eml.2021.101368.

[2] G. Sal-Anglada, D. Yago, J. Cante, J. Oliver, and D. Roca. "Optimal design of Multiresonant Layered Acoustic Metamaterials (MLAM) via a homogenization approach", *Engineering Structures*, 293, 116555 (2023). DOI: 10.1016/j.engstruct.2023.116555.

[3] D. Yago, G. Sal-Anglada, D. Roca, J. Cante, and J. Oliver. "Machine learning in solid mechanics: application to acoustic metamaterial design". *International Journal for Numerical Methods in Engineering*. Under Review.

TS14: Computational modelling in mechanobiology and tissue engineering

This page intentionally left blank

Congress on Numerical Methods in Engineering 2024
4-6 September 2024, University of Aveiro, Portugal

Graded porous scaffolds mimic in vivo bone regeneration mechanical environment

Mora-Macías J.[1], Santos J.E.[2], Castro A.P.G. [2,3], Fernandes P.R.[2]

[1] Departamento de Ingeniería Minera, Mecánica, Energética y de la Construcción, Escuela Técnica Superior de Ingeniería, Universidad de Huelva, España.
Email: juan.mora@dimme.uhu.es

[2] IDMEC, Instituto Superior Técnico, Universidade de Lisboa, Portugal.
Email: jorge.e.santos@tecnico.ulisboa.pt, andre.castro@tecnico.ulisboa.pt, paulo.rui.fernandes@tecnico.ulisboa.pt

[3] ESTSetúbal, Instituto Politécnico de Setúbal, Portugal

ABSTRACT

It is accepted in bone tissue engineering that scaffolds should mimic the mechanical environment for bone healing, i.e., to allow cell and tissue deformations that lead to optimal mechanical signals for ossification [1]. The mechanical properties of the callus, softer than intact bone, are totally different throughout a bone regeneration process [2,3] and, therefore, it is difficult to establish a reference in terms of mechanical strain when manufacturing a scaffold. Our hypothesis is that, for the treatment of large bone defects requiring fixation devices, the strain field within the scaffold should mimic this within the callus at the moment of maximum bone tissue production observed in alternative bone regeneration processes to treat the same defect.

The strain field within the callus in a bone regeneration process for treatment of a 15 mm critical size defect in a sheep metatarsus, by bone transport, has been analysed computationally, based on CT images obtained previously [2,3]. Different models of triply periodic minimal surface (TPMS) 3D printable scaffolds with graded porosity (from 60 to 80%, 65 to 85% and 70 to 90%) and appropriate dimensions to cover the same initial defect of 15mm, have been designed [4] and simulated using real boundary conditions measured during the alternative regeneration process in vivo [3].

The outputs show that the proposed scaffolds allow for a strain distribution close to this within the callus at the maximum ossification period. This means that it shall be possible, in a future work, to define a procedure to optimize these graded porous scaffolds; such scaffolds shall generate a mechanical environment similar to what is found in a callus during the period of maximum ossification.

JMM would like to acknowledge the funding from Spanish State Research Agency (PID2020-113790RB-I00/AEI/10.13039/501100011033); JES, APGC and PRF would like to thank Fundação para a Ciência e Tecnologia (FCT, Portugal) for the funding provided, through IDMEC, under LAETA projects UIDB/50022/2020 and UIDP/50022/2020, and PhD Grant UI/BD/150995/2021.

REFERENCES

[1] B.M. Willie et al., "Designing biomimetic scaffolds for bone regeneration: why aim for a copy of mature tissue properties if nature uses a different approach?", *Soft. Matter.*, 6:4976–4987 (2010)
[2] J. Mora-Macías et al., "Comparison of methods for assigning the material properties of the distraction callus in computational models", *J. Numer. Method. Biomed. Eng*., 35(9):e3227 (2019)
[3] J. Mora-Macías et al., "In vivo mechanical characterization of the distraction callus during bone consolidation", *Ann. Biomed. Eng.,* 43(11):2663-74 (2015)
[4] A.P.G. Castro et al., "Permeability versus Design in TPMS Scaffolds", *Materials (Basel),* 22;12(8):1313 (2019)

Congress on Numerical Methods in Engineering 2024
4-6 September 2024, University of Aveiro, Portugal

Advancements in Finite Element Formulations for Accurate Simulation of Melanoma Cancer Stem Cells Growth

R. Palma[†], B. Blanco[*], H. Gómez[+], J. Soler[^], and G. Rus[†]

† Department of Structural Mechanics and Hydraulic Engineering, University of Granada, Spain
Email: rpalgue,grus@go.ugr.es

[*] Department of Electronics and Computing, Universidade de Santiago de Compostela, Spain
Email:Beatriz.blanco@usc.es

[+]School of Mechanical Engineering, Purdue University, USA
Email: hectorgomez@purdue.edu

^Department of Applied Mathematics, University of Granada, Spain
Email:jsoler@ugr.es

ABSTRACT

Cancer stem cells, resistant to conventional therapies, stand as pivotal targets in cancer research. An emerging technique aimed at disrupting the growth and migration of these resilient cells involves mechanotransduction through low-intensity ultrasounds [1]. Nevertheless, understanding and modeling tumor growth presents a significant challenge for the computational mechanics community before implementing these mechanotransduction techniques.

This work focuses on melanoma cancer stem cells, specifically the A375 cell line, within a poroelastic framework that incorporates solid and fluid stresses over the timescale of days to explore the intricate interplay between mechanical forces and fluid dynamics. Consequently, the poroelastic constitution offers a realistic representation of the tumor microenvironment, including factors such as interstitial fluid and cytoskeleton dynamics.

Theoretically, tumor growth may be conducted by two continuum theories: Classical Continuum Mechanics (CCM) and Micropolar Mechanics (MM). In the case of MM, each material point at the continuum level is linked to a rigid body, thereby transmitting both linear and angular momenta. The initial model, proposed by the author of the present work in [1], is based on CCM and under the assumption of small strain. The main aim of this research is to enhance the model by integrating micro-structure within the framework of MM.

On this ground, this work presents a numerical formulation based on MM and within the Finite Element (FE) method [2] for modeling tumor growth. Furthermore, the model assumes a poro-visco-elastic material constitution, incorporating Volterra-Lotka interactions among different cell phases. Subsequently, the FE formulation is implemented in the research code FEAP, which belongs to the University of California at Berkeley, and the code is validated against experimental results obtained from the Ultrasonic Laboratory at the University of Granada.

REFERENCES

[1] B. Blanco et al. “Mechanotransduction in tumor dynamic modeling”, *Physics of Life Reviews*, 44, 279-301 (2023).

[2] O.C. Zienkiewicz and R.L. Taylor, *The finite element method*, McGraw Hill, Vol. I., 1989, Vol. II, (1991).

Congress on Numerical Methods in Engineering 2024
4-6 September 2024, University of Aveiro, Portugal

Pore size evaluation as a tool to design TPMS-based scaffolds for tissue engineering

J. E. Santos[1], P. R. Fernandes[1] and A. P. G. Castro[1,2]

[1] IDMEC, Instituto Superior Técnico, Universidade de Lisboa, Portugal,
Email: jorge.e.santos@tecnico.ulisboa.pt, paulo.rui.fernandes@tecnico.ulisboa.pt, andre.castro@tecnico.ulisboa.pt

[2] ESTSetúbal, Instituto Politécnico de Setúbal, Portugal

ABSTRACT

The purpose of a Tissue Engineering (TE) scaffold is to provide support for cells adhesion, proliferation and differentiation into a specific phenotype. These cellular phenomena depend on the scaffold design and its structural properties (geometry, porosity, pore size, pore interconnectivity and surface area (SA)). Pore size has been reported to directly influence the differentiation of Mesenchymal Stem Cells (MSCs) [1] and affect the scaffolds mechanical and transport properties [2], [3]. Larger pores may result in decreased compressive strength, while smaller pores can enhance mechanical stability. Well-connected pores distribute the applied load more evenly, preventing localized stress concentrations. Therefore, pore size quantification, control and correlation with the mechanical properties is crucial to the successful design of TE scaffolds.

TPMS-based scaffolds have been considered for TE applications due to their high surface area per volume ratios and can be designed/adapted to various geometrical and topological configurations including density gradients, cell size gradients and/or hybrid structures, according to the desired application. It is, therefore, difficult and unclear how to quantify the pore size distribution (PSD) of such structures. This work shows how common image segmentation methods, namely the Local Thickness (LT) and Medial Axis/Skeleton, can be applied and used as auxiliary design tools to accurately extract the PSD of four TPMS-based scaffolds (Fischer-Koch S surface, Schwartz Diamond, Schoen Gyroid and Schwartz Primitive, with linear or graded porosity) for correlation with the mechanical and biological output of the scaffolds.

To achieve pore sizes greater than 300 μm, ideal for Bone TE, the outcomes show that TPMS-based scaffolds should have cell size superior to 1.625 mm, and porosities superior to 50%. The Schwartz Primitive have the largest pore diameters, contrasting with the Fischer-Koch S surface. To conclude, porous structures for application in TE and other engineering fields can be developed with controlled pore size, evolving from porosity-controlled frameworks.

The authors would like to thank Fundação para a Ciência e Tecnologia (FCT, Portugal) for the funding provided, through IDMEC, under LAETA projects UIDB/50022/2020 and UIDP/50022/2020, and PhD Grant UI/BD/150995/2021.

REFERENCES

[1] V. Karageorgiou and D. Kaplan, "Porosity of 3D biomaterial scaffolds and osteogenesis," *Biomaterials*, 26, 27, 5474–5491 (2005)

[2] A. P. G. Castro, J. Santos, T. Pires, and P. R. Fernandes, "Micromechanical Behavior of TPMS Scaffolds for Bone Tissue Engineering," *Macromol Mater Eng*, 305, 12, 2000487 (2020)

[3] J. E. Santos, T. Pires, B. P. Gouveia, A. P. G. Castro, and P. R. Fernandes, "On the permeability of TPMS scaffolds," *J Mech Behav Biomed Mater*, 110, 103932 (2020)

Congress on Numerical Methods in Engineering 2024
4-6 September 2024, University of Aveiro, Portugal

Computational Fluid Dynamics with mesh morphing in comparison with Fluid-Structure Interaction in Ascending Thoracic Aortic Aneurysm

Rodrigo Valente[1,2,*], André Mourato[1,2], Moisés Brito[1,2], José Xavier[1,2], Stéphane Avril[3], António Tomás[4], José Fragata[4,5]

[1] UNIDEMI, Department of Mechanical and Industrial Engineering, NOVA School of Science and Technology, Universidade NOVA de Lisboa, Portugal,
rb.valente@campus.fct.unl.pt, af.mourato@campus.fct.unl.pt, moisesbrito@fct.unl.pt, jmc.xavier@fct.unl.pt
[2] Laboratório Associado de Sistemas Inteligentes, LASI, Portugal,
[3] École des Mines de Saint-Étienne, University of Lyon, Inserm, Sainbiose U1059, France, avril@emse.fr
[4] Department of Cardiothoracic Surgery, Santa Marta Hospital, Portugal, acruztomas@gmail.com
[5] Department of Surgery and Human Morphology, NOVA Medical School, Portugal, jose.fragata@nms.unl.pt

ABSTRACT

Ascending Thoracic Aorta aneurysm (ATAA) is a pathology characterised by permanent dilatation of the vessel, caused mainly by ageing, genetics, or disturbed hemodynamics. Current guidelines diagnose the ATAA if an increase of 50% of the healthy diameter is present, and corrective surgery is applied if it surpasses 55 mm.
Computational Fluid Dynamics (CFD) models have been developed to predict the hemodynamics in the aorta. However, by not including wall dynamics in those models, Fluid-Structure Interaction (FSI) models have gained more relevance [1]. Besides, the FSI allows an increase in accuracy with an increase in computational cost. Augment CFD with a mesh morphing method based on a displacement vector to each node of the outside wall allows for a change in the area of interest across the computational time, resulting in a numerical model with a computational cost very similar to a regular CFD but including the wall motion effects as in an FSI model. This paper aims to improve the CFD model with patient-specific mesh morphing to approximate the hemodynamics without compromising the computational effort of FSI methods. The mesh morphing, incorporated as a boundary condition in the CFD model, was extracted from an angiogram CT scan with ECG. These results are compared to an FSI model with prestress [2]. Furthermore, the Young Module in the FSI was calibrated to match the volume variation in the wall deformation data.

REFERENCES

[1] Mourato A, Valente R, Xavier J, Brito M, Avril S, de Sá JC, Tomás A, Fragata J. Computational Modelling and Simulation of Fluid Structure Interaction in Aortic Aneurysms: A Systematic Review and Discussion of the Clinical Potential. Applied Sciences. 2022;12(16):8049. https://doi.org/10.3390/app12168049

[2] S. Bäumler K, Vedula V, Sailer AM, Seo J, Chiu P, Mistelbauer G, Chan FP, Fischbein MP,Marsden AL, Fleischmann D. Fluid-structure interaction simulations of patient-specific aortic dissection. Biomech Model Mechanobiol. 2020 Oct;19(5):1607-1628. doi: 10.1007/s10237-020-01294-8. Epub 2020 Jan 28. PMID: 31993829.

ACKNOWLEDGEMENT

The authors acknowledge the Portuguese Fundação para a Ciência e a Tecnologia (FCT - MCTES) for its financial support via the project AneurysmTool (doi: 10.54499/PTDC/EMDEMD/1230/2021). A. Mourato and R. Valente are also grateful to FCT for the PhD grants UI/BD/151212/2021 and 2022.12223.BD, respectively.

Congress on Numerical Methods in Engineering 2024
4-6 September 2024, University of Aveiro, Portugal

Using Simple Unidimensional Networks to Estimate Pressure Spatial and Temporal Variations in Ascending Thoracic Aortic Aneurysms

André Mourato [1,2]*, Rodrigo Valente[1], Moisés Brito[1,2], José Xavier[1,2], Stéphane Avril[3], António Tomás[4], José Fragata[4,5]

[1] UNIDEMI, Department of Mechanical and Industrial Engineering, NOVA School of Science and Technology, Universidade NOVA de Lisboa, Portugal
Email: af.mourato@campus.fct.unl.pt, rb.valente@campus.fct.unl.pt
[2] Laboratório Associado de Sistemas Inteligentes, LASI, Portugal
Email: moisesbrito@fct.unl.pt, jmc.xavier@fct.unl.pt
[3] École des Mines de Saint-Étienne, University of Lyon, Inserm, Sainbiose U1059, France
Email: avril@emse.fr
[4] Department of Cardiothoracic Surgery, Santa Marta Hospital, Portugal
Email: acruztomas@gmail.com
[5] Department of Surgery and Human Morphology, NOVA Medical School, Portugal
Email: jose.fragata@nms.unl.pt

ABSTRACT

Numerical models emerged as robust tools for replicating the biomechanics of Ascending Thoracic Aortic Aneurysms (ATAA), allowing the development of digital twins which can enhance current clinical guidelines. Nonetheless, the extensive reporting time is identified as a primary issue hindering the integration into clinical practice. This spurred the need to explore numerical techniques that strike an optimal balance between accuracy and reporting time [1]. This study explored the hypothesis that simple unidimensional networks accurately estimate the pressure field and time series of ATAA. To investigate this, the results of a Reduced Order Model (ROM) and Fluid-Structure Interaction (FSI) simulations were compared. Two simulations were conducted with a timestep of 0.001 s until a periodic steady state was achieved. Patient-specific flow rate and calibrated three-element Windkessel models served as inlet and outlet boundary conditions, respectively. The results revealed that both quantitative and qualitative analyses revealed strong agreement between the two approaches. This confirmation of our hypothesis suggests significant research potential, particularly in applying Physical-Informed Neural Networks for surrogate modelling.

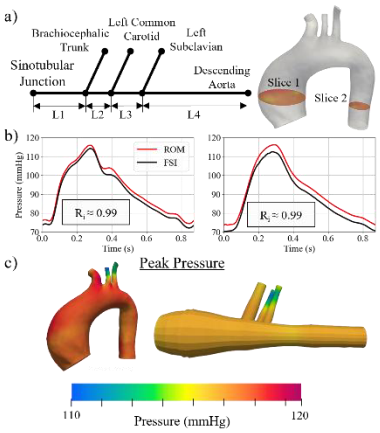

REFERENCES

[1] M.E. Biancolini, K. Capellini, E. Costa, C. Groth and S. Celi, "Fast interactive CFD evaluation of hemodynamics assisted by RBF mesh morphing and reduced order models: The case of aTAA modelling", *Int. J. Interact. Des. Manuf.*, 14, 1227-1238 (2020).

ACKNOWLEDGEMENT

This research was funded by Portuguese Foundation for Science and Technology (FCT) under the project AneurysmTool (DOI: 10.54499/PTDC/EMD-EMD/1230/ 2021), and projects UIDB/00667/2020 and UIDP/00667/2020 (UNIDEMI). A. Mourato and R. Valente are also grateful to FCT for the PhD grants UI/BD/151212/2021 and 2022.12223.BD, respectively.

Congress on Numerical Methods in Engineering 2024
4-6 September 2024, University of Aveiro, Portugal

Evolution of the woven bone mechanical properties: relation with changes in composition

Blázquez-Carmona P. [1], Mora-Macías J. [2], Soriano-López G. [1], Mármol-Martínez A. [2], Domínguez J. [1], Reina-Romo E. [1]

[1] Departamento de Ingeniería Mecánica y Fabricación, Escuela Técnica Superior de Ingeniería, Universidad de Sevilla, España.
Email: pbcarmona@us.es, jaime@us.es, gabrielsorian99@gmail.com, jaime@us.es, erreina@us.es

2 Departamento de Ingeniería Minera, Mecánica, Energética y de la Construcción, Escuela Técnica Superior de Ingeniería, Universidad de Huelva, España.
Email: alvaro.marmol441@alu.uhu.es, juan.mora@dimme.uhu.es

ABSTRACT

Woven bone, generated during bone regeneration processes, is a disorganized tissue with dynamic mechanical and mineral properties until reaching its mature bone state. The evolution of the woven bone stiffness has been characterized using numerical models based on computed tomography (CT) images [1]. This work aims to explore if these changes in the mechanical properties are related to changes observed in the composition of the woven bone [2].

Ex vivo samples at different time points after surgery in a previous bone lengthening study [3] were used. The three-dimensional morphology of the callus was thresholded and meshed with Avizo software using CT images of the bone-lengthening callus. Mechanical properties of the model were assigned according to the gray level in CT images according to previous works [1]. Subsequently, the mechanical behavior of the callus under *in vivo* loads was simulated using Abaqus, thus providing the callus' apparent stiffness at the analyzed time points. Finally, volumetric composition of each sample was measured by ash fraction analysis (volumetric composition of mineral, collagen and water; content in Ca, P and C).

Results demonstrate a correlation between the evolution of the stiffness reported by computational models based on CT images and the increasing volumetric composition of mineral fraction and calcium content.

Authors would like to acknowledge the funding from Spanish State Research Agency (PID2020-113790RB-I00/AEI/10.13039/501100011033).

REFERENCES

[1] J. Mora-Macías et al., "Comparison of methods for assigning the material properties of the distraction callus in computational models", *Int J Numer Method Biomed Eng*, 35(9):e3227 (2019)
[2] J. Martínez-Reina et al., "Comparison of the volumetric composition of lamellar bone and the woven bone of calluses", *Proc Inst Mech Eng H,* 232(7):682-689 (2018)
[3] P. Blázquez-Carmona et al., "Mechanobiology of bone consolidation during distraction osteogenesis: bone lengthening vs. bone transport", *Ann Biomed Eng*, 49(4):1209-1221 (2021)

Congress on Numerical Methods in Engineering 2024
4-6 September 2024, University of Aveiro, Portugal

Model-order reduction and unfitted methods for patient-specific medical decision making in arterial section analysis

Pedro Díez*, Stephan Gahima*, Marco Stefanati†, José Félix Rodríguez Matas† and Alberto García-González*

* LaCàN, Universitat Politècnica de Catalunya (UPC-BarcelonaTech) &
Centre Internacional de Mètodes Numèrics en Enginyeria (CIMNE)
Email: pedro.diez@upc.edu
† Laboratory of Biological Structure Mechanics (LaBS) Department of Chemistry, Materials and Chemical Eng. "Giulio Natta" Politecnico di Milano, 20133 Milan, Italy

ABSTRACT

Geometries of arterial cross-sections are extremely diverse from patient to patient, as well as the distribution of their atherosclerotic plaque intrusions. Medical decision on whether a patient has low or high risk of rupture is made on the basis of this information, mostly of geometrical nature. Mechanical models analyzing stress distribution under internal pressure and the corresponding stress concentrations are of great help to support decision making. This is far of being integrated in clinical practice because the conversion of medical images into mechanical outputs of interest is a laborious process. The standard approach to tackle this problem consists in 1) processing the medical image into a segmented geometry, 2) to generate a compliant finite element mesh for the analysis, and 3) to solve the mechanical problem and compute the outputs of interest. Each of three steps is time demanding and jeopardizes the practical and translational use of these tools.

The aim of this research is to provide further tools allowing a seamless integration of the full process, minimizing the human intervention and providing robust and reliable computational outputs to support clinical decision making. First, an unfitted approach is devised for this specific case, allowing to encapsulate all the geometrical information in form of level sets supported in a background mesh to be used also in the computation of the mechanical problem. This presents the advantage of precluding the need of a constructing computational mesh, conformal with all the geometrical features of the section and its inclusions.

Moreover, this approach paves the way for a using Reduced Order Models (ROM) and therefore to drastically accelerate the computation. Nevertheless, the variability of the arterial cross-sections is a serious drawback for using ROM. The elements of the training set (snapshots) are too diverse to extract common features, and the new elements to be analyzed have little in common with the database from which the ROM has learned.

The work contributes to shape the mechanical problem statement with new boundary conditions, to provide insightful analysis of the dispersion of the observed different geometries, to devise a specific unfitted approach, and to test the ROM strategy in this scenario.

REFERENCES

[1] Gahima, S.; Stefanati, M.; Rodríguez Matas, J. F.; Díez, P.; García-González, A., *An Unfitted Method with Elastic Bed Boundary Conditions for the Analysis of Heterogeneous Arterial Sections*, Mathematics, **11**(7) 1748 (2023) https://doi.org/10.3390/math11071748

Congress on Numerical Methods in Engineering 2024
4-6 September 2024, University of Aveiro, Portugal

Non-linear modelling of isotropic and anisotropic damage in a hyperelastic material using three parameters

Laura Moreno Corrales *, Miguel A. Sanz-Gómez†, Luis Saucedo-Mora†, José María Benítez†, and Francisco Javier Montáns Leal†

* Departamento de Aeronaves y Vehículos Espaciales, Universidad Politécnica de Madrid, Spain
Email: laura.mcorrales@upm.es

† Departamento de Aeronaves y Vehículos Espaciales, Universidad Politécnica de Madrid, Spain
Email: miguelangel.sanz@upm.es, luis.saucedo@upm.es, josemaria.benitez@upm.es, fco.montans@upm.es

ABSTRACT

The behaviour of the hyperelastic materials, also extended to the soft tissues [1], can be understood from the classical statistical theory of elastomers [2]. In this theory, it is established that through the behaviour of the macromolecule, the behaviour of the hyperelastic can be generated as if it were continuous due to a perfect connection between the micro-macro scale of the material. Such a connection has usually been considered as an affine-orientation of the chains that make up the material causing inconsistencies with respect to the traditional computational homogenization approach that provides the average Piola stresses and the strain gradient. However, the integration in a representative volume of the complete network of chains to generate the continuum provides results more in line with the experimental evidence when it is considered the orientation of the chain with a non-affine behaviour [3].

This work presents a model that is able to characterize and predict the behaviour of the hyperelastic materials under any loading condition from a single experimental curve (reference curve) in a uniaxial test ([4], [5]). This model has been extended to study the isotropic and anisotropic damage behaviour of hyperelastic damage behaviour of hyperelastic models known as Mullins effect [6]. The three characteristic parameters of the model (Po, μ^*, λ) are determined using one of the damaged curves of a material with isotropic behaviour as a reference. From them, it is possible to characterize the rest of the curves of the damaged material keeping Po and μ^* constant, and modifying only the parameter, λ, this parameter being associated with the blocking of each of the polymeric chain that make up the material.

REFERENCES

[1] Benítez, J. M., & Montáns, F. J. (2017). The mechanical behavior of skin: Structures and models for the finite element analysis. *Computers & Structures*, *190*, 75-107.
[2] Treloar, L. R. (1976). The mechanics of rubber elasticity. *Proceedings of the Royal Society of London. A. Mathematical and Physical Sciences*, *351*(1666), 301-330.
[3] Miehe, C., Göktepe, S., & Lulei, F. (2004). A micro-macro approach to rubber-like materials—part I: the non-affine micro-sphere model of rubber elasticity. *Journal of the Mechanics and Physics of Solids*, *52*(11), 2617-2660.
[4] Amores, V. J., Moreno, L., Benítez, J. M., & Montáns, F. J. (2023). A model for rubber-like materials with three parameters obtained from a tensile test. *European Journal of Mechanics-A/Solids*, *100*, 104931.
[5] Moreno-Corrales, L., Sanz-Gómez, M. Á., Benítez, J. M., Saucedo-Mora, L., & Montáns, F. J. (2024). Using the Mooney Space to Characterize the Non-Affine Behavior of Elastomers. *Materials*, *17*(5), 1098.
[6] Diani, J., Fayolle, B., & Gilormini, P. (2009). A review on the Mullins effect. *European Polymer Journal*, *45*(3), 601-612.

TS15: Fluid mechanics applied to engineering

This page intentionally left blank

Congress on Numerical Methods in Engineering 2024
4-6 September 2024, University of Aveiro, Portugal

Fire in road tunnels. The influence of the heat release rate in the smoke flow

Ulisses Fernandes*, João C. Viegas* and Pedro J. Coelho†

* LNEC, Laboratório Nacional de Engenharia Civil, 1700-099 Lisbon, Portugal
Email: ufernandes@lnec.pt, jviegas@lnec.pt

† IDMEC, Instituto de Engenharia Mecânica, Mechanical Engineering Department, Instituto Superior Técnico, Universidade de Lisboa, 1049-001 Lisbon, Portugal
Email: pedro.coelho@tecnico.ulisboa.pt

ABSTRACT

Fire accidents in road tunnels may cause a significant number of fatalities and severe damages in the tunnel structure. The tunnel European directive [1] applies to trans-European road network and requires the use of active smoke control systems for most tunnels longer than 500 m. Research has been carried out to investigate if shorter tunnels are safe when the smoke flow occurs due to buoyancy [2, 3]. The FireFoam computer code has been used to model the Memorial Tunnel fire ventilation tests [4] to validate the tunnel model. This model was used to produce a set of simulations to investigate the effect of the wind velocity and of the tunnel slope on the smoke buoyant flow.

In a first step, the effect of the wind velocity on the smoke flow in a horizontal tunnel showed that the contamination of the lower layer (where the people egress) with smoke may start as close as 138 m from the fire source [2]. This contamination (depending on its intensity) may impair the visibility disturbing the people egress, and may cause intoxication and, eventually, death. In a second step, the effect of the slope (without wind) may increase the tendency to the lower layer contamination [3], when compared to the horizontal tunnel. Lower layer contamination may start as close as 210 m to fire source. An analytical model has been developed to predict the distance from the fire source where the lower layer contamination with smoke may occur.

In this communication, the effect of the variation of the heat release rate (HRR) both with and without wind is studied in the same tunnel model. It shows that, although the velocity due to buoyancy increases with the HRR, the location of the lower layer contamination with smoke does not vary significantly due to the increment of the flow rate. The analytical model extension to the HRR variation is also presented.

REFERENCES

[1] Council of European Union, 2004. Directive 2004/54/EC.
[2] A. Galhardo, J. Viegas and P. Coelho, *The influence of wind on smoke propagation to the lower layer in naturally ventilated tunnels*. Tunn. Undergr. Space Technol. 2022, 128, 104632.
[3] E. Ortega, J.C. Viegas, P.J. Coelho. *The contamination of the lower layer in sloped tunnel fires*. Fire, 2023, 6, 245.
[4] Bechtel/Parsons Brinckerhoff, 1995. *Memorial Tunnel Fire Ventilation Test Program*. Test Report. Massachusetts Highway Department.

Congress on Numerical Methods in Engineering 2024
4-6 September 2024, University of Aveiro, Portugal

Numerical simulation of laboratory combustors: a comparison of two commercial codes

Bruno M. Pinto, Afonso Santoalha, Gonçalo P. Pacheco, Pedro J. Coelho* and Miguel A. A. Mendes

* IDMEC, Mechanical Engineering Department, Instituto Superior Técnico, Universidade de Lisboa, 1049-001 Lisboa, Portugal
Email: pedro.coelho@tecnico.ulisboa.pt

ABSTRACT

The mathematical and physical modelling of combustion chambers involve complex interacting physical phenomena, namely turbulence, chemical kinetics, convective and diffusive transport and heat transfer. These phenomena are governed by conservation equations that include terms that need to be modelled. The numerical solution of the governing equations is based on algorithms that are often complex. A few decades ago, the mathematical modelling and the numerical solution was only based on in-house codes written at universities and research laboratories. As more advanced models and more precise numerical methods were developed, commercial codes also appeared. The recognition by the industry of the potential of these codes in the development of better products has boosted the improvement of the commercial codes. They have progressively become more sophisticated and user-friendly, including a wide variety of mathematical/physical models and numerical methods. Their robustness and accuracy has also been improved. Due to these features, they are nowadays widely used in research rather than only in the industry. However, they largely remain like black boxes, since the source code is not available to the users. Even though they have been validated for a huge amount of different problems, the validation is always an issue when a new problem needs to be solved. In this context, the following question arises: to what extent can we be confident on the results computed using a commercial code? In the present work, a detailed comparison of two leading CFD commercial codes (Ansys Fluent and Star-CCM+) is presented for the numerical simulation of a laboratory combustor. The calculations for both codes are performed using the same mesh, the same mathematical and physical models, the same discretization methods of the governing equations, and the same solution algorithm. Preliminary simulations are performed for an isothermal flow. Then, combustion is included and finally radiation is also considered. It is shown that despite the mathematical, physical and numerical methods are identical for both codes, there are differences between the predicted results, even for isothermal flow.

Congress on Numerical Methods in Engineering 2024
4-6 September 2024, University of Aveiro, Portugal

A very high-order Chimera method based on Mean Preserving Moving Least Squares (MP-MLS) for Fluid Structure Interaction – CNM 2024

L. Edreira*†, L. Ramírez†, X. Nogueira† and I. Colominas†

† Group of Numerical Methods in Engineering (GMNI), Center for Technological Innovation in Construction and Civil Engineering (CITEEC). Civil Engineering School, Universidade da Coruña, Campus de Elviña, 15071, A Coruña, Spain
Email: laura.edreiram@udc.es, web page: https://caminos.udc.es/gmni

ABSTRACT

The interaction between fluids and structures is frequent in physics and engineering, such as the aeronautical and automotive industries, turbomachinery, long-span bridges, and biomedical engineering. Precise simulation is essential, as the forces that fluids exert on structures can compromise their response by causing deformations, vibrations, and even failure, leading to safety, reliability, and durability concerns. Thus, it is crucial to have reliable and cost-effective tools to assess the designing process that can simulate and analyze fluid-structure interaction problems, guaranteeing the system's structural integrity throughout its lifespan.

Our approach to analyzing phenomena involving moving bodies - such as Vortex-Induced Vibrations (VIV) - employs a Chimera/overset grid approach, originally introduced by Steger et al. [1]. We employ the very high-order Finite Volume method based on Mean Preserving Moving Least Squares (FV-MP-MLS), developed in [2], to solve the Euler and Navier-Stokes equations. The MP-MLS approximants interpolate the flow variables following the general framework derived in [3] to facilitate information transfer between the grids' boundaries.

The proposed method has been tested by solving a diverse set of benchmark problems, where the accuracy and performance of the method have been thoroughly evaluated and demonstrated.

REFERENCES

[1] G. Starius, “Composite Mesh Difference Methods for Elliptic and Boundary Value Problems”, *Numerische Mathematik*, 28, 243-258 (1977).

[2] L. Ramirez, L. Edreira, I. Couceiro, P. Ouro, X. Nogueira, I. Colominas, “A new Mean Preserving Moving Least Squares method for Arbitrary Order Finite Volume schemes”, *Applied Mathematics and Computation*, 443 (2023).

[3] L. Ramírez, X. Nogueira, P. Ouro, F. Navarrina, S. Khelladi,I. Colominas, “A Higher-Order Chimera Method for Finite Volume Schemes”, *Archives of Computational Methods in Engineering*, 25(3), 691-706 (2018).

Congress on Numerical Methods in Engineering 2024
4-6 September 2024, University of Aveiro, Portugal

Numerical simulation of sediment transport problems under non-saturated conditions

R. Bravo Pareja*, J. Molina Moya* and P. Ortiz*

* Department of Structural Mechanics and Hydraulic Engineering, University of Granada, Spain
Email: rbravo@ugr.es
Email: jorgemolina@urg.es
Email: portiz@urg.es

ABSTRACT

The numerical simulation of sediment transport problems is essential for maintenance and security of civil infrastructures and avoid catastrophes for the population. Traditionally, the dynamics and interactions of sediment with structures under air or water flow conditions has been studied experimentally obtaining very basic approaches. In the last decade, the numerical simulation of sediment transport problems (transport equation one-way coupled with hydrodynamics) has been studied in detail using finite elements [1] or lagrangian methods (see e.g. particle finite element method Pfem [2]). All of them implement the sediment flow in the transport equation with a term that takes considers the sediment flow formulated under saturated conditions in an experimental way. In this work this term is numerically formulated simulated the physics of the sediment transport with two additional transport equations, one for momentum and one for density of the flow which permits to model the dynamics of the sediment and, consequently, the non-saturated conditions, see [3]. The CBS technique is applied for the hydrodynamics and sediment transport equations, obtaining results very similar to the experiments.

REFERENCES

[1] P. Ortiz, P. K. Smolarkiewicz, Coupling the dynamics of boundary layers and evolutionary dunes, Phys. Rev. E 79 (2009) 041307–1.

[2] R. Bravo, P. Ortiz, S. Idelsohn, P. Becker, Sediment transport problems by the particle finite element method (Pfem), Computational Particle Mechanics 7 (1) (2020) 139–149.

[3] G. Sauermann, K. Kroy, H. K. Herrmann, Continuum saltation model for sand dunes, Phys. Rev.E 64 (2001) 031305–1.

Congress on Numerical Methods in Engineering 2024
4-6 September 2024, University of Aveiro, Portugal

A NUMERICAL STUDY ON FIRE PROTECTION OPTIMIZATION DESIGN OF STEEL WAREHOUSE STRUCTURES

Pegah Aghabozorgi[1], Luís Laím[1] and Aldina Santiago[1]

1: ISISE, ARISE, Department of Civil Engineering,
University of Coimbra, Coimbra, Portugal
3030-788
e-mail: {pa,luislaim}@uc.pt & aldina@dec.uc.pt https://isise.net/

Keywords: Steel warehouse, Numerical analysis, Fire protection mortars, Fire design, Fire protection optimization, Temperature distribution.

Abstract *This paper presents an optimization study aimed at enhancing the resistance and overall stability of steel warehouse structures in fire. 3D finite element (FE) models of steel portal frames protected with gypsum-based insulation boards were developed for heat transfer and thermo-mechanical analysis. The thermal properties of fire protection materials were temperature-dependent and defined based on previous thermal analysis tests.*

The optimization was carried out in terms of the thickness of the fire protection coating layer through an iterative process. Optimal thicknesses were determined for achieving a frame fire resistance rating of R60 under various thermal actions, including ISO-834 standard time-temperature curve as well as advanced curves generated by fire simulation software (CFAST).

Furthermore, a novel formula was proposed to predict steel temperature evolution in protected structural H-shaped elements. Then, a comparison was made between the predicting temperature distribution from this formula with the corresponding one taken from Eurocode design methods as well as FE analysis results (heat transfer analysis). The objective is to evaluate the fire protection optimization in terms of thermal actions.

The study contributes to a more precise evaluation of fire resistance in steel-framed warehouses protected with fire protection boards by taking into account the temperature evolution distribution within steel elements under elevated temperatures. These findings are also crucial for developing optimized fire design strategies that ensure structural integrity and safety of industrial steel warehouses under various fire conditions.

Congress on Numerical Methods in Engineering 2024
4-6 September 2024, University of Aveiro, Portugal

A HIGH ACCURATE MESHLESS METHOD FOR FREE SURFACE FLOW

José Maciñeira*, Luis Ramírez[a] y Antonio Eirís[b]

[*a] Group of Numerical Methods in Engineering-GMNI, Center for Technological Innovation in Construction and Civil Engineering-CITEEC, Civil Engineering School
Universidad de A Coruña
Campus de Elviña, 15071, A Coruña, Spain
[b] Defense University Center at the Spanish Naval Academy
Plaza de España, s/n, 36920 Marín, Spain.

Email: jose.macineira@udc.es, web page: http://caminos.udc.es/gmni/

RESUMEN

Nowadays, advances in engineering and CFD have led us to face problems with more complex geometries and higher accuracy needs.

Traditionally, mesh – based methods have been employed to solve this CFD problems, but with today's computational facilities, meshless methods have become very popular for dealing with large deformation or complex geometries problems, like free-surface or wave breaking problems.

In this work we present a high–accurate meshless method based on the use of Moving Least Squares (MLS) approximants [1] for the resolution of the Weakly-Compressive Navier Stokes equations [2] on an ALE approach. The method was developed to overcome some of the grand challenges [3] of traditional Lagrangian SPH methods, like boundary conditions, accuracy and the treatment of the free surface.

The accuracy and robustness of the proposed method are demonstrated by performing tests cases. In these test cases the new methodology will be compared to the traditional kernel-based method of Vila [4].

REFERENCIAS

[1] L. Ramírez, A Eirís, I Couceiro, J París, X Nogueira. An Arbitrary Lagrangian-Eulerian SPH-MLS method for the computation of compressible viscous flows. JCP, 111172, 2022

[2] A Eirís, L Ramírez, J Fernández-Fidalgo, I Couceiro, X Nogueira. SPH-ALE Scheme for Weakly Compressible Viscous Flow with a Posteriori Stabilization. Water, 13 (3), 245, 2021.

[3] R. Vacondio, C. Altomare, M.D. Leffe, X. Hu, D.L. Touzé, S. Lind, J.C. Marongiu, S. Marrone, B. Rogers, A. Souto-Iglesias, Grand challenges for smoothed particle hydrodynamics numerical schemes, Comput. Part. Mech. 8 (2020) 575–588.

[4] J.P. Vila, On particle weighted methods and smooth particle hydrodynamics, Math. Models Methods Appl. Sci. 09(02) (1999) 161–209.

Congress on Numerical Methods in Engineering 2024
4-6 September 2024, University of Aveiro, Portugal

Efecto de la malla de cálculo en el cálculo del flujo asimétrico a altos ángulos de ataque en cuerpos esbeltos

José Jiménez Varona*, Gabriel Liaño†

* Área de Aerodinámica Teórica y Computacional, Departamento de Física del Vuelo, INTA, España
Email: jimenezj@inta.es

† Área de Aerodinámica Teórica y Computacional, Departamento de Física del Vuelo, INTA, España
Email: liagno@inta.es

RESUMEN

El cálculo numérico del flujo alrededor de cuerpos esbeltos, tales como bombas, misiles o cohetes, es una tarea difícil cuando se determina en la zona de altos ángulos de ataque. A esta condición, se ha detetctado experimentalmente que el flujo es asimétrico aunque se trate de cuerpos axilsimétricos. La causa está en una inestabilidad global, que se activa en función de determinados factores o parámetros, tales como la turbulencia del flujo de la corriente libre, así como el número de Reynolds, el número de Mach o el ángulo efectivo de la nariz. Existe un ángulo de ataque a partir del cual, si el régimen es subsónico o transónico, aparece un flujo asimétrico sobre el cuerpo. El resultado es que aparece una fuerza lateral, bien negativa o positiva. El flujo simétrico es inestable y cualquier perturbación lleva a una solución asimétrica bi-estable. Existe una dificultad añadida para el cálculo. Muy pequeñas irregularidades de la configuración, como excentricidad o asimetría de la nariz o rugosidad alta, llevan a que exista una inestabilidad convectiva, que se añade a la global, produciendo un flujo sobre el cuerpo que depende del ángulo de orientación. No sólo es muy difícil tener configuraciones de ensayo perfectamente simétricas y pulidas. Numéricamente, las mallas estructuradas permiten simular cuerpos simétricos, con rugosidad muy baja. Y se pueden añadir irregularidades controladas en determinados ángulos de orientación para simular los efectos en el flujo. Por otro lado, es muy normal la simulación numérica mediante el empleo de mallas no estructuradas, que son asimétricas intrínsecamente, y su nivel de irregularidades -e incluso de "rugosidad numérica"- puede ser elevado, llevando a una gran dependencia de las fuerzas y momentos del ángulo de orientación, cuando el flujo se determina a ángulos de ataque por encima del ángulo de comienzo de la asimetría. Es preciso realizar los cálculos, cuando se usan métodos basados en las ecuaciones promediadas de Navier-Stokes (RANS), con modelos de turbulencia poco disipativos, que permitan la captura de los torbellinos desprendidos en la zona de sotavento del cuerpo. En el Área de Aerodinámica Teórica y Experimental del INTA se han realizado cálculos de varias configuraciones de cuerpos esbeltos a altos ángulos de ataque usando el código FLUENT de ANSYS Inc, con varios modelos de turbulencia y diferentes mallas de cálculo, que ha mostrado la gran dependencia de los resultados en función de la malla de cálculo usada.

REFERENCIAS

[1] José Jiménez Varona, Gabriel Liaño, "Asymmetric Flow at High Incidence on Slender Bodies: Mesh Influence" Nota Técnica INTA, AT/TNO/7160/006/INTA/023 (2023).
[2] José Jiménez Varona, Gabriel Liaño, José L. Castillo, Pedro L. García Ybarra, "Roughness Effect on the Flow past Axisymmetric Bodies at High Incidence", *Aerospace 2022 (MDPI),* 9, 668 (2022).
[3] José Jiménez Varona, Gabriel Liaño, José L. Castillo, Pedro L. García Ybarra, "Steady and Unsteady Asymmetric Flow Regions past an Axisymmetric Body", *AIAA Journal* 59-9, 3375-3386, (2021).

This page intentionally left blank

TS16: Recent advances in shape and topology optimization

This page intentionally left blank

Congress on Numerical Methods in Engineering 2024
4-6 September 2024, University of Aveiro, Portugal

Optimization and dehomogenization of structures with spatially varying complex inclusions

A. Ferrer*†

* Universidad Politécnica de Cataluña, Campus ESEIAAT UPC, 08222 Barcelona, Spain

† Centre Internacional de Mètodes Numèrics a l'Enginyeria (CIMNE)
C/Gran Capitán S/N UPC Campus Nord, Edifici C1, 08034 Barcelona, Spain

email: aferrer@cimne.upc.edu

ABSTRACT

In recent years, additive manufacturing has facilitated the creation of lattice structures characterized by intricate microscale features. This advancement has prompted the topology optimization community to devise innovative techniques capable of accommodating a vast number of design variables. While certain approaches, such as multi-scale topology optimization, have been explored, their computational demands have rendered them less appealing.

In response, the dehomogenization method has emerged as a promising alternative, demonstrating noteworthy performance and computational efficiency in many problems [1]. The dehomogenization process involves identifying a conformal map that deforms a regular grid to coincide with the optimal orientation, considering singularities in the orientation field through the incorporation of singular functions.

In this work, we extend the super-ellipsoidal holes as optimal inclusions for stress minimization [2] to more complex inclusions, in particular to the superformula inclusion, which enlarges the design space and allows the design of optimal structures with spatially varying complex microscale features. Several numerical examples are presented to validate the proposed methodology of this work.

REFERENCES

[1] Grégoire Allaire, Perle Geoffroy-Donders, and Olivier Pantz. Topology optimization of modulated and oriented periodic microstructures by the homogenization method. Computers and Mathematics with Applications, 78(7):2197–2229, 2019.

[2] Alex Ferrer, Perle Geoffroy-Donders, and Grégoire Allaire. Stress minimization for lattice structures. Part I: Micro-structure design. Philosophical Transactions of the Royal Society A (2021), 2020

Congress on Numerical Methods in Engineering 2024
4-6 September 2024, University of Aveiro, Portugal

Topological derivative in constrained optimization problems via the null-space algorithm

Torres, J.[*,1], Ferrer, A.[1,2] and Otero, F.[2,3]

1 Universidad Politécnica de Cataluña, Campus ESEIAAT UPC, 08222 Barcelona, Spain.

2 Universidad Politécnica de Cataluña, Campus FNB UPC, 08003 Barcelona, Spain

3 Centre Internacional de Mètodes Numèrics a l'Enginyeria (CIMNE) C/Gran Capitán S/N UPC Campus Nord, Edifici C1, 08034 Barcelona, Spain

* e-mail: jatorres@cimne.upc.edu

ABSTRACT

The optimization of structural designs through topology optimization techniques has become pivotal in achieving efficient and lightweight structures, especially in the transport industry.

The topological derivative plays a crucial role in topology optimization by providing valuable information about the sensitivity of an objective function with respect to infinitesimal perturbations in the material distribution. In the last years, the topological derivative has been succesfully used in many engineering problems when combined with level-set and incorporated in a fixed point algorithm: the slerp algorithm [1].

However, when dealing with constrained optimization problems, the slerp algorithm needs to incorporate additional numerical schemes. In the last years only the augmented Lagrangian scheme has been used in this scenario and in general it has shown a slow rate of convergence.

We propose to incorporate the slerp algorithm to the null-space optimizer to deal with the constraints. The Null-space has exhibit solid performance when considering the level-set and the shape derivative in the Hamilton-Jacobi algorithm [2]. In other words, we extend the null space algorithm from shape to topological changes.

Through a series of case studies, we demonstrate the efficacy of this approach.

References

[1] Amstutz, S., & Andrä, H. (2006). A new algorithm for topology optimization using a level-set method. Journal of computational physics, 216(2), 573-588.

[2] Feppon, F., Allaire, G., & Dapogny, C. (2020). Null space gradient flows for constrained optimization with applications to shape optimization.ESAIM: Control, Optimisation and Calculus of Variations, 26, 90.

Congress on Numerical Methods in Engineering 2024
4-6 September 2024, University of Aveiro, Portugal

Finite electro-magneto-elasticity with physics-augmented neural networks

R. Ortigosa*, J. Martínez-Frutos*, D. Klein† and O. Weeger†

* Technical University of Cartagena, Multiphysics Simultation & Optimization Group, r.ortigosa@upct.es, jesus.martinez@upct.es

† Technical University of Darmstadt, Cyber-Physical Simulation Group, klein@cps.tu-darmstadt.de, weeger@cps.tu-darmstadt.de

ABSTRACT

In the present work, a machine learning based constitutive model for electro-mechanically coupled material behavior at finite deformations is proposed. Using different sets of invariants as inputs, an internal energy density is formulated as a convex neural network [**1**]. In this way, the model fulfills the polyconvexity condition which ensures material stability, as well as thermodynamic consistency, objectivity, material symmetry, and growth conditions. Depending on the considered invariants, this physics-augmented machine learning model can either be applied for compressible or nearly incompressible material behavior, as well as for arbitrary material symmetry classes. The applicability and versatility of the approach is demonstrated by calibrating it on transversely isotropic data generated with an analytical potential, as well as for the effective constitutive modeling of an analytically homogenized, transversely isotropic rank-one laminate composite and a numerically homogenized cubic metamaterial. These examinations show the excellent generalization properties that physics-augmented neural networks offer also for multi-physical material modeling such as nonlinear electro-elasticity and magneto-elasticity [**2**].

Research funded by Grants PID2022-141957OA-C22 by MCIN/AEI/10.13039/5011000110233 "ERDF A way of making Europe" and 21996/PI/22 Fundación Séneca

REFERENCES

[**1**] D. Klein, R. Ortigosa, J. Martínez-Frutos, A. J. Gil, Finite electro-elasticity with physics-augmented neural networks, *Computer Methods in Applied Mechanics and Engineering*, 400 (2022)

[**2**] R. Zhao, Y. Kim, S. A. Chester, P. Sharma, X. Zhao, Mechanics of hard-magnetic soft materials, *Journal of the Mechanics and Physics of Solids*, 124 (2019), 244-263

Congress on Numerical Methods in Engineering 2024
4-6 September 2024, University of Aveiro, Portugal

Geometric Constraints to minimum length scale in topology optimization

Jose A. Postigo*, Alain Garaigordobil † and Rubén Ansola †

University of the Basque Country (UPV/EHU)
Department of Mechanical Engineering
Campus of Biscay, 48013 Bilbao, Spain

* e-mail: joseantonio.postigo@ehu.eus, web page: https://www.ehu.eus/en/web/optitrans/structural

† e-mail: alain.garaigordobil@ehu.eus, web page: https://www.ehu.eus/en/web/optitrans/structural

† e-mail: ruben.ansola@ehu.eus web page: https://www.ehu.eus/en/web/optitrans/structural

ABSTRACT

The goal of this study is to propose new geometrical restrictions for density-based topology optimization. Specifically, the research aims to develop new approaches to designing structures with a strict minimum length-scale.

One significant contribution to this field is the method proposed by [1], which involves creating a structural indicator function that compares eroded and dilated designs and ensures it forms a consistent design. In this geometrical restriction, the structural indicator function can be changed to another structural representation, for example, the media-zone. The advantage of the media-zone over the structural indicator function is that the former is not such sensitive to parameters. However, there are some disadvantages, for example, the most usual method to obtain the media-zone (Morphological Skeletonization) is not easily differentiable and can be computationally expensive. To overcome these limitations, we propose a new method based on the PDE filter that allows for an efficient and differentiable generation of the media-zone to impose the minimum length scale.

On the other hand, considering this media-zone, different alternatives are explored to impose the minimum size of solids and voids. One of these alternatives is to use the PDE filter to expand the representation of the media-zone up to the minimum length scale so that we can impose it over the structure. Another alternative is to use the structure perimeter to evaluate the overlapping between two perimeters at this media-zone and restrict it to a maximum value.

REFERENCES

[1] M. Zhou, B. S. Lazarov, F. Wang, and O. Sigmund, “Minimum length scale in topology optimization by geometric constraints,” *Comput Methods Appl Mech Eng*, vol. 293, pp. 266–282, Aug. 2015, doi: 10.1016/j.cma.2015.05.003.

Congress on Numerical Methods in Engineering 2024
4-6 September 2024, University of Aveiro, Portugal

Multifunctional topology optimization for shape-morphing electroactive materials

Jesús Martínez-Frutos[1], Rogelio Ortigosa[1], Antonio J. Gil[2]

[1] Technical University of Cartagena. Multiphysics Simulation & Optimization Group.
jesus.martinez@upct.es , rogelio.ortigosa@upct.es

[2] Zienkiewicz Centre for Computational Engineering, Faculty of Science and Engineering, Swansea University, Bay Campus, SA1 8EN, United Kingdom. a.gil@swansea.ac.uk

ABSTRACT

This presentation addresses a novel engineering strategy for the design of Dielectric Elastomer (DE) based actuators, capable of attaining complex electrically induced shape morphing configurations. In this approach, a multilayered DE prototype, interleaved with compliant electrodes spreading across the entire faces of the DE, is considered. Careful combination of several DE materials, characterised by different material properties within each of the multiple layers of the device, is pursued. The resulting layout permits the generation of a heterogenous electric field within the device due to the spatial variation of the material properties within the layers and across them. An in-silico or computational approach has been developed in order to facilitate the design of new prototypes capable of displaying predefined electrically induced target configurations. Key features of this framework are: (i) use of a standard two-field Finite Element implementation of the underlying partial differential equations in reversible nonlinear electromechanics, where the unknown fields ot the resulting discrete problem are displacements and the scalar electric potential; (ii) introduction of a novel phase-field driven multi-material topology optimisation framework allowing for the consideration of several DE materials with different material properties, favouring the development of heterogeneous electric fields within the prototype. This novel multi-material framework permits, for the first time, the consideration of an arbitrary number of different DE materials, by means of the introduction of phase-field functions, evolving independently over the different layers across the thickness of the device through Allen-Cahn type evolution equations per layer. A comprehensive series of numerical examples is analysed, with the aim of exploring the capability of the proposed methodology to propose efficient optimal designs.

Research founded by Grants PID2022-141957OA-C22 by MCIN/AEI/ 10.13039/501100011033 "ERDF A way of making Europe" and 21996/PI/22 Fundación Séneca

REFERENCES

[1] J. Martínez-Frutos, R. Ortigosa, A.J. Gil. In-silico design of electrode meso-architecture for shape morphing dielectric elastomers. J. Mech. Phys. Solids, 157 (2021)

[2] R. Ortigosa, J. Martínez-Frutos. Topology optimisation of stiffeners layout for shape-morphing of dielectric elastomers Struct. Multidiscip. Optim., 64 (2021), pp. 3681-3703

Topology optimization of flexoelectric lattice metamaterials

Juan Carlos Tarín[1], David Codony[1], Francesco Greco[1], Sonia Fernández-Méndez[1], and Irene Arias[1,3]

[1]Laboratori de Càlcul Numèric (LaCàN), Universitat Politècnica de Catalunya (UPC), Campus Nord UPC-C2,E-08034, Barcelona, Spain
[3]Centre Internacional de Mètodes Numèrics en Enginyeria (CIMNE), 08034 Barcelona, Spain

January 17, 2024

This work focuses on the development of an innovative topological optimization framework for periodic lattice metamaterials, specifically designed to optimize its flexoelectric response. Flexoelectricity is the two way coupling between polarization and strain gradient and conversely, the coupling between polarization gradient and strain. Flexoelectric metamaterials offer a promising alternative to traditional piezoelectric materials, overcoming challenges such as toxicity and biocompatibility limitations [1]. The present framework comprehensively addresses the topological optimization of flexoelectric metamaterials exhibiting macroscopic apparent piezoelectricity although made from non-piezoelectric base materials [2], facilitating the creation of structures with enhanced electromechanical properties.

At the core of this work, topological and shape optimization is carried out through a combination of bit-array representations and the levelset method. This combination allows for the representation of any geometry with a smooth contour, which is essential for high-order mathematical models such as flexoelectricity. The versatility of the framework is further enhanced by its ability to accurately model complex geometries, a critical aspect in the optimization of flexoelectric materials where the electromechanical properties are highly geometry-dependent.

The Dijkstra algorithm is integrated into the framework to efficiently resolve continuity and connectivity challenges, which are fundamental in topological optimization. This algorithm ensures that the resulting optimized structures maintain structural integrity and are viable for practical applications.

The framework has proven to be very effective in the optimization of flexoelectric metamaterials, demonstrating its adaptability and precision in handling diverse geometrical challenges. This adaptability makes the framework not only suitable for flexoelectric devices but also potentially applicable to a wide range of other materials and structures requiring sophisticated geometrical optimizations.

References

[1] P. Zubko, G. Catalan, and A. K. Tagantsev, "Flexoelectric effect in solids," *Annual Review of Materials Research*, vol. 43, no. 1, pp. 387–421, 2013.

[2] A. Mocci, J. Barceló-Mercader, D. Codony, and I. Arias, "Geometrically polarized architected dielectrics with apparent piezoelectricity," *Journal of the Mechanics and Physics of Solids*, vol. 157, p. 104643, 2021.

Congress on Numerical Methods in Engineering 2024
4-6 September 2024, University of Aveiro, Portugal

Nonlocal optimal design of conducting domains

José C. Bellido* and Anton Evgrafov†

* Departamento de Matemáticas, Universidad de Castilla-La Mancha, Spain
Email: JoseCarlos.Bellido@uclm.es

† Department of Mathematics, Aalborg University, Denmark
Email: anev@math.aau.dk

ABSTRACT

We consider the problem of optimal distribution of a limited amount of conductive material in systems governed by local and non-local scalar diffusion laws. Of particular interest for these problems is the study of the limiting case, which appears when the amount of available material is driven to zero. Such a limiting process is of both theoretical and practical interest and continues to be a subject of active study. In the local case, the limiting optimization problem is convex and has a well understood basis pursuit structure. Still this local problem is quite challenging both analytically and numerically because it is posed in the space of vector-valued Radon measures. Surprisingly, the nonlocal counterpart admits solution and convergence to local problem when the nonlocality vanishes holds.

REFERENCES

[1] A. Evgrafov and J.C. Bellido, *Nonlocal basis pursuit: nonlocal optimal design of conductive domains in the vanishing material limit*, SIAM Journal of Mathematical Analysis, 55(4), 2023.

Congress on Numerical Methods in Engineering 2024
4-6 September 2024, University of Aveiro, Portugal

Neighbourhood-based acceleration strategies in 2-level topology optimization with Cartesian grids

M. Bosch-Galera*[1], R. Merli[1], J.J. Ródenas[1], E. Nadal[1] and J.M. Navarro-Jiménez[1]

[1] Institute of Mechanical Engineering and Biomechanics (I2MB),
Universitat Politècnica de València (UPV), Spain
Email: marbosga@upv.es, ramergis@upv.es, jjrodena@upv.es,
ennaso@upv.es, jonaji@upv.es

ABSTRACT

High-definition topology optimization (TO) is a trending design method used to obtain complex trabecular structures that resemble nature. In our implementation, material is first distributed over the domain (discretized by cells) at the *coarse-level* and then finely redistributed into each cell at the *fine-level*, in both cases, by solving a TO problem. Note that the cell TO can only be properly posed when an adequate traction recovery procedure, such as the one proposed in Ladevèze and Maunder [1], is applied. Despite being a powerful approach, it presents two main drawbacks: the computational cost derived from the concurrent optimizations of the *fine-level* cells and the structural discontinuity between adjacent cells due to both the finite size of the elements at the *fine-level* and the also discontinuous density field.

Given a fine enough discretization of the *coarse-level* Cartesian grid mesh, one may assume that the loads acting on contiguous elements are essentially the same and, therefore, expect the material distributions resulting from the *fine-level* TO to be very close as well. Based on this intuition, this work explores the possibility of significantly reducing the iterations of the *fine-level* TOs (up to convergence) by setting the initial density distribution into each cell as the converged solution of a near cell (neighbour).

Then, by cleverly grouping the *coarse-level* cells into cells to be fully solved and cells to be solved from their neighbours, and by preventing in the latter group the contour *fine-level* elements to be updated within the TO algorithm, structural continuity may be enforced regardless of the aforementioned hurdles.

Acknowledgements: The authors would like to thank the financial support granted by Generalitat Valenciana (Prometeo/2021/046) and *Ministry of Science and Innovation* (FPU20/04828 and /AEI/10.13039/501100011033/FEDER, UE, project PID2022-141512NB-I00).

REFERENCES

[1] P. Ladevèze, E.A.W. Maunder, *A general methodology for recovering equilibrating FE tractions and stress fields for plate and solid elements*, CAMES, 4:533−548, 1997.

Congress on Numerical Methods in Engineering 2024
4-6 September 2024, University of Aveiro, Portugal

Computational homogenization of flexoelectricity-based metamaterials: application to topology optimization for apparently piezoelectric devices

David Codony[1], Jordi Barceló-Mercader[1], Francesco Greco1, Alice Mocci[1], Hossein Mohammadi[1], Sonia Fernández-Méndez[1], and Irene Arias[1,2]

[1] Laboratori de Càlcul Numàric (LaCàN), Universitat Politècnica de Catalunya (UPC), Campus Nord UPC-C2,E-08034, Barcelona, Spain

[2] Centre Internacional de Mètodes Numèrics en Enginyeria (CIMNE), 08034 Barcelona, Spain

ABSTRACT

The optimization of structural designs through topology optimization techniques has become pivotal in achieving efficient and lightweight structures, especially in the transport industry.

We present a method for the numerical computation of representative volume element (RVE) in the context of high-order electromechanical theory, which relies on the construction of a generalized periodic Cartesian B-Spline approximation space [1]. The geometry is unfitted to the mesh, and described by a periodic level set function. The imposition of generic macroscopic fields (strains/stresses and electric fields/electric displacements) is naturally allowed as strong Dirichlet/Neumann macroscopic conditions.

We apply the proposed method to study non-piezoelectric architected metamaterials with apparent piezoelectric behavior thanks to the flexoelectric effect (coupling between polarization and strain gradient). In particular, we perform multi-objective topology optimization of flexoelectric metamaterial RVEs by means of genetic algorithms [2]. We find the Pareto fronts where area fraction is minimized and different apparent piezoelectric coefficients (stress/strain sensor/actuator) are maximized.

Overall, we find RVE topologies exhibiting a competitive apparent piezoelectric behavior as compared to reference piezoelectric materials such as quartz and PZT ceramics.

References

[1] J. Barceló-Mercader, D. Codony, A. Mocci, and I. Arias, “Computational homogenization of higher-order electro-mechanical materials with built-in generalized periodicity conditions,” arXiv preprint arXiv:2311.08196, 2023.

[2] F. Greco, D. Codony, H. Mohammadi, S. Fernández-Méndez, and I. Arias, “Topology optimization of flexoelectric metamaterials with apparent piezoelectricity,” Journal of the Mechanics and Physics of Solids, vol. 183, p. 105477, 10 2023.

Congress on Numerical Methods in Engineering 2024
4-6 September 2024, University of Aveiro, Portugal

Computational framework for the design of multiresonant layered acoustic metamaterials

D. Roca*[1,2], G. Sal-Anglada[1,2], D. Yago[1,2], J. Cante[1,2] and J. Oliver[1,3]

[1] International Center for Numerical Methods in Engineering (CIMNE), Spain
* Email: david.roca.cazorla@upc.edu

[2] Escola Superior d'Enginyeries Industrial, Aeroespacial i Audiovisual de Terrassa (ESEIAAT), Universitat Politècnica de Catalunya · BarcelonaTech (UPC), Spain

[3] Escola Tècnica Superior d'Enginyeria de Camins, Canals i Ports de Barcelona (ETSECCPB), Universitat Politècnica de Catalunya · BarcelonaTech (UPC), Spain

ABSTRACT

Acoustic metamaterials are built with specifically engineered structures that trigger certain phenomena in the material's lower scale, which translates into an unusual response in the macro-scale. This can cause huge levels of attenuation at specific frequency ranges without necessarily increasing the mass, making them interesting for soundproofing applications. Despite the numerous advances in the past years, the acoustic metamaterial technology still faces challenges mostly related to manufacturing—with overcomplicated designs—and to the ability to tackle broadband ranges of attenuation at frequencies below 1000 Hz. In this context, Multiresonant Layered Acoustic Metamaterial (MLAM) designs were proposed recently as a promising solution to solve both these issues [1].

In this work, we present a general computational design strategy aimed at optimizing MLAM-based panels for high-performance soundproofing applications at lower frequency ranges [2]. The framework is based on a layer-by-layer homogenization model capable of capturing the local resonance phenomena inside the MLAM structure, as well as the coupling effect between resonating layers—a fundamental aspect of the MLAM design to increase its attenuating performance. This homogenization model is used to build a database linking the effective properties of a layer design to relevant geometric features of the same. The database is then used to solve an optimization problem—by means of a genetic algorithm—to get an optimal MLAM design maximizing the attenuation in a target frequency range with restrictions in terms of weight.

We demonstrate how the proposed computational design strategy is effective even when more than two resonating layers are considered, which greatly enhances the properties of the MLAM panel in terms of increasing the levels of attenuation and/or broadening the effective frequency range.

REFERENCES

[1] D. Roca, J. Cante, O. Lloberas-Valls, T. Pàmies, and J. Oliver. "Multiresonant Layered Acoustic Metamaterial (MLAM) solution for broadband low-frequency noise attenuation through double-peak sound transmission loss response", *Extreme Mechanics Letters*, 47, 101368 (2021). DOI: 10.1016/j.eml.2021.101368.

[2] G. Sal-Anglada, D. Yago, J. Cante, J. Oliver, and D. Roca. "Optimal design of Multiresonant Layered Acoustic Metamaterials (MLAM) via a homogenization approach", *Engineering Structures*, 293, 116555 (2023). DOI: 10.1016/j.engstruct.2023.116555.

Congress on Numerical Methods in Engineering 2024
4-6 September 2024, University of Aveiro, Portugal

Surrogate-based topology optimisation of elastic structures via parametric autoencoders

Matteo Giacomini[1,2,*], Guillem Barroso[3], and Antonio Huerta[1,2]

[1] Laboratori de Càlcul Numèric (LaCàN), E.T.S. de Ingeniería de Caminos, Canales y Puertos, Universitat Politècnica de Catalunya, Barcelona, Spain.

[2] Centre Internacional de Mètodes Numèrics en Enginyeria (CIMNE), Barcelona, Spain.
Email: {matteo.giacomini, antonio.huerta}@upc.edu

[3] ANSYS, Inc, Canonsburg, Pennsylvania, USA.

ABSTRACT

To perform optimal design of structures, topology optimisation algorithms rely on the iterative solution of state (and, possibly, adjoint) equations. In the context of finite element-based topology optimisation, it follows that the accuracy of the computed solutions and the quality of the designed layouts significantly depend on the underlying computational mesh used for discretisation. While a single instance of such problems can be solved with reasonable time and resources, conducting parametric studies involving topology optimisation, and therefore many-queries, becomes computationally intractable.

Here, surrogate models based on machine learning strategies will be presented to accelerate topology optimisation of linear elastic structures. In particular, a parametric autoencoder, trained on a dataset of optimal topologies obtained by the homogenisation method for different positions and orientations of the external load, will be encapsulated in the optimisation pipeline to reduce the overall computing time by predicting *quasi-optimal*, homogenised topologies [1].

Numerical results will be presented to illustrate the ability of the proposed parametric autoencoder to reconstruct the homogenised topologies, both interpolating and extrapolating in the parametric space. Moreover, the computational gains provided by the integration of the surrogate model into the full-order optimisation pipeline will be numerically assessed.

REFERENCES

[1] M. Giacomini, G. Barroso, and A. Huerta, “A surrogate model for topology optimisation of elastic structures via parametric autoencoders”, *In preparation*.

Congress on Numerical Methods in Engineering 2024
4-6 September 2024, University of Aveiro, Portugal

A variational framework for thermodynamic topology optimisation

Edmund Bell-Navas[+], David Portillo[+] and Ignacio Romero[+]*

[+]

Escuela Técnica Superior de Ingenieros Industriales, Universidad Politécnica de Madrid, Spain
Email: edmund.bell@upm.es, david.portillo@upm.es, ignacio.romero@upm.es

ABSTRACT

Topology optimisation has become an essential technique in mechanical design. The mathematical analysis of its governing equations reveals the enormous difficulties involved in its solution. To start, even the existence of such solutions is in question. Formulating a numerical method that can find optimal solutions to these problems invariably involves some kind of regularisation and this opens the door to many families of algorithms.

In this work, we will focus on a numerical method for topology optimisation based on the solution of an ancillary Cahn-Hilliard problem whose phase field solution can be understood as the optimal density distribution. More specifically, we will design a method that couples the Cahn-Hilliard problem with small strain elasticity and obtains a discrete trajectory whose limit coincides with an optimal density. The method, moreover, will be based on an incremental variational formulation (following [1]) that yields all the equations of coupled phase-field/mechanical problems as the stationarity points of a single functional.

In the original method [1], to enforce that the phase-field variable takes values only in the interval [0,1], Lagrange multipliers and Nonlinear Complementary Conditions (NCP) functions are introduced in the algorithmic unconstrained variational problem. By doing so, the symmetry of the underlying variational framework is spoiled, i.e. the tangent stiffness matrix of the FEM implementation is no longer symmetric. In the present method, a number of alternatives to Lagrange multipliers and NPC functions are proposed. These modifications maintain the symmetry of the tangent stiffness matrix without compromising convergence. Thus, the reduction in computational cost is achieved by elimination of two variables per node (Lagrange multipliers) in the whole domain and by enabling the use of much more efficient numerical schemes that take advantage of matrix symmetry.

The numerical performance of the proposed framework will be illustrated by optimising a series of structures of minimum compliance and fixed mass. The results will serve as a benchmark against SIMP [2, 3], Allen-Cahn phase-field [4] and variational Cahn-Hilliard [1] phase-field methods.

REFERENCES

[1] Bartels, A., Kurzeja, P., & Mosler, J. (2021). Cahn–Hilliard phase field theory coupled to mechanics: Fundamentals, numerical implementation and application to topology optimization. Computer Methods in Applied Mechanics and Engineering, 383, 113918.

[2] Andreassen, E., Clausen, A., Schevenels, M., Lazarov, B. S., & Sigmund, O. (2011). Efficient topology optimization in MATLAB using 88 lines of code. Structural and Multidisciplinary Optimization, 43, 1-16.

[3] Ferrari, F., & Sigmund, O. (2020). A new generation 99 line Matlab code for compliance topology optimization and its extension to 3D. Structural and Multidisciplinary Optimization, 62, 2211-2228.

TS17: Crashworthiness, Impact and Blast Wave Dynamics

This page intentionally left blank

Congress on Numerical Methods in Engineering 2024
4-6 September 2024, University of Aveiro, Portugal

Real-time brain response to sporting impact using pose estimation and finite element head models

T. Aston*, F. Teixeira-Dias*

* Institute for Infrastructure and Environment, School of Engineering, University of Edinburgh, United Kingdom
Email: thomas.aston@ed.ac.uk

ABSTRACT

Exposure to repetitive sub-concussive head impact through activities such as routine soccer heading and boxing sparring can lead to immediate cognitive impairment [1], and an increased risk of developing a neurodegenerative disease in later life through participation in contact sports such as soccer and rugby has been observed [2]. Numerous studies have aimed to quantify and categorise the kinematics associated with sporting head impact to obtain a better understanding of the mechanisms of brain injury resulting from contact sport participation [3], and brain injury criteria which translate kinematics into spatially detailed mechanical response of the brain for a given head impact have been developed using finite element head models (FEHM) [4]. Typically, skull kinematics are obtained using a custom-fit instrumented mouthguard and used as input boundary conditions for FEHM simulations in a process that can take days before results are obtained. To move towards a model of efficient player welfare management and on-field injury assessment informed by simulation results, the present study examines the feasibility of a near real-time approach to obtaining brain injury predictions in a sporting context. Experimental measurements of skull kinematics experienced by a cohort of participants during routine soccer heading practice is obtained using a custom-fit instrumented mouthguard, and visual confirmation of impact is automated using previously developed deep learning action classification and human pose estimation techniques [5,6]. Instantaneous predictions of entire brain strains are then acquired using the 'CNN-brain-strains' model developed by Ghazi et al. [7]. Results from this model are compared with those obtained using the in-house isDynamics 50th Percentile Male FEHM [8], to assess the accuracy of the proposed approach compared with traditional FEHM methods.

REFERENCES

1. Di Virgilio, T. G., Ietswaart, M., Wilson, L., Donaldson, D. I. & Hunter, A. M. Understanding the Consequences of Repetitive Subconcussive Head Impacts in Sport: Brain Changes and Dampened Motor Control Are Seen After Boxing Practice. *Front. Hum. Neurosci.* **13**, (2019).
2. Mackay, D. F. *et al.* Neurodegenerative Disease Mortality among Former Professional Soccer Players. *N. Engl. J. Med.* **381**, 1801–1808 (2019).
3. O'Connor, K. L., Rowson, S., Duma, S. M. & Broglio, S. P. Head-Impact–Measurement Devices: A Systematic Review. *J. Athl. Train.* **52**, 206–227 (2017).
4. Takhounts, E. G. *et al.* Investigation of traumatic brain injuries using the next generation of simulated injury monitor (SIMon) finite element head model. *Stapp Car Crash J.* **52**, 1–31 (2008).
5. Rezaei, A. & Wu, L. C. Automated soccer head impact exposure tracking using video and deep learning. *Sci. Rep.* **12**, 9282 (2022).
6. Aston, T. & Teixeira-Dias, F. An automatic, markerless approach to measuring head kinematics in soccer. in *International Research Council on Biomechanics of Injury: IRCOBI Europe Conference 2023* (International Research Council on Biomechanics of Injury, 2023).
7. Ghazi, K., Wu, S., Zhao, W. & Ji, S. Instantaneous Whole-Brain Strain Estimation in Dynamic Head Impact. *J. Neurotrauma* **38**, 1023–1035 (2021).
8. McGill, K. Investigation into Brain and Intracranial Structure Representations in FE Head Models. (2022) doi:10.7488/era/2544.

Congress on Numerical Methods in Engineering 2024
4-6 September 2024, University of Aveiro, Portugal

Numerical modelling of fragmentation in armour piercing bullet cores

Maisie Edwards-Mowforth, Miguel Costas†, Filipe Teixeira-Dias*, and Tore Børvik†**

* Institute of Infrastructure and Environment (IIE), School of Engineering, The University of Edinburgh, UK

† Structural Impact Laboratory (SIMLab), Department of Structural Engineering, NTNU – Norwegian University of Science and Technology, Trondheim, Norway

ABSTRACT

High-strength and high-hardness materials are considered effective armour against threats from small-arms ammunitions and often play a significant role in armour systems which may protect vehicles, structures, equipment, or personnel. The mechanism by which such materials offer ballistic protection is in their capacity to break up the hard steel core of armour piercing bullets, thus reducing the capacity for further penetration and damage [1].

The optimisation of armour systems to improve performance relies heavily on accurate simulations of the ballistic impact. Target failure mechanisms in cases where a rigid bullet core is considered are well established. However, once the bullet core experiences fragmentation, the scope for accurate simulations is limited by the commonly used but rather simple methods of modelling failure with finite element methods such as element erosion, as well as a lack of data in the literature on ammunition materials [2].

The present work addresses the numerical modelling of fragmentation in APM2 armour piercing bullet cores using the IMPETUS Afea Solver [3]. The model consists of an elastic-thermo-viscoplastic constitutive law [4] combined with node splitting based on two damage criteria: the Cockcroft-Latham criterion and a tensile fracture criterion. Material characterisation tests were carried out in order to calibrate the work hardening behaviour and inform a heterogenous distribution of material properties as well as material failure.

The mass, shape and residual velocity of bullet core fragments recorded in experiments of impacts against a rigid wall were used to evaluate the model performance. Comparisons were also drawn against alternative damage criteria and modelling techniques, and a parameter sensitivity analysis was carried out. Good performance of the numerical model was observed over a range of impact velocities.

REFERENCES

[1] M. Costas, M. Edwards-Mowforth, M. Kristoffersen, F. Teixeira-Dias, V. Brøtan, C. Paulsen, and T. Børvik, “Ballistic impact resistance of additive manufactured high-strength maraging steel: an experimental study”, *The International Journal of Protective Structures,* 12:577–603 (2021).

[2] S. Dey, T. Børvik, X. Teng, T. Wierzbicki, OS. Hopperstad, “On the ballistic resistance of double-layered steel plates: an experimental and numerical investigation”, *Int J Solids Struct*, 44:6701–23 (2007).

[3] L. Olovsson, J. Limido, J-L. Lacome, AG. Hanssen, J. Petit, “Modeling fragmentation with new higher order finite element technology and node splitting”, *In: Proceedings of the 11th international conference on the mechanical behaviour of materials under dynamic loading,* 1–6. 04050 (2015).

[4] T. Børvik, OS. Hopperstad, T. Berstad, M. Langseth, “A computational model of visco-plasticity and ductile damage for impact and penetration”, *Eur J Mech A/Solids*, 20:685–712 (2001).

Congress on Numerical Methods in Engineering 2024
4-6 September 2024, University of Aveiro, Portugal

Shock response analysis and optimisation of functionally-graded ceramic composite shield for hypervelocity impact

K. Fowler* and F. Teixeira-Dias*

* Institute for Infrastructure and Environment (IIE), School of Engineering, The University of Edinburgh, Edinburgh, EH9 3FG, United Kingdom

Email: k.r.fowler@ed.ac.uk
f.teixeira-dias@ed.ac.uk

ABSTRACT

Recent advancements in space exploration have led to an increase in Micro-Meteoroid and Orbital Debris (MMOD), significantly heightening the threat of Hypervelocity Impact (HVI) on space structures [1]. HVI refers to velocities exceeding the speed of sound through a material, typically ≥ 6 km/s for metals [2], resulting in catastrophic damage. Effective passive protection measures are therefore imperative, necessitating improvements to conventional Whipple shield designs [3]. This study employs adaptive coupled Finite Element (FE) - Smoothed Particle Hydrodynamic (SPH) numerical techniques to eliminate mesh-based distortion issues while maintaining computational efficiency and enabling post-impact debris cloud modelling. The incorporation of failure criteria within the simulated material triggers a conversion from an FE mesh to discrete SPH particles upon reaching predefined thresholds. These particles inherit volume and material properties, remaining coupled with the FE mesh throughout the simulation [4]. This technique is utilised for the analysis and optimisation of functionally graded ceramic composite shields aimed at increasing shield fragmentation and reducing the kinetic energy of impacting projectiles. Shield compositions of SiC, NbC, and B_4C composite architectures, have yielded positive results due to an advantageous shock response and wave impedance effects. An experimental campaign is conducted, subjecting ceramic-metal composite plates with consistent areal densities to impacts from spherical 1 mm diameter aluminium projectiles. Utilizing a two-stage light gas gun, the experimental results closely align with the numerical simulations, validating the effectiveness of the proposed approach.

REFERENCES

[1] European Space Agency (ESA) Space Debris Office, *European Space Agency's Annual Space Environment Report*, Darmstadt, Germany. (Report No. ESA/ESOC-SRO(2022)401), (2022).

[2] J. Zukas, *Introduction to Hydrocodes*, Studies in Applied Mechanics, 49, (2004).

[3] L.C. Eric, *Handbook for Designing MMOD Protection*, Astromaterials Research and Exploration Science Directorate Human Exploration Science Office NASA Johnson Space Center, (2009).

[4] Q.G. He, X. Chen, and J.F. Chen, "Finite element-smoothed particle hydrodynamics adaptive method in simulating debris cloud", *Acta Astronaut*, 175, 99–1 (2020).

Congress on Numerical Methods in Engineering 2024
4-6 September 2024, University of Aveiro, Portugal

Numerical validation of Dyneema HB80 and Silicon Carbide plates using experimental results

A. Azevedo*, A. Miranda-Vicario*. F. Coghe* and F.Teixeira-Dias†

* Department of Weapon Systems and Ballistics, Royal Military Academy, Renaissance Avenue, 30, B-1000 Brussels, Belgium
Email: ana.ferreira@mil.be

† School of Engineering, The University of Edinburgh
Edinburgh EH9 3FG, United Kingdom

ABSTRACT

Armour systems made of ceramic and composite materials are widely used in ballistic applications to defeat high energy projectiles. Finite element models with settled material laws are indispensable in understanding the interaction between the projectile and armour, and finding effective ways of developing lightweight protection solutions. In this research the authors use explicit finite element analyses and explain how the models are built and the results verified. A numerical approach is proposed to validate the ceramic plate model. Due to the brittle nature of the ceramic, a multi-component armour target was used, such as a hard-faced ceramic armour with a composite backing. The used ammunition was the FSP 0.22 projectile and the target consisted of a silicon carbide (SiC) 4.2 mm thick tile, supported by a 5 mm Dyneema HB80 plate. One of the most widely used constitutive laws for ceramic materials in ballistic research is the Johnson-Holmquist model, which is also relatively easy to implement. This research uses the Johnson-Holmquist-2 (JH-2) model to simulate the ceramic material as it can incorporate both intact and failed material curves. The JH-2 model is gradually softened as damage accumulates, gradually increasing the bulking pressure as the damage accumulates [1, 2]. The composite material (Dyneema HB80) was modelled as set of orthotropic laminates using the orthotropic simplified damage material model. Cross-plies have been homogenised to represent the composite layup as a sub-laminate, and these sub-laminates are then stacked and separated by a tied contact. The simulation results in terms of ballistic limit are in good agreement with the experimental observations, illustrated for example by the <4% difference between the numerical and experimental ballistic limit velocity (BLV).

REFERENCES

[1] Johnson, G. R., Holmquist, T. J., and Beissel, S. R. (2003). Response of aluminum nitride (including a phase change) to large strains, high strain rates, and high pressures. Journal of Applied Physics, 94(3):1639-1646.

[2] Anderson, C. E., Johnson, G. R., and Holmquist, T. J. (1995). Ballistic experiments and computations of confined 99.5% Al2O3 ceramic tiles. In 15th International Symposium on Ballistic, pages 65{72, Jerusalem, Israel.

Numerical applications

This page intentionally left blank

Congress on Numerical Methods in Engineering 2024
4-6 September 2024, University of Aveiro, Portugal

MANIFEM, A C++ LIBRARY FOR MESH GENERATION AND FINITE ELEMENTS

Cristian Barbarosie[1], Anca-Maria Toader[1]

[1] Centro de Matemática, Aplicações Fundamentais e Investigação Operacional,
Faculdade de Ciências da Universidade de Lisboa, Campo Grande 1749-016 Lisboa Portugal

Key Words: *Finite element method, mesh generation, C++ library, tessellation, computational mathematics*

Many softwares exist for solving partial differential equations through the finite element method [1]. We propose a new library, written from scratch entirely in C++, called maniFEM [2]. The name comes from “finite elements on manifolds". ManiFEM is free software (LGPL).

ManiFEM was designed with the goal of coping with very general meshes, in particular meshes on Riemannian manifolds, including quotient manifolds like the flat torus. Also, maniFEM was written with the goal of being conceptually clear and easy to read. We hope it will be particularly useful for people who want fine control over the mesh, e.g. for implementing their own meshing or remeshing algorithms.

Below is a very short program using maniFEM, and the produced mesh.

```
Manifold RR3 ( tag::Euclid, tag::of_dim, 3 );
Function xyz = RR3 .build_coordinate_system ( tag::Lagrange, tag::of_degree, 1 );
Function x = xyz[0], y = xyz[1], z = xyz[2];
Function seg_len = 0.1 + 0.05*x;
Manifold ellipse_manif = RR3 .implicit ( z == 0., x*x + 3.*y*y == 1. );
Mesh ellipse  // 'ellipse_manif' is used by default as working manifold
   ( tag::frontal, tag::desired_length, seg_len, tag::orientation, tag::random );
Manifold surface_manif = RR3 .implicit ( x*x + 3.*y*y + 3.*z*z == 1. );
Mesh surface  // 'surface_manif' is used as working manifold
   ( tag::frontal, tag::boundary, ellipse, tag::desired_length, seg_len );
```

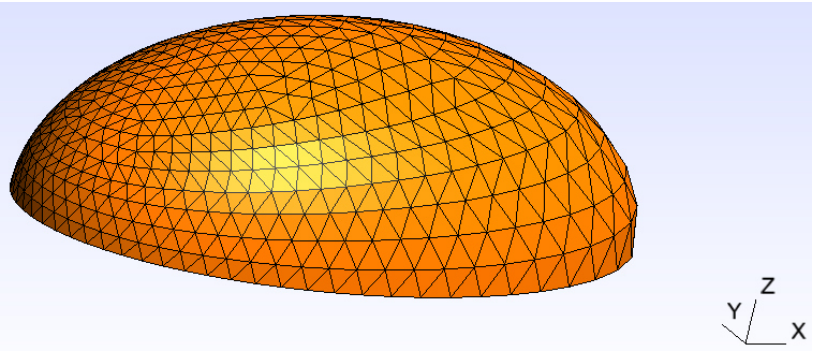

REFERENCES

[1] deal.II: https://dealii.org/, FEniCS/Dolphin: https://fenicsproject.org/, FreeFem++: http://www3.freefem.org/, GetFEM: https://getfem.org/, libMesh: https://libmesh.github.io/, PolyFEM: https://github.com/polyfem/polyfem

[2] maniFEM: https://manifem.rd.ciencias.ulisboa.pt/

Congress on Numerical Methods in Engineering 2024
4-6 September 2024, University of Aveiro, Portugal

Numerical tests for interpreting diffuse map cracking in laminar elements affected by concrete expansions

Dias I. F.*[1], Santos C. F.†[2], Batista A.L.*[3], Santos L.O.†[4]

*Departamento de Barragens de Betão, Laboratório Nacional de Engenharia Civil, Portugal
Email: [1]idias@lnec.pt ; [2]albatista@lnec.pt

† Departamento de Estruturas, Laboratório Nacional de Engenharia Civil, Portugal
Email: [3]cfsantos@lnec.pt ; [4]luisosantos@lnec.pt

ABSTRACT

The map cracking patterns that occur on the surfaces of concrete structures affected by internal expansions can be modelled and interpreted by considering the spatial variability of the expansions, at the scale of aggregates, according to a normal distribution.

In this context, for interpreting diffuse cracking in laminar concrete elements affected by expansions, three-dimensional finite element meshes with centimeter-scale discretization were considered. The spatial variability of the expansions was generated from the long-term expansion mean value and a coefficient of variation, assumed constant over time. The structural analysis considered the time evolution of the expansive action (of the sigmoidal type) [1], the viscoelastic [2] and nonlinear tensile behavior of the concrete [3], and the depreciation of the concrete properties, along time, due to the expansions [4].

The obtained results are promising concerning the interpretation of diffuse map cracking in laminar concrete elements, considering the spatial variability of the expansive action in a straightforward manner.

REFERENCES

[1] I.F. Dias, A.L. Batista and S. Ferra, Influence of temperature and stress field seasonal variations in the development of concrete swelling in dams. Application to the case of Covão do Meio dam (Portugal). *Proceedings of the 16th International Conference on Alkali-Aggregate Reaction in Concrete*, Volume II, Lisbom (2022).

[2] A.L. Batista, *Analysis of the behaviour over time of arch dams (in Portuguese).* PhD thesis, Instituto Superior Técnico, Lisbon (1998).

[3] R. Faria, J. Oliver and M. Cervera, A strain-based plastic viscous-damage model for massive concrete structures. *Int. J. Solids Structures*, Vol.35, No.14, pp 1533-1558, Pergamon (1998).

[4] J. Pan, Y.T. Feng, F. Jin and C. Zhang, Numerical prediction of swelling in concrete dams affected by alkali-aggregate reaction. *European Journal of Environmental and Civil Engineering*, 17:4, pp. 231-247 (2013)

Other topics in Numerical Methods in Engineering

This page intentionally left blank

Congress on Numerical Methods in Engineering 2024
4-6 September 2024, University of Aveiro, Portugal

Estudio de los ciclos de operación a corto plazo para el almacenamiento subterráneo de hidrógeno en cavernas salinas

F. Figueiras[1,*], A. Soage[1,2], J. París[1], I.Colominas[1] and L. Cueto-Felgueroso[2]

[1] Group of Numerical Methods in Engineering-GMNI, Center for Technological Innovation in Construction and Civil Engineering-CITEEC. Civil Engineering School, Universidade da Coruña, Campus de Elviña, s/n, 15071 A Coruña, Spain. web page: http://caminos.udc.es/gmni, e-mail: {f.fvelo, a.soage, jose.paris, ignacio.colominas}@udc.es

[2] Department of Civil Engineering: Hydraulics, Energy and Environment. Universidad Politécnica de Madrid. Madrid, Spain, e-mail: luis.cueto@upm.es

RESUMEN

La idea de emplear hidrógeno como fuente de energía renovable está creciendo en nuestros días [1]. Entre sus diferentes orígenes destaca el hidrógeno verde, obtenido de los excedentes energéticos de fuentes renovables. Para aprovechar de manera eficiente la energía transformada en hidrógeno se debe almacenar de alguna manera.

El almacenamiento subterráneo de hidrógeno se está convirtiendo en una opción viable frente al empleo de tanques metálicos en superficie, debido a los problemas de permeabilidad que presentan las estructuras metálicas frente al hidrógeno. Dentro de las posibles alternativas se encuentra el acondicionamiento y creación de cavernas salinas [2], puesto que la baja permeabilidad de la halita (roca de sal) permite confinar de manera eficiente el hidrógeno, sin producirse filtraciones.

Este estudio trata de comprobar la viabilidad de este tipo de almacenamiento, centrándose en los ciclos de operatividad a corto plazo, 30 años de vida útil. Los ciclos de operación se componen de cuatro fases diferentes, ordenadas de la siguiente manera: fase de carga, fase de mantenimiento a presión máxima o presión de trabajo, fase de descarga, y fase de mantenimiento a presión mínima o presión de gas colchón. Actualmente no existe una idea generalizada de cual es el periodo ideal de las fases en estos ciclos de operación para obtener mayor eficiencia y seguridad en la caverna.

En este estudio, se ha analizado mediante simulación numérica la influencia en la estabilidad de la caverna de dichos ciclos centrándonos en los tiempos de duración de cada una de las fases que componen el ciclo.

REFERENCIAS

[1] Kruck, O.; Crotogino, F.; Prelicz, R.; Rudolph, (2013). "*Overview on All Known Underground Storage Technologies for Hydrogen*", HyUnder. Grant Agreement 303417 Deliverable; p. 93.

[2] D. G. Caglayan, N. Weber, H. U. Heinrichs, J. Linßen, M. Robinius, P. A. Kukla and D. Stolten, (2020). "*Technical potential of salt caverns for hydrogen storage in Europe*", International Journal of Hydrogen Energy, Volume 45, Issue 11, Pages 6793-6805.

Congress on Numerical Methods in Engineering 2024
4-6 September 2024, University of Aveiro, Portugal

Envolvente de temperatura para la construcción de cavernas salinas

B. Fernández[1,*], A. Soage[1,2], J. París[1], I. Colominas[1], L. Cueto- Felgueroso[2]

[1] Grupo de Métodos Numéricos em la Ingeniería (GMNI), Centro de Innovación Tecnológica en Edificación e Ingeniería Civil (CITEEC). E.T.S. de Ingeniería de Caminos, Canales y Puertos. Universidade da Coruña
Campus de Elviña, s/n, 15071 A Coruña, España
Email: {blanca.fernandeza, a.soage, jose.paris, ignacio.colominas}@udc.es

[2] Departamento de Ingeniería Civil: Hidráulica, Energía y Medio Ambiente. Universidad Politécnica de Madrid. Madrid, España.
Email: luis.cueto@upm.es

RESUMEN

Disponer de energía abundante, limpia y a un precio razonable es uno de los retos a los que la humanidad lleva enfrentándose desde hace siglos. A su vez, dentro de este ámbito se pueden plantear numerosos hitos que aún no se ha conseguido resolver satisfactoriamente. El almacenamiento de energía de forma eficiente y en grandes cantidades es un aspecto fundamental de esta problemática sobre el que todavía no se tienen grandes avances.

El objetivo principal de este trabajo es estudiar el uso de cavernas salinas como sistema de almacenamiento masivo de hidrógeno. Es decir, se pretende alcanzar una visión global del comportamiento de las cavernas salinas que permita clasificar diferentes localizaciones terrestres como factibles o no para la construcción de cavernas salinas.

Los autores han analizado una caverna tipo en domos salinos a través de un modelo estructural aplicando el método de los elementos finitos que tiene en cuenta la evolución de la temperatura y la profundidad. Para poder conocer la respuesta estructural de la caverna ha sido necesario combinar un modelo elástico lineal con un modelo de fluencia de Norton [1], que se ha implementado para una vida útil de 30 años.

Los resultados de estos modelos permiten determinar si se garantiza la seguridad de la estructura para su vida útil o si, por el contrario, se experimentarán grandes deformaciones y tensiones; lo que puede provocar que se pierda resistencia en el macizo rocoso y su colapso. En cualquier caso, estas excesivas deformaciones provocarán una pérdida del volumen de la caverna que es necesario tener en cuenta.

La metodología desarrollada se ha aplicado con éxito a ejemplos reales de cavernas construidas en EEUU recientemente, y se ha comprobado que ninguna de ellas excede los valores límite de estabilidad determinados. Estos resultados abalan la metodología empleada en el estudio.

REFERENCIAS

[1] Ramesh Kumar, K., Makhmutov, A., Spiers, C. J. & Hajibeygi, H. (2021). Geomechanical simulation of energy storage in salt formations. Scientific Reports, 11(1), 19640. Engng. Comput., Vol. 10, pp. 543–561, 1993.

Congress on Numerical Methods in Engineering 2024
4-6 September 2024, University of Aveiro, Portugal

Multi-scale modelling of deformation-coupling and size effects in mechanical metamaterials

Wanderson F. dos Santos[1], Igor A. Rodrigues Lopes*[2], Francisco M. Andrade Pires[2,3] and Sergio P.B. Proença[1]

[1] Escola de Engenharia de São Carlos, Universidade de São Paulo, Av. Trabalhador São-Carlense, 13566-590 São Carlos, Brasil

[2] INEGI, Universidade do Porto, Rua Dr. Roberto Frias, 400, 4200-465 Porto, Portugal, Email: ilopes@inegi.up.pt

[3] DEMec, Faculdade de Engenharia, Universidade do Porto, Rua Dr. Roberto Frias, 4200-465 Porto, Portugal

ABSTRACT

Computational modelling of the exotic behaviour of mechanical metamaterials can be challenging due to intriguing properties and higher-order effects that cannot be predicted by classical continuum mechanics. Direct Numerical Simulations (DNS) of micro-architected structures are computationally demanding and multi-scale analyses based on FE^2 approaches are an interesting alternative. However, classical first-order homogenisation may also fail to capture some deformation mechanisms since it is based on classical Cauchy continua.

Therefore, a novel multi-scale second-order computational homogenisation formulation at finite strains [1], based on the Method of Multi-scale Virtual Power, is employed to explore the deformation-mode coupling in artificial materials with functional properties. The macro-scale is described by a second gradient theory, and the micro-scale Representative Volume Element (RVE) is modelled with the classical continuum theory, where the presence of a void phase is considered. The kinematics is defined only in the solid domain of the RVE, where an appropriate expression is postulated for the homogenisation of the second-order gradient. The framework provides the construction of three different sets of micro-scale kinematic constraints over the RVE: minimal (lower bound), periodic and direct (upper bound).

Several 2D and 3D multi-scale numerical examples of architected materials are employed to assess the robustness and predictive capability of the second-order computational homogenisation-based formulation. These examples encompass distinct deformation modes, including bending, tension/compression-induced undulation, and compression-induced torsion. Comparisons with the results obtained from first-order homogenisation and Direct Numerical Simulations are provided. In general, second-order computational homogenisation is better suited to capture coupling deformation mechanisms and size effects.

REFERENCES

[1] W.F. Dos Santos, I.A. Rodrigues Lopes, F.M. Andrade Pires and S.P.B. Proença. “Second-order multi-scale modelling of natural and architected materials in the presence of voids: Formulation and numerical implementation”, *Comput. Methods Appl. Mech. Eng.*, 416: 116374 (2023).

Congress on Numerical Methods in Engineering 2024
4-6 September 2024, University of Aveiro, Portugal

BUCKLING ANALYSIS OF ELASTIC COLUMNS AND FRAMES: MIXED FINITE ELEMENT FORMULATION AND ERROR ASSESSMENT

H.A.F.A. Santos[1] **and J.P. Moitinho de Almeida**[2]

1: Departamento de Engenharia Mecânica,
CIMOSM, UnIRE,
Instituto Superior de Engenharia de Lisboa, Instituto Politécnico de Lisboa,
Rua Conselheiro Emídio Navarro 1, 1959-007 Lisboa, Portugal,
e-mail: hugo.santos@isel.pt

2: Departamento de Engenharia Civil, Arquitetura e Ambiente,
Instituto Superior Técnico, Universidade de Lisboa,
Av. Rovisco Pais, 1049-001 Lisboa, Portugal,
e-mail: moitinho@civil.ist.utl.pt

Keywords: Elastic columns and frames, buckling analysis, Hellinger-Reissner energy, finite elements, lower bounds, upper bounds, error assessment.

Abstract *Various numerical techniques have been proposed in the literature for the buckling analysis of elastic framed structures. In a finite element framework, the so-called displacement-based finite element formulation is the most popular one. Complementary formulations, in which only force/moment like-quantities are taken as approximation functions, have also been employed. However, both types of formulations lead to numerical buckling loads that are upper bounds of the exact ones. Hence, by themselves, such formulations are not entirely useful, as they do not provide information on how far the estimated buckling loads lie above the true buckling loads. To have a validated buckling analysis study, it is necessary to find error estimates or, ideally, to determine lower bounds of the buckling loads. A mixed finite element formulation for the buckling analysis of elastic framed structures is proposed in this work. This formulation relies on a complementary form of the Hellinger-Reissner variational principle, involving the bending moment and rotation fields as fundamental unknowns. It will be numerically verified that, for a specific set of approximations, the solutions rendered by the formulation can be used to estimate both lower and upper bounds of the buckling loads.*

Congress on Numerical Methods in Engineering 2024
4-6 September 2024, University of Aveiro, Portugal

A C^0- Interior Penalty Finite Element method for flexoelectricity-enhanced photovoltaic effects at Finite deformations

S. Perez-Escudero*, I. Arias† and S. Fernàndez-Méndez†

Universitat Politècnica de Catalunya, Laboratori de Càlcul Numèric (LaCàN), Barcelona (08034)
Email: {sergi.perez.escudero, irene.arias, sonia.fernandez}@upc.edu

Supported by the European Research Council (StG-679451 to I.A.), the Spanish Government (RTI2018-101662-B-I00, CEX2018-000797-S) and the Generalitat de Catalunya (ICREA Academia to I.A., FI-AGAUR fellowship to S.P, and Grant No. 2021-SGR-010490)}

ABSTRACT

Keywords: *Flexo-photovoltaic effect, Flexoelectricity, Interior penalty method, 4th-order PDE, Finite Elements.*

In the last decades, many researchers have focused on improving the efficiency of existing photovoltaic techniques. In that direction, the study of the flexoelectric phenomena [1] has opened the path to another line of research referred to as flexo-photovoltaics [2]. There is, however, very scarce work done in its computational modelling and solution. In this work, a simple yet revealing model consisting on coupling the flexoelectricity [3] and the semiconductor modelling equations [4] is considered together with its Finite Element (FE) solution. The photovoltaic part of the model is discretized by means of standard C^0-FE approximations. However, flexoelectricity is modeled by 4th order PDE and, consequently, standard finite element formulations cannot be used. In infinitesimal deformations, its solution is carried out by means of the C^0-Interior Penalty Method described in [3]. The extension of the C^0-IPM formulation for the finite deformations (nonlinear) framework [5] is presented here. The coupling of photovoltaic and flexoelectric effects at finite deformations is currently under development.

REFERENCES

[1] Pavlo Zubko, Gustau Catalan, Alexander K. Tagantsev. “Flexoelectric Effect in Solids”. *The Annual Review of Materials Research, 33, 1, pp. 387-421. 2013*.
[2] Ming-Min Yang, Jik Kim, Marin Alexe. “Flexo-photovoltaic effect”. *Science, 2018*.
[3] Jordi Ventura, David Codony, Sonia Fernández-Méndez. “A C0 Interior Penalty Finite Element Method for Flexoelectricity”. *Journal of Scientific Computing. 2021*
[4] W. R. Van Roosbroeck. “Theory of flow of electrons and holes in germanium and other semiconductors”. *Bell System Technical J, 29: 560–607. 1950.*
[5] D. Codony, P. Gupta, O. Marco, I. Arias. “Modeling flexoelectricity in soft dielectrics at finite deformation”. *Journal of the Mechanics and Physics of Solids, 146. 2021*

Congress on Numerical Methods in Engineering 2024
4-6 September 2024, University of Aveiro, Portugal

A proposal of a numerical tool to design traditional timber pavements during inspection – A contribution

Filipe Silva[†] and Jorge Pinto*

[†] Departamento de Engenharias, Universidade de Trás-os-Montes e Alto Douro, Portugal
filipe_silva11@hotmail.com

* C MADE, Departamento de Engenharias, Universidade de Trás-os-Montes e Alto Douro, Portugal
tiago@utad.pt

ABSTRACT

The rehabilitation of traditional construction is an important sector in the building industry. It may be a proper economical and sustainable option considering that we may save building materials and gain time. At the same time, we are may contribute to keep the identity of a place. It is a fact, that main traditional Portuguese buildings include an expressive part of timber building elements. In particular, structural timber elements such as walls, beams, pavements, trusses, stairs, among other. This research work is related on studying traditional buildings in Pedras Salgas Village, Portugal. In particular, it is focused on studying the traditional timber pavements used in this Village such as the one presented in Figure 1. Therefore, a surveying form was proposed for this context. In addition, this form is linked with an Excel page that allows an automatically numerical design of traditional timber pavement according to EC5 [1]. By this way, during an inspection process, it is possible to have a clue about the safety of a traditional pavement. This proposal may give a contribution for a Construction 4.0 [2].

Figure – Example of a traditional timber pavement of Pedras Salgadas Village

REFERENCES

[1] Eurocode 5: Design of timber structures - Part 1-1: General -. Common rules and rules for buildings.
[2] Miguel Branco-Teixeira et al. (2023). MANUAL DE INOVAÇÃO E SUSTENTABILIDADE. Os Desafios e as Soluções na Reabilitação Urbana 4.0 - Materiais, Tecnologias, Recursos Humanos e Segurança. Universidade Fernando Pessoa e Associação dos Industriais da Construção Civil e Obras Públicas. pp. 337

Predicting failure of structures with second-order homogenisation and non-local damage models

Guilherme F. Gonçalves*,[1], Igor A. R. Lopes[2], Francisco M. A. Pires[1]

[1] DEMec FEUP, Departamento de Engenharia Mecânica da Faculdade de Engenharia da Universidade do Porto

[2] INEGI, Institute of Science and Innovation in Mechanical and Industrial Engineering

RESUMO

Finite element simulations supported by non-local constitutive models introduce the effect of an internal length scale parameter on the predicted mechanical response. This kind of description is of particular relevance for the analysis of structures where the stress state in regions close to a crack tip or in the presence of strain localization becomes paramount.

In the framework of multi-scale models based on computational homogenization, where the effect of heterogeneous microstructures is naturally accounted for in the macroscopic response, second-order homogenization models are characterized by the introduction of a length scale parameter and, consequently, of non-local effects. However, the relationship between second-order homogenization models and macroscopic non-local models is still under-explored.

Therefore, this work focuses on the application of this kind of multi-scale approach to model the progressive failure of structural details, considering microstructures containing voids as damage precursors. First, standard single-scale local damage models and multi-scale models based on first-order computational homogenization of RVEs with voids are employed in the analysis of structural failure. Second, the analysis is repeated with non-local damage models and second-order homogenization. The mesh regularization obtained with each approach is meticulously compared, in what concerns the length scale parameter and its influence on the failure mode. Finally, a connection between the non-local characteristic length and the second-order intrinsic length-scale parameter will be established.

Congress on Numerical Methods in Engineering 2024
4-6 September 2024, University of Aveiro, Portugal

Enriched discretizations for accurate phase field models with sharp interfaces: applications to fracture.

Miguel Castillón[*1], Javier Segurado[1,2] and Ignacio Romero[1,3]

[*1] Instituto IMDEA Materiales, Eric Kandel 2, Tecnogetafe, 28906 Madrid
Email: miguel.castillon.demiguel@imdea.org

[2] Universidad Politécnica de Madrid, Departamento de Ciencia de Materiales, E.T.S.I. Caminos, 28040, Madrid
Email: javier.segurado@imdea.org

[3] Universidad Politécnica de Madrid, Departamento de Ingeniería Mecánica, E.T.S.I. Industriales, 28006, Madrid
Email: ignacio.romero@imdea.org

ABSTRACT

One of the main limitations of phase field-based models is their high computational cost. Within the framework of finite elements, the size of the finite elements must be orders of magnitude smaller than the scale factor responsible for regularizing the diffuse field. This requirement necessitates many elements to capture the interface or discontinuity. Additionally, the solution exhibits a strong dependence on the orientation of the elements.
In order to reduce the computational cost and improve the convergence rate of the solution, a non-conforming finite elements formulation is presented. This formulation enriches the Galerkin solution space with non-conforming functions, including incompatible bubbles. All of this is carried out within a consistent variational formulation. The developed formulation demonstrates better convergence errors than the standard formulation and reduces the influence of the element's orientation. The application of this formulation is proposed for phase-field-fracture models.

Congress on Numerical Methods in Engineering 2024
4-6 September 2024, University of Aveiro, Portugal

Variational methods for the simulation of hydrogen transport in metals

Eva M. Andrés[1], Ignacio Romero*[,2] and Javier Segurado[3,4]

[1] Universidad Politécnica de Madrid, José Gutiérrez Abascal, 28006, Madrid, España
Email: eva.andres.lopez@upm.es

[*] Universidad Politécnica de Madrid, José Gutiérrez Abascal, 28006, Madrid, España
Email: ignacio.romero@upm.es

[2] IMDEA Materials Institute, Eric Kandel, 28906, Madrid, España
Email: ignacio.romero@imdea.org

[3] Universidad Politécnica de Madrid, Profesor Aranguren, 28040, Madrid, España
Email: javier.segurado@upm.es

[4] IMDEA Materials Institute, Eric Kandel, 28906, Madrid, España
Email: javier.segurado@imdea.org

ABSTRACT

The diffusion of atomic hydrogen through metals is governed by the hops of such atoms among interstitial lattice sites and their chances of remaining trapped in heterogeneities (dislocations, grain boundaries, voids, interfaces, impurities, etc.). In order to study their effects on the ductility and fracture resistance of metals, these complex mechanisms need to be understood and modeled. Additionally this motivates the development of numerical methods.

As far as hydrogen transport in metals is concerned, the main difficulties are the treatment of the boundary conditions and distinguishing the evolution of the free and trapped hydrogen atoms. In this work, we will propose a new formulation modeling transient solutions to this problem in which we use an incremental variational principle whose stationarity conditions include the thermodynamic equilibrium between the two types of hydrogen atoms, following [1]. This formulation ensures, among other things, the symmetry of the tangent operator leading to large computational savings.

Numerical simulations of stationary and transient solutions obtained with this method will be presented.

REFERENCES

[1] I. Romero, E. M. Andrés, and Á. Ortiz-Toranzo. Variational updates for general thermo-chemo-mechanical processes of inelastic solids. *Computer Methods in Applied Mechanics and Engineering*, 385:114013, Nov 2021.

Congress on Numerical Methods in Engineering 2024
4-6 September 2024, University of Aveiro, Portugal

Análisis de Estabilidad de Cavernas de Sal en Formaciones Salinas Estratificadas para el Almacenamiento de Hidrógeno Verde

A. Soage[1,2] *, F. Navarrina[1], R. Juanes[3,4], J. Paris[1], I. Colominas[1] y Luis Cueto-Felgueroso[2]

[1] Grupo de Métodos Numéricos en Ingeniería (GMNI), Centro de Innovación Tecnológica en Edificación e Ingeniería Civil (CITEEC), Universidad de A Coruña (UDC), Campus de Elviña, A Coruña, 15008, Galicia, España.
Email: a.soage@udc.es (A.S.); fermin.navarrina@udc.es (F.N.); jose.paris@udc.es (J.P.); ignacio.colominas@udc.es (I.C.).

[2] Departamento de Ingeniería Civil: Hidráulica, Energía y Medio Ambiente. Universidad Politécnica de Madrid (UPM), Madrid, 28006, España.
Email: andres.soage@externos.upm.es (A.S.), luis.cueto@upm.es (L.C.-F.)

[3] Department of Civil and Environmental Engineering, Massachusetts Institute of Technology. Cambridge, MA, 02139, USA.
E-mail: juanes@mit.edu. (R.J.)
[4] Department of Earth, Atmospheric and Planetary Sciences, Massachusetts Institute of Technology, Cambridge, MA,02139, USA.
E-mail: juanes@mit.edu

RESUMEN

Las cavernas ejecutadas en formaciones salinas mediante procesos de lixiviación se postulan como uno de los mejores sistemas de almacenamiento de hidrógeno verde.

En este contexto, las formaciones de sal aprovechables están muy bien distribuidas por todo el mundo y pueden clasificarse en dos tipos: formaciones tipo domo, es decir, grandes formaciones subterráneas de geometría fúngica con diámetros de hasta 2 km, y por otro lado, capas horizontales estratificadas con un espesor de capa de 50 a 200 m. Se estima que la mitad de las formaciones salinas son de un tipo y la otra mitad de otro tipo.

En el diseño de cavernas en formaciones estratificadas existe una clara restricción geométrica ya que el espesor y por tanto la altura de la caverna será bastante limitada. Por este motivo, para conseguir diseños de mayor volumen será necesario aumentar el tamaño de las cavernas en dirección horizontal manteniendo su estabilidad. En este tipo de cavernas la cantidad de energía almacenada está restringida por la deformación vertical de la caverna en su eje central

Como metodología para este análisis utilizamos la simulación numérica, barriendo diferentes tamaños de geometrías esféricas-cilíndricas y definiendo los criterios de estabilidad que permitan la elección de un diseño estable a largo plazo.

Nuestros descubrimientos apuntan a que se pueden construir geometrías capaces de almacenar grandes cantidades de hidrógeno verde en formaciones estratificadas. Para ello se requiere de un delicado equilibro entre la vida útil de la infraestructura, el tamaño de la caverna y la presión de gas colchón almacenada.

REFERENCIAS

[1] K. Ramesh Kumar, A. Makhmutov, C.J. Spiers y H. Hajibeygi. Geomechanical Simulation of Energy Storage in Salt Formations. Scientific Reports, 2021, 11(1), 19640.

Congress on Numerical Methods in Engineering 2024
4-6 September 2024, University of Aveiro, Portugal

DYNAMIC SIMULATION WITH NUMERICAL MODEL TO CALIBRATE HOT-BOX PARAMETERS FOR LIGHT STEEL FRAME

Langner, M[1], Figueiredo, A[1], Vicente, R[1], Almeida, R.S.F[2,3], Soares, T[1]

1: RISCO-Risks and Sustainability in Construction, Civil Engineering Department, University of Aveiro
3810-193 Aveiro | Portugal
e-mail: marcelolangner@ua.pt, web: https://www.ua.pt/pt/risco

2: Department of Civil Engineering, Polytechnic Institute of Viseu, School of Technology and Management
Campus Politécnico de Repeses,
3504-510 Viseu | Portugal
3: Institute of R&D in Structures and Construction-LFC (CONSTRUCT-LFC), Faculty of Engineering (FEUP), University of Porto, Rua Dr. Roberto Frias s/n,
4200-465 Porto | Portugal

Keywords: Hot-box, Numerical Methods, Ansys, Light Steel Frame, Dynamic Simulation, Thermal Simulation.

Abstract *The use of dynamic simulation with numerical methods during the design phase allows for the efficient and economical analysis of various scenarios, minimizing costs related with real-test and maximizing reliability in solving complex problems. This study includes heat flow data obtained through experimental testing with Hot-box equipment in a wall constructed using Light Steel Frame (LSF) technology. This data was used to calibrate the numerical model developed in Ansys for the thermal analysis impact of adding a steel member in the middle of the LSF system and determining the thermal transmittance of the analysed system. To achieve this purpose, dynamic simulation under the same boundary conditions as the real experiment using the Transient Thermal module of Ansys Mechanical was performed. As a secondary objective, was also evaluated the needed time until to attain equilibrium conditions in terms of heat flow by dynamic simulation. This works aims not only to improve the accuracy and reliability of thermal transmittance results but also to contribute by providing reliable and validated data for the development of innovative construction solutions in the civil construction market.*

Congress on Numerical Methods in Engineering 2024
4-6 September 2024, University of Aveiro, Portugal

Nonlinear behavior of tunable metamaterials: the General Auxetic Metamaterials (GAM) lattice.

Juan A. López-Salido*, Miguel A. Sanz-Gomez†, Luis Saucedo-Mora†, Laura Moreno Corrales†, and Francisco Javier Montáns Leal†

* Departamento de Aeronaves y Vehículos Espaciales, Universidad Politécnica de Madrid, Spain
Email: juanantonio.lopez.salido@alumnos.upm.es

† Departamento de Aeronaves y Vehículos Espaciales, Universidad Politécnica de Madrid, Spain
Email: miguelangel.sanz@upm.es, luis.saucedo@upm.es, laura.mcorrales@upm.es, fco.montans@upm.es

ABSTRACT

Auxetic metamaterials are based on an unique counter-intuitive property: negative Poisson's Ratio. This objective is based on the analysis of non-linear behaviour of metamaterial structures in large strains.

Additionally, a wide variety of indentation tests are carried out and the macroscopic behaviour of the different structures under these tests is characterized. It is very interesting to obtain significant information from the elastoplastic region, as very few analysis have been carried out about it. In addition, the auxetic behaviour presented by the cell patented by Polytechnic University of Madrid is characterized [1]. This cell has recently obtained the patent and presents unique characteristics: it has a double configuration (one with negative Poisson's Ratio and another with positive Poisson's Ratio) very similar and chosen by user, so that a transition can be implemented.

In addition, this new cell is perfectly tunable, and the variation of its parameters can substantially change the behavior of the whole structure. Other objective of this dissertation will focus on modifying one of the parameters and see how the structure responds to the same load case.

Auxetic metamaterials have negative Poisson's ratio, increasing their performance when it comes to impact behaviour and offering a new research field. A while ago, it might have been thought that such complex geometries were impossible to manufacture with the technology of that time. However, the development of new 3D printing technologies offers a truly viable path for the creation of huge metamaterial structures [2].

REFERENCES

[1] Ismael Ben-Yelun, Guillermo Gómez-Carano, Francisco J. San Millán, Miguel Ángel Sanz, Francisco Javier Montáns, and Luis Saucedo-Mora. Gam: General auxetic metamaterial with tunable 3d auxetic behavior using the same unit cell boundary connectivity. Materials, 16(9):3473, April 2023.

[2] Ismael Ben-Yelun Insenser, Elemer José San Miguel Niddam, Luis Saucedo-Mora, Miguel Ángel Sanz Gómez, José María Benitez Baena, and Francisco Montans Leal. 3dmecmet: A package to fill with metamaterials cad designs and export them to structural calculation softwares and 3d printable formats. Software Impacts, 18:100594, November 2023.).

Congress on Numerical Methods in Engineering 2024
4-6 September 2024, University of Aveiro, Portugal

MEASUREMENT AND MODELLING OF IN-PLANE DEFORMATIONS IN PINE WOOD AND MEDIUM DENSITY FIBREBOARD AT ELEVATED TEMPERATURES

Matheus Alves[1], Luís Mesquita[2], Paulo Piloto[3] and Nuno Lopes[4]

1: RISCO, Research Centre for Risks and Sustainability in Construction
Department of Civil Engineering
Universidade de Aveiro
Campus Universitário de Santiago, 3810-193, Aveiro, Portugal
e-mail: matheus.alves@ipb.pt

2: ISISE, Institute for Sustainability and Innovation in Structural Engineering
3: LAETA-INEGI, Instituto Politécnico de Bragança
4: RISCO, Research Centre for Risks and Sustainability in Construction

Keywords: wood, wood-based, coefficient of thermal expansion, thermomechanical analysis, high temperature testing

Abstract *The need to reduce the environmental impact of the construction industry along with innovations in engineered wood-based products has contributed to the promotion of wood-based constructions as viable alternatives to traditional methods. In fire conditions, thermal strains and stresses develop in wood and wood-based materials. A thermomechanical analysis is required to account for such thermal strains and stresses, but material properties such as the coefficient of thermal expansion (CTE) at elevated temperatures are usually not available. In this work, in-plane deformations in small-scale Pinus pinaster and medium-density fibreboard (MDF) samples are investigated through experiments and finite element heat transfer and thermal strain simulations. The CTE was calculated on the basis of the experimental findings and used as input to the thermal strain analysis. The results obtained in the transient heat transfer model showed good agreement for the internal temperature evolution, but accounting for internal heat generation and mass transfer could improve the temperature predictions. The numerical results for the in-plane displacement showed good predictions but require further validation for other experimental setups and scales. The data provided in this work could be useful to investigate the loss of integrity of wood and wood-based materials under fire through thermomechanical models, and an alternative methodology is proposed to measure the temperature-dependent CTE. Efforts are still required to obtain reliable thermomechanical properties above 300 ° C, when large deformations are expected, thus contributing to understanding the fire behaviour of wood-based structures.*

Congress on Numerical Methods in Engineering 2024
4-6 September 2024, University of Aveiro, Portugal

ANÁLISE NUMÉRICA SOBRE A INFLUÊNCIA DAS PROPRIEDADES VISCOELÁSTICAS DOS INTERCALARES NA DEFLEXÃO DE PAINÉIS DE VIDRO LAMINADOS SIMPLESMENTE APOIADOS

Hugo Delgado[1], Eliana Inca[2] e Sandra Jordão[3]

1: ISISE, Departamento de Engenharia Civil
Faculdade de Ciências e Tecnologia
Universidade de Coimbra
Rua Sílvio Lima, Pólo II da Universidade de Coimbra, 3030-790 Coimbra
e-mail: hugo.delgado@uc.pt

2: Departamento de Engenharia Civil
Faculdade de Ciências e Tecnologia
Universidade de Coimbra
Rua Sílvio Lima, Pólo II da Universidade de Coimbra, 3030-790 Coimbra
e-mail: e.inca.cabrera@uc.pt

3: Departamento de Engenharia Civil
Faculdade de Ciências e Tecnologia
Universidade de Coimbra
Rua Sílvio Lima, Pólo II da Universidade de Coimbra, 3030-790 Coimbra
e-mail: sjordao@dec.uc.pt

Palavras-chave: Intercalares Viscoelásticos, Painéis de Vidro, Reologia, Métodos Numéricos, PVB, SentryGlas,

Resumo. *Este artigo investiga a influência das propriedades viscoelásticas em painéis de vidro laminados simplesmente apoiados quando submetidos a uma carga lateral uniformemente distribuída. Um modelo numérico foi desenvolvido em ABAQUS e validado frente a resultados experimentais, obtidos no Laboratório de Engenharia Civil da Universidade de Coimbra. O modelo é usado para examinar a influência da temperatura e da velocidade de carregamento na deflexão dos painéis. A análise abrange os dois principais intercalares do mercado, o PVB e o SentryGlas.*

List of Full Articles

This page intentionally left blank

Congress on Numerical Methods in Engineering 2024
4-6 September 2024, University of Aveiro, Portugal

A NUMERICAL STUDY ON FIRE PROTECTION OPTIMIZATION DESIGN OF STEEL WAREHOUSE STRUCTURES

Pegah Aghabozorgi[1], Luís Laím[1] and Aldina Santiago[1]

1: ISISE, ARISE, Department of Civil Engineering,
University of Coimbra, Coimbra, Portugal
3030-788
e-mail: {pa,luislaim}@uc.pt & aldina@dec.uc.pt https://isise.net/

Keywords: Steel warehouse, Numerical analysis, Fire protection mortars, Fire design, Fire protection optimization, Temperature distribution.

Abstract *This paper presents an optimization study aimed at enhancing the resistance and overall stability of steel warehouse structures in fire. 3D finite element (FE) models of steel portal frames protected with gypsum-based insulation boards were developed for heat transfer and thermo-mechanical analysis. The thermal properties of fire protection materials were temperature-dependent and defined based on previous thermal analysis tests.*

The optimization was carried out in terms of the thickness of the fire protection coating layer through an iterative process. Optimal thicknesses were determined for achieving a frame fire resistance rating of R60 under various thermal actions, including ISO-834 standard time-temperature curve as well as advanced curves generated by fire simulation software (CFAST).

Furthermore, a novel formula was proposed to predict steel temperature evolution in protected structural H-shaped elements. Then, a comparison was made between the predicting temperature distribution from this formula with the corresponding one taken from Eurocode design methods as well as FE analysis results (heat transfer analysis). The objective is to evaluate the fire protection optimization in terms of thermal actions.

The study contributes to a more precise evaluation of fire resistance in steel-framed warehouses protected with fire protection boards by taking into account the temperature evolution distribution within steel elements under elevated temperatures. These findings are also crucial for developing optimized fire design strategies that ensure structural integrity and safety of industrial steel warehouses under various fire conditions.

1. INTRODUCTION

Steel structures have long been preferred for constructing long-span industrial buildings like warehouses due to their remarkable strength-to-weight ratio, design flexibility, and increasing emphasis on sustainability. However, in terms of fire resistance, steel structures face challenges compared to other alternative materials like concrete due to their high thermal conductivity and lower specific heat capacity. Hence, implementing effective fire protection measures becomes crucial to maintain structural integrity during fire incidents, allowing safe evacuation and intervention to minimize risks.

Among different fire protection materials aimed to improving the fire performance of steel portal frame elements within warehouses, gypsum-based coatings have emerged as a practical solution due to their excellent thermal properties such as low thermal conductivity, high specific heat capacity as well as cost-effectiveness. Moreover, the effectiveness of these fire protection materials in providing the thermal protection and improving fire resistance of steel structures have been proven to us from previous studies [1]–[4]. For example, in a study conducted by Aghabozorgi *et al.* [5], the fire performance of gypsum-based fire protection boards has been evaluated when they are protecting the main structural elements of one-story industrial shed. Based on the analysis results from this study, 5-6 mm layer of gypsum-based insulation coatings could provide adequate resistance to one-hour ISO-834 fire curve [6].

Moreover, previous works showed that different factors such as opening factors, lateral restraints, thermal properties, and thermal actions can significantly affect the fire performance and optimal fire protection requirements in these structures [7]. For example, removing lateral restraints doubled the required fire protection thickness layer or considering the temperature-dependent nature of thermal properties of fire protection materials increased the required fire protection thickness up to 50%. In another example, removing the roof opening resulted in a threefold increase in required fire protection thickness compared to a 5% roof opening scenario. Besides that, the analysis results from the second case study portal frame demonstrated that usually the optimal FP thickness from the FDS fire simulation [8] is trivial (5mm) due to the short duration of high temperatures experienced by the columns.

However, there remains a gap in the literature regarding the optimization design of such structures using the same fire protection materials while considering all influential parameters simultaneously to develop an optimized fire design approach.

Therefore, this paper conducts fire protection optimization for a one-story industrial shed without roof opening under two different thermal actions, including ISO-834 standard time-temperature curve [6] and natural fire curve from CFAST (Consolidated model of Fire and Smoke Transport) [9]. The thermal properties of fire protection materials are based on previous thermal analysis tests conducted at the ISISE laboratory at the University of Coimbra. The objective is to determine the optimal fire protection thickness required for steel elements under one-hour fire exposure while accounting for the thermal properties as a function of temperature. FE models were developed in Abaqus (version 2021) [10] for linear buckling, heat transfer, and thermo-mechanical analysis. In addition, a formula is proposed to predict the temperature distribution of steel in protected elements of the warehouses under fire conditions as an alternative to prediction equations established in Eurocode 1993-1-2:2005 [11]. The

temperature distribution curves in steel elements taken from standard Eurocode, heat transfer results, and new proposed formula are compared considering different thermal actions to evaluate the optimization in terms of thermal actions. This study aims to develop a suitable fire protection optimization approach for steel industrial warehouses, ensuring both safety and efficiency to enhance competitiveness of steel in long-span industrial construction and promote advantages over alternative materials like concrete.

2. CASE STUDY

A one-story steel industrial sheds was selected as a case study to do the optimization fire design in terms of fire protection. This optimization was based on predicted temperature profiles from fire environment and obtained from either standard fire curve ISO-834 or two-zone fire model in fire simulation software CFAST. The main objective was to identify the optimal fire protection thickness required for steel elements, rafter and column, to provide the safety measures for large-space warehouse buildings during one-hour fire exposure.
Figure 1 shows a sketch view of the portal frame used in the simulation with some dimensions. As shown in this figure, the frame geometry had a span of 25 m (L), total height of 8.9 m, and pitch of 5.71º. The length of the frame was equal with four times the span distance and each frame spacing of one-quarter 6.25 m (L/4) of the span. The length and depth of the haunch part rafter were determined according to the design standards and equal to 2.5 m (L/10), and 0.714 m (L/25), respectively. The purlins and façade rail beams typically placed at every 2.5 m and 1.875 m over the rafters and columns, respectively, were excluded from this finite element (FE) analysis. This exclusion allows for examining a critical scenario with optimized fire protection without secondary beams, ensuring the portal frame´s structural integrity under the extreme conditions.
The structure was made of steel hot rolled profiles; IPE450 for rafters and HEB 260 for columns. All four sides of structural elements were protected against fire by a layer of gypsum-based fire protection coating. Moreover, the portal frame was pinned at the column bases and laterally restrained by horizontal bracing members.
The load acting on the frame is 2.2 KN/m vertical uniformly distributed load based on ULS load combination (i.e., 1.35G + 1.5Q + 0.75 S) with the maximum utilization factor calculated according to EN 1990 [12], being G the permanent load, Q the variable imposed load (calculated from EN 1991-1-1:2003 [13]), S the variable load of snow.

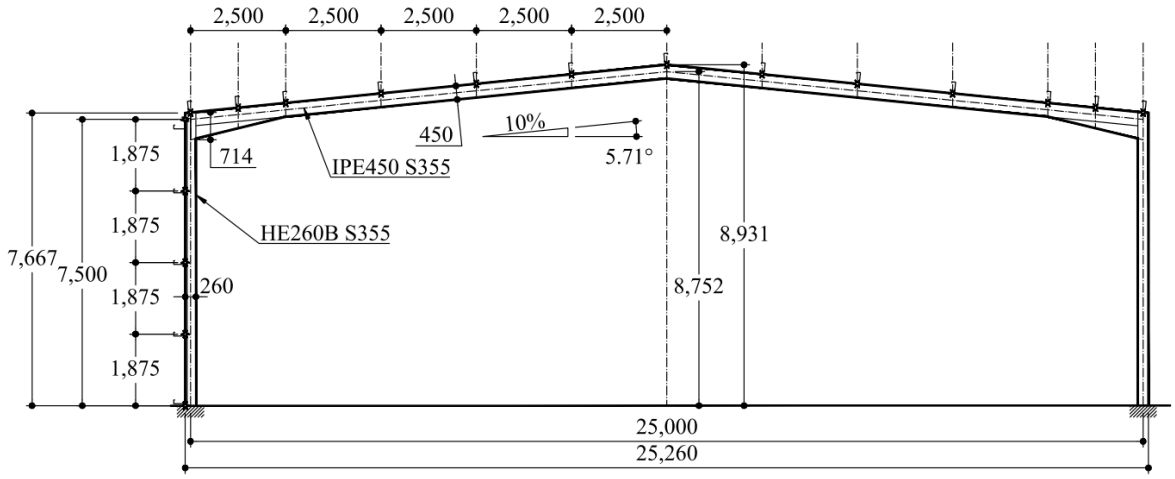

Figure 1. Two-pitched industrial shed to be analysed: reference case study [14].

3. DEVELOPMENT OF NUMERICAL SIMULATIONS

To evaluate the fire resistance of a single portal frame from the industrial shed in Figure 1 and optimize the fire protection applied to its main steel elements, FE models were created using Abaqus software (version 2021) [10]. The analysis involved three sequential steps: (i) linear buckling analysis evaluating the buckling susceptibility of the members and applying the global imperfection corresponding to primary buckling mode for each element with the magnitude of L/100 (EN 1993-1-1 [15]) for the thermo-mechanical analysis, and (ii) heat transfer analysis predicting the temperature distribution along the members under fire conditions, and finally (iii) thermo-mechanical analysis combined the results from previous steps to evaluate the structural response of the portal frame members under combined thermal and dynamic actions. Note that, fire optimization design was achieved through an iterative process. This approach allowed for a comprehensive evaluation of the frame's fire resistance and the optimization of its fire protection for optimal performance.
As previously mentioned, a parametric study was conducted to optimize fire protection for steel warehouses. This involved selecting an appropriate design fire model and comparing the optimization results obtained with this model against those using the standard fire design model on the structural elements. The chosen fire design model serves as input for calculating the temperature distribution within the compartment. Therefore, a two-zone model was implemented using the fire modelling software CFAST (version 7.7.0) [16] to simulate the impact of a localized fire on the building. This focus on localized fires aligns with the more common fire scenario in steel warehouses compared to generalized fires.

3.1. Finite Element Model

A simplified 3D FE model of half the portal frame was created, leveraging symmetry (Figure 2). All elements, including columns, rafters, and their fire protection coating (gypsum-based mortar), were modelled using 4-node shell elements with reduced integration (S4R). A

consistent mesh size of 25 mm was used for the cross-section and 50 mm along the member length.

To accurately simulate the real-world support conditions, two reference points were defined: one at the column base centroid and another at the rafter-end (left and right ends) (see Figure 2). The kinematic coupling constraint method was then employed to connect each reference point to its corresponding cross-section surface. This coupling ensured that all six degrees of freedom (three translational (U1, U2, and U3) and three rotational (UR1, UR2, and UR3)) at the cross-section points were constrained to match the motion of their respective reference points. Besides that, each surface at the connection was coupled to a reference point, and these reference points were further tied together to simulate the connection between rafter and column (see Figure 2).

Pinned support condition at the column base were achieved by constraining all displacements (U1=U2= U3= 0) and one rotation (UR2=0) at the column base reference point. While at the right end, all the displacements and rotations were constrained except for the vertical displacement (U3=0) at the reference point, simulating a roller support. Vertical loads were applied over the rafters at the mid-points where the purlins are located. Lateral restraints were applied to the outer flange of the rafters and columns at their connection points.

A multi-step analysis was conducted sequentially to assess the overall structural response of the industrial metal shed with enhanced gypsum-based mortar protection. This analysis included: buckling analysis, heat transfer thermal analysis, and nonlinear geometric and material static analysis.

3.1.1 Description of material properties

The main components of the portal frame were made of steel with yield strength of 355 MPa (S355) and Young's modulus of 200 GPa. A nonlinear isotropic material model with von Mises yield criterion was used. At ambient temperature, Young's modulus and yield strength were incorporated. To account for the temperature dependence of steel properties during fire events, Eurocode 1993-1-2:2005 [17] was followed. True stress-strain curve was used to capture the steel behaviour under fire-induced deformations. Moreover, a constant density (7850 Kg/m^3) and Poisson’s ratio (0.3) were assigned in the FE analyses.

In terms of fire protection material, the thermal properties used in the FE analysis were established from previous thermal analysis tests carried out at the laboratory of Civil Engineering Department at the University of Coimbra (DEC-UC) [1]. Tests were performed at three different temperature levels: 25 ºC, 250 ºC, and 350 ºC [2]. Figure 3 presents the apparent experimentally derived apparent thermal properties of the gypsum-based mortar coating as a function of temperature.

The fire protection material is estimated to have a modulus of elasticity of 1.3 GPa, a Poisson's ratio of 0.2, and a compressive strength of 1.2 MPa.

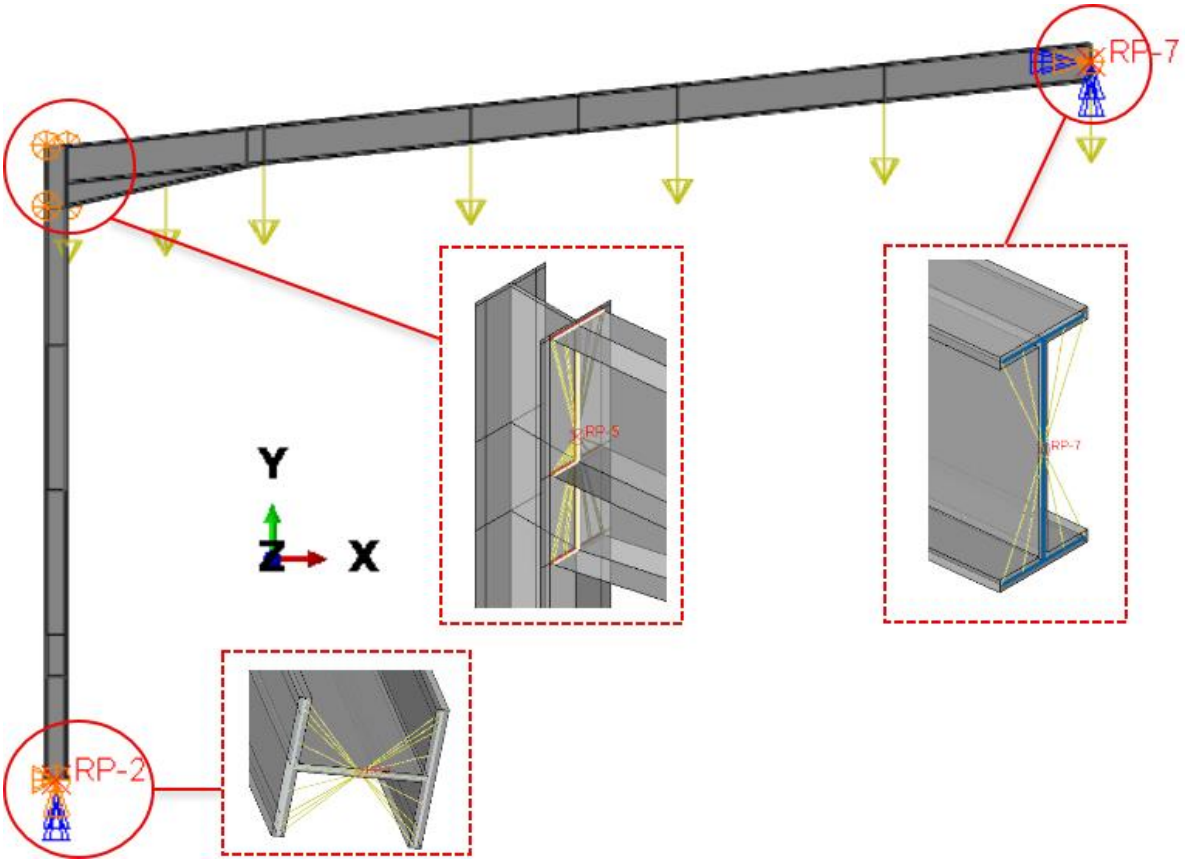

Figure 2. Finite element model of half portal frame with fire protection [7].

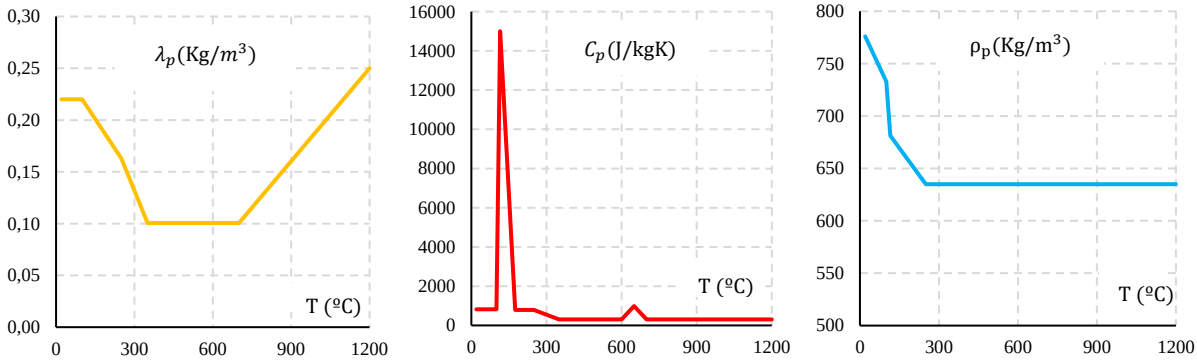

(a) (b) (c)

Figure 3. Thermal properties of gypsum-based fire protection mortar [5].

3.2. CFAST Natural Fire Model

To predict the gas temperature distribution inside a warehouse compartment using a two-

zone model, key features like fire loads, openings, and the compartment dimensions were defined in CFAST simulation software. This case study considered a fire located at the center of a 25m×25m warehouse compartment. Two façade openings measured 3m×3m each, while the roof remained sealed. Due to the industrial nature of the structure, a fast fire growth rate was assumed. The fire load density (FLD) was set to 1755 MJ/m^2, with a maximum heat release rate (HRR) of 35 MW (compliant with EN 1991-1-2 [18]). The fire load area was 36 m^2, and wood, with a heat combustion value of 17500 kJ/kg, was chosen as the primary fuel.

The gas temperature-time curves for different zones obtained from the simulation in CFAST software were plotted in

Figure **4** (a). These curves showed that CFAST fire heats up slower compared to the ISO-834 temperature-time curve but reaches higher peak temperatures in both hot-air and plume air zones.

Since the fire was centered, the heat distribution on the steel elements (see Figure 4 (b)) corresponded to their zone location. The lower column section, exposed to the cold air zone, experienced a maximum temperature of 597 ºC. Conversely, the upper column section, located in the hot air zone, reached a maximum temperature of 899 ºC. The rafter was divided into two sections based on proximity to the fire. The section closer to the center was exposed to the plume air with a peak temperature of 1500 ºC, while the section closer to the column was exposed to the hot air, reaching a maximum temperature of 899 ºC (same as the upper column). The hot and cold zone boundaries were defined by the temperature height profile obtained from CFAST.

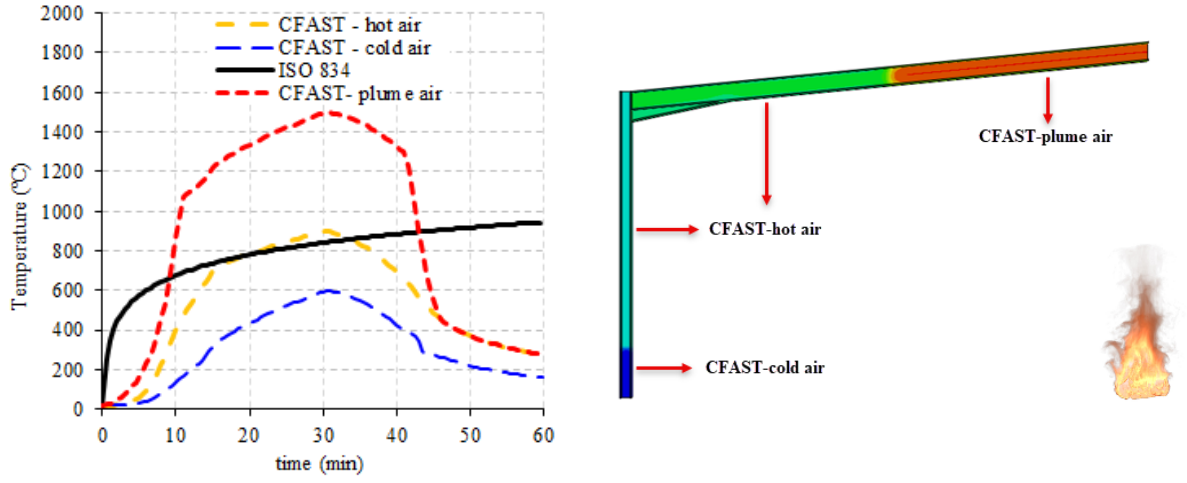

(a) (b)

Figure 4. (a) Evolution of gas temperature in the warehouse compartment simulated with CFAST software (b) Schematic illustration of steel frame configuration with specified fire scenario applied to each section of steel elements [7].

4. DESIGN AND NUMERICAL PARAMETRIC RESULTS AND DISCUSSION

4.1. Influence of thermal actions on optimization design (parametric analysis)

A parametric analysis was conducted in this section to evaluate the influence of different fire scenarios on the optimization of fire protection design in warehouse structures. The analysis focuses on determining the optimal fire protection thickness required for structural stability during a one-hour exposure to both standard and natural fire scenarios. This process considers the structure's failure time and fire resistance rating, while also accounting for the temperature-dependent thermal properties of the fire protection coating.

Figure **5** and
Figure **6** present the thermo-mechanical results regarding the optimal fire protection thickness obtained for the main components of the steel portal frame (rafter and column) based on two different thermal actions: standard and natural fire curve.

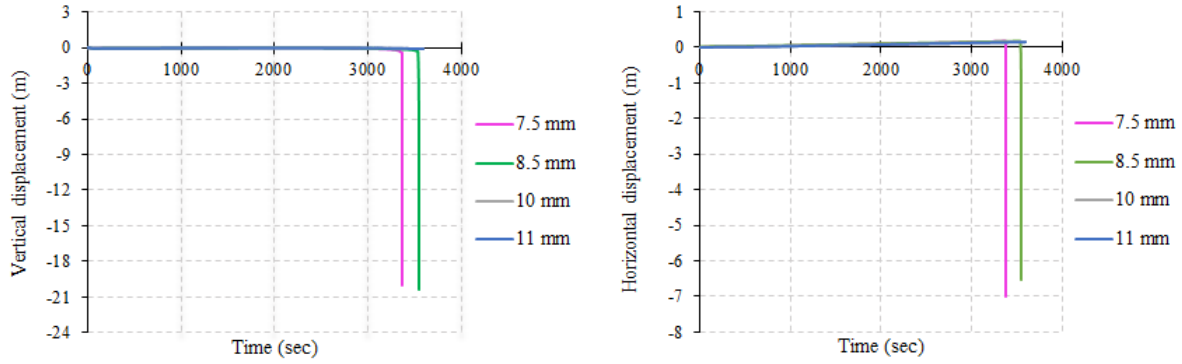

(a) (b)

Figure 5. Evolution of vertical displacement at frame peak and (b) maximum horizontal displacement at the column for different FP thicknesses under one-hour exposure to ISO-834 standard fire curve.

Figure 5 displays the results of a thermo-mechanical analysis performed using Abaqus FE software when the standard ISO-834 fire curve was applied to the elements as the thermal action. As the figure shows, a significant increase in frame displacement (vertical for rafters or horizontal for columns) or even frame failure happened when the fire protection thickness, reached around 9 mm for both elements (column and rafter).
On the other hand, a more realistic fire scenario with cooling and heating phases, achieved through fire simulation in CFAST (as explained in section 3.2), presents a different picture. Here, to maintain structural integrity during a one-hour fire exposure, rafters require approximately 13 mm of fire protection thickness, while columns need only 5 mm to prevent failure. This difference, marked by a 5 mm increase in fire protection requirement for rafters and a 3.5 mm decrease observed in columns, can be attributed to the distribution of natural fire curve along the frame elements (refer to

Figure 4 (b)). In contrast, the standard fire curve assumes a rapid and continuous temperature rise, which may not be always representative of real fire conditions.
Thus, it is clear from the analysis that relying solely on the standard fire curve for fire safety design in large compartments like warehouses might lead to underestimating the actual fire resistance required for metal structures, depending on the specific fire scenario encountered.

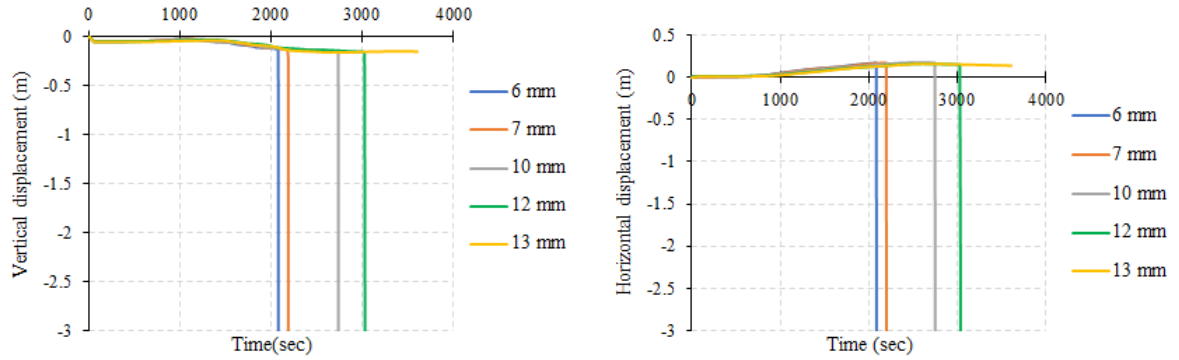

(a) (b)

Figure 6. Evolution of vertical displacement at frame peak and (b) maximum horizontal displacement at column for different FP thicknesses under one-hour exposure to natural fire curve from CFAST software.

4.2. Proposal of modifications to design methods

Building upon the findings from the parametric study in previous section, a modification to the design formula for estimating temperatures in steel elements protected with gypsum-based fire protection mortars is proposed in this section. The modification incorporates additional parameters into the existing design prediction equations established by EN 1993-1-2:2005 [11] (Equations (1) and (2)). These additional parameters account for the temperature dependent thermal properties of fire protection mortars, which is a factor being ignored in the Eurocode-based fire design calculations for steel members. This modification aims to enhance the accuracy of the Eurocode predictions by aligning them more closely with the results obtained from FE analysis in Abaqus. In addition, this proposed formula allows for a more realistic comparison with FE results by considering a natural fire curve, being derived from gas temperature predictions surrounding the elements using CFAST software for different fire zones.
Equations (3) to (9) present the newly proposed formula applicable to protected I-shaped steel elements, such as IPE and HE sections.

$$\Delta\theta_{a,t} = \frac{\lambda_p A_p/V\left(\theta_{g,t}-\theta_{a,t}\right)}{d_p c_a \rho_a (1+\phi/3)}\Delta t - \left(e^{\phi/10}-1\right)\Delta\theta_{g,t}\,, \quad \left(\Delta\theta_{a,t} \geq 0, \text{if } \Delta\theta_{g,t} > 0\right) \tag{1}$$

$$\phi = \frac{c_p \rho_p}{c_a \rho_a} d_p A_p / V \tag{2}$$

$$\begin{cases} \lambda_p^* = \lambda_{p,350} & , \quad \theta_g < \theta_d \\ \lambda_p^* = \dfrac{(\lambda_{p,1200}^* - \lambda_{p,350})(\theta_g - \theta_d)}{\varphi \times (1200 - \theta_d)} + \lambda_{p,350} & , \quad \theta_g \geq \theta_d \end{cases} \tag{3}$$

$$\varphi = 1/(0.95 + (d_p \times 5 \times 10^{-5} \times e^{d_p * \psi})) \tag{4}$$

$$\psi = 0.23 \times (\frac{0.15825}{\lambda_{p,350}})^{0.75} \tag{5}$$

$$t^* = t + 0.04 d_p^2 - 0.55 d_p + 8.0 \tag{6}$$

$$\theta_d = -d_p + (-0.9524 t_m^2 + 25.2381 t_m + 762.8571) + \frac{\overline{w}}{10} \tag{7}$$

$$\overline{w} = b - \left(100 \times \frac{b}{2 \times |h - b|}\right); \ |h - b| \geq 8 \tag{8}$$

$$t_m = \frac{t_f + t_w}{2} \tag{9}$$

As mentioned earlier, the newly proposed formula takes into account several factors influencing the temperature evolution predictions on steel elements. These factors include the dry thermal properties of FP materials at 350 ºC, denoted by $\lambda_{p,350}$ (thermal conductivity), $\rho_{p,350}$ (mass density), $c_{p,350}$ (specific heat capacity). Besides that, the formula considers adjustments to thermal conductivity of FP materials for higher temperatures (λ_p^*) and the impact of moisture inside FP materials (t^*), which delays the temperature rise within the steel material. Furthermore, the formula incorporates the influence of different mortar compositions through a factor denoted by "φ". This factor is dependent on both the fire protection thickness and the thermal conductivity limits of the FP materials at two key temperatures: 350 ºC and 1200 ºC (Equations (3) and (4)).

The gas temperature corresponding to the deploit of thermal degradation of such mortars is estimated by Equation (7): θ_d. This parameter is adjusted for I-shaped cross-sectional type, and it depends on the fire protection thickness, column thickness, and dimensions.

The scalar values used within the formulas (Equations (3)-(7)) were derived using a linear regression method. This method aims to minimize the mean absolute percentage error in predicting steel temperatures within column.

Therefore, the temperature evolution curves derived from proposed design formula are compared with finite element analysis results as well as design methods considering the optimal FP thickness achieved for each element under different fire scenarios (i.e., ISO-834 standard curve and natural fire curve CFAST) (see Figure 7 and Figure 8).

A comparison of the temperature evolution curves obtained using newly developed design formulas with different methods, including FE analysis and Eurocode-based design methods, shows a good improvement in the results, even when the natural fire curves have been used in

the analysis, as can be seen in Figure 7 and Figure 8. As evident from these figures, standard design method tends to be overly conservative or under conservative during the one-hour fire exposure. In contrast, the time-temperature curves based on proposed formula exhibit a good agreement with FE analysis results, with an average error of less than 10%.
This method presents a potential alternative to fire design methods based standard Eurocode regarding the fire resistance predictions. It can effectively predict fire resistance in steel elements with I-shaped cross-sections within warehouse. Notably, this method remains effective even when elements are exposed to a more realistic natural fire curve, unlike standard Eurocode methods that rely on nominal temperature curves only (e.g., ISO-834 standard fire curve).

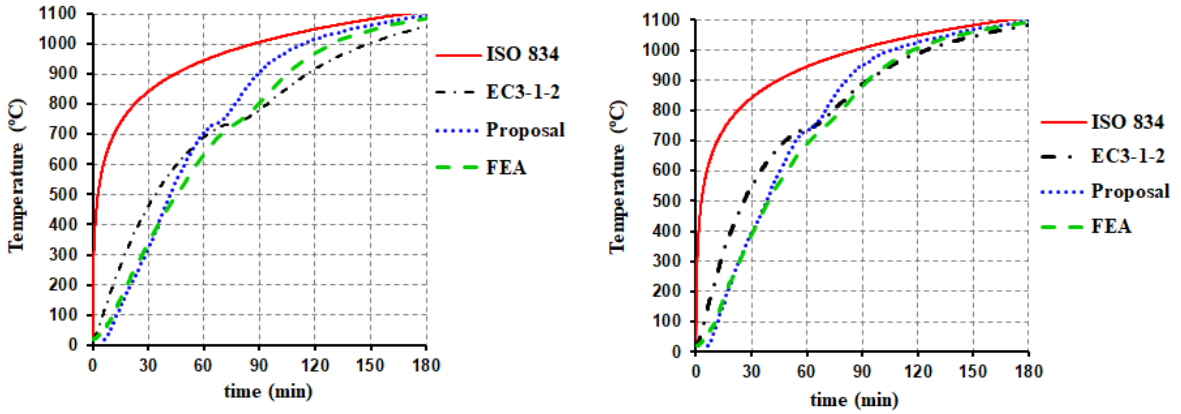

Figure 7. Temperature predictions in steel elements of the frame (column (a) and rafter (b)) for optimization fire design based on ISO-834 standard fire curve.

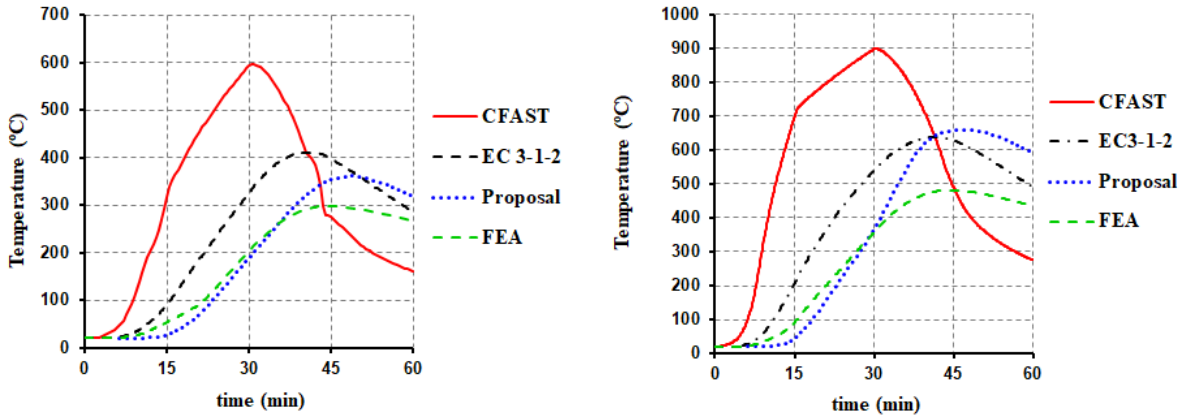

(a) column in cold air zone (b) column in hot air zone

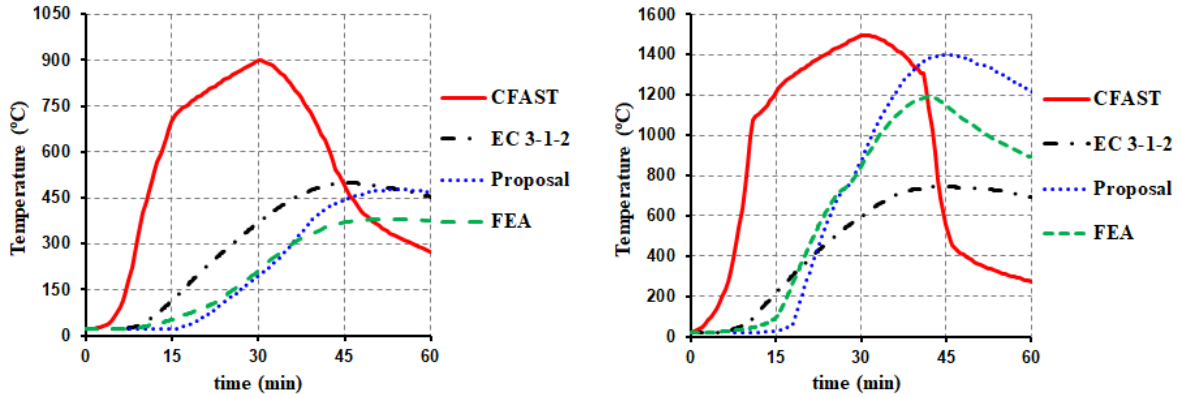

(c) rafter in hot air zone

(d) rafter in plume air zone

Figure 8. Temperature predictions in steel elements of the frame (column (a) and rafter (b)) for optimization fire design based on natural fire curve CFAST.

5. CONCLUSION

This study employed numerical simulations to optimize fire protection design for structural elements in industrial steel warehouses while considering the thermal properties of gypsum-based fire protection materials as a function of temperature.

The results from thermo-mechanical analysis showed that relying solely on standard fire curves in optimization design of large-space structures like warehouses can underestimate their actual fire resistance. Compared to a natural fire scenario simulated in CFAST software, the optimized fire protection thickness for rafters based on the standard fire curve (ISO) was underestimated by 5 mm. This highlights the importance of considering realistic fire scenarios beyond standardized curves for accurate fire safety design.

Furthermore, a novel formula was proposed as an alternative to the EN 1993-1-2 [17] design methods. This formula demonstrated higher accuracy in predicting steel element temperatures under both standard and natural fire scenarios, with an average difference below 10% compared to finite element analysis results. This signifies the formula's broader applicability beyond standard fire conditions, unlike existing design code calculations.

In conclusion, this study provides crucial insights for developing optimized fire design approaches. By considering realistic fire scenarios and employing more accurate temperature prediction methods, the proposed formula ensures the structural integrity and safety of industrial steel warehouses under diverse fire conditions. Ultimately, these findings offer valuable guidance for enhancing fire safety strategies in steel-framed structures.

ACKNOWLEDGEMENTS

This work is financed by national funds through the FCT – Foundation for Science and Technology in Portugal, under grant agreement unmber 2022.10619.BD awarded to the first author within the research project PCIF/AGT/0061/2019 (EVACUARFLORESTA). We

gratefully acknowledge their support.

REFERENCE

[1] H. Caetano, A. Santiago, and A. Shahbazian, “Cement mortar as passive fire protection in steel columns,” no. June, pp. 9–11, 2021.

[2] L. Laím, A. Santiago, H. Caetano, D. Craveiro, and A. Shahbazian, “Numerical analysis and structural fire design of protected SHS steel columns with thermally enhanced gypsum-based mortars,” vol. 54, 2022, doi: 10.1016/j.jobe.2022.104629.

[3] P. Aghabozorgi, L. Laím, A. Santiago, and N. Cândido, “STRUCTURAL FIRE BEHAVIOUR OF PROTECTED TUBULAR STEEL COLUMNS IN INDUSTRIAL WAREHOUSES UNDER STANDARD AND SIMULATED FIRE CONDITIONS,” in *Proceedings of IFireSS 2023-International Fire Safety Symposium*, 2023.

[4] P. Aghabozorgi, A. Santiago, L. Laím, and N. Cândido, “A parametric study of tubular steel columns protected with gypsum-based mortars under fire load using finite element modelling,” in *Proceedings of the 12th International Conference on Structures in Fire (SiF 2022)*, 2022, pp. 693–702.

[5] P. Aghabozorgi, L. Laím, and A. Santiago, “a Numerical Investigation on Fire Performance of Industrial Steel Warehouses Protected With Gypsum-Based Boards,” *Ce/Papers*, vol. 7, no. 1–2, pp. 175–185, 2024, doi: 10.1002/cepa.3034.

[6] ISO, “ISO 834-1 Fire resistance tests -Elements of building construction, Part 1: General requirements,” *International Organization for Standardization, Geneva, Switzerland*, 1999.

[7] P. Aghabozorgi, A. Santiago, and L. Laím, “A NUMERICAL INVESTIGATION ON FIRE RESISTANCE OF STEEL WAREHOUSE BASED ON FIRE PROTECTION OPTIMIZATION,” *Proc. 13th Int. Conf. Struct. Fire (SiF 2024)*, no. Submitted, 2024.

[8] K. McGrattan, S. Hostikka, R. McDermott, J. Floyed, C. Weinschenk, and K. Overholt, “Fire Dynamics Simulator (FDS) (version 5), technical reference guide, National Institute of Standards and Technology, U.S. Department of Commerce,” 2007.

[9] R. D. Peacock, P. A. Reneke, and G. P. Forney, “CFAST-Consolidated Model of Fire Growth and Smoke Transport (Version 7) Volume 2 : User ’ s Guide,” *Nist*, vol. 2, no. Version 7, 2017.

[10] “ABAQUS/CAE,” *ABAQUS/CAE, Standard User’s Manual, Version 2021, Dessault systems, Simulia Crop.,USA*. 2021.

[11] E. 1993-1-2, “‘Design of steel structures. General Rules. Structural Fire Design’ European Committe for Standardization, Brussels, Belgium.,” 2005.

[12] B. S. En, “BS EN 1990: 2002. Eurocode - Basis of structural design,” *Bs En 19902002*, vol. 3, 2002.

[13] Eurocode - BS EN and W. Schwind, “BS EN 1991-1-1-1: Eurocode 1 - Actions on structures - Part 1-1: General actions - Densities, self-weight, imposed loads for buildings,” *Bauingenieur*, vol. 86, no. JULY-AUGUST, 2011.

[14] F. Ljubinković *et al.*, “Optimized fire design for steel industrial sheds,” *ce/papers*, vol. 6, no. 3–4, 2023, doi: 10.1002/cepa.2703.

[15] E. 1993-1-1, “Eurocode 3 : Design of steel structures - Part 1-1: General rules and rules for buildings.”
[16] W. Jones, G. Forney, R. Peacock, and P. Reneke, “A technical reference for CFAST: an engineering tool for estimating fire and smoke transport,” *NIST Tech. Note*, 2000, [Online]. Available: http://fire.nist.gov/bfrlpubs/fire00/art004.html
[17] CEN. EN 1993-1-2, “Eurocode 3 : Design of steel structures - Part 1-2 : General rules - Structural fire design. Brussels, Belgium, European Committee for Standardization.”
[18] E. 1991-1-2, “Eurocode 1 : Actions on structures - Part 1-2: General actions - Actions on structures exposed to fire,” 2002.

Congress on Numerical Methods in Engineering 2024
4-6 September 2024, University of Aveiro, Portugal

ANÁLISE COMPARATIVA DE CRITÉRIOS DE COLAPSO DE ESTRUTURAS PORTICADAS EM AÇO CARBONO E INOXIDÁVEL EM SITUAÇÃO DE INCÊNDIO

Nuno Lopes[1], João Cabral[1] e Paulo Vila Real[1]

1: RISCO, Departamento de Engenharia Civil,
Universidade de Aveiro
Campus universitário de santiago, 28, 3810-193 Aveiro, Portugal
e-mail: {nuno.lopes,jaoacabral5,pvreal}@ua.pt, web: https://www.ua.pt/pt/decivil/

Palavras-chave: Aço Inoxidável, Estruturas Porticadas, Comportamento Global, Cenários de Incêndio, Critérios de Colapso

Resumo. *O aço inoxidável possui, a altas temperaturas, melhor comportamento mecânico que o aço carbono convencional, que pode conduzir a estruturas que não necessitem de proteção ao fogo, tornando-o mais competitivo para uma mais ampla gama de aplicações estruturais. O aço inoxidável é caracterizado por possuir uma relação tensão-extensão sempre não linear, apresentando maiores endurecimento e ductilidade a temperaturas elevadas que o aço carbono. Uma formulação de Ramberg-Osgood de duas fases foi recentemente proposta, para modelação da lei constitutiva em estruturas de aço inoxidável sujeitas ao fogo, na segunda geração do Eurocódigo 3 (EC3), que se encontra em preparação. Com o objetivo de aumentar o conhecimento sobre o cálculo ao fogo de estruturas porticadas, este trabalho aplica métodos avançados de cálculo, por meio da utilização do método dos elementos finitos (MEF) com o programa SAFIR, para analisar e discutir a sua resistência ao fogo, aplicando diferentes critérios de colapso. Adicionalmente, as resistências de diferentes estruturas em aço inoxidável, submetidas a diferentes cenários de incêndio, são comparadas com casos similares em aço carbono, para estudar a influência das diferentes reduções de resistência e de rigidez, dos materiais a altas temperaturas, no comportamento global das referidas estruturas. Os métodos de cálculo simplificados do EC3 são também considerados neste estudo, incluindo as abordagens recentemente propostas para inclusão na segunda geração do EC3.*

1. INTRODUÇÃO

O uso do aço inoxidável para fins estruturais tem sido limitado a projetos com alto valor arquitetónico, onde o caráter inovador das soluções adotadas é um fator de valorização para a estrutura. O alto custo inicial do aço inoxidável, aliado à falta de conhecimento dos benefícios adicionais do seu uso como material estrutural, são algumas das razões que têm influenciado os projetistas a evitar a aplicação do aço inoxidável em estruturas [1-4]. No entanto, uma análise mais cuidada pode concluir que o aço inoxidável tem um bom desempenho do como material

estrutural, quando comparado com o aço carbono convencional.
A maior vantagem do aço inoxidável é sua resistência à corrosão. No entanto, as suas aparência estética, fácil manutenção, alta durabilidade e custos reduzidos do ciclo de vida (podendo ser considerado que tem uma vida útil mais longa, e no final da vida da estrutura maior valor residual e reutilização mais fácil dos perfis) também são aspetos importantes. O aço inoxidável tem um melhor comportamento a temperaturas elevadas quando comparado com o aço carbono, existindo ainda a necessidade de melhor compreender como esta vantagem influencia o comportamento das estruturas em situações de incêndio e possa evitar a necessidade de proteção ao fogo. A possibilidade de eliminação da proteção ao fogo com a aplicação de aço inoxidável em estruturas resultará em menores custos e menores prazos de construção, um uso mais eficiente de espaços interiores, ambiente de trabalho mais saudável, melhor aparência estética do edifício e eliminação dos custos do ciclo de vida do material de proteção.
Ao contrário do aço carbono, o aço inoxidável possui, a temperatura normal e a temperaturas elevadas, um comportamento mecânico sempre não linear, mesmo para pequenas deformações, não apresentando uma tensão de cedência claramente definida, pelo que se considera igual à tensão limite convencional de proporcionalidade a 0.2%. A Tabela 1 compara as propriedades mecânicas à temperatura normal dos aços inoxidáveis 1.4301 (também conhecido como 304) e 1.4401 (também conhecido como 316), as classes mais comuns na construção e utilizadas neste trabalho, com o aço carbono S235 [5-7]. O aço carbono S235 foi escolhido devido ao seu valor de tensão de cedência ser similar aos valores nominais de tensão limite de proporcionalidade a 0.2% das classes de aço inoxidável 1.4301 e 1.4401.

Propriedades mecânicas	Aço carbono S235	Aço inoxidável 1.4301	Aço inoxidável 1.4401
Tensão de cedência [MPa]	235	210	220
Tensão última [MPa]	360	520	520
Extensão última	15%	45%	45%
Módulo de Young [GPa]	210	200	200

Tabela 1. Propriedades mecânicas dos aços à temperatura normal.

O endurecimento não é geralmente considerado no aço carbono a temperaturas elevadas. Recentemente foi proposta para incorporação na segunda geração da Parte 1-2 do EC3 (parte dedicada ao projeto de estruturas em aço ao fogo) [8] uma formulação de Ramberg-Osgood de duas fases para a modelação da lei constitutiva do aço inoxidável a temperaturas elevadas [9], considerando os seus endurecimento e ductilidade. Adicionalmente, as reduções de resistência e rigidez do aço inoxidável a temperaturas elevadas são menores do que as do aço carbono [8]. A Figura 1a representa as relações tensão-extensão do S235, 1.4301 e 1.4401 propostas no EC3 a 600 ºC, onde se observa um comportamento significativamente melhor do aço inoxidável.
Relativamente às propriedades térmicas dos referidos materiais, a Figura 2 ilustra as diferenças existentes na condutividade térmica e no calor específico entre o aço carbono e o aço inoxidável [8]. Embora o aço inoxidável tenha uma condutividade térmica menor que o aço carbono, o que faria supor uma velocidade de aquecimento mais lenta no aço inoxidável, o calor específico do aço carbono é maior. Assim, a diferença, entre as evoluções de temperatura de ambos os

materiais, é relativamente pequena, como pode ser observado na Figura 1b. Por fim, a expansão térmica do aço inoxidável é também pouco diferente da do aço carbono.

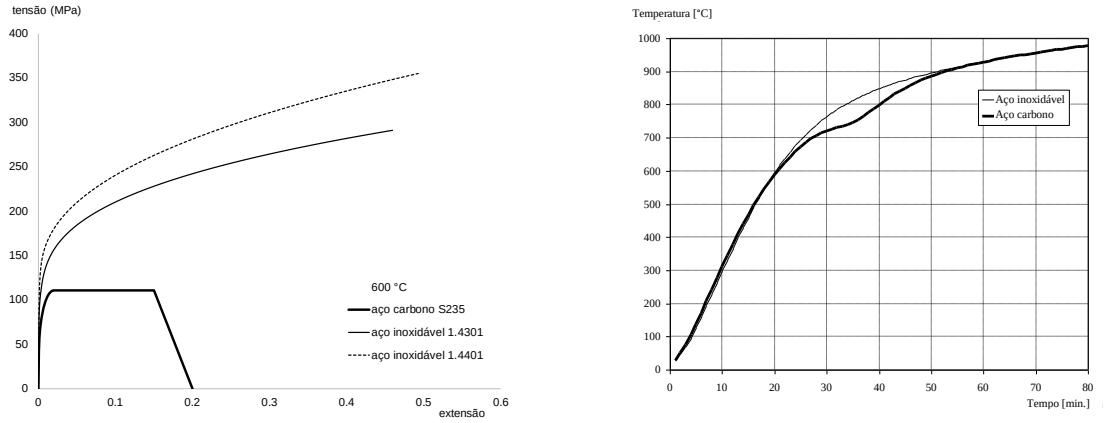

Figura 1. a) Leis constitutivas do aço carbono S235 e aços inoxidáveis 1.4301 e 1.4401 a 600 ºC [8]; b) Evolução da temperatura na secção transversal.

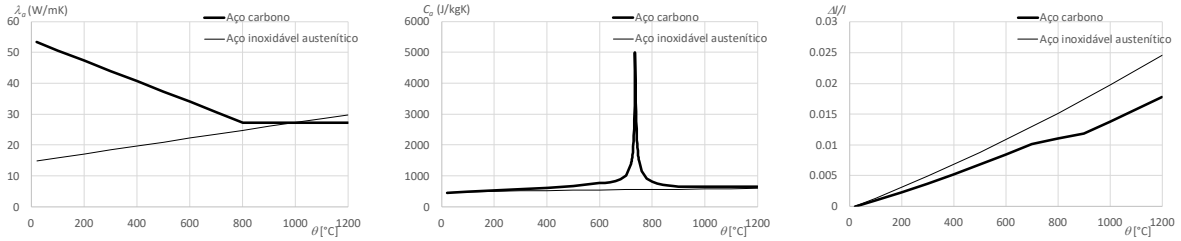

Figura 2. a) Condutividade térmica; b) Calor específico; c) Expansão térmica [8].

A Parte 1.2 do EC3 prevê a aplicação de métodos de cálculo simplificados e avançados para a determinação da resistência ao fogo de estruturas em aço [10,11].

As regras simplificadas consistem num conjunto de formulações analíticas, para o dimensionamento de elementos estruturais (como colunas, vigas e vigas-coluna), considerando as reduções de resistência e rigidez dos materiais a altas temperaturas no comportamento mecânico e a suscetibilidade a fenómenos de instabilidade, mas baseadas em esforços internos, obtidos em estado limite de acidente à temperatura normal. Note-se que a segunda geração do EC3, incluirá novas abordagens cálculo ao fogo de elementos estruturais em aço inoxidável.

Os métodos avançados de cálculo referem-se à aplicação de modelação numérica, para obtenção do comportamento ao fogo de partes ou estruturas completas. O critério de colapso da estrutura é tipicamente definido como o instante em que a matriz de rigidez deixa de ser positiva definitiva, tornando assim impossível estabelecer o equilíbrio da estrutura. No entanto, limites de deformação podem ser importantes para estabelecer critérios seguros de colapso na

aplicação destas análises numéricas. Por exemplo, a norma EN1363-1 [12] prescreve o uso de limites para a deformação e velocidade de deformação em ensaios experimentais de resistência ao fogo a elementos estruturais (que são analisados no presente trabalho).
A investigação sobre o comportamento estrutural de estruturas em aço inoxidável ao fogo tem-se focado na resistência de elementos, sendo estudos sobre o comportamento estrutural global de estruturas completas ainda escassos. Este comportamento global tem recebido recentemente maior atenção [13,14], no entanto, são ainda necessários mais estudos para melhor entender o colapso dessas estruturas em situação de incêndio.
Com o objetivo de melhor compreender o comportamento de estruturas porticadas ao fogo, este estudo aplica métodos avançados de cálculo, utilizando o MEF com o programa SAFIR [15], para analisar e discutir falhas estruturais usando diferentes critérios. Adicionalmente, o estudo compara a resistência de diferentes estruturas porticadas em aço inoxidável, expostas a diferentes cenários de incêndio, com casos similares em aço carbono. Esta análise visa investigar a influência das reduções de resistência e rigidez dos dois materiais a altas temperaturas no respetivo comportamento estrutural. Por fim, os métodos simplificados de cálculo do EC3 são também analisados, com o objetivo de analisar as aproximações fornecidas por estas regras às capacidades últimas obtidas numericamente das estruturas porticadas.

2. AVALIAÇÃO DA RESISTÊNCIA AO FOGO DE ESTRUTURAS EM AÇO CARBONO E AÇO INOXIDÁVEL

2.1. Métodos simplificados de cálculo do Eurocódigo 3

O EC3 fornece formulações analíticas para o cálculo ao fogo de colunas axialmente comprimidas, vigas e vigas-coluna (elementos sujeitos a flexão composta com compressão), considerando os fenómenos relevantes de instabilidade. Com estas formulações, é possível obter as temperaturas críticas dos elementos, impostas pelas combinações de ações acidentais, que são aplicadas para determinar as previsões de tempo de resistência ao fogo, a partir das evoluções de temperatura-tempo no aço [10,11].
Na EN 1993-1-2:2005 [16], a resistência ao fogo de elementos em aço inoxidável é calculada com as mesmas fórmulas do aço carbono, alterando as propriedades mecânicas.
No entanto, a FprEN 1993-1-2:2023 [8] propõe novas abordagens de cálculo ao fogo para estruturas em aço inoxidável, que incluem uma nova metodologia de classificação das secções transversais em esbeltas e não-esbeltas [17], diferente das quatro classes definidas para elementos em aço carbono a temperaturas elevadas [8] e para o projeto à temperatura normal de elementos em aço carbono e aço inoxidável [5,6]. Novas fórmulas para verificação de elementos em aço inoxidável foram desenvolvidas com base em estudos de elementos com secções em I [18,19], mantendo a formulação de base proposta pelo EC3, mas considerando 2% de extensão total para a definição da tensão de cedência, independentemente da classe da secção transversal, e modificando algumas das expressões relativas aos fatores de redução de encurvadura (como em colunas) e fatores de interação (em vigas-coluna). Relativamente ao aço carbono, na FprEN 1993-1-2:2023 são apenas introduzidas novas propostas de cálculo para elementos com secções de Classe 4. O presente

estudo considera apenas secções de Classes 1 e 2.
Neste trabalho, apenas alguns casos de estudo são analisados com as regras simplificadas de cálculo, pois são tipicamente usadas em elementos estruturais isolados. Sendo que este procedimento não considera a expansão térmica resultante da análise da estrutura porticada, e adicionalmente, os comprimentos de encurvadura dos elementos variarão com a variação da rigidez da estrutura circundante devido ao incêndio. Nos casos testados, que correspondem a estruturas porticadas de nós fixos, o comprimento de encurvadura l_{fi} de uma coluna contínua foi considerado como $l_{fi} = 0.5L$ nos pavimentos intermédios e $l_{fi} = 0{,}7L$ nos pavimentos superiores, onde L é a altura da coluna no respetivo piso [8].

2.2. Métodos avançados de cálculo

O EC3 também prevê a aplicação de métodos avançados de cálculo para a verificação da segurança ao fogo de estruturas em aço. Análises geométrica e materialmente não lineares considerando imperfeições (GMNIA) podem ser realizadas aplicando o MEF.
O programa SAFIR [15], utilizado neste trabalho, possui dois módulos de cálculo distintos, um para a análise térmica da estrutura e outro para a análise do comportamento mecânico. A evolução da distribuição de temperaturas em cada secção é primeiro calculada sendo posteriormente aplicada no módulo mecânico do programa para a determinação do comportamento termomecânico da estrutura numa análise estática incremental.
Neste estudo, foram utilizados elementos finitos de viga, sendo a respetiva análise térmica da secção transversal realizada com elementos bidimensionais. A secção transversal dos elementos é simulada utilizando um modelo de fibra, onde a temperatura, a tensão, a deformação e outras propriedades materiais são consideradas constantes em cada fibra. A condutividade térmica e o calor específico apresentados na Figura 2 são aplicadas nas análises térmicas. A emissividade relativa à superfície do aço foi considerada igual a 0.7 para aço carbono e 0.4 para aço inoxidável.
A nova lei constitutiva do aço inoxidável a temperaturas elevadas proposta na FprEN 1993-1-2:2023 foi introduzida no SAFIR [20]. O elemento finito de viga utilizado não considera a encurvadura local. Este elemento finito apresenta 3 nós [13]. Os nós de extremidade têm três graus de liberdade (duas translações e uma rotação) e o terceiro nó do elemento da viga um grau de liberdade (o deslocamento axial), totalizando 7 graus de liberdade.
As análises do programa, incrementais em função do tempo, são interrompidas no instante em que a matriz de rigidez deixa de ser positiva definida, tornando assim impossível estabelecer o equilíbrio da estrutura. Este instante tem sido tipicamente considerado o instante de colapso. Nestas análises de colapso, a deformação é considerada apenas indiretamente pelas deformações últimas dos materiais.
A aplicação, nas análises numéricas de estruturas porticadas, dos critérios de desempenho para ensaios experimentais de resistência ao fogo à determinação da capacidade de suporte de carga dos elementos (prescritos na EN1363-1 [12]), também é aqui estudada. As seguintes definições (deformação limite e velocidade de deformação limite) são utilizadas para elementos fletidos (neste trabalho, vigas) [12]:

$$D_{limit} = \frac{L^2}{400d}\,[\text{mm}] \tag{1}$$

$$\left(\frac{dD}{dt}\right)_{limit} = \frac{L^2}{9000d}\,[\text{mm/min}] \tag{2}$$

Sendo definido para elementos verticais de suporte de carga (neste trabalho, colunas), a contração vertical limite (expansão negativa) e a velocidade de contração vertical limite:

$$C_{limit} = \frac{h}{100}\,[\text{mm}] \tag{3}$$

$$\left(\frac{dC}{dt}\right)_{limit} = \frac{3h}{1000}\,[\text{mm/min}] \tag{4}$$

Assim, os critérios de colapso aplicados foram [12]:

- para elementos fletidos: i) deformação medida ≥ 1.5D_{limite} ou ii) tanto D_{limite} e $(dD/dt)_{\text{limite}}$ são excedidos;
- para elementos verticais de suporte de carga: i) contração vertical medida ≥ C_{limite} ou ii) $(dC/dt)_{limite}$ são excedidos.

3. CASO DE ESTUDO

Um estudo paramétrico é aqui apresentado no qual estruturas porticadas planas, com diferentes geometrias (variando o número de pavimentos e vãos) e dimensões, foram analisadas, considerando diferentes cenários de incêndio com a curva de incêndio padrão ISO 834 [21]. As estruturas porticadas escolhidas são apresentadas na Figura 3. Para consideração dos efeitos das imperfeições de montagem, possíveis excentricidades e imperfeições geométricas, foi introduzida uma imperfeição inicial de flexão, de acordo com a Parte 1-1 do EC3 [5], correspondente a um ângulo de rotação de 0,0033 radianos.

As estruturas foram projetadas para suportar ações correspondentes a edifícios de escritórios, sendo analisadas com secções transversais I não esbeltas não protegidas em aço carbono da classe S235 e nos aços inoxidáveis 1.4301 e 1.4401.

As secções transversais escolhidas resultaram de análises numéricas à temperatura normal com os objetivos: i) de as estruturas serem de nós fixos - fator carga crítica de instabilidade ≥ 10 [5] (aplicando o programa SAP2000 [22] para as análises de instabilidade das respetivas estruturas porticadas); e ii) fornecer capacidades de suporte carga seguras com o modelo numérico desenvolvido no SAFIR, para combinações de ações de estado limite último, de acordo com a EN1990 [23] - equação (5). Os pesos próprios, sobrecargas, ações de vento e neve foram considerados de acordo com o EC1 [24-26]. Considerando edifícios com estruturas porticadas espaçadas de 5 m, as combinações de ações mais desfavoráveis para os estados limite último e acidental são apresentadas na Tabela 2. Nas combinações de estado limite acidental (necessárias para o projeto ao fogo) aplica-se a equação (6), determinada de acordo com a NP EN 1990 [27], onde $\Psi_{1,1}$ é usado para se poder considerar a ação de vento como ação variável de base.

$$\sum_{j\geq 1} \gamma_{G,j} G_{k,j} + \gamma_{Q,1} Q_{k,1} + \sum_{i\geq 1} \gamma_{Q,i} \Psi_{0,i} Q_{k,i} \tag{5}$$

$$\sum_{j\geq 1} G_{k,j} + \left(\Psi_{1,1} \text{ or } \Psi_{2,1}\right) Q_{k,1} + \sum_{i\geq 1} \Psi_{2,i} Q_{k,i} + A_d \quad (6)$$

Estado limite	Carga na cobertura (q1)	Carga nos pavimentos (q2)	Ação do vento (q3)
Último	51.5	65.0	4.9
Acidental	36.5	41.0	0.7

Tabela 2. Cargas consideradas [kN/m] (ver Figura 3).

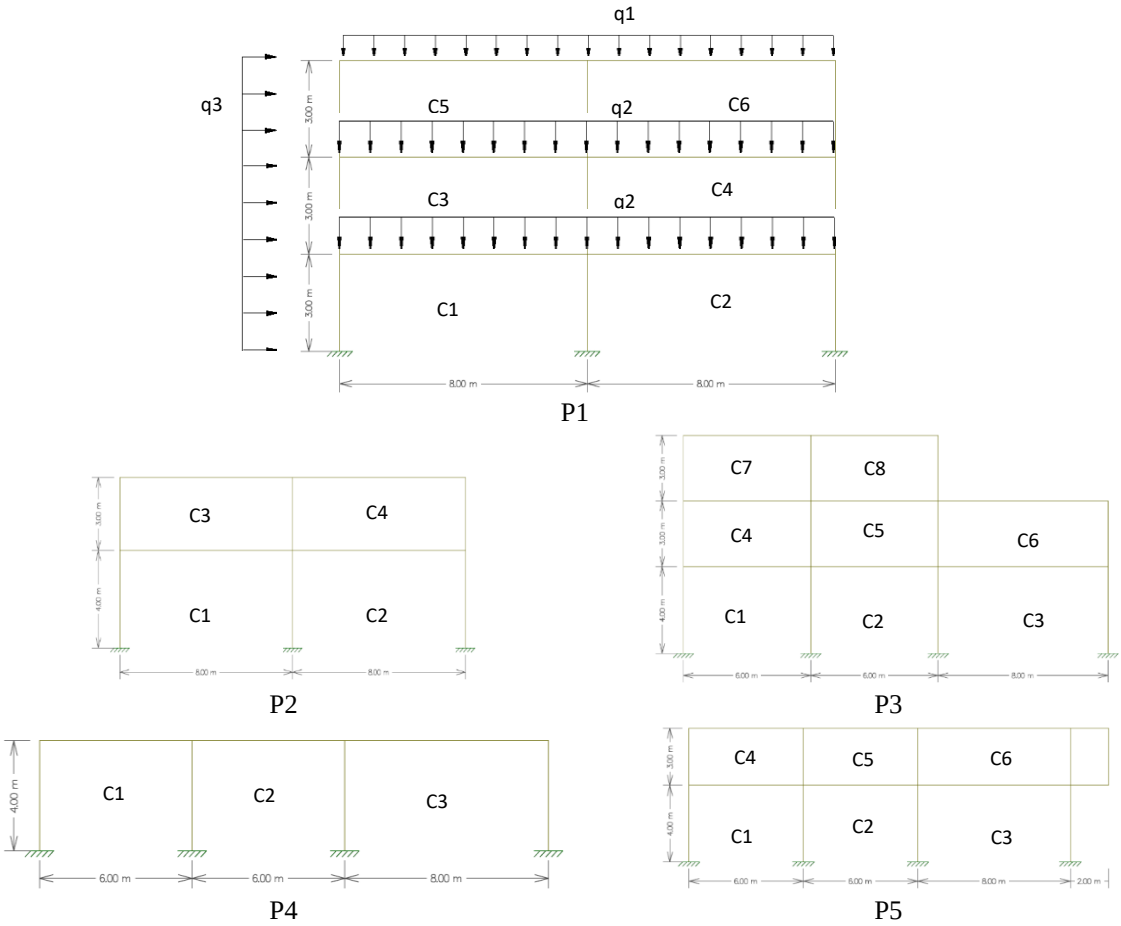

Figura 3. Estruturas porticadas analisadas.

Foram adotadas as mesmas secções transversais em I (apresentadas na Tabela 3) para cada estrutura porticada nos diferentes materiais S235, 1.4301 e 1.4401.

	P1	P2	P3	P4	P5
Colunas	HE260A	HE220A	HE260A	HE220A	HE220A
Vigas	IPE500	IPE450	IPE450	IPE400	IPE360

Tabela 3. Secções transversais escolhidas para cada estrutura porticada.

Diferentes cenários de incêndio foram considerados para as cinco estruturas porticadas, de acordo com o apresentado na Tabela 4.

Estrutura	P1	P2	P3	P4	P5
Cenário 1	Fogo em todos compartimentos	Fogo em todos compartimentos	Fogo em todos compartimentos	Fogo em todos compartimentos	Fogo em todos compartimentos
Cenário 2	Fogo em C1	Fogo em C4	Fogo em C5	Fogo em C2	Fogo em C6
Cenário 3	Fogo em C4	Fogo no rés-do-chão	Fogo no rés-do-chão	-	Fogo no rés-do-chão
Cenário 4	Fogo no rés-do-chão	Fogo no 1º andar	Fogo no 1º andar	-	Fogo no 1º andar
Cenário 5	Fogo no 1º andar	-	Fogo no 2º andar	-	-
Cenário 6	Fogo no 2º andar	-	-	-	-

Tabela 4. Cenários de incêndio considerados para cada estrutura porticada.

As secções transversais em I das vigas, localizadas em compartimentos sujeitos à ação do fogo, foram consideradas aquecidas em três lados, simulando a influência de uma laje de betão nos banzos superiores. As colunas localizadas entre dois compartimentos sujeitos à ação do fogo foram aquecidas nos seus quatro lados, e as colunas que têm um compartimento sujeito à ação do fogo apenas num lado foram consideradas aquecidas em três lados. A variação de temperaturas obtida na secção transversal dos perfis é não uniforme. Os métodos simplificados de cálculo prescritos no Eurocódigo 3 assumem que a variação de temperaturas é uniforme na secção transversal dos perfis. No entanto, a ocorrência provável de gradientes térmicos elevados nas secções analisadas podem originar mudanças significativas no comportamento termomecânico.
A Figura 1b representa a evolução da temperatura num ponto específico de uma secção transversal de uma viga. Verifica-se que a curva de aquecimento do aço inoxidável é semelhante à curva de aquecimento do aço carbono, com exceção de temperaturas entre os 600 ºC e 900 ºC. O atraso temporal representado para o aço carbono deve-se à transformação de fase metalúrgica e é provocado pelo pico de calor específico do aço carbono, que não existe no aço inoxidável, como foi ilustrado na Figura 2.

4. DISCUSSÃO DE RESULTADOS

A Figura 4 apresenta os deslocamentos obtidos imediatamente antes do colapso de dois dos casos de estudo (estrutura porticada P1 com cenário 4, onde o colapso ocorreu numa coluna, e estrutura porticada P5 com cenário 2, onde o colapso ocorreu numa viga) e os gráficos correspondentes da evolução dos deslocamentos verticais máximos ao longo do tempo, mostrando a obtenção dos critérios de colapso da EN1363-1 (limites de deformação e velocidade de deformação) e o último cálculo de equilíbrio obtido com o SAFIR (correspondendo ao último instante registado).

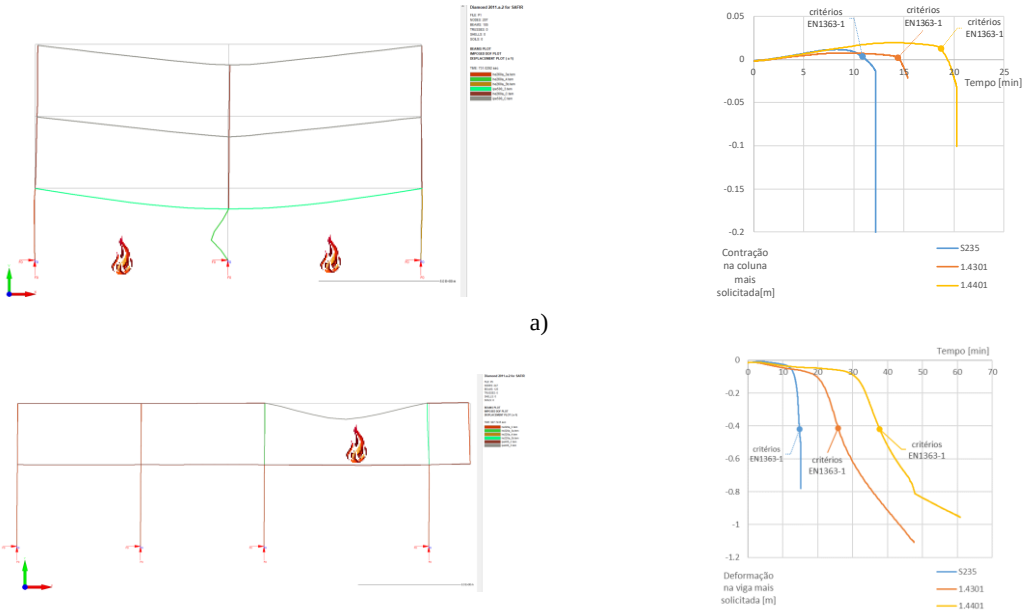

Figura 4. Exemplos de análises, deformadas antes do colapso (x1) e deslocamentos verticais máximos em função do tempo: a) P1 com cenário 4; b) P5 com cenário 2.

A Tabela 5 detalha os respetivos resultados, considerando também as previsões de cálculo da versão atual do EC3 (EN1993-1-2:2005) e da sua segunda geração (FprEN 1993-1-2:2023). O método proposto para a segunda geração do EC3 fornece tempos de resistência ao fogo mais baixos para o aço inoxidável, melhorando as previsões do EC3 para a resistência da coluna em P1 com o cenário 4, mas fornecendo resultados conservativos para estrutura porticada P5 com o cenário 2, onde a colapso ocorre na viga.

A Tabela 6 apresenta todo o conjunto completo de tempos de colapso obtidos, considerando o instante em que não foi possível estabelecer o equilíbrio de cada estrutura testada com os diferentes cenários de incêndio. Os tempos correspondentes à obtenção dos critérios EN1363-1 em cada caso testado são listados na Tabela 7. Por baixo de cada tempo apresentado é sinalizado se a falha foi devido aos limites de contração vertical ou velocidade de contração vertical para as colunas "C" ou devido aos limites de deformação e velocidade de deformação para as vigas "B". A Figura 5 apresenta uma comparação entre todos os resultados obtidos numericamente considerando os dois diferentes critérios de colapso.

Os critérios de colapso adotados nas análises de MEF podem ter uma influência significativa nos resultados obtidos para estruturas porticadas em aço inoxidável, principalmente para os cenários de incêndio em que a colapso ocorre em vigas. Nestes casos, os critérios correspondentes à perda de equilíbrio fornecem tempos de resistência ao fogo significativamente maiores do que os critérios da EN1363-1, o que pode ser justificado pelo endurecimento do aço inoxidável. Estruturas porticadas com cenários correspondentes a incêndio em apenas um compartimento apresentam tipicamente maiores diferenças entre os dois critérios de colapso testados. A menor redução de rigidez na estrutura envolvente do

compartimento de incêndio pode permitir uma melhor distribuição de esforços, mesmo quando ocorrem grandes deformações e redução da suscetibilidade a instabilidades.
Como esperado, e apesar de terem tensões de cedência e módulos de elasticidade semelhantes à temperatura normal, as estruturas em aço inoxidável fornecem resistências ao fogo significativamente mais elevadas quando comparadas às estruturas em aço carbono.

		Métodos simplificados de cálculo		Métodos avançados de cálculo	
		EN1993-1-2:2005	FprEN1993-1-2:2023	Critérios da EN1363-1	Perda de equilibrio
P1 com cenário 4	S235	14.6		10.8	12.2
	1.4301	20.3	13.5	14.4	15.4
	1.4401	27.0	19.5	18.7	20.3
P5 com cenário 2	S235	13.8		14.7	15.1
	1.4301	16.6	10.9	25.9	47.6
	1.4401	23.3	17.5	37.3	60.8

Tabela 5. Resistências ao fogo obtidas para os dois exemplos da Figura 4 [min].

Estrutura	P1			P2			P3			P4			P5		
	S235	1.4301	1.4401	S235	1.4301	1.4401	S235	1.4301	1.4401	S235	1.4301	1.4401	S235	1.4301	1.4401
Cenário 1	11.7	14.6	19.6	10.6	10.9	16.3	13.4	18.4	26.9	11.1	17.4	23.0	10.9	10.1	16.0
Cenário 2	15.2	24.0	29.6	15.0	30.2	42.2	21.9	44.5	52.6	16.4	52.2	76.8	15.1	47.6	60.8
Cenário 3	19.2	28.1	39.5	10.5	10.1	15.4	13.1	17.9	26.0	-	-	-	10.7	9.4	14.0
Cenário 4	12.2	15.4	20.3	15.0	28.7	41.6	15.4	26.9	36.0	-	-	-	14.7	28.3	40.9
Cenário 5	14.2	20.3	27.1	-	-	-	22.0	51.6	69.9	-	-	-	-	-	-
Cenário 6	17.7	39.7	47.8	-	-	-	-	-	-	-	-	-	-	-	-

Tabela 6. Instantes de colapso obtidos com o SAFIR considerando perda de equilíbrio [min].

Estrutura	P1			P2			P3			P4			P5		
	S235	1.4301	1.4401	S235	1.4301	1.4401	S235	1.4301	1.4401	S235	1.4301	1.4401	S235	1.4301	1.4401
Cenário 1	10.5 C	14.5 C	19.5 C	10.4 C	10.8 C	16.3 C	12.9 C	18.4 C	26.9 C	11.0 B	14.5 B	19.6 B	10.8 C	10.1 C	16.0 C
Cenário 2	14.9 C	16.1 C	23.3 C	14.9 B	25.9 B	37.5 B	21.4 B	41.9 C	51.9 C	16.3 B	37.6 B	47.5 B	14.7 B	25.9 B	37.3 B
Cenário 3	19.0 C	25.6 C	38.3 C	10.2 C	10.1 C	15.4 C	12.7 C	17.9 C	25.4 C	-	-	-	10.5 C	9.4 C	13.9 C
Cenário 4	10.1 C	14.4 C	18.7 C	14.7 B	25.6 B	37.3 B	15.3 C	25.1 C	34.7 C	-	-	-	14.3 C	24.5 B	35.8 B
Cenário 5	12.7 C	19.7 C	27.0 C	-	-	-	21.9 B	47.0 B	69.9 B	-	-	-	-	-	-
Cenário 6	17.6 B	34.7 B	47.4 B	-	-	-	-	-	-	-	-	-	-	-	-

Tabela 7. Instantes de colapso obtidos com o SAFIR considerando os critérios da EN1363-1 [min].

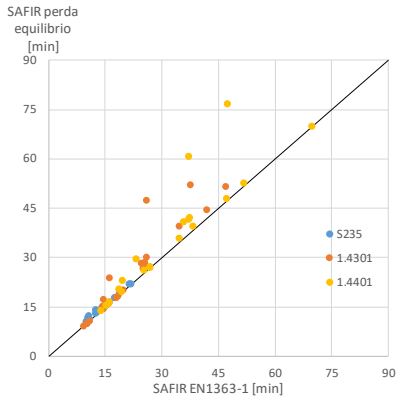

Figura 5. Resultados obtidos numericamente considerando os diferentes critérios de colapso.

5. CONCLUSÕES

Os principais objetivos deste trabalho foram analisar a aplicação de possíveis critérios de colapso na determinação das resistências ao fogo de estruturas porticadas obtidas por meio de análises numéricas pelo MEF e apresentar uma comparação entre as capacidades de carga últimas de estruturas em aço carbono e aço inoxidável. Foi possível concluir que, para as 5 estruturas porticadas estudadas, de diferentes geometrias e dimensões:

- Os critérios de colapso prescritos para ensaios experimentais de resistência ao fogo, da EN1363-1 de elementos estruturais, forneceram tempos de resistência ao fogo significativamente menores quando comparados à perda de equilíbrio, nas estruturas porticadas em aço inoxidável. Nestes casos, é possível tirar partido do endurecimento do aço inoxidável a temperaturas elevadas. No entanto, deve-se observar que a aplicação de critérios de deformação na análise de estruturas porticadas em aço pode ser importante para fazer opções de projeto mais seguras quando necessário, como por exemplo, em vias de evacuação;
- As estruturas porticadas estudadas em aço inoxidável 1.4401 forneceram tempos de resistência ao fogo relativamente mais altos do que as mesmas estruturas em aço inoxidável 1.4301, que por sua vez também apresentaram resistência ao fogo maiores do que as mesmas estruturas em aço carbono S235. Estas superiores resistências poderão permitir a utilização de estruturas em aço inoxidável sem proteção ao fogo.

Por fim, foram realizadas comparações com estimativas obtidas pelos métodos simplificados de cálculo do EC3. Essas avaliações analíticas não consideram a expansão térmica dos elementos em aço e os comprimentos de encurvadura são constantes, o que não reproduz de forma precisa a variação da rigidez dos pórticos analisados com a temperatura.

REFERÊNCIAS

[1] Baddoo, N., “Stainless steel in construction: A review of research, applications, challenges and opportunities”, *J. of Constr. Steel Research*, 64(11), 1199-1206, 2008.

[2] Gardner, L., Stability and design of stainless steel structures – Review and outlook, *Thin-Walled Structures*, Elsevier, 141, pp. 208-216, 2019.

[3] Steel Construction Institute (SCI), *Design Manual for Structural Stainless Steel*, SCI publication P413 (4th edition), 2017.
[4] Mirambell, E., Real, E., "On the calculation of deflections in structural stainless steel beams: an experimental and numerical investigation", *JCSR*, 54(1), 109-133, 2000.
[5] European Committee for Standardisation (CEN), FprEN 1993-1-1, Eurocode 3, Design of Steel Structures – Part 1-1. General rules and rules for buildings. Belgium, 2022.
[6] CEN, prEN1993-1-4, Eurocode 3, Design of Steel Structures – Part 1-4. General rules – Supplementary Rules for Stainless Steels, Brussels, Belgium, 2023.
[7] CEN, EN10088-4, Stainless steels. Part 4: Technical delivery conditions for sheet/plate and strip of corrosion resisting steels for construction purposes, Belgium, 2009.
[8] CEN, FprEN1993-1-2, Eurocode 3, Design of Steel Structures – Part 1-2. General rules – Structural fire design, Brussels, Belgium, 2023.
[9] Liang, Y., Manninen, T., Zhao, O., Walport, F., Gardner, L. "Elevated temperature material properties of a new high-chromium austenitic stainless steel", *JCSR*, 152, 2019.
[10] Franssen, J.-M., Vila Real, P., *Fire Design of Steel Structures*, ECCS; Ernst & Sohn, a Wiley Company, 2nd Ed., 2015.
[11] Vila Real, P., Manual de dimensionamento ao fogo de estruturas metálicas, Edição CMM, ISBN: 978-989-99251-8-2, 2021.
[12] CEN, EN1363-1, Fire resistance tests - Part 1: General requirements, Belgium, 2020.
[13] Segura, G., Arrayago, I., Mirambell, E. "Plastic redistribution capacity of stainless steel frames in fire", *Journal of Constructional Steel Research*, Volume 208, 108019, 2023.
[14] Segura, G., Pournaghshband, A., Afshan, S., Mirambell, E. "Numerical simulation and analysis of stainless steel frames at high temperature", *Eng. Struct.*, 227, 111446, 2021.
[15] Franssen, J.-M. and Gernay, T. "Modeling structures in fire with SAFIR: theoretical background and capabilities", *J. of Structural Fire Engineering*, 8(3), 300–323, 2017.
[16] CEN, EN1993-1-2, Eurocode 3, Design of Steel Structures – Part 1-2. General rules – Structural fire design, Brussels, Belgium, 2005.
[17] Xing, Z., Kucukler, M. and Gardner, L., "Local buckling of stainless steel I-sections in fire: finite element modelling and design", *Thin-Walled Structures*,161:107486, 2021.
[18] Kucukler, M., Xing, Z., Gardner, L., "Behaviour and design of stainless steel I-section columns in fire", *Journal of Constructional Steel Research*, Vol. 165, 105890, 2020.
[19] Kucukler, M., Xing, Z., "Gardner, L., Stability of stainless steel I-section beam–columns at elevated temperatures", *I. J. of Struct. Stab. and Dyna.*, Vol. 21, No. 3, 2150037, 2021.
[20] Pinho-da-Cruz, J., Lopes, N., Vila Real, P., Couto, C. "Numerical modelling and benchmark study of fire resistance of stainless steel structural elements", *JFT*, 2022.
[21] CEN, NP EN1991-1-2, Eurocódigo 1: Acções em estruturas - Parte 1-2: Acções gerais - Acções em estruturas expostas ao fogo, IPQ, Caparica, Portugal 2010.
[22] Computers and Structures, Inc. SAP2000. Version 25, 2024.
[23] CEN, EN1990, Eurocode – Basis of structural design, Brussels, Belgium, 2002.
[24] CEN, EN1991-1-1, Eurocode 1: Actions on structures - Part 1-1: General actions - Densities, self-weight, imposed loads for buildings, Brussels, Belgium, 2002.
[25] CEN, EN1991-1-4, EC1: Part 1-4: General actions – Wind actions, Belgium, 2005.
[26] CEN, EN1991-1-3, EC1: Part 1-3: General actions – Snow loads, Belgium, 2003.

Congress on Numerical Methods in Engineering 2024
4-6 September 2024, University of Aveiro, Portugal

ANÁLISE NUMÉRICA SOBRE A INFLUÊNCIA DAS PROPRIEDADES VISCOELÁSTICAS DOS INTERCALARES NA DEFLEXÃO DE PAINÉIS DE VIDRO LAMINADOS SIMPLESMENTE APOIADOS

Hugo Delgado[1], Eliana Inca[2] e Sandra Jordão[3]

1: ISISE, Departamento de Engenharia Civil
Faculdade de Ciências e Tecnologia
Universidade de Coimbra
Rua Sílvio Lima, Pólo II da Universidade de Coimbra, 3030-790 Coimbra
e-mail: hugo.delgado@uc.pt

2: Departamento de Engenharia Civil
Faculdade de Ciências e Tecnologia
Universidade de Coimbra
Rua Sílvio Lima, Pólo II da Universidade de Coimbra, 3030-790 Coimbra
e-mail: e.inca.cabrera@uc.pt

3: Departamento de Engenharia Civil
Faculdade de Ciências e Tecnologia
Universidade de Coimbra
Rua Sílvio Lima, Pólo II da Universidade de Coimbra, 3030-790 Coimbra
e-mail: sjordao@dec.uc.pt

Palavras-chave: Intercalares Viscoelásticos, Painéis de Vidro, Reologia, Métodos Numéricos, PVB, SentryGlas,

Resumo. *Este artigo investiga a influência das propriedades viscoelásticas em painéis de vidro laminados simplesmente apoiados quando submetidos a uma carga lateral uniformemente distribuída. Um modelo numérico foi desenvolvido em ABAQUS e validado frente a resultados experimentais, obtidos no Laboratório de Engenharia Civil da Universidade de Coimbra. O modelo é usado para examinar a influência da temperatura e da velocidade de carregamento na deflexão dos painéis. A análise abrange os dois principais intercalares do mercado, o PVB e o SentryGlas.*

1. INTRODUÇÃO

A arquitetura moderna primazia fachadas com elevadas áreas envidraçadas, estas permitem uma maior luminosidade natural, um contacto mais envolvente com o exterior e a paisagem, contribuindo para o aumento do conforto. Quando um projeto de engenharia e de arquitetura é devidamente executado, a implementação do vidro possibilita um aumento da eficiência energética do edifício e a redução de custos com a obra. O vidro também tem sido utilizado para substituir outros materiais tradicionais da construção civil, como peitoris, corrimões, revestimentos de fachadas, coberturas, entradas, anexos/extensões de edifícios, divisões internas, portas, etc. Além do mercado habitacional, outras aplicações também têm encontrado no vidro a solução, como por exemplo, pequenos pavilhões de exposição e a preservação de património histórico. Como consequência, o mercado do vidro tem tido um crescimento sólido de 4.6% ao ano nas décadas recentes e as expetativas são ainda bastante otimísticas.

Devido à sua reduzida capacidade de deformação plástica, o vidro comporta-se como um material frágil que se fragmenta sem apresentar sinais de rutura. Apesar de no momento de produção ser um material com uma impressionante resistência à rutura de cerca de 21GPa, devido às suas tensões residuais que contribuem para a abertura e crescimento de micro-fendas superficiais durante os primeiros meses de vida, que tornam o vidro mais frágil, e reduzem consideravelmente a sua resistência à tensão de rotura. Não existem valores exatos da resistência à rotura, e para uma investigação experimental são necessárias várias amostras, pois a variância pode ser considerável. Para vidros flutuantes, a norma Europeia prEN 19100 de 2023 estabelece como valores de referência de 45MPa para vidro flutuante recozido, 70MPa para termicamente reforçado e 120MPa para vidro temperado. A resistência à compressão é em torno de 1000 MPa. A qualidade e o tipo de polimento nos bordos do painel também têm um impacto significativo. Portanto, a imprevisibilidade do comportamento mecânico do vidro dificulta a sua implementação segura em aplicações estruturais.

Por isso, em aplicações onde a rutura frágil do vidro é indesejável, este é implementado como laminado em que duas ou mais camadas de vidro são unidas com peliculas poliméricas. Os painéis de vidro laminados têm um comportamento plástico melhorado, pois a sua película interna permite manter os detritos unidos e continuar a transferir as tensões, além de aumentar a sua segurança. Outro campo de estudo que tem sido alvo de investigação recentemente, é o uso de conexões embutidas no intercalar, sem a necessidade de efetuar cortes adicionais ao vidro, como furos, que aumentam as tensões residuais. Este aspeto não será detalhado neste artigo, mas será relevante na continuidade do projeto em que está inserido. Portanto é de extrema importância conhecer detalhadamente a interação dos intercalares com o vidro.

Os elementos de vidro laminado exibem um comportamento geometricamente não linear e sensível à temperatura e duração de carga, pois são constituídos por materiais poliméricos viscoelásticos [1]. Em algumas partes do globo, a temperatura do ar pode atingir 50°C e as temperaturas de superfícies podem exceder este valor. Isto tem vários efeitos nas propriedades do material do intercalar, afetando assim a sua rigidez e consequentemente o seu desempenho estrutural, como a resistência à deflexão do laminado [2].

Verificando-se que existe uma certa lacuna na literatura, sobre o impacto das propriedades viscoelásticas, no comportamento mecânico de painéis de vidro laminado, este artigo pretende

contribuir para o aprofundamento do tema. Desta forma, o presente estudo tem como principal objetivo investigar o comportamento de painéis de vidro laminados sob o efeito de cargas laterais uniformemente distribuídas, numa ampla gama de temperaturas e para diferentes tempos de duração de carga, usando um modelo numérico desenvolvido no software comercial ABAQUS 2023.

2. MODELO DA VISCOELÁSTICIDADE LINEAR

As propriedades reológicas são geralmente fornecidas pelo fabricante na forma de tabelas, que registram o módulo de resistência ao corte relaxado do polímero sob tensão de corte constante em função da temperatura e do tempo. O código europeu prEN 19100 de 2023 estipula que para cálculos de projeto, se usem esses valores, considerando o polímero como um material elástico linear cujo módulo de resistência ao corte é escolhido de acordo com a temperatura ambiente e a duração característica da carga de projeto também definida pelo código. A suposição de que tanto o vidro quanto o polímero são linearmente elásticos permite simplificações drásticas na análise estrutural. No entanto, dependendo do polímero, o módulo de resistência ao corte relaxado pode variar consideravelmente. Assumindo o PVB como exemplo, este módulo tem cerca de 0.01 MPa a 60°C e sob carga permanente ou 300MPa para 0°C e 1s de duração de carga [3].

Para obter uma análise reológica mais precisa, pode-se considerar o polímero como um material viscoelástico linear. O modelo comumente usado para descrever a viscoelasticidade linear é o de Maxwell-Wiechert, que geralmente pode ser interpretado por uma série de unidades de Prony dispostas no modelo de Maxwell-Wiechert, representado na Figura 1. Este, combina em paralelo uma série de unidades de mola-amortecedor (com constante de mola G_i e viscosidade do amortecedor η_i) e uma mola de Hook. Este modelo leva em consideração que a relaxação não ocorre em uma única escala de tempo, mas em diversas escalas de tempo diferentes. Os parâmetros da série de Prony que definem as propriedades constituintes podem ser determinados experimentalmente através de testes de fluência (“creep test”) em que uma tensão constante é aplicada durante um período de tempo, que no caso dos intercalares pode corresponder a alguns meses, ou relaxação em que é aplicada uma deformação constante, ou medindo a resposta a oscilações cíclicas onde o material viscoelástico é submetido a uma carga sinusoidal e a resposta atrasada com uma mudança de fase é medida e processada (DMTA - Dynamical-Mechanical-Thermal Analysis).

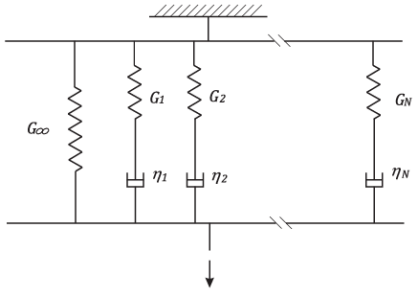

Figura 1. Representação esquemática do modelo Maxwell-Wiechert, retirado de [3]

Quando submetido a uma deformação de corte fixa e constante, o módulo de resistência ao corte do material viscoelástico decai com o tempo de acordo com uma expressão geralmente referida como série de Prony, definida como:

$$G(t) = G_\infty + \sum_{i=1}^{n} G_i e^{-\frac{t}{\tau_i}} = G_0 - \sum_{i=1}^{n} G_i (1 - e^{-\frac{t}{\tau_i}}) \quad (1)$$

onde G_∞ é o módulo de resistência ao corte de longo prazo, n representa o número de unidades viscoelásticas, G_i denota o módulo de resistência ao corte da i-ésima unidade, $\tau_i = \eta_i / G_i$ é o tempo de relaxação relacionado à viscosidade η_i e $G_0 = G_\infty + \sum_{i=1}^{n} G_i$ é o módulo de resistência ao corte instantâneo.

A dependência da temperatura pode ser considerada utilizando o princípio da superposição tempo-temperatura de Williams–Landel–Ferry [4]. A equação é definida como:

$$\log(a_T) = \frac{-C_1(T - T_0)}{C_2 + T - T_0} \quad (2)$$

em que C_1 e C_2 são constantes do material, e T e T_0 são as temperaturas atual e de referência, respetivamente.

Para um material isotrópico, E e G estão relacionados por:

$$G = \frac{E}{2(1 + \nu)} \quad (3)$$

É importante ressaltar que ν também é dependente da temperatura, apesar de ter um impacto menos significativo que a temperatura e a duração de carga.

O mercado é dominado principalmente por dois filmes poliméricos. O PVB (Polivinil Butiral) e o SentryGlas (Ionómero). Atualmente, o uso do intercalar (PVB) domina a LG, com mais de 70% de quota de mercado. O SentryGlas é geralmente usado em aplicações que requerem uma maior resistência mecânica, o seu modulo de elasticidade é cerca de 100 vezes superior ao PVB e a tensão de rutura é de cerca 5 vezes, e tem também uma elevada temperatura de transição vítrea (T_g=55°C).

As séries de Prony dos intercalares foram retiradas de [5] para o PVB e de [6] para o SentryGlas e podem ser visualizadas na tabela 1. Os respetivos módulos de resistência ao corte em função do tempo de carga são apresentados na Figura 2.

Tabela 1. Séries de Prony usadas para a modelação da viscoelasticidade

PVB				SentryGlas		
T_{ref}	19.2	°C		T_{ref}	20	°C
C_1	33.2	-		C_1	23.36	-
C_2	212.42	-		C_2	31.12	-
G_0	97.37	MPa		G_0	375	MPa
τ_i	g_i			τ_i	g_i	
1.00E+07	2.77E-03			5.00E-02	0.029733	
1.00E+06	8.26E-04			5.00E+00	0.049333	
1.00E+05	6.07E-04			5.00E+02	0.041493	
1.00E+04	1.25E-03			5.00E+04	0.186187	
1.00E+03	4.37E-03			5.00E+06	0.076347	
1.00E+02	2.07E-02			5.00E+08	0.2204	
1.00E+01	9.12E-02			5.00E+10	0.08472	
1.00E+00	2.79E-01			5.00E+12	0.011893	
1.00E-01	3.00E-01			5.00E+14	0.005147	
1.00E-02	2.99E-01			5.00E+16	0.0028	
				5.00E+18	0.00112	

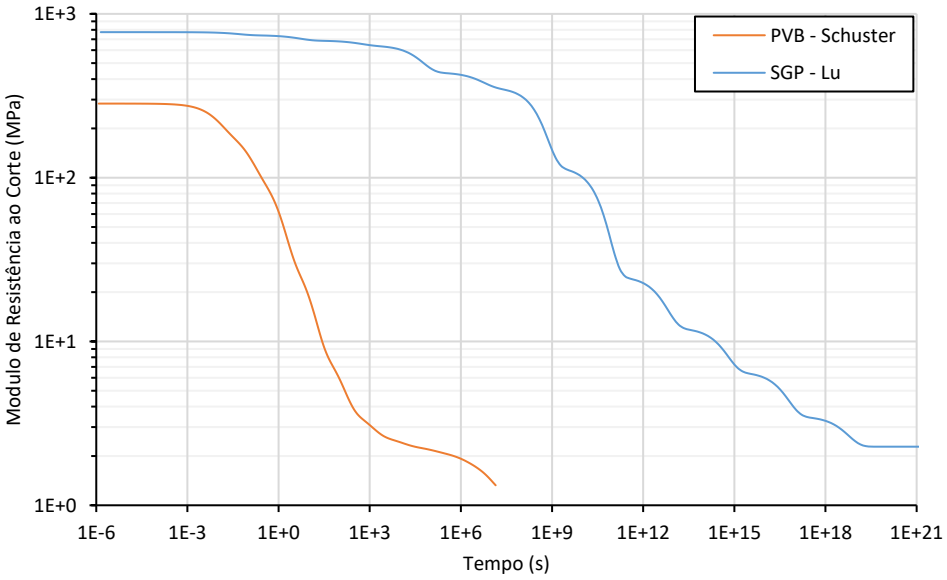

Figura 2. Módulo de resistência ao corte à temperatura ambiente de 20°C

3. METODOLOGIA EXPERIMENTAL

Os resultados experimentais foram retirados de [7] e [8], onde pode ser encontrada uma descrição mais pormenorizada. A campanha de testes experimentais foi realizada no Laboratório de Engenharia Civil da Universidade de Coimbra em 2019. Os painéis consistem em vidro laminado duplo com PVB ou SentryGlas. Têm uma área frontal de 1.5x1.5m, as camadas de vidro têm uma espessura de 5mm e o intercalar de 1,52mm. O painel de vidro é simplesmente apoiado em quatro vigas metálicas, suficientemente rígidas para se desprezar a sua deformação durante o teste. Os provetes estão assentes numa banda de EPDM (material usualmente utilizado no contacto direto com o vidro nas fachadas) com 20mm de largura que cobre todo o perímetro dos mesmos, para assim prevenir o contacto direto com o metal. A carga é exercida através de pressão hidrostática, tendo para isso sido construído um reservatório de água, em que no fundo foi colocado o provete em teste.
De acordo com a Figura 3, foram colocados vários extensómetros unidirecionais na face superior e inferior do provete a ¼ do vão e rosetas a ½ de vão. Os defletómetros foram instalados na parte inferior do laminado, exceto os defletómetros D1, D2, D3 e D4 que foram instalados na viga o qual se verificou que que estas são suficientemente rígidas e, portanto, as deformações que ocorrem durante os ensaios podem ser desprezadas.

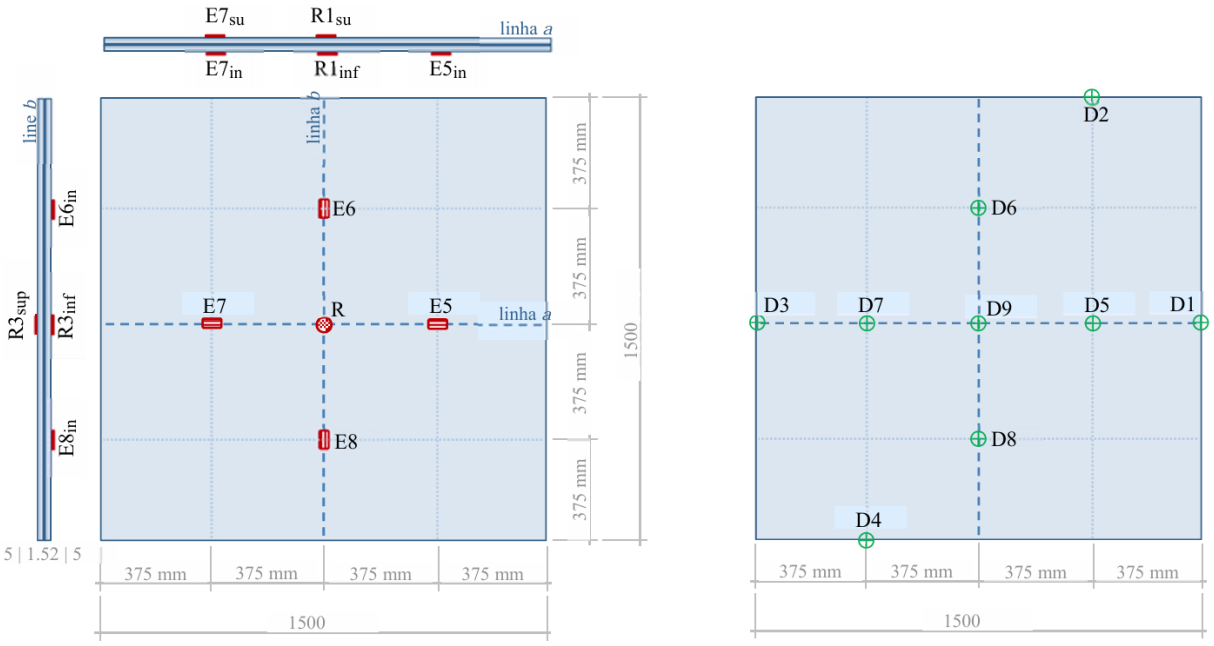

Figura 3. Posição dos extensómetros (esquerda) e dos defletómetros (direita) retirado de [8]

Foram construídos 3 provetes de cada intercalar. E cada provete foi testado diversas vezes até ao máximo de 3. A taxa de carregamento ocorreu de acordo com o disposto no gráfico da Figura 4:

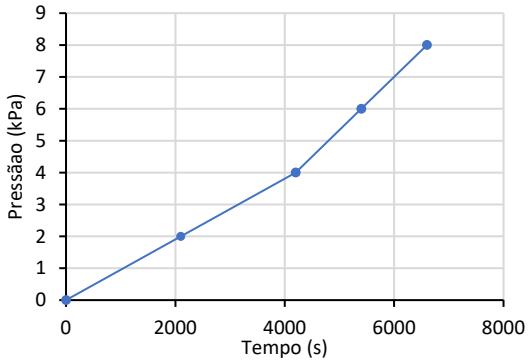

Figura 4. Evolução da pressão em função do tempo

4. METODOLOGIA NUMÉRICA

As simulações numéricas foram feitas com o código de elementos finitos do Abaqus 2023, utilizando uma malha 3-D com elementos sólidos de 20 nós C3D20R com integração reduzida e controlo de "hourglass" selecionados. Estes elementos por terem nodos no meio das faces e das arestas permitem computar as tensões de corte entre os diferentes materiais. O vidro foi modelado como um material linear com E_{vidro}=70GPa e ν_{vidro}=0.23. A gravidade também foi considerada ortogonal ao plano. A malha estruturada foi criada com elementos de 20mm de largura e ao longo da espessura de cada camada foram usados 3 elementos. O contacto entre o intercalar e o vidro, foi definido como Tie. No contacto entre o vidro e a banda EPDM foi definido sem penetração e sem atrito. Para o EPDM foram usadas as propriedades E_{EPDM}=6GPa e ν_{EPDM}=0.49. O apoio foi definido nas superfícies da banda EPDM em contacto com as vigas metálicas. Foi ainda inserido um apoio com restrições aos deslocamentos e momentos no plano num dos cantos do provete. Este apoio não tem qualquer influência nos resultados, apenas garante uma maior estabilidade numérica. Apenas ¼ do provete foi simulado definido com condições de fronteira de simetria. As condições de fronteira podem ser visualizadas na Figura 5.

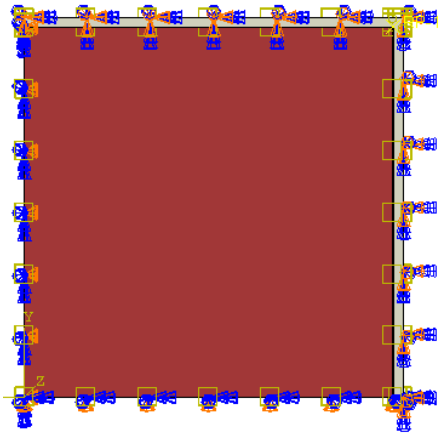

Figura 5. Condições de fronteira aplicadas no modelo

5. VALIDAÇÃO DOS RESULTADOS EXPERIMENTAIS

Para cada intercalar foram utilizados três provetes, porém estes foram testados mais de uma vez e até ao máximo de três vezes. Todos os testes foram contabilizados para realizar uma média global das leituras obtidas com os defletómetros e os extensómetros nas posições homólogas, esta simplificação é viável de ser feita, pois todos os testes foram feitos com a mesma taxa de carregamento, e, portanto, está-se a considerar que a fadiga estática do vidro, que ocorre devido ao crescimento do tamanho das microfissuras superficiais, não afeta as propriedades elásticas, esta apenas tem impacto na tensão de rotura, o qual não é objetivo deste trabalho aprofundar este tema.

Os resultados experimentais da deflexão e o respetivo desvio padrões calculados podem ser visualizados na Figura 6. Para ambos os intercalares e para quatro patamares de pressão, 2, 4, 6 e 8kPa. Para o cálculo do desvio padrão a ¼ do vão, foram consideradas as quatro leituras dos defletómetros (D5, D6, D7 e D8) de cada provete, e, portanto, o gráfico da deflexão é simétrico relativamente à posição central que se encontra a ½ vão. Na posição central, apenas foi considerada uma leitura por provete efetuada com a roseta.

O desvio padrão calculado, e que pode ser visualizado na Figura 6, é notavelmente superior a ¼ do vão do que a ½ do vão, a contribuir para esta diferença, deve-se ao fato de a deformação do painel não ser perfeitamente simétrica e devido ao maior número de medições consideradas para esta posição, como descrito acima.

A temperatura de execução dos testes, T_{amb}=12°C, foi obtida por processo iterativo, até obter a melhor aproximação para os quatro patamares de pressão e para ambos os intercalares.

Os resultados numéricos são bastante próximos dos resultados experimentais, e na maioria das vezes, as diferenças estão dentro do desvio padrão calculado. Porém é notável, que nos resultados com PVB, a ¼ do vão, a diferença acentua-se, isto pode-se dever ao facto de o código numérico não simular com precisão suficiente o efeito de placa que está mais presente neste intercalar. O efeito de placa caracteriza-se pela deformação com um declive quase horizontal na região próxima ao centro do provete, e para o qual contribuem os efeitos de ancoramento presentes no bordo. Desta forma, não existem evidências de que este efeito esteja presente nos provetes com SentryGlas.

As diferenças são ainda mais notáveis nas extensões, Figura 7, principalmente na camada de vidro superior que está sujeita a esforços de compressão e para os maiores patamares de pressão. Nos resultados com SentryGlas, estes resultados são bem mais próximos, porém as diferenças acentuam-se com o aumento de carga, mas neste caso, a diferença não parece estar relacionada com o efeito de placa, que se espera que seja mínimo, mas devido ao aumento da diferença na deformação entre os resultados experimentais e numéricos presentes na Figura 6.

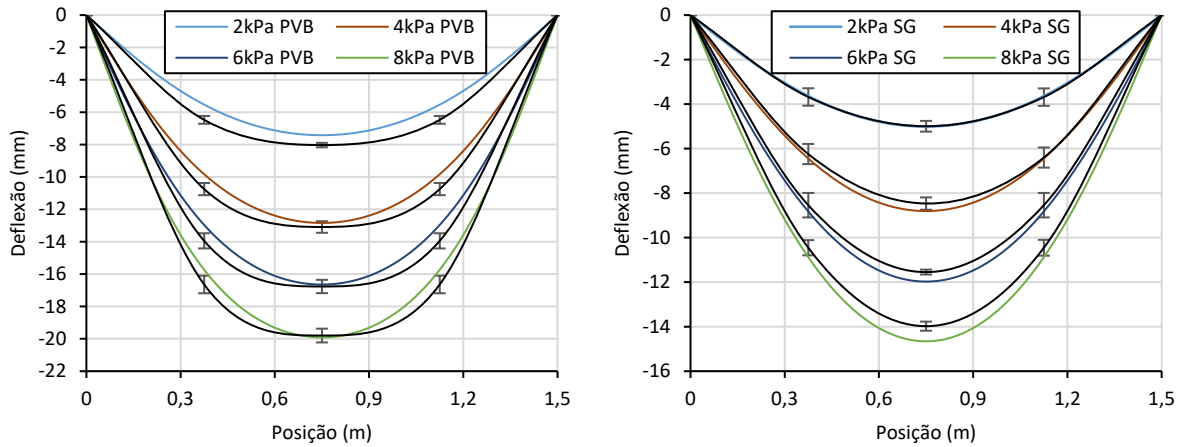

Figura 6. Comparação dos resultados numéricos da deflexão com os experimentais para T_{amb} =12°C, PVB (gráfico da esquerda) e SentryGlas (gráfico da direita)

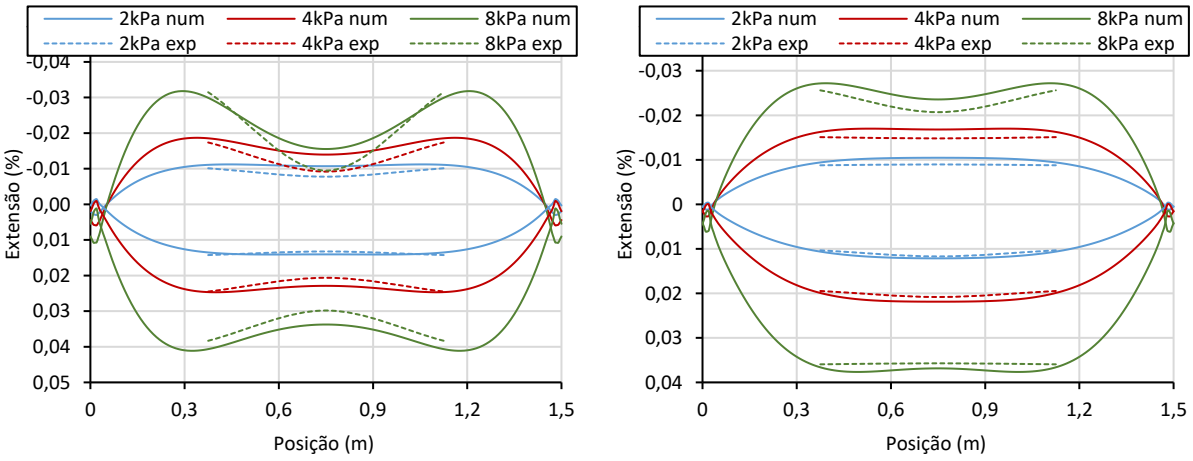

Figura 7. Comparação dos resultados numéricos da extensão com os experimentais para T_{amb} =12°C, PVB (gráfico da esquerda) e SentryGlas (gráfico da direita)

6. ANÁLISE NUMÉRICA DA INFLUÊNCIA DA TEMPERATURA E DO TEMPO DE CARREGAMENTO

Uma análise numérica do impacto da temperatura pode ser visualizada na Figura 8, onde foi considerada a taxa de carregamento da Figura 4. Para o PVB, a deflexão máxima aumenta a uma taxa aproximadamente constante, dos 5°C até aos 20°C, a partir desta temperatura, a deflexão máxima aumenta a uma taxa consideravelmente menor, indicando que o módulo de resistência ao corte do intercalar atingiu o seu valor mínimo. Para o SentryGlas, verifica-se que o impacto da temperatura é mínimo para a gama de temperaturas estudadas.

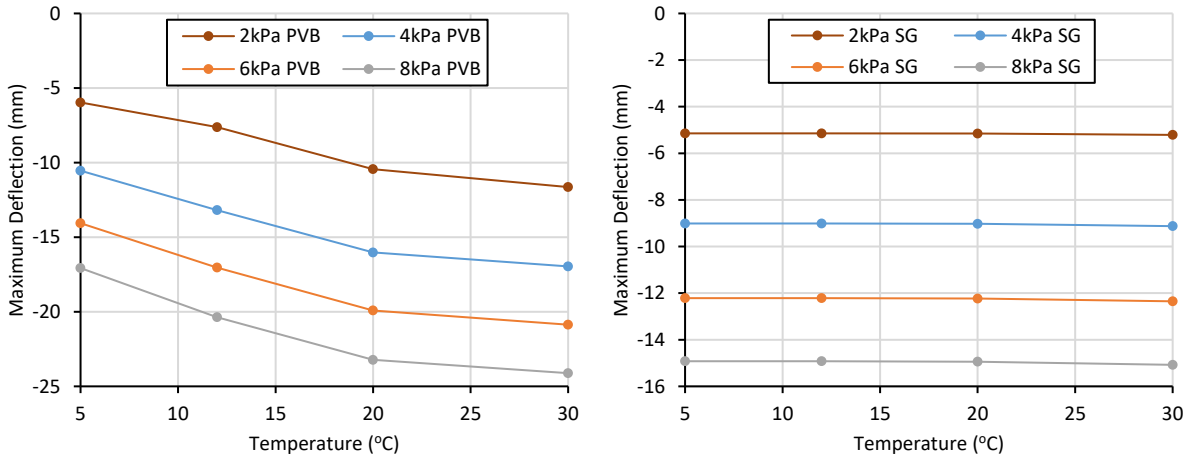

Figura 8. Influência da temperatura na deflexão máxima para a taxa de carregamento da Figura 4, PVB (gráfico da esquerda) e SentryGlas (gráfico da direita)

Para o PVB foi analisada a influência de diferentes velocidades de carregamento constante, para uma temperatura de 12°C. O tempo de carregamento apresentado é por cada patamar de carga, ou seja, por cada incremento de 2kPa. Os resultados podem ser visualizados na Figura 9. Para tempos de carregamento superiores a 3000s/2kPa, verifica-se que o impacto na deflexão máxima é mínimo, pois o intercalar já se comporta como um material elástico G_{∞}. As diferenças na deflexão máxima do painel aumentam até aos 2kPa, sendo que a partir dos 4kPa mantêm-se quase constantes. Aos 2kPa a diferença máxima na deflexão é de 1.54 mm, aos 4kPa é 2.11mm e aos 8kPa é 2.41mm. Demonstrando que a velocidade de carregamento inicial é determinante para as diferenças observadas.

A temperatura tem um maior impacto na deflexão máxima do que a taxa de carregamento. No caso do PVB entre os 5°C e os 20°C a diferença é em torno de 6mm independentemente do patamar de carga, ou seja, cada grau centigrado tem um impacto de cerca 0.4mm na deflexão máxima do provete para as condições analisadas.

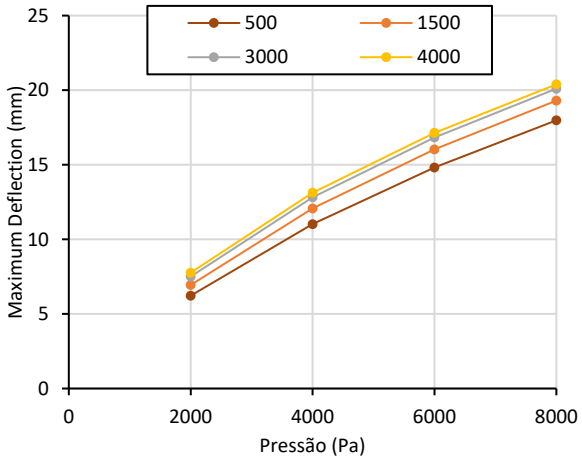

Figura 9. Influência do tempo de carregamento por patamar de carga na deflexão máxima para T_{amb}=12°C

7. CONCLUSÕES

O modelo numérico obtém resultados bastante satisfatórios quando comparado aos resultados experimentais. No entanto, é ainda necessário melhorar a modelação do efeito de placa presente nos modelos com PVB. Este poderá ser usado para planear futuras campanhas de testes experimentais em laboratório, principalmente quando estas podem demorar vários meses e, portanto, existem ciclos de temperatura que podem ter efeitos notáveis no comportamento mecânico do vidro laminado. Este modelo permitirá antecipar a variância de resultados relacionadas com a temperatura do provete.

A variação de temperatura e da velocidade de carregamento foi analisada para ambos os intercales. No caso do PVB, este é mais sensível a variações de temperatura entre os 5°C e os 20°C nesta gama de temperaturas para a deflexão máxima pode variar até 6mm. A velocidade de carregamento, para a gama estudada, tem uma influência menor, de cerca 2,41mm, onde a velocidade de carregamento no instante inicial é crucial para esta diferença. No caso do SentryGlas, a temperatura e a velocidade de carregamento tem um impacto reduzido na deflexão máxima dos provetes para os intervalos analisados.

AGRADECIMENTOS

Financiado no âmbito do Projeto N.º 7254 — R2U Technologies | modular systems, apoiado pelo PRR — Plano de Recuperação e Resiliência e pelos Fundos Europeus Next Generation EU

REFERÊNCIAS

[1] A. Zemanová, J. Zeman, e M. Šejnoha, "Comparison of viscoelastic finite element models for laminated glass beams", *Int J Mech Sci*, vol. 131–132, p. 380–395, out. 2017, doi: 10.1016/J.IJMECSCI.2017.05.035.

[2] M. A. Samieian *et al.*, "Temperature effects on laminated glass at high rate", *Int J Impact Eng*, vol. 111, p. 177–186, jan. 2018, doi: 10.1016/J.IJIMPENG.2017.09.001.

[3] L. Galuppi e G. Royer-Carfagni, "Laminated beams with viscoelastic interlayer", *Int J Solids Struct*, vol. 49, nº 18, p. 2637–2645, set. 2012, doi: 10.1016/J.IJSOLSTR.2012.05.028.

[4] M. L. Williams, R. F. Landel, e J. D. Ferry, "The Temperature Dependence of Relaxation Mechanisms in Amorphous Polymers and Other Glass-forming Liquids", *J Am Chem Soc*, vol. 77, nº 14, p. 3701–3707, jul. 1955, doi: 10.1021/ja01619a008.

[5] M. Schuster, K. Thiele, e J. Schneider, "Investigations on the viscoelastic material behaviour and linearity limits of PVB", *ce/papers*, vol. 4, nº 6, p. 207–223, dez. 2021, doi: https://doi.org/10.1002/cepa.1633.

[6] Y. Lu, S. Chen, e X. Shao, "Shear modulus of ionomer interlayer: Effects of time, temperature and strain rate", *Constr Build Mater*, vol. 302, p. 124224, out. 2021, doi: 10.1016/J.CONBUILDMAT.2021.124224.

[7] M. A. S. A. Gonçalves, "Análise comparativa de intercalares para vidro estrutural: SGP|

PVB. Ações de curta e longa duração", 2019.
[8] S. Jordão, M. Gonçalves, P. Freitas, e E. Inca, "Comportamento de painéis de fachada em vidro: avaliação experimental", em *XII Congresso de Construção Metálica e Mista*, Coimbra, 2019.

Congress on Numerical Methods in Engineering 2024
4-6 September 2024, University of Aveiro, Portugal

BUCKLING ANALYSIS OF ELASTIC COLUMNS AND FRAMES: MIXED FINITE ELEMENT FORMULATION AND ERROR ASSESSMENT

H.A.F.A. Santos[1] **and J.P. Moitinho de Almeida**[2]

1: Departamento de Engenharia Mecânica,
CIMOSM, UnIRE,
Instituto Superior de Engenharia de Lisboa, Instituto Politécnico de Lisboa,
Rua Conselheiro Emídio Navarro 1, 1959-007 Lisboa, Portugal,
e-mail: hugo.santos@isel.pt

2: Departamento de Engenharia Civil, Arquitetura e Ambiente,
Instituto Superior Técnico, Universidade de Lisboa,
Av. Rovisco Pais, 1049-001 Lisboa, Portugal,
e-mail: moitinho@civil.ist.utl.pt

Keywords: Elastic columns and frames, buckling analysis, Hellinger-Reissner energy, finite elements, lower bounds, upper bounds, error assessment.

Abstract *Various numerical techniques have been proposed in the literature for the buckling analysis of elastic framed structures. In a finite element framework, the so-called displacement-based finite element formulation is the most popular one. Complementary formulations, in which only force/moment like-quantities are taken as approximation functions, have also been employed. However, both types of formulations lead to numerical buckling loads that are upper bounds of the exact ones. Hence, by themselves, such formulations are not entirely useful, as they do not provide information on how far the estimated buckling loads lie above the true buckling loads. To have a validated buckling analysis study, it is necessary to find error estimates or, ideally, to determine lower bounds of the buckling loads. A mixed finite element formulation for the buckling analysis of elastic framed structures is proposed in this work. This formulation relies on a complementary form of the Hellinger-Reissner variational principle, involving the bending moment and rotation fields as fundamental unknowns. It will be numerically verified that, for a specific set of approximations, the solutions rendered by the formulation can be used to estimate both lower and upper bounds of the buckling loads.*

1. INTRODUCTION

Buckling of framed structures is the most important buckling problem for civil and structural engineers, and it is often encountered by mechanical and aerospace engineers as well. Buckling is an instability phenomenon in structural systems subjected to compression loads, being associated with the transition from a straight configuration to a laterally deformed state [8]. The critical (or buckling) load describes the load at which this transition occurs.

The buckling loads of a structural system may, in theory, be predicted by formulating its governing differential equation in order to obtain its exact solution. However, finding the exact solutions is often difficult, or even impossible in practice. Therefore, approximate methods, such as the finite-element method or the finite-difference method are usually employed. The classical displacement-based formulation of the finite-element method is equivalent to the well known Rayleigh-Ritz method. Complementary formulations, in which force/moment like-quantities are taken as approximation functions satisfying the equilibrium in a strong sense, have also been employed [7, 4]. However, these formulations provide approximate buckling loads that are upper bounds to those of the elastic structural system.

In other words, unlike what happens in linear elastic analysis, where bounds of the error in energy can be obtained from complementary solutions [6], these formulations do not provide information on how far their approximate buckling loads lie above the true buckling loads of the system under consideration.

This violates the basic precept of the philosophy of engineering design, specifically that the design of a structure based on an approximate theory should be conservative.

Therefore, to improve the process of estimating buckling loads it is necessary to develop methodologies that can be used to predict the accuracy of the obtained solutions. A methodology that can be used to produce upper bounds of the errors of the numerical solutions is therefore of utmost importance. A possible direction to accomplish this is to develop a technique that gives lower bounds of the buckling loads.

Although some techniques that provide lower bounds can be found in the literature [5, 2, 1], to the best of the authors' knowledge, none of them have been formulated within the framework of the finite element method.

The goal of this work is to propose a finite element formulation that can be used to provide lower bounds of the buckling loads of two-dimensional columns and frames and, therefore, that can be used to provide an upper bound of the true errors of their numerical solutions. The introduced finite element formulation is developed within the framework of a complementary form of the Hellinger-Reissner variational principle [4], and makes use of the approximation of both bending moment and rotation fields. The adopted bending moment and rotation approximations ensure C^0-continuity and, simultaneously, satisfy the equilibrium and kinematic boundary conditions, respectively. It was numerically verified that, for all tested problems, the solutions rendered by the

proposed formulation can be used to obtain both lower and upper estimates of the buckling loads, which, when combined, provide a true upper bound of the error in the buckling loads. The accuracy and feasibility of the formulation will be shown and discussed by considering the analysis of two simple problems.

2. BOUNDARY-VALUE PROBLEM

This work is based on a geometrically non-linear column theory in which the following assumptions are considered: (i) the Euler-Bernoulli hypothesis holds, that is, plane sections perpendicular to the column axis before deformation remain so after deformation, *i.e.*, shear deformations are neglected; (ii) the cross sections are uniform along the column, have an axis of symmetry and bending is about this axis; (iii) axial deformations are disregarded and (iv) the column is under moderately large deformations.
Under these assumptions, consider a planar column whose geometry in the current configuration is described by its centroidal axis denoted by C. The centroidal axis C is parameterized by $x \in [0, L]$, with L denoting the length of the column in its reference configuration. C is decomposed into an internal part, represented by $\Omega =]0, L[$, and a boundary part, identified by $\Gamma = \Gamma_N \cup \Gamma_D = \{0, L\}$, where Γ_N and Γ_D correspond to the Neumann and Dirichlet boundaries, respectively, such that $\Gamma_N \cap \Gamma_D = \emptyset$.
Let the column be subjected to a compressive axial load P. The loads are assumed to be conservative and to act at the centroidal axis of the column.
The kinematical differential equations (often also called strain-displacement or compatibility relationships) of the problem are as follows

$$u' = -\frac{\theta^2}{2}, \text{ in } \Omega \tag{1a}$$

$$w' = \theta, \text{ in } \Omega \tag{1b}$$

$$\kappa = \theta', \text{ in } \Omega \tag{1c}$$

where u and w are the axial and transverse displacements of the column, respectively, θ represents the cross-section rotation, and κ represents the curvature of the column. Prime denotes differentiation with respect to x. The reference axis is taken as the centroidal axis of the column, *i.e.*, the axis passing through the centroid of the column cross-sections.
As it will be shown later on, in the context of the buckling problem, the relevant Dirichlet (kinematical) boundary condition is

$$\theta = 0, \text{ on } \Gamma_D \tag{2}$$

The equilibrium equations of the geometrically non-linear column under study can be obtained using the well known Principle of Virtual Work (PVW). Let us beforehand

introduce the following function spaces

$$\mathcal{U}_k = \{\theta \in \mathcal{H}^1(\Omega) |\ \theta = 0 \text{ on } \Gamma_D\}$$
$$\mathcal{V}_k = \{\delta\theta \in \mathcal{H}^1(\Omega) |\ \delta\theta = 0 \text{ on } \Gamma_D\}$$

with $\mathcal{U}_k$ a trial space and $\mathcal{V}_k$ a test space. $\mathcal{H}^1(\Omega)$ represents the standard Sobolev space. $\mathcal{U}_k$ and $\mathcal{V}_k$ are referred to as the kinematically and the homogeneous kinematically admissible spaces, respectively.

Proposition 1. If $\theta \in \mathcal{U}_k$ represents an equilibrium configuration, then, for any given virtual configuration defined by $\delta\theta \in \mathcal{V}_k$, the internal virtual work equals the external virtual work, *i.e.*

$$\int_\Omega (M\delta\kappa - V\delta\theta)\, d\Omega = \int_\Omega P\theta\delta\theta\, d\Omega,\ \forall\ \delta\theta \in \mathcal{V}_k \tag{5}$$

where M represents the bending moment and V the transverse force (which is constant) of the column.

Proof. We first note that, on insertion of the kinematical differential equation (1c) into this equation yields

$$\int_\Omega M\delta\theta'\, d\Omega = \int_\Omega (P\theta + V)\delta\theta\, d\Omega,\ \forall\ \delta\theta \in \mathcal{V}_k \tag{6}$$

This, after integration by parts, gives

$$\int_\Omega (M' + P\theta + V)\delta\theta\, d\Omega - [nM\delta\theta]_{\Gamma_N} = 0,\ \forall\ \delta\theta \in \mathcal{V}_k \tag{7}$$

Finally, since the variation $\delta\theta$ is completely arbitrary, the terms in parentheses must vanish, giving rise to the following Euler-Lagrange equations

$$M' + P\theta + V = 0,\ \text{in } \Omega \tag{8}$$

and

$$nM = 0,\ \text{on } \Gamma_N \tag{9}$$

with

$$n = \begin{cases} 1 & \text{if } x = L \\ -1 & \text{if } x = 0 \end{cases}$$

These equations represent the equilibrium differential equations and Neumann (static) boundary conditions of the boundary-value problem stated above. □

Remark 1. Conditions on the transverse displacement are not directly enforced since, after making use of (1b), the term in (5) that involves V results as

$$\int_\Omega V\delta\theta \, d\Omega = \int_\Omega V\delta w' \, d\Omega \tag{10}$$

which, after integrating, can be rewritten as

$$\int_\Omega V\delta\theta \, d\Omega = V(\delta w_L - \delta w_0) \tag{11}$$

Also, since for the column we have either $V = 0$ or $\delta w_L = \delta w_0$, it always yields

$$\int_\Omega V\delta\theta \, d\Omega = 0 \tag{12}$$

It is also worth noting that no assumptions regarding the material behavior have been considered so far. Let us hereafter assume a linear elastic (homogeneous and isotropic) material response. Under this assumption, the strain energy density defined per unit reference length can be written as the following differentiable and convex function

$$W(\varepsilon, \kappa) = \frac{1}{2} EI\kappa^2$$

and the following constitutive equations can be defined

$$M = \frac{\partial W}{\partial \kappa} = EI\kappa, \text{ in } \Omega \tag{13}$$

where E stands for the Young's modulus of the material and I represents the cross-section moment of inertia with respect to the centroidal axis.
Due to the differentiability and convexity of W with respect to κ, a one-to-one correspondence between κ and M can be established and, therefore, a new function $W_c(M)$, referred to as the complementary strain energy density, can be introduced by means of the following Legendre transformation

$$W_c(M) = -W(\kappa) + M\kappa \tag{14}$$

which gives

$$W_c(M) = \frac{1}{2}\frac{M^2}{EI}$$

This, in turn, after differentiation with respect to M, gives rise to the inverse form of the constitutive relations (13) as follows

$$\kappa = \frac{\partial W_c}{\partial M} = \frac{M}{EI}, \text{ in } \Omega \tag{15}$$

Accordingly, the boundary-value problem consists of the sets of kinematical differential equations (1), equilibrium differential equation (8), constitutive equation (13) or (15) and Neumann and Dirichlet boundary conditions (9) and (2), respectively.

3. VARIATIONAL SETTING

Let us beforehand introduce the total potential energy functional $\Pi_p : \mathcal{U}_k(\Omega) \to \mathcal{R}$ given by

$$\Pi_p(\theta) = U(\kappa(\theta)) + F(\theta) \tag{16}$$

where U and F represent the strain energy and the external potential energy, respectively, given by

$$U(k) = \int_\Omega W(\kappa)\, d\Omega \tag{17a}$$

$$F(\theta) = -\int_\Omega P\frac{\theta^2}{2}\, d\Omega - \int_\Omega V\theta\, d\Omega \tag{17b}$$

The principle of stationary total potential energy can be stated as follows:

Proposition 2. θ is a stationary point of Π_p if, and only if, its first-order Gâteaux derivative defined at $\theta \in \mathcal{U}_k$ in any direction $\delta\theta \in \mathcal{V}_k$ vanishes, that is, if the following condition holds

$$\delta\Pi_p = 0,\ \forall\ \delta\theta \in \mathcal{V}_k \tag{18}$$

Proof. We first note that, the first-order Gâteaux derivative of Π_p, defined at $\theta \in \mathcal{U}_k$, in the direction of $\delta\theta \in \mathcal{V}_k$, assumes the following form

$$\delta\Pi_p = \int_\Omega \left(\frac{\partial W}{\partial \kappa}\delta\kappa - P\theta\delta\theta - V\delta\theta\right) d\Omega$$

This, upon substitution of the constitutive relation (13), gives rise to

$$\delta\Pi_p = \int_\Omega (M\delta\kappa - P\theta\delta\theta - V\delta\theta)\, d\Omega$$

which shows that the variational form (18) is formally equivalent to the PVW given by Proposition 1. Hence, the stationarity of the total potential energy implies the equilibrium of the system and vice-versa. Therefore, it can be stated that, of all kinematically admissible fields θ, those that satisfy the equilibrium equations of the column are the ones for which the total potential energy assumes a stationary value. □

The condition for buckling can be obtained from setting the second variation of Π_p to 0, which gives

$$P_R = \frac{\int_\Omega EI\delta\theta'^2\, d\Omega}{\int_\Omega \delta\theta^2\, d\Omega} \tag{19}$$

This formula is well known as the Rayleigh quotient.

Conventional finite element formulations can be constructed on the basis of the variational principle of total potential energy presented above. In a buckling analysis setting, such formulations lead to upper bounds of the exact buckling loads through the Rayleigh quotient.
Making use of the Legendre transformation (14) and the compatibility relationship (1c), the total potential energy (16) gives rise to the complementary Hellinger-Reissner functional $\Pi_{H-R} : \times\mathcal{H}^0(\Omega) \times \mathcal{H}^1(\Omega) \rightarrow \mathcal{R}$ defined as

$$\Pi_{H-R}(M,\theta) = \int_\Omega \left(\frac{1}{2}\frac{M^2}{EI} - M\theta' + P\frac{\theta^2}{2} + V\theta\right) d\Omega \tag{20}$$

The condition for buckling in the framework of the Hellinger-Reissner variational principle results from setting the second variation of Π_{H-R} to 0, which can be written as

$$P_{HR} = \frac{\int_\Omega \left(2\delta M\delta\theta' - \frac{\delta M^2}{EI} - 2\delta V\delta\theta\right) d\Omega}{\int_\Omega \delta\theta^2 \, d\Omega} \tag{21}$$

This formula will be, herein, regarded as the Hellinger-Reissner quotient.
The mixed finite element formulation proposed in this work is developed on the basis of the Hellinger-Reissner variational principle in which both Dirichlet and Neumann boundary conditions are *a priori* satisfied.

4. FINITE ELEMENT FORMULATION

The following trial finite element approximations are assumed for the bending moments and rotations

$$M^h = M_i\left(1 - \frac{x}{L_e}\right) + M_j\frac{x}{L_e} \tag{22a}$$

$$\theta^h = \theta_i\left(1 - \frac{x}{L_e}\right) + \theta_j\frac{x}{L_e} \tag{22b}$$

where the pairs M_i, θ_i and M_j, θ_j represent the nodal bending moments and nodal rotations, defined at $x = 0$ and $x = L$, respectively. L_e stands for the finite element length.
A Galerkin approach is adopted, *i.e.*, the problem is numerically approached assuming the same trial and test approximation function spaces.
These approximations ensure C^0-continuity of both bending moments and rotations. Furthermore, the bending moment/rotation approximations are such that both static and kinematic boundary conditions are satisfied.
The stationarity of Π^h_{H-R} with respect to all the unknown element parameters gives rise to a governing system of equations that involves the axial load P as an additional unknown as follows

$$\begin{bmatrix} \boldsymbol{F} & \boldsymbol{A}^T \\ \boldsymbol{A} & P\boldsymbol{K}_G \end{bmatrix} \begin{bmatrix} \boldsymbol{M} \\ \boldsymbol{\theta} \end{bmatrix} = \begin{bmatrix} \boldsymbol{0} \\ \boldsymbol{0} \end{bmatrix} \tag{23}$$

where $\boldsymbol{F}$, $\boldsymbol{A}$ and $\boldsymbol{K}_G$ represent the flexibility, equilibrium and geometric stiffness matrices, respectively, and $\boldsymbol{M}$ and $\boldsymbol{\theta}$ stand for the vectors that collect the nodal bending moments and rotations, respectively. This system of equations can be regarded as an eigenvalue problem, in which the obtained eigenvalues and corresponding eigenvectors represent the critical (buckling) loads and the critical (buckling) modes of the problem, respectively.

Remark 2. Note that, the obtained eigen-solutions for θ are admissible within the framework of the potential energy principle discussed above. Therefore, they can be used to compute upper bounds of the exact buckling loads using the Rayleigh's quotient as given in (19).
As it will be numerically shown in the following section, this mixed finite element formulation leads to spurious solutions, although it correctly approximates the non-spurious ones. A strategy to filter out these solutions becomes, therefore, necessary. This will be further discussed in the following section. It is worth noting that, despite alternative formulations free from this issue could be easily designed and used for the analysis, the proposed formulation has the following capabilities: (i) to produce lower bounds of the exact buckling loads using the Hellinger-Reissner's quotient as defined in (21); (ii) to give upper bounds of the exact buckling loads using the Rayleigh's quotient as given in (19); (iii) to allow to obtain true upper bounds of the error to the exact solutions using the results from (i) and (ii).

5. NUMERICAL TESTS

To validate and assess the accuracy and effectiveness of the proposed finite element formulation, a clamped-simply-supported column and a statically indeterminate frame are analyzed. Uniform meshes of 2, 4, 8, 16, 32 and 64 finite elements per member were considered. The bending stiffness EI and length L of the members were set as $EI = 1$ and $L = 1$ in both numerical tests.
Herein, LB stands for a critical load computed using the Hellinger-Reissner quotient formula (21), whereas UB denotes a critical load computed using the Rayleigh quotient formula (19).

5.1 Clamped-Pinned Column

Firstly, a clamped-pinned column under compressive axial load as depicted in Figure 1 is analyzed.
The numerical results obtained for the first critical loads of the column are displayed in Table 1.
The exact analytical buckling loads were computed using the well known transcendental equation of the clamped-pinned column given by

$$\lambda L = \tan(\lambda L) \tag{24}$$

Figure 1: Clamped-pinned column.

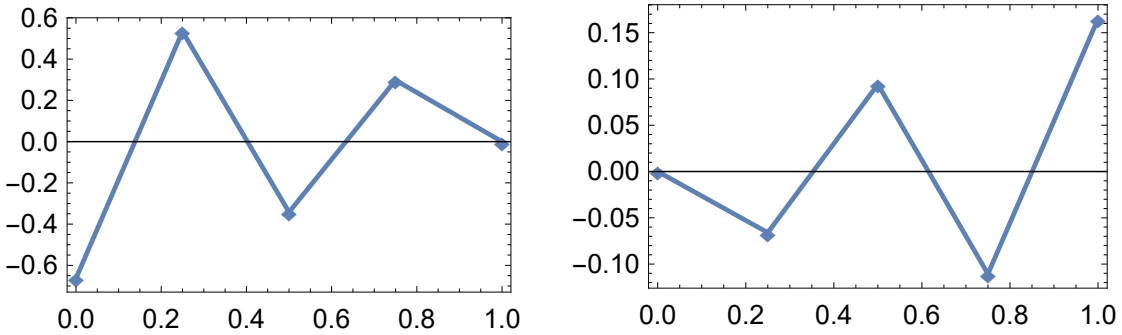

Figure 2: Clamped-pinned column - First spurious eigen-solution obtained on the 4-element mesh, $P_{cr}^{(1)} = 18.0795$. Bending moment M^h (left); Rotation θ^h (right).

with $\lambda^2 = \frac{P}{EI}$.

As it can be seen, while some of the obtained LB solutions converge to their corresponding exact solutions, others do not. A common feature is that, for such LB solutions, the corresponding LB/UB ratios are too high. In fact, for such solutions, the corresponding eigenvectors of either θ^h or M^h exhibit an exaggerated number of waves. All these features are consequence of the spurious character of such solutions. Furthermore, the spurious solutions do not disappear on mesh refinement. This is a feature of some mixed finite element formulations when applied to eigenvalue problems, and it seems to be well known in the Mathematics literature, see, *e.g.*, [3]. This phenomenon is illustrated in Figure 2, which corresponds to the first buckling solution obtained on the 4-element mesh. As is well known, the first exact buckling mode θ of the clamped-pinned column exhibits two roots. However, as it can be observed in Figure 2, the first eigen-solution θ^h obtained by the proposed mixed finite element formulation possesses four roots.

A strategy to filter out the spurious solutions is, therefore, needed. The following criteria are considered: (i) an eigen-solution is considered to be spurious if, for a specific mesh refinement, the ratio UB/LB of such solution is above the ratio of the preceding eigen-solution (note that the ratio UB/LB should increase from mode i to mode $i + 1$), and, in addition, (ii) the ratio R=UB/LB is above a specified threshold (taken as 2 in this work). In Table 1, the results that simultaneously satisfy conditions (i) and (ii) were marked in red.

n_e		$P_{cr}^{(1)}$	$P_{cr}^{(2)}$	$P_{cr}^{(3)}$	$P_{cr}^{(4)}$	$P_{cr}^{(5)}$	$P_{cr}^{(6)}$
2	*LB*	10.2857					
	UB	30.0000					
	R	2.91667					
4	*LB*	18.0795	19.8112	45.8372			
	UB	164.155	29.4897	79.9551			
	R	9.07962	1.48854	1.74433			
8	*LB*	20.1557	21.1092	59.0112	113.150	129.984	168.607
	UB	27.9948	738.882	64.6662	139.163	599.971	252.397
	R	1.38893	35.0028	1.09583	1.22990	4.61572	1.49695
16	*LB*	20.1889	21.9238	59.6411	118.593	178.424	196.406
	UB	20.9094	3049.30	60.8961	123.680	2880.96	211.459
	R	1.03569	139.086	1.02104	1.04289	16.1467	1.07664
32	*LB*	20.1906	22.1354	59.6772	118.881	194.190	197.774
	UB	20.3427	12265.7	59.9816	120.080	12087.6	203.987
	R	1.00753	554.121	1.00510	1.01009	62.2463	1.03141
64	*LB*	20.1907	22.1888	59.6794	118.899	197.852	198.422
	UB	20.2273	49129.8	59.7549	119.194	228.116	48923.3
	R	1.00181	2214.17	1.00127	1.00248	1.15296	246.562
Exact		20.1907	59.6795	118.900	197.858	296.554	414.990

Table 1: Critical loads of the clamped-pinned column (results in red correspond to the cases that simultaneously satisfy conditions (i) and (ii).

After filtering out the spurious solutions, the remaining solutions were reorganized and displayed in Table 2. A thorough analysis of Table 2 leads us to also doubt of the quality of the solution corresponding to $P_{cr}^{(4)} = 197.852$ (marked in blue in Table 2), since the corresponding UB critical load does not decrease, as one would expect, from the 32- to the 64-element mesh. In other words, it does not satisfy condition (i), though it satisfies condition (ii).
True upper bounds of the errors of the obtained solutions can now be straightforwardly obtained using the LB and UB solutions.

5.2 Statically Indeterminate Frame

A statically indeterminate frame under compressive load as depicted in Figure 3 is now analyzed. The corresponding exact analytical solutions are not known *a priori* in this case. The numerical results obtained for the first critical loads of the frame are displayed in Table 3. After filtering out the spurious solutions, the remaining solutions were reorganized and displayed in Table 4.

n_e		$P_{cr}^{(1)}$	$P_{cr}^{(2)}$	$P_{cr}^{(3)}$	$P_{cr}^{(4)}$	$P_{cr}^{(5)}$
2	*LB*					
	UB					
4	*LB*	19.8112	45.8372			
	UB	29.4897	79.9551			
8	*LB*	20.1557	59.0112	113.150	168.607	
	UB	27.9948	64.6662	139.163	252.397	
16	*LB*	20.1889	59.6411	118.593	196.406	291.461
	UB	20.9094	60.8961	123.680	211.459	326.415
32	*LB*	20.1906	59.6772	118.881	197.774	296.266
	UB	20.3427	59.9816	120.080	203.987	303.839
64	*LB*	20.1907	59.6794	118.899	197.852	296.537
	UB	20.2273	59.7549	119.194	228.116	298.363
Exact		20.1907	59.6795	118.900	197.858	296.554

Table 2: First five critical loads of the clamped-pinned column after filtering out the spurious solutions.

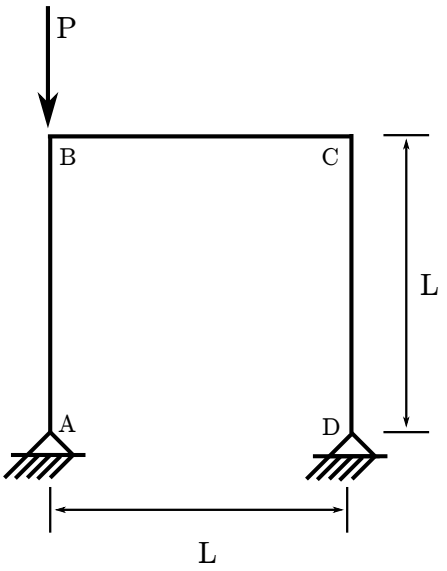

Figure 3: Statically indeterminate frame.

n_e		$P_{cr}^{(1)}$	$P_{cr}^{(2)}$	$P_{cr}^{(3)}$	$P_{cr}^{(4)}$	$P_{cr}^{(5)}$	$P_{cr}^{(6)}$
2	LB	3.58564	14.3429				
	UB	4.44932	54.8389				
	R	1.24087	3.82342				
4	LB	3.59015	15.4392	39.9396	47.2848		
	UB	3.80082	18.7801	82.9275	515.427		
	R	1.05868	1.21639	2.07632	10.9005		
8	LB	3.59043	15.5520	45.5923	73.0004	92.9777	149.465
	UB	3.64272	16.3148	49.8662	2945.93	171.871	265.248
	R	1.01456	1.04905	1.09374	40.3550	1.84852	1.77465
16	LB	3.59044	15.5585	45.8335	84.4219	95.3028	163.847
	UB	3.60349	15.7447	46.8506	14345.9	129.965	189.137
	R	1.00363	1.01197	1.02219	169.931	1.36371	1.15435
32	LB	3.59044	15.5589	45.8475	87.6950	95.4263	164.576
	UB	3.59370	15.6052	46.0983	60404.3	109.134	170.459
	R	1.00091	1.00298	1.00547	688.800	1.14365	1.03575
64	LB	3.59044	15.5590	45.8484	88.5417	95.4335	164.619
	UB	3.59126	15.5705	45.9109	244723.	99.4969	166.064
	R	1.00023	1.00074	1.00136	2763.93	1.04258	1.00878

Table 3: Critical loads of the statically indeterminate frame (results in red correspond to the cases that simultaneously satisfy conditions (i) and (ii).

n_e		$P_{cr}^{(1)}$	$P_{cr}^{(2)}$	$P_{cr}^{(3)}$	$P_{cr}^{(4)}$	$P_{cr}^{(5)}$
2	LB	3.58564				
	UB	4.44932				
4	LB	3.59015	15.4392			
	UB	3.80082	18.7801			
8	LB	3.59043	15.5520	45.5923	92.9777	149.465
	UB	3.64272	16.3148	49.8662	171.871	265.248
16	LB	3.59044	15.5585	45.8335	95.3028	163.847
	UB	3.60349	15.7447	46.8506	129.965	189.137
32	LB	3.59044	15.5589	45.8475	95.4263	164.576
	UB	3.59370	15.6052	46.0983	109.134	170.459
64	LB	3.59044	15.5590	45.8484	95.4335	164.619
	UB	3.59126	15.5705	45.9109	99.4969	166.064

Table 4: First five critical loads of the statically indeterminate frame after filtering out the spurious solutions.

6. CONCLUSIONS

A mixed finite element formulation for the buckling analysis of elastic framed structures was proposed in this work. This formulation relies on a complementary form of the Hellinger-Reissner variational principle, involving the bending moment and rotation fields as fundamental unknowns. It was numerically demonstrated that if C^0-continuous bending moment and rotation approximations that simultaneously satisfy their corresponding equilibrium and kinematical boundary conditions are adopted, the solutions rendered by the formulation can be used to estimate both lower and upper bounds of the buckling loads, which, when combined, allow to estimate true upper bounds of the error of the exact buckling loads. The main drawback of the formulation is that spurious solutions are obtained, which requires a strategy for filtering out such solutions.

REFERENCES

[1] A. Vrouwenvelder and J. Witteveen. Lower bound approximation for elastic buckling loads. *HERON*, 20(4), 1975.

[2] C. H. Popelar. Lower bounds for the buckling loads and the fundamental frequencies of elastic bodies. *Journal of Applied Mechanics*, 41:151–154, 1974.

[3] D. Boffi. Finite element approximation of eigenvalue problems. *Acta Numerica*, 19:1–120, 2010.

[4] H. A. F. A. Santos. Variationally consistent force-based finite element method for the geometrically non-linear analysis of Euler-Bernoulli framed structures. *Finite Elements in Analysis and Design*, 53:24–36, 2012.

[5] H. L. Schreyer and P. Y. Shih. Lower bounds to column buckling loads. *Journal of Engineering Mechanics Division (ASCE)*, 99:1011–1022, 1973.

[6] J. P. M. Almeida and E. A. W. Maunder. *Equilibrium Finite Element Formulations*. John Wiley & Sons, 2017.

[7] K. Washizu. *Variational methods in elasticity and plasticity*. Pergamon Press, 1968.

[8] Z. Bazant and L. Cedolin. *Stability of structures*. Oxford University Press, New York, 1991.

This page intentionally left blank

Congress on Numerical Methods in Engineering 2024
4-6 September 2024, University of Aveiro, Portugal

COMPARACIÓN DE REDES NEURONALES Y KRIGING PARA LA OPTIMIZACIÓN ENERGÉTICA DE PUENTES Llosa PRETENSADOS

Lorena Yepes-Bellver[1], Alejandro Brun-Izquierdo[2] , Julián Alcalá[2] y Víctor Yepes[2]

1: Departamento de Mecánica de los Medios Continuos y Teoría de Estructuras
Universitat Politècnica de València
Camino de Vera, s/n, 46022 Valencia, Spain
e-mail: loyebel@alumni.upv.es

2: ICITECH. Departamento de Ingeniería de la Construcción y Proyectos de Ingeniería Civil
Universitat Politècnica de València
Camino de Vera, s/n, 46022 Valencia, Spain
e-mail: albruiz1994@gmail.com;{jualgon,vyepesp}@cst.upv.es

Palabras clave: Optimización, metamodelos Kriging, redes neuronales, metaheurísticas, puente losa postesado, sostenibilidad, energía

Resumen *El objetivo principal de este estudio es evaluar y comparar la eficacia de varios métodos de predicción espacial en una simulación aplicada para optimizar la energía incorporada durante la construcción de tableros de puentes pretensados. Se lleva a cabo una exhaustiva revisión bibliográfica para realizar un análisis transversal e identificar los parámetros de diseño cruciales. A partir de este análisis, se determinan las variables de diseño clave que pueden mejorar la eficiencia energética del forjado. Los métodos analizados son el Kriging ordinario y una red neuronal Perceptrón multicapa. Aunque el estudio de simulación indica que el rendimiento de predicción espacial de la red neuronal es algo más débil que el del método Kriging, sigue siendo un buen competidor. Para mejorar la eficiencia energética se recomiendan relaciones de esbeltez elevadas (en torno a 1/28) y emplear hormigones de 40 MPa de resistencia característica a compresión.*

1. INTRODUCCIÓN

La construcción representa entre el 25% y el 40% del consumo mundial de energía [1]. La cantidad de energía utilizada en la construcción de una estructura, así como las emisiones de gases de efecto invernadero asociadas, se consideran indicadores clave de su sostenibilidad [2,3]. Por tanto, el interés por optimizar la sostenibilidad ambiental en la industria de la construcción ha aumentado significativamente en los últimos años [4].

La selección adecuada de materiales y la optimización contribuyen a mejorar la sostenibilidad de las estructuras. De hecho, algunos estudios han utilizado la energía como un objetivo clave en este proceso [5,6]. Miller *et al*. [7] han demostrado que las losas postesadas consumen menos energía que las de hormigón armado. Sin embargo, la reducción en el consumo energético no se garantiza únicamente con la disminución del peso de la estructura [8].

Nuestro equipo ha optimizado el consumo energético en puentes. En el estudio de Yepes *et al*. [9], se aplicó esta optimización a un puente de tres vanos continuos, con longitudes de 20-36-20 m y una anchura de tablero de 11 m, utilizando 33 variables de diseño. Se observó que la solución que minimizaba la energía era un 9,7% más costosa que aquella obtenida al optimizar el costo. Por otro lado, Alcalá *et al*. [10] encontraron que la solución de menor costo solo requería un aumento del 5,3% en el consumo de energía. En otro estudio, Martí *et al*. [11] lograron ahorros energéticos del 24% para un puente prefabricado de 30 m. Además, Penadés-Plà *et al*. [12] presentaron un algoritmo de optimización basado en Kriging para una pasarela de tres vanos con longitudes de 40-50-40 m. Como se puede apreciar, son escasas las investigaciones que abordan la optimización energética en puentes con losa de hormigón.

La optimización heurística de estructuras puede conllevar un alto costo computacional, lo que lleva a la utilización de metamodelos para abordar este desafío. Uno de los más eficaces es el Kriging, el cual reemplaza a un modelo de simulación y ofrece una interpolación óptima basada en la regresión de valores observados [13]. Sin embargo, son escasos los estudios que han empleado Kriging en el diseño de estructuras reales. Martínez-Frutos y Martí [14] han aplicado esta metodología para resolver el diseño óptimo robusto de estructuras articuladas y separar la evaluación de la incertidumbre del proceso de optimización en sí. Recientemente, se ha utilizado en la optimización de aerogeneradores [15], en la planificación de vías ferroviarias [16], de puentes postesados [17-19], o en la optimización de estructuras de hormigón armado en edificación [20,21]. Una revisión reciente del estado del arte de los metamodelos aplicados en la optimización estructural puede verse en el trabajo de Negrín *et al*. [22].

Otro tipo de metamodelo lo constituyen las redes neuronales artificiales (RNA). Su estructura se compone de una red formada por nodos (o neuronas) y conexiones, lo que les confiere una semejanza con el cerebro humano. Estas redes encuentran aplicación en una amplia gama de problemas, desde el reconocimiento de patrones hasta la aproximación de funciones, gracias a su flexibilidad y facilidad de uso. son un método de aprendizaje automático. Las RNA aprenden a partir de ejemplos de entrenamiento y proporcionan una respuesta o salida aproximando funciones no lineales de sus entradas. Se han aplicado RNA para predecir el comportamiento estructural [23] o como apoyo a la optimización multiobjetivo de puentes [24].

2. DESCRIPCIÓN DEL TABLERO DE PUENTE LOSA ALIGERADO

La utilización de losas de hormigón postesado hiperestáticas en puentes de entre 10 y 45 m es una práctica común. Con una luz principal de más de 50 m, esta estructura no es competitiva, y da paso a las vigas de sección en cajón. En la práctica habitual, al diseñar losas para carreteras con tres o más vanos, se suele mantener una relación canto/luz de aproximadamente 1/25. Esta solución compite con las vigas prefabricadas debido a sus ventajas estructurales, que incluyen una mayor rigidez a flexión y torsión, una mayor durabilidad y seguridad atribuida al comportamiento hiperestático. Además, se adapta fácilmente a formas constructivas complejas, simplificando los procesos de encofrado y vertido de hormigón. Además, elimina las juntas y proporciona una mayor flexibilidad en la colocación de pilas, mejorando la estética.

El objetivo de este estudio es mejorar el diseño de una losa aligerada pretensada con luces de 24-34-28 m, una configuración común en pasos superiores que atraviesan autopistas de doble carril y doble vía. Como se muestra en la Figura 1, la losa de hormigón in situ presenta un canto constante y sigue un trazado rectilíneo. La plataforma tiene un ancho de 8,30 m, que permite dos carriles de 3,50 m, y pretiles a ambos lados de 0,65 m cada uno junto con un pedestal de hormigón (ver Figura 2).

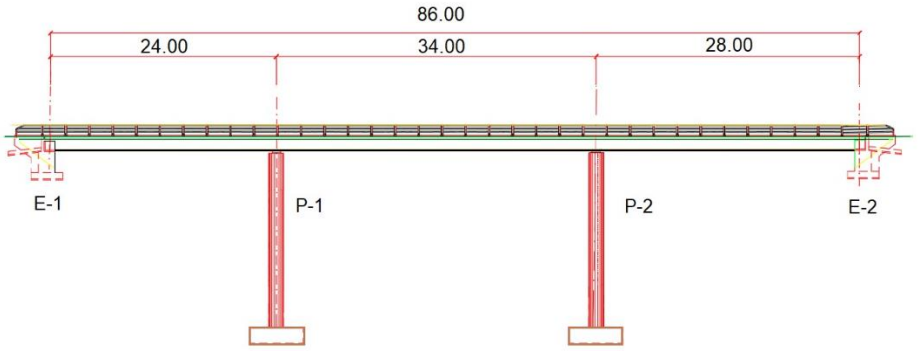

Figura 1. Alzado del puente losa pretensado aligerado.

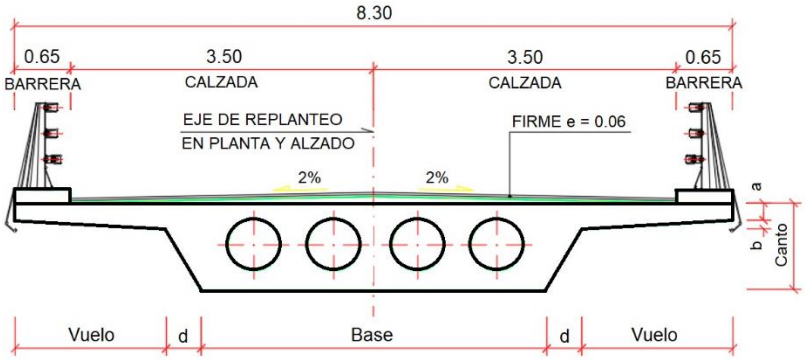

Figura 2. Sección transversal tipo del tablero de puente losa pretensado aligerado.

Se trata de un paso superior situado en el kilómetro 441 de la autovía A-7, en el término municipal de Cocentaina (Alicante). En la Figura 3 se puede observar una imagen aérea del paso superior. Este puente se diseñó con un canto de 1,35 m, con una base inferior de 4,00 m, un vuelo de 1,75 m, siendo a = 0,20 m, b = 0,10 m y d = 0,40 m. Los aligeramientos interiores fueron cuatro secciones circulares de diámetro 0,60 m. Estas dimensiones suponen un aligeramiento interior de 0,14 m^3/m^2 y exterior de 0,51 m^3/m^2.

Figura 3. Imagen aérea del paso superior en el kilómetro 441 de la autovía A-7, en el término municipal de Cocentaina (Alicante). Imagen: Google Maps.

La teoría de los estados límite se emplea para verificar la resistencia estructural mediante coeficientes parciales de seguridad. En cada situación de diseño, se asegura que no se exceda ningún estado límite, tanto para condiciones últimas como de servicio. En este caso, se utilizó el software CSiBridge v.21.0.0 para modelar, analizar y dimensionar el tablero. Se analizó cada alternativa para determinar las cargas actuantes y resistentes, las cuales se representan mediante esfuerzos seccionales. Estas cargas se obtienen para cada elemento estructural y se detallan en los trabajos de Yepes-Bellver *et al*. [18,19].

3. METODOLOGÍA

Cada tablero consume energía en su construcción. Para comparar diferentes diseños, se analizan diversos elementos como el tipo de hormigón, la superficie de encofrado, la cantidad de acero y el volumen de aligeramientos. En la Tabla 1 se recogen los distintos costes correspondientes a las funciones objetivo de coste, emisiones y consumo energético [18,19].
En este trabajo se utilizan dos tipos de metamodelos predictivos: Kriging y redes neuronales. Ambos se aplican sobre 42 datos empleados anteriormente para optimizar el puente losa propuesto [18,19], y que recogen en la Tabla 2. Los 30 primeros corresponden con la fase de

diversificación de la optimización de la superficie de respuesta generada por el metamodelo Kriging. Los 10 siguientes, corresponden a la fase de intensificación. El dato número 41 corresponde con el óptimo local de la fase de diversificación, mientras que el número 42 es el óptimo local correspondiente a la fase de intensificación.

Tipo de material	kWH/m^3	kWH/kg	kWH/m^2
Hormigón HP-30	596,91		
Hormigón HP-35	612,22		
Hormigón HP-40	646,61		
Hormigón HP-45	681,00		
Hormigón HP-50	715,39		
Acero (B 500S)		10,44	
Acero Y1860-S7		12,99	
Encofrado			8,70
Aligeramiento	1137,50		

Tabla 1. Coste energético de las unidades de obra [12].

#	Canto (m)	Base (m)	f_{ck} (MPa)	Coste energético (MW·h)
1	1,65	3,65	35	1149,88
2	1,70	3,80	45	1182,89
3	1,20	3,85	40	1065,87
4	1,55	3,60	45	1140,79
5	1,20	4,85	50	1170,72
6	1,15	4,50	50	1199,59
7	1,35	3,95	30	1103,18
8	1,30	4,45	30	1180,31
9	1,35	4,25	45	1132,71
10	1,50	4,55	30	1138,00
11	1,60	4,20	40	1267,85
12	1,25	4,70	40	1191,65
13	1,50	4,05	45	1183,17
14	1,45	4,35	35	1119,17
15	1,65	3,45	45	1145,07
16	1,55	4,10	35	1162,92
17	1,25	3,50	45	1073,75
18	1,40	3,30	40	1152,33
19	1,45	3,90	45	1145,21
20	1,35	3,60	35	1094,86
21	1,50	3,35	45	1134,93
22	1,50	4,50	45	1189,53
23	1,55	3,20	30	1103,41
24	1,25	3,00	50	1101,04
25	1,40	3,45	45	1201,73
26	1,50	3,55	35	1105,44
27	1,70	3,85	45	1165,47
28	1,20	3,60	40	1083,41
29	1,30	4,90	40	1215,82
30	1,45	4,75	35	1163,59
31	1,20	3,40	40	1059,87
32	1,15	3,90	35	1129,22
33	1,05	3,50	35	1237,89
34	1,10	3,80	45	1178,72
35	1,15	3,35	45	1074,77
36	1,25	3,60	45	1078,71
37	1,10	3,45	40	1124,21
38	1,20	3,35	45	1065,44
39	1,25	3,40	45	1084,92
40	1,15	3,60	45	1104,77
41	1,15	3,35	40	1051,00
42	1,15	3,70	40	1038,28

Tabla 2. Valores obtenidos para las variables de diseño dentro de los rangos establecidos [18,19].

Una vez se ajusta una superficie de respuesta a un metamodelo, se puede medir el error de la predicción a través de la raíz del error cuadrático medio (RMSE), que tendrá las mismas unidades que los valores de salida del modelo predictivo.

$$RMSE = \sqrt{\sum_{i=1}^{n} \frac{(\hat{y}_i - y_i)^2}{n}} \quad (1)$$

Donde $\hat{y}_i$ son los valores estimados, y_i son los valores observados y n es el número de observaciones.

3.1. Metamodelo Kriging

La metodología utilizada es una optimización bifase de la superficie de respuesta generada por un metamodelo Kriging [18,19]. Se utiliza el muestreo de hipercubo latino (LHS) para seleccionar números aleatorios uniformemente distribuidos. Para cada alternativa, se analiza la energía embebida y se optimiza una superficie de respuesta generada por un metamodelo Kriging. Este muestreo genera diseños que se utilizan como entrada en el modelo de optimización.

Kriging se fundamenta en la predicción del valor de un atributo z en un punto de coordenadas *u*, a partir de *n* valores de *z* (ver Figura 4). En este contexto, el atributo en cuestión es la energía requerida para ejecutar el tablero, y los puntos corresponden al conjunto de soluciones obtenidas mediante un muestreo LHS. Este proceso permite predecir la respuesta sin la necesidad de llevar a cabo un análisis estructural completo. Para ello, se ha empleado el "MATLAB Kriging Toolbox" (DACE), el cual construye un modelo de Kriging utilizando datos de un experimento computacional que consta de pares de entradas y respuestas del modelo [25]. Los modelos son deterministas, por lo que una respuesta del modelo carece de error aleatorio, es decir, ejecuciones repetidas para los mismos parámetros de entrada proporcionan la misma respuesta del modelo. Se pueden construir diversos modelos Kriging eligiendo polinomios de orden 0, 1 y 2 para los modelos de regresión. Se ha llamado a estos modelos Kriging 1, Kriging 2 y Kriging 3 para los polinomios de orden 0, 1 y 2, respectivamente.

Se emplea el Muestreo de Hipercubo Latino (LHS, por sus siglas en inglés) para seleccionar números aleatorios distribuidos uniformemente. LHS produce una menor varianza de la media de la muestra en comparación con una muestra aleatoria simple [26]. Esta técnica selecciona aleatoriamente una muestra dentro de cada intervalo para cada variable, y el modelo numérico se ejecuta tantas veces como intervalos haya en la división de la distribución de probabilidad. Esto asegura la selección de valores iniciales dentro de cada rango de datos. LHS ofrece una comprensión más completa del espacio de diseño que el muestreo aleatorio simple. Es especialmente adecuado en experimentos computacionales que se centran en errores sistemáticos en lugar de aleatorios y garantiza una muestra aleatoria uniforme. LHS proporciona la flexibilidad para ajustar el tamaño de la muestra según las necesidades experimentales específicas. Además, destaca por su facilidad de generación, ofreciendo resultados eficientes en un período de tiempo razonable, lo que lo convierte en una opción práctica para diversas aplicaciones.

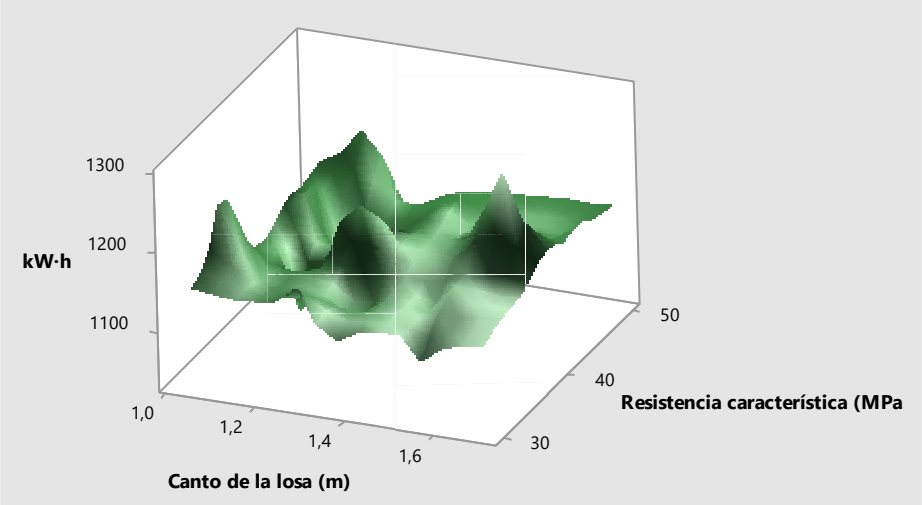

Figura 4. Ejemplo de superficie de respuesta

3.2. Redes neuronales

La ANN consiste en una red de nodos o neuronas y conexiones que es capaz de detectar relacionas complejas y no lineales entre las variables. Las neuronas pueden organizarse en diferentes capas. Las redes neuronales más simples constan de una capa de entrada, una capa oculta y una capa de salida. El modelo aprende de los elementos de entrada ajustando los pesos a través de un proceso iterativo en el cual las salidas del modelo se comparan con las salidas medidas y los errores se propagan hacia atrás. La red alimentada hacia adelante de múltiples capas está formada por una capa oculta de neuronas sigmoideas seguida por una capa de salida de neuronas lineales. Las neuronas de la capa oculta están conectadas a todas las neuronas en las capas de entrada y salida (ver Figura 5). El número de neuronas en las capas de entrada y salida corresponde con el número de parámetros de entrada y salida. Las entradas (x_i) se multiplican por pesos ($w_{i,j}$) y se combinan linealmente con un término independiente o sesgo (b_j). Cada neurona oculta sigue esta ecuación ($\sum x_i \cdot w_{i,j} + b_j$). Luego, cada neurona de la capa oculta produce una salida aplicando una función tangente sigmoide a la combinación lineal. La capa de salida sigue el mismo procedimiento, pero aplicando una función lineal.
Básicamente, este es el conocido y ampliamente utilizado modelo de Perceptrón Multicapa (MLP). Incluso con una sola capa oculta y con una amplia gama de funciones de activación, el MLP es un aproximador universal [27]. Además, existe un algoritmo básico de retropropagación [28] con muchas variantes y mejoras que permiten un uso efectivo de este modelo de ANN para muchos problemas prácticos de clasificación y regresión a partir de algunos datos de entrenamiento para los cuales se conoce su valor deseado u objetivo.

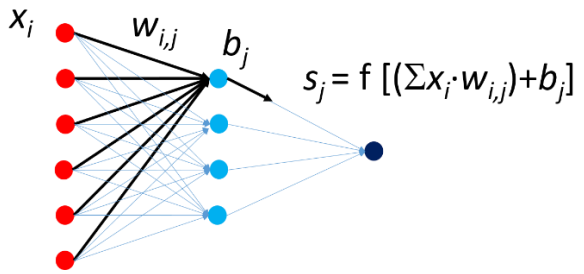

Figura 5. Ejemplo de red neuronal con una capa oculta

Se ha utilizado una red neuronal de propagación hacia delante (*feed-forward*), donde las conexiones van en un solo sentido, desde la capa de entrada hacia la capa de salida. El aprendizaje es supervisado, pues los datos (o entrada) tienen una respuesta conocida (o salida), con la cual se entrena la red.

Para evaluar si una red neuronal se ha sobreajustado, se divide el conjunto de datos en tres grupos distintos: los datos de entrenamiento, utilizados para ajustar los parámetros de la red y que deben ser representativos del conjunto completo; los datos de validación, empleados después de cada iteración durante el entrenamiento para detectar sobreaprendizaje; y finalmente, los datos de test, que se utilizan únicamente al finalizar el proceso de entrenamiento.

A partir de la división de datos en los grupos mencionados, se puede implementar una técnica para prevenir el sobreajuste conocida como "early stopping". Durante el proceso iterativo de optimización de los parámetros de la red, se compara el error obtenido tanto en los datos de entrenamiento como en los de validación. Si en iteraciones sucesivas el error en los datos de entrenamiento disminuye mientras que el error en los datos de validación aumenta, se detiene el proceso de ajuste como un criterio de parada adicional.

La red neuronal ha utilizado 42 datos, destinando un 34 de ellos para el entrenamiento, 4 de ellos para la validación y 4 para el test, todos ellos elegidos al azar. Se han empleado 5 neuronas en la capa oculta.

Después de entrenar una red neuronal, se puede evaluar su rendimiento al proporcionarle datos de entrada y observar los resultados obtenidos. Este procedimiento se denomina simulación, ya que los datos de entrada pueden ser aquellos utilizados durante el entrenamiento o pueden ser datos nuevos para los cuales se busca una predicción.

El primer paso implica comparar los datos de salida utilizados durante el entrenamiento con los datos generados por la red neuronal en la simulación. Este proceso se conoce como validación cruzada y facilita la representación gráfica de la precisión del ajuste de la red neuronal. En caso de un ajuste perfecto, la representación de estos valores coincidiría con la línea $y = x$. La validación cruzada se puede realizar para los datos de entrenamiento, validación, test o todos los datos, de modo que se puede comprobar si se ha producido sobreaprendizaje o no. En la Figura 6 se representa un ajuste de la red para el caso estudiado, con la validación cruzada de datos de entrenamiento, validación, test y total de datos. Se hace notar que cada vez que se ejecuta la red, se eligen de forma aleatoria los datos que sirven para la validación y, por tanto, los ajustes cambian cada vez.

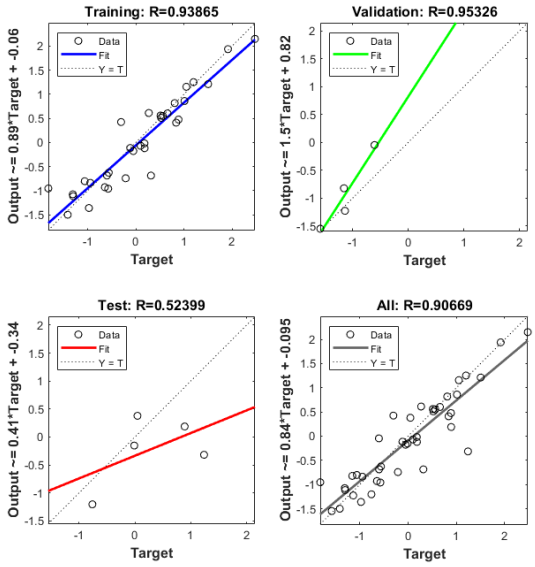

Figura 6. Validación cruzada de datos de entrenamiento, validación, test y total de datos

4. RESULTADOS Y DISCUSIÓN

Antes de aplicar los metamodelos, se pueden representar los datos observados en una superficie de respuesta para observar el aspecto abrusco que tiene la superficie de respuesta. Para ello se ha utilizado Minitab v17. En las Figuras 4 y 7 se han representado los 42 datos observados (Tabla 2), habiéndose representado como variable de respuesta el consumo energético. En la Figura 8 se ha representado la gráfica de contorno correspondiente a los datos observados. Se aprecian que existen diversos óptimos locales, por lo que es necesario usar modelos predictivos y de optimización para comprobar cuál es el mejor óptimo de este espacio de soluciones.

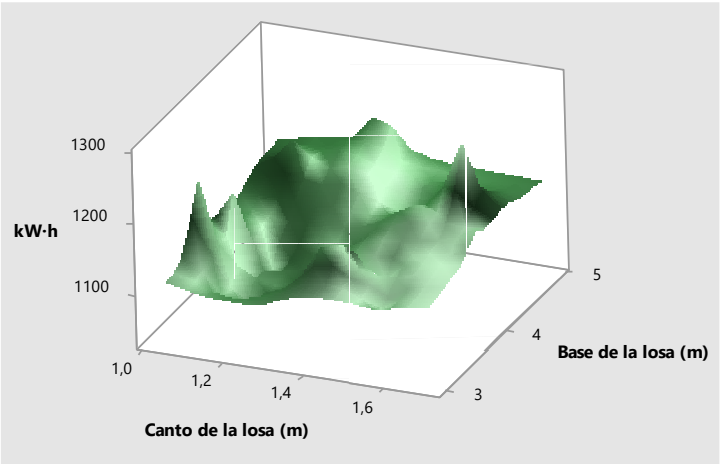

Figura 7. Superficie de respuesta de los 42 datos observados de la losa (Tabla 2)

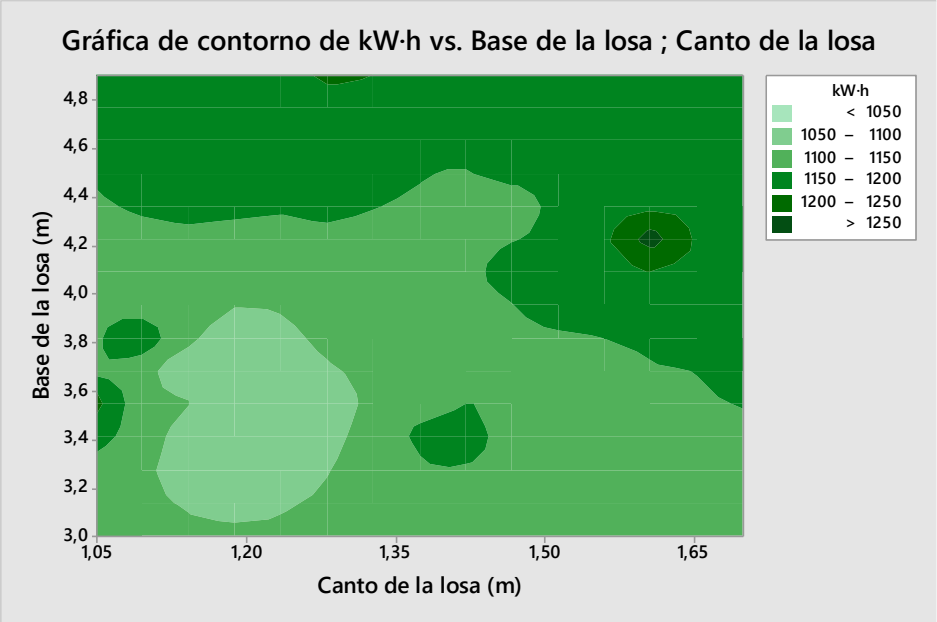

Figura 8. Gráfica de contorno de los 42 datos observados de la losa (Tabla 2)

En la Tabla 3 se indican los valores observados, los tres modelos Kriging empleados y el promedio de 16 ejecuciones de redes neuronales para los óptimos locales obtenidos en la fase de diversificación (puente #41) y de intensificación (puente #42) en la optimización de la superficie de respuesta. Se hace notar que los modelos predictivos Kriging son deterministas, mientras que las redes neuronales no lo son, pues cada vez que se ejecutan, se eligen de forma aleatoria los datos que se emplean para el aprendizaje y para la validación. Por tanto, se ha ejecutado la red neuronal un total de 16 veces, para estabilizar la desviación típica de los valores medios (que queda dividida por 4).
Se puede comprobar que los modelos predictivos ofrecen valores por encima de los valores observados. El modelo Kriging 3, que utiliza un polinomio de regresión de orden 2, es el que menor error proporciona. No obstante, el promedio de los valores predichos por 16 ejecuciones de una red neuronal, ofrece un error similar al modelo Kriging 2, que utiliza un polinomio de regresión de orden 1.

	#41	#42	Error absoluto #41	Error relativo #41	Error absoluto #42	Error relativo #42
Observado	1051,00	1038,28	0,00	0,00%	0,00	0,00%
Kriging 1	1130,68	1091,95	79,68	7,58%	53,67	5,17%
Kriging 2	1073,98	1085,84	22,98	2,19%	47,56	4,58%
Kriging 3	1060,58	1079,81	9,58	0,91%	41,53	4,00%
Promedio RNA	1073,06	1091,85	22,06	2,10%	53,57	5,16%

Tabla 3. Valor observado y predicción para los óptimos locales en fase de diversificación (#41) e intensificación (#42), así como sus errores absolutos y relativos.

Sin embargo, los errores medidos como error cuadrático medio (MSE) y la raíz del error cuadrático medio (RMSE), son menores para el caso de la red neuronal (Tabla 4). Los valores de los errores para el caso de los modelos Kriging se han obtenido para la predicción de los valores #31 a #42, mientras que en el caso de la red neuronal se han obtenido usando los 42 casos. Por tanto, esta supuesta ventaja de las redes neuronales no es homologable.

Modelos predictivos	MSE	RMSE
Kriging 1	2212,98	47,04
Kriging 2	3923,49	62,64
Kriging 3	4976,80	70,55
Promedio RNA	1037,22	30,95

Tabla 4. Errores MSE y RMSE de los modelos predictivos empleados

Se quiere comprobar a continuación hasta qué punto es capaz la red neuronal de detectar los valores óptimos. Para ello se ha representan en las Figuras 7-9 que siguen los valores medios de las predicciones ejecutadas.
En la Figura 9 se comprueba que la red neuronal predice bien donde se encuentra el valor mínimo del canto del tablero considerando una base de 3,70 m y un hormigón de 40 MPa de resistencia característica. Se observa un mínimo claro en un canto de 1,20 m, que es sensiblemente parecido al obtenido en el óptimo obtenido por Kriging.

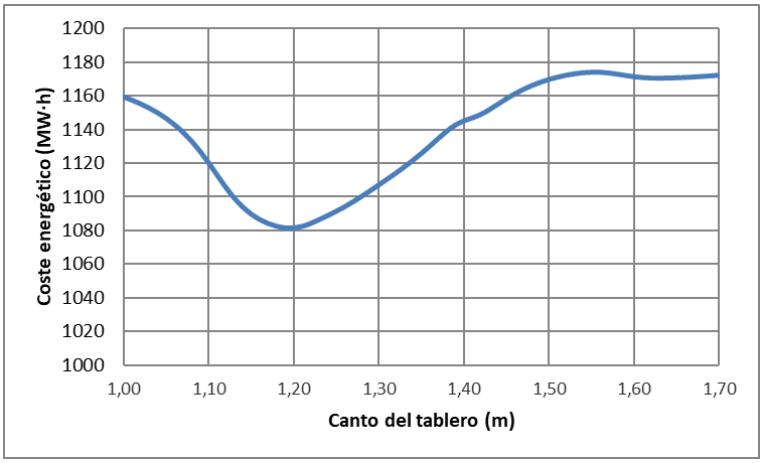

Figura 9. Predicción del coste energético con RNA en función del canto del tablero, considerando una base de 3,70 m y un hormigón de 40 MPa de resistencia característica

Si ahora se fija el canto en 1,20 m y la resistencia característica en 40 MPa, entonces la red neuronal indica (Figura 10) que el mínimo coste energético apenas varía entre una base comprendida entre 3,00 y 3,50 m, siendo 3,35 m el valor más bajo.

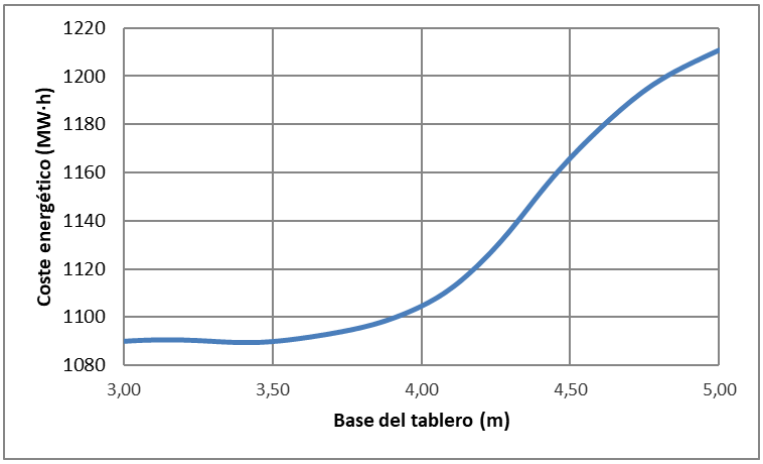

Figura 10. Predicción del coste energético con RNA en función de la base del tablero, considerando un canto de 1,20 m y un hormigón de 40 MPa de resistencia característica

Si se fija un canto de 1,20 m y una base de 3,35 m, entonces la red neuronal indica (Figura 11) que el valor de la resistencia característica que ofrece un menor coste energético es de 41 MPa, próximo a los 40 MPa, que es el valor estandarizado que se puede utilizar en la construcción de la estructura.

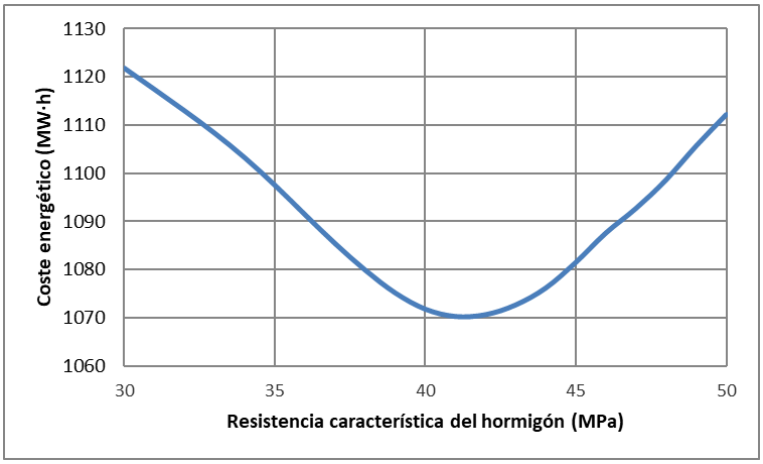

Figura 11. Predicción del coste energético con RNA en función de la resistencia característica del tablero, considerando un canto de 1,20 m y una base de 3,35 m

Los resultados obtenidos por la red neuronal son consistentes con las conclusiones obtenidas por el trabajo de Yepes-Bellver *et al*. [19], donde se analizaba el óptimo conseguido de la optimización de la superficie de respuesta originada por Kriging. En dicho trabajo se comprobó que para reducir las emisiones en un puente losa pretensado de tres vanos y una luz principal de 34 m, se recomienda una esbeltez en torno a 1/28, una cuantía de hormigón entre 0,55 y 0,60 m^3/m^2 de tablero, un cuantía de armadura pasiva entre 100 y 130 kg/m^3,

la cuantía de armadura activa debe rondar los 17 kg/m^2 de tablero, la resistencia característica del hormigón debe ser de 40 MPa, los aligeramientos interiores deben ser inferiores a 0,18 m^3/m^2 de tablero y los exteriores deben estar comprendidos entre 0,45 y 0,55 m^3/m^2 de tablero.

Por tanto, la red neuronal es capaz de situar dónde se encuentra el óptimo local, que es bastante parecido al valor encontrado tras la optimización de la superficie de respuesta del metamodelo Kriging. Sin embargo, la predicción de la energía no es suficientemente precisa, ni con los modelos Kriging ni tampoco con las redes neuronales. Es por ello que, si bien los metamodelos pueden determinar una superficie de respuesta, deberá optimizarse dicha superficie para llegar a determinar un mínimo local.

5. CONCLUSIONES

El artículo compara el rendimiento de Kriging y una red neuronal Perceptrón multicapa para la optimización energética en puentes de losas aligeradas pretensadas. Para ello se han empleado 42 soluciones de un paso superior de carretera real donde, para cada una de ellas, se ha evaluado el consumo energético necesario para su construcción. Se ha comprobado que la superficie de respuesta que evalúa el consumo energético es compleja y muy escarpada, con numerosos óptimos locales, lo cual muestra la complejidad del problema. Se ha verificado en este problema que tanto los modelos Kriging como las redes neuronales ofrecen predicciones por encima de los valores observados. El modelo Kriging que utiliza polinomios de orden 2, ofrece un error relativo del 4% en el óptimo local, inferior al de la red neuronal. Sin embargo, los errores cuadráticos medios y sus raíces (RMSE), son menores para el caso de la red neuronal. No obstante, y a diferencia de los modelos Kriging, que son deterministas, para estabilizar las respuestas de las redes neuronales, se deben ejecutar varias veces para determinar sus valores medios. Además, se ha verificado para este problema estructural que la red neuronal tiene la capacidad de identificar la ubicación del óptimo local, que guarda similitudes significativas con el valor obtenido tras optimizar la superficie de respuesta obtenida mediante Kriging. Con todo, tanto los modelos Kriging como las redes neuronales no logran predicciones precisas de la función objetivo, pero orientan sobre la zona del espacio de soluciones más prometedora. Por este motivo, aunque los metamodelos puedan establecer una superficie de respuesta, es necesario optimizar dicha superficie para alcanzar la determinación de un mínimo local.

AGRADECIMIENTOS

Grant PID2020-117056RB-I00 funded by MCIN/AEI/ 10.13039/501100011033 and by “ERDF A way of making Europe”.

REFERENCIAS

[1] IEA, UNEP, *Global Status Report: Towards a zero-emission, efficient and resilient buildings and construction sector*, International Energy Agency and the United Nations Environment Programme, (2018).

[2] T. Wang, I.S. Lee, A. Kendall, J. Harvey, E.B. Lee and C. Kim, "Life cycle energy consumption and GHG emission from pavement rehabilitation with different rolling resistance", *J. Clean. Prod.,* Vol. **33,** pp. 86-96, (2012).
[3] E. Wang and Z. Shen, "A hybrid Data Quality Indicator and statistical method for improving uncertainty analysis in LCA of complex system - application to the whole-building embodied energy analysis", *J. Clean. Prod.,* Vol. **43,** pp. 166-173, (2013).
[4] C. Maureira, H. Pinto, V. Yepes and J. García, "Towards an AEC-AI industry optimization algorithmic knowledge mapping", *IEEE Access,* Vol. **9**, pp. 110842-110879, (2021).
[5] D. Yeo and R.D. Gabbai, "Sustainable design of reinforced concrete structures through embodied energy optimization", *Energy Build.,* Vol. **43**, pp. 2028-2033, (2011).
[6] C.P. Quaglia, N. Yu, A.P. Thrall and S. Paolucci, "Balancing energy efficiency and structural performance through multi-objective shape optimization: case study of a rapidly deployable origami-inspired shelter. *Energy Build.,* Vol. **82**, pp. 733-745, (2014).
[7] D. Miller, J.H. Doh and J. Mulvey, "Concrete slab comparison and embodied energy optimisation for alternate design and construction techniques", *Constr. Build. Mater.,* Vol. **80**, pp. 329-338, (2015).
[8] P. Foraboschi, M. Mercanzin and D. Trabucco, "Sustainable structural desgin of tall buildings base don embodied energy", *Energy Build.,* Vol. **68**, pp. 254-269, (2014).
[9] V. Yepes, P. Villalba, J. Alcalá and F. González-Vidosa, *Energy consumption optimization design of prestressed concrete slab bridge decks, Proceedings of 4th Intenational Congress on Energy and Environment Engineering and Management*, Mérida (Spain), 2011, pp. 153.
[10] J. Alcalá, F. González-Vidosa, V. Yepes and J.V. Martí, "Embodied energy optimization of prestressed concrete slab bridge decks", *Technologies*, Vol. **6**, pp. 43, (2018).
[11] J.V. Martí, T. García-Segura and V. Yepes, "Structural design of prescast-prestressed concrete U-beam road bridges based on embodied energy", *J. Clean. Prod.,* Vol. **120**, pp. 231-240, (2016).
[12] V. Penadés-Plà, T. García-Segura and V. Yepes, "Accelerated optimization method for low-embodied energy concrete box-girder bridge design", *Eng. Struct*., Vol. **179**, 556-565, (2019).
[13] N. Cressie, "The origins of Kriging", *Math. Geol.*, Vol. **22**, pp. 239-252, (1990).
[14] J. Martínez-Frutos and P. Martí, "Diseño óptimo robusto utilizando modelos Kriging: Aplicación al diseño óptimo robusto de estructuras articuladas", *Rev. Int. Metod. Numer.,* Vol. **30**, pp. 97-105, (2014).
[15] A. Mathern, V. Penadés-Plà, J. Armesto Barros and V. Yepes, "Practical metamodel-assisted multi-objective design optimization for improved sustainability and buildability of wind turbine foundations", *Struct. Multidiscip. Optim.,* Vol. **65**, pp. 46, (2022).
[16] P. Martínez Fernández, I. Villalba Sanchis, R. Insa Franco and V. Yepes, "Slab track optimisation using metamodels to improve rail construction sustainability", *J. Constr. Eng. Manag.*, Vol. **148**, pp. 04022053, (2022).
[17] T. García-Segura, V. Penadés-Plà and V. Yepes, "Sustainable bridge design by metamodel-assisted multi-objective optimization and decision-making under uncertainty", *J. Clean. Prod*., 202, 904-915 (2018).
[18] L. Yepes-Bellver, A. Brun-Izquierdo, J. Alcalá and V. Yepes. "CO_2-Optimization of Post-Tensioned Concrete Slab-Bridge Decks Using Surrogate Modeling", *Materials*, Vol. **15**, pp. 4776, (2022).
[19] L. Yepes-Bellver, A. Brun-Izquierdo, J. Alcalá and V. Yepes. "Embodied Energy Optimization of Prestressed Concrete Road Flyovers by a Two-Phase Kriging Surrogate Model", *Materials*, Vol. **16**, pp. 6767, (2023).

[20] P.E. Mergos, "Surrogate-based optimum design of 3D reinforced concrete building frames to Eurocodes", *Dev. Built. Environ.*, Vol. **11**, pp. 100079, (2022).
[21] I. Negrín, M. Kripka and V. Yepes, "Metamodel-assisted meta-heuristic design optimization of reinforced concrete frame structures considering soil-structure interaction", *Eng. Struct.*, Vol. **293**, pp. 116657, (2023).
[22] I. Negrín, M. Kripka and V. Yepes, "Metamodel-assisted design optimization in the field of structural engineering: a literature review", *Struct.*, Vol. **52**, pp. 609-631, (2023).
[23] J.R. Martí-Vargas, F.J. Ferri and V. Yepes, "Prediction of the transfer length of prestressing strands with neural networks", *Comput. Concr.*, Vol. **12**, pp. 187-209, (2013).
[24] T. García-Segura, V. Yepes and D. Frangopol, "Multi-Objective Design of Post-Tensioned Concrete Road Bridges Using Artificial Neural Networks", *Struct. Multidiscipl. Optim*, 56(1), 139-150 (2017).
[25] N.S. Lophaven, H.B. Nielsen and J. Sondergaard, *MATLAB Kriging Toolbox DACE* (Design and Analysis of Computer Experiments) Version 2.0, (2002).
[26] M.D. McKay, R.J. Beckman and W.J. Conover, "A comparison of three methods for selecting values of input variables in the analysis of output from a computer code", *Technometrics*, Vol. **21**, pp. 239-245, (1979).
[27] K. Hornik, M. Stinchcombe and H. White, "Multilayer feedworward networks are universal approximator", *Neural Netw.*, Vol. **2**, pp. 359-366, (1989).
[28] D.E. Rumelhart, J.L. McClelland and the PDP Research Group, *Parallel distributed processin: explorations in the microstructure of cognition*, MIT Press, Cambridge, UK, Vol. 1: Foundations, (1986).

This page intentionally left blank

Congress on Numerical Methods in Engineering 2024
4-6 September 2024, University of Aveiro, Portugal

COMPUTATIONAL INVESTIGATION OF THE FLOW AND GEOMETRICAL CONFIGURATION OF AN INTERMEDIATE TEMPERATURE SOLID OXIDE FUEL CELL

João Paulo C. P. de Freitas, Ana Filipa Ferreira and Pedro J. Coelho

IDMEC, Mechanical Engineering Department, Instituto Superior Técnico, Universidade de Lisboa, 1049-001 Lisboa, Portugal
email: pedro.coelho@tecnico.ulisboa.pt

Keywords: Solid oxide fuel cell, Computational fluid dynamics, Parametric Study

Abstract *Fuel cells are devices that convert directly chemical energy into electrical energy by means of electrochemical reactions. Over the last two decades, numerical simulations have been used as a cost-effective way of studying configurations and working parameters of fuel cells. The numerical simulation of a fuel cell is a challenging task, due to the multiple physical phenomena taking place in different cell components. Among the most studied ones is the intermediate temperature solid oxide fuel cell. Intermediate temperature functioning (500-700ºC) is a recurring research theme among the solid oxide fuel cell scientific literature due to benefits such as faster start-up and shutdown times and reduced thermal stresses, leading to material cost savings and selection flexibility, along with longer lifetimes. Despite lower efficiencies, intermediate temperatures permit solid oxide types to be used in applications requiring more flexibility, such as in auxiliary automobile power units. To study the flow behaviour, computational fluid dynamics is employed in this work using the ANSYS Fluent unresolved electrolyte module. A structured mesh is built, the mesh independence is verified, and the model is validated using published data for the voltage as a function of the current density. Different geometrical and flow configurations are studied to investigate the effect on the maximum temperature and efficiency of the fuel cell. The temperature, species concentration and current density field allow explaining the reasons behind the observed macro changes and the overall performance of the fuel cell.*

1. INTRODUCTION

The world is facing a major change in the energy sector dictated by the depletion of fossil fuels and the need to shift to clean energy technologies in order to mitigate greenhouse gas emissions and global warming. Among these clean technologies, the fuel cells are gaining popularity in the research and industrial fields [1, 2], with governments pushing for hydrogen-powered projects and industrial players looking for solutions that appeal to consumers and investors, and

which satisfy increasingly strict emission regulations. Although fuel cells were developed almost two centuries ago, only in the last few decades they have been the subject of active research from the scientific community and interest from the industry. This is due to several advantages over other power sources, namely the low or zero emissions, high efficiency, versatility, reliability, and scalability.

The main objective of a fuel cell is to convert the chemical energy stored in a fuel into electrical energy. There are several types of fuel cells, the most common ones being the proton exchange membrane fuel cells (PEMFC), which are widely used for mobile applications, and the solid oxide fuel cells (SOFC), which are the most common and efficient ones for stationary applications and operate at much higher temperatures compared to other fuel cells, ranging from 600 to 1000ºC [3]. These temperatures generally increase the catalytic properties of materials and consequently the reaction rates, approaching the optimum ionic conductivity for electrochemical reaction and increasing the efficiency. An advantage of the SOFC is that the high temperature excess heat from exhaust gases can be used in regeneration and hybrid power production cycles, improving further the overall efficiency of the system. Another advantage, due to the high temperatures and a solid electrolyte, is the reduced probability of corrosion. However, the high operating temperature of the SOFC requires relatively expensive materials to withstand the thermal stresses, as opposed to other fuel cells, such as the PEMFC.

A SOFC comprises a pair of electrodes (anode and cathode), designed for facilitating gas diffusion and ion transport. These electrodes are separated by a solid electrolyte, creating a distinct boundary for the electrochemical reactions to occur. The assembly is further supported by a pair of current collectors, positioned on each side of the electrodes, which form the pathway for the flow of fuel and oxidant gases and act as conduits for the transport of electrons. The fuel may be H_2, either pure or diluted with water vapour or impurities, synthetic gas, biogas or a hydrocarbon (e.g., CH_4). The oxidant is either air or oxygen. Figure 1 shows a schematic of a planar SOFC.

The incoming air travels along the air channel and diffuses across the cathode, which is made of a porous material. The oxygen reaches the triple-phase boundary (TPB), in the near vicinity of the cathode-electrolyte interface, where a catalyst accelerates the electrochemical reduction of oxygen according to the following reaction:

$$\frac{1}{2}\mathrm{O}_2 + 2e^- \rightarrow \mathrm{O}^{2-} \tag{1}$$

The oxygen ions are then conducted across the electrolyte to the anode side. Meanwhile, the incoming fuel gas travels along the fuel channel and diffuses across the anode, which is also made of a porous material. The fuel (hydrogen in the present work) reaches the active TPB at the anode-electrolyte interface where it reacts and oxidizes with the oxygen ions, according to reaction (2):

$$\mathrm{H}_2 + \mathrm{O}^{2-} \rightarrow \mathrm{H}_2\mathrm{O} + 2e^- \tag{2}$$

The overall reaction is written as:

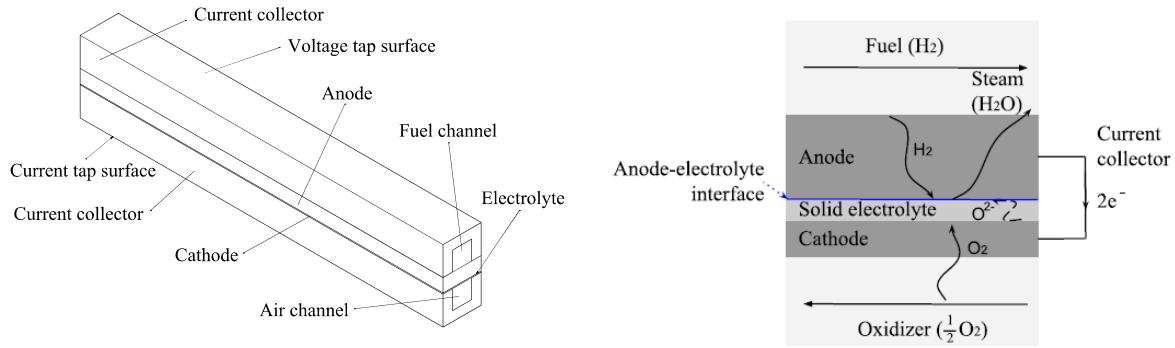

Figure 1. Schematic of a solid oxide fuel cell.

$$H_2 + \frac{1}{2}O_2 \rightarrow H_2O \tag{3}$$

The electrons released in reaction (2) travel across the anode to the current collector, then through an external circuit to a load, and back to the cathode current collector and across the cathode, closing the circuit.

The electrolyte and the electrodes should have high ionic conductivity at high temperatures to facilitate ionic movement. The electrodes should be good electrical conductors to allow for the electrons to travel to the current collector. The electrolyte must be non-porous and impermeable to prevent gas crossover between the electrodes. Ideally, the electrolyte serves as a pure ionic conductor, devoid of any electronic conductivity, thus safeguarding against short-circuiting within the cell.

This work is concerned with the numerical simulation of a SOFC. The influence of the flow configuration and geometrical parameters on the performance of the fuel cell is investigated. The main goal is to enhance the power output while minimizing the temperature gradients created when the fuel cell components have different thermal expansion coefficients. These gradients increase the thermal stresses and the probability of internal fracture.

2. MATHEMATICAL MODEL

The mathematical model relies on the following assumptions: the fuel cell operates under steady-state conditions, the flow is incompressible, laminar and fully developed at the channels' inlet, the electrodes and the electrolyte are homogeneous and isotropic, the chemical species behave as ideal gases, the buoyancy is negligible, and there is no leakage of gas or electrons. The viscous dissipation, Dufour and Soret effects, heat flux due to mass diffusion and thermal radiation are also neglected.

2.1. Governing equations

The governing equations for mass, momentum, energy, and species mass fractions in the gas channels may be written as follows:

$$\nabla \cdot (\rho \mathbf{u}) = 0 \tag{4}$$

$$\rho \mathbf{u} \cdot \nabla \mathbf{u} = -\nabla p + \nabla \cdot \left[\mu \left[\nabla \mathbf{u} + (\nabla \mathbf{u})^T \right] - \frac{2}{3} \mu (\nabla \cdot \mathbf{u}) \mathbf{I} \right] \tag{5}$$

$$\rho c_p \mathbf{u} \cdot \nabla T = \nabla \cdot (\lambda \nabla T) \tag{6}$$

$$\rho \mathbf{u} \cdot \nabla y_i = \nabla \cdot (\rho D_i \nabla y_i) \tag{7}$$

where $\mathbf{u}$ is the velocity vector, p the pressure, T the temperature, y_i the mass fraction of species i, ρ the density, μ the dynamic viscosity, c_p the specific heat capacity, λ the thermal conductivity, D_i the effective diffusion coefficient of species i, and $\mathbf{I}$ the unit tensor. In Eq. (7) it is assumed that the mass diffusion is governed by Fick's law and that there are no chemical reactions in the channels.

The electrodes are made of porous material, allowing for electrons and ions transport. Mass conservation is expressed by Eq. (8):

$$\nabla \cdot (\rho_f \phi \mathbf{u}_f) = 0 \tag{8}$$

where the subscript f has been included to make clear that the density and the velocity refer to the fluid phase, i. e., $\mathbf{u}_f$ denotes the intrinsic average velocity over the fluid phase in a representative elementary volume. The porosity, ϕ, is defined as the fraction of the total volume of the porous medium occupied by void space. The product $\phi_f \mathbf{u}_f$ represents the Darcy velocity, i.e., the average velocity over the total volume in a representative elementary volume.

The momentum equation may be written as [4]:

$$\begin{aligned} \rho_f \phi \mathbf{u}_f \cdot \nabla \mathbf{u}_f = & -\nabla(\phi p) + \nabla \cdot \left[\mu \left[\nabla(\phi \mathbf{u}_f) + (\nabla(\phi \mathbf{u}_f))^T \right] - \frac{2}{3} \mu \left(\nabla \cdot \left(\phi \mathbf{u}_f \right) \right) \mathbf{I} \right] \\ & - \phi^2 \frac{\mu}{K} \mathbf{u}_f - \phi^3 \frac{c_F \rho_f \mu}{\sqrt{K}} |\mathbf{u}_f| \mathbf{u}_f \end{aligned} \tag{9}$$

where K is the permeability of the medium and c_F is a dimensionless form-drag constant. The last but one term on the right-hand side accounts for the Darcy drag force and the last one represents the modification of the Darcy's model introduced by Forchheimer. The convective and diffusive terms are often negligible in porous media flows, particularly when the Reynolds number is small, as in the case of fuel cells. In such a case, the term on the left-hand side and the second term (term into square brackets) on the right-hand side vanish and the Forchheimer's equation is obtained. If, in addition, the Reynolds number of the flow based on the typical pore size is equal to unity or lower, than the last term of Eq. (9) is also negligible and the Darcy's equation is obtained.

Zheng *et al*. [5] showed that the local thermal equilibrium assumption is valid for fuel cells. Therefore, the energy conservation equation may be written as follows [4]:

$$\rho_f \, c_{p,f} \, \phi \mathbf{u}_f \cdot \nabla T = \nabla \cdot \left(k_m \nabla T \right) + S_q \tag{10}$$

where the effective thermal conductivity of the medium, k_m, is evaluated as:

$$k_m = (1-\phi) k_s + \phi k_f \tag{11}$$

The subscripts *s* and *f* denote the solid and fluid phases, respectively. The electrochemical reactions (1) and (2) take place in a thin layer, referred to as triple-phase boundary, in the vicinity of the interfaces of the electrolyte with the cathode and the anode, respectively. In fact, the electrical conductivity of the electrodes is much higher than the ionic conductivity. Here, it is assumed that those reactions are confined to the interfaces between the electrodes and the electrolyte. In this case, the source term of the energy equation is only due to the ohmic resistance, which leads to the Joule heating effect:

$$S_q = \sigma_{el} \nabla \phi_{el} \cdot \nabla \phi_{el} \tag{12}$$

where σ_{el} is the electrical conductivity and ϕ_{el} is the electric potential.
The equation of mass conservation for species *i*, assuming again Fickian diffusion, is written as follows [4]:

$$\phi \rho_f \, \mathbf{u}_f \cdot \nabla y_i = \nabla \cdot \left(\rho D_m \nabla y_i \right) \tag{13}$$

where $D_m = \phi D / \tau$ is the mass diffusivity of the porous medium, D is the binary diffusion coefficient for a two-component mixture and τ is the tortuosity.
The unresolved electrolyte modelling approximation is used in this work. This means that the electrolyte and the triple phase boundary are not included in the computational domain. The effect of the electrochemical reactions on the mass and energy transport is taken into account either through the boundary conditions of these equations at the electrode-electrolyte interface or via mass and energy source/sink terms added to the mass species and energy conservation equations, respectively, at the control volumes adjacent to the electrolyte. According to this approximation, the equation of conservation of electrical charge in the electrodes is written as:

$$\nabla \cdot \mathbf{J} = 0 \tag{14}$$

where **J** is the current density vector, which is related to the electrical potential by means of Ohm's law:

$$\mathbf{J} = -\sigma_{el} \nabla \phi_{el} \tag{15}$$

$$\nabla^2 \phi_{el} = 0 \tag{16}$$

In the current collectors, also referred to as interconnects, the conservation equations for energy and electrical charge are solved. They may be written according to Eq. (10), with ϕ=0, and Eq. (16), respectively.

2.2. Boundary and interface conditions

The fluid velocity, the temperature and the gas composition (mass fraction of the species) are prescribed at the inlet boundary of the gas channels. At the outlet of the gas channels, the pressure is set to atmospheric, and the temperature and species mass fraction gradients are set to zero. The boundary of the gas channels coincident with the solid surface of the current collector is assumed to be adiabatic, no-slip velocity is prescribed, and the mass flux is zero.

At the outer surfaces of the electrodes and current collectors, the velocity and the fluxes of mass, heat and electrical current are equal to zero, except at the outer surfaces that are in contact with the external electric circuit. At these outer contact boundaries, the voltage is set to zero on the anode side and to the prescribed cell voltage on the cathode side.

At the interface between the gas channels and the porous electrodes, there is continuity of mass and energy fluxes, and there is no flux of electrons or ions. The velocity is continuous across the interface, i.e., the normal velocity component on the gas channel side is equal to the Darcy velocity normal to the interface on the electrode side.

At the interface between an electrode and the current collector, there is no gas species flux nor ion flux, and the heat flux and electrical current are continuous.

The no-slip boundary condition is used for the momentum equation in the electrodes at the interfaces between the electrodes and the electrolyte. At these interfaces, the boundary condition for the equation of conservation of electrical charge is given by the Butler-Volmer equation [6]:

$$\mathbf{J}\cdot\mathbf{n} = \pm J_{\mathrm{o}}\left[\exp\left(\frac{\alpha_1 n F \eta_{act}}{RT}\right)\right] - \exp\left(\frac{-\alpha_2 n F \eta_{act}}{RT}\right) \tag{17}$$

where the positive sign is applied to the cathode and the negative one to the anode. In this equation, **n** is the outer unit vector normal to the boundary, J_{o} is the exchange current density, α_1 and α_2 are the anodic and cathodic transfer coefficients, respectively, of the electrode under consideration, n the number of electrons transferred in the electrochemical reaction, F the Faraday constant, which is defined as the electrical charge of a mole of electrons, R the ideal gas constant, T the temperature and η_{act} the activation overpotential. The latter is also referred to as activation loss or activation polarization, and corresponds to the energy required for the electrochemical reactions to proceed at the electrodes. It is assumed here that the sum of the transfer coefficients of the anode and cathode is equal to unity. The activation energy is related to the cell voltage, V, as follows [6]:

$$V = E_o - \eta_{act} - \eta_{ohm} - \eta_{con} \tag{18}$$

where E_{o} is the theoretical open circuit voltage, η_{ohm} the ohmic overpotential and η_{con} the concentration overpotential. The theoretical open circuit voltage is given by the Nernst equation [6]:

$$E_o = -\frac{\Delta G^o}{n\,F} - \frac{RT}{nF}\ln\left(\frac{p_{H_2O}/p_{ref}}{\left(p_{H_2}/p_{ref}\right)\sqrt{\left(p_{O_2}/p_{ref}\right)}}\right) \tag{19}$$

where ΔG^o denotes the variation of the free Gibbs energy of reaction (3) at standard state conditions (25ºC and 1 atm), p_i is the partial pressure of species i, and p_{ref} the reference pressure. The factor n that appears in the denominator of both terms on the right-hand side of Eq. (19) is the number of moles of electrons exchanged in reaction (3) per mole of hydrogen. The first term on the right-hand side of Eq. (19) is the theoretical open circuit voltage at standard state conditions.

The exchange current density for the anode and cathode are given by [6]:

$$J_{o,anode} = \gamma_{anode}\left(\frac{p_{H_2}}{p_{ref}}\right)\left(\frac{p_{H_2O}}{p_{ref}}\right)\exp\left(-\frac{E_{act,anode}}{RT}\right) \tag{20}$$

$$J_{o,cathode} = \gamma_{cathode}\left(\frac{p_{O_2}}{p_{ref}}\right)^{0.25}\exp\left(-\frac{E_{act,cathode}}{RT}\right) \tag{21}$$

where γ_{anode} and $\gamma_{cathode}$ are the pre-exponential coefficients and E_{act} is the activation energy of the electrochemical reaction.

The activation overpotential can be determined from Eq. (17). The Ohmic overpotential, which is due to the resistance to the transport of ions through the electrolyte and the transport of electrons through the electrodes and current collectors, is given by:

$$\eta_{ohm} = J\,R_{AS} \tag{22}$$

where J is the current density and R_{AS} the total area specific resistance, which may be calculated by the sum of the ratios of the thickness to the electrical conductivity for the anode, cathode and electrolyte (see [7] for details). The concentration overpotential is given by [3]

$$\eta_{con} = \frac{RT}{nF}\ln\left(\frac{J_L}{J_L - J}\right) \tag{23}$$

where J_L is the limiting current density.

At the interface between the anode and the electrolyte, the boundary condition for the energy equation is given by [6]:

$$\left(\mathbf{q}\cdot\mathbf{n}\right)_{anode-electolyte} = -\frac{J}{nF}\;T\Delta S_{\mathrm{H_2O}} - J\,\eta_{act} \tag{24}$$

A similar equation may be written for the interface between the cathode and the electrolyte:

$$\left(\mathbf{q}\cdot\mathbf{n}\right)_{cathode-electrolyte} = -\frac{J}{2nF}\;T\Delta S_{\mathrm{O_2}} - J\,\eta_{act} \tag{25}$$

where **q** denotes the heat flux vector and ΔS represents the change of entropy associated with reaction (2) for the anode, and reaction (1) for the cathode. The minus sign is due to the orientation of the normal, which points into the electrolyte, so that the term on the left-hand side of the equations is negative, i.e., there is a source of energy at the interface due to electrochemical reactions at the triple phase boundary (first term of the right-hand side of the equations) and to the activation overpotential (last term on the right-hand side of the equations). The factor 2 in the denominator of Eq. (25) is due to the factor ½ in reaction (1).

The boundary condition of the transport equations for the species mass fractions at the interface between the anode and the electrolyte are [6]:

$$\left(\dot{\mathbf{m}}_{\mathrm{H}_2} \cdot \mathbf{n}\right)_{anode-electolyte} = \frac{\mathbf{J}\cdot\mathbf{n}}{nF} M_{\mathrm{H}_2} \tag{26}$$

$$\left(\dot{\mathbf{m}}_{\mathrm{H}_2\mathrm{O}} \cdot \mathbf{n}\right)_{anode-electolyte} = -\frac{\mathbf{J}\cdot\mathbf{n}}{2nF} M_{\mathrm{H}_2\mathrm{O}} \tag{27}$$

Similarly, at the interface between the cathode and the electrolyte, the boundary condition is given by:

$$\left(\dot{\mathbf{m}}_{\mathrm{O}_2} \cdot \mathbf{n}\right)_{cathode-electolyte} = -\frac{\mathbf{J}\cdot\mathbf{n}}{2nF} M_{\mathrm{O}_2} \tag{28}$$

In these equations, $\dot{\mathbf{m}}_i$ denotes the mass flux of species *i*. At the triple face boundary on the anode side, **J**.**n** > 0 (the current flux is opposite to that of the electrons flux). Therefore, noting that the normal unit vector points to the outer side of the electrode under consideration, the electrochemical reaction (2) yields a sink of hydrogen and a source of water vapour to the anode. At the triple face boundary on the cathode side, **J**.**n** < 0. Therefore, the electrochemical reaction (1) yields a sink of oxygen.

3. VALIDATION

All simulations were performed using the Ansys Fluent software and rely on the SOFC with unresolved electrolyte model. This implies that the electrolyte is modelled as a surface rather than a volume. The voltage jump across the electrolyte, oxygen ion transport, and heat dissipation within the electrolyte are accounted for through the boundary conditions at the interfaces between the electrolyte and the electrodes.

Preliminary calculations were performed for the SOFC numerically investigated by Yakabe *et al*. [8]. The size of the gas channels is 100 mm in length, 1 mm in height and 2 mm in width. The current collectors have a width of 4 mm and a height of 2 mm. The anode, electrolyte and cathode are 0.15, 0.1 and 0.1 mm thick, respectively. The input data were defined according to Pulagam [9], who simulated this fuel cell using COMSOL. Figure 2 shows the present predictions of the voltage as a function of the current density. The results

are close to those computed by Yakabe *et al.* [8] using the STAR-CD software.
The calculations reported in the remainder of this paper were obtained for the planar anode-supported SOFC experimentally investigated by Keegan *et al.* [10]. The fuel is humidified hydrogen (97% H_2 and 3% H_2O on a molar basis) and the oxidizer is air. The geometrical dimensions of the fuel cell are given in Table 1, the thermophysical properties of the materials are provided in Table 2, and the operating conditions and other input data are listed in Table 3. A mesh with about 270,000 control volumes was selected to compute the results presented in this work. Additional calculations performed using meshes with about 97,000 and 816,000 control volumes were performed, the former being too coarse and the latter yielding results similar to those of the selected mesh. The grid convergence index [11] approach for mesh refinement studies was used, yielding an order of convergence of 0.81, and a discrepancy between the extrapolated open circuit voltage (OCV) and the OCV computed for the mesh with 270,000 control volumes of 1.04%.
The polarization curve of the present simulations is shown in Fig. 3, along with the experimental data [10], and the predictions of two other references [12, 13].

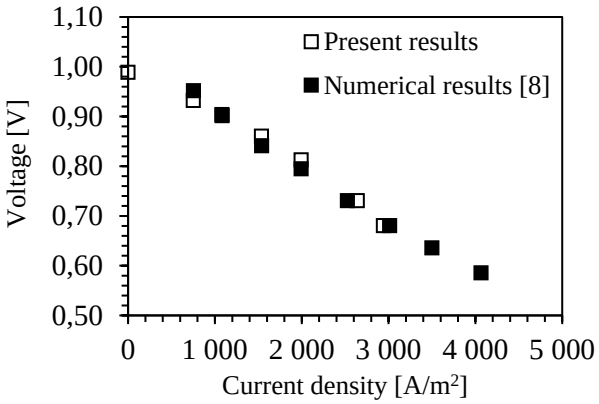

Figure 2. Voltage as a function of the current density for the SOFC modelled by Yakabe *et al.* [8].

Geometrical quantity	Value
Cell length	19 mm
Cell width	2.0 mm
Gas channels height	1.0 mm
Gas channels width	1.0 mm
Cathode thickness	0.05 mm
Anode thickness	0.70 mm
Electrolyte thickness	0.01 mm
Current collector height	1.5 mm

Table 1. Geometric dimensions of the SOFC.

Thermophysical property	Value
Anode density	4,200 kg/m^3
Anode specific heat	377 J/kg.K
Anode thermal conductivity	11 W/m.K
Cathode density	6,350 kg/m^3
Cathode specific heat	377 J/kg.K
Cathode thermal conductivity	2.37 W/m.K
Current collector density	4,640 kg/m^3
Current collector specific heat	300 J/kg.K
Current collector thermal conductivity	2.2 W/m.K
Electrolyte density	6.010 kg/m^3
Electrolyte specific heat	2,000 J/kg.K
Electrolyte thermal conductivity	2.7 W/m.K

Table 2. Thermophysical properties [12, 13].

Quantity	Value
Fuel inlet mass flow rate	1.14×10^{-8} kg/s
Air inlet mass flow rate	2.29×10^{-7} kg/s
Fuel inlet temperature	1023 K
Air inlet temperature	1023 K
Anode reference exchange current density	5630 A/m^2
Cathode reference exchange current density	2320 A/m^2
Anode pre-exponential coefficient	7.55×10^{9} Ω^{-1}m^{-2}
Cathode pre-exponential coefficient	9.61×10^{8} Ω^{-1}m^{-2}
Anode activation energy	120 kJ/mol
Cathode activation energy	110 kJ/mol
Anode reaction – anodic transfer coefficient	2.0
Anode reaction – cathodic transfer coefficient	1.0
Cathode reaction – anodic transfer coefficient	1.4
Cathode reaction – cathodic transfer coefficient	0.6
Anode tortuosity	8.5
Cathode tortuosity	2.5
Anode porosity	0.3
Cathode porosity	0.3
Anode electrical conductivity	28,586 Ω^{-1}m^{-1}
Cathode electrical conductivity	12,098 Ω^{-1}m^{-1}
Electrolyte electrical conductivity	1.416 Ω^{-1}m^{-1}
Current collectors electrical conductivity	4×10^{6} Ω^{-1}m^{-1}

Table 3. Operating conditions and input data [12,13].

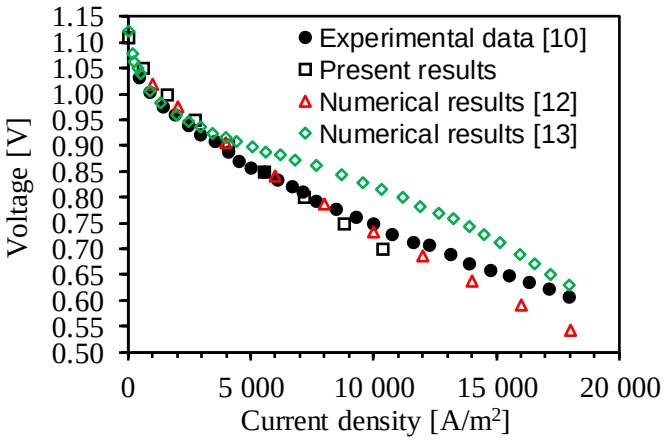

Figure 3. Voltage as a function of the current density for the SOFC experimentally investigated by Keegan *et al*. [10].

The present predictions are very close to those of Barzi *et al*. [12]. Both of them are in good agreement with the experimental data for voltages greater than about 0.75 V and underestimate the current density at lower voltages. The numerical results of Chaisantikulwat *et al*. [13] are very accurate for low current densities but significantly overestimate the current density for voltages lower than 0.9 V. Keegan *et al*. [10] found that there was leakage of oxygen into the anode in the experiments, and so the measured open circuit voltage was about 0.06 V lower than that predicted from the Nernst equation. Since the leakage was not accounted for in the present mathematical model, the open circuit voltage is overpredicted by about that value. The same behaviour is visible in the numerical results of Chaisantikulwat *et al*. [13], while Barzi *et al*. [12] did not present results for the open circuit voltage.

The predicted temperature and species mass fraction fields are displayed in Fig. 4. The current collectors are not shown to allow a better visualization of the temperature and species concentration fields in the gas channels. The flow configuration is of the counterflow type. Hydrogen is introduced through the left side of the top channel and air through the right side of the bottom channel. The results show an increase of the temperature from the left to the right side of the fuel cell, by more than 200ºC, as a result of the electrochemical reactions, and the production of steam along with the consumption of hydrogen and oxygen along the streamwise direction.

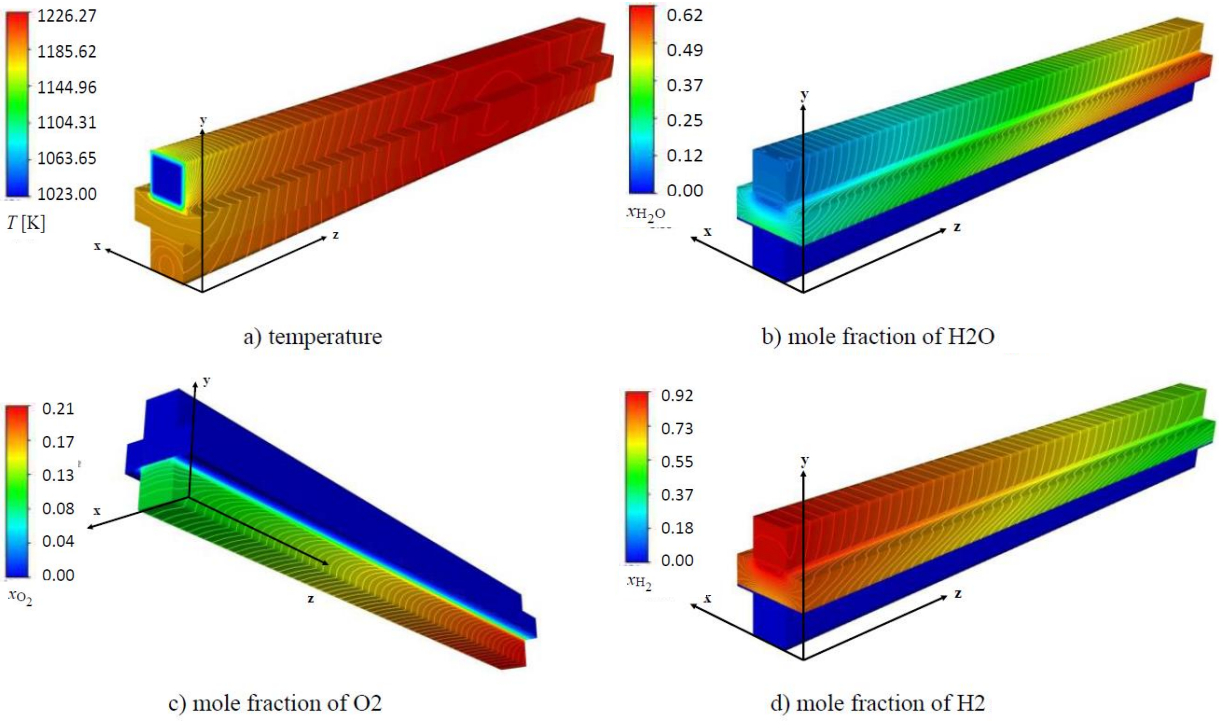

Figure 4. Predicted temperature and species mass fractions for the SOFC experimentally investigated by Keegan *et al*. [10].

4. PARAMETRIC STUDY

4.1. Flow configuration

The counterflow configuration used in the experiments of Keegan *et al*. [10] is compared here with a coflow arrangement, maintaining the geometry, the boundary conditions and all the other parameters unchanged.

The polarization curves shown in Fig. 5 are very similar for both flow configurations. However, as the current increases, subtle deviations between them become apparent. At 0.7 V, which will be considered the standard operating voltage from now on, the counterflow arrangement leads to a 3% increase in the peak power density compared with the coflow configuration, from 7,048 W/m^2 to 7,264 W/m^2.

The overall efficiency and fuel conversion increase with the power density (see Fig. 5). The overall efficiency, defined as the ratio of the electrical energy output generated by the fuel cell to the chemical energy input provided by the fuel and oxidant, increases linearly, at least in the range of voltages under investigation. The counterflow configuration has an overall efficiency of 20%, which is about 1% higher than that of the coflow configuration for 0.7 V. The fuel usage efficiency, defined as the ratio of the electrical energy output produced by the fuel cell to the chemical energy content of the fuel consumed by the cell, differs by a higher amount (about 3%) in the two flow configurations. The higher overall efficiency of the counterflow over the coflow configuration is due to both a higher fuel usage efficiency and a higher current density at the standard operating conditions. However, the counterflow and coflow efficiencies only differ as power density increases above ~5 kW/m^2, since the efficiency curves overlap at low current densities.

The maximum and average temperatures increase with the power density, as also shown in Fig. 5. The maximum temperature is about 1% lower for the counterflow (1226 K) than for the coflow configuration (1239 K), particularly at high power. The average temperature of both cells is roughly the same at around 1,213 K. This corresponds to an increase of 190ºC relative to the initial temperature of the gases, which is due to the heat generated in the electrochemical reactions and to the ohmic heating. The ratio of the difference between the maximum and the minimum cell temperatures to the maximum power density provides a measure of how the cell power performance relates to the temperature change. In this case, the maximum temperature increase, per unit of power density increase, is lower for the counterflow design (27.9 vs. 30.6 K/kW/m2). This suggests a higher efficiency in managing heat by the counterflow configuration as opposed to the coflow one. The results in Fig. 5 further reveal that although higher temperatures favour the performance by improving the reaction rates, higher temperatures may not yield higher peak power and efficiency, but depend on where the highest temperatures occur.

The better fuel conversion of a counterflow arrangement can be seen in Figs. 6 and 7. In that arrangement, the molar fraction of H_2 decreases by a greater amount in the streamwise direction and the steam production occurs further downstream of the fuel inlet, in comparison with the coflow configuration. This is explained by the fact that the oxidant flows in a direction opposite to the fuel flow direction, thus the electrochemical reaction rates are higher further away from

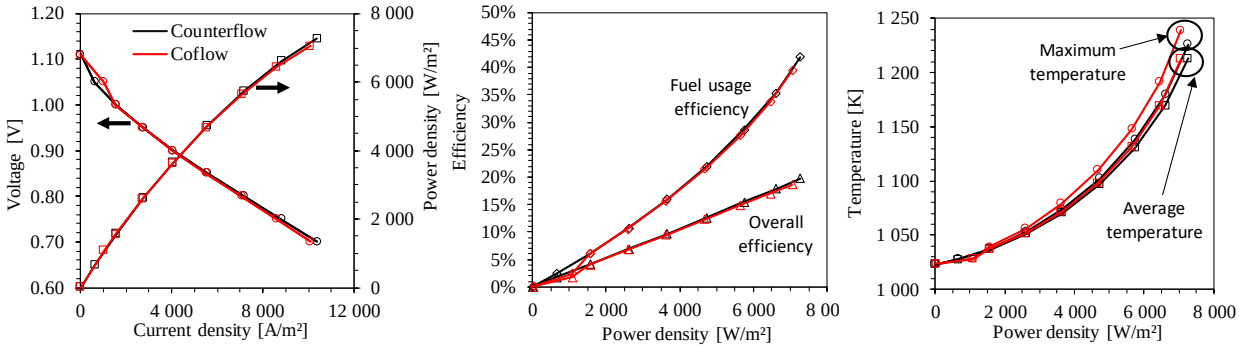

Figure 5. Comparison of polarization and power density, fuel usage and overall efficiencies, maximum and average temperatures for counterflow and coflow configurations.

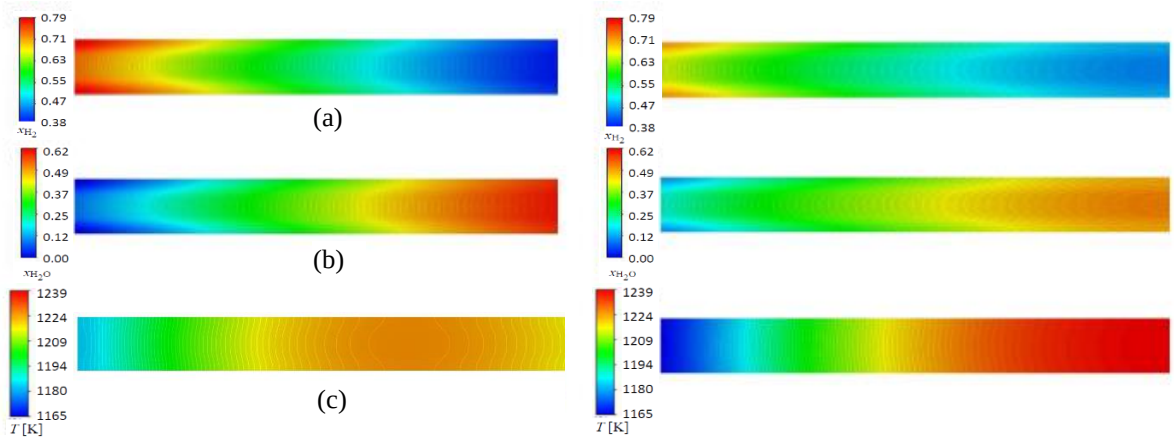

Figure 6. Temperature and mole fraction contours at a horizontal plane through the electrolyte for counterflow (left) and coflow (right) configurations. (a) H_2 mole fraction; (b) H_2O mole fraction; (c) Temperature.

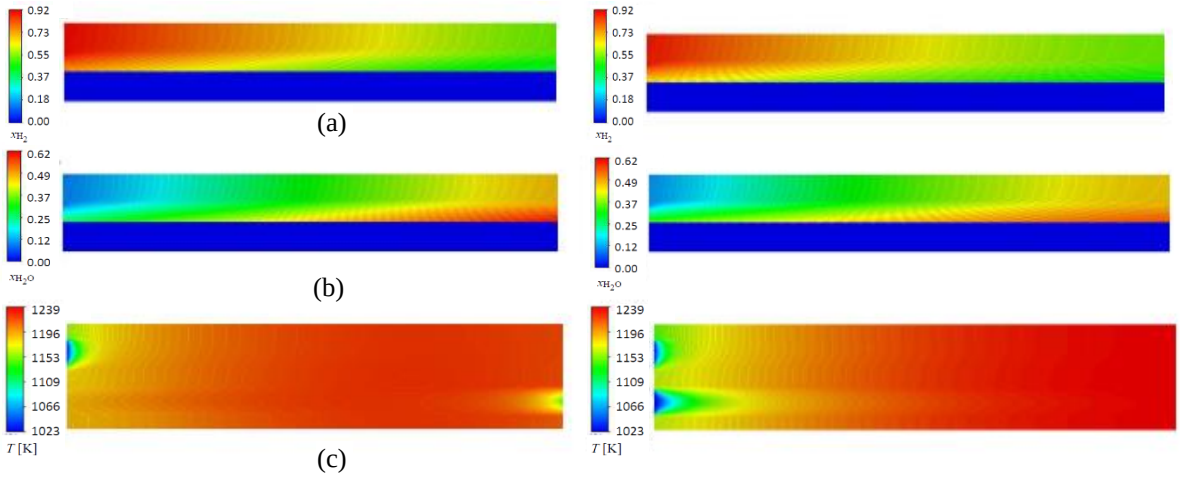

Figure 7. Temperature and mole fraction contours at a longitudinal, vertical symmetry plane for counterflow (left) and coflow (right) configurations. (a) H_2 mole fraction; (b) H_2O mole fraction; (c) Temperature.

the fuel inlet. In the counterflow case, the relative difference between the inlet and outlet fuel molar fractions is about 52%, while in the case of coflow is about 37%.

In coflow, the temperature increases continuously from the channel inlets and along the streamwise direction, due to the electrochemical reaction and the heat exchange between the fluids taking place along the fuel cell. The higher mass flow rate of the oxidant (about one order of magnitude) allows more heat to be removed, thus the temperature in the air channel and cathode is, overall, lower than in the fuel channel and anode. Additionally, the coflow yields a minimum temperature near the inlets, where both reacting species begin diffusing through the electrodes and thus the temperatures at the TPB are relatively low, hindering the electrochemical reaction activity, which reduces the performance. Counterflow is an efficient solution to this limitation because the peak of the electrochemical reaction occurs away from both inlets, at a point where the temperature of both fluids increased due to the heat generated by the reactions along the cell, providing a combination of temperature and species diffusion that maximizes the rate of reaction.

In the coflow configuration, the maximum temperature occurs near the outlets, as illustrated in Fig. 8, which shows the temperature profile along the fuel streamwise direction, *z*, at the symmetry plane of the electrolyte. Note that the electrolyte is not modelled, so this plane corresponds to the interface between the anode and the cathode. In the counterflow arrangement, the temperature near the outlets decreases because the fuel is cooled down due to the heat transferred to the incoming air in the air channel and, similarly, the air is cooled down close to the exit of the air channel due to the heat transferred to the fuel entering through the fuel channel.

Despite the benefit in performance and simultaneous reduction of the maximum temperature in the counterflow design, the thermal gradients in the direction perpendicular to the flow are higher than in the coflow configuration at both the air and fuel inlets. This is illustrated in Fig. 9 for the fuel inlet (see also Fig. 7). This figure shows the temperature profile at a vertical line passing through the centre of the fuel inlet. The vertical dashed lines represent the interfaces between different fuel cell components (the electrolyte, located between the anode and cathode, is not represented but its width is very small, as shown in Table 1, and is modelled as an interface in the unresolved electrolyte model used in the present work).

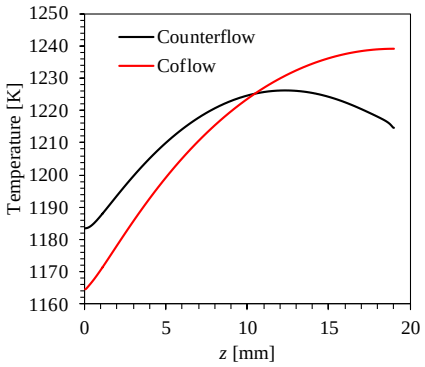

Figure 8. Temperature profiles along the fuel streamwise direction, at the symmetry plane of the electrolyte.

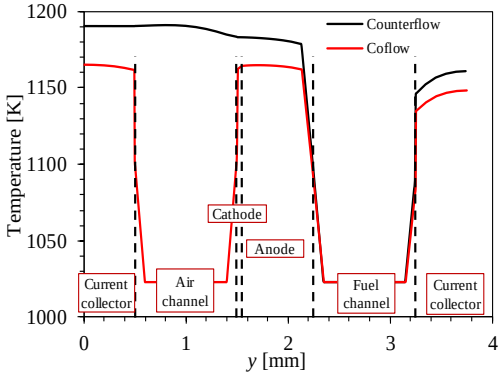

Figure 9. Temperature profiles along a vertical centreline at *z*=0 mm.

4.2. Mass flow rate

The influence of the mass flow rates of air and fuel on the performance of the fuel cell was assessed by carrying out simulations for the cases summarized in Table 4. Case 1 stands for the fuel cell experimentally investigated by Keegan *et al.* [10], as described in section 3. The mass flow rates are denoted by subscript *st* (standard), and their values were given in Table 1. The influence of the air mass flow rate was investigated in case 2, while the influence of the fuel mass flow rate was addressed in cases 3 and 4.

The polarization, efficiency and temperatures are presented in Fig. 10. They show that, as the fuel flow rate increases, so does the maximum temperature, while the power density increases by a greater amount. Therefore, the ratio of the difference between the maximum and minimum temperatures to the power density drops by 16% with the increase of the fuel flow rate from 31.1 K/kW/m^2 in case 3 to 26.8 K/kW/m^2 in case 4. The fuel usage efficiency is lower at higher fuel flow rates because the fuel cell is not able to consume the greater amount of hydrogen in the fuel stream.

The rise in power density as the mass flow rate increases can be attributed to the augmented mass of hydrogen in the fuel stream or oxygen in the air stream, while maintaining the molar masses constant. The higher mass flow rate of fuel or oxygen promotes more electrochemical reactions and thus generates more current and power for a given voltage. In addition, since the inlet area and density are constant, a higher mass flow rate implies higher inlet velocities. Convection is directly related to velocity, affecting the transport phenomena in the flow. Hence, higher flow rates improve the rate of convective mass transfer and the diffusion rate of species.

Case	$\dot{m}_{air}$	$\dot{m}_{fuel}$
1	$\dot{m}_{air,st}$	$\dot{m}_{fuel,st}$
2	$4\times \dot{m}_{air,st}$	$\dot{m}_{fuel,st}$
3	$\dot{m}_{air,st}$	$0.5\times \dot{m}_{fuel,st}$
4	$\dot{m}_{air,st}$	$1.5\times \dot{m}_{fuel,st}$

Table 4. Air and fuel mass flow rates.

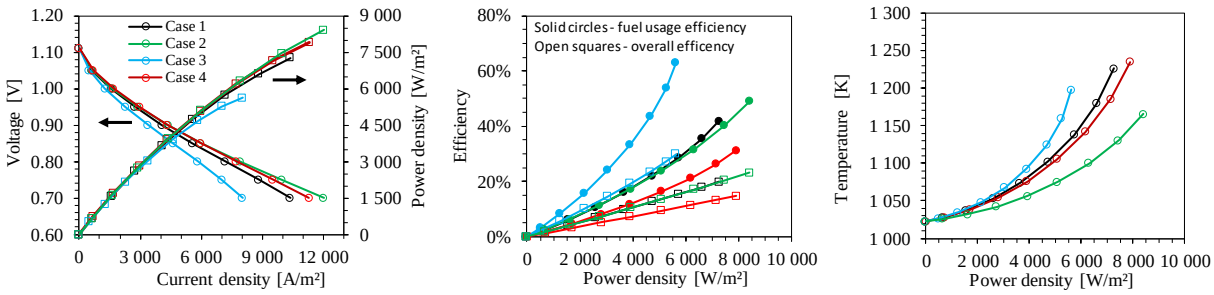

Figure 10. Polarization and power density, fuel usage and overall efficiencies, and maximum temperature for various fuel and air mass flow rates (see Table 4).

The improvement of the performance becomes especially visible at high current densities, where the demand for hydrogen greatly increases to comply with the high reaction rate requirement.
Figure 10 shows the improved fuel consumption efficiency that results from increasing the air mass flow rate. As the fuel flow rate increases, the maximum temperature marginally rises, and the curves approach each other. Moreover, the influence of the fuel flow rate on the efficiency attenuates with the increase of the fuel flow rate. This shows that a fuel cell has a limit above which the performance and the temperature will not increase further, since the cell is not able to consume the surplus of hydrogen or oxygen. Figure 10 also shows the cooling effect of a higher mass flow rate, especially at higher power output.

4.3. Fuel cell length

As the cell length increases while the width remains constant, the available active site area for the electrochemical reactions expands. To explore this, two cell length variations are compared against the reference length of 19 mm (see Table 1): an extended length of 30 mm and a shortened length of 10 mm. These choices aim to gauge the impact of roughly 50% increase or decrease in length on performance. Given that the overall reaction in the SOFC is exothermic and heat generation is proportional to the active site area, it is anticipated that the maximum temperature will rise with increased length. To ensure fair comparison among different cell lengths, current values are normalized based on the electrolyte-electrode contact area of the reference case.
The longest fuel cell consistently achieves the highest power density, even after normalization, as depicted in Figure 11. This result is expected, given the increased surface area available for electrochemical reactions. In addition to greater power density, the overall efficiency also increases for longer cells. The fuel usage efficiency rises from 25% for a cell length of 10 mm to approximately 43% for the reference length of 19 mm, and further to about 53% for 30 mm length. The change from a length of 10 to 19 mm yields a more pronounced efficiency increase compared to that from 19 to 30 mm, where the efficiency gains are proportionally smaller.

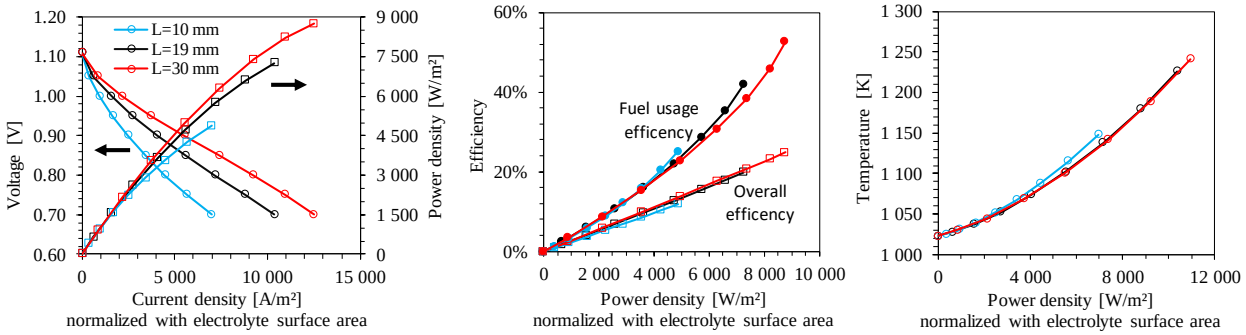

Figure 11. Polarization and power density, fuel usage and overall efficiencies, and maximum temperature for fuel cells with different length.

Another advantage of lengthening the cell is the diminished temperature gradient per unit length. Higher temperatures spread across a longer distance, resulting in a lower thermal gradient relative to shorter cells. Notably, when comparing temperatures for the same power output, the longest cell exhibits the lowest maximum temperature, albeit marginally higher than the 19 mm length cell, as shown in Figure 10. Conversely, the longer fuel cell has a higher temperature rise per unit of power density increase (31.3 vs. 29.7 K/kW/m² for 30 mm and 10 mm length, respectively).

4.4. Electrode thickness

The influence of the thickness of the electrodes and electrolyte was investigated by performing simulations for the cases listed in Table 5. Case 1 is the standard simulation described in section 3. Cases 5 and 6 are anode-supported cells, like case 1, but with a thinner anode. Case 7 is a cathode-supported cell, while case 8 is an electrolyte-supported cell. The component with the largest thickness defines the cell as either anode-, electrolyte-, or cathode-supported.
The power density, fuel usage efficiency, and temperature for the cases listed in Table 5 are displayed in Fig. 12. The analysis reveals that electrode-supported cells exhibit higher power output, efficiency, and values of the difference between the maximum and the minimum temperature per unit of power output compared to electrolyte-supported cells. The electrode-supported cells boast a broader operating range of current densities. Additionally, thinner anodes marginally enhance the performance and efficiency at standard operating conditions, albeit with elevated temperatures and increased temperature gradients per unit of power output.

Case	Anode thickness [mm]	Cathode thickness [mm]	Electrolyte thickness [mm]
1	0.70	0.05	0.01
5	0.35	0.05	0.01
6	0.07	0.05	0.01
7	0.07	0.25	0.01
8	0.07	0.05	0.10

Table 5. Electrodes and electrolyte thickness.

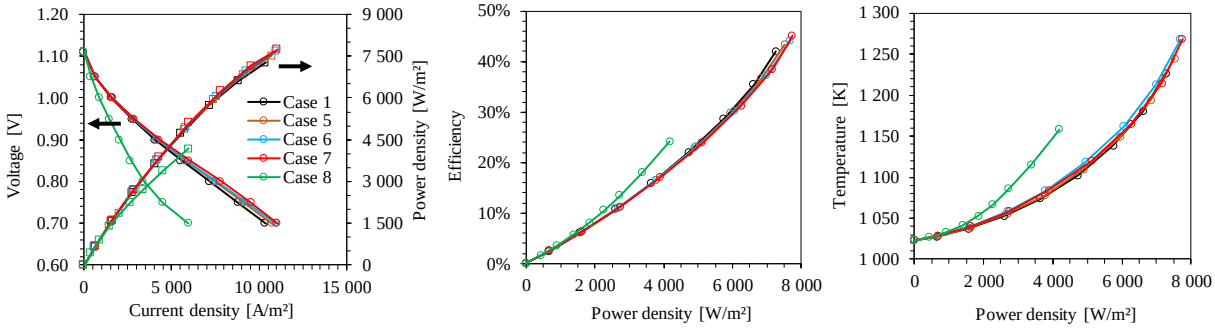

Figure 12. Polarization and power density, fuel usage efficiency, and maximum temperature for fuel cells with different electrode and electrolyte thickness.

Although the difference in power output between anode- and cathode-supported cells is minimal, the enhanced current range afforded by thinner anodes is evident from the power curves. Reducing the thickness of the anode enhances the hydrogen mass transfer rate by mitigating concentration losses, while simultaneously diminishing ohmic polarization due to shorter electron paths.

The electrolyte-supported cell allows for higher efficiencies at lower current densities. However, electrode-supported designs are more efficient for the normal operation of the fuel cell, at higher power outputs. The electrolyte-supported cell operates at lower current densities and reaches much higher temperatures at such current densities, thereby improving the reaction rates. However, the power output is lower due to the overpotential losses that harm the performance. The large ohmic polarization in the electrolyte is a significant issue of an electrolyte-supported SOFC, hence a thin-film electrolyte is usually employed to decrease the ohmic losses.

4.5. Channels height

The influence of the height of the fuel and air channels was investigated by performing simulations for a reduced height of 0.5 mm. Optimizing the height of the channel may be useful because the volume of material required for the current collectors must be reduced as well as the length the current must travel, decreasing losses due to the ohmic resistance. In this case, however, the current collector height was kept the same while reducing the channel height, and only the effects due to channel height will be considered.

To compare the performance of fuel cells with different channel heights, it is important to ensure that the amount of fuel and air entering the cell is the same for the different heights. The consequence of a lower channel height is a higher velocity, such that the mass flow rates remain unchanged. This leads to a higher convective mass transfer.

The lower height yields a slightly lower current density and an average cell temperature that is 40ºC higher, while the overall and fuel usage efficiencies are marginally improved as shown in Fig. 13. Although the higher temperatures lead to higher reaction rate, the diffusion of species is hindered by the thinner channels, which explains the reduction of the current density.

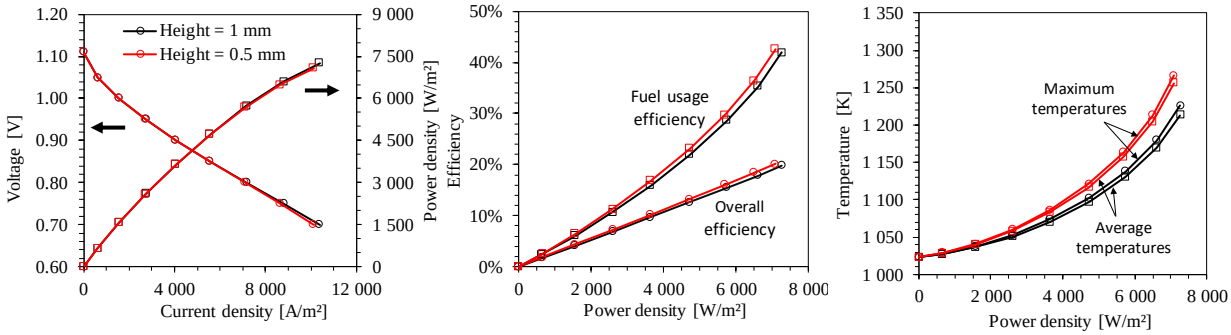

Figure 13. Polarization and power density, fuel usage and overall efficiencies, and maximum and average temperatures for fuel cells with different channels height.

5. CONCLUSIONS

An SOFC was numerically simulated using the Ansys Fluent software. The predictions were validated for two fuel cells using results reported in the literature. A parametric study was carried out to assess the influence of the flow configuration (counterflow vs. coflow), the fuel and air mass flow rates, the length of the cell, the thickness of the electrodes and electrolyte, and the height of the air and fuel channels on the performance of the fuel cell. The following conclusions may be drawn from the analysis carried out:

(i) The counterflow configuration performed slightly better than the coflow arrangement since the power density was higher and the maximum temperature was a little lower.
(ii) The increase in the fuel flow rate leads to higher power output because more hydrogen is available for the electrochemical reactions, and therefore the electrical current increases. The maximum temperature rose but the fuel usage and overall efficiency were lower for the studied conditions.
(iii) The increase in the air flow rate also leads a higher power output because more oxygen is available at the cathode, promoting more electrochemical reactions and increasing the current density. The temperature decreases due to the cooling effect of the additional air, while the efficiency is a little higher.
(iv) Lengthening the cell proves advantageous for performance, enhancing both power output and efficiency. However, the magnitude of these gains diminishes with each incremental increase in length.
(v) Anode- and cathode-supported cells offer significant power advantages over electrolyte-supported cells due to the higher temperatures, which improve the reaction rates and the species diffusion.
(vi) The reduction of the height of the air and fuel channels leads to a significant increase of the maximum temperature, but the current density decreases due to the lower diffusion of species.

ACKNOWLEDGEMENTS

The authors acknowledge Fundação para a Ciência e a Tecnologia (FCT) for its financial support via the project LAETA Base Funding (DOI: 10.54499/UIDB/50022/2020).

REFERENCES

[1] N. Sammes (ed.), *Fuel cell technology*, Springer, London (2006).
[2] N.H. Behling, *Fuel cells: Current technology challenges and future research needs*, Elsevier, Amsterdam (2013).
[3] B. Sundén, *Hydrogen, batteries and fuel cells*, Academic Press, London (2019).
[4] D.A. Nield and A. Bejan, *Convection in porous media*, 3rd ed., Springer, New York (2006).
[5] Z. Zheng, Y. Qian, Y. Zhang, C. Hao, D. Dan and W. Zhuge, A review of heat transfer and thermal management methods for temperature gradient reduction in solid oxide fuel cell (SOFC) stacks. *Applied Energy* Vol. **280**, 115899, (2020).
[6] R. Bove and S Ubertini, *Mathematical models: A general overview*. R. Bove and S

Ubertini (eds.). *Modeling solid oxide fuel cells*, Springer (2008), pp. 51–93.
[7] S.A. Hajimolana, M.A. Hussain, W.M.A.W. Daud, M. Soroush and A. Shamiri, Mathematical modeling of solid oxide fuel dells: A review. *Renewable and Sustainable Energy Reviews* Vol **15**, pp. 1893-1917, (2011).
[8] H. Yakabe, T. Ogiwara, M. Hishinuma and I. Yasuda, 3D model calculation for planar SOFC. *Journal of Power Sources* Vol. **102**, pp. 144-154, (2001)
[9] K. C. Pulagam, Optimization of solid oxide fuel cell interconnect design, *M.Sc. Thesis*, University of Nevada, Las Vegas, (2009).
[10] K. Keegan, M. Khaleel, L. Chick, K. Recknagle, S. Simner, and J. Deibler, Analysis of a planar solid oxide fuel cell based automotive auxiliary power unit, SAE 2002 *World Congress Exhibition*, paper 2002-01–0413, (2002).
[11] P.J. Roache, Perspective: A method for uniform reporting of grid refinement studies. *J. Fluids Engineering* Vol. **116**, pp. 405-413, (1994).
[12] Y.M. Barzi, A. Raoufi, N.M. Rasi, and S. Davari, Three dimensional simulation of a counter-flow planar solid oxide fuel cell. *ECS Transactions* Vol. **35**, pp. 1021–1033, (2011).
[13] A. Chaisantikulwat, C. Diaz-Goano, and E. S. Meadows, Dynamic modelling and control of planar anode-supported solid oxide fuel cell, *Computers & Chemical Engineering* Vol. **32**, pp. 2365–2381, (2008).

Congress on Numerical Methods in Engineering 2024
4-6 September 2024, University of Aveiro, Portugal

DYNAMIC SIMULATION WITH NUMERICAL MODEL TO CALIBRATE HOT-BOX PARAMETERS FOR LIGHT STEEL FRAME

Langner, M[1], Figueiredo, A[1], Vicente, R[1], Almeida, R.S.F[2,3], Soares, T[1]

1: RISCO-Risks and Sustainability in Construction, Civil Engineering Department, University of Aveiro
3810-193 Aveiro | Portugal
e-mail: marcelolangner@ua.pt, web: https://www.ua.pt/pt/risco

2: Department of Civil Engineering, Polytechnic Institute of Viseu, School of Technology and Management
Campus Politécnico de Repeses,
3504-510 Viseu | Portugal
3: Institute of R&D in Structures and Construction-LFC (CONSTRUCT-LFC), Faculty of Engineering (FEUP), University of Porto, Rua Dr. Roberto Frias s/n,
4200-465 Porto | Portugal

Keywords: Hot-box, Numerical Methods, Ansys, Light Steel Frame, Dynamic Simulation, Thermal Simulation.

Abstract *The use of dynamic simulation with numerical methods during the design phase allows for the efficient and economical analysis of various scenarios, minimizing costs related with real-test and maximizing reliability in solving complex problems. This study includes heat flow data obtained through experimental testing with Hot-box equipment in a wall constructed using Light Steel Frame (LSF) technology. This data was used to calibrate the numerical model developed in Ansys for the thermal analysis impact of adding a steel member in the middle of the LSF system and determining the thermal transmittance of the analysed system. To achieve this purpose, dynamic simulation under the same boundary conditions as the real experiment using the Transient Thermal module of Ansys Mechanical was performed. As a secondary objective, was also evaluated the needed time until to attain equilibrium conditions in terms of heat flow by dynamic simulation. This works aims not only to improve the accuracy and reliability of thermal transmittance results but also to contribute by providing reliable and validated data for the development of innovative construction solutions in the civil construction market*.

1. INTRODUCTION

When developing an object, preliminary tests and studies are required before its manufacture and release for unrestricted use. This requirement stems from the need to demonstrate its effectiveness and efficiency under the natural conditions to which it will be subjected. These conditions include physical factors inherent to its nature and use, as well as the environmental

conditions of exposure throughout its estimated life cycle.

Throughout history, these preliminary tests were conducted using real prototypes, allowing for an analysis limited to the physical and environmental conditions accessible to the researcher. With technological advances in computing in the 20th and 21st centuries, it has become possible to develop research through computational simulations. These simulations, which are rapid and efficient, simplify reality to emulate the behavior of the object in a virtual environment, including its natural dynamic characteristics. Simulations are particularly useful in contexts where practical experiments are impracticable, costly, or potentially hazardous. They allow for the exploration of hypothetical scenarios and the analysis of possible outcomes without the risks, costs and efforts associated with experimentation [1].

Although computational simulation offers significant advancements in the design process, especially in engineering, it does not completely replace the need for testing with real prototypes. Simulations attempt to replicate physical reality, which often requires the calibration of boundary conditions and the selection of mathematical models that best represent this reality. Therefore, simulation serves as an exploratory approach in research, being validated through comparison with real models. This creates a complementarity that facilitates significant advances in various scientific areas.

In the last decade, demands for innovation in building components in the construction sector have accelerated due to the need to reduce the environmental impacts caused by the construction industry. Similarly, there is a demand to reduce the energy consumption of buildings, which directly contributes to global warming. Thus, innovative systems and construction solutions that minimize material waste and increase the energy efficiency of buildings have been extensively explored [2].

An alternative construction system that has shown great promise in meeting the construction demands and needs is the Light Steel Frame, commonly known by the acronym LSF. This system consists of a light steel structure, complemented by closures in oriented strand board (OSB) panels, drywall, cementitious boards, and thermal insulation with a finishing layer.

For the study of wall construction systems, such as the Light Steel Frame (LSF), the literature indicate that the use of simulation tools with Finite Element Methods yields reliable [3] [4]. However, tests with experimental models to investigate thermal properties using hot-box approach, as described in the European EN ISO 8990 [5] and American ASTM C1363-05 [6] standards, are also recommended [7] [3].

Hotbox tests demonstrate that thermal conductivity varies with temperature in a linear and increasing manner, underscoring the importance of integrating experimental approaches and simulations to comprehend this behavior, as studies by Figueiredo et al. [8] and Rebelo et al. [9] illustrate.

The hot-box approach consists in a structure that accommodates a sample of the material or assembly of materials to be tested in a mounting ring, that is placed between two climate chambers. Sensors to record the temperatures and also the heat flow through the sample are required in the hot-box test.

Although there are studies on the thermal efficiency of LSF systems through simulations and experimental methods, the thermal characteristics of these systems can vary due to differences in the geometry and the correspondent material layers, as well as due to the ratios between the

steel profiles and the current zone without steel. In this context, the studies propose the verification and calibration of a computational model of an LSF system, used in the construction of two building at University of Aveiro, in Portugal. The methodology includes the use of the hot-box approach and computational simulation by finite element methods with the Ansys tool, highlighting the importance of these tools as complementary research resources. Additionally, by numerical simulation was evaluated the thermal effect of adding a steel member in this construction solution, by comparing the heat flow of both solutions, with and without the referred steel member.

2. METHODOLOGY

The methodology is divided into the following stages:
Experimental Hot-Box Test: Conducting tests on a prototype of the Light Steel Frame (LSF) construction system using hot-box equipment. This test aims to evaluate the thermal performance of the prototype under controlled conditions, simulating the thermal behavior in pre-set conditions. All the test details and results are presented in Figueiredo [8].
Computational Simulation with Ansys Mechanical: Simulation of a computational LSF model identical to the one used in the experimental hot-box test. This simulation allows for a detailed analysis of the thermal interactions in the system, using Ansys Mechanical software to replicate the experimentally tested conditions.
Thermal Bridging Modelling: Adding a steel member in the middle of the construction frame to investigate the impact on the system heat flux by increasing the total number of thermal bridges. This study is crucial to understanding how steel members influence heat transfer through the system, potentially identifying critical aspects that require attention in the design phase.
The wall specimen used is composed of materials developed by Saint Gobain. The composition of the system layers are described Figure 1. The thermal characteristics and dimensions of the systems are detailed in Table 1.

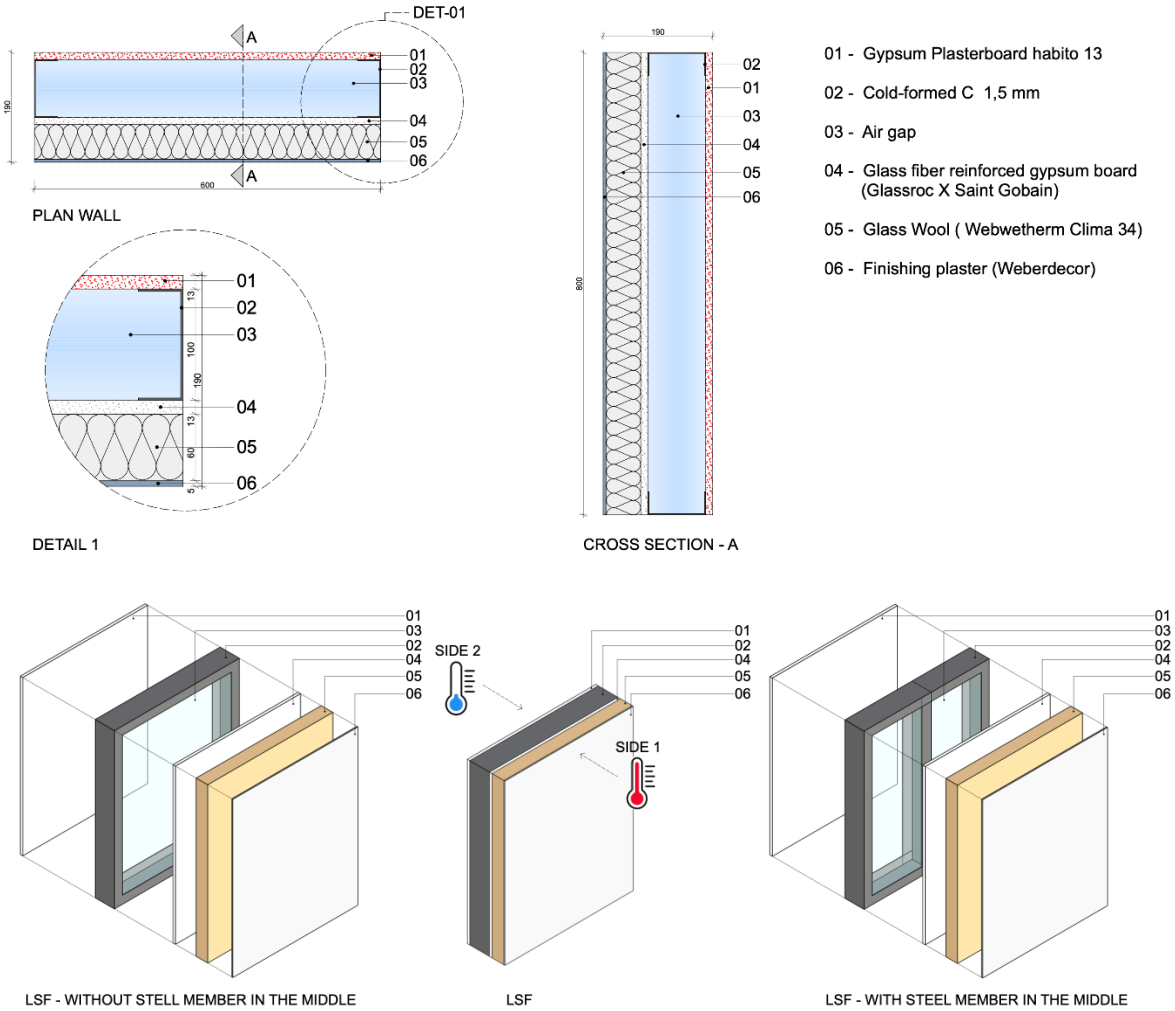

Figure 1. Wall specimen: dimensions and 3D view.

Table 1. Thermal Characteristics of Materials.

Material (industrial reference)	Thickness (m)	Density (Kg/m³)	Conductivity (W/m·K)	Specifc Heat (J/kg.K)
Finishing plaster (Weberdecor)	0.0050	1200	0.40	1090
Glass Wool (Webwetherm Clima 34)	0.060	115	0.034	840
Glass fiber reinforced gypsum board (Glassroc X Saint Gobain)	0.0125	872	0.186	840
Air gap	0.1000	1,225	0.024	1006
Gypsum Plasterboard (habito 13)	0.0125	944	0.25	950
Cold-formed C 1.5 mm	0.0015	7850	60.5	434

2.1.1 Hot-box - Experimental Research

The methodology used for the experimental test was based on the guidelines of ISO 8990, 'Thermal Insulation. Determination of Steady-State Thermal Transmission Properties — Calibrated and Guarded Hot Box' [5]. The hot-box approach consists of two climate chambers joined together by a mounting ring (Figure 2). Sensors placed on both sides of the wall specimen to measure temperature and thermal flux are also needed. The location of the sensors is shown in Figure 3.

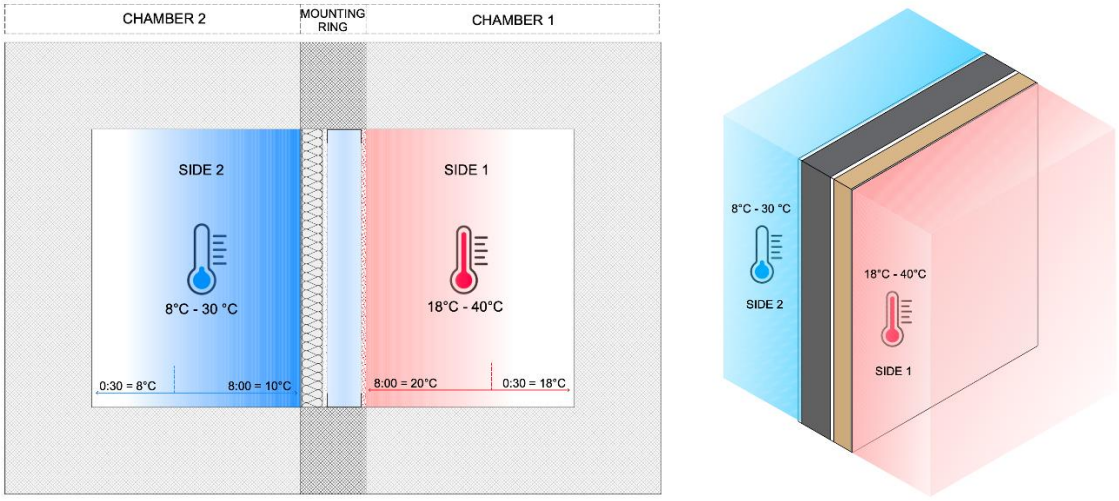

Figure 2. Illustrative Figure of the Hot-box apparatus and temperature range information.

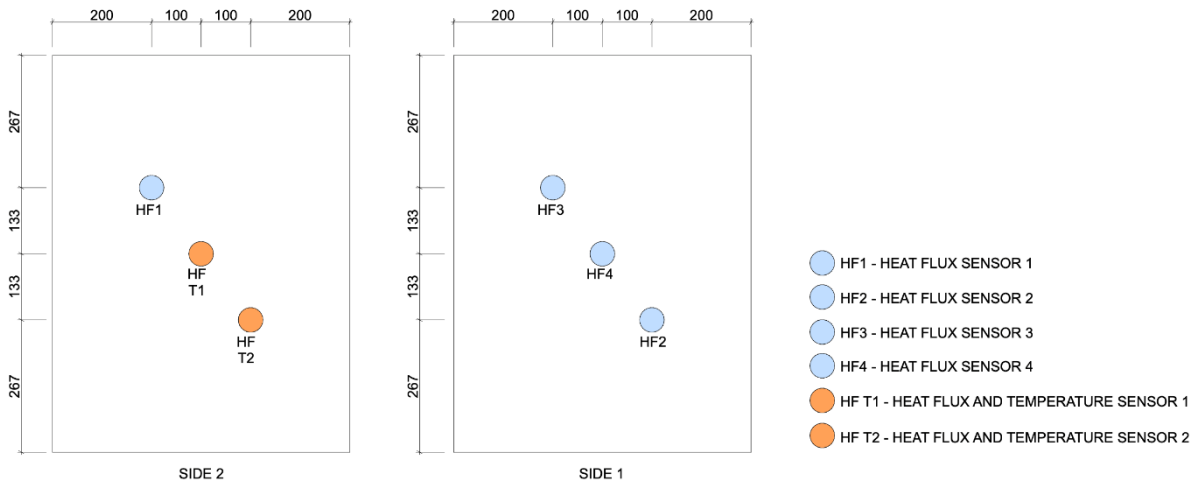

Figure 3. Locations of temperature sensors installed in the LSF system (wall specimen) on sides 1 and 2.

The test ran for 5800 minutes (96 hours and 40 minutes), during which the temperature in

chamber 1 (side 1) was initially maintained at 18°C, increasing by 2°C every 480 minutes until reaching 40°C. Chamber 2 had its temperature adjusted starting from 8°C, with increments of 2°C every 480 minutes until reaching 30°C, while always maintaining a temperature difference of 10°C between chamber 1 (side 1) and chamber 2 (side 2). Detailed information regarding the experimental campaign could be consulted in Figueiredo et al. [8].

2.1.2 FEM - Simulation Research

For computational simulation using the Finite Element Method (FEM), the Ansys Mechanical software version R1 2024 was used. The mesh model was discretized using the Automatic (Primemesh) method, with mesh characteristics presented in Table 2 and Figure 4.

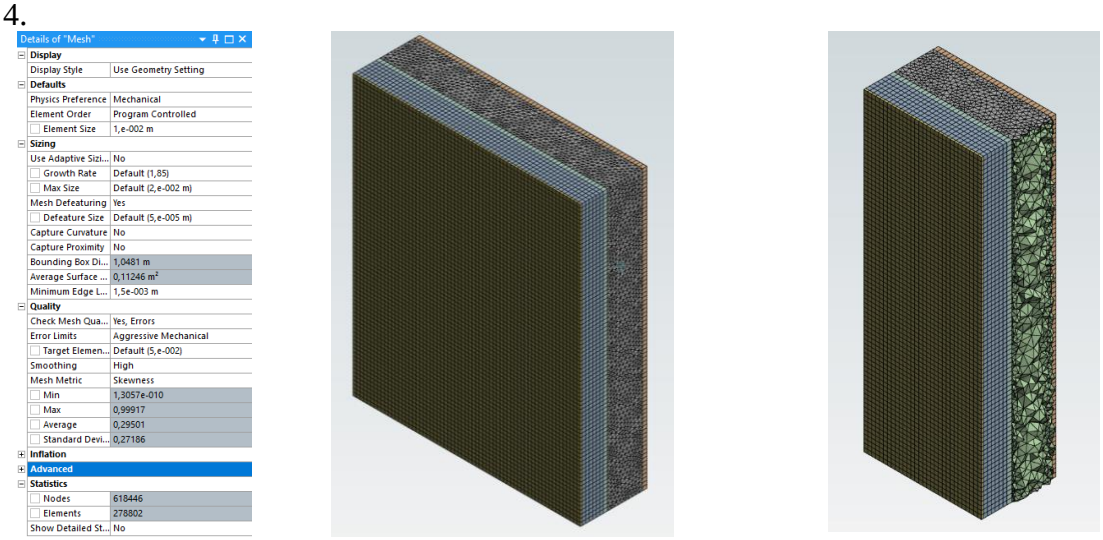

Figure 4. Images of mesh configuration, mesh perspective, and a detail with a cross section.

Table 2. Features of the simulated mesh.

Feature: Mesh without profile in the middle		
Method Control	Automatic (Prime mesh)	
Element Size	0,01 m	
Element Quality	Average 0,7725	Standard Deviation 0,2224
Skewness	Average 0,2950	Standard Deviation 0,2718
Statistic	Nodes 618446	Elements 278802
Feature: Mesh with profile in the middle		
Method Control	Automatic (Prime mesh)	
Element Size	0,01 m	
Element Quality	Average 0,7484	Standard Deviation 0,2385
Skewness	Average 0,3253	Standard Deviation 0,2905
Statistic	Nodes 634259	Elements 282895

For the simulation in Ansys Mechanical, the Transient Thermal module was used with the following boundary conditions:

- Temperature on side 1 - 8°C for 480 min, increasing by 2°C every 480 min until

reaching 30°C.

- Temperature on side 2 - 18°C for 480 min, increasing by 2°C every 480 min until reaching 40°C.
- The other boundaries were specified as adiabatic.
- The thermal characteristics of the materials were configured according to Table 1.

The methodology scheme adopted to study the influence of adding a steel member is depicted in Figure 5.

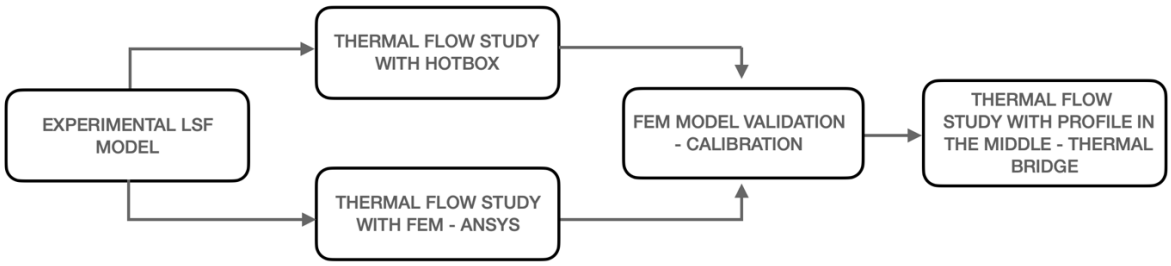

Figure 5. Scheme of the methodological research procedure.

3. ANALYSES AND RESULTS

3.1. Experimental Characterization

A construction wall assembled with a LSF solution was developed and them thermal characterized under laboratory condition (Figure 6).

Figure 6. Image of the LSF wall and hot-box equipment.

The results of the thermal flux, as well as the temperatures evolution, are presented in Figure 7. From the results it is possible to conclude that apparently steady state conditions were attained

after 250 minutes of test, with specimen exposed to the same temperature conditions in both sides.

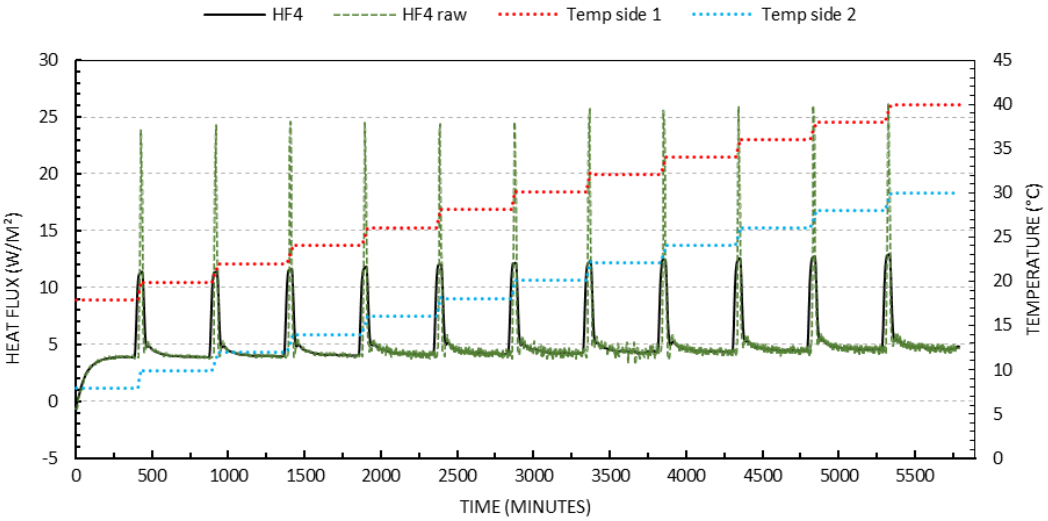

Figure 7. The results from Heat Flux Sensor 4 (HF4) and Raw Heat Flux 4 (HF4 raw) are expressed in W/m², with a temperature delta of 10°C over 5800 minutes.

The Heat Flux Sensor 4 was chosen to calibrate the model due to its location in the center of the LSF system and, among the sensors, the one with the least amount of noise in the raw file, as can be seen in Figueiredo et al. [8].

3.2. Numerical model calibration

A numerical model of the construction solution tested in the laboratory was developed in the software Ansys. The results can be seen in Figures 8.

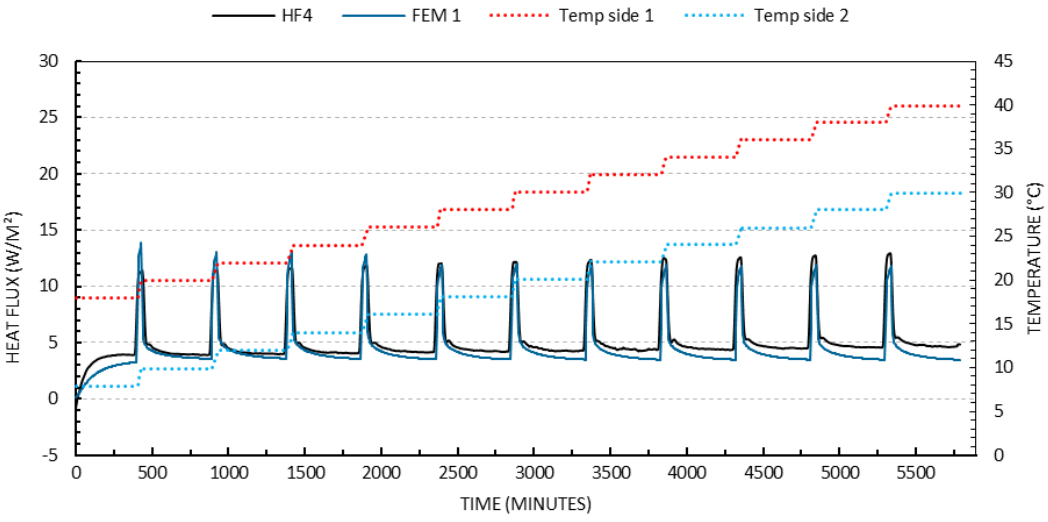

Figure 8. Results comparison between Ansys, FEM 1 and experimental tests.

Based on the plot, it is evident that the behavior of the system simulated in Ansys, compared to the real experiment of the hotbox, exhibits a similar thermal flux behavior. However, with the temperature increase the error between the simulated and real data becomes larger. This difference is related to the influence of material thermal conductivity with temperature increase, therefore a dynamic function for the thermal conductivity parameter should be considered for this type of analysis.

It was observed that the margin of error in the first simulation cycle (from 480 min to 960 min) was 8%, and in subsequent cycles, there was an increase of 1.7% in average. Based on this, it can be inferred that the influence of temperature on the thermal conductivity of this LSF wall is 1.7% for every 2°C increase.

To calibrate the model, an equivalent thermal conductivity based on the experimental test was used for the specimen.

In Figure 8, it is possible observe the result of FEM 1, with a function representing the system equivalent thermal conductivity, according to the hotbox results.

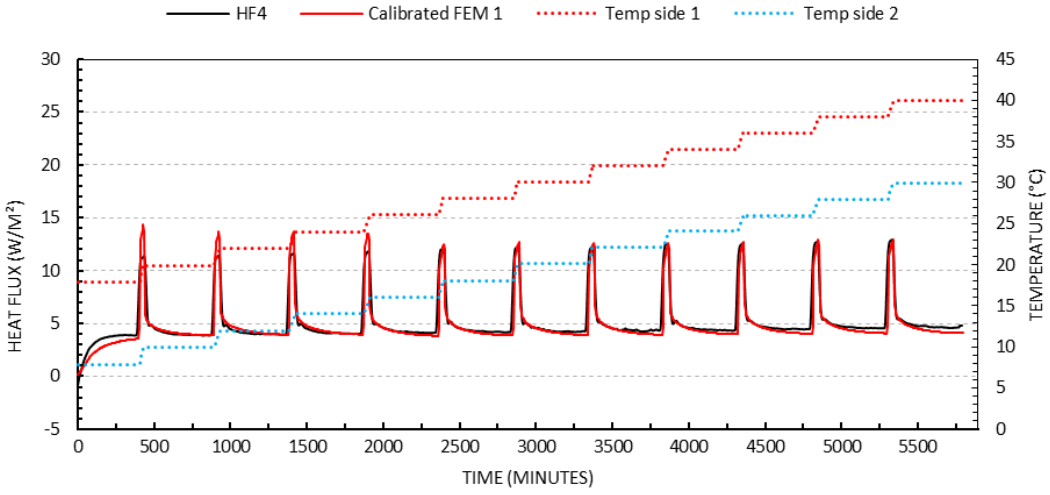

Figure 8. Heat flux ant temperature evolution after the model calibration

3.3. Characterization of the impact of introducing an LSF profile on the specimen thermal performance

As previous refereed, this study proposed the addition of a steel member in the central zone of the specimen (in the simulation model) to assess the percentage increase in the global heat flux. Typically, such profiles are added every 600mm in LSF (Light Steel Frame) structures for structural support purposes. The aim of employing a computational model, as mentioned in the introduction, is to conduct a parametric study enabling the quantification of thermal bridging and its influence on the flow within the constructive solution with the incorporation of a centrally positioned LSF profile. The outcome of the LSF specimen with a steel member in the central zone can be analysed in Figure 9, where the specimen with the

steel member is referred to as FEM 2.

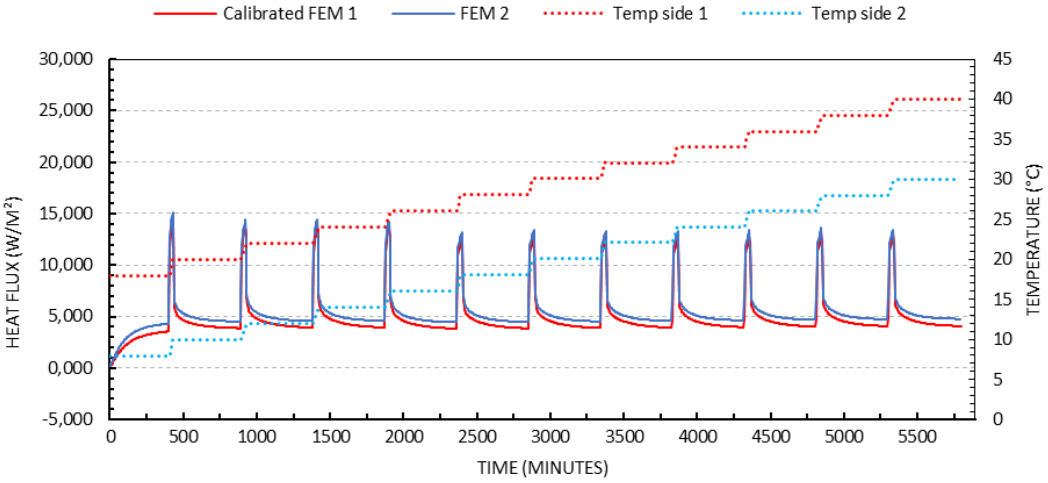

Figure 9. Simulation results from Ansys, calibrated FEM 1 and FEM 2.

The heat flow behaviour is observed in plot being in average 16% (0.62 W/m²) higher when compared to the LSF system without the steel member.

3.3. Characterization of the thermal performance of the LSF in the research

Based on the heat flux transfer rate (Q) obtained from the calibrated simulation results it was possible, using Equation (2), to determine the thermal transmittance of the studied LSF system (with and without the steel member placed in the middle of the specimen), with temperature variation presented in Table 4.

$$U\ (\text{Thermal Conductivity}) = \frac{\text{Surface Area (A)} \times \text{Temperature Gradient (dT)}}{\text{Heat Transfer Rate (Q)}} \quad (2)$$

Table 4. Thermal conductivity of the LSF system as a function of temperature.

	20 °C	22 °C	24 °C	26 °C	28 °C	30 °C	32 °C	34 °C	36 °C	38 °C	40 °C
Equivalent Thermal Conductivity LSF (w/m²k)	0.389	0.394	0.402	0.416	0.419	0.424	0.436	0.435	0.444	0.452	0.460
Equivalent Thermal conductivity of the LSF frame center (W/m²K)	0.451	0.458	0.467	0.482	0.486	0.492	0.506	0.504	0.515	0.524	0.534

An increase of 16% in the equivalent thermal conductivity was observed by the addition of the steel member. This value is consistent with the literature, which reports an increase of 25% in Santos' study [10] of LSF walls with and without a steel member.

12. CONCLUSIONS

This research aims to study the impact on thermal performance of introducing an additional steel member into an LSF construction solution. Therefore, a numerical model was developed calibrated and then simulated in the software Ansys.

From the calibration process it was observed that the FEM model can incur significant errors, ranging from 8% to 28%, as noted in this case study. In this case, the need to validate numerical models with real data is reinforced, thus ensuring greater precision in the results generated in subsequent parametric studies.

From the results regarding the influence of adding a steel member in the construction solution and its impact in the thermal behaviour, it was possible to determine that the thermal transmittance of the investigated LSF specimen changes from 0.389 to 0.46 W/m²·K without the steel member and can range from 0.451 to 0.534 W/m²·K with the additional steel member.

REFERENCES

[1] L. N. Groat and D. Wang, *Architectural Research Methods*, vol. 2. Hoboken, New Jersey, 2013.

[2] Z. Ma *et al.*, "An Overview of Emerging and Sustainable Technologies for Increased Energy Efficiency and Carbon Emission Mitigation in Buildings," *Buildings*, vol. 13, no. 10, p. 2658, Oct. 2023.

[3] P. Keerthan and M. Mahendran, "Thermal Performance of Composite Panels Under Fire Conditions Using Numerical Studies: Plasterboards, Rockwool, Glass Fibre and Cellulose Insulations," *Fire Technol.*, vol. 49, no. 2, pp. 329–356, Apr. 2013.

[4] P. Santos, G. Lemes, and D. Mateus, "Analytical Methods to Estimate the Thermal Transmittance of LSF Walls: Calculation Procedures Review and Accuracy Comparison," *Energies*, vol. 13, no. 4, p. 840, Feb. 2020.

[5] ISO 8990, "Thermal Insulation. Determination of Steady-State Thermal Transmission Properties–Calibrated and Guarded Hot Box." European Committee for Standardization, 1996.

[6] ASTM C1363-19, "Standard Test Method for Thermal Performance of Building Materials and Envelope Assemblies by Means of a Hot Box Apparatus." ASTM International, 2021.

[7] F. Asdrubali and G. Baldinelli, "Thermal transmittance measurements with the hot box method: Calibration, experimental procedures, and uncertainty analyses of three different approaches," *Energy Build.*, vol. 43, no. 7, pp. 1618–1626, Jul. 2011.

[8] A. Figueiredo, F. Rebelo, A. Samagaio, R. Vicente, and J. Lira, "Design and Thermal Characterization of Two Construction Solutions with and without Incorporation of Macroencapsulated PCM," *Infrastructures*, vol. 7, no. 3, p. 27, Feb. 2022.

[9] F. Rebelo, A. Figueiredo, R. Vicente, and V. M. Ferreira, "Study of a thermally enhanced mortar incorporating phase change materials for overheating reduction in buildings," *J. Energy Storage*, vol. 46, p. 103876, Feb. 2022.

[10] P. Santos, D. Mateus, D. Ferrandez, and A. Verdu, "Numerical Simulation and Experimental Validation of Thermal Break Strips' Improvement in Facade LSF Walls," *Energies*, vol. 15, no. 21, p. 8169, Nov. 2022.

This page intentionally left blank

Congress on Numerical Methods in Engineering 2024
4-6 September 2024, University of Aveiro, Portugal

DYNAMIC STRUCTURAL ANALYSIS OF STEEL TOWERS USED IN POWER TRANSMISSION LINES WHEN SUBJECTED TO NON-DETERMINISTIC DYNAMIC WIND LOADING

M. S. Rechtman[1] and José Guilherme S. da Silva[1]

1: Postgraduate Programme in Civil Engineering (PGECIV).
State University of Rio de Janeiro (UERJ).
São Francisco Xavier St., N° 524, Maracanã, 20550-900, Rio de Janeiro/RJ, Brazil.
e-mail: jgss@uerj.br or jgss@eng.uerj.br

Keywords: Latticed steel towers, power transmission lines, nonlinear dynamic analysis.

Abstract *The lattice steel towers have been widely used as supports for power transmission lines. On the other hand, in the current design practise of steel latticed towers used to support electrical transmission lines, the structure's dynamic behaviour is not considered [1-4]. However, the main loading to be taken into account in the structural analysis of electrical transmission lines steel towers is produced by the wind loadings, which acts dynamically over the structural system composed by towers and cables [1-4]. In addition, it's not uncommon for slender towers to present disadvantageous dynamic properties, making them vulnerable to the wind action. Considering that many accidents associated to this kind of structure occur even for wind velocities below that specified in project, it's possible that most of these accidents have been produced by dynamic actions [1-4]. This way, this research work proposes an analysis methodology that can accurately simulate the coupled behaviour between the transmission line cables and the suspension structures, when subjected to wind non-deterministic loads, including in the dynamic analysis the effects of the geometric nonlinearity and the aerodynamic damping [1]. Therefore, the main objective of this research work is to develop an analysis regarding the structural behaviour of power transmission lines, when subjected to wind dynamic loadings, having in mind the assessment of the displacements and forces of the steel towers. In this work, a transmission steel tower was investigated, considering the wind non-deterministic dynamic characteristic, and the wind loads modelled by an aleatory process based on their statistical properties. The results have shown important quantitative differences associated to the displacements and forces values when the structural response of the transmission steel tower was calculated based on a static linear analysis and a dynamic geometric non-linear and non-deterministic analysis.*

1. INTRODUCTION

The lattice steel towers have a significant importance as supports for overhead power transmission lines. The stability of the structural system is crucial to the perfect functioning and electrical safety of transmission systems [1]. In current day-to-day practice, the project of lattice steel towers used for power transmission lines considers the first-order elastic structural

analysis, assuming static equivalent loads related to the own weight, the transmission line components (conductor, shield wires and insulators) and the wind action [2].
It is widely recognized that a second-order elastic structural analysis provides additional structural displacements and imposing members forces in addition to those computed in a first-order elastic analysis. Consequently, performing a second-order elastic analysis may show that towers will be subjected to additional displacements and additional forces [3].
On the other hand, the main loading to be taken into account in the structural analysis of electrical transmission lines steel towers is produced by the wind loadings, which acts dynamically over the structural system composed by towers and cables [1-5]. In addition, it's not uncommon for slender towers to present disadvantageous dynamic properties, making them vulnerable to the wind action. Having in mind, that many accidents associated to this kind of structure occur even for wind velocities below that specified in project, it's possible that most of these accidents have been produced by dynamic actions [1-5].
Additionally, the dynamic characteristic of the wind action is essential for a more realistic analysis based on the use of the Spectral Representation Method (SRM) [1,4,6]. With this purpose, wind series can be generated with the wind fluctuant part determined as a sum of a finite number of harmonics with randomly generated phase angles. Thus, a power spectrum and a coherence function can be used to calculate the amplitude of each harmonic, aiming to keep the resemblance to the natural wind [1,6].
This way, in this research work the series of nondeterministic wind dynamic loads can be used to assess the structure nonlinear geometric response, based on the displacements and forces values. Therefore, the main objective of this study is to develop an investigation regarding the structural behaviour of lattice steel towers, aiming to assess the displacements and member forces acting in the suspension tower, comparing with the expected values indicated in current design practice methodologies. Therefore, a transmission line system section, comprising a suspension tower and two spans with total length of 900 m was analysed, based on the use of three different developed analysis methodologies (see Table 1).

Model	Structural model	Wind loads	Structural analysis
I	Isolated steel tower	Equivalent static [7]	Linear static
II	Transmission line system	Equivalent static [7]	Geometric nonlinear static
III	Transmission line system	Nondeterministic loads	Geometric nonlinear dynamic

Table 1. Performed structural analysis: static and dynamic.

2. INVESTIGATED STRUCTURAL MODEL

The investigated transmission line system, including the steel towers, conductors and shield wire types were extracted from the study developed by Oliveira [8]. The studied section of the transmission line system presents two spans of 450 m (see Figure 1), comprehended a main suspension tower in the centre with total height of 32.86 m (see Figure 2), and other two towers at the ends. The cross sections of the main suspension tower present rectangular base, pyramidal body and hollow configuration at the top, where the phases and the shield wires were fixed. Angle profiles and steel ASTM A36 type were used in this structural system [8].

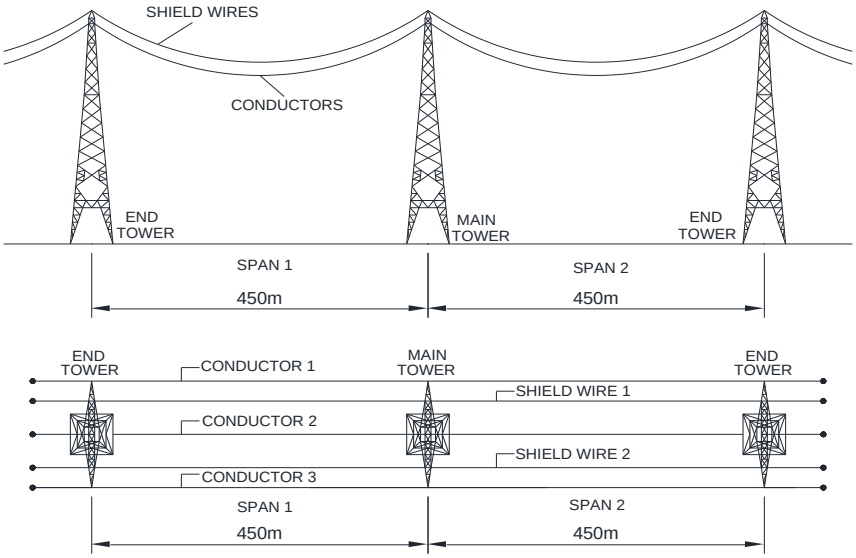

Figure 1. Investigated structural system.

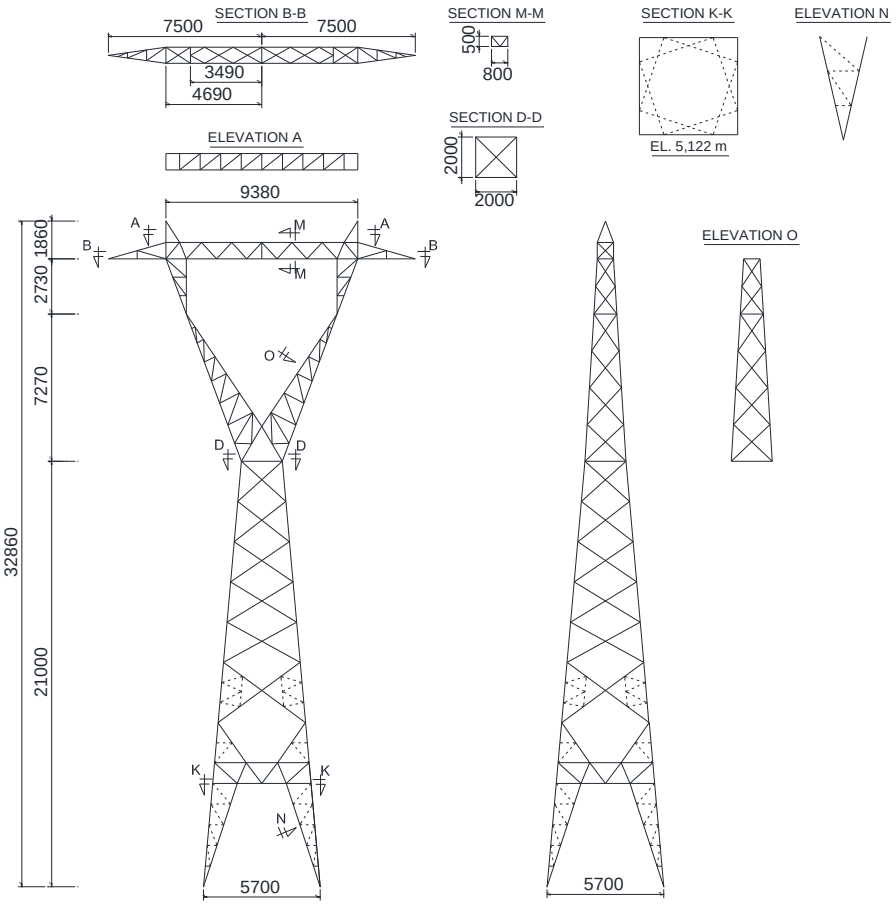

Figure 2. Main steel tower (dimensions in mm).

3. FINITE ELEMENT MODELLING

In this research work, the transmission line system was modelled based on the use of the Finite Element Method (FEM), utilising the ANSYS software. The beam finite element BEAM4 was used for modelling the main steel tower, the truss finite element LINK8 was utilised to represent the insulators, the beam finite element BEAM189 was used for simulate the conductors and shield wires, and the BEAM188 was adopted to modelling the end towers (see Fig. 3). In this investigation, the cables were represented based on the use of BEAM189 finite elements, having in mind the complexity of the numerical modelling due to the cables low stiffness against bending and compression forces. The boundary conditions were applied to the nodes that represent the towers foundations, considering restrictions to the horizontal translational displacements related to the three global axes. The developed finite element model is illustrated in Figure 3.

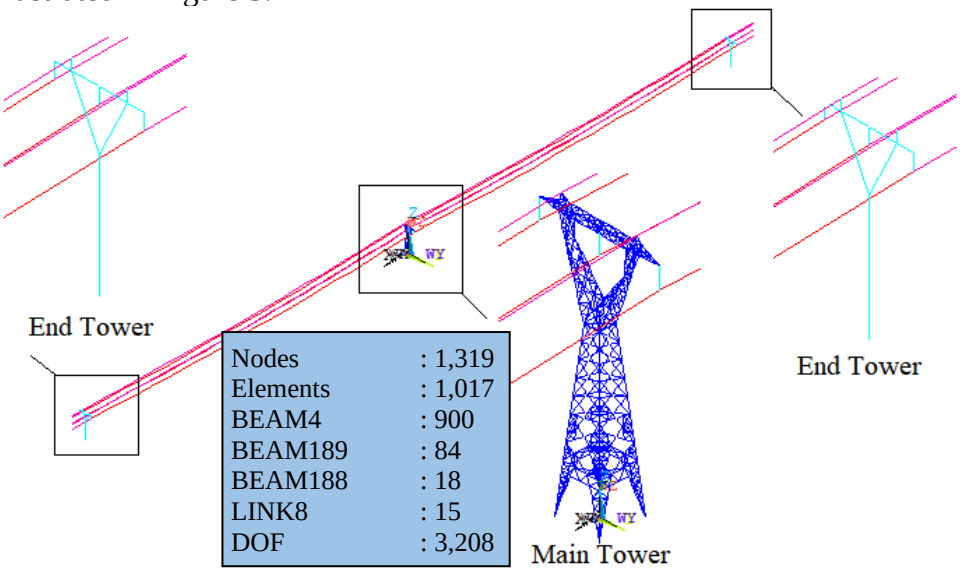

Figure 3. Finite element model of the investigated structural system

4. DEVELOPED STRUCTURAL ANALYSES

Initially, the free vibration analysis of the isolated steel tower resulted in a fundamental frequency equal to 2.60Hz (f_{01} = 2.60Hz: steel tower fundamental vibration mode). However, when the full transmission line system (steel tower and cables) was considered in the free vibration analysis, the calculated fundamental frequency was equal to 0.153Hz (f_{01} = 0.153Hz: cables and steel tower fundamental vibration mode). It was concluded that the cables (conductors and shield wires) have influenced significantly the first vibration modes of the transmission line system. Considering that the conductors, shield wires and insulator chain present a relatively elevated weight (elevated mass) when compared with their low stiffness, the influence of the cables on the transmission line non-linear dynamic behaviour is relevant.
After that, the linear elastic analysis was performed to Model I and nonlinear geometric analysis to Models II and III. Basically, the geometric nonlinearity was included in the

structural analysis based on the total Lagrangian formulation, which allows large displacements and rotations, and the Newton-Raphson method was utilised. Considering the Model III, the Newmark's time integration method was adopted for the solution of the dynamic equilibrium equations. The Newton-Raphson method was used along with Newmark's formulation. This strategy for solving the nonlinear equations is based on the implicit time integration method, which despite being more complicated in terms of calculation, is the most appropriate, given the problem high nonlinearity.

The load hypotheses are related to the forces imposed on the system associated to the basic wind velocity acting at 0^o with the line direction. Considering the Model I, the loads related to the cables, shield wires and insulators were applied to the attachment points of the main tower (see Figure 4), and calculated based on the use of the Brazilian standard NBR 5422 "Design of overhead power transmission lines" (in Portuguese) [9]. The displacement at point A and forces in element B was determined (see Figure 5).

The wind loads applied on the main tower (Model I), and the transmission line system (Model II), were determined based on the use of the Brazilian standard NBR 6123 "Forces due to wind on buildings" (in Portuguese) [7] (see Figure 6). The nondeterministic dynamic wind loads applied on the Model III (see Fig. 6) were modelled by an aleatory process based on the statistical properties. This way, the nondeterministic wind load series were generated using the Spectral Representation Method (SRM) [1,4,6]. In this study, seven wind velocities (υ = 50 m/s, υ = 45 m/s, υ = 40 m/s, υ = 35 m/s, υ = 30 m/s, υ = 25 m/s and υ = 20 m/s) were considered and selected based on significant wind velocities applied to Brazilian transmission lines regions, with mean of 3 seconds, height at 10 meters from the ground, and return period of 50 years [7]. The wind series were generated as lagged random series from a time interval τ, calculated from the use of the auto covariance and covariance functions [1,4,6].

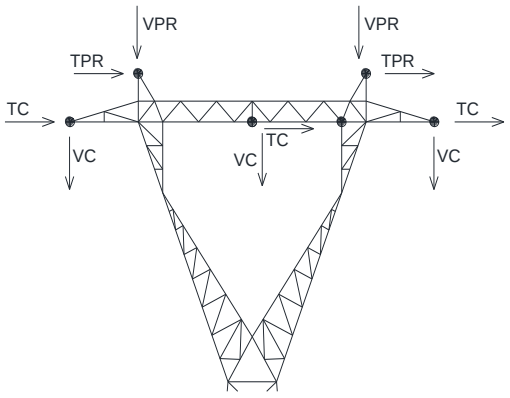

T_C: Transversal load (conductor)
T_{PR}: Transversal load (shield wire)
V_C: Vertical load (conductor)
V_{PR}: Vertical load (shield wire)

Figure 4. Loads: conductors and shield wires (Model I).

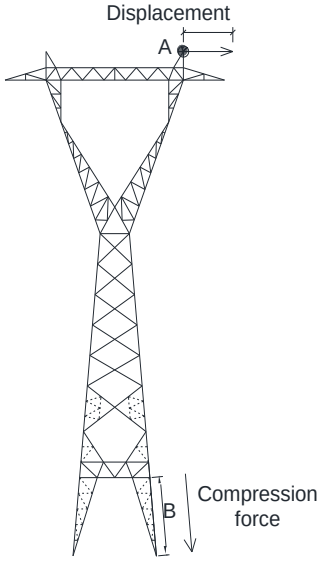

Figure 5. Calculated displacement and force.

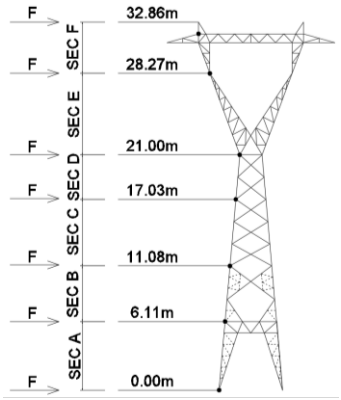

a) Static equivalent wind loads applied on the main tower: Models I and II.

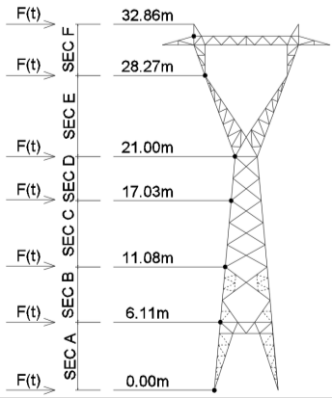

b) Nondeterministic dynamic wind loads applied on the main tower: Model III.

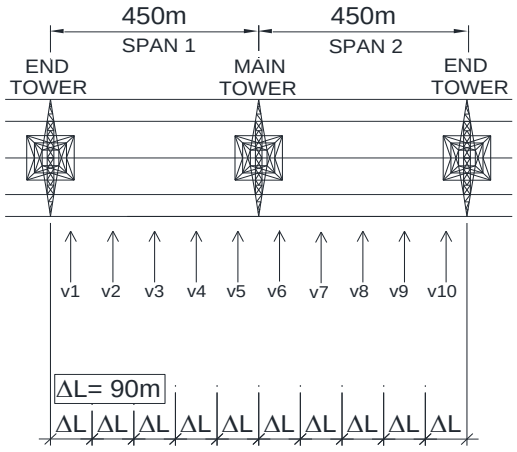

c) Static equivalent wind loads applied on the conductors and shield wires: Model II.

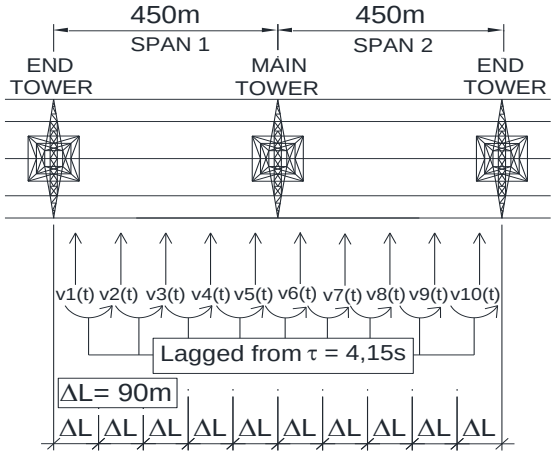

d) Nondeterministic wind loads applied on the conductors and shield wires: Model III.

Figure 6. Definition of the applied wind loads: static equivalent and nondeterministic wind loads.

In sequence, Figure 7 presents a typical example of the tower displacement in time domain, when subjected to non-deterministic dynamic wind loads. Figure 8 illustrates this displacement in frequency domain determined through Fast Fourier Transform (FFT), where it is possible to see the displacement amplitude associated to the fundamental frequency of the transmission line system [f_{01} = 0.153 Hz: 1st vibration mode (Model III)].

The horizontal translational displacement at the main tower structural section A and compression force acting on member B (see Figure 5) determined based on the use of the Mode I (linear static analysis) and Model II (nonlinear static analysis) are presented in Table 2. Tables 3 and 4 present the statistical analysis of the investigated structural system dynamic response [mean values (μ); standard deviation (σ); reliability index ($D_{95\%}$ and $F_{95\%}$)], associated to the horizontal translational displacement at the section A and compression force related to the structural element B (see Figure 5), respectively, calculated considering ten series of nondeterministic wind loads based on the use of Model III.

It must be emphasized that the element B structural capacity (see Figure 5), which was calculated equal to 242kN, was determined according to the Brazilian standard NBR 8850 "Design and execution of lattice steel towers for transmission lines - Procedure" (in Portuguese) [10]. This way is possible to assess the investigated member capacity ratio based on the results related to the reliability index ($F_{95\%}$) (see Tables 4 and 5).

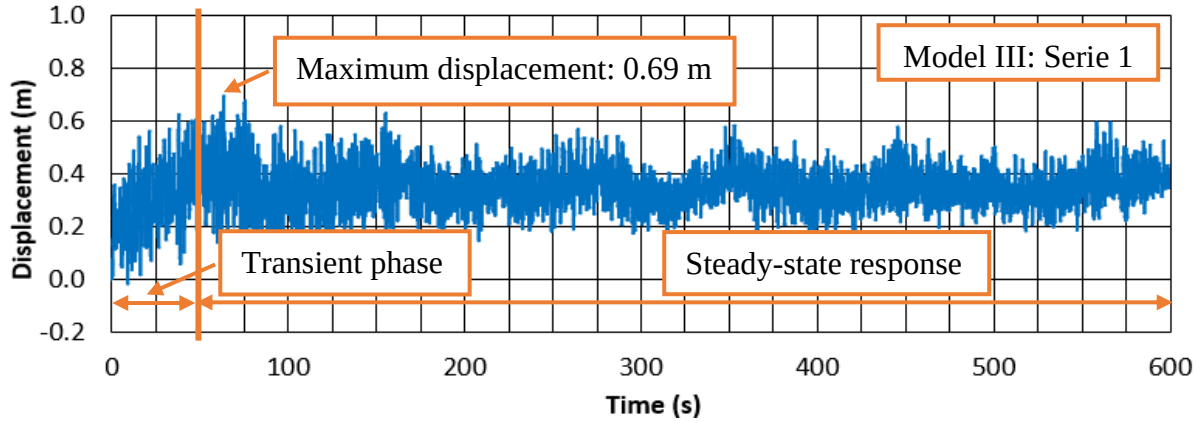

Figure 7. Typical horizontal translational displacement on point A (see Figure 5): time domain.

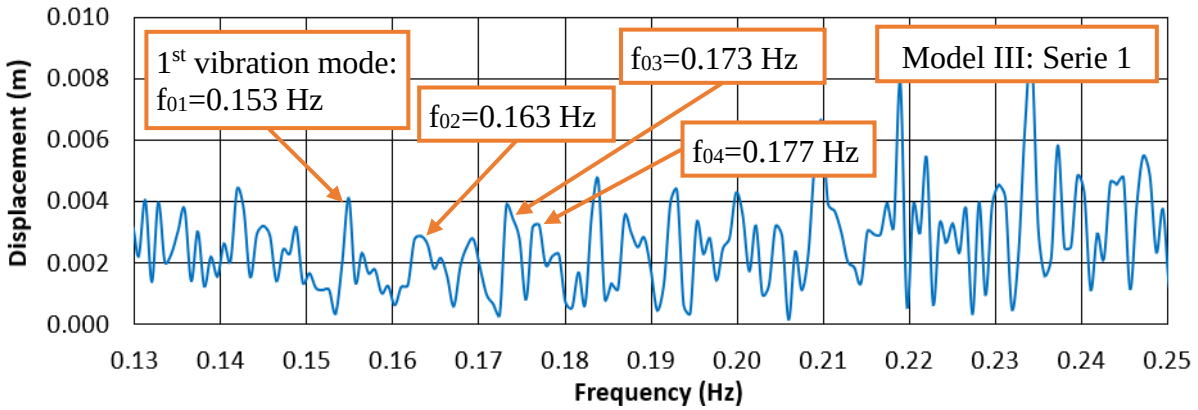

Figure 8. Typical horizontal translational displacement on point A (see Figure 5): frequency domain**.**

Model I							
Velocity υ (m/s)	50m/s	45m/s	40m/s	35m/s	30m/s	25m/s	20m/s
Displacement (m)	0.29	0.23	0.18	0.14	0.10	0.07	0.05
Force (kN)	165	136	110	87	67	50	36
Model II							
Velocity υ (m/s)	50m/s	45m/s	40m/s	35m/s	30m/s	25m/s	20m/s
Displacement (m)	0.29	0.23	0.19	0.15	0.12	0.09	0.07
Force (kN)	167	140	117	96	79	64	52

Table 2. Displacement at point A and compression force on member B (see Fig. 5): Model I and Model II.

Horizontal translational displacements in (m) at point A (see Fig. 5): Model III							
Series	υ = 50m/s	υ = 45m/s	υ = 40m/s	υ = 35 m/s	υ = 30m/s	υ = 25m/s	υ = 20 m/s
1	0.693	0.579	0.469	0.360	0.254	0.164	0.104
2	0.700	0.552	0.461	0.327	0.242	0.169	0.100
3	0.727	0.547	0.402	0.351	0.256	0.164	0.105
4	0.635	0.626	0.454	0.354	0.253	0.193	0.100
5	0.772	0.569	0.427	0.331	0.237	0.153	0.088
6	0.770	0.516	0.501	0.336	0.252	0.162	0.108
7	0.704	0.587	0.491	0.359	0.240	0.172	0.099
8	0.590	0.570	0.523	0.355	0.263	0.155	0.105
9	0.647	0.597	0.411	0.351	0.289	0.171	0.096
10	0.664	0.619	0.462	0.351	0.248	0.144	0.089
11	0.638	0.558	0.430	0.316	0.230	0.175	0.101
12	0.747	0.567	0.454	0.337	0.218	0.212	0.107
13	0.631	0.576	0.470	0.313	0.279	0.161	0.089
14	0.702	0.529	0.488	0.316	0.248	0.159	0.100
15	0.696	0.622	0.516	0.341	0.197	0.183	0.107
16	0.658	0.535	0.520	0.386	0.243	0.148	0.110
17	0.602	0.526	0.398	0.350	0.273	0.151	0.100
18	0.619	0.549	0.473	0.021	0.218	0.156	0.107
19	0.719	0.608	0.444	0.358	0.220	0.156	0.138
20	0.616	0.631	0.448	0.360	0.232	0.169	0.121
21	0.649	0.528	0.497	0.327	0.232	0.143	0.098
22	0.654	0.635	0.457	0.351	0.224	0.179	0.102
23	0.611	0.632	0.541	0.354	0.200	0.161	0.103
24	0.722	0.533	0.434	0.331	0.230	0.160	0.113
25	0.620	0.559	0.476	0.336	0.220	0.165	0.103
26	0.644	0.586	0.483	0.359	0.238	0.174	0.106
27	0.733	0.588	0.488	0.355	0.249	0.184	0.110
28	0.714	0.596	0.540	0.351	0.222	0.156	0.099
29	0.708	0.635	0.444	0.351	0.229	0.157	0.121
30	0.635	0.538	0.453	0.316	0.216	0.171	0.105
μ	0.674	0.576	0.469	0.337	0.238	0.166	0.105
σ	0.050	0.037	0.037	0.313	0.021	0.014	0.010
$D_{95\%}$	0.692	0.590	0.482	0.316	0.246	0.171	0.108

Table 3. Horizontal translational displacements in (m) at point A (see Fig. 5): Model III.

Compression forces in (kN) acting on member B (see Fig. 5): Model III.							
Series	υ = 50m/s	υ = 45m/s	υ = 40m/s	υ = 35 m/s	υ = 30m/s	υ = 25m/s	υ = 20 m/s
1	416	342	279	231	152	100	65
2	436	322	285	236	146	101	64
3	458	316	241	208	150	100	67
4	393	368	267	190	149	117	64
5	471	341	252	206	145	93	59
6	471	316	304	214	150	98	70
7	423	355	297	208	145	104	64
8	365	341	318	210	152	93	66
9	391	368	244	210	174	105	61
10	401	382	273	222	146	88	58
11	375	336	257	223	136	107	65
12	447	346	276	217	133	127	68
13	369	351	280	205	167	96	59
14	430	310	295	199	145	97	65
15	421	396	302	214	118	111	68
16	394	327	318	188	145	92	69
17	368	320	239	210	161	91	65
18	373	338	273	213	130	96	67
19	440	371	266	196	133	96	85
20	377	394	266	202	139	102	76
21	391	318	306	216	139	87	62
22	392	369	276	210	132	108	64
23	372	376	335	211	119	97	66
24	433	328	267	205	135	100	70
25	377	339	293	187	133	102	66
26	383	354	282	200	139	106	68
27	462	364	284	184	151	113	69
28	446	368	325	185	136	96	64
29	442	386	261	204	140	97	77
30	380	320	266	226	130	105	66
μ	410	349	281	208	142	101	66
σ	34	25	24	13	12	8	5
$F_{95\%}$	422	358	290	212	147	104	68

Table 4. Compression forces in (kN) acting on member B (see Fig. 5): Model III.

Model	Member force ratio (%)						
	υ=50m/s	υ=45m/s	υ=40m/s	υ=35m/s	υ=30m/s	υ=25m/s	υ=20m/s
I	68	56	45	36	28	21	15
II	69	58	48	40	33	26	21
III	174	148	120	88	61	43	28

Table 5. Assessment of the load capacity of the investigated structural element B (see Fig. 5).

It should be noted that the static structural analysis (Model I and Model II) provided lower values of displacements and compression forces when compared to those determined based on the dynamic structural analysis (Model III) (see Tables 2 to 5). This way, the dynamic amplification factor (DAF) related to displacements and compression forces of the investigated models are approximately three (DAF = 2.5). The differences between the results calculated based on the use of Models I and II are not significant (see Table 2).

On the other hand, it can be seen from Table 5 results, that the differences between the model's response (Model I; Model II; Model III), in terms of members force ratio could be relevant and up to 106%. It must be emphasized that according to the Brazilian standard NBR 8850 [10], the admitted maximum force ratio is equal to 93%, and clearly the results provided by Model III have surpassed this limit for higher wind velocities (see Table 5).

The results obtained in this investigation reflect relevant differences between the displacement and force values according to the chosen finite element model and structural analysis. It is important to emphasize that the structural member's capacity analysis shows that the maximum member force ratio is equal to 174% [$F_{95\%}$ = 422 kN > 242 kN] (see Table 5). This member force ratio value is enough to surpass the structural member capacity determined by NBR 8850 [10] and could cause structural failure.

5. CONCLUSIONS

The final conclusions on this work are presented based on the structural response assessment of a transmission line system section comprising a suspension tower and two spans with total length of 900m, based on the development of three different analysis methodologies: static linear analysis considering the main isolated tower (Model I); static geometric nonlinear analysis based on a transmission line system section (Model II); geometric nonlinear dynamic analysis associated to a transmission line system section (Model III). This way, the following conclusions can be drawn from the results presented in this study:

1. The results have shown relevant quantitative differences between the displacement and force values established by the design standards and those calculated through a geometric nonlinear dynamic analysis. Based on the comparisons between the results calculated from Model I (static linear analysis), Model II (static geometric nonlinear analysis) and Model III (geometric nonlinear dynamic analysis), it is possible to verify differences: up to 257% (displacements), 263% (member's compression forces), and 106% (member force ratio).
2. It is important to notice that the structural member's capacity analysis shows that the force ratio increase is enough to surpass the structural member capacity for higher wind velocities, when the Model III (geometric nonlinear dynamic analysis) was considered, as result of the

differences between the forces provided by the standard methodology and those obtained from the finite element analysis.
3. This investigation has revealed that the geometric nonlinear dynamic analysis is very important to understand the structural behaviour, loads distribution, structural stability and design of transmission lines. This work considered a case study, based on four seven velocities (50m/s, 45m/s, 40m/s, 35m/s, 30m/s, 25m/s and 20m/s), which can be used as a reference for similar studies, highlighting the importance of considering the wind dynamic effects on the design of transmission lines.

ACKNOWLEDGEMENTS

The authors gratefully acknowledge the financial support for this research work provided by the Brazilian Science Foundation's CNPq, CAPES and FAPERJ.

REFERENCES

[1] M.S. Rechtman. *Nonlinear dynamic structural modelling of transmission lines steel towers when subjected to the nondeterministic wind dynamic loads*. DSc Thesis (In development / In Portuguese). State University of Rio de Janeiro (UERJ), Rio de Janeiro/RJ, Brazil, (2023).

[2] S.P. Troian. *On the dynamic structural response of a cable-stayed transmission line tower subjected to EPS-type winds*. MSc Dissertation (In Portuguese). Federal University of Rio Grande do Sul (UFRGS), Porto Alegre/RS, Brazil, (2018).

[3] N.P. Rao, S.J. Mohan, N. Lakshmanan. A study on failure of cross arms in transmission line towers during prototype testing. *International Journal of Structural Stability and Dynamics*, Vol. **5(3)**, pp. 435-455, (2005).

[4] L. Kempner Jr. Wind load methodologies for transmission line towers and conductors. *Proceedings of the Electrical Transmission and Substation Structures Conference*, Texas, USA, (2009).

[5] R.R. Roman, L.F.F. Miguel; F. Alminhana; J. Pimenta, Numerical simulation of full-scale tests in transmission line towers. *XLI CILAMCE: Ibero-Latin American Congress on Computational Methods in Engineering*, Foz do Iguaçu/PR, Brazil, pp. 1-7, (2020).

[6] A. Barile, L.S. Bastos, J.G. Santos da Silva. Human comfort assessment of buildings sub jected to nondeterministic wind dynamic loadings, *IBRACON Structures and Materials Journal*. Vol. **13(4)**, e13402, (2020).

[7] Brazilian Association of Technical Standards (ABNT). NBR 6123: Forces due to wind on buildings (In Portuguese), Rio de Janeiro/RJ, Brazil, (2023).

[8] M.I.R. Oliveira, *Structural analysis of transmission line steel towers subjected to wind induced dynamic effects*. MSc Dissertation (In Portuguese). State University of Rio de Janeiro (UERJ), Rio de Janeiro/RJ, Brazil, (2006).

[9] Brazilian Association of Technical Standards (ABNT). NBR 5422: Design of overhead power transmission lines (In Portuguese), Rio de Janeiro/RJ, Brazil, (1985).

[10] Brazilian Association of Technical Standards (ABNT). NBR 8850: Design and execution of lattice steel towers for transmission lines - Procedure (In Portuguese), Rio de Janeiro/RJ, Brazil, (2013).

This page intentionally left blank

Congress on Numerical Methods in Engineering 2024
4-6 September 2024, University of Aveiro, Portugal

EFECTO DE LA MALLA EN EL CÁLCULO DEL FLUJO ASIMÉTRICO A ALTOS ÁNGULOS DE ATAQUE EN CUERPOS ESBELTOS

José Jiménez Varona[1], Gabriel Liaño[2]

1: Área de Aerodinámica Teórica y Computacional
Departamento de Física del Vuelo
INTA (Instituto Nacional de Técnica Aeroespacial)
Carretera de Ajalvir km 4.5, 28850 Torrejón de Ardoz (Madrid), España
e-mail: jimenezj@inta.es, web: https://www.inta.es

2: Área de Aerodinámica Teórica y Computacional
Departamento de Física del Vuelo
INTA (Instituto Nacional de Técnica Aeroespacial)
Carretera de Ajalvir km 4.5, 28850 Torrejón de Ardoz (Madrid), España
e-mail: liagno@inta.es web: https://www.inta.es

Palabras clave: Aerodinámica, flujo asimétrico, cuerpos esbeltos, cálculo numérico, mallas de cálculo

Resumen *El cálculo numérico del flujo alrededor de cuerpos esbeltos es una tarea difícil cuando se determina en la zona de altos ángulos de ataque. A esta condición, se ha detetctado experimentalmente que el flujo es asimétrico, aunque se trate de cuerpos axilsimétricos. La causa está en una inestabilidad global, que se activa en función de determinados factores o parámetros. El resultado es que aparece una fuerza lateral, bien negativa o positiva. El flujo simétrico es inestable y cualquier perturbación lleva a una solución asimétrica bi-estable. Existe una dificultad añadida para el cálculo. Muy pequeñas irregularidades de la configuración llevan a que exista una inestabilidad convectiva, que se añade a la global, produciendo un flujo sobre el cuerpo que depende del ángulo de orientación.. Numéricamente, las mallas estructuradas permiten simular cuerpos simétricos, con rugosidad muy baja. Y se pueden añadir irregularidades controladas en determinados ángulos de orientación para simular los efectos en el flujo. Por otro lado, es muy normal la simulación numérica mediante el empleo de mallas no estructuradas, que son asimétricas intrínsecamente, y su nivel de irregularidades puede ser elevado, llevando a una gran dependencia de las fuerzas y momentos con el ángulo de orientación o azimut. En este trabajo se muestra esta dependencia de las soluciones numéricas con las mallas de cálculo utilizadas, sean estructuradas o no estructuradas. Su nifluencia en la solución es muy alta, lo que lleva a incertidumbre en el análisis de los resultados y a la necesidad de validación exhaustiva y comparación con datos experimentales.*

1. INTRODUCCIÓN

Computational Fluid Dynamics (CFD) es actualmente una herramienta fiable y robusta para la caracterización del flujo sobre una aeronave. Los coeficientes aerodinámicos se pueden estimar con buena precisión usando métodos CFD, siempre que se cumplan los requisitos de utilizar mallas de cálculo finas, métodos de alto orden y modelos de turbulencia de alto nivel. Existen muchos códigos CFD que implementan las ecuaciones promediadas de Navier-Stokes ('Reynolds Average Navier-Sokes', RANS). También existen muchos métodos que implementan los métodos de filtrado espacial 'Large Eddy Simulation (LES)'. Estos últimos son más apropiados para cálculos no estacionarios, pero requieren una potencia de cálculo de bastante superior, al requerir para flujos a altos números de Reynolds mallas de cálculo mucho más finas, pasos de tiempo mucho menores y determinar la solución en períodos mayores, lo que lleva a valores de varios órdenes de magnitud sobre los cálculos RANS, que hacen prohibitivo a nivel industrial su uso [1].

A diferencia de los cálculos sobre aviones de configuración estándar, el cálculo numérico sobre cuerpos axil-simétricos a altos ángulos de ataque aún es un problema difícil de abordar.

Muchos estudios y experimentos han demostrado que a altos ángulos de ataque el flujo sobre cuerpos axil-simétricos no es simétrico. Existen fuerzas laterales y momentos de guiñada asociados. Estas fuerzas laterales pueden llegar a ser de magnitud similar a la de las fuerzas normales. Es más, el campo de presiones, y por tanto las fuerzas y momentos, dependen del ángulo de orientación del cuerpo. Esta dependencia con el ángulo de orientación de cuerpos axil-simétricos macroscópicamente hablando ha generado ríos de tinta en la literatura especializada. Las referencias [2-18] muestran un breve resumen de los resultados y conclusiones de expertos teóricos y experimentalistas, desarrolladas desde los años 80 del siglo pasado.

Existen dos parámetros aerodinámicos que tienen una enorme influencia en el desarrollo de un patrón de flujo asimétrico: el número de Mach y el número de Reynolds. El flujo asimétrico desaparece cuando el número de Mach del flujo cruzado sobrepasa cierto valor. Por tanto, este es un fenómeno básicamente de flujos subsónico y transónico. Con respecto al número de Reynolds, la fuerza lateral es máxima bien en flujo laminar o bien en flujo completamente turbulento, mientras que a número de Reynolds crítico su valor es mínimo [2-4].

Este comportamiento llevó a muchos investigadores a sugerir que existe una inestabilidad de naturaleza no viscosa que hace que el flujo llegue a una solución asimétrica bi-estable. A determinados valores del ángulo de ataque, el patrón de flujo simétrico es inestable, y una pequeña perturbación del flujo (corriente libre no homogénea, turbulencia, etc.) produce una de los dos posibles estados asimétricos estables. A esto se le denomina inestabilidad global o temporal del flujo [2], [6], [12], [18]. Esta inestabilidad está relacionada también con la geometría del cuerpo axil-simétrico, en las que el ángulo de la nariz, el alargamiento y las imperfecciones en términos de excentricidad o rugosidad, juegan un papel decisivo [5-18].

La punta es muy importante. Estudios empíricos para cuerpos de alargamiento pequeño condujeron a obtener una correlación entre el ángulo de ataque de comienzo de la asimetría y el ángulo de la punta [2], [6-7]. A ángulos de ataque por encima de éste, el par de torbellinos simétricos que se desarrolla en barlovento se modifica por el fenómeno llamado "vortex

crowding". Una inestabilidad no viscosa -denominada global o temporal- ocurre tal que uno de los torbellinos se aleja del cuerpo y el otro se mueve bajo el otro [6]. El ángulo de ataque al que ocurre esto se define como: $\alpha_{onset} = 2 \cdot \delta_{nose}$ siendo δ_{nose} el ángulo de la punta. El redondeo de estos cuerpos incrementa de forma efectiva este ángulo, y por tanto se retrasa la asimetría, dado que el ángulo de ataque de comienzo de asimetría se incrementa.

Las irregularidades geométricas son muy importantes en el desarrollo del flujo sobre estos cuerpos cuando el ángulo de ataque es alto. En estos flujos, sobre todo en régimen turbulento, la rugosidad es muy importante. Uno de los efectos es la dependencia de las fuerzas y momentos con el ángulo de orientación, y siendo en principio cuerpos axil-simétricos no debería producirse. En palabras de B. L. Hunt: "One of the most curious, fascinating and infuriating flow problems to have been encountered in recent years is the body side force problem. This roll angle variation is one of the most perplexing features of the side force problem" [7].

Muchos ensayos en túnel no reprodujeron repetitividad de las soluciones. Ensayos diferentes llevaban a soluciones diferentes en las fuerzas laterales. Modificaciones de la punta de la maqueta llevaban también a diferentes fuerzas laterales. Existe pues una dependencia enorme de las fuerzas laterales con el ángulo de orientación. Esto se ha comprobado en multitud de ensayos en diferentes túneles. Esto se detalla muy bien en la referencia [2]; por un lado se obtuvo un patrón de flujo asimétrico bi-estable de la fuerza lateral (bien positiva o bien negativa de igual magnitud) cuando se ensayaba un cuerpo muy pulido, con una rugosidad adimensional de $\frac{r_a}{D} = 5 \cdot 10^{-6}$. Posteriormente, este modelo pulido fue mecanizado para tener tomas de presión y pintado. El resultado fue un modelo con una rugosidad relativa de $\frac{r_a}{D} = 40 \cdot 10^{-6}$. Ensayos con este modelo llevaban a una forma sinusoidal de la fuerza lateral con el ángulo de orientación, y a valores más altos en magnitud en determinados ángulos y variaciones de hasta 50% entre unos valores y otros de ángulo de orientación.

Otra consecuencia de la rugosidad e incluso de las irregularidades geométricas en términos de excentricidad, es que el ángulo de ataque de comienzo de asimetría, del que se tiene una correlación para cuerpos de poca esbeltez, se reduce bastante respecto al ángulo de ataque de comienzo de asimetría del modelo pulido. Esta reducción la demuestran Champigny [2-4] y Deane *et al*. [19] para un cuerpo axil-simétrico -ojiva-cilindro- a bajos números de Mach. Otros investigadores han hecho ensayos con maquetas pulidas y rugosas y éstos mostraban un mismo comportamiento: una solución bi-estable con el ángulo de orientación para la fuerza lateral, si se trataba del cuerpo pulido, y una solución sinusoidal para el cuerpo rugoso [13-16]. Este efecto tan importante de las micro-imperfecciones ha llevado a muchos experimentalistas a perturbar bien la punta del cuerpo o a introducir rugosidad. También se ha investigado esto desde un punto de vista numérico [13-18]. La forma de hacerlo numéricamente es modificar la malla de superficie añadiendo micro-imperfecciones o rugosidad numérica.

Esta es la segunda fuente de asimetría: la dependencia de las fuerzas y momentos con el ángulo de orientación están relacionadas con estas asimetrías geométricas. El ángulo de orientación o azimut es una buena variable para establecer la influencia de la rugosidad e irregularidades geométricas. El mecanismo que actúa se denomina como una inestabilidad espacial o

convectiva [6], [12]. Bridges define en la referencia [6] que una inestabilidad convectiva tiene las siguientes características: (i) una perturbación infinitesimal asimétricamente dispuesta se fija cerca de la punta y el resultado es un flujo con fuerza lateral finita (ii) un pequeño cambio de la perturbación genera un cambio finito de la fuerza lateral (iii) cuando la perturbación se quita, el flujo vuelve a su estado original. Bao-Feng Ma [12] define la inestabilidad convectiva (o espacial) como la causa para la aparición de torbellinos asimétricos debidos a las imperfecciones geométricas.

Como conclusión, a altos ángulos de ataque para cuerpos rugosos actúan dos mecanismos de inestabilidad: el no viscoso o global (temporal) y el convectivo (espacial). Los diferentes ensayos, tanto de Champigny [2-4] o de Deane *et al.* [19] para cuerpos pulidos y rugosos de una configuración ojiva-cilindro, refuerzan esta idea. La dependencia de las fuerzas y momentos con el ángulo de orientación del modelo rugoso, así como las curvas polares de las dos configuraciones indican la acción de ambos mecanismos.

Desde un punto de vista numérico, para poder realizar estudios de este tipo de configuraciones, hemos de tener en cuenta especialmente las mallas de cálculo, pues éstas juegan un papel crucial en la simulación, mucho más en este tipo de flujos. Los efectos de las irregularidades geométricas pueden medirse en forma de alejamiento de la forma axil-simétrica ideal, muy especialmente en la punta, que juega el papel decisivo para la activación de la inestabilidad convectiva (o espacial), que lleva a la dependencia de las fuerzas con el ángulo de orientación. Otro problema que se debe abordar es la necesidad de realizar cálculos no estacionarios, ya que a altos ángulos de ataque el flujo es inestable y no estacionario. Se desarrollan torbellinos asimétricos, y a medida que el alargamiento es alto y se incrementa el ángulo de ataque, hay un patrón de torbellinos oblicuos que tiende a la calle de torbellinos de von Kármán en la parte trasera del cuerpo.

Finalmente, aparece otro aspecto clave en la simulación. La mayoría de los modelos de turbulencia que se usan en códigos RANS son excesivamente disipativos y resuelven solamente frecuencias mucho más bajas que las fluctuaciones turbulentas. La razón es que ellos no resuelven el espectro correcto de escalas turbulentas, incluso con pasos de tiempo pequeños y tamaños de celdas de malla de suficiente resolución [1], [20-23]. Esto ha llevado a numerosos investigadores a explorar métodos RANS-LES o métodos mixtos RANS-DDES para abordar este tipo de flujos [24]. Sin embargo, sin ir a métodos LES y centrarnos en métodos RANS que siguen siendo los métodos estándar más realistas a un coste computacional asumible [24], el método "Scale Adaptive Simulation (SAS)" implementado por Menter *et al.* [1], [20-23], [25] para dos modelos de turbulencia – uno el modelo k-ω SST y otro el modelo basado en ω para esfuerzos de Reynolds (ω-RSM)- es un método adecuado para abordar este tipo de problemas no estacionarios.

Una gran ventaja de este método es que se adapta al tamaño de la celda de malla y al paso de tiempo, resultando en una variación continua de la simulación desde LES a RANS [1].

En este trabajo, nos centraremos en el efecto de la malla de cálculo en simulaciones de dos configuraciones: una ojiva-cilindro a baja velocidad y una bomba (M823) a régimen transónico. Una estimación de la desviación sobre la configuración ideal se realiza para los cuerpos de las dos configuraciones. En el caso de la bomba, la influencia de los torbellinos de la nariz se amplifica a altos ángulos de ataque por la diferente interacción con las aletas dependiendo de

la mayor o menor irregularidad y/o rugosidad de la nariz.

2. MÉTODOS NUMÉRICOS: CÁLCULO DEL FLUJO ASIMÉTRICO SOBRE CUERPOS AXIL-SIMÉTRICOS

Las mallas de cálculo son absolutamente determinantes en la solución numérica en el cálculo del flujo alrededor de una configuración aeronáutica. Desafortunadamente para un ingeniero teórico, aún no es posible tener una solución independiente de la malla, al menos para una configuración tan simple como es un cuerpo axil-simétrico. Para alas, es posible tener soluciones más o menos independientes a partir de un determinado grado de refinado, particularmente para la sustentación o momento de cabeceo. Y existen métodos de extrapolación -con el número de nodos como variable- bastante precisos para poder determinar los coeficientes aerodinámicos con un buen grado de precisión. Sin embargo, en los cuerpos axil-simétricos a altos ángulos de ataque se ha comprobado experimentalmente que la rugosidad o pequeñas y microscópicas irregularidades son suficientes para activar una inestabilidad convectiva. El resultado no es sólo un flujo asimétrico, con fuerzas laterales de magnitud importante, sino que éstas dependen del ángulo de orientación; es decir, son función de la distribución de las irregularidades y de la rugosidad, que se convierte en un parámetro vital, tanto como el número de Reynolds o el número de Mach. Además, existe un ángulo de ataque a partir del cual, una pequeña perturbación produce una inestabilidad global tal que existen dos soluciones posibles del flujo, una espejo de la otra, con fuerzas laterales iguales en magnitud y diferentes en signo.
Por tanto, nos debemos hacer las siguientes preguntas cuando abordamos un cálculo numérico:

I. Es posible capturar el flujo asimétrico a altos ángulos de ataque, fruto de la acción de las inestabilidades global y convectiva?
II. Qué parámetros debemos tener en cuenta para que el resultado reproduzca la realidad: número de Mach (Ma), número de Reynolds (Re), rugosidad relativa $\left(\frac{r_a}{L}\right)$

    Se necesita semejanza cinemática, dinámica y geométrica hasta niveles microscópicos. Las ecuaciones de Navier-Stokes permiten soluciones bi-estables en función de las perturbaciones iniciales.
III. Las inestabilidades numéricas en forma de turbulencia de la corriente libre y otras, reproducen la inestabilidad real del flujo tal que a veces se tendrá una solución de fuerza lateral negativa y otras veces positiva?
IV. Se podrá capturar el flujo detectado experimentalmente en cuerpos esbeltos en los que existen dos o tres zonas definidas en barlovento, una en el morro de flujo estacionario y las otras atrás; de flujo fluctuante con un número de Strouhal tendiendo al de los cilindros en flujo cruzado en las zonas traseras?

Utilizaremos un código RANS con un modelo de turbulencia avanzado –ω-RSM-SAS- en muchos de los casos estudiados, que ha sido esbozado en la introducción y es robusto y menos disipativo, y ha demostrado mayor capacidad de resolución que otros modelos; en

particular los basados en la hipótesis de Bousinessq para la viscosidad [1], [20-23], [25].

3. CONFIGURACIÓN OJIVA-CILINDRO A BAJA VELOCIDAD

La primera configuración estudiada dispone de abundante información experimental: es una ojiva-cilindro ensayada por ONERA (Office National d'Etudes et de Recherches Aérospatiales) [19], [26]. El modelo es un cuerpo cilíndrico de 120 mm de diámetro con una ojiva tangente de 3 calibres. La longitud total es de 15 calibres (*L/D = 15*). Este cuerpo fue ensayado en el túnel presurizado ONERA F1 en Le Fauge-Mauzac (France). Las condiciones del flujo para el caso de referencia eran número de Mach (Ma) 0.2, número de Reynolds basado en el diámetro $Re_D = 2\times10^6$ y ángulo de ataque $\alpha = 45.43$ deg.

Muy importante para las comparaciones teóricas es el hecho de que dos modelos con diferente rugosidad fueron ensayados. El primer modelo tenía una rugosidad media de 0.1 μm, mientras que el segundo tenía mucha mayor rugosidad; estaba pintado y con 354 tomas de presión distribuidas en 22 secciones. Se usó también para visualizaciones [2], [4]. El diámetro del modelo computacional era D = 1 m. La temperatura del aire es T = 288 K y la presión fue ajustada para obtener un número de Reynolds similar al de los experimentos. Para este estudio numérico, las condiciones del caso de referencia son Ma = 0.20, $Re_D = 2.2\times10^6$ y $\alpha = 45.00$ deg.

4. CONFIGURACIÓN BOMBA M823 A RÉGIMEN TRANSÓNICO

La otra configuración es una bomba clásica -M823 bomb- que se compone de un cuerpo axil-simétrico y un grupo de cuatro aletas [27-28]. Se utilizaron dos modelos para los ensayos en túnel, a escala 1:10. Un esquema de la configuración se muestra en la Figura 1.

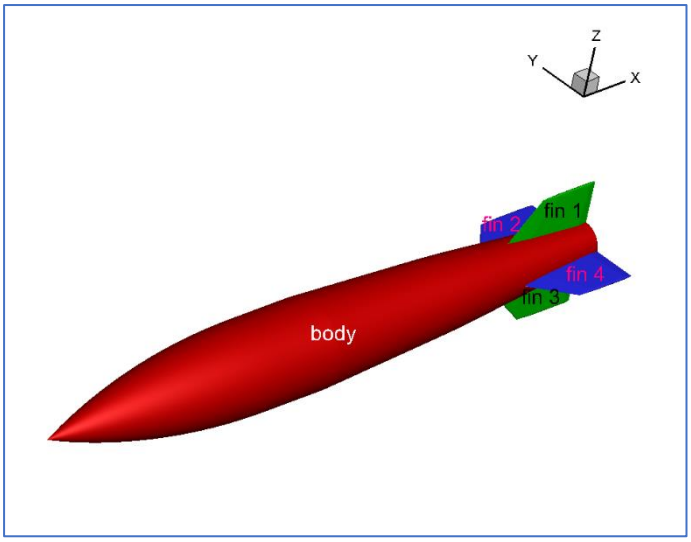

Figura 1. Bomba M823: esquema de la configuración.

Los cálculos se realizan para atmósfera ISA con las condiciones:

- Altitud h = 10000 m, Presión p_∞ = 26500 Pa.
- Temperatura T_∞ = 226 ºK, Número de Mach (Ma) = 0.85.

El número de Reynolds es: $\mathrm{Re}_D = \dfrac{\rho_\infty \cdot v_\infty \cdot D}{\mu_\infty}$ siendo D el diámetro máximo. Éste tiene el valor: D = 0.47625 m (18.75 pulgadas). Como todos los cálculos se hacen a la misma altitud el número de Reynolds es $\mathrm{Re}_D = 3.4\times10^6$. Existe información experimental acerca de ensayos en dos túneles diferentes (NOL y ARA) que está en la referencia [27]. Eso sí, el número de Reynolds era menor: $\mathrm{Re}_D = 6.48\times10^5$

5. MALLAS ESTRUCTURADAS Y NO ESTRUCTURADAS

Existen las mallas estructuradas y no estructuradas para realizar cálculos numéricos. En el caso de cuerpos axil-simétricos las mallas estructuradas son sencillas de realizar, pudiendo generar una 2D y luego girarla para tener por definición axil-simetría. Para cuerpos tipo la bomba M823 que incorpora 4 aletas, sería necesario realizar mallas multi-bloques para que puedan ser estructuradas. Otra forma más sencilla es generar mallas híbridas no estructuradas, compuestas por prismas y tetraedros. Estas mallas son intrínsecamente asimétricas. Así pues, para el primer caso de ojiva-cilindro se pueden generar los dos tipos de malla. La estructurada claramente será axil-simétrica pero en función del número de celdas y de la definición de la punta, la malla de superficie tendrá de alguna manera una rugosidad numérica, que se irá reduciendo con el incremento de densidad de la malla, y dependerá también del alargamiento de las celdas en la malla de superficie. Si la inestabilidad global del flujo depende solamente de las condiciones de éste y del ángulo de ataque, es de esperar no encontrar dependencia de las fuerzas laterales con el ángulo de orientación, pero deben encontrarse las dos soluciones bi-estables. Eso no significa que no exista inestabilidad convectiva si hay rugosidad, pero debe añadirse a la global de forma axil-simétrica. Sin embargo, con las mallas no estructuradas esto es más complicado, dado que son asimétricas intrínsecamente, y puede encontrarse dependencia de las fuerzas con el ángulo de orientación. Asimismo, la generación de la punta es mucho más compleja y tendrá un peso mayor e influencia en el flujo calculado. Medir de alguna manera el grado de asimetría y rugosidad de estas mallas de superficie que simulan al cuerpo con un número finito de celdas, es muy importante para valorar nuestra precisión en los cálculos.

5.1. Malla estructurada de la ojiva-cilindro

Una malla 2D se generó, y luego rotada sobre el eje longitudinal se generó la malla 3D. La malla se compone de 450·240·140 nodos. Esto es, 450 celdas en dirección longitudinal, 240 en dirección azimutal y 140 en dirección radial. Al usar esplines cúbicas para interpolar la ojiva, en la punta se generaron algunas oscilaciones de curvatura, pero axil-simétricas. Es equivalente a tener alguna rugosidad en dirección longitudinal. En la Figura 2 se muestra un detalle de esta malla estructurada. La altura de la primera celda en dirección radial era 10^{-5} m lo que lleva a valores de y^+ de orden 1 o menor.

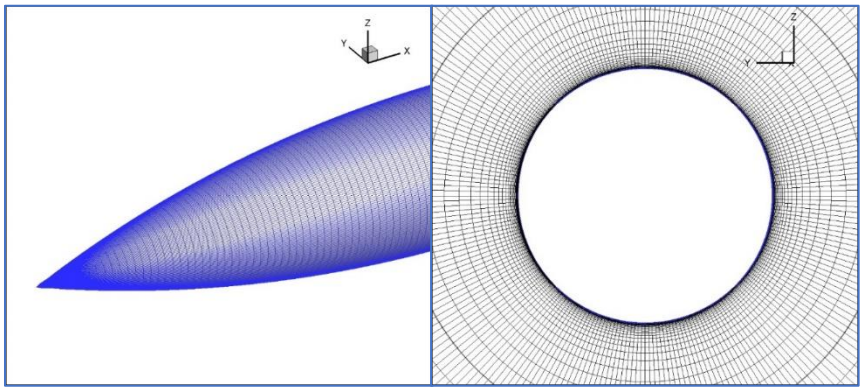

Figura 2. Detalle de la malla estructurada de la ojiva-cilindro Izquierda: región de la nariz. Derecha: plano transversal y-z.

5.2. Mallas no estructuradas de la ojiva-cilindro y bomba M823

Se han generado varias mallas híbridas para la ojiva-cilindro y también para la bomba M823; en este caso se usaron dos generadores de malla diferentes, en los que uno de ellos genera mallas menos irregulares como se verá. En la Figura 3 se muestra un detalle de una malla híbrida no estructurada.

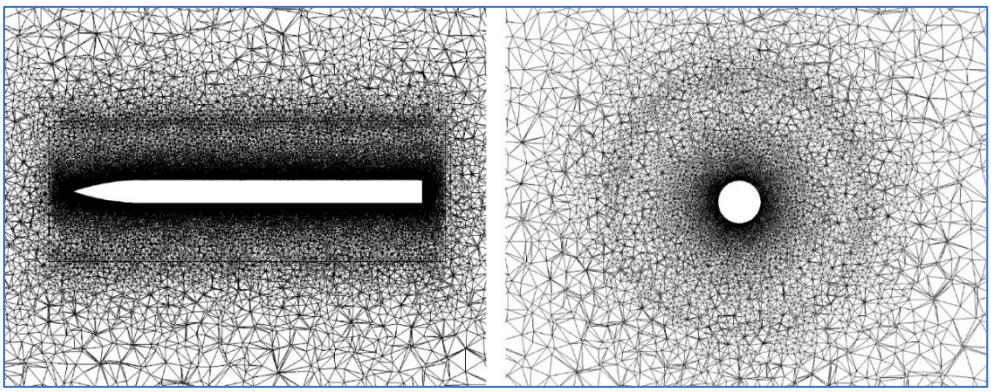

Figura 3. Detalle de una malla no estructurada de la ojiva-cilindro Izquierda: campo cercano en el plano x-z. Derecha: plano transversal y-z.

En la Tabla 1 se muestran algunas características de las mallas generadas para las dos configuraciones. La malla S1 es la malla estructurada de la ojiva-cilindro. El resto son mallas híbridas no estructuradas. La malla de superficie de la malla U2 ha sido derivada de la malla de superficie de la malla U1. Los nodos se han movido tal que cumplan lo más posible la ley ideal del cuerpo, reduciendo así la "rugosidad numérica". Esto se muestra más adelante. Adicionalmente, la malla MU2 ha sido derivada de la malla MU1 realizando el mismo procedimiento de ajuste, para tener una geometría más axil-simétrica y regular que la de la malla MU1. La malla MU3 ha sido generada diferente a las otras, utilizando otro generador de

malla (código Centaur©).

Grid	Surface elements	Prismatic layers	Number of faces	Number of cells
Grid (S1)	78720	-	45114720	15012000
Grid (U1)	196612	48	37346792	16240213
Grid (U2)	196612	48	37333372	16233653
Grid (U3)	236722	48	89205448	38880331
Grid (MU1)	215840	48	32226602	13459149
Grid (MU2)	215840	48	32222496	13457096
Grid (MU3)	106712	48	23362843	10539527

Tabla 1. Características de las malla generadas para la ojiva-cilindro y bomba M823.

5.3. Irregularidades geométricas de las mallas de superficie

Las mallas de superficie están definidas por un número finito de nodos. En nuestro caso varía de 78720 nodos en la estructurada S1 a 236722 nodos en la malla U3, si bien los de la malla estructurada están simétricamente distribuidos en dirección azimutal. La rugosidad se puede definir de varias maneras, una de ellas es: $Ra = \frac{1}{N}\sum_{i=1}^{N}|Z_i|$ siendo Z_i la altura respecto a la altura media en la región de muestra. Se puede medir en dirección longitudinal o azimutal. En lugar de usar una definición de rugosidad estándar, usaremos un cálculo de la siguiente manera: en primer lugar medimos la separación del cuerpo ideal axil-simétrico. En diferentes anillos de espesor $2\Delta(x/D)$ determinamos los nodos que están contenidos y evaluamos a su posición longitudinal su radio real –definido como $r(x_i) = \sqrt{y_i^2 + z_i^2}$, y lo comparamos con el radio ideal $r_{ideal}(x_i)$-definido por la ley que define al cuerpo- a esa posición longitudinal. En el caso de la bomba no hacemos esto para las aletas, que no son cuerpos axil-simétricos; tan sólo para el cuerpo, porque a valores altos de ángulo de ataque o con puntas de la nariz mal definidas, el efecto en los torbellinos de punta será enorme y la influencia en el flujo global es grande, pues afecta a la intensidad de la interacción con las aletas.

La diferencia $diff(x_i) = \left(r(x_i) - r_{ideal}(x_i)\right)$ y el valor de su integral en cada anillo - $Dif(x) = \int_{x=cte} diff(x_i)\cdot dr$ - nos da una medida de la separación de la malla de superficie respecto la ideal. En las regiones de la ojiva en las que el radio no es constante con la coordenada longitudinal, esta medida es más compleja de hacer y depende del tamaño del

anillo y la densidad de malla, pero nos da una idea buena de la asimetría en esta región. Este valor $diff\,(x)$ se representa en la Figura 4 para la ojiva-cilindro y las diferentes mallas. Con respecto a la malla estructurada S1 hemos de decir que en la ojiva-cilindro por razones prácticas se utilizó un radio de 0.495 m en lugar de 0.5 m, por lo que la separación del radio ideal en realidad es mínima (se ve en la zona cilíndrica a partir de x/D = 3.0).

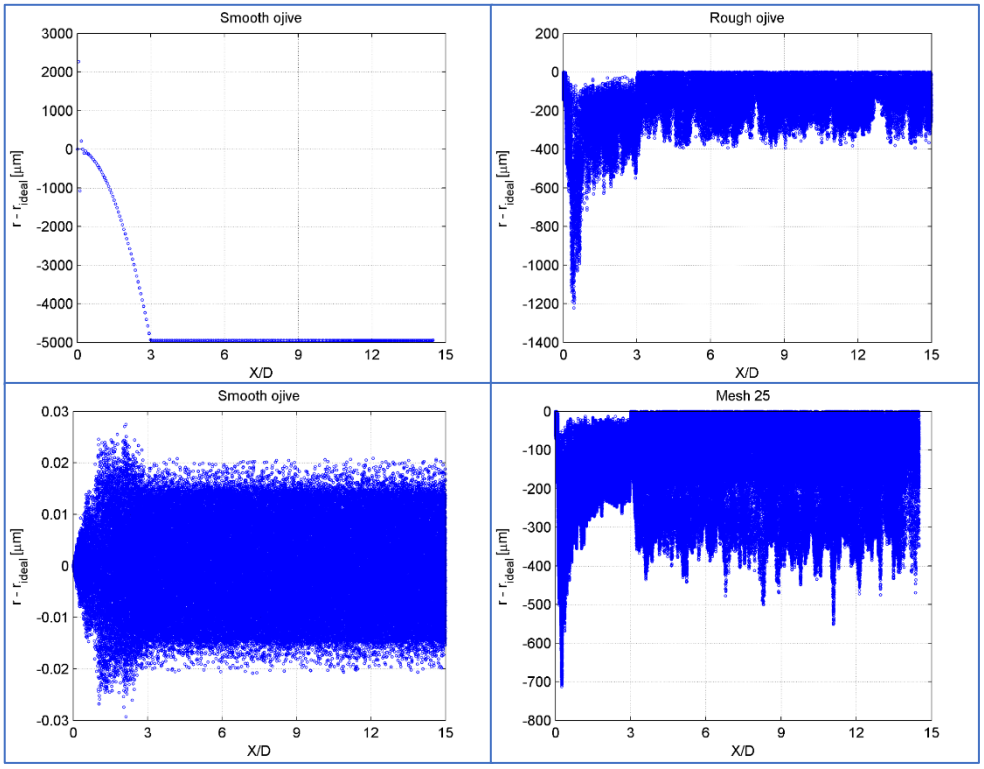

Figura 4. Valor *diff (x)* en función de la coordenada longitudinal para la ojiva-cilindro. Arriba izquierda: Malla S1. Arriba derecha: Malla U1. Abajo izquierda: Malla U2. Abajo derecha: Malla U3.

Con respecto a las mallas U1 y U2 hemos de decir que la malla de superficie de la U2 muestra realmente una "rugosidad numérica" mínima con respecto a la malla U1. Pero, es muy importante remarcar que **no solamente es importante que la malla no tenga rugosidad**, sino su densidad y la forma en la punta. Veremos más adelante que hay efectos del ángulo de orientación en las fuerzas con la malla U2 tan importantes como con la malla U1 debido a que la punta no está bien definida, porque hay muy pocos nodos. Esto se ve en la figura siguiente (Figura 5). Vemos que en la sección x/D = 0.05 cerca de la punta hay 240 nodos que la definen si se usa la malla S1 (izquierda, Figura 5). Y están distribuidos axil-simétricamente. El resultado es que no habrá efectos del ángulo de orientación en las fuerzas y momentos. Sin embargo, aunque la sección x/D = 0.05 define un polígono más cercano a una circunferencia con la malla U3 (derecha, Figura 5) que si se usa la malla U2 (centro, Figura 5), no están distribuidos axil-simétricamente en ningún caso, y su número

es mucho menor que 240 (nodos de la sección de la malla S1). Una lección sacada del procedimiento interno de generación de mallas híbridas es que las mallas no estructuradas deben ser mucho más densas en la punta, además de buscar una reducción de su "rugosidad numérica".

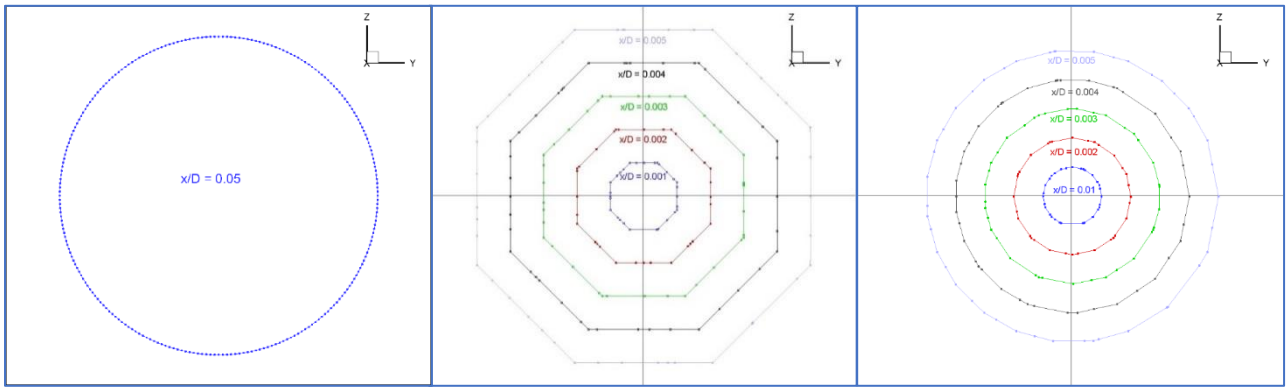

Figura 5. Izquierda: sección x/D = 0.05 de la malla S1 (240 nodos). Centro: Secciones x/D = 0.01 hasta x/D = 0.05 de la malla U1. Derecha: Secciones x/D = 0.01 hasta x/D = 0.05 de la malla U2.

Con relación a la bomba, se ha hecho algo similar. La malla MU1 es con diferencia la más irregular y con mayor "rugosidad numérica". La malla MU2 –realizada suavizando la malla MU1- es más suave, pero su punta sigue estando pobremente definida e influye en la determinación de los torbellinos de barlovento generados en la nariz. La malla MU3 tiene poca densidad de malla pero es más suave y su punta está mejor definida que las otras. La razón es la utilización de un generador de malla –código Centaur©- que permite generar mallas más continuas y con mejor métrica. En la Figura 6 se muestra la nariz de las mallas de superficie MU1, MU2 y MU3. Se puede ver que la MU1 es muy irregular, y la MU3 a pesar de ser menos densa, es más simétrica.

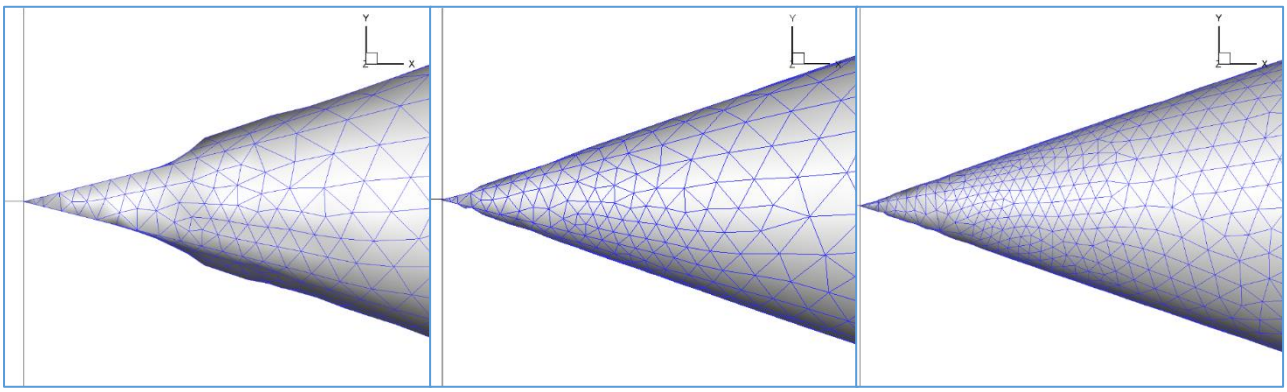

Figura 6. Detalle de la malla de superficie (x/D < 0.05) en la nariz de la bomba M823. Izquierda: Malla MU1. Centro: Malla MU2. Derecha: Malla MU3.

En la Figura 7 se muestran los valores $diff(x_i) = \left(r(x_i) - r_{ideal}(x_i)\right)$ en la región cilíndrica de la bomba (x/D = 3.0) para las mallas MU1 y MU3.

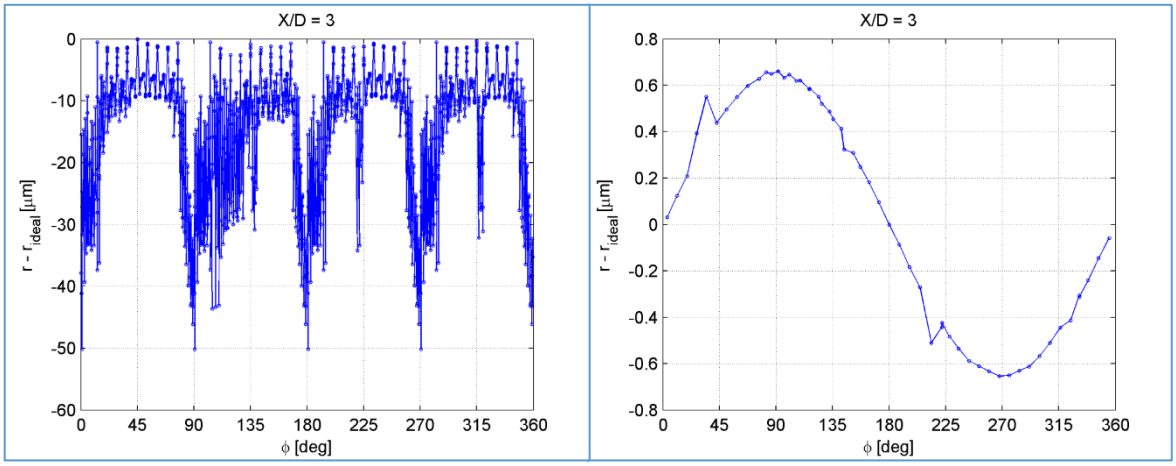

Figura 7. Valor *diff (x)* en la sección x/D = 3.0 de la bomba M823. Izda: Malla MU1. Dcha: Malla MU3.

6. INESTABILIDADES GLOBAL Y CONVECTIVA

Tal como se ha definido en el capítulo 1 (Introducción), a altos ángulos de ataque se ha comprobado experimentalmente que el flujo desarrolla sobre cuerpos axil-simétricos un patrón asimétrico bi-estable debido a una inestabilidad global del flujo. Pequeñas perturbaciones del flujo dan como resultado un par de torbellinos no simétricos, bien orientados a babor o estribor y con resultado global de una fuerza lateral de una magnitud igual y diferente signo según la orientación de la perturbación inicial. Además, cuerpos con una rugosidad importante o con irregularidades, sobre todo en la punta, desarrollan fuerzas que dependen del ángulo de orientación o azimut. Estas irregularidades contribuyen a la aparición de una inestabilidad geométrica o convectiva.

6.1. Inestabilidad global: patrón bi-estable

La malla estructurada S1 se ha construido para un cuerpo puramente axil-simétrico y es axil-simétrica con rugosidad numérica muy pequeña y de tamaño medio (unos 15 millones de celdas). Los cálculos realizados con esta malla [29-30] a diferentes ángulos de orientación a un ángulo de ataque alto, por encima del ángulo de ataque de aparición de asimetría, llevaron a la conclusión de que numéricamente es posible capturar la solución bi-estable. Son las condiciones iniciales y pequeñas oscilaciones numéricas las que determinan la solución negativa o positiva. En la referencia [29] se muestran soluciones de fuerza lateral iguales en magnitud pero de distinto signo según el ángulo de orientación. Y también, dos soluciones de distinto signo al mismo ángulo de orientación pero con diferentes condiciones iniciales. En un caso, la condición inicial era del mismo signo, y en el otro se produce un

salto a la solución espejo durante el transitorio numérico.
Se realizaron nuevos cálculos numéricos no estacionarios usando el modelo de turbulencia *ω-RSM-SAS* [1], [20-23], [25] a la condición $M_\infty = 0.2$, $Re_D = 2 \cdot 10^6$ y ángulo de ataque α = 45 deg. El paso de tiempo elegido fue $\Delta t = 5 \cdot 10^{-4}\ s$. Con esa malla y paso de tiempo, los valores de y^+ en la primera celda del cuerpo eran de orden 1 y los valores del número de Courant CFL eran menores a 5 en las regiones de interés. Conviene remarcar nuevamente que una característica del modelo de turbulencia elegido es su capacidad para una variación continua de soluciones de tipo LES a RANS dependiendo del paso de tiempo y los tamaños de las celdas de la malla [1], [20-23].
En la Figura 8 se muestran las historias de los coeficientes de fuerzas lateral y normal para cuatro ángulos de orientación. Para el de referencia (Φ = 0 deg.), el tiempo total de cálculo fue el doble que en los otros.
Un análisis PSD (Power Spectral Density) dio valores medios del coeficiente de fuerza lateral entre C_S = [2,97, 3.1] y para el coeficiente de fuerza normal C_N = [7.79, 7.83]. Son variaciones pequeñas, pero las de fuerza normal un orden de magnitud menor que las de fuerza lateral.

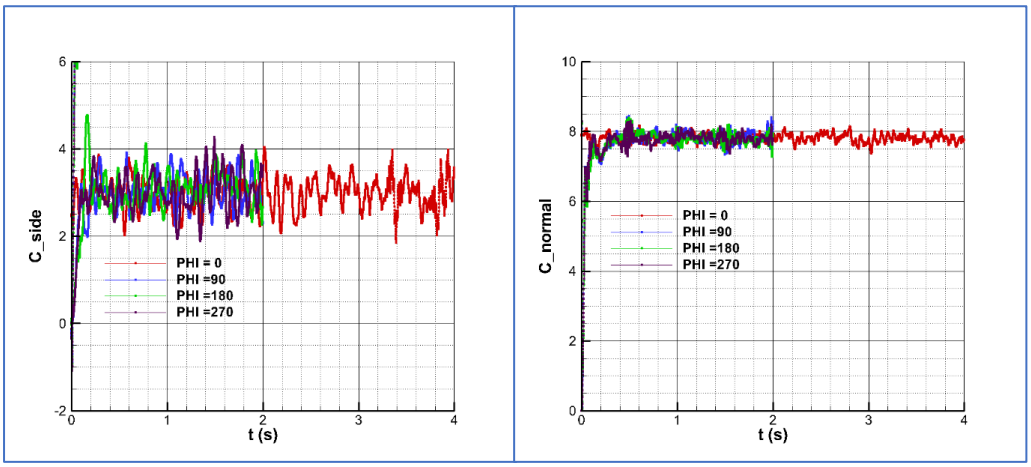

Figura 8. Historia temporal del coeficiente de fuerza lateral (izquierda) y normal (derecha) de la configuración ojiva-cilindro a Ma = 0.2, $Re_D = 2 \cdot 10^6$ y α = 45 deg. a diferentes ángulos de orientación. Malla S1.

El análisis del espectro de frecuencias de la fuerza lateral indica un número de Strouhal que variaba algo según el ángulo de orientación en un valor $St \approx 0.156$-0.2. En la referencia [26] se menciona que el número de Strouhal experimental de esta configuración era St = 0.160. El efecto del ángulo de orientación en el número de Strouhal es mayor. Pero hemos de tener en cuenta que el tiempo de cálculo es bajo. Para una predicción correcta de la parte de baja frecuencia del espectro de las fuerzas se necesita un tiempo de integración grande, según especifica Egorov [23].

6.2. Inestabilidad convectiva: dependencia con el ángulo de orientación

A las mismas condiciones de flujo, y usando los mismos esquemas y modelos de turbulencia que para la malla estructurada S1, se hicieron cálculos con las mallas U1, U2 y U3. Se ha mencionado antes que la malla U2 es más suave que la U1, al haber sido modificada a partir de la U1. Y que la malla U3 es más densa, en particular en la punta del cuerpo, por lo que las secciones transversales son más circulares que las de las otras mallas, a la misma coordenada longitudinal. Pero, es claro que el flujo cruzado encuentra esquinas y celdas deformadas con alargamientos grandes en direcciones longitudinal y normal, y cómo puede afectar al cálculo del flujo se muestra en las siguientes figuras. La Figura 9 muestra los valores medios absolutos de los coeficientes de fuerzas lateral y normal a ocho diferentes ángulos de orientación o azimut.

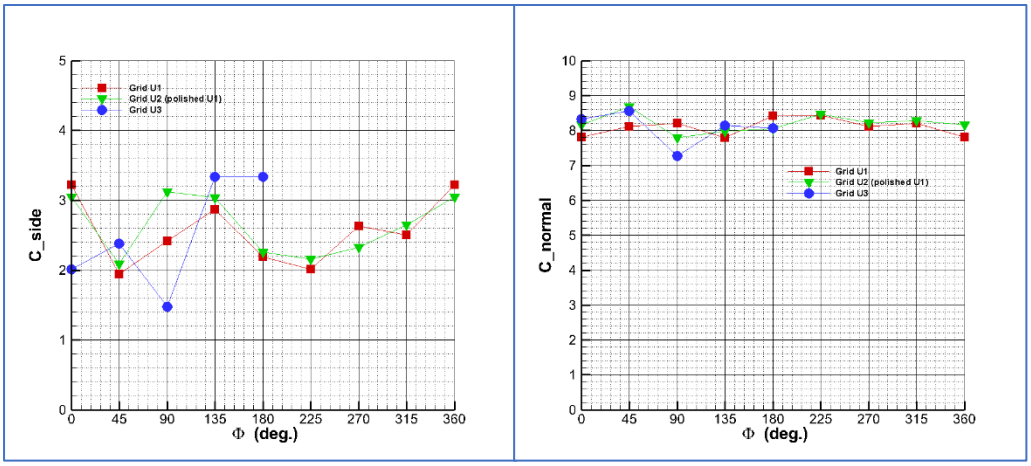

Figura 9. Valores medios absolutos de los coeficientes de fuerza lateral (izquierda) y normal (derecha) de la configuración ojiva-cilindro a Ma = 0.2, $Re_D = 2 \cdot 10^6$ y α = 45 deg. a diferentes ángulos de orientación. Mallas U1, U2 y U3.

Como sucede con la malla estructurada S1, la variación de la fuerza normal es un orden de magnitud inferior a la de la fuerza lateral. La fuerza normal es independiente de la asimetría a derechas o izquierdas de los torbellinos. Pero ahora, los valores medios del coeficiente de fuerza lateral oscilan entre C_S = [1.47, 3.34] y para el coeficiente de fuerza normal C_N = [7.78, 8.54]. Son variaciones que llegan al 100% entre un ángulo de orientación y malla (U3 y Φ = 90 deg.) y otra malla y ángulo (U3, Φ = 180 deg.).

Se puede calcular un valor medio del coeficiente de fuerza lateral para cada malla tal que $\left|C_{Yavg}\right| = \frac{1}{N}\sum_{i=1}^{N}\left|C_{Yi}\right|$. Una expresión similar se usa para la fuerza normal.

Para la malla U1 este valor es $\left|C_{Yavg}\right| = 2.4725$ y para la fuerza normal es $\left|C_{Zavg}\right| = 8.1362$. En

el caso de la malla U2 estos valores son $\left|C_{Yavg}\right| = 2.5845$ y $\left|C_{Zavg}\right| = 8.2022$. No son muy distintos entre sí. Sorprendentemente, la curva del coeficiente de fuerza lateral de la malla U2 no difiere demasiado de la de la malla U1. Se esperaba que el procedimiento de suavizado reduciendo la rugosidad numérica fuertemente tuviera influencia en hacer las curvas de coeficientes de fuerzas independientes del ángulo de orientación en forma parecida a la de la malla estructurada. Pero, no ha sido así porque la región de la punta de la nariz, que tiene una influencia decisiva en el patrón del flujo, está pobremente definida. La malla estructurada está siempre definida en cada sección por 240 nodos en dirección de azimut, mientras que la no estructurada tiene pocos nodos en la punta y muchos más al alejarse, pero no uniformemente distribuidos. Es importante señalar que se han hecho cálculos a un número limitado de ángulos de orientación. Es posible que estos valores tiendan a asemejarse si el número de casos de prueba aumenta. Con relación a la malla U3, que es más densa y tiene una forma más ideal que las otras en la nariz, los valores que obtenemos son $\left|C_{Yavg}\right| = 2.5029$ y $\left|C_{Zavg}\right| = 8.0649$.

Aunque por falta de espacio no se muestra aquí, otro efecto de las mallas no estructuradas es reducir el ángulo de ataque de comienzo de asimetría a valores en torno a $\alpha_{onset} \approx 20$ deg. para las mallas U1 y U2, y $\alpha_{onset} \approx 25$ deg. para la malla U3. Para la malla estructurada este valor se ha determinado en $\alpha_{onset} \approx 34$ deg. Hemos de recordar que el valor empírico para la ojiva es $\alpha_{onset} \approx 2 \cdot \delta_{nose} = 37.84$ deg. Experimentalmente se ha demostrado que las maquetas rugosas tienen un ángulo de ataque de comienzo de asimetría bastante menor que el de las maquetas pulidas [2], [19]. Por tanto, esto nos indica que las mallas no estructuradas semejan a cuerpos rugosos o con irregularidades grandes, tales que la inestabilidad convectiva es suficientemente intensa para que a valores más bajos de ángulos de ataque que los ideales relacionados con la geometría de la punta comience el flujo asimétrico, que se superpone a partir de determinado ángulo de ataque a la inestabilidad global intrínseca del flujo. Las mallas estructuradas capturan solamente la inestabilidad global a valores cercanos a los teóricos, obtenidos de correlaciones basadas en ensayos.

7. EFECTO DEL ÁNGULO DE ORIENTACIÓN EN LA INTERACCIÓN CUERPO ALETA PARA LA BOMBA M823

Hemos visto la importancia de la punta del cuerpo en el desarrollo de un patrón de torbellinos asimétricos en barlovento, y el efecto de las irregularidades geométricas, en forma de excentricidades o rugosidad numérica, que reproducen teóricamente algunas de las observaciones y mediciones experimentales sobre cuerpos pulidos y rugosos, o cuerpos con irregularidades añadidas, especialmente en la nariz. Estos cálculos son cálculos no estacionarios y con un modelo de turbulencia de alto nivel: ω-RSM-SAS.

En el caso de la bomba M823, este es un cuerpo axil-simétrico compuesto de ojiva-cilindro-flare y cuatro aletas. A altos ángulos de ataque existe interacción del par de torbellinos que se inician en el morro con las aletas. Es muy importante la configuración en este caso: las aletas van desde una posición cruciforme con orientación + (ángulo de orientación Φ = 0 y Φ = 90 deg.) a una posición cruciforme con orientación x (ángulo de orientación Φ = 45

deg.) pasando por una intermedia (Φ = 22.5 o Φ = 67.5 deg.).
Los cálculos se realizaron a la condición Ma = 0.85, $Re_\infty = 3.4 \cdot 10^6$ y varios ángulos de ataque en el rango {0.30} y tres ángulos de orientación [0, 22.5, 45]. Se usaron dos modelos de turbulencia: k-ω SST (eddy-viscosity) y RSM y cálculos estacionarios.
En la Figura 10 se muestran los resultados de los coeficientes de fuerza normal y de momento de cabeceo (sobre el centro de gravedad) para las mallas MU1 y MU2 a los tres diferentes ángulos de orientación.

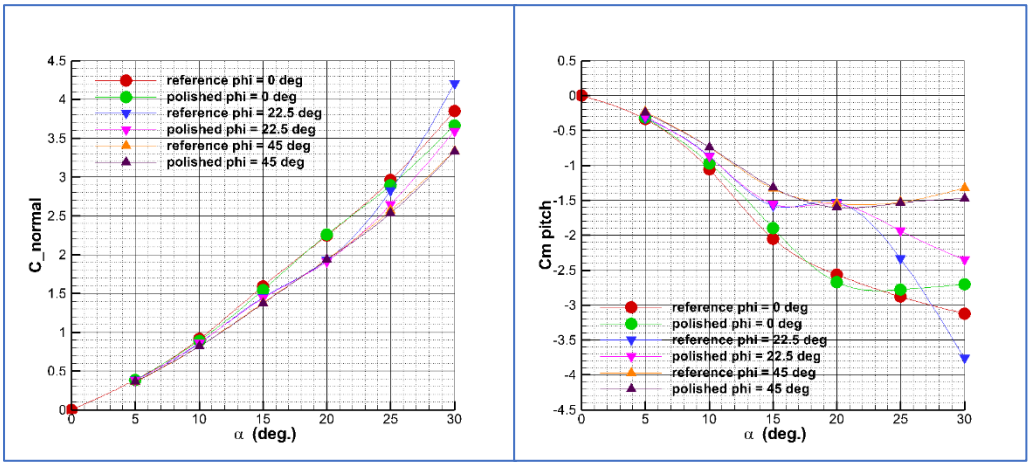

Figura 10. Coeficientes de fuerza normal (izquierda) y momento de cabeceo (derecha) de la configuración M823 a Ma = 0.85, $Re_D = 3.4 \cdot 10^6$ y varios ángulos de ataque a diferentes ángulos de orientación. Mallas MU1 y MU2.

Hay algo fundamental en esta figura, que se observa también en la figura de fuerza lateral (no mostrada). A la condición de ángulo de orientación Φ = 22.5 deg. las diferencias de los resultados de las dos mallas son muy importantes a partir del ángulo de ataque α = 25 deg. A ese ángulo aparece una fuerza lateral muy importante si se usa la malla MU1 mientras que con la malla MU2 esa fuerza lateral es bastante menor. La siguiente figura (Figura 11) aclara lo que ocurre, en relación al efecto de malla. Se muestran los coeficientes de fuerza normal y de momento de cabeceo (sobre el centro de gravedad) para las mallas MU2 y MU3 a los tres diferentes ángulos de orientación, comparados con datos experimentales (obtenidos a un número de Reynolds algo más bajo).
Los resultados de la malla MU3 -generada con el código Centaur©- se ajustan más a los datos experimentales. Y los de la malla MU2 se parecen más a los de la malla MU3 a partir de los ángulos de ataque altos.
La Figura 12 muestran los contornos de función Q positiva (junto a líneas de fricción en el cuerpo) para la condición de ángulo de ataque más alto (α = 30 deg.) y la condición de ángulo de orientación donde las soluciones son más dispares entre sí; esto es, Φ = 22.5 deg. A esa condición, con la malla MU1 se genera en la nariz del cuerpo un par de torbellinos muy asimétrico, y el más intenso (babor) interacciona fuertemente con la aleta 4 (ver Figura 1), provocando además de fuerza lateral, momentos de guiñada y de balance grandes. También

contribuye a una mayor fuerza normal, básicamente debida al cuerpo. Sin embargo, con la malla MU2 (en la que la punta se ha suavizado) los torbellinos son más similares, reduciéndose ampliamente la interacción con la aleta 4, que se compensa con la de la aleta 1 en parte, y se reduce la fuerza normal, al ser este par de torbellinos menos intenso. En las configuraciones con ángulos de orientación $\Phi = 0$ y $\Phi = 45$ deg. los torbellinos son más simétricos también para la misma configuración MU1, y además la interacción de éstos con las aletas es mínima a $\Phi = 45$ deg., haciendo más similares las soluciones de las dos mallas.
Por tanto, la falta de una buena definición de la punta genera una solución que se aleja de la experimental a medida que el ángulo de ataque se incrementa.

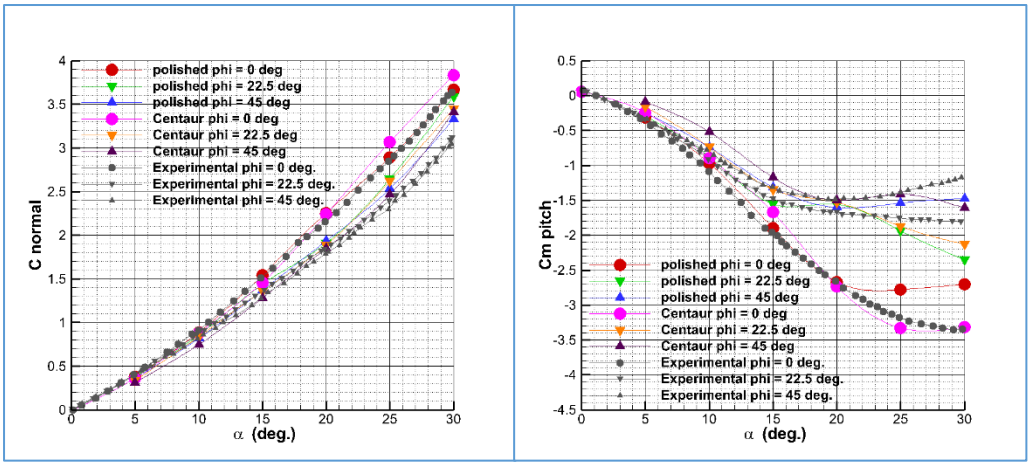

Figura 11. Coeficientes de fuerza normal (izquierda) y momento de cabeceo (derecha) de la configuración M823 a Ma = 0.85, $Re_D = 3.4 \cdot 10^6$ y varios ángulos de ataque a diferentes ángulos de orientación. Mallas MU2 (polished) y MU3 (Centaur) y datos experimentales.

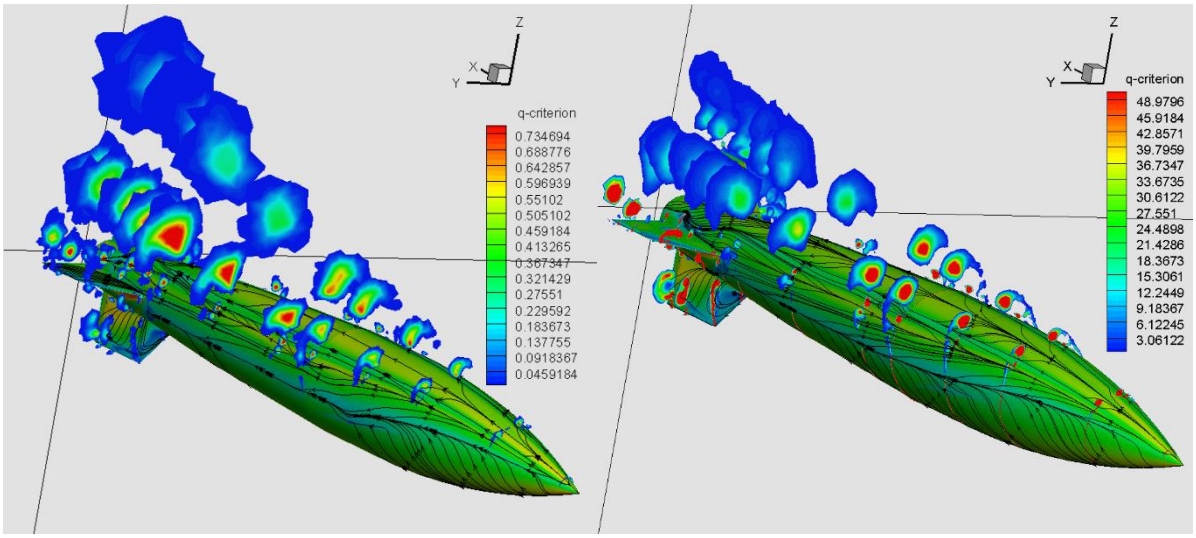

Figura 12. Contornos de función Q positiva y líneas de fricción de la configuración M823 a Ma = 0.85, $Re_D = 3.4 \cdot 10^6$ y $\alpha = 30$ deg.; ángulo de orientación $\Phi = 22.5$ deg. Mallas MU1 (izda) y MU2 (dcha).

8. CONCLUSIONES

La Aerodinámica Computacional (CFD) es actualmente una buena herramienta para la determinación del flujo sobre diversas configuraciones aeronáuticas. Esto es posible siempre y cuando se usen mallas finas, métodos de alto orden y modelos de turbulencia de alto nivel. Sin embargo, el flujo sobre cuerpos axil-simétricos y misiles es aún un problema no bien resuelto. La causa es que a altos ángulos de ataque estas configuraciones desarrollan un patrón de flujo asimétrico, debido a la actuación de dos inestabilidades, una intrínseca al flujo, de naturaleza no viscosa, y otra debida a las imperfecciones geométricas y rugosidad del cuerpo, que tiene una influencia decisiva. En particular, los efectos de la nariz son muy importantes a la hora de desarrollar un par de torbellinos asimétricos, que están influidos por la propia orientación del cuerpo. En el caso de misiles y/o bombas, en los que hay varias aletas de control y de estabilización, la interacción de los torbellinos con las aletas es también decisiva y las fuerzas laterales, así como los momentos de guiñada o balance, varían mucho dependiendo de las condiciones y la geometría. Reproducir numéricamente esto requiere de mallas de cálculo muy finas y sobre todo, que sean uniformes y axil-simétricas en todo el cuerpo, pero especialmente en la punta.

En este trabajo se ha mostrado la influencia de la malla de cálculo en el flujo sobre el cuerpo. Pequeños cambios llevan a cambios muy importantes en los valores de las fuerzas y momentos, por lo que la precisión y confianza en los resultados numéricos queda cuestionada si no se comprueban todos los posibles efectos.

La diferencia de la malla estructurada con respecto a las mallas híbridas es clara con respecto a los cuerpos axil-simétricos; en configuraciones de misiles las mallas estructuradas son posibles si se generan mallas multibloques, por lo que en general se usan mallas híbridas no estructuradas. Para evitar tiempos de cálculos muy elevados, se deben usar mallas medianas, pero se ha de tener mucho cuidado en la modelización de la punta y tener una estimación de las irregularidades geométricas. Conviene usar varias mallas para valorar mejor la dispersión de soluciones, y tener en lo posible datos experimentales que guíen el procedimiento a seguir. Es necesario seguir modelizando y afinando los métodos.

7. REFERENCIAS

[1] F.R. Menter, J. Schütze, K.A. Kurbatskii, M. Gritskevich and A. Garbaruk, “Scale-Resolving Simulation Techniques in Industrial CFD”, in *6th AIAA Theoretical Fluid Mechanics Conference*, 27-30 June 2011, Honolulu, Hawaii, https://doi.org/10.2514/6.2011-3474.

[2] P. Champigny, “High Angle of Attack Aerodynamics”, in *AGARD R-804 Special Course on Missile Aerodynamics*; Specialized Printing Services Limited: Loughton, UK, pp 5-1 5-19, 1994.

[3] P. Champigny, “Side Forces at high angles of attack. Why, When, How?”, *La Recherche Aerospatiale*, nº 4, pp. 269-282, 1994.

[4] P. Champigny, “Reynolds Number Effect on the Aerodynamics Characteristics of an Ogive-Cylinder at high Angles of Attack”, in *AIAA 2nd Applied Aerodynamics Conference*, Seattle, WA, USA, 1984. https://doi.org/10.2514/6.1984-2176.

[5] L.E. Ericsson, J.P. Reding, "Vortex Induced Asymmetric Loads in 2-D and 3-D Flows", in *AIAA 18th Aerospace Sciences Meeting*, Pasadena, California, USA, 1980. https://doi.org/10.2514/6.1980-181

[6] D.H. Bridges, "The Asymmetric Vortex Wake Problem-Asking the Right Question", in *36th AIAA Fluid Dynamics Conference and Exhibit*, San Francisco, CA, USA, 2006. https://doi.org/10.2514/2006-3553.

[7] B.L. Hunt, "Asymmetric Vortex Forces and Wakes on Slender Bodies", in *AIAA 9th Atmospheric Flight Mechanics Conference*, San Diego, CA, USA, 1982. https://doi.org/10.2514/6.1982-1336.

[8] S.E. Ramberg, "The effects of Yaw and Finite Length upon the Vortex Wakes of Stationary and Vibrating Circular Cylinders", *Journal of Fluid Mechanics*, Vol. **128**, pp. 81-107, (1983). https://doi.org/10.1017/S0022112083000397.

[9] D. Degani, M. Tobak, "Numerical Experimental and Theoretical Study of Convective Instability of Flows over Pointed Bodies at Incidence", in *29th Aerospace Sciences Meeting*, Reno, Nevada, USA, 1991. https://doi.org/10.2514/6.1991-291.

[10] G. Zilliac, D. Degani, M. Tobak, "Asymmetric Vortices on a Slender Body of Revolution", *AIAA Journal*, Vol **29**, nº 5, (1991). https://doi.org/10.2514/3.59934.1-2.

[11] D. Degani, "Development of nonstationary Side Forces along a Slender Body of Revolution at Incidence", *Physical Review Fluids*, Vol **7**, 124101, (2022). https://doi.org/10.1103/PhysRevFluids.7.124101.

[12] B-F. Ma, Y. Huang, X.-Y. Deng, "Dynamic Responses of Asymmetric Vortices over Slender Bodies to a rotating tip perturbation", *Exp. Fluids 2016*, 57:54, (2016). https://doi.org/10.1007/s00348-016-2139-3.

[13] S. Mahadevan, J. Rodríguez, R. Kumar, "Effect of Controlled Imperfections on the Vortex Asymmetry of a Conical Body at high Incidence", in *35th AIAA Applied Aerodynamics Conference*, Denver, Colorado, USA, 2017. https://doi.org/10.2514/6.2017-3240.

[14] J. Taligoski, E. Fernández, A. Uzun, R. Kumar, "Study of the Roll Orientation Effects on Vortex Asymmetry of a Conical Forebody at high Angles of Attack", in *53rd AIAA Aerospace Sciences Meeting*, Kissimmee, Florida, USA, 2015. https://doi.org/10.2514/6.2015-0547.

[15] J. Taligoski, E. Fernández, R. Kumar, "Experimental Investigation of Vortex Asymmetry on a Conical Forebody at High angles of Incidence", in *52nd AIAA Aerospace Sciences Meeting*, National Harbor, Maryland, USA, 2014. https://doi.org/10.2514/6.2014-0051.

[16] J. Taligoski, A. Uzun, R. Kumar, "Numerical Investigation of Vortex Asymmetry on a Conical Forebody at High angles of Incidence", in *52nd AIAA Aerospace Sciences Meeting*, National Harbor, Maryland, USA, 2014. https://doi.org/10.2514/6.2014-0052.

[17] R. Kumar, T. Kumar Guha, R. Kumar, "Role of Secondary shear-layers Vortices in the Development of Flow Asymmetry on a cone-cylinder Body at High Angles of Incidence", *Experiments in Fluids (2020)*, 61:215, (2020). https://doi.org/10.1007/s00348-020-03045-y.

[18] K. Wei, S. Chen, Y. Xu, D. Tang, "Influence of roughness on the Asymmetric Flow Field of a Slender Body", *International Journal of Aerospace Engineering*, Vol **2022**,

(2022). https://doi.org/10.1155/2022/6590152.
[19] J. R. Deane, "An Experimental and Theoretical Investigation into the Asymmetry Vortex Flow Characteristics of Bodies of Revolution at High Angles of Incidence in low Speed Flow", *GARTEUR TP 109 (also BT 16482).* Final Report of Group for Aeronautical Research and Technology in Europe GARTEUR-AG04 (1984).
[20] F. R. Menter, Y. Egorov, "A Scale Adaptive Simulation Model using Two Equation Models", in *43rd Aerospace Sciences Meeting and Exhibit*, Reno, Nevada, USA, 2005. https://doi.org/10.2514/6.2005-1095.
[21] F.R. Menter, Y. Egorov, "The Scale-Adaptive Simulation Method for Unsteady Turbulent Flow Predictions. Part I: Theory and Model Description", *Flow Turbulence Combustion (2010)* **85**:113-138, June 2010. https://doi.org/10.1007/s10494-010-9264-5.
[22] F. R. Menter, M. Kuntz, R. Bender, "A Scale Adaptive Simulation Model for Turbulent Flow Predictions", in *41st Aerospace Sciences Meeting and Exhibit*, Reno, Nevada, USA, 2003. https://doi.org/10.2514/6.2003-767.
[23] Y. Egorov, F.R. Menter, R. Lechner, D. Cokljat, "The Scale-Adaptive Simulation Method for Unsteady Turbulent Flow Predictions. Part II: Application to Complex Flow", *Flow Turbulence Combustion (2010)* **85**:139-165, June 2010. https://doi.org/10.1007/s10494-010-9265-4.
[24] M. Tormalm, J. DeSpirito, C. Schnepf, E. Dikbaş, "The Influence of Scale Resolving Simulation in Predictions of Vortex Interaction about a Generic Missile Airframe" in *AIAA SciTech Forum (2022)*, San Diego, California, USA, 2022. https:/doi.org/10.2514/6.2022-1685.
[25] ANSYS FLUENT "Theory Guide" pp. 92-95 Release 19.1. ANSYS Inc. Southpointe 2600 ANSYS Drive, Canonsburg, PA 15317, USA (2018).
[26] B.B. Prananta, S. Deck, P. d'Éspiney, A. Jirasek, A. Kovak, M. Leplat, C. Nottin, K. Petterson, I. Wrisdale, "Numerical Simulation of Turbulent and Transonic Flows about Missile Configurations", *Final Report of Group for Aeronautical Research and Technology in Europe GARTEUR (AD) AG42 (NLR-TR-2007-704)*. (2007).
[27] F.J. Regan, J.H.W. Shannon, F.J. Tanner, "The joint NOL/RAE/WRE Research Programme on Bomb Dynamics Part III. A Low-Drag Bomb with Freely Spinning Stabilizers", *WRE Report-904 (WR&D)*, Department of Supply, Australian Defence Scientific Service, Salisbury, South Australia (1973).
[28] N.E. Gilbert, "The Use of Rate Gyroscopes in the Free Flight Measurement of Aerodynamic Lateral Force and Moment Coefficients", *Technical Note HAS 164*, Department of Supply, Australian Defence Scientific Service, Salisbury, South Australia (1973).
[29] J. Jiménez Varona, "Flujo Asimétrico alrededor de Cuerpos de Revolución a Altos Ángulos de Ataque", *Tesis Doctoral*, Universidad Nacional de Educación a Distancia (UNED), Madrid (2021).
[30] J. Jiménez-Varona, G. Liaño, "Numerical Study of the Influence of the Geometrical Irregularities on Bodies of Revolution at high Angles of Attack", *Computation 2022, 10, 173*. MDPI (2022). https://doi.org/10.3390/computation10100173.

Congress on Numerical Methods in Engineering 2024
4-6 September 2024, University of Aveiro, Portugal

FIRE IN ROAD TUNNELS. THE INFLUENCE OF THE HEAT RELEASE RATE IN THE SMOKE FLOW

Ulisses Fernandes[1], João C. Viegas[1] and Pedro J. Coelho[2]

1: LNEC, Laboratório Nacional de Engenharia Civil
1700-099 Lisbon, Portugal
e-mail: ufernandes@lnec.pt, jviegas@lnec.pt

2: IDMEC, Instituto de Engenharia Mecânica, Mechanical Engineering Department
Instituto Superior Técnico
Universidade de Lisboa
1049-001 Lisbon, Portugal
e-mail: pedro.coelho@tecnico.ulisboa.pt

Keywords: Tunnel fire, natural ventilation, wind, *fireFoam*, smoke propagation, CFD

Abstract *Fire accidents in road tunnels may cause a significant number of fatalities and severe damages in the tunnel structure. The tunnel European directive [1] applies to trans-European road network and requires the use of active smoke control systems for most tunnels longer than 500 m. Research has been carried out to investigate if shorter tunnels are safe when the smoke flow occurs due to buoyancy [2, 3]. The FireFoam computer code has been used to model the Memorial Tunnel fire ventilation tests [4] and validate the tunnel model. This model was used to produce a set of simulations to investigate the effect of the wind velocity and of the tunnel slope on the smoke buoyant flow.*

In a first step, the effect of the wind velocity on the smoke flow in a horizontal tunnel showed that the contamination of the lower layer (where the people egress) with smoke may start as close as 138 m from the fire source [2]. This contamination (depending on its intensity) may impair the visibility disturbing the people egress, and may cause intoxication and, eventually, death. In a second step, the effect of the slope (without wind) may increase the tendency to the lower layer contamination [3], when compared to the horizontal tunnel. Lower layer contamination may start as close as 210 m to fire source. An analytical model has been developed to predict the distance from the fire source where the lower layer contamination with smoke may occur.

In this communication, the effect of the variation of the heat release rate (HRR) both with and without wind is studied in the same tunnel model. It shows that, although the velocity due to buoyancy increases with the HRR, the location of the lower layer contamination with smoke does not vary significantly due to the increment of the flow rate. The analytical model extension to the HRR variation is also presented.

1. INTRODUCTION

Natural ventilation avoids the significant costs of mechanical ventilation in road tunnels. However, it can only be relied on as a smoke control strategy if the lower layer contamination does not happen (i.e. if the smoke remains above the occupants' height). Hence, an accurate understanding of this phenomenon under several different scenarios is important [4].
In a horizontal tunnel, the flow from a fire source is symmetrical, and the smoke forms a hot upper layer flowing from the fire plume to the tunnel portals, while a cold lower layer of outside air flows from the portals and feeds the fire plume with fresh air [3]. It is well known that the contamination of the cold lower layer with the smoke from the hot upper layer starts at some distance from the fire source, and the contaminated region increases as the smoke flows to the portals (Figure 1) [2, 3]**Erro! A origem da referência não foi encontrada.Erro! A origem da referência não foi encontrada.**. The contaminated cold lower layer flow transports the smoke to the fire, and any smoke-free zone, subsisting from the beginning in the lower layer near the fire, will eventually be fully contaminated by the smoke.

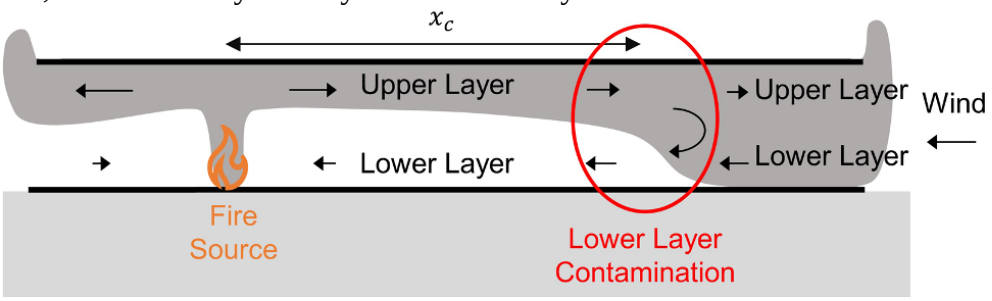

Figure 1 – Flow of smoke in a tunnel with length higher than x_c, leading to lower layer contamination [2].

The problem of the contamination of the cold layer with smoke must be analysed under three different conditions: (i) when the tunnel is completely horizontal, (ii) when the tunnel has a slope (in general, the slope does not exceed 10% and Directive 2004/54/EC [1] does not allow more than 5%) and (iii) when the wind generates a flow inside the tunnel in opposition to the smoke flow. However, most of the tunnels have a slope that, even being small, will significantly change the smoke flow and it is always necessary to consider that unfavourable wind may occur during the fire event [4]. The smoke control is used to keep the environmental conditions compatible with the occupants' safety, during the egress period of a fire, and later maintain the environmental conditions favourable for the firefighting. In this way, the smoke control may contribute to the success of the firefighting and thus prevent catastrophic consequences on the availability of infrastructure [4].
This research aims to analyse the contamination of the lower layer with smoke in horizontal tunnels with opposing wind and varying heat release rate (HRR) and this work will consider different heat release rates in the range from 6 MW to 100 MW.

2. LITERATURE REVIEW

Fires in the confined infrastructure of tunnels are critical hazards due to the potential for

fatalities and damage to the structures [5]. The tunnel European directive (Directive 2004/54/EC [1]) applies to Trans-European Road Network and states that “mechanical ventilation systems shall be installed in all tunnels longer than 1000 m with a traffic volume higher than 2000 vehicles per lane”. Therefore, there are many tunnels in Europe where the flow of smoke in the event of a fire is controlled by natural ventilation. Research has been carried out to investigate if shorter tunnels are safe when the smoke flow occurs due to buoyancy [2, 3].

Most of the studies concerned with naturally ventilated tunnels focus on horizontal tunnels, and little research has been carried out on sloped tunnels. However, most tunnels are sloped for geographical reasons, being relevant to study the smoke flow due to fires in those tunnels. In the case of fires in naturally ventilated horizontal tunnels, there are two main flows, namely, an upper layer flow that exits the tunnel and a lower layer flow that moves towards the fire. Galhardo et al. studied the effect of the wind velocity on the smoke flow in a horizontal tunnel showing that the contamination of the lower layer (where the people egress) with smoke may start as close as 138 m from the fire source [2]. The authors concluded that this contamination (depending on its intensity) may impair the visibility disturbing the people egress, and may cause intoxication and, eventually, death [2].

Ortega et al. investigated the effect of the tunnel slope on the contamination of the cold lower layer and concluded that the slope (without wind) may increase the tendency to the lower layer contamination, when compared to the horizontal tunnel, but above a certain slope, due to the stack effect, the air entering through the lower part of the tunnel changes the fire and the flow dynamics in terms of flame, temperature, velocity and smoke layer thickness [3].

One of the largest sources of experimental data from fires in a single tunnel is the Memorial Tunnel Fire Ventilation Test Program (MTFVTP) (Bechtel and Brinckerhoff, 1995 [6]). This consisted of a series of fires with varying HRR and ventilation conditions in an 853-m long tunnel with a 3.2% slope in West Virginia, USA. Natural ventilation was tested for fires with nominal HRR of 20 MW and 50 MW.

CFD simulations have become an increasingly common tool for the study of tunnel fires. Caliendo et. al [7] analysed the impact of HRR variation from 8 MW to 100 MW on the flow of smoke in a road tunnel. Kong et al. [8] investigated the effect of tunnel slope on hot gas movement and smoke distribution in a tunnel fire. They carried out a set of fire simulations, using the Fire Dynamics Simulator (FDS) software, varying the slope from 0 to 10%. More recently, Ortega et al. investigated the effect of the tunnel slope on hot gas movement and smoke distribution in a tunnel fire. They carried out a set of fire simulations, using the CFD (FireFoam) software, varying the slope from 0 to 7% [3].

In this work, CFD simulations were performed with the goal of improving the knowledge of the physical mechanisms that lead to lower layer contamination in a naturally ventilated tunnel fire. The effect of the variation of the HRR from 6 MW to 100 MW both with and without wind is studied in the same tunnel model. It shows that, although the velocity due to buoyancy increases with the HRR, the location of the lower layer contamination with smoke does not vary significantly due to the increment of the flow rate. The effect of natural wind on the flow of smoke and on the hazard to human health was analysed by comparing

predictions from simulations with varying wind velocities.

3. METHODS

3.1. CFD model

This work is based on CFD simulations using the open-source FireFOAM software package (version 1912). This code solves the Favre-filtered, three-dimensional Navier-Stokes equations using the finite volume technique and employing the pressure-implicit with splitting of operators (PISO) algorithm. Turbulence was modelled using large-eddy simulation (LES). The governing equations for mass, momentum, energy and species mass fractions are solved.
The relevant physical phenomena of the flow were modelled using the Smagorinsky model for turbulence, the Eddy Dissipation Model for combustion, and the Finite Volume/Discrete Ordinates Method for radiation. These models were briefly described in Galhardo et al. [2].

3.2. CFD implementation

The CFD model was employed to perform a series of simulations of tunnel fires. The necessity of predicting the three-dimensional flow of smoke in regions spanning several hundred meters in length resulted in large computational domains. To limit the computational cost, the size of the computational domains under study was decreased by taking advantage of the symmetry of the mean flow: in all simulations, only one half of the tunnel width was simulated. On the other hand, the entire length of the tunnels under analysis was simulated, as well as two 50 m-long extensions outside the portals [4].
The CFD simulations were performed using an unstructured mesh. The control volumes of this are finest near the fire and coarser away from it, to ensure an accurate simulation of the complex flow in the vicinity of the fire source while avoiding excessively long computational times. The characteristic dimension of the control volumes, $\Delta=V^{1/3}$ (where V is the cell volume), was equal to 8 cm in the vicinity of the fire source, 16 cm in a transition region, and 32 cm elsewhere [4]. Figure 2 shows the mesh in the vertical symmetry plane for simulations shown in Table 1, where L is the tunnel length, P is the percentage of the time when the wind velocity adopted in the simulation is exceeded, V is the wind velocity, ΔP is the pressure difference generated by the wind between portals and v is the average velocity of the flow inside the tunnel due to wind velocity. The tunnel is horizontal.
The fire source was simulated as a horizontal rectangular surface and treated as a source of dodecane at boiling temperature with a vertical velocity calculated based on the desired HRR. At the walls, a no-slip condition with wall functions was used for velocity, while a zero-gradient condition was used for mass fractions of chemical species. An energy balance boundary condition was implemented to calculate the wall surface temperature. The gradient of all variables was set to 0 at the symmetry planes.
At the open borders, the ambient values of temperature and species mass fractions were prescribed for the case of inflow and a zero gradient boundary condition was set for the case of outflow. The variable p', which represents the pressure deviation from the hydrostatic field, had different values for outflow and inflow, according to the following equation:

$$p' = \begin{cases} p_0 - \frac{1}{2}\rho|\mathbf{u}|^2 & flow\ into\ the\ domain \\ p_0 & flow\ out\ of\ the\ domain \end{cases} \quad (1)$$

where ρ, **u** and p_o stand for the density, velocity vector and free stream pressure, respectively. The values of p_0 at the two ends of the computational domain can be adjusted to create a pressure difference between the two portals, which simulates longitudinal wind flow. In the simulations the wind is acting from right to left.

L [m]	P [%]	V [m/s]	ΔP [Pa]	v [m/s]	$HRR_{nominal}$ [MW]
600	20	3.13	3.61	1.19	100
600	35	2.04	1.54	0.771	6
600	35	2.04	1.54	0.771	15
600	35	2.04	1.54	0.771	50
600	35	2.04	1.54	0.771	70
600	35	2.04	1.54	0.771	100
600	100	0	0	0	6
600	100	0	0	0	50
600	100	0	0	0	100

Table 1 - Simulation parameters

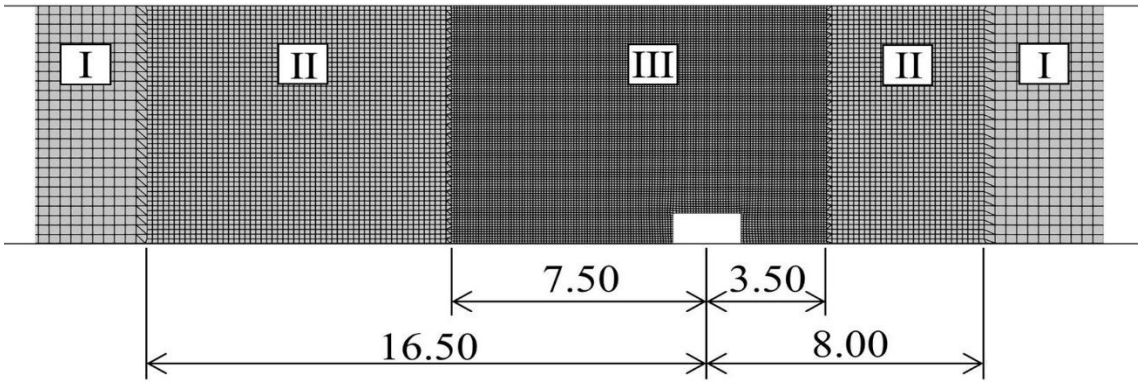

Figure 2 – Mesh refinement near the fire source in simulations (dimensions in m)

3.3. CFD validation

The CFD model was validated by simulating the test 502 of the Memorial Tunnel Fire Ventilation Test Program (MTFVTP); details about the tunnel geometry and the test conditions may be found in Bechtel and Brinckerhoff [6]. The tests were carried out for a naturally ventilated tunnel. The fire source was a pool fire of Fuel Oil No.2 (modelled as dodecane). The nominal heat release rate ($HRR_{nominal}$) was 50 MW.

Figure 2 shows the validation for the HRR of 50 MW (temperatures in Fahrenheit). The

predicted temperature field is slightly colder in comparison with the experimental data [4].

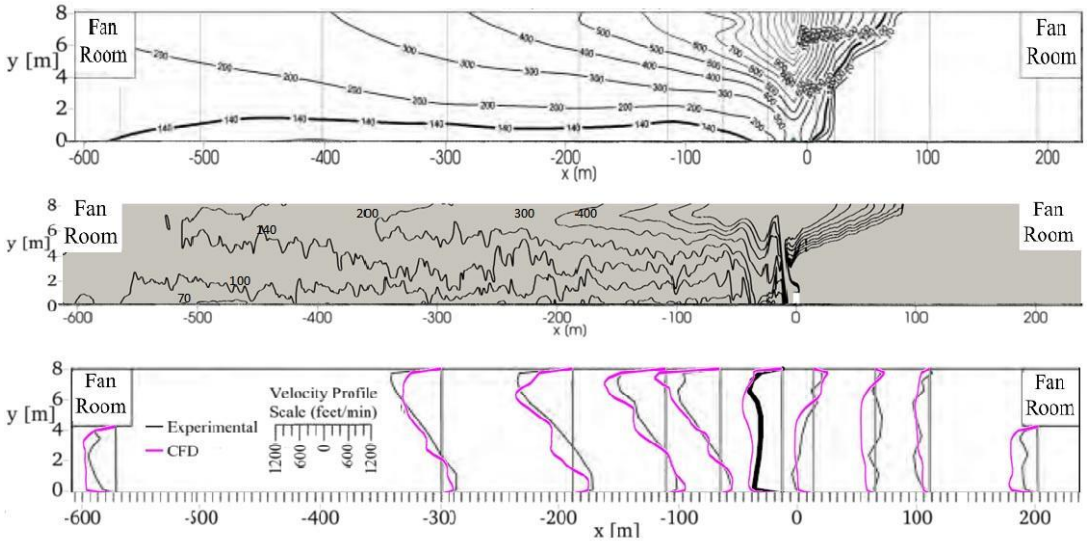

Figure 2 – Comparison of the temperature and velocity measurements obtained for the MTFVTP test 502 with the CFD predictions (natural ventilation, $HRR_{nominal}$=50 MW, t = 10 min)

4. SIMULATION RESULTS

The purpose of this work is to better understand the processes of contamination of the tunnel lower cold layer with the smoke coming from the hot upper layer, considering different conditions of HRR and velocity of the external wind.

After the validation, several cases were studied to assess the effect of the HRR in horizontal naturally ventilated fire tunnels and its impact on the distance from the fire source to the location where the contamination of the lower layer with smoke starts. CFD simulations for HRR ranging from 6 MW to 100 MW were carried out, with wind effect and without wind action and considering only natural ventilation.

Figure 3 presents the longitudinal profiles of the average temperature at the cross section of the upper layer (calculated according to the equation 2, where T_∞ is the ambient temperature, ρ is the density, u is the velocity, $\overline{Cp}$ is the specific heat at constant pressure, is the mass flow rate and A is the cross section area) and Richardson Number (Ri) along the horizontal tunnel (from fire to the portal) for simulations with varying HRR (v=0.77 m/s and P=35%). The Ri is defined in the equation 3, where h_u represents the upper layer thickness and Δρ the difference between layer densities.

$$\overline{T} = T_\infty + \frac{\int_{UL} \rho u \overline{c_p} (T - T_\infty) dA}{\dot{m} \overline{c_p}} \tag{2}$$

$$Ri = \frac{\Delta \rho g h_u}{\rho \left(|u_u| + |u_l| \right)^2} \tag{3}$$

Figure 4 presents the profiles of the same quantities for HRR=100 MW with wind (v=1.19 m/s and P=20%) and Figure 5 shows the profiles for varying HRR without wind (v=0 m/s and P=100%).
For the horizontal tunnel, the temperature decays exponentially from the fire source to the exit portal (Figures 3, 4 and 5).

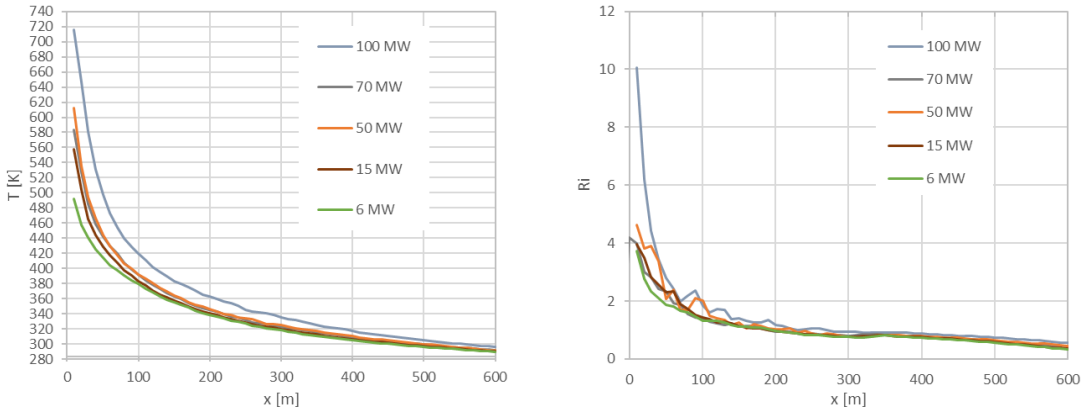

Figure 3 – Temperature and Richardson Number profiles with wind at t = 30 min (v=0.77)

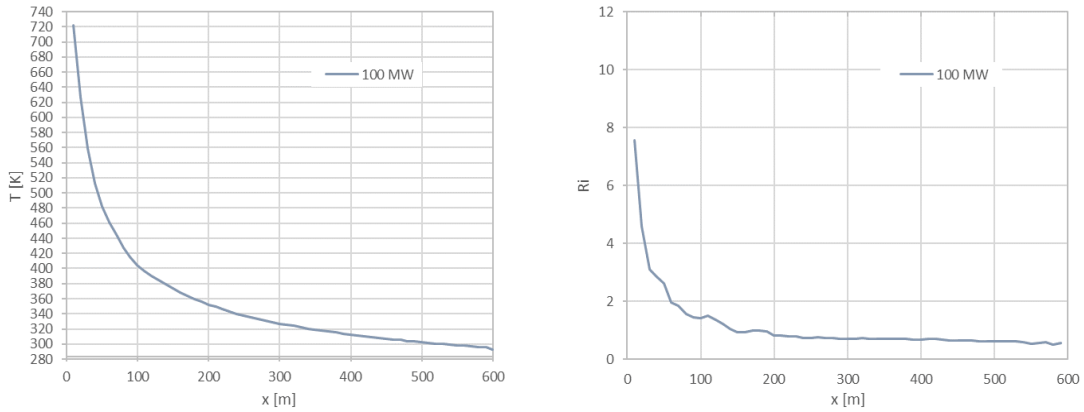

Figure 4 – Temperature and Richardson Number profiles with wind at t = 30 min (v=1.19 m/s)

Figure 6 presents the contours of soot concentration in the vertical symmetry plane for a horizontal tunnel without wind action and with wind driven velocity of v =0,77 m/s. The red line corresponds to the zero velocity; thus, it represents the boundary between the upper layer outflow and the lower layer inflow. The white lines represent soot concentration of 80 mg/m³ and 300 mg/m³, corresponding to visibility distances for reflecting signs of 5.0 m and 1.3 m, respectively.

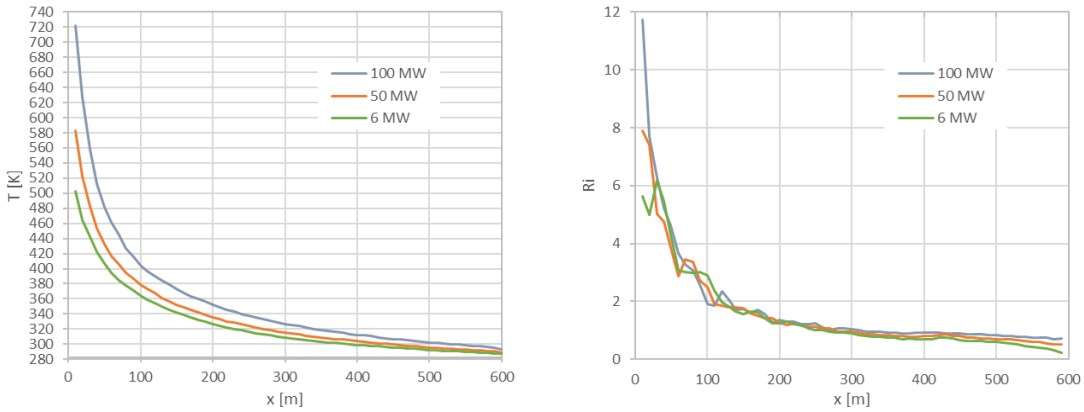

Figure 5 – Temperature and Richardson Number profiles without wind at t = 30 min (v=0 m/s)

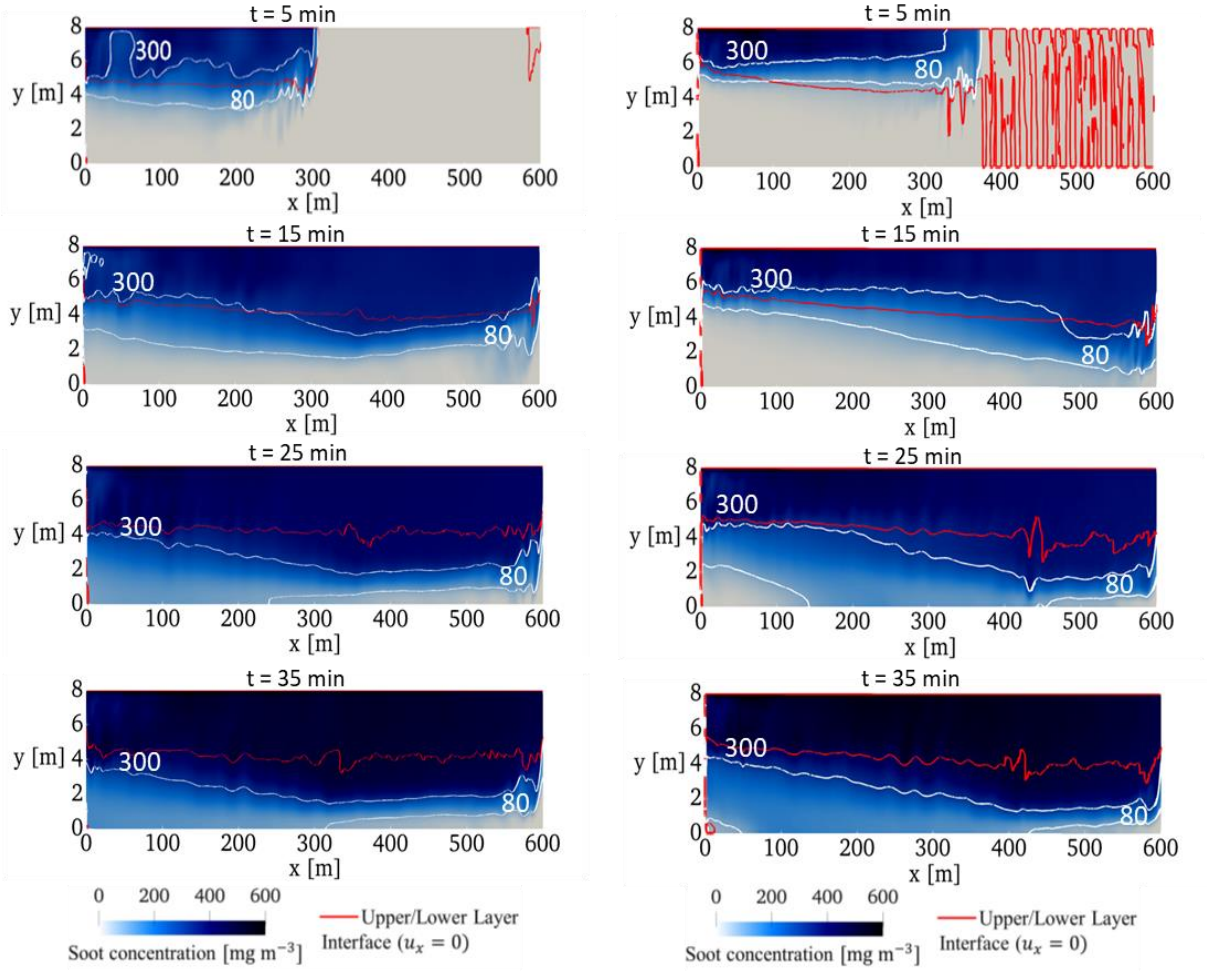

Figure 6 – Comparison of the soot concentration with wind (left), v =0.77 m/s and without wind (right), for a fire with $HRR_{nominal}$=50 MW in a horizontal tunnel

Figure 7 presents the soot concentration in the vertical symmetry plane for a horizontal tunnel with wind velocity of v =0.77 m/s for two different fire source sizes. The development of the smoke contamination is similar but is much more intense for the higher HRR. Moreover, the comparison between Figures 6 and 7 shows that the contamination of the lower inflow layer with smoke increases with the wind velocity v.

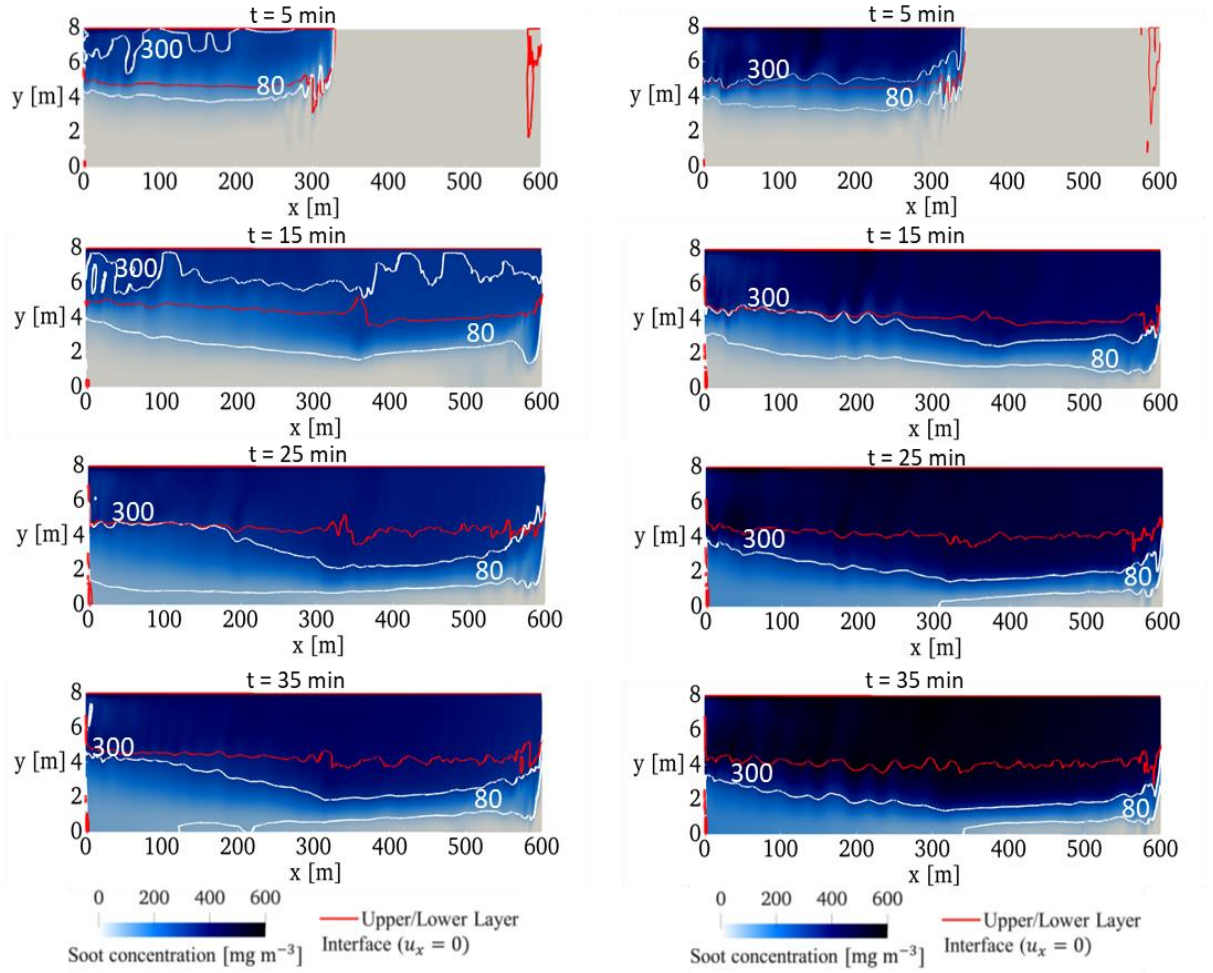

Figure 7 – Comparison of the soot concentration for $HRR_{nominal}$=15 MW (left) and $HRR_{nominal}$=70 MW (right) in a horizontal tunnel and with external wind, v =0.77 m/s

Figures 8 and 9 show the mass flow rate in the upper outflow layer, $\dot{m}$, and the difference between the velocity magnitudes in the upper and lower layers, Δu, for v=0.77 m/s (with wind) and v=0 m/s (without wind), respectively. When the outflow (higher layer) velocity magnitude is higher ($\Delta u>0$), the mass entrainment from the lower to the higher layer dominates, thus increasing the upper layer mass flow rate (left side of the figure). However, for v=0.77 m/s, $\Delta u=0$ occurs at a distance from the fire source smaller than the distance beyond which the decay of the upper layer mass flow rate occurs.

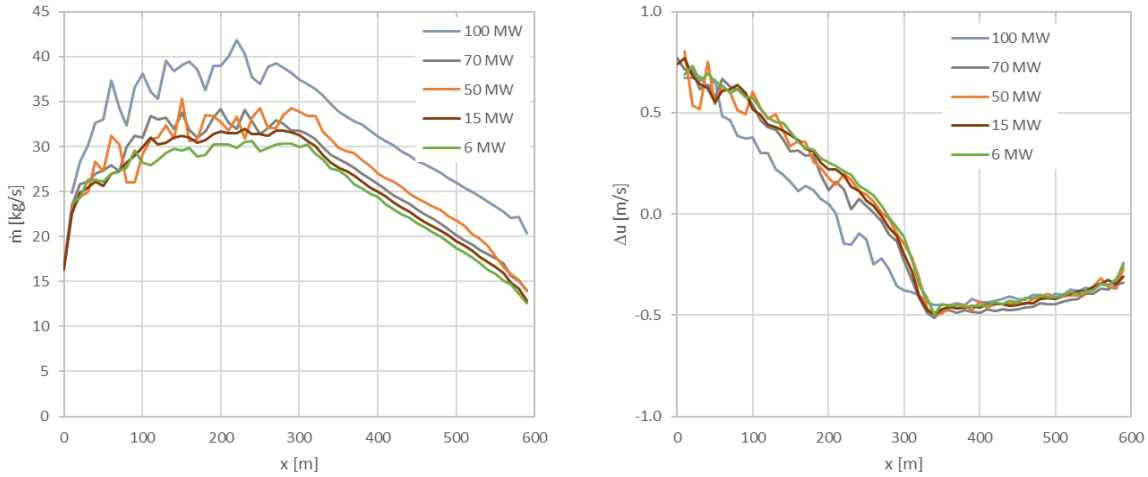

Figure 8 – Mass flow rate in the upper outflow layer, ṁ, and difference between velocity magnitudes in the upper and lower layers, Δu, at t = 30 min (v=0.77 m/s)

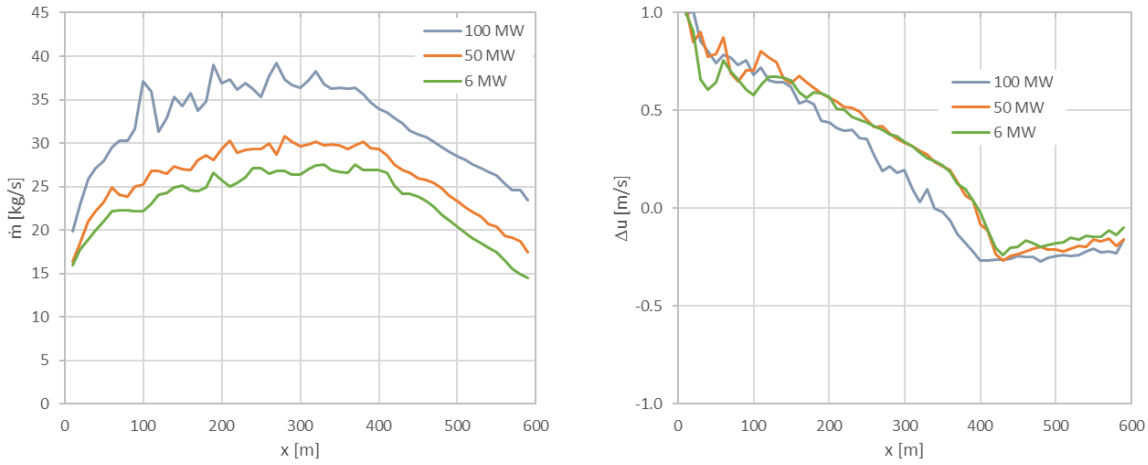

Figure 9 – Mass flow rate in the upper outflow layer, ṁ, and difference between velocity magnitudes in the upper and lower layers, Δu, at t = 30 min (v=0 m/s)

5. DISCUSSION

5.1. General

In this section, several quantities, obtained by CFD simulations, related with the lower layer contamination with smoke during tunnel fires (namely, upper layer mass flow rate, upper layer velocity and lower layer velocity) are analysed. Using the methods proposed by Galhardo et al. [2] and Ortega et al. [3], the results calculated using algebraic equations available in the

literature are compared with the CFD results to clarify the role of the influencing variables. While in the work presented by Galhardo et al. [2] a horizontal tunnel subjected to wind action was studied, Ortega et al. [3] studied the influence of the tunnel slope for the same tunnel and heat release rate. In this work, the same horizontal tunnel is used again, but different heat release rates from the fire source combined with the wind action were considered. This does not constitute a predictive model yet, because several data were taken from the CFD results, but it is intended to be a step towards an algebraic model able to predict the beginning of the lower layer contamination with smoke.

As noticed by Galhardo et al. [2], the shear layer between the upper and lower layer is responsible by the entrainment of air from the lower layer to the upper layer causing the mass transfer that increased the upper layer mass flow rate, while the upper layer absolute velocity is higher than the lower layer absolute velocity. When the upper layer absolute velocity is lower than the lower layer absolute velocity, the mass transfer from the upper layer to the lower layer dominates, and the contamination of the lower layer with smoke starts or is strengthened. Ortega et al. [3] observed that this simple criterium is not possible to apply to slopped tunnels because, due to the stack effect, the mass flow rates in the upper and lower layers are not equal. Consequently, the contamination of the lower layer with smoke starts even when the upper layer absolute velocity is higher than the lower layer absolute velocity. According to Ortega et al. [3], the mass transfer from the upper to the lower layer starts when the lower layer mass flow rate is not able to increase, due to geometric limitation of the tunnel, to satisfy the mass balance. In this section, the equations proposed by Ortega et al. [3] are used and, whenever necessary, they are adapted considering the physical constraints.

5.2. Upper layer velocity

The upper layer velocity in the vicinity of the fire is obtained from equation 4 [3]:

$$\Delta v_u = \frac{S_u \rho_\infty \left(1-\frac{T_\infty}{T_u}\right) cg - S_u f \rho_\infty \frac{T_\infty v_u^2}{2 T_u D_{H\,u}} - v_u W \rho_\infty C_\beta (v_u - v_l)}{\dot{M}_u} \Delta x \quad (4)$$

where S_u is the area of the cross-section of the upper layer, ρ_∞ is the density of air at temperature T_∞, T_∞ is the ambient air temperature, T_u is the average upper layer temperature, c is a proportionality constant, g is the acceleration of gravity, f is the friction factor, v_u is the upper layer average velocity, $D_{H\,u}$ is the upper layer hydraulic diameter, W is the width of the interface between the upper and lower layers, C_β is a model constant related to the entrainment, v_l is the lower layer average velocity and $\dot{M}_u$ is the upper layer mass flow rate.

On the right side of the equation, the first term is related with the momentum source due to buoyancy, the second one is related with the friction losses in the tunnel walls, ceiling and shear layer (between upper and lower layers) and the third term is related with the momentum losses due to mass transfer from the upper to the lower layer.

The initial velocity (v_u for x=10 m), the coefficient c (that affects the term of increment of velocity due to buoyancy) and the friction factor (f) are obtained by the least squares method best fit. The solutions obtained showed that the coefficient $C_\beta = 0$, meaning that the momentum losses due to mass transfer from the upper to the lower layer is much less relevant than the buoyancy and friction losses; therefore, the equation was simplified to equation 5:

$$\Delta v_u = \frac{S_u \rho_\infty \left(1-\frac{T_\infty}{T_u}\right) cg - S_u f \rho_\infty \frac{T_\infty v_u^2}{2 T_u D_{H\,u}}}{\dot{M}_u} \Delta x \quad (5)$$

The values obtained are presented in the Table 2 and some selected results are presented in Figure 10, where $v_u(10)$ means the value of v_u for x=10 m.

HRR [MW]	100	50	6	100	70	50	15	6	100
Wind [m/s]	0	0	0	0.771	0.771	0.771	0.771	0.771	1.19
$v_u(10)$ [m/s]	1.35	1.09	0.98	1.62	1.40	1.25	1.34	1.21	1.59
c	0.0010	0.0011	0.0011	0.001	0.002	0.002	0.002	0.002	0.0009
f	0.017	0.018	0.017	0.021	0.031	0.031	0.032	0.034	0.021

Table 2. Best fit obtained by the least squares method.

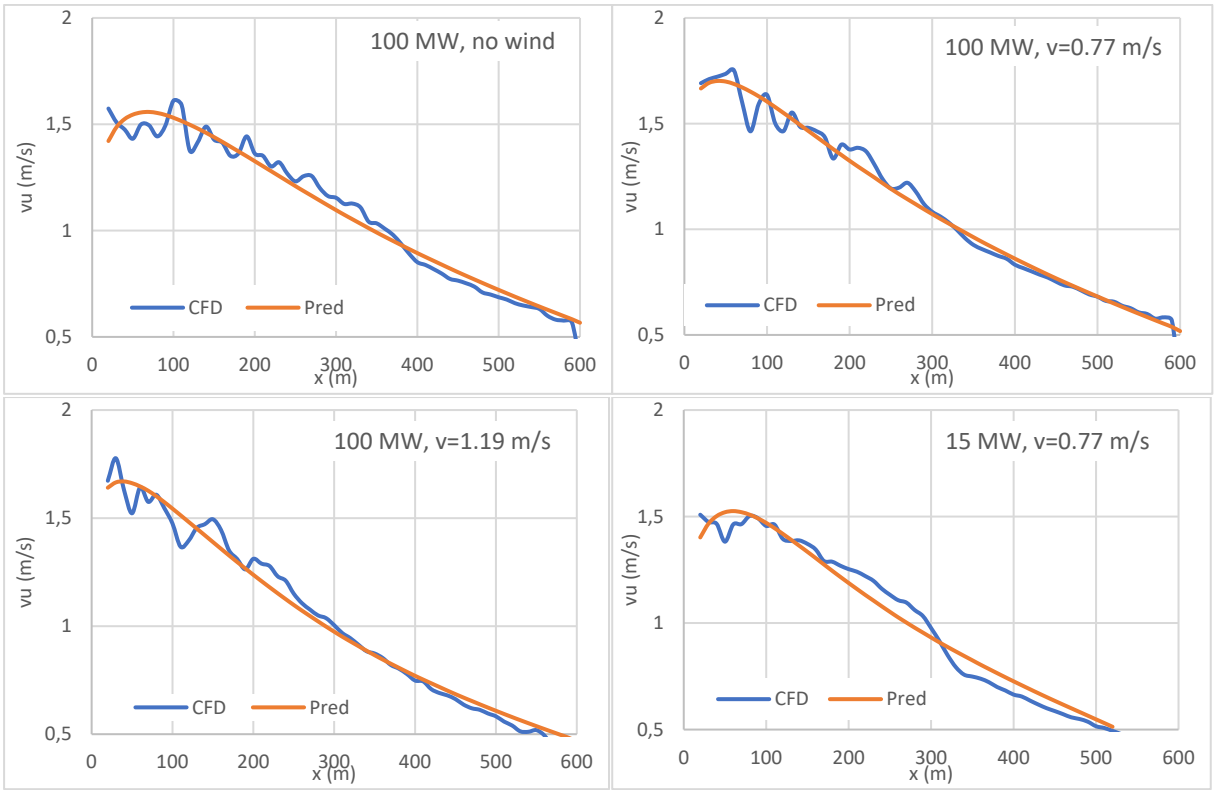

Figure 10. Comparison between the predicted (Pred2) and simulated (CFD) upper layer velocity for 100 MW (without wind, v= 0.771 m/s and v=1,19 m/s) and for 15 MW (v= 0.771 m/s).

Figure 10 shows that the upper layer velocity slightly increases close to the fire source and decreases farther downstream. The increment of the upper layer velocity as the distance from the fire increases is due to the buoyancy term, where the parameter "*c*" lies in the range of 0.0009 to 0.002. This range is about two orders of magnitude smaller when compared with the values obtained by Ortega *et al.* [3] for sloped tunnels. In our case, the tunnel is horizontal,

therefore the buoyancy effect is weaker because it is just related with the upper hot layer thickness and not with the height difference between tunnel extremities. The decrease of the upper layer velocity at a larger distance from the fire is due to the friction loss term. The friction factor lies in the range of 0.017 to 0.034. Ortega *et al*. [3] reported a range from 0.020 to 0.035, which is very similar. This factor also includes the friction losses in the shear layer between the upper and lower layers, which are not explicitly considered in Equation 5. The value f = 0.020 is currently used in tunnels with concrete walls [9]. The f value is higher for the cases under the wind action and increases when the heat release rate is reduced. The wind effect is not explicitly considered in equation 4, then the least squares fit reflects the wind effect on the friction losses term.

The Figure 10 shows that the upper layer velocity increases with the heat release rate of the fire source. The opposing wind effect reduces the upper layer velocity far from the fire source.

5.3. Upper layer mass flow rate

The initial mass flow rate is obtained from the CFD simulation for x=10 m. The upper layer mass flow rate variation is obtained from equation 6 [3]:

$$\Delta \dot{M}_u = \rho_\infty W C_\beta (v_u - v_l) \Delta x \tag{6}$$

where $C_\beta = 0.004$ is a model constant related to the entrainment coefficient β.

Figure 11 shows the prediction of the upper layer mass flow rate using equation 6. Is clear that, far from the fire source, the entrainment process is weaker, and it is not possible to express it by equation 6. Beyond some distance from the fire source, the upper layer mass flow rate decreases, meaning that the upper layer starts losing mass to the lower layer and contaminates the lower layer with smoke.

5.4. Lower layer velocity

The lower layer velocity is obtained from equation 7 [3]:

$$v_l^* = \frac{\dot{M}_u}{\rho_\infty (S - S_u)} \tag{7}$$

where S is the tunnel cross section area. This equation expresses the mass balance between the upper and the lower layer without wind and for a horizontal tunnel.

The lower layer velocity is modified by the wind effect (the wind increments the lower layer velocity). The lower layer velocity v_l was predicted by treating the flow as a superposition of a tunnel fire without wind (in which case v_l^* can be calculated by equation 7) and a wind flow without a fire (with the average velocity v inside the tunnel), according to equation 8 [2].

$$v_l = \sqrt{v_l^{*2} - v^2} \tag{8}$$

Figure (12) compares the lower layer average velocity obtained by CFD and by equations (7) and (8). As the prediction of the lower layer average velocity depends on the upper layer mass flow rate prediction, the lower layer velocity increases with x to satisfy mass balance when the upper layer mass flow rate increases (the lower layer is at ambient air temperature). Far from the fire source, the lower layer velocity predicted by Equation 8 diverges from the CFD results due to the process of mass transfer from the upper to the lower layer.

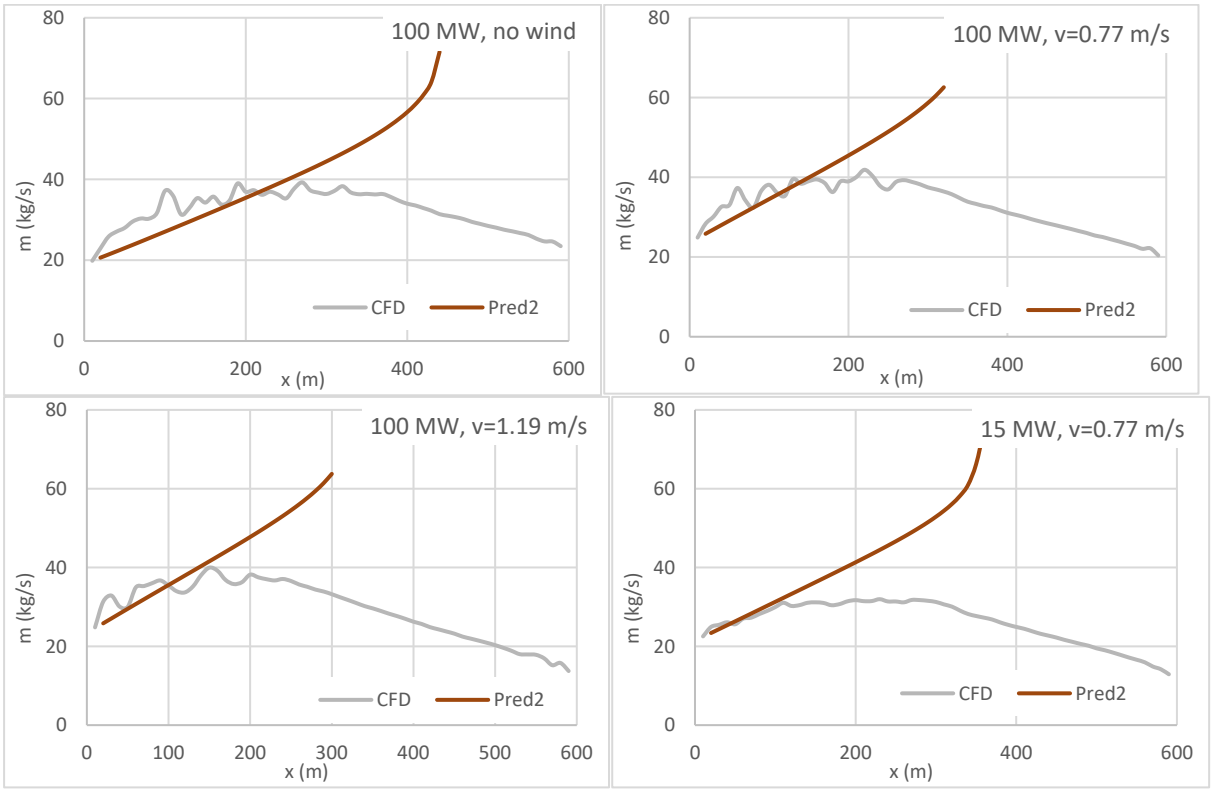

Figure 11. Comparison between the predicted (Pred2) and simulated (CFD) upper layer mass flow rate for 100 MW (without wind, v= 0.771 m/s and v=1,19 m/s) and for 15 MW (v= 0.771 m/s).

5.5. Origin of the lower layer contamination

equations (5) and (7) may be used to determine when it is physically unrealistic to consider the upper- and lower-layer flows without significant mixing. These flows are driven by the buoyancy. The maximum difference between the upper layer and lower layer velocities of the flow due to buoyancy may be predicted by the equation 9 [3]:

$$\Delta v = \sqrt{2g\left(\frac{T_u}{T_\infty} - 1\right)h_u} \tag{9}$$

The prediction of the distance x_c from the fire source where the contamination of the lower layer with smoke starts is based on the comparison between the difference of the predicted upper and lower layer velocities (using equations (5) and (7)) with the maximum difference between the upper layer and lower layer velocities of the flow due to buoyancy (equation (9)). Figure 13 shows the lines corresponding to the predicted difference between the upper layer and lower layer velocities (u_dif_pred), which is obtained using Equations (5) and (7), and the maximum allowed velocity difference due to the temperature inside the tunnel (u_dif_max), which is given by equation (9).

The blue arrows indicate the intersection of the lines u_dif_pred and u_dif_max. For large

distance from the fire source, namely beyond this intersection, it is not possible to increase the velocity difference between both layers because the buoyancy action is insufficient; therefore, the only physical solution is to transfer mass from the upper layer to the lower layer. The red arrows indicate the points where the upper layer mass flow rate starts to decrease significantly according to the CFD predictions. These points correspond to the beginning of a significant contamination with smoke of the lower layer. Table 3 compares the values of the distance x_c obtained by CFD and by the predictions from equations (5) and (7).

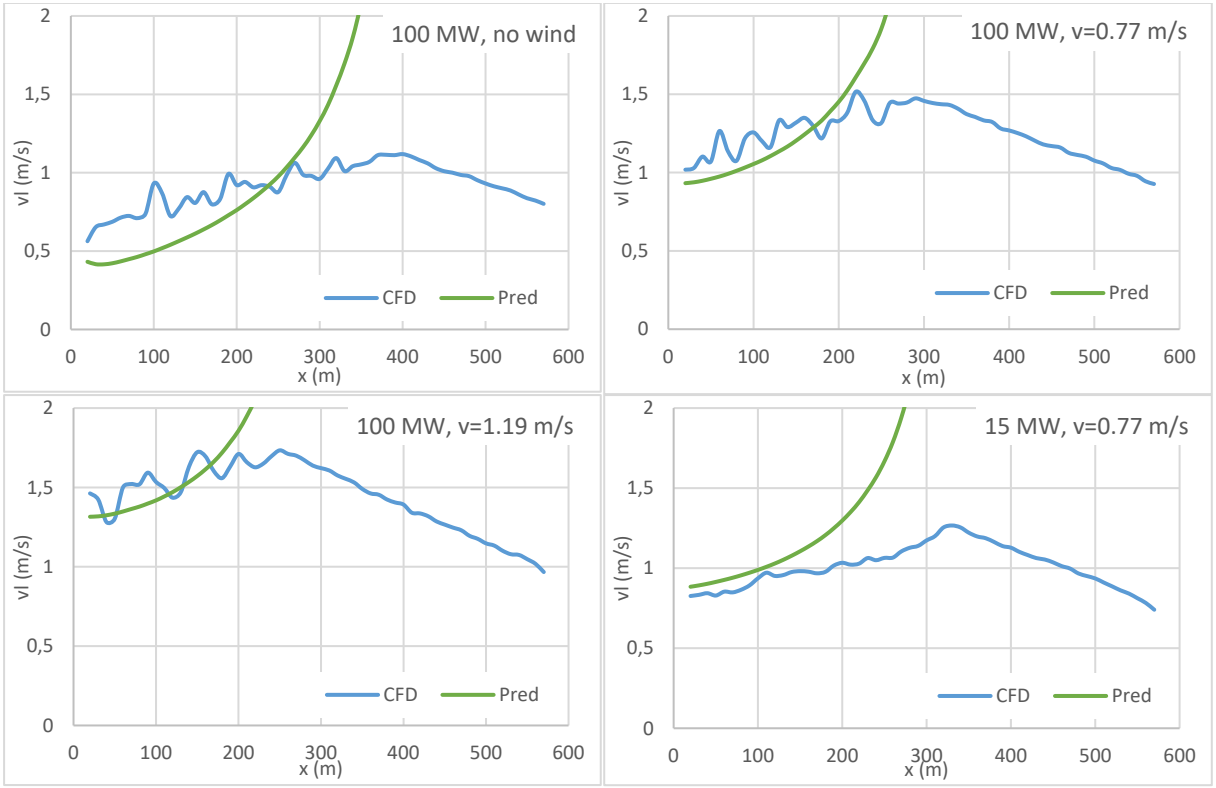

Figure 12. Comparison between the predicted (Pred2) and simulated (CFD) lower layer velocities for 100 MW (without wind, v= 0.771 m/s and v=1,19 m/s) and for 15 MW (v= 0.771 m/s).

Table 3 shows that the values of the distance x_c obtained by CFDand by the predictions from equations (5) and (7) are quite close. The relative error of the prediction based on the algebraic equations, and taking the CFD results as reference, is higher for the lower heat release rate and for the condition without wind. The predicted x_c value is always smaller than that obtained by the CFD simulations, thus it is in the safe side. The value of x_c obtained for Ri=0.8 is a general criterium that is used to assess the possibility of loss of thermal stratification when the difference of temperature between the hot and cold layers is too small and the opposing velocities of both layers too high [10, 11]. Observing the difference between the values of x_c determined from the CFD results and the values obtained for Ri=0.8, this criterium is not applicable in tunnel fire scenarios, where the flow is constrained.

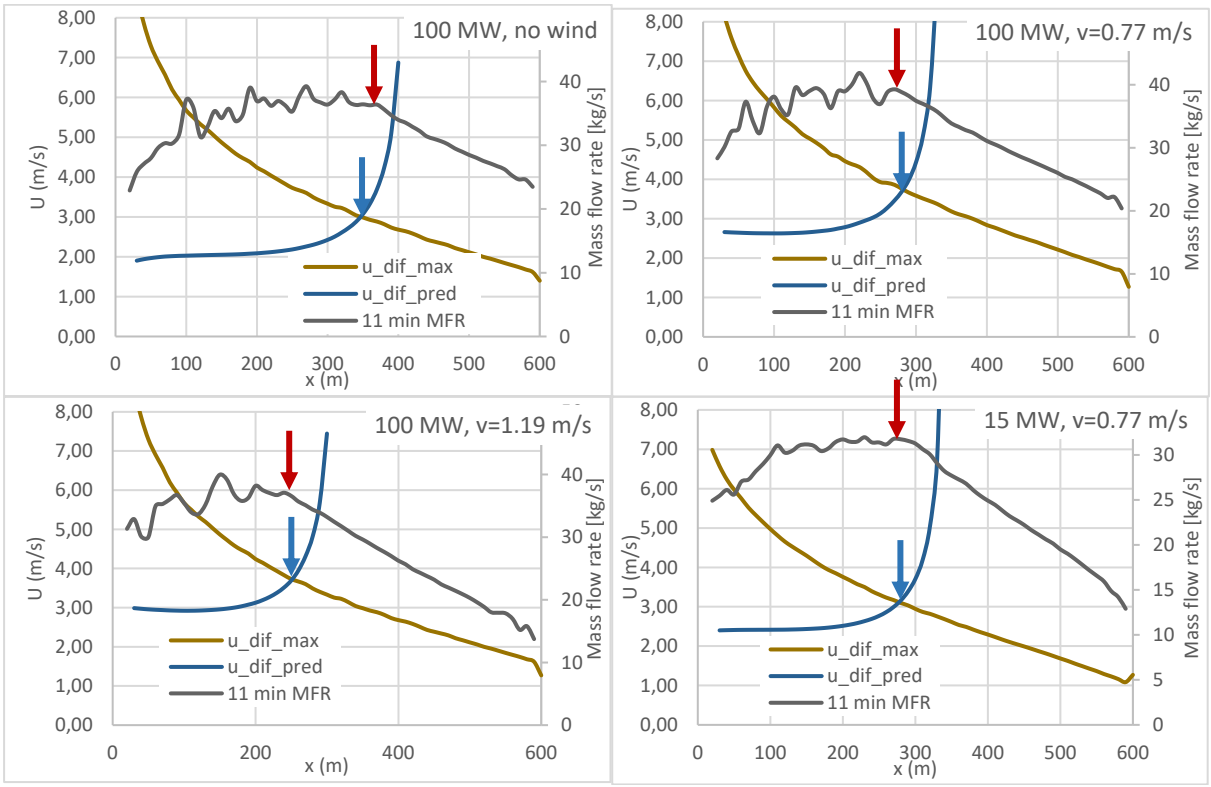

Figure 13. Comparison between the predicted difference between the upper layer and lower layer velocities (u_dif_pred) and the maximum allowed velocity difference for 100 MW (without wind, v= 0.771 m/s and v=1.19 m/s) and for 15 MW (v= 0.771 m/s).

HRR [MW]	100	50	6	100	70	50	15	6	100
Wind v [m/s]	0	0	0	0.771	0.771	0.771	0.771	0.771	1.19
CFD x_c [m]	380	380	380	270	270	290	270	310	250
x_c for Ri=0.8 [m]	520	450	320	450	370	370	350	260	220
Predicted x_c [m]	350	360	350	280	270	280	270	270	250
Error [%]	8	5	8	4	0	3	0	13	0

Table 3. Longitudinal coordinate x_c corresponding to the beginning of the lower layer smoke contamination: comparison between simulated (CFD) and predicted values.

The distance x_c decreases when the opposing wind velocity increases, as concluded by Ortega et al. [3], but seems insensitive to the variation of the heat release rate. When the heat release rate increases, the velocity increases; this seems to be the reason why the distance x_c is not significantly affected by the heat release rate variation.

6. CONCLUSIONS

Large eddy simulations of naturally ventilated tunnel fires were performed with fireFoam to study the effect of the variation of the heat release rate (HRR) both with and without wind in a naturally ventilated tunnel. Experimental data available in the literature for the Memorial Tunnel was used for validation purposes. It shows that, although the velocity due to buoyancy increases with the HRR, the location of the lower layer contamination with smoke does not vary significantly. It is concluded that the criterium based on the Richardson Number (Ri=0.8), commonly used to assess the possibility of thermal stratification loss, is not applicable when the flow is constrained in tunnel fire scenarios.

It is also shown that the criterium based on the higher and the lower layer velocities and the balance of the mass flow rates of the layers, formerly proposed by Ortega *et al.* [3], may correctly predict the distance from the fire source where the lower layer contamination with smoke starts.

REFERENCES

[1] Directive 2004/54/EC of the European Parliament and of the Council of 29 April 2004, on minimum safety requirements for tunnels in the Trans-European Road Network.

[2] A. Galhardo, J. Viegas and P. Coelho. *The influence of wind on smoke propagation to the lower layer in naturally ventilated tunnels*. Tunn. Undergr. Space Technol. 2022, 128, 104632.

[3] E. Ortega, J.C. Viegas and P.J. Coelho. *The contamination of the lower layer in sloped tunnel fires*. Fire, 2023, 6, 245.

[4] A. Galhardo, J. Viegas, P. Coelho, E. Ortega and U. Fernandes. *Smoke control in naturally ventilated tunnels*. 2nd International Conference on Road Tunnel Operations and Safety. Granada (spain), 25th - 28th October 2022.

[5] H. Guo, Z. Yang, P. Zhang, Y. Gao, Y. Zhang. *Experimental Investigation on Fire Smoke Temperature under Forced Ventilation Conditions in a Bifurcated Tunnel with Fires Situated in a Branch Tunnel*. Fire 2023, 6, 473. https://doi.org/10.3390/fire6120473.

[6] Bechtel/Parsons Brinckerhoff, 1995. *Memorial Tunnel Fire Ventilation Test Program*. Test Report. Massachusetts Highway Department.

[7] C. Caliendo, G. Genovese, I. Russo. *Risk analysis of road tunnels: A computational fluid dynamic model for assessing the effects of natural ventilation*. Applied Sciences, 11(1):32, 2021.

[8] J. Kong, W. You, Z. Xu, H. Liu, H. Li. *A Numerical Study on Smoke Behaviors in Inclined Tunnel Fires under Natural Ventilation*. Journal of Safety Science and Resilience (2022).

[9] Centre d'Etudes des Tunnels. *Dossier Pilote des Tunnels Équipements*; Centre d'Etudes des Tunnels: Bron, France, 2003.

[10] P. L. Hinkley. *The flow of hot gases along an enclosed shopping mal. A tentative theory*. 1970.

[11] D. Yang, L.H. Hu, R. Huo, Y.Q. Jiang, S. Liu, F. Tang. *Experimental study on buoyant*

flow stratification induced by a fire in a horizontal channel. Applied Thermal Engineering 30 (2010) 872–878.

Congress on Numerical Methods in Engineering 2024
4-6 September 2024, University of Aveiro, Portugal

HUMAN COMFORT ASSESSMENT OF STEEL AND STEEL-CONCRETE COMPOSITE FOOTBRIDGES BASED ON THE USE OF DESIGN RESPONSE SPECTRA

Paula O. Diniz[1], Jorge M. Souza[1], Amanda B. Oliveira[1] and José Guilherme S. da Silva[1]

1: Postgraduate Programme in Civil Engineering (PGECIV).
State University of Rio de Janeiro (UERJ).
Rio de Janeiro/RJ, Brazil.
Email: jgss@uerj.br or jgss@eng.uerj.br

Keywords: Pedestrian footbridges, dynamic analysis, excessive vibrations, human comfort.

Abstract *The pedestrian footbridges are more and more becoming the modern landmarks of urban areas. The designers seem to continuously move the safety border, aiming to increase the footbridges slenderness and lightness. However, more and more footbridges are carried out as light weight structures with low frequencies and low damping. These facts have generated very slender structures, sensitive to dynamic excitations, and consequently changed the serviceability limit states associated to the design [1-2]. The current design codes and technical guides recommend the use of deterministic models to assess the dynamic structural behaviour of footbridges [3-4]. On the other hand, the effect of the uncertainties in mass, stiffness and damping of the investigated structure are relevant and lead to uncertainties on the values of the footbridges natural frequencies. Nevertheless, the human walking is a stochastic phenomenon and the dynamic force generated at each step depends of the weight, the step frequency and the step length of each pedestrian [1-2]. This research work aims to contribute with the structural designers based on the development of a probabilistic approach to assess the dynamic behaviour of steel and steel-concrete composite footbridges, based on the use of design response spectra, considering the stochastic nature of the pedestrian's walking, aiming to assess the structural response with regard to excessive vibrations that may cause human discomfort. Based on the use of probabilistic methods, it becomes possible to determine the probability of the footbridge's peak acceleration values exceeding or not the human comfort criteria. The results obtained in this work reveal that the peak accelerations calculated through the deterministic methods may be overestimated in design situations.*

1. INTRODUCTION

The pedestrian footbridges are more and more becoming the modern landmarks of urban areas. This way, the designers seem to continuously move the safety border, aiming to increase slenderness and lightness of the pedestrian footbridges. However, more and more footbridges are carried out as light weight structures with low frequencies and low damping [1-6]. These facts have generated very slender footbridges, sensitive to dynamic excitations, and consequently changed the serviceability limit states associated to the design.

The current design codes and project guides recommend the use of deterministic models to assess the dynamic behaviour of footbridges [3-4]. On the other hand, the effect of the uncertainties in mass, stiffness and damping of the investigated structure are relevant and lead to uncertainties on the values of the footbridges natural frequencies. Nevertheless, the human walking is a stochastic phenomenon and the dynamic force generated at each step depends of the weight, the step frequency and the step length of each pedestrian.
This way, opposite to the deterministic approach, this work aims to present a probabilistic model to assess the dynamic behaviour of footbridges, when subjected to pedestrian walking, considering the stochastic nature of the human walking [1-2]. The probabilistic dynamic analysis methodology considered the uncertainty related to the pedestrian weight [W (N)], pedestrian step frequency [f_p (Hz)], and pedestrian step length [l_p (m)]. The proposed probabilistic model takes into consideration both inter-subject [Inter] and intra-subject [Intra] step variability [1-2]. These uncertainties in pedestrian weight, step frequency, step length, inter-subject and intra-subject step variability were modelled as random variables and included in the Monte Carlo simulations.
The proposed probabilistic methodology is used to assess the dynamic response of steel and steel-concrete composite footbridges located at Rio de Janeiro/RJ, Brazil [1-2]. The results are presented and discussed based on design response spectra that allow the assessment of the vibration serviceability of footbridges. These results have demonstrated that the peak accelerations calculated using the deterministic methods [3-4] may be overestimated

2. MAXIMUM ACCELERATIONS CALCULATED BY ANALYTHIC METHODS

The human walking generates periodic loadings on the footbridge slabs and the two feet move alternately from one position to another and do not simultaneously leave the surface. The dynamic part of the load-time history of a single pedestrian can be modelled based on the Fourier series expansion that represents a combination of sinusoidal forces, whose frequencies are multiples of the step frequency, as presented in Eq. (1).

$$F(t) = P\left[1 + \sum \alpha_i \cos(2\pi i\, f_p\, t + \phi_i\right] \tag{1}$$

Where:
$F(t)$: dynamic loading function (N);
P : pedestrian weight (N);
α_i : dynamic coefficient of the harmonic force;
i : harmonic multiple (1, 2, 3, etc.);
f_p : pedestrian step frequency (Hz);
t : time (s);
ϕ_i : phase angle to the harmonic i (rad).

The analytical expressions used in this investigation considered the footbridges represented by a single degree of freedom system (SDOF). This way, it is well known that the dynamic behaviour of a SDOF for a given generic mode vibration i can be represented by the dynamic equilibrium equation presented in Eq. (2).

$$a(t) + 2\xi_i \omega_i v(t) + \omega_i^2 u(t) = \frac{\phi_i F(t)}{m_i} \quad (2)$$

Where:

a(t) : acceleration (m/s²);
v(t) : velocity (m/s);
u(t) : displacement (m);
ξ_i : modal damping coefficient;
m_i : modal mass;
ω_i : excitation frequency (rad/s);
ϕ_i : vibration mode function;
F(t) : dynamic loading function (N).

It is noteworthy that in this research work the analytical solution proposed by Živanović [7-9] was considered for investigate the pedestrian footbridges peak acceleration, having in mind that for this purpose the first vibration mode of the structure can be represented by a half sine wave function *sen* ($\pi \upsilon_p t/L$). This way, the equation that governs the first vibration mode of the investigated footbridge is presented in Eq. (3).

$$a(t) + 2\xi\omega v(t) + \omega^2 u(t) = \frac{1}{m} \alpha P \, sen(2\pi f_p t) \, sen\left(\frac{\pi v_p}{L} t\right) \quad (3)$$

Where:

a(t) : peak acceleration (m/s²);
ξ : damping coefficient;
m : footbridge modal mass (kg);
α : dynamic coefficient;
P : pedestrian weight (N);
f_p : pedestrian step frequency (Hz);
l_p : pedestrian step length (m);
v_p : pedestrian step velocity [$v_p = f_p \, l_p$] (m/s);
L : footbridge span (m).

3. PROBABILISTIC ANALYSIS METHODOLOGY: RESPONSE SPECTRA

In this investigation, the proposed probabilistic dynamic analysis methodology assumes that the independent random variables associated to the pedestrian weight [W (N)], pedestrian step frequency [f_p (Hz)], and pedestrian step length [l_p (m)] follow a normal distribution [1-2]. The proposed analysis methodology was computationally implemented and the generated design response spectra allow structural engineers the evaluation of the vibration serviceability of pedestrian footbridges.

Hausdorff et al. [10] have demonstrated that the step frequency is not constant during walking. Each pedestrian walks freely with a preferential step frequency. However, at each step, the frequency varies because the pedestrian cannot repeat the same motion with the same frequency. This step-by-step variation is called the intra-subject step variability, whereas the step frequency variation between different people represents the inter-subject step variability.
In this study, the proposed probabilistic model takes into consideration both inter-subject [Inter] and intra-subject [Intra] step variability [1-2]. Table 1 shows the mean values (μ) and respective standard deviations (σ) of the random variables adopted in the Monte Carlo simulations [3,7,10,11] to assess the dynamic behaviour of simply supported footbridges.

Variable	Unities	Mean (μ)	Standard deviation (σ)	References
W	(N)	727	145	Ingólfsson [11]
f_p	(Hz)	2.00	0.2	Bachmann [3]
l_p	(m)	0.71	0.071	Zivanovic [7]
Intra	(Hz)	-	1.3 + 0.1% μ	Hausdorff [10]

Table 1: Statistical parameters used to simulate the pedestrian walking.

Thus, for each pedestrian, a preferential step frequency was randomly generated. At each step period, the step frequency varied by 1.3% around the preferential pedestrian's step frequency to account the intra-subject step variability [10]. The dynamic load factors were calculated using the mathematical formulations proposed by Rainer et al. [12] and Young apud Hauksson [6]. In sequence, Figure 1 presents the developed analysis methodology in details.
It must be emphasized that there are significant differences between the analysis methodologies I [9] and II [1-2]. In fact, analysing the Figure 1, it is possible to conclude that when the methodology I (M-I) is utilised in this investigation, the effect of the intravariability is considered only to the calculation of the dynamic coefficients (α_i) [Step 3: see Equation (1)], and used to determine the peak accelerations [Step 4: see Figure 1]. On the other hand, when the analysis methodology II (M-II) is investigated, the intravariability is considered on the dynamic coefficient (α_i) calculations and on the sinusoidal harmonic function sen ($2\pi f_p$) [Step 3 and Step 4: see Equation (1)]. After that the peak acceleration percentile 95% ($a_{95\%}$) is determined, based on Step 5, as illustrated in Figure 1.

4. INVESTIGATED PEDESTRIAN FOOTBRIDGES

In this research work two pedestrian footbridges located at the Rio de Janeiro city (Rio de Janeiro/RJ, Brazil) were investigated, aiming to compare the results calculated based on the use of the proposed analysis methodologies I and II (see Figure 1), and the results determined based on experimental tests developed on the analysed pedestrian footbridges [5,13]. The main characteristics related to the investigated structural models FB-I (Footbridge I: see Figure 2) and FB-II (Footbridge II: see Figure 3) are presented in Table 2.

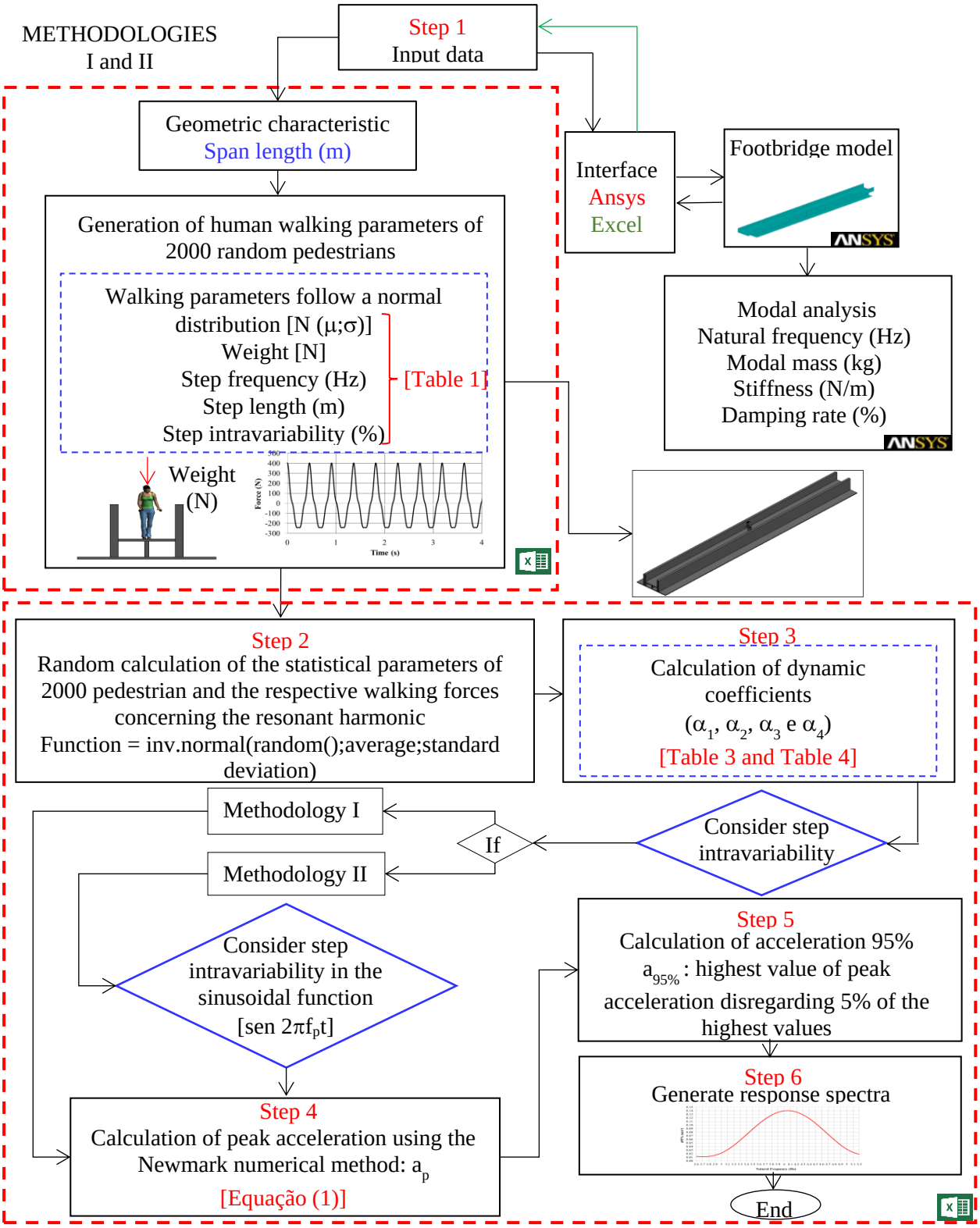

Figure 1: Proposed analysis methodology to generate the project response spectra.

The first analysed structural model (FB-I) is located at the Osvaldo Aranha Street, route of great importance and very heavy traffic of vehicles along the day, next to the new Maracanã Stadium, in the city of Rio de Janeiro/RJ, Brazil [5]. The footbridge is made of a steel-concrete composite structural system, and presents two spans with length equal to 29.5m and 24m, respectively, and a total length of 53.5m [5], as presented in Figure 2.

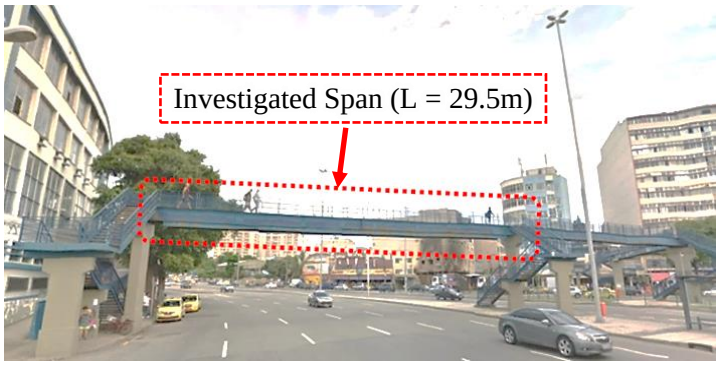

Figure 2: Steel-concrete composite footbridge: FB-I (L = 53.5 m).

The second analysed footbridge (FB-II) is associated to a simply-supported inverted-queen-post-truss steel footbridge spanning 68.6 m, with all beams and columns made of steel [13]. The deck floor is made of precast concrete slabs 7 cm thick, and the two parallel trusses are braced at their top and bottom. The cross-sections of the truss members, the reinforcement beams and the primary members of the bracing systems are made of steel with double-U profiles welded at theirs flanges to form a box section [13], as illustrated in Figure 3.

Figure 3: Inverted-queen-post-truss steel footbridge: FB-II (L = 68.6 m).

Footbridges	Frequency f_{01} (Hz)	Vibration mode	Harmonic resonant	Length L (m)	Modal mass m (kg)	Damping ratio ξ (%)
FB-I	3.83	1st	2nd	53.5	10674.24	1.50
FB-II	1.85	1st	1st	68.6	39490.00	0.23

Table 2: Characteristics of the investigated pedestrian footbridges.

5. PROBABILISTIC DESIGN RESPONSE SPECTRA

Initially, it is worth to mention that the results obtained based on the proposed probabilistic analysis methodology was calculated from 2,000 analyses associated with pedestrian crossings. Therefore, the probabilistic response spectra were constructed based on an extensive parametric study (see Table 3), based on the calculation of the maximum acceleration values (peak accelerations), corresponding to each pedestrian crossing, varying the fundamental frequency in the vertical transverse direction in the range of 0.5 Hz to 10 Hz of the reference footbridges, FBI and FB-II (see Table 2). Peak acceleration values were determined using the analysis methodologies I and II (M-I [9] and M-II [1-2]), see Figure 1.

Investigated parameters	Parametric variation
Fundamental frequency: f_{01}	0.5 Hz to 10 Hz
Structural damping: ξ	0.5% to 2.0%

Table 3: Dynamic structural analysis: parametric study.

The calculation of the dynamic coefficients (α_i), see Eq. (1), was considered based on the use of the mathematical formulations proposed by Rainer et al. [12] and Young apud Hauksson [6], as illustrated in Figures 4 and 5, and also presented in Tables 3 and 4. The determination of dynamic coefficients is intrinsically associated to the resonance between the harmonic frequency of the dynamic excitation and the footbridge fundamental frequency.

The 95% percentile values ($a_{95\%}$) were determined from the calculated probabilistic peak accelerations. The 95% percentile corresponds to the value with a 95% probability of occurrence, that is, by calculating the maximum structure dynamic response 100 times, it is expected that in 95 cases the peak acceleration values will be equal to or lower than the representative value of the 95% percentile ($a_{95\%}$).

Based on the values associated with the 95% percentile ($a_{95\%}$), the probabilistic response spectra were generated based on a total of 760,000 and 950,000 dynamic analyses considering the assessment of the dynamic response of the reference footbridges (FB-I: L = 53.5 m; m = 10,674.24 kg; f_{01} = 3.83 Hz [5]; see Figure 2 and Table 2; and FB-II: (L = 68.6 m; m = 34,490 kg; f_{01} = 1.85 Hz [13]; see Figure 3 and Table 2), respectively. This way, Figures 6 and 7 present the design response spectra associated to the investigated pedestrian footbridges utilising the two analysis methodologies (M-I [9] and M-II [1-2]: see Figure 1), having in mind the dynamic coefficients (α_i) proposed by Rainer et al. [12] and Young apud Hauksson [6], respectively.

After that, Figures 8 and 9 present the design response spectra related to the reference footbridges (FB-I: L = 53.5 m; m = 10,674.24 kg; f_{01} = 3.83 Hz [5]; see Figure 2 and Table 2; and FB-II: (L = 68.6 m; m = 34,490 kg; f_{01} = 1.85 Hz [13]; see Figure 3 and Table 2), considering only the analysis methodology M-II [1,2] (see Figure 1), the variation of the structural damping (ξ), and the dynamic coefficients (α_i) determined according to the mathematical formulation proposed by Rainer et al. [12].

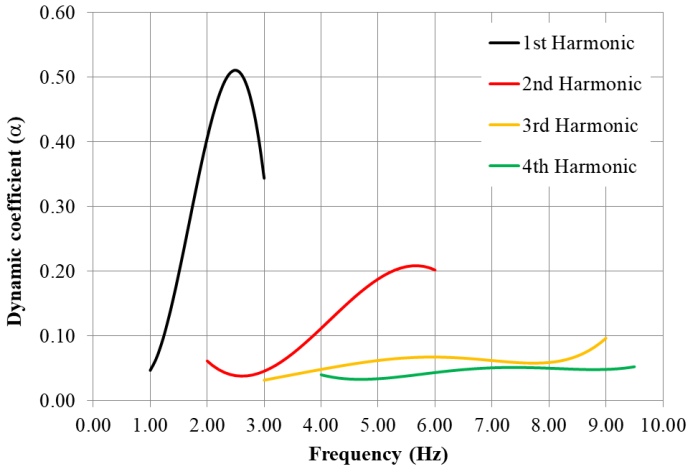

Figure 4: Variation of the dynamic coefficients α_i proposed by Rainer et al.[12].

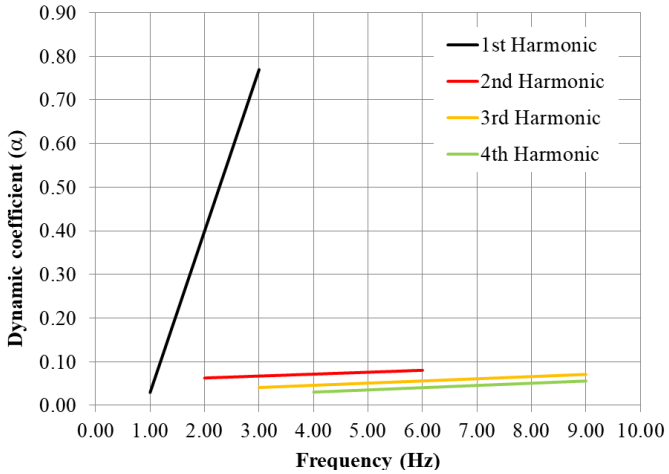

Figure 5: Variation of the dynamic coefficients α_i proposed by Young apud Hauksson [6].

Dynamic coefficients (α_i)
$\alpha_1 = -0.22169f_p^3 + 1.11946\ f_p^{\ 2} - 1.44748\ f_p + 0.5967$
$\alpha_2 = -0.012037(2\ f_p)^3 + 0.1494(2\ f_p)^2 - 0.53146(2\ f_p) + 0.6285$
$\alpha_3 = 0.00009068(3f_p)^5 - 0.0021066(3fp)^4 + 0.018364(3f_p)^3 - 0.077278(3f_p)^2 + 0.17593(3f_p) - 0.1477$
$\alpha_4 = 0.00051715(4\ f_p)^4 - 0.014388(4\ f_p)^3 + 0.14562(4\ f_p)^2 - 0.6018469$

Table 3: Dynamic coefficients proposed by Rainer et al. [12]: footbridge vertical direction.

Dynamic coefficients (α_i)
$\alpha_1 = 0.37\ (f_p - 0.92)$
$\alpha_2 = 0.054 + 0.0044f_p$
$\alpha_3 = 0.026 + 0.0050f_p$
$\alpha_4 = 0.010 + 0.0051f_p$

Table 4: Dynamic coefficients proposed by Young apud Hauksson [6]: footbridge vertical direction.

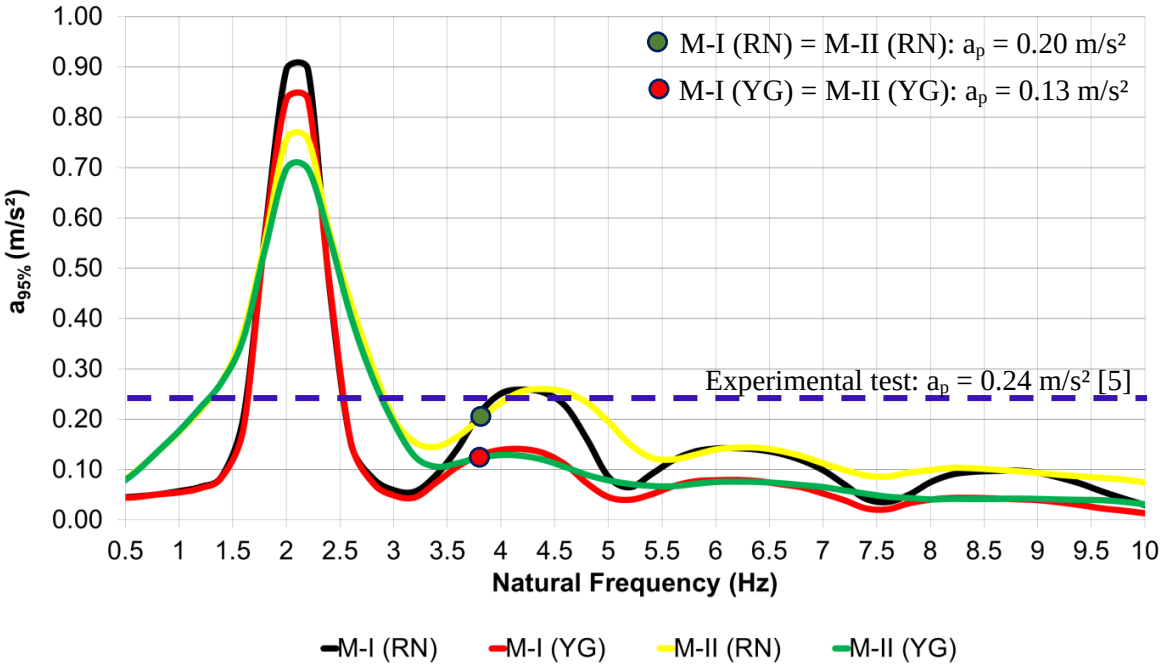

Figure 6: Response spectrum for peak accelerations: FB-I (ξ = 1.5%) (see Figure 2 and Table 2).

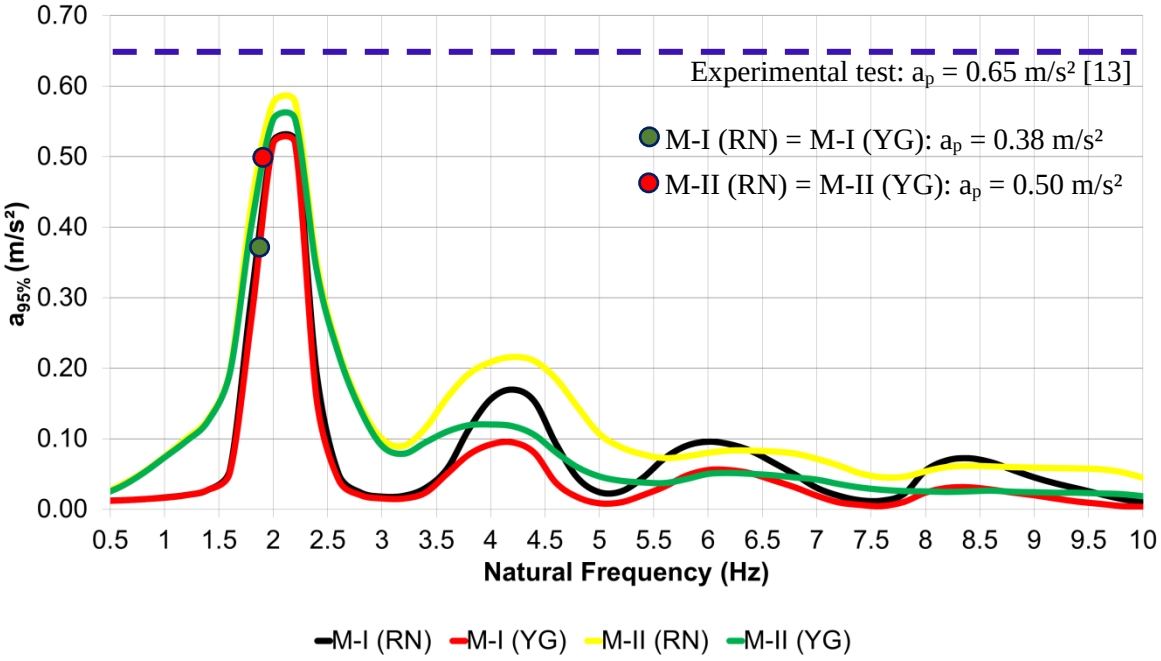

Figure 7: Response spectrum for peak accelerations: FB-I (ξ = 0.23%) (see Figure 3 and Table 2).

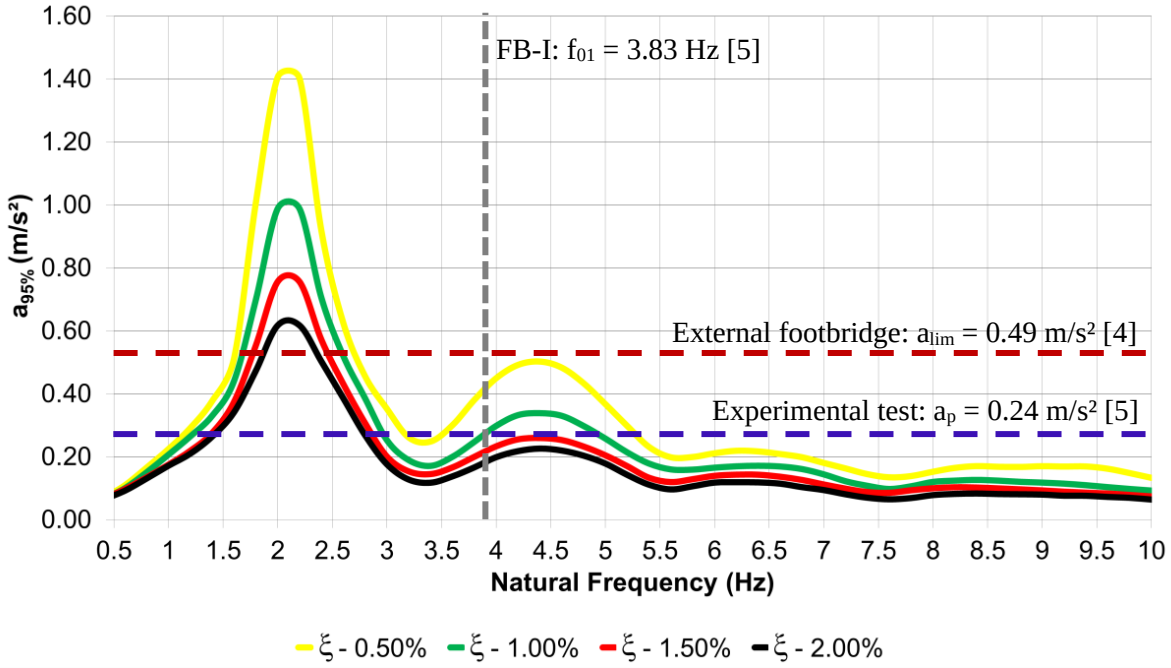

Figure 8: Response spectrum for peak accelerations: L = 53.5 m.

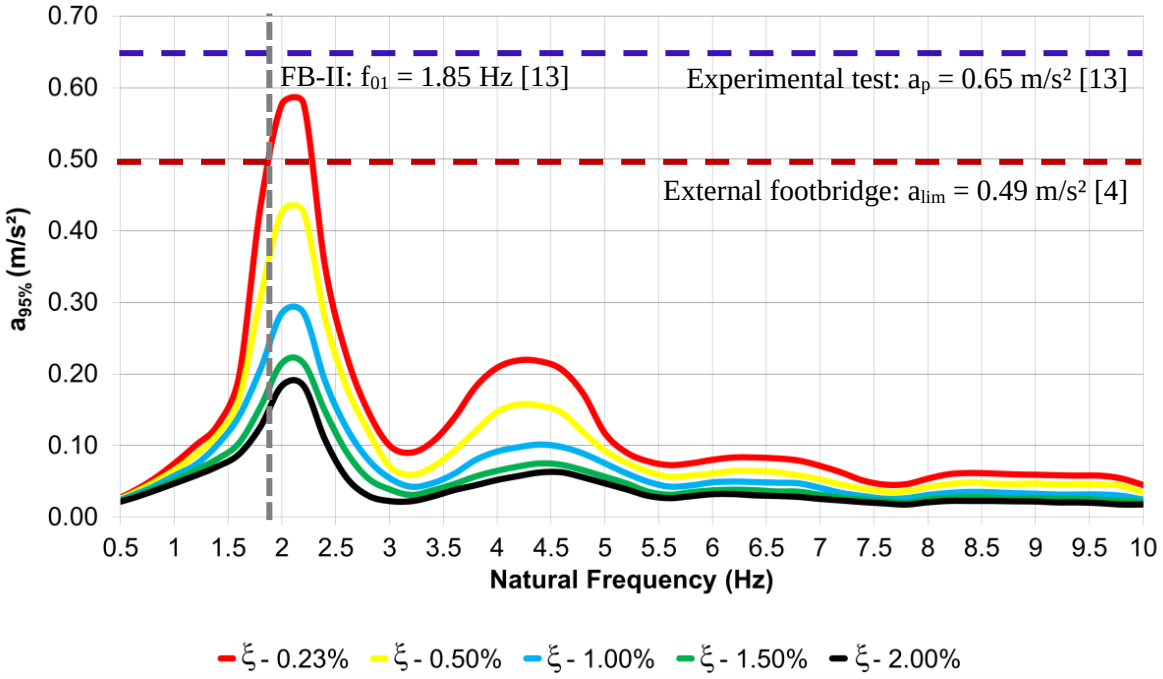

Figure 9: Response spectrum for peak accelerations: L = 68.6 m.

6. ANALYSIS AND DISCUSSION RESULTS

Having in mind the assessment of the 95% percentile values ($a_{95\%}$), determined based on the use of methodologies I and II (M-I [9] and M-II [1-2]), the experimental results are presented and delimited by dashed lines (see Figures 6 and 7). Following the investigation, the results comparison is presented considering the damping coefficient (ξ) variation from 0.5% to 2.0%, as well as the analysis of the human comfort criterion recommended by design standards for external footbridges (a_{lim} = 0.49 m/s² [4]) (see Figures 8 and 9). After that, Tables 5 and 6 present the $a_{95\%}$ values calculated based on the investigated analysis methodologies I and II (M-I [9] and M-II [1-2]), and utilising different mathematical formulations to determine the dynamic coefficients α_i [6,11].

Model	Frequency f_{01} (Hz)	Damping ratio ξ (%)	Experimental results a_p (m/s²)	$a_{95\%}$ (m/s²) Rainer [12]	$a_{95\%}$ (m/s²) Young [6]
FB-I	3.83	1.50	0.24	0.20	0.13
FB-II	1.85	0.23	0.65	0.38	0.38

Table 5: Comparison between the experimental results and those determined by methodology I (M-I).

Model	Frequency f_{01} (Hz)	Damping ratio ξ (%)	Experimental results a_p (m/s²)	$a_{95\%}$ (m/s²) Rainer [12]	$a_{95\%}$ (m/s²) Young [6]
FB-I	3.83	1.50	0.24	0.20	0.13
FB-II	1.85	0.23	0.65	0.50	0.50

Table 6: Comparison between the experimental results and those determined by methodology I (M-II).

Based on the results presented in Figures 6 and 7 and Tables 5 and 6, it is possible to conclude that the 95% percentile values ($a_{95\%}$), determined using the proposed design response spectra (M-I [9] and M-II [1,2]) are lower when compared to the experimental tests peak accelerations. This comparison is consistent and can be explained due to the fact that the experimental tests induced a resonant pedestrian walking with the investigated footbridges, keeping the step frequency constant as much as possible and considering only one pedestrian crossing. On the other hand, the probabilistic analysis methodology (M-I [9] and M-II [1,2]) has considered 2,000 pedestrians with different step frequencies, taking to account the randomness of the variables involved in the probabilistic study.

It must be emphasized that when the FB-I (Harmonic resonant: 2nd; see Figure 2 and Table 2) is considered in the investigation, the $a_{95\%}$ values determined based on the use of the design spectra were the same for the two analysis methodologies (M-I [9] and M-II [1,2]), but presented different values when the dynamic coefficients mathematical formulation [6,12] was modified, see Figures 6 and 7 and Tables 5 and 6. On the other hand, when analysing the FB-II (Harmonic resonant: 1nd; see Figure 3 and Table 2), the determined $a_{95\%}$ values considering the M-II [1,2] were greater than those obtained based on the use of M-I [9], to the both dynamic coefficients mathematical formulation [6,13].

These observations can be verified in Figures 6 and 7, looking at design spectra behaviour, and Tables 5 and 6, when assessing the first and second harmonic.
Having in mind the structural damping variation related to the investigated pedestrian footbridges (see Figures 8 and 9), when the reference footbridge FB-I (Harmonic resonant: 2^{nd}; see Figure 2 and Table 2) was investigated it is possible to observe that the $a_{95\%}$ values are higher than the experimental accelerations (a_{exp} = 0.24 m/s²), when the damping rates of 0.5% and 1.0% (ξ = 0.5% and 1.0%) are considered. On the other hand, all the $a_{95\%}$ values are lower than the design standard limit acceleration (External footbridges: a_{lim} = 0.49m/s² [4]) to all investigated damping rates (ξ = 0.5% to 2.0%), as illustrated in Figure 8.
Considering the design response spectrum of the reference footbridge FB-II (Harmonic resonant: 1^{nd}; see Figure 3 and Table 2), see Figure 9, it is noted that the $a_{95\%}$ values are lower than the experimental accelerations (a_{exp} = 0.65 m/s²) to all investigated structural damping rates (ξ = 0.23% to 2.0%). It was verified that the $a_{95\%}$ values slightly surpass the design standard limit acceleration (a_{lim} = 0.49 m/s² [4]) to the damping rate ξ = 0.23% (damping experimental value [13]). However, all the $a_{95\%}$ values are lower the recommended design limit to external footbridges when the structural damping rates are equal to 0.5%, 1.0%, 1.5% and 2.0% (ξ = 0.5%, 1.0%, 1.5% and 2.0%).

7. CONCLUSIONS

In this research work, design spectra response are proposed, based on development of a probabilistic analysis methodology, aiming to assess the dynamic structural behaviour of pedestrian footbridges when subjected to human induced loadings considering the stochastic nature of the walking. This way, the following conclusions can be drawn from the results presented in this investigation:
1. The proposed probabilistic design response spectra clearly demonstrated that the dynamic response of simply supported footbridges [95% percentile ($a_{95\%}$)], when subjected to pedestrian walking, can be modified based on the effect of the step intravariability, as well as the randomness of the other variables used in the probabilistic analysis methodology.
2. Considering a quantitative analysis, based on the 2,000 pedestrians crossing the investigated pedestrian footbridges, the results calculated through the proposed probabilistic analysis methodology indicates that the first studied footbridge (FB-I) attends the human comfort for all investigated damping rates (ξ = 0.5%, to 2.0%). On the other hand, when the second footbridge (FB-II) was analysed, it was concluded that the $a_{95\%}$ value slightly exceeds the design standard recommended limit when the experimental damping rate of ξ = 0.23% is considered, and is lower than this limit when the structural damping rates are equal to 0.5% to 2.0% (ξ = 0.5%, to 2.0%).

ACKNOWLEDGEMENTS

The authors gratefully acknowledge the financial support for this research work provided by the Brazilian Science Foundation's CNPq, CAPES and FAPERJ.

REFERENCES

[1] P.O.B. Diniz, *Human comfort assessment of footbridges based on the development of probabilistic design response spectra* (In Portuguese / In development). MSc Dissertation. Postgraduate Programme in Civil Engineering (PGECIV). State University of Rio de Janeiro (UERJ). Rio de Janeiro/RJ, Brazil, (2024).

[2] J.M.S. Souza, *Dynamic response analysis of pedestrian footbridges considering a human walking probabilistic modeling* (In Portuguese). MSc Dissertation. Postgraduate Programme in Civil Engineering (PGECIV). State University of Rio de Janeiro (UERJ). Rio de Janeiro/RJ, Brazil, (2012).

[3] H. Bachman and W. Amman, *Vibration in Structures Induced by Man and Machine*, Structural Engineering Document 3, International Association for Bridge and Structural Engineering (IABSE), Zurich, Switzerland, (1987).

[4] T.M. Murray, D.E. Allen, E.E. Ungar and D.B. Davis, *Steel Design Guide Series Nbr. 11: Vibrations of Steel-framed Structural Systems due to Human Activity*. American Institute of Steel Construction (AISC), 2nd Edition, Chicago, USA, (2016).

[5] I.A.R. da Silva and J.G.S. da Silva, Experimental and numerical dynamic analysis of steel-concrete composite footbridges subjected to pedestrians walking. *CE/Papers*, Vol. **1**, 458-467, (2017).

[6] F Hauksson,. *Dynamic behaviour of footbridges subjected to pedestrian induced vibrations*. MSc Dissertation. Lund University. Sweden, (2005).

[7] S. Živanović, *Probability-based estimation of vibration for pedestrian structures due to walking*. PhD Thesis. Department of Civil and Structural Engineering. University of Sheffield. England, UK, (2006).

[8] S. Živanović, A. Pavic and P. Reynolds, Probability based estimation of footbridge vibration due to walking. *Proceedings of the 25th International Modal Analysis Conference (IMAC XXV)*, Orlando, Florida, USA, (2007).

[9] K. Wan, S. Živanović and A Pavic. Design spectra for single person loading scenario on footbridges. *Proceedings of the 27th Conference and Exposition on Structural Dynamics (IMAC XXVII)*, Orlando, Florida, USA, (2009).

[10] J.M. Hausdorff, L. Zemany, C.K. Peng, Goldberger A.L., Maturation of gait dynamics: stride-to-stride variability and its temporal organization in children. *Journal of Applied Physiology*, Vol. **86(3)**, pp. 1040-1047, (1999).

[11] E.T. Ingólfsson, *Pedestrian-induced lateral vibrations of footbridges: experimental studies and probabilistic modelling*. PhD Thesis. Department of Civil Engineering. Technical University of Denmark, (2011).

[12] Rainer J.H., Pernica G., Allen D.E., Dynamic loading and response of footbridges, *Canadian Journal of Civil Engineering*, Vol. **15(1)**, pp. 66-71, (1988).

[13] F.A. Rezende, W.D. Varela, E.M.L. Carvalho and A.M.B. Pereira, Vibration performance assessment of a long-span steel footbridge. *Proceedings of the Institution of Civil Engineers - Structures and Buildings*, Vol. **175(6)**, pp. 500-512, (2022).

This page intentionally left blank

Congress on Numerical Methods in Engineering 2024
4-6 September 2024, University of Aveiro, Portugal

INVESTIGAÇÃO DE VIGAS ALVEOLARES EM CONDIÇÕES DE INCÊNDIO

Luana V. Silva[1,2], Mychel Sandri[1], Nickolas Giacomitti[1,2] e Luís M. R. Mesquita[2]

1: Instituto Politécnico de Bragança
Campus Santa Apolónia, 5300-253 Bragança, Portugal
e-mail: luana.silva@ipb.pt, a46686@alunos.ipb.pt, nickolas.giacomitti@gmail.com

2: Grupo de Investigação em Construção Sustentável (GICoS)
Instituto Politécnico de Bragança
Campus Santa Apolónia, 5300-253 Bragança, Portugal
e-mail: lmesquita@ipb.pt

Palavras-chave: Vigas Alveolares de Aço, Resistência ao Fogo, Desempenho Estrutural, Ensaios experimentais; Simulações numéricas.

Resumo. *Vigas de aço alveolares são amplamente utilizadas na indústria da construção. Suas aberturas circulares na alma permitem a integração de serviços e oferecem uma solução eficaz para estruturas de grande vão. O processo de fabricação requer duas passagens de corte térmico de uma viga seção-I sólida, originando uma viga alveolar maior que sua seção original. Essas aberturas presentes nas vigas alveolares causam modos de falha local, como a encurvadura do montante da alma e o mecanismo de Vierendeel. A encurvadura do montante da alma envolve deslocamentos laterais no montante da alma com deformações de torção, enquanto o mecanismo de Vierendeel é causado pelo desenvolvimento de quatro rótulas plásticas nas seções Tê inferior e superior. A estrutura desse tipo de viga geralmente fica exposta e desprotegida, o que a torna mais vulnerável em situações de incêndio. A degradação do aço em contato com o fogo reduz sua resistência e capacidade de suporte de carga. Embora o comportamento desse tipo de viga mereça atenção devido à influência das aberturas da alma em seus modos de falha, não se dispõe de orientações para tais vigas quando sujeitas a temperaturas elevadas. Portanto, considerando a importância da verificação de segurança, este estudo analisa experimentalmente e numericamente vigas alveolares em temperaturas ambiente e elevadas. Os resultados de testes experimentais de flexão em quatro vigas alveolares com uma das extremidades encastradas são demonstrados. Não-linearidades materiais e geométricas foram consideradas no modelo de elementos finitos desenvolvido, o qual é validado com sucesso pela consistência entre os resultados numéricos e experimentais. Um estudo paramétrico com o modelo numérico é apresentado para expandir o conhecimento sobre a viga alveolar em condições de incêndio. O estudo analisa como os parâmetros geométricos da viga alveolar afetam sua resistência e as cargas de falha em diferentes condições de temperatura. Os principais modos de falha observados foram o mecanismo de Vierendeel e a encurvadura do montante da alma.*

1. INTRODUÇÃO

As seções de aço em forma de I, especialmente as vigas alveolares com suas aberturas circulares na alma, são amplamente utilizadas como elementos estruturais nas estruturas de edifícios. No entanto, a presença dessas aberturas influencia os modos de colapso da viga. As aberturas originam modos de falha como o mecanismo de Vierendeel [1,2] e a encurvadura do montante da alma [3,4]. Além disso, as vigas alveolares apresentam alterações aos modos de instabilidade já pré-existentes em vigas sólidas, como a encurvadura lateral torsional (ELT) [5,6]. Para além disso, a exposição a temperaturas elevadas tem um impacto negativo na resistência do aço, que ao se juntar às imperfeições geométricas iniciais pode resultar em uma combinação dos modos de falha. Os guias de dimensionamento disponíveis para vigas com aberturas na alma à temperatura ambiente, incluindo o Eurocódigo EN1993-1-13 [7], o P100 [8] e o P355 [9] da SCI, e o Steel Design Guide 31 [10] da AISIC, apresentam abordagens que são consideradas conservadoras, antieconómicas, ou por vezes inseguras de acordo com estudos [11-13]. Além disso, não estão disponíveis guias para estas vigas a temperaturas elevadas. Devido à importância da verificação da segurança, as vigas com aberturas na alma têm sido recentemente investigadas na procura de novos métodos de dimensionamento para condições de incêndio, adaptando frequentemente os procedimentos concebidos para vigas maciças ao dimensionamento de vigas com furos [14-18].

Embora os ensaios experimentais sejam essenciais para avaliar o comportamento da viga alveolar e validar o modelo numérico para um posterior estudo paramétrico, poucos ensaios experimentais foram efetuados a temperaturas elevadas [19,20]. Uma vez que a estrutura deste tipo de viga está normalmente exposta e desprotegida, o que a torna mais vulnerável em situação de incêndio, o comportamento das vigas de aço alveolares será investigado através da realização de ensaios experimentais a temperaturas ambiente e elevada. Adicionalmente, devido à necessidade de atualizar as normas de dimensionamento relativas às vigas alveolares, será conduzida uma investigação numérica paramétrica, validada pelos ensaios experimentais, para analisar a influencia dos parâmetros geométricos nos modos de colapso das vigas alveolares em condições de incêndio.

2. ENSAIOS EXPERIMENTAIS EM VIGAS ALVEOLARES

Os ensaios experimentais foram realizados em quatro vigas alveolares, variando os parâmetros geométricos e a temperatura de um ensaio. As vigas alveolares foram fabricadas de um perfil sólido IPE 220 em aço S275, no qual a abertura na alma foi feita sem alterar a altura original do perfil.

2.1. Descrição das amostras e configuração experimental

Enquanto a Figura 1(a) apresenta configuração geométrica das vigas alveolares ensaiadas e a configuração experimental, a Tabela 1 descreve as dimensões geométricas médias de cada uma. O número de furos é igual a três para todas as vigas, assim como a largura do montante da alma inicial (w_0) e o comprimento L são fixos para todos os casos.

Tabela 1. Dimensões geométricas médias das vigas alveolares ensaiadas.

Viga	L [mm]	H [mm]	b [mm]	t_f [mm]	t_w [mm]	a_0 [mm]	S [mm]	w_0 [mm]
B1	1503.0	221.0	110.9	8.9	6.6	109.8	219.9	151.0
B2	1499.0	219.0	110.2	8.9	6.6	109.6	241.8	151.0
B3	1501.0	222.0	112.2	9.3	6.6	131.8	197.7	152.0
B4	1496.0	222.0	112.1	9.1	5.9	140.7	219.7	149.8

As vigas B1, B2 e B3 foram ensaiadas a temperatura ambiente, e a viga B4 a 600 °C. Os testes foram feitos em vigas em console, com uma extremidade encastrada e carga concentrada na extremidade oposta. Para evitar falhas por encurvadura lateral torsional, foram instaladas contenções laterais a 300 mm da extremidade livre da viga.

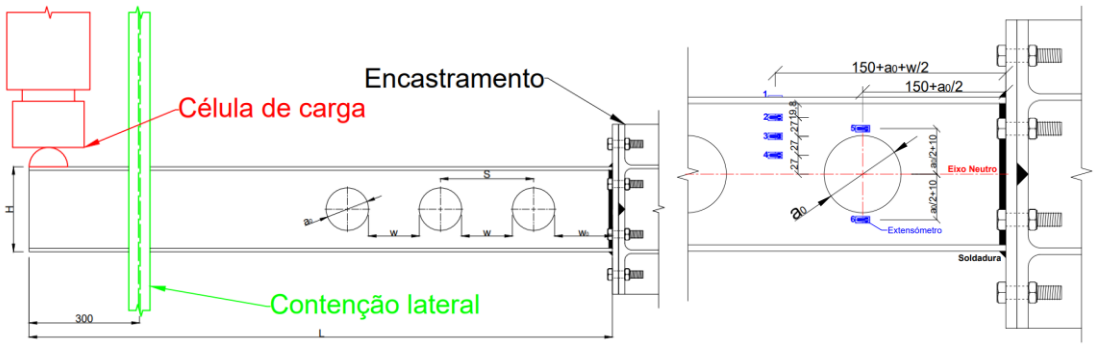

(a) (b)

Figura 1. (a) Design das vigas alveolares e setup experimental em [mm]; (b) Disposição dos extensómetros em [mm].

Um transdutor potenciométrico de fio foi utilizado para obter o deslocamento vertical da extremidade livre da viga no banzo inferior. Além disso, as deformações do montante da alma e dos banzos foram medidas utilizando seis extensómetros elétricos nos ensaios a temperatura ambiente. A localização dos extensómetros nas vigas é apresentada na Figura 1(b). Durante o ensaio em alta temperatura, utilizou-se dezasseis termopares distribuídos ao longo de cinco seções transversais da viga, que estão indicadas na Figura 2(a).

Para elevar a temperatura da viga, foram utilizadas resistências elétricas conectadas ao MANNINGS 16300, um sistema de aquecimento configurado em 800 °C/h, conforme mostrado na Figura 2(b). Além disso, aplicou-se mantas de lã de vidro com 50 mm de espessura para isolar a viga, deixando sem isolamento apenas as extremidades sujeitas à aplicação de carga e a placa de encastramento. O momento de iniciar a aplicação da carga mecânica foi determinado pela uniformidade e proximidade da temperatura ao redor de 600 °C ao longo da viga.

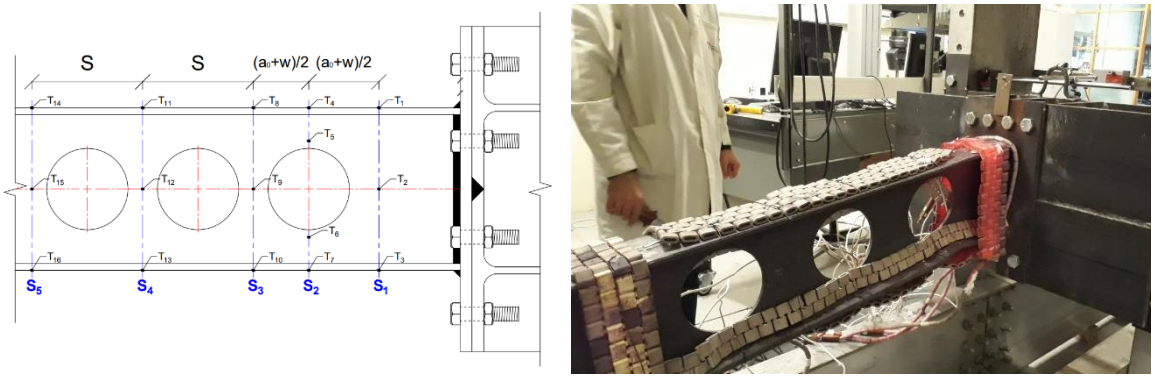

(a) (b)

Figura 2. (a) Disposição dos termopares; (b) Disposição das resistências.

2.2. Resultados experimentais

A Figura 3(a) apresenta um gráfico com as temperaturas médias das secções durante o ensaio da viga B4, em que a temperatura desejada foi alcançada após aproximadamente 50 minutos. Na Figura 7 são exibidos os resultados dos quatros ensaios experimentais com as curvas da força aplicada em função do deslocamento vertical. Em todas as vigas ensaiadas em temperatura ambiente, o mecanismo de Vierendeel foi identificado como o principal modo de falha. O montante da alma entre as duas aberturas não demonstrou grandes instabilidades, ao contrário da abertura e do banzo inferior na seção da primeira abertura, que apresentaram deformações significativas. Em relação a viga B4 ensaiada a 600 °C, o modo de falha observado foi semelhante ao das vigas ensaiadas em temperatura ambiente, pelo mecanismo de Vierendeel. No entanto, a carga máxima foi reduzida em cerca de 50 %, devido aos efeitos da temperatura na resistência do aço.

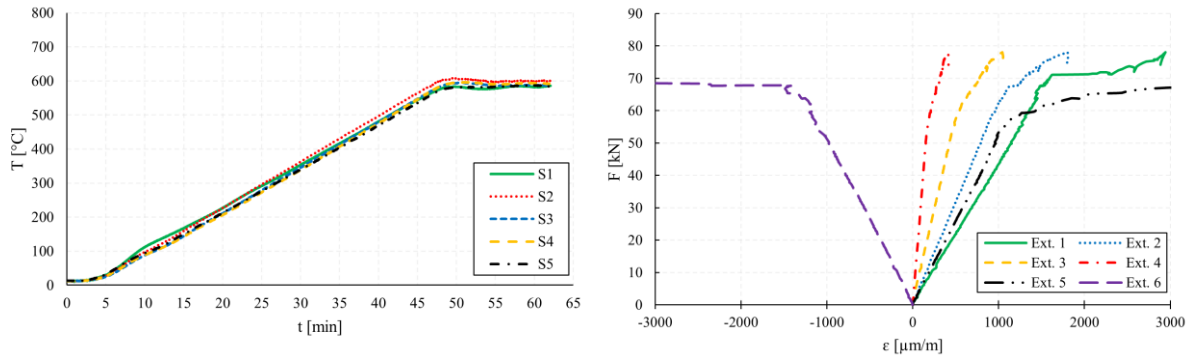

(a) (b)

Figura 3. (a) Temperatura média das secções da viga B4; (b) Curvas deformação vs. força registadas para viga B2.

A Figura 3(b) ilustra as deformações registadas pelos extensómetros instalados na viga B2 submetida ao ensaio em condições de temperatura ambiente. A partir das curvas

apresentadas, verifica-se que as deformações plásticas próximas ao furo (extensómetros 5 e 6) são mais significativas e iniciaram antes das registadas no montante da alma. Além do mais, as deformações no montante da alma foram influenciadas pelo momento de flexão presente na viga, conforme demonstrado pelas maiores deformações registadas nos extensómetros posicionados mais afastados do eixo neutro (2 e 3). Esse padrão de comportamento também foi observado nas vigas B1 e B3.

3. MODELO NUMÉRICO

A fim de realizar um estudo paramétrico, um modelo numérico foi desenvolvido e validado com base nos testes experimentais. Todas as simulações numéricas foram efetuadas com o software ANSYS Mechanical. Para as simulações em temperatura ambiente, o modelo é analisado em duas fases: análise elástica da encurvadura e análise não linear pós-encurvadura. Na primeira análise, considera-se apenas as propriedades elásticas do material. Na análise não linear, além da plasticidade do material são consideradas não linearidades geométricas, inserindo imperfeições geométricas locais, com base no primeiro modo de encurvadura da análise elástica. Para os casos em condições de incêndio, realizou-se também uma análise térmica estacionária a fim de inserir as temperaturas elevadas e incluí-las na análise não linear de forma constante. Com isso, a análise não linear pós-encurvadura fornece a capacidade de suporte e o modo de falha da estrutura.

3.1. Descrição, materiais e condições de contorno

O aço de classe S355 (f_y =355 MPa) foi usado em todos os casos do estudo paramétrico, com um módulo de elasticidade de 210 GPa e coeficiente de Poisson de 0,3. A relação tensão-deformação foi definida conforme o Eurocódigo 3 Parte 1-2 [21]. O modelo numérico foi desenvolvido com elemento de casca SHELL181, traçando a secção transversal pelas coordenadas da superfície média do perfil e o raio de concordância entre o banzo e alma não foi considerado. A malha foi definida com elementos de 10 mm de tamanho.

Assim como nos testes experimentais, as vigas foram modeladas com uma extremidade encastrada e a outra extremidade livre com aplicação de carga. Para isso, aplicou-se um suporte fixo (deslocamento e rotação iguais a zero em todos os eixos) nas linhas dos banzos e da alma da extremidade encastrada. Na extremidade livre da viga, aplicou-se um deslocamento vertical incremental (Uy) na linha do banzo superior e uma restrição de deslocamento lateral (Ux=0) na linha da alma, a fim de impedir falhas por encurvadura lateral torsional. As temperaturas elevadas foram inseridas de forma uniforme por toda a viga e as imperfeições geométricas locais foram aplicadas com uma amplitude de H/200, conforme recomendado no Eurocódigo 1993-1-5. A malha do modelo numérico e as condições de contorno aplicadas podem ser observadas na Figura 4(a).

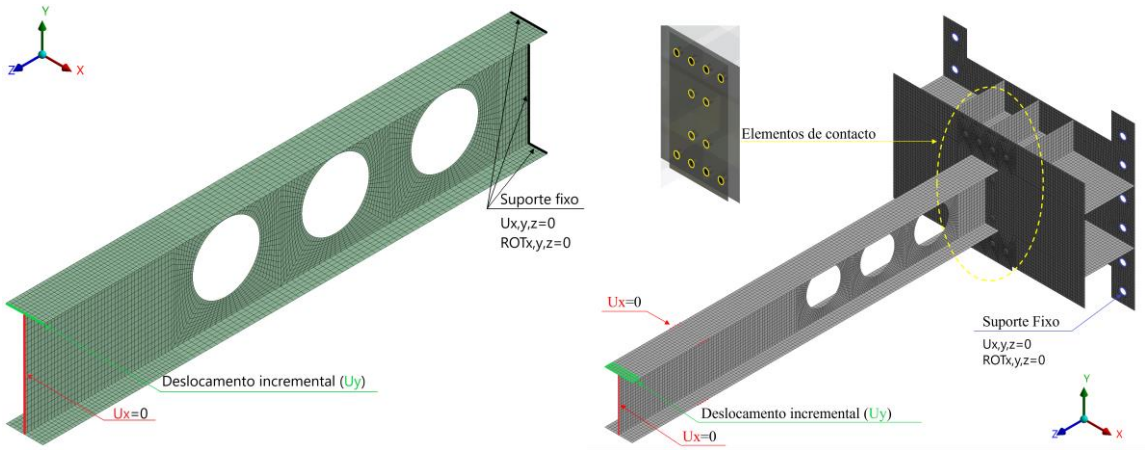

(a) (b)

Figura 4. Condições de contorno: (a) Estudo paramétrico; (b) Validação do modelo numérico.

3.2. Validação do modelo numérico

Para atender de forma mais próxima possível aos requisitos da viga encastrada conforme o teste experimental, foram realizados ajustes na geometria e nas condições de contorno no modelo numérico de validação, conforme ilustrado na Figura 4(b). Além da viga, acrescentou-se a estrutura de encastramento. Os valores de tensões foram derivados dos testes de tração conduzidos em [22], em que a tensão de cedência é de 318,16 MPa e a tensão de rutura é de 433,97 MPa. À temperatura ambiente foi considerado um comportamento bilinear com um módulo tangente de E/100. Os parafusos de classe 8.8 também foram inseridos como elementos de viga, entre os furos da placa e do suporte. Entre a placa de extremidade da viga e o encastramento foram considerados elementos de contato com um coeficiente de atrito de 0.2. A placa e os parafusos foram analisados com um comportamento material linear.

As vigas foram modeladas de acordo com as dimensões reais especificadas na Tabela 1. Além disso, para representar as contenções laterais utilizadas nos ensaios experimentais, aplicou-se a restrições de deslocamento no eixo X dos nós dos banzos, impedindo a ELT.

A fixação da placa de encastramento com o pórtico de ensaios foi modelada aplicando um suporte fixo nas linhas associadas aos parafusos. Já a união entre a placa de encastramento e a placa de fixação foi feita usando elementos de contato, inseridos nas linhas dos furos para representar os parafusos e garantir um contato perfeito. A Figura 4(b) ilustra a disposição do suporte fixo e dos elementos de contato. Para a análise térmica estacionária da viga B4, foram inseridas as temperaturas médias de cada seção registadas no momento da aplicação da carga durante os ensaios experimentais, conforme mostra a Figura 5(a).

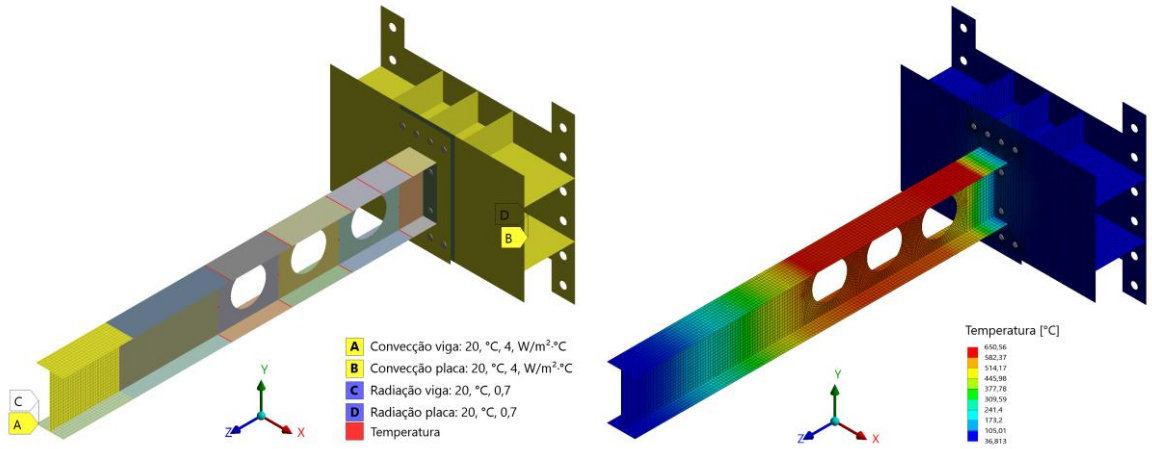

(a) (b)

Figura 5. (a) Análise térmica estacionária; (b) Distribuição de temperatura na Viga B4.

Nas áreas que não estavam isoladas, extremidade da viga e placa de encastramento, foram considerados os efeitos de convecção e radiação. A convecção foi simulada com um valor de 4W/m2K, com base no Eurocódigo 1991-1-2 [23], para situações em que a superfície não esta exposta a incêndios. Quanto a radiação, adotou-se o valor de emissividade de 0,7 para o aço carbono, conforme especificado pelo Eurocódigo 1993-1-2 [21]. A distribuição da temperatura da viga B4 é mostrada na Figura 5(b).

A partir da força de reação no suporte fixo, foi possível analisar a relação entre a carga máxima aplicada e o deslocamento vertical da viga, possibilitando comparações com os dados experimentais. A Figura 6 mostra a similaridade entre a deformação plástica da viga B4 registada no ensaio experimental e a prevista pelo modelo numérico. Em ambas as abordagens, a falha ocorreu na primeira abertura da viga pelo mecanismo de Vierendeel.

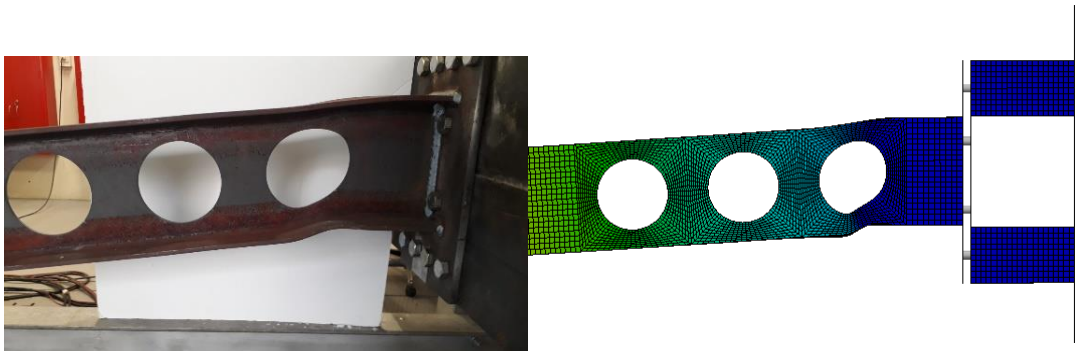

(a) (b)

Figura 6. Deformação plástica da viga B4: (a) Experimental (b) Modelo numérico.

Na Figura 7(a) e (b), são apresentados os gráficos com os resultados das curvas força vs. deslocamento, das vigas testadas à temperatura ambiente e temperaturas elevadas, respetivamente. Ao analisar este gráfico, observa-se uma boa proximidade entre os valores

numéricos e experimentais, validando a eficácia do modelo numérico em reproduzir o comportamento observado experimentalmente. O modelo numérico demonstrou uma rigidez superior no domínio elástico indicada pela inclinação mais acentuada da curva. Este facto se justifica devido ao deslocamento causado no encastramento durante, devido à existência de uma rotação no encastramento, não se verificando uma restrição perfeita. Por outro lado, no domínio plástico, as curvas numéricas permaneceram abaixo das curvas experimentais para todas as vigas testadas.

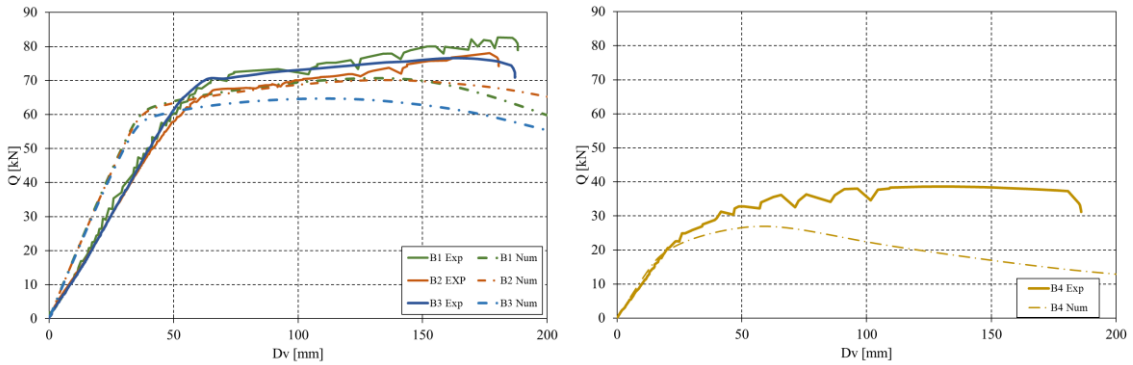

(a) (b)

Figura 7. Resultados dos ensaios experimentais (EXP) e do modelo numérico (NUM) de validação: (a)Temperatura ambiente; (b) Temperatura elevada.

4. ESTUDO PARAMÉTRICO

A partir da validação do modelo numérico, desenvolveu-se um estudo paramétrico para analisar a influência de diferentes parâmetros geométricos nos modos de colapso da viga alveolar em situações de incêndio. Para isso, manteve-se a seção do IPE 220, o comprimento L=1.5 m e o número de furos igual a 3. Os demais parâmetros foram variados conforme os três casos de estudo apresentados na Tabela 2. As simulações não lineares foram feitas para temperatura ambiente e para temperaturas elevadas a 500 °C, 600 °C e 700 °C.

Para efeitos de comparação, calculou-se o momento plástico resistente analítico, $M_{pl,Rd} =$ 159.29 [kN.m], para a secção I transversal sem abertura (sólida), conforme definido na secção 6.2.5 do EC3-1-1 [24] para temperatura ambiente. A Tabela 2 apresenta o momento plástico resistente para a secção transversal dois Tês ($M_{pl,Rd,2T}$), o qual é o mesmo para os casos de estudo I e II, porém é variável para o caso de estudo III, que analisa diferentes diâmetros do furo. O $M_{pl,Rd,2T}$ foi calculado conforme as Equações 1 e 2 [9], [18].

$$M_{pl,Rd,2T} = \frac{W_{pl,2T}\, f_y}{\gamma_{M0}} = \frac{2A_T Z_c f_y}{\gamma_{M0}} \tag{1}$$

$$Z_c = \left[\frac{A_f\left(H - t_f\right)}{2} + A_{wT}\left(\frac{H - 2t_f + a_0}{4}\right)\right] / \left(A_f + A_{wT}\right) \tag{2}$$

Em que: $W_{pl,2T}$ é o módulo de elasticidade plástico da secção dois Tês; $\gamma_{M0} = 1$ é o

coeficiente parcial de segurança para resistência de secções transversais de qualquer classe; Z_c é a distância entre o centróide local da área de uma secção Tê e o centroide global; A_T é a área de uma secção Tê, $A_T = A_f + A_{wT}$; A_f é a área do banzo de um Tê; A_{wT} é a área da alma de uma secção Tê.

Tabela 2. Estudo paramétrico.

Casos de estudo	H [mm]	a_0 [mm]	S [mm]	w_0 [mm]	$M_{pl,Rd,2T}$ [kN.m]
I	320	230	325	100, 150, 200, 250, 300, 350, 400, 450, 500	131.59
II	320	230	250, 275, 300, 325, 350, 375, 400, 425, 450	150	131.59
III	320	100, 125, 150, 175, 200, 225, 250, 275, 300	325	150	154.05, 151.10, 147.50, 143.25, 138.34, 132.78, 126.56, 119.69, 112.16

5. RESULTADOS E DISCUSSÕES

Nesta secção são apresentados os resultados do estudo paramétrico, analisando a influência da variação dos parâmetros geométricos nos modos de colapso da viga alveolar em diferentes temperaturas e comparando com valores de cálculo do Eurocódigo para regras de projeto de resistência das vigas alveolares.

Os momentos de colapso para as cargas máximas suportadas pelas vigas estão apresentados na Figura 8. Para o caso de estudo I, em que o montante inicial da viga é variado, pode-se observar na Figura 8(a) que o momento é quase constante, e não sofreu grande influência. Em todos os tamanhos de w_0 analisados, a viga falhou na secção dois Tês, e o momento de colapso para temperatura ambiente é próximo ao valor de cálculo do momento plástico resistente da secção sólida dois Tês de 131.59 kN.m. Já para o caso de estudo II, que analisa a variação do espaçamento entre os furos, o momento de colapso tem grande variação nos primeiros espaçamentos analisados, mas é constante nos outros em diante. Nos primeiros espaçamentos, a viga falha por uma junção da encurvadura do montante da alma, devido aos pequenos espaçamentos considerados, mais o mecanismo de Vierendeel. A partir de $S = 1.41a_0$ a falha passa a ser apenas pelo mecanismo de Vierendeel na secção dois Tês, o que é confirmando pela proximidade do momento de colapso constante, de cerca de 127 [kN.m] mostrado no gráfico da Figura 8(b), com o valor do $M_{pl,Rd,2T} = 131.59$ [kN.m].

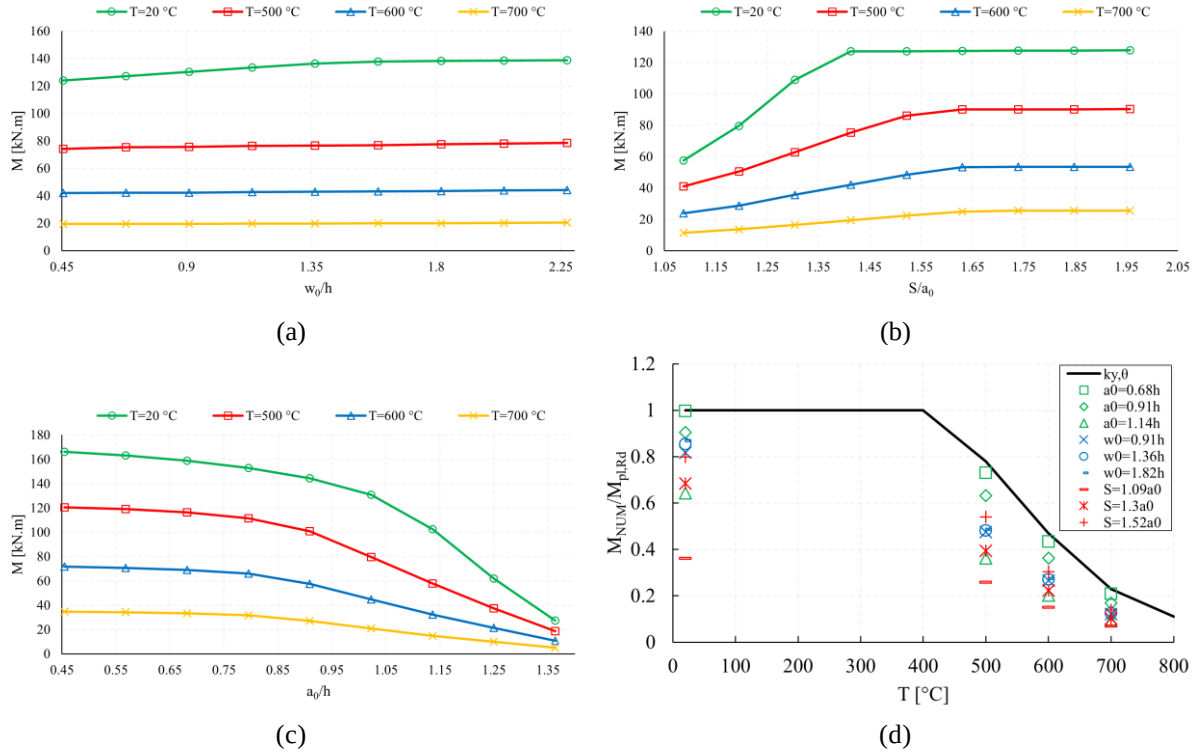

Figura 8. Resultados do estudo paramétrico.

Considerando o caso de estudo III, em que a influência do diâmetro do furo é analisada, pode-se concluir pela Figura 8(c) que quanto maior o diâmetro do furo, menor o momento resistente da viga alveolar. Para os primeiros diâmetros analisados, de $0.45h$ a $0.68h$, a falha ocorreu na secção sólida do montante inicial da viga, com um momento de colapso mais alto e próximo ao momento plástico resistente da secção sólida de 159.29 [kN.m]. Com o aumento do diâmetro ($a_0 = 0.79h \; e \; a_0 = 0.91h$), a falha passa a ocorrer pelo mecanismo de Vierendeel, e nos últimos casos, tem-se uma combinação de Vierendeel mais encurvadura do montante da alma. A Figura 8(d) analisa o momento de colapso resistente numérico normalizado pelo momento plástico da secção I sólida a temperatura ambiente, a fim de comparar com o coeficiente de redução à temperatura ($k_{y,\theta}$) para a tensão de cedência efetiva, fornecido pelo EC3 parte 1-2 [23]. As conclusões relativas aos modos de colapso se confirmam com a comparação com o coeficiente $k_{y,\theta}$, visto que quando os pontos do gráfico se distanciam para abaixo da linha de $k_{y,\theta}$ é devido ao momento de colapso numérico ser menor do que o $M_{pl,Rd}$ da secção solida I, então a falha ocorreu na secção dois Tês, por Vierendeel ou pela combinação deste último com a encurvadura do montante da alma.

6. CONCLUSÕES

Este trabalho investigou o comportamento de vigas de aço alveolares em temperatura

ambiente e em condições de temperaturas elevadas. A partir de ensaios experimentais, validou-se o modelo numérico desenvolvido, considerando uma análise não linear e com imperfeições geométricas. Com isso, um estudo paramétrico foi realizado para analisar a influência da largura do montante inicial da viga, do espaçamento entre os furos e do diâmetro do furo na capacidade resistente das vigas e seus modos de falha. As vigas apresentaram modos de falha semelhantes à temperatura ambiente e elevadas, porém com perda de rigidez e resistência causada pelo aumento da temperatura. Para o caso de estudo I, o montante inicial da viga apresentou baixa influência no momento de colapso, sendo o mecanismo de Vierendeel o modo de falha predominante. No entanto, no caso de estudo II, que analisa o espaçamento entre os furos, para espaçamentos entre $1.09a_0$ e $1.41a_0$, a viga falha com uma combinação entre mecanismo de Vierendeel e a encurvadura do montante da alma. Já para espaçamentos acima de $1.41a_0$, o modo de falha passa a ser exclusivamente por Vierendeel. No último caso de estudo, o diâmetro do furo apresentou grande influência nos modos de colapso das vigas alveolares. Para os menores diâmetros analisados, o colapso ocorreu na secção transversal I do montante inicial da viga. Com o aumento do furo, o colapso passou a ser por Vierendeel e depois pela combinação de Vierendeel mais encurvadura do montante da alma.

REFERÊNCIAS

[1] G. M. França, C. M. Weidlich, E. D. Sotelino, and D. C. T. Cardoso, "An appraisal of the Vierendeel mechanism capacity of cellular beams with sinusoidal openings," *J Constr Steel Res*, vol. 198, p. 107539, Nov. 2022, doi: 10.1016/J.JCSR.2022.107539.

[2] B. M. Zeytinci, M. Şahin, M. A. Güler, and K. D. Tsavdaridis, "A practical design formulation for perforated beams with openings strengthened with ring type stiffeners subject to Vierendeel actions," *Journal of Building Engineering*, vol. 43, p. 102915, Nov. 2021, doi: 10.1016/J.JOBE.2021.102915.

[3] V. Limbachiya and R. Shamass, "Application of Artificial Neural Networks for web-post shear resistance of cellular steel beams," *Thin-Walled Structures*, vol. 161, p. 107414, Apr. 2021, doi: 10.1016/J.TWS.2020.107414.

[4] L. F. Grilo, R. H. Fakury, A. L. R. de Castro e Silva, and G. de S. Veríssimo, "Design procedure for the web-post buckling of steel cellular beams," *J Constr Steel Res*, vol. 148, pp. 525–541, Sep. 2018, doi: 10.1016/J.JCSR.2018.06.020.

[5] D. Sonck and J. Belis, "Lateral–torsional buckling resistance of cellular beams," *J Constr Steel Res*, vol. 105, pp. 119–128, Feb. 2015, doi: 10.1016/J.JCSR.2014.11.003.

[6] L. V. da Silva and L. M. R. Mesquita, "Elastic lateral-torsional buckling of cellular beams," *Structures*, vol. 63, p. 106392, May 2024, doi: 10.1016/j.istruc.2024.106392.

[7] CEN, "prEN 1993-1-13, Eurocode 3 - Part 1.13: Steel Beams with Large Web Openings." European Committee for Standardization, Brussels, Belgium, 2022.

[8] J. K. Ward, *Design of composite and non-composite cellular beams*, P100 ed. SCI, 1994.

[9] R. M. Lawson and S. J. Hicks, *Design of composite beams with large web openings: in accordance with Eurocodes and the UK National Annexes*, P355 ed. SCI, 2011.

[10] S. S. Fares, J. Coulson, and D. W. Dinehart, *Steel design guide 31: castellated and cellular beam design*. American Institute of Steel Construction, 2016.
[11] M. F. Ertenli, E. Erdal, A. Buyukkaragoz, I. Kalkan, C. Aksoylu, and Y. O. Özkılıç, "Lateral torsional buckling of doubly-symmetric steel cellular I-Beams," *Steel and Composite Structures*, vol. 46, no. 5, pp. 709–718, Mar. 2023, doi: 10.12989/scs.2023.46.5.709.
[12] A. Moghbeli and Y. Sharifi, "New predictive equations for lateral-distortional buckling capacity assessment of cellular steel beams," *Structures*, vol. 29, pp. 911–923, Feb. 2021, doi: 10.1016/J.ISTRUC.2020.12.004.
[13] N. Boissonnade, J. Nseir, and H. Somja, "Design of cellular steel beams subjected to lateral torsional buckling," *Thin-Walled Structures*, vol. 197, p. 111604, Apr. 2024, doi: 10.1016/J.TWS.2024.111604.
[14] X. Chen, X. Chen, and G. Li, "Practical Design Methods for Fire Resistance of Restrained Cellular Steel Beams," *International Journal of Steel Structures*, vol. 19, no. 6, pp. 1814–1839, Dec. 2019, doi: 10.1007/S13296-019-00248-W.
[15] L. G. Justino, J. C. L. Ribeiro, G. de S. Veríssimo, J. L. R. Paes, and L. G. Pedroti, "Shear buckling strength of web-posts in castellated steel beams in fire," *Eng Struct*, vol. 209, p. 109960, Apr. 2020, doi: 10.1016/J.ENGSTRUCT.2019.109960.
[16] C. de F. Correa, H. Carvalho, R. H. Fakury, and L. F. Grilo, "Lateral-torsional buckling resistance of cellular steel beams at room temperature and fire situation," *Eng Struct*, vol. 237, p. 112046, Jun. 2021, doi: 10.1016/J.ENGSTRUCT.2021.112046.
[17] V. K. Kotapati and A. P. Khatri, "A new proposal for the design of laterally unrestrained cellular steel beams under moment gradient at elevated temperatures," *Fire Saf J*, vol. 140, p. 103812, Oct. 2023, doi: 10.1016/J.FIRESAF.2023.103812.
[18] S. B. Oribi, A. Kada, B. Lamri, and L. Mesquita, "Behaviour of cellular steel beams at ambient and high-temperature conditions," *J Constr Steel Res*, vol. 207, p. 107969, Aug. 2023, doi: 10.1016/J.JCSR.2023.107969.
[19] J. Claasen, R. Walls, A. Cicione, and D. Streicher, "Structural behaviour of a novel modular cellular steel beam system at elevated temperatures based on large-scale experimental testing and numerical modelling," *J Constr Steel Res*, vol. 197, p. 107512, Oct. 2022, doi: 10.1016/J.JCSR.2022.107512.
[20] K. A. Cashell, M. Malaska, M. Khan, M. Alanen, and K. Mela, "Experimental and numerical analysis of stainless steel cellular beams in fire," *Fire Saf J*, vol. 121, p. 103277, May 2021, doi: 10.1016/J.FIRESAF.2021.103277.
[21] CEN, "EN 1993-1-2 - Design of steel structures - Part 1-2: General rules - Structural fire design." European Committee for Standardization, Brussels, Belgium, 2005.
[22] P. H. Bortolozzo, "Instabilidade do montante da alma de vigas alveolares: estudo experimental e numérico," Instituto Politécnico de Bragança, Bragança, 2020.
[23] CEN, "EN 1991-1-2, Eurocode 1 - Actions on structures - Part 1.2: General actions - actions on structures exposed to fire." European Committee for Standardization, Brussels, 2002.
[24] CEN, "EN 1993-1-1, Eurocode 3 - Design of steel structures - Part 1-1: General rules and rules for buildings." European Committee for Standardization, Brussels, Belgium, 2005.

Congress on Numerical Methods in Engineering 2024
4-6 September 2024, University of Aveiro, Portugal

MEASUREMENT AND MODELLING OF IN-PLANE DEFORMATIONS IN PINE WOOD AND MEDIUM DENSITY FIBREBOARD AT ELEVATED TEMPERATURES

Matheus Alves[1], Luís Mesquita[2], Paulo Piloto[3] and Nuno Lopes[4]

1: RISCO, Research Centre for Risks and Sustainability in Construction
Department of Civil Engineering
Universidade de Aveiro
Campus Universitário de Santiago, 3810-193, Aveiro, Portugal
e-mail: matheus.alves@ipb.pt

2: ISISE, Institute for Sustainability and Innovation in Structural Engineering
3: LAETA-INEGI, Instituto Politécnico de Bragança
4: RISCO, Research Centre for Risks and Sustainability in Construction

Keywords: wood, wood-based, coefficient of thermal expansion, thermomechanical analysis, high temperature testing

Abstract *The need to reduce the environmental impact of the construction industry along with innovations in engineered wood-based products has contributed to the promotion of wood-based constructions as viable alternatives to traditional methods. In fire conditions, thermal strains and stresses develop in wood and wood-based materials. A thermomechanical analysis is required to account for such thermal strains and stresses, but material properties such as the coefficient of thermal expansion (CTE) at elevated temperatures are usually not available. In this work, in-plane deformations in small-scale Pinus pinaster and medium-density fibreboard (MDF) samples are investigated through experiments and finite element heat transfer and thermal strain simulations. The CTE was calculated on the basis of the experimental findings and used as input to the thermal strain analysis. The results obtained in the transient heat transfer model showed good agreement for the internal temperature evolution, but accounting for internal heat generation and mass transfer could improve the temperature predictions. The numerical results for the in-plane displacement showed good predictions but require further validation for other experimental setups and scales. The data provided in this work could be useful to investigate the loss of integrity of wood and wood-based materials under fire through thermomechanical models, and an alternative methodology is proposed to measure the temperature-dependent CTE. Efforts are still required to obtain reliable thermomechanical properties above 300 ° C, when large deformations are expected, thus contributing to understanding the fire behaviour of wood-based structures.*

1. INTRODUCTION

Wood-based construction has gained more popularity around the world. In Europe, significant progress is expected until 2030, mainly driven by increased consumption of engineered wood products [1], as well as policies and regulations proposed under the European Green Deal that highlight the role of wood and wood-based resources in promoting a sustainable construction sector to meet the energy goals of the European Union [2]. However, the perception of wood-based construction as a viable alternative to more traditional methods faces limitations in construction practice due to concerns related to the fire, acoustic, and durability performance of wood and wood-based products [3], although stringent requirements must be met for commercialisation according to the Construction Products Regulation [4]. In terms of fire safety performance, timber structures are designed to maintain integrity and limit the spread of fire through compartments and adjacent constructions, allowing safe evacuation and rescue [4]. For that purpose, the use of coverings and protective membranes to delay the onset of charring of critical members is a common practice, and wood-based panels can achieve a fire protection ability of 10 or 30 min. depending on their density and thickness [5]. However, when exposed to fire, due to a thermomechanical instability, the protective cladding may fall off from the structure it is attached to, thus exposing the underlying structure and losing its protective function. Simplified methods, such as the Fire Separating Method and the European Charring Model proposed in Eurocode 5, are capable of accounting for the phenomenon of protection fall off in structures under standard fire, where the fall off criterion is the temperature behind the protection layer [6]. In advanced numerical simulations, a thermomechanical analysis is performed to obtain the stress-strain response of the material under fire, which requires temperature-dependent physical, thermal, and mechanical properties. However, properties such as the coefficient of thermal expansion (CTE) of wood and wood-based materials have not been well reported.

Cueff et al. [7] investigated the thermomechanical behaviour of particleboard in fire. In-plane and out-of-plane CTE of particleboard was measured using 33.5 mm square samples up to 260 ° C. They identified that the CTE in the out-of-plane direction was about six times higher than in the in-plane direction. The thermal expansion of dry, moist and charred beechwood was measured by Cziegler and Kaschnitz [8] up to 900 ° C using a dilatometer. The sample sizes were 25 x 5 x 5 mm (dry and moist wood) and 12 x 5 x 5 mm (charred wood). The thermal expansion of dry and moist wood was highly dependent on the moisture content and the fibre direction, while for the charred sample, the thermal expansion had a small dependence on the fibre direction. Goli et al. [9] and Espinoza-Herrera [10] focused on measuring the CTE of wood at low temperatures (up to 60 ºC), also indicating the strong dependence of the CTE on the fibre direction and moisture content. Furthermore, Adibaskoro et al. [11] evaluated the temperature dependence of the elastic modulus, thermal expansion, and pyrolysis shrinkage of 40 x 10 x 1 mm Norway spruce samples up to 325 ºC using a dynamic thermomechanical analyser. The measured thermal expansion followed a linear expansion trend up to 200 ° C, above which shrinkage of the sample was observed.

Calculating thermal strains and pyrolysis shrinkage is necessary to understand how surface cracks and surface stresses develop in samples exposed to external heat sources [12], [13], [14].

To the knowledge of the authors, no studies have evaluated the effects of high temperatures on the thermal expansion behaviour of MDF samples. Therefore, the objective of this work is to provide a first assessment of in-plane deformations in small-scale MDF and pine wood samples (*Pinus pinaster*) samples at temperatures up to 300 ° C. Experimental tests were performed to calculate the CTE for both materials. The finite element method is used to predict the temperature distribution and the in-plane displacement through transient heat transfer and thermal strain analyses.

2. EXPERIMENTAL TESTS

2.1. Materials and samples

Table 1 shows the density and sample dimensions of the materials used in this study. The density and moisture content of the samples were determined according to EN 323 [15] and EN 322 [16], respectively.

Material	Thickness (mm)	Moisture content (%)	Wet density (kg/m3)	Dry density (kg/m3)	Surface sample size (mm)
Medium density fibreboard (MDF)	16	6,7	752	705	200 x 200
Pine (*Pinus pinaster*)	20	11	660	594	200 x 40

Table 1. Physical and geometric characteristics of the MDF and pine wood samples at room temperature.

2.2. Experimental apparatus

To measure the in-plane displacement of the samples, a universal testing machine (Shimadzu Autograph AGS -X) with a load capacity of 10 kN was used; see Figure 1a. A small nominal compression force of 1 N was applied on the upper surface of the sample to maintain contact between the sample and the steel rod throughout the test; see Figures 1b, 1c. As the sample expands or shrinks, the machine adjusts the cross-head speed according to a maximum displacement rate of 0.2 mm/s to maintain the minimum compression force on the sample. Under these conditions, it was assumed that the cross-head displacement corresponded to the in-plane displacement of the sample. The cross-head displacement and the force applied were recorded with a data acquisition frequency of 1 Hz. The results indicated that the compression force was maintained at 1.0 ± 0,06 N when testing the MDF sample, and at 1.0 ± 0,2 N in the case of the pine wood sample.

A furnace with internal dimensions of 35 x 35 x 35 cm equipped with electrical resistance was used to achieve the desired temperature, see Figure 1a. The interfaces between the sample and the aluminium stand and steel rod were protected with calcium silicate to minimise heat exchange in these areas.

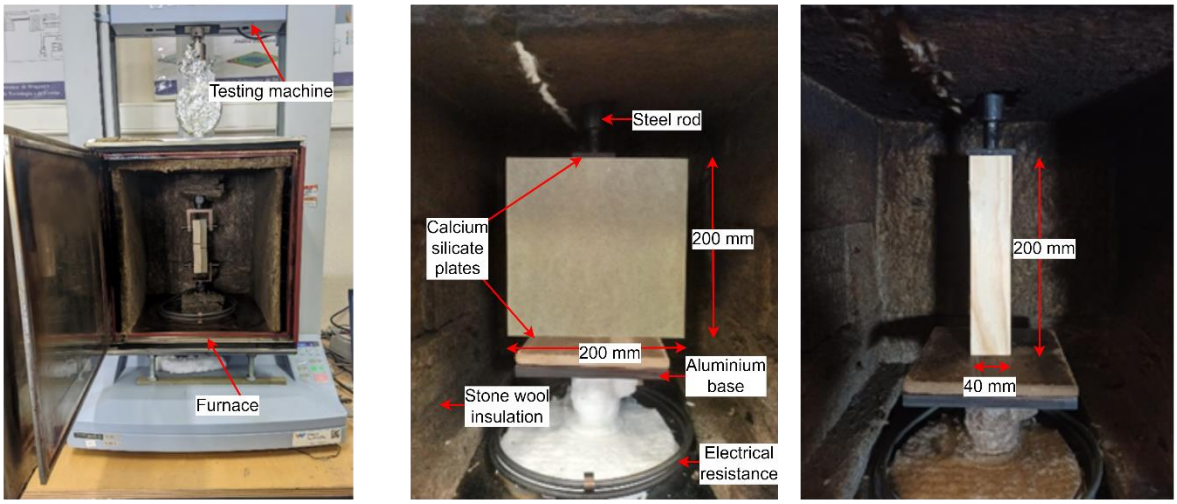

(a) Tensile tensting machine/furnace (b) MDF sample (c) Pine wood sample

Figure 1. Experimental setup to measure the in-plane displacement of MDF and pine wood samples at elevated temperatures.

A PID controller was used to control the temperature inside the furnace according to the readings of two type K thermocouples placed near the sample surface and inside the sample at 20 mm from the right edge and at mid-thickness. The temperatures were collected through a portable temperature meter (Extech SDL200) with a data acquisition frequency of 1 Hz. Figure 2 shows the temperature evolution inside the furnace and inside each sample. Although the temperature controller does not allow one to set a heating rate, it can be observed that after 2000 s, the temperature inside the furnace increases roughly at a heating rate of 1 ° C/min. As a result of the onset of thermal decomposition reactions in the MDF sample, the temperature inside the sample surpasses the furnace temperature towards the end of the test. The maximum temperature inside the pine wood sample was 294 ° C, when the furnace temperature was recorded at 298 ° C. This was due to difficulties in achieving the desired temperature level of 300 ° C in this test.

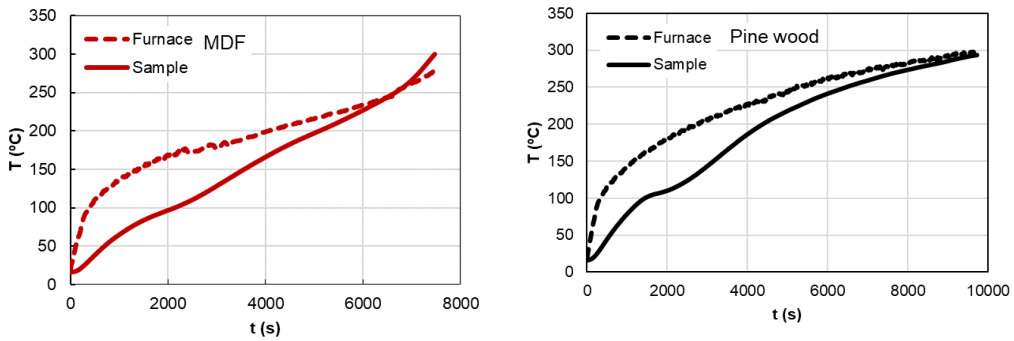

Figure 2. Temperatures inside the furnace and inside the MDF and pine wood samples during heating.

Figure 3 shows the MDF and pine wood samples after being tested and cooled to room temperature. Although the test was stopped when the temperature inside the samples reached around 300 ° C, the samples were kept inside the furnace to cool off before being removed. However, the temperature inside the sample continued to increase, reaching almost 350 ° C, and char shrinkage was expected at temperatures above 300 ° C, causing large deformations that were not measured due to experimental limitations. Also, shrinkage occurs while the sample cools off. This explains the reduced dimensions of the samples after testing, which was around 190 mm in height for the MDF and 192 mm for the pine wood, corresponding to 4% and 5 % shrinkage, respectively. As seen in Section 3, measuring the char contraction rate was not possible and the samples only expanded while heating.

Figure 3. MDF and pine wood samples after being cooled to room temperature.

The thermal expansion coefficient, CTE (/ºC), was calculated according to Equation 1, where ΔL is the in-plane deformation, taken as equal to the cross-head displacement, L is the initial sample's length and ΔT is the temperature difference between the actual temperature measured inside the sample and the reference temperature, taken as 20 ºC.

$$\mathrm{CTE}=\frac{\Delta \mathrm{L}}{\mathrm{L}\cdot\Delta \mathrm{T}} \tag{1}$$

The experimental results (EXP) for the in-plane displacement, d (mm) and the CTE for the MDF and pine wood samples are shown in Figure 4. The results obtained for the CTE were used as input to perform the thermal strain analysis in Section 3.

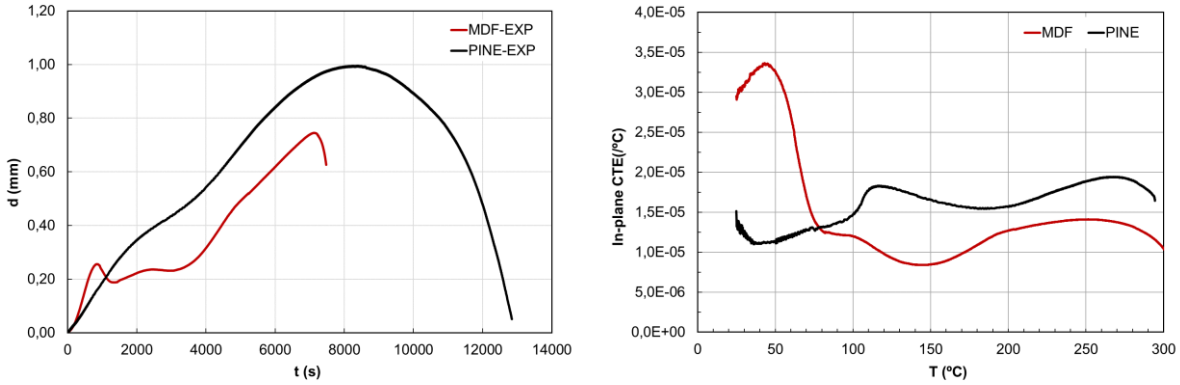

Figure 4. In-plane displacement and measured CTE values for the MDF and pine wood samples.

3. NUMERICAL MODELS

3.1. Heat transfer analysis

The 3D transient heat transfer analysis was developed in the finite element software Ansys Workbench (2022 R2). The model does not include the internal generation or absorption of heat as a result of the thermal decomposition reactions occurring in both MDF and pine wood. The thermophysical properties of virgin material and char were measured, calculated, or obtained in the literature and are shown in Table 2. The char line is assumed to be the position of the 300 ° C isotherm [6].

Solid material	Property	Unity	MDF	Pine wood	References
Virgin	Wet density	(kg/m3)	752	660	
	Dry density	(kg/m3)	705	594	
	Thermal conductivity	(W/m.K)	0,12	0,16	
	Specific heat	(J/ kg.K)	1463	1397	[17]
	Peak specific heat at 110 ºC	(J/ kg.K)	3269	4172	[18]
	Surface emissivity	(kg/m3)	0,8	0,8	[19]
Char	Density	(kg/m3)	190	220	[20], [21]
	Thermal conductivity	(kg/m3)	0,1	0,12	[20], [21]
	Specific heat	(W/m.K)	622	622	[17]
	Surface emissivity	(J/ kg.K)	0,8	0,8	[19]

Table 2. Thermophysical properties of MDF and pine wood for the heat transfer analysis.

Inspired by the work of Vermesi et al. [20], the temperature dependence of density, thermal conductivity, and specific heat is expressed as in Equation 2, where $X\ (T)$ is the temperature-dependent property, X_0 is the reference property value, T is the material temperature in Kelvin, T_0 is the reference temperature (T_0 = 20 ºC), and a is a calibrated exponent value; see [20].

$$X\ (T) = X_0 \cdot \left(\frac{T}{T_0+273,15}\right)^a \tag{2}$$

The net heat transfer ($\dot{h}_{net}$) to the exposed surfaces is a combination of natural convection and radiation, as defined in Equation 3. This boundary condition was applied to all surfaces, except the lower surface in contact with the calcium silicate board (Figures 1b, 1c), which was considered adiabatic.

$$\dot{h}_{net} = \alpha_{cv} \cdot (T_g - T_m) + \varepsilon_{res} \cdot \sigma \cdot (T_g^4 - T_m^4) \quad (3)$$

In Equation 3, α_{cv} = 4 W/m²K is the heat transfer coefficient for natural convection [19], ε_{res} = 0.8 is the resultant emissivity and $\sigma = 5.67 \times 10^{-8}$ W/m²K^4 is the Stefan-Boltzmann constant. The surface temperature is denoted by T_m. The furnace temperature measured in the experimental tests (Figure 2) was used to represent the variation of the gas temperature (T_g). The initial nodal temperature is T_0 = 20 ° C. Figure 5 shows the finite element mesh for both materials, with 8 elements along the thickness of the 16 mm thick MDF board, and 10 elements along the thickness of the 20 mm thick pine wood board. The SOLID278 finite element was selected to perform the 3D heat transfer analysis. This finite element has 8 nodes, each with one degree of freedom (temperature), and linear shape functions are used to approximate the temperature field. For this analysis, the heat flow convergence criterion was selected, with a tolerance of 0,1 % and a reference value of 1,0E-6 W. The initial time step of the solution was 0,1 s, with a minimum time step of 0,1 s, and a maximum time step of 5 s.

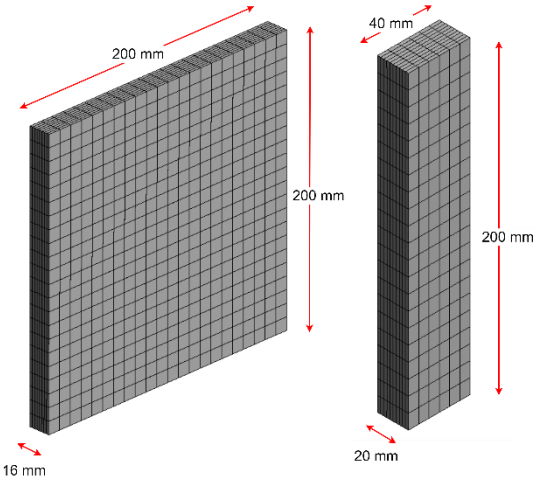

Figure 5. Finite-element mesh for the heat transfer and thermomechanical analysis.

3.2. Thermal strain analysis

In this work, thermal strains (ε^T) result from the non-uniform temperature difference obtained in the heat transfer analysis and are calculated according to Equation 4. The CTE was determined in Section 2 and used as a material property in Ansys Workbench.

$$\varepsilon^{T} = CTE \cdot (\Delta T) \quad (4)$$

The finite element mesh for the 3D thermal strain analysis, which is performed by means of a static structural analysis in the Ansys Workbench, is shown in Figure 5. In this case, the SOLID185 finite element is used. This element has eight nodes, each with three degrees of freedom (translations in each direction) and with a thermal strain capability. The body temperature obtained in the heat transfer analysis is imported as a thermal load at specified time intervals. The displacement convergence criterion was selected for this case, with a tolerance of 0,5 % and a reference value of 1E-4 mm. The initial time step of the solution was 1 s, with a minimum of 0,1 s and a maximum of 20 s. Displacement constraints (UX, UY, UZ) were applied to the bottom surface (UZ = 0) and the symmetry axes (UX = 0, UY = 0), as shown in Figure 6. The small compression force applied to the upper surface of the samples in the experimental tests was not considered in the models. In addition, the upper surface of the specimen was kept unrestrained.

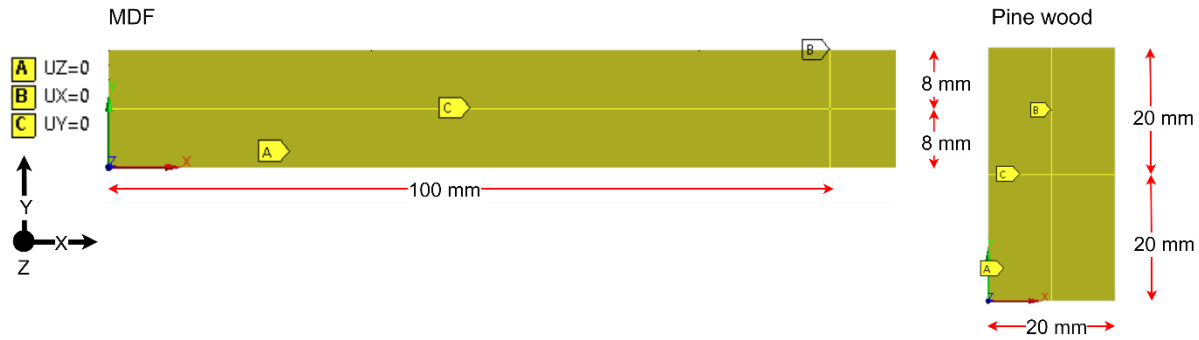

Figure 6. Boundary conditions for the thermal strain analysis of MDF and pine wood.

3.2. Results and discussion

Figure 7 presents the comparison between the experimental results (EXP) and the numerical results (NUM) for the internal temperature and the in-plane displacement of the MDF and pine wood samples. The central node at mid-thickness of the numerical models was selected to represent the internal temperature evolution. The average in-plane displacement in the Z direction corresponds to the displacement of the unrestrained upper edge at mid-length.

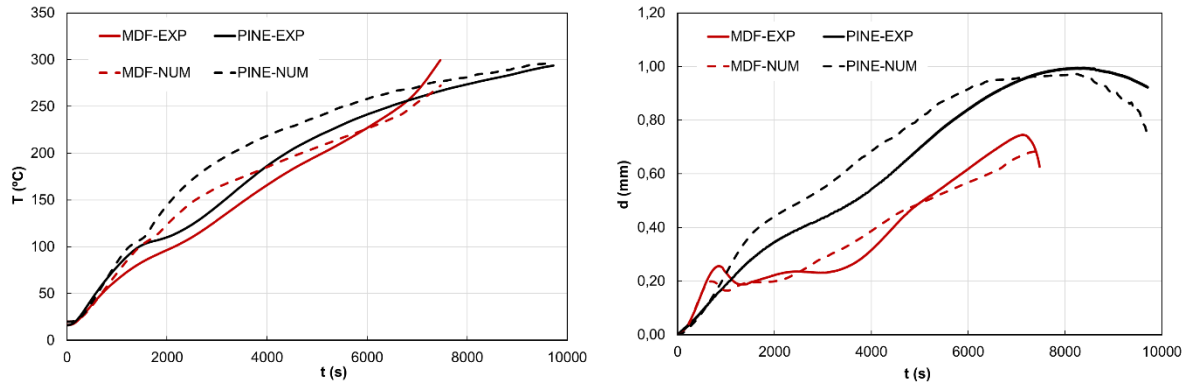

Figure 7. Comparison between experimental (EXP) and numerical (NUM) results for the internal temperature evolution and the in-plane displacement of the MDF and pine wood samples.

As seen in Figure 7, the trend of temperature evolution is well simulated throughout most of the heating period. Root mean square error (RMSE) was calculated for the entire time series, resulting in 19 ° C for the MDF and 23 ° C for pine wood. In the case of MDF, a higher temperature difference is observed at the end of the test because the heat transfer models are not able to account for the heat generation from thermal decomposition reactions. At 100 ° C, a temperature slowdown caused by dehydration is observed in the experimental values, being more evident for the pine wood sample due to its higher moisture content. This is not accurately captured by the heat transfer model, because property uncertainties and the lack of a mass transport model can significantly influence the duration of this temperature plateau [7].

Figure 8 shows the temperature distribution along the horizontal middle section of the samples at different time instants. The temperature gradient along the thickness tends to reduce with time. This indicates that the outer layers of the material are at a higher temperature during the initial stages of heating. Thus, since the calculation of the CTE was based on the temperature evolution at the centre, the effects of heating rate and adequate sample dimensions should be considered in future investigations. Temperature gradients may have a higher effect on the out-of-plane CTE, which is significantly higher than the in-plane CTE [7], [8], [11].

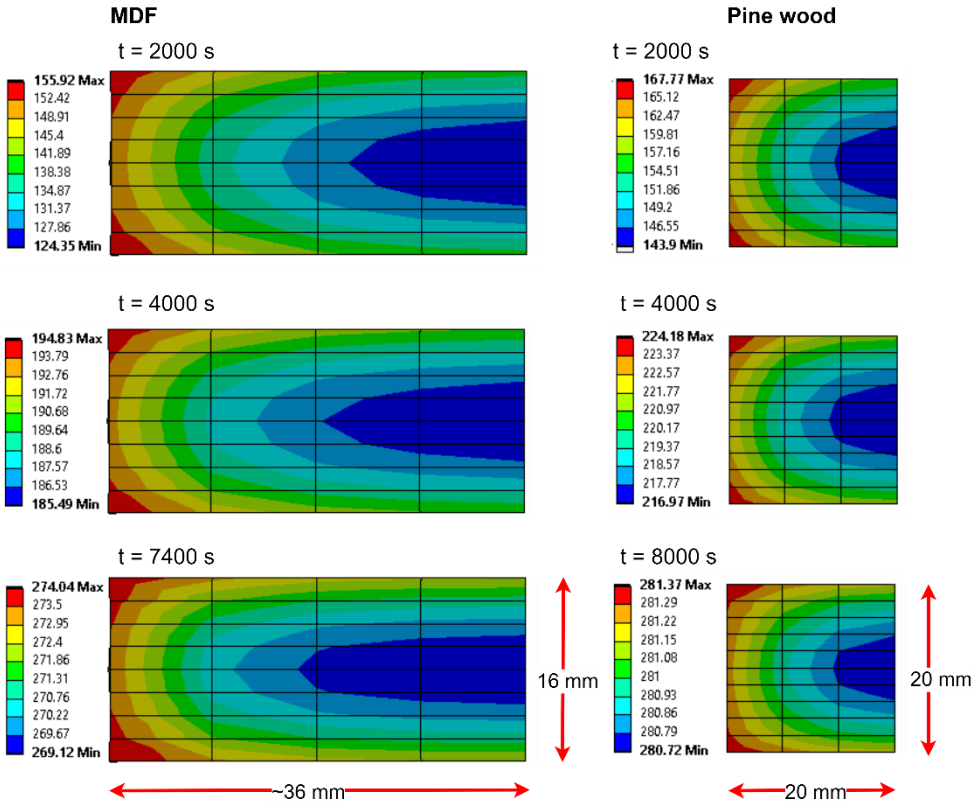

Figure 8. Temperature distribution in the horizontal middle section of the MDF and pine wood models at different time instants.

Good agreement is observed between the experimental and modelled values for the in-plane displacement; see Figure 7. This was expected because the thermal strain depends on the CTE values, which were experimentally determined, and the temperature distribution, which, as seen in Figure 7, also agrees well with the experimental findings. The RMSE resulted in 0,04 mm for the MDF sample and 0,12 mm for pine wood. The differences between the predicted and experimental deformation values are mainly related to the accuracy of the non-uniform temperature field. Figure 9 shows the final distribution of the in-plane deformations in the Z direction.

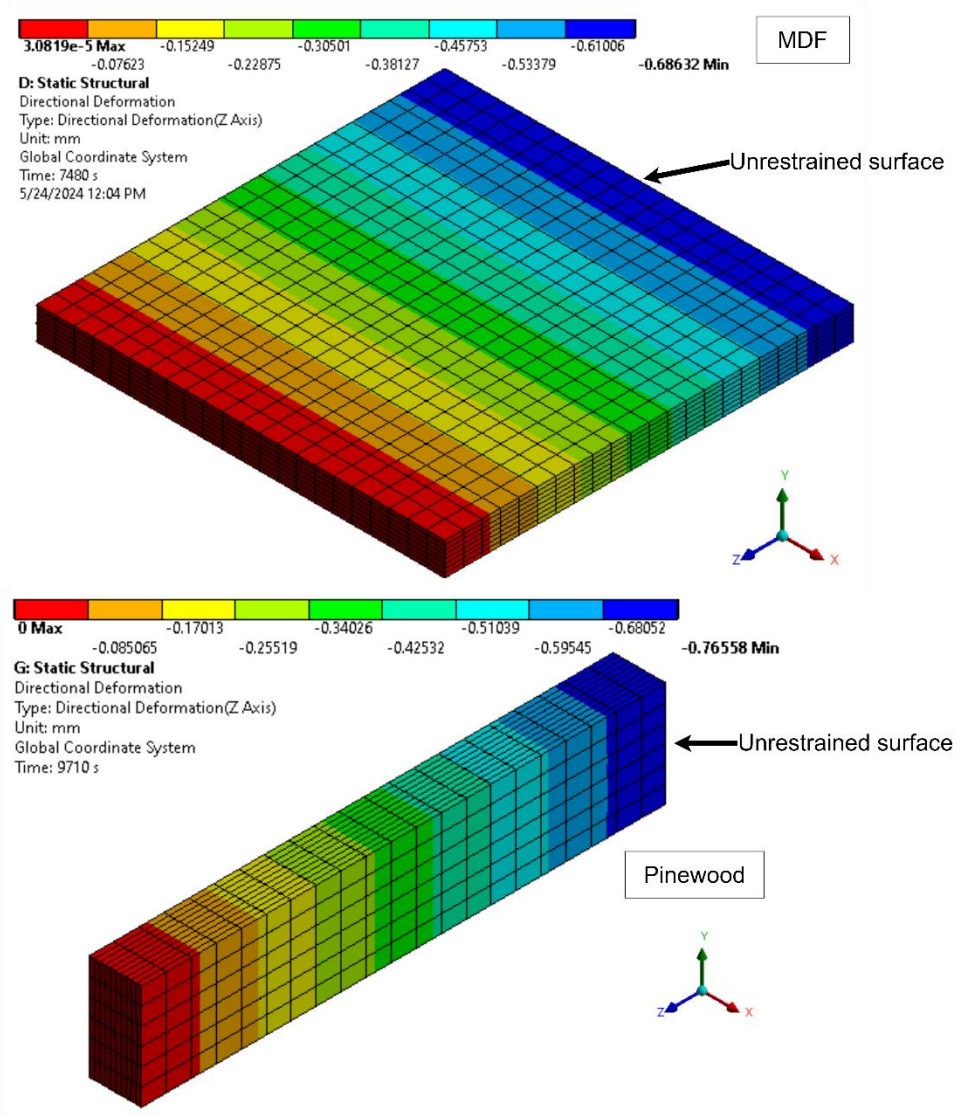

Figure 8. Distribution of the deformation in the Z direction at the final time instant of the thermal strain models of MDF and pine wood.

3. CONCLUSION

This study presents a preliminary assessment of the in-plane strain behaviour of pine wood and MDF boards at elevated temperatures. The in-plane coefficient of thermal expansion (CTE) was determined using a universal testing machine and an electric furnace, yielding consistent results at temperatures up to 300 º C. However, these results still require validation against additional experimental data. The experimental setup to measure deformations was unable to capture the char shrinkage behaviour at temperatures over 300 ° C, and further investigations are required to obtain the CTE during the char shrinkage stage of medium-sized samples and thus provide better predictions for the thermal strain

behaviour at elevated temperatures. Additionally, out-of-plane displacements are significant in wood and wood-based materials, and the CTE in this direction should be determined. Furthermore, the effects of the heating rate and sample dimensions should be taken into account in future investigations.

The transient heat transfer model provided good predictions for the temperature evolution inside the samples. Additional considerations are necessary to account for the internal heat generation from thermal decomposition reactions, which become relevant at high temperatures. Considering moisture transfer can also lead to better temperature predictions in the initial stages of heating.

The in-plane displacement of the samples was calculated through a thermal strain analysis, and a good agreement was observed between the experimental and numerical values.

Investigations are currently being conducted to measure out-of-plane displacements in wood and wood-based materials, as well as to understand the role of connections and restraints in the stress-strain response of wood-based structures. This should be useful to build thermomechanical models to analyse the thermostructural behaviour of wood-based structures at elevated temperatures.

REFERENCES

[1] J. Hildebrandt, N. Hagemann, and D. Thrän, "The contribution of wood-based construction materials for leveraging a low carbon building sector in europe," *Sustain Cities Soc*, vol. 34, no. June, pp. 405–418, 2017, doi: 10.1016/j.scs.2017.06.013.

[2] Comité Económico e Social Europeu, "Construção em madeira para reduzir as emissões de CO2 no setor da construção," 2023.

[3] J. Švajlenka and T. Pošiváková, "Innovation potential of wood constructions in the context of sustainability and efficiency of the construction industry," *J Clean Prod*, p. 137209, Apr. 2023, doi: 10.1016/j.jclepro.2023.137209.

[4] European Commission, "Regulation (EU) 305/2011 of the European Parliament and of the Council of 9 March 2011 laying down harmonised conditions for the marketing of construction products and repealing Council Directive 89/106/EEC," 2011.

[5] B. Östman and L. Boström, "Fire Protection Ability of Wood Coverings," *Fire Technol*, vol. 51, no. 6, pp. 1475–1493, Nov. 2015, doi: 10.1007/s10694-014-0452-z.

[6] CEN, "Draft prEN 1995-1-2: Eurocode 5: Design of timber structures - Part 1-2: General - Structural fire design." European Commission, 2020.

[7] G. Cueff, J.-C. Mindeguia, V. Dréan, D. Breysse, and G. Auguin, "Experimental and numerical study of the thermomechanical behaviour of wood-based panels exposed to fire," *Constr Build Mater*, vol. 160, pp. 668–678, 2018, doi: 10.1016/j.conbuildmat.2017.11.096.

[8] A. Cziegler and E. Kaschnitz, "Thermophysical Properties of Beech Wood in the Range from Room Temperature to 900 °C," *Int J Thermophys*, vol. 45, no. 2, p. 26, Feb. 2024, doi: 10.1007/s10765-023-03319-7.

[9] G. Goli, F. Becherini, M. C. Di Tuccio, A. Bernardi, and M. Fioravanti, "Thermal expansion of wood at different equilibrium moisture contents," *Journal of Wood Science*, vol. 65, no. 1, p. 4, Dec. 2019, doi: 10.1186/s10086-019-1781-9.
[10] R. Espinoza-Herrera, L. Olmos, I. A. Trujillo, and P. Garnica-Gonzalez, "STUDY OF THERMAL EXPANSION AND COMPRESSION STRENGTH OF THREE WOOD SPECIES FROM PLANTATIONS," *CERNE*, vol. 26, no. 2, pp. 256–264, Jun. 2020, doi: 10.1590/01047760202026022723.
[11] T. Adibaskoro, M. Makowska, A. Rinta-Paavola, S. Fortino, and S. Hostikka, "Elastic Modulus, Thermal Expansion, and Pyrolysis Shrinkage of Norway Spruce Under High Temperature," *Fire Technol*, vol. 57, no. 5, pp. 2451–2490, Sep. 2021, doi: 10.1007/s10694-021-01123-z.
[12] A. Ferrantelli, D. Baroudi, S. Khakalo, and K. Y. Li, "Thermomechanical surface instability at the origin of surface fissure patterns on heated circular MDF samples," *Fire Mater*, vol. 43, no. 6, pp. 707–716, Oct. 2019, doi: 10.1002/fam.2722.
[13] D. Baroudi, A. Ferrantelli, K. Y. Li, and S. Hostikka, "A thermomechanical explanation for the topology of crack patterns observed on the surface of charred wood and particle fibreboard," *Combust Flame*, vol. 182, pp. 206–215, Aug. 2017, doi: 10.1016/j.combustflame.2017.04.017.
[14] K. Li, M. Mousavi, and S. Hostikka, "Char cracking of medium density fibreboard due to thermal shock effect induced pyrolysis shrinkage," *Fire Saf J*, vol. 91, pp. 165–173, Jul. 2017, doi: 10.1016/j.firesaf.2017.04.027.
[15] CEN, "EN 323: Wood-Based Panels - Determination of Density." European Commission, 1993.
[16] CEN, "EN 322: Wood-based panels - Determination of moisture content." European Commission, 1993.
[17] K. Y. Li, C. M. Fleischmann, and M. J. Spearpoint, "Determining thermal physical properties of pyrolyzing New Zealand medium density fibreboard (MDF)," *Chem Eng Sci*, vol. 95, pp. 211–220, May 2013, doi: 10.1016/j.ces.2013.03.019.
[18] Y. Wang, I. Burgees, F. Wals, and M. Gillie, *Performance-based fire engineering of structures*. 2013.
[19] CEN, "EN 1991-1-2: Eurocode 1: Actions on structures - Part 1-2: General actions - Actions on structures exposed to fire." European Commission, 2002.
[20] I. Vermesi, F. Richter, M. Chaos, and G. Rein, "Ignition and Burning of Fibreboard Exposed to Transient Irradiation," *Fire Technol*, vol. 57, no. 3, pp. 1095–1113, 2021, doi: 10.1007/s10694-020-01017-6.
[21] F. Richter, F. X. Jervis, X. Huang, and G. Rein, "Effect of oxygen on the burning rate of wood," *Combust Flame*, vol. 234, p. 111591, 2021, doi: 10.1016/j.combustflame.2021.111591.

This page intentionally left blank

Congress on Numerical Methods in Engineering 2024
4-6 September 2024, University of Aveiro, Portugal

MÉTODO DA RESISTÊNCIA DIRETA NA DETERMINAÇÃO DA CAPACIDADE RESISTENTE DE VIGAS DE AÇO COM ABERTURAS NA ALMA SUJEITAS A INTERAÇÃO LOCAL-GLOBAL

Flávia Gimenez Berti[1], Adriano Silva de Carvalho[2], Alexandre Rossi[3] e Carlos Humberto Martins[1]

1: Departamento de Engenharia Civil, Universidade Estadual de Maringá (UEM), Brasil. e-mail: chmartins@uem.br, web: http://www.gpnum.com.br

2: Universidade de Luxembrugo, e-mail: adriano.ce7@gmail.com, web: http://www.gpnum.com.br

3: Faculdade de Engenharia Civil, Universidade Federal Uberlândia, e-mail: alexandre-rossi@hotmail.com, web: http://www.gpnum.com.br

Palavras-chave: Flambagem no Montante da Alma; Método da Resistência Direta; Vigas Alveolares.

Resumo. *As formas de colapso das vigas alveolares, são comumente estudadas e abordadas na literatura, isso pelo fato desses perfis possuírem maior suscetibilidade à flambagem, por conta das aberturas presentes na alma, que aumentam a inércia do perfil, porém reduzem a rigidez a torção da viga. A Flambagem Lateral com Torção (FLT), uma forma de colapso global muito estudada, também, para perfis de alma cheia, ocorre com maior facilidade nesses outros modelos de viga, justamente por conta das aberturas. Já a Flambagem no Montante da Alma (FMA), ocorre localizada no elemento, na região entre as aberturas da alma (montante), sendo um modo de falha exclusivo para os perfis alveolares. Individualmente, ambos modos de falha são bastante abordados na literatura, entretanto, quando se trata da interação entre eles, poucos estudos são referenciados e por isso torna-se importante a análise de vigas alveolares sob essas condições. Dessa forma, o objetivo deste trabalho será compreender a interação entre FLT e FMA, exclusivamente em vigas alveolares de aberturas circulares, caracterizadas como vigas celulares, propondo o desenvolvimento de uma curva de projeto, utilizando o Método da Resistência Direta (MRD). Desse modo, pretende-se analisar numericamente 120 modelos considerando a interação entre FLT e FMA e assim extrair uma curva normalizada pela esbeltez global-local destes perfis e determinar uma equação para o momento último de vigas celulares submetidas a esses dois modos de falha simultâneos.*

1. INTRODUÇÃO

Os perfis de aço com aberturas na alma, conhecidos como perfis alveolares, são caracterizados pelo padrão de aberturas que possuem. As vigas celulares apresentam um padrão de corte circular e, assim como outros perfis alveolares, são amplamente utilizadas para vencer grandes vãos, conforme ilustrado na Figura 1. Além disso, facilitam a passagem de tubulações e garantem uma estética agradável a estrutura.

Figura 1. Vigas celulares em um ginásio poliesportivo, [1]

Esse tipo de viga é fabricado a partir do corte térmico em perfis laminados de alma cheia, seguido pelo deslocamento e soldagem das duas faces da viga, como mostra a Figura 2. Esse processo garante a expansão na altura da peça, resultando em uma melhor proporção entre peso próprio e resistência mecânica, uma vez que se aumenta a inércia utilizando a mesma quantidade de material. No entanto, esse aumento na seção transversal torna o perfil mais suscetível a falhas, o que se torna ainda mais crítico devido à abertura na alma que reduz a rigidez à torção da viga.

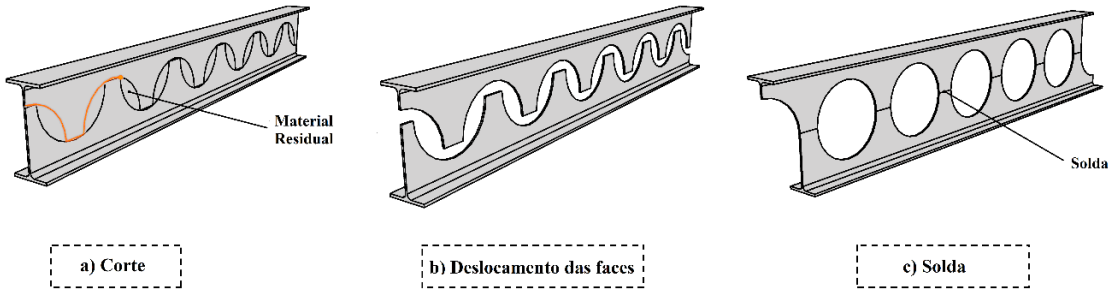

Figura 2. Processo de fabricação das vigas celulares

Quando submetidas aos carregamentos nas estruturas, as vigas alveolares ficam sujeitas às seguintes formas de colapso: flambagem lateral com torção (FLT), flambagem no montante da alma (FMA), flambagem por mecanismos de Vierendeel (MV) e interações entre estes, [2]. Além disso, as tensões residuais provenientes do processo de fabricação desses perfis, impactam diretamente nos modos de falha citados, visto que a modificação dessas altera significativamente a resistência da viga, [3].

A Flambagem Lateral com Torção (FLT), causada pelo momento fletor atuante no eixo de maior inércia da seção, é um fenômeno comum também para vigas de perfil cheio, porém as aberturas na alma afetam a capacidade das vigas celulares, tornando-as menos resistentes. Segundo [4], a FLT pode ser subdividida em três regimes de flambagem:

1. Regime elástico: comum para vigas esbeltas, no qual a estrutura passa de uma configuração estável para instável, tornando-se estável novamente;
2. Regime inelástico: situação em que algumas fibras já atingiram a resistência ao escoamento;
3. Regime de plastificação: não se observa o fenômeno da flambagem, uma vez que a plastificação da seção transversal ocorre primeiro.

Já a Flambagem no Montante da Alma (FMA), exclusiva para perfis com aberturas, ocorre devido aos esforços cortantes, que geram tensões de cisalhamento no montante da alma, especialmente evidente quando se têm seções de largura reduzida. A Flambagem no Montante da Alma pode ser causada por compressão, ou cisalhamento, onde a força de cisalhamento presente na região da solda da peça, solicita as bordas à flexão, fazendo com que haja deslocamento e torção da seção, como mostra a Figura 3. Diferentemente, para FMA por compressão, não se observa a torção do elemento, [1].

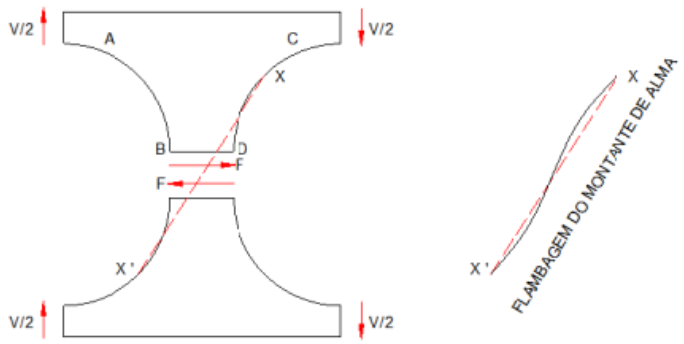

Figura 3. Esquema de solicitações para FMA por cisalhamento, [1]

A capacidade resistente da FMA depende do diâmetro das aberturas, o espaçamento entre elas e a espessura da alma, sendo predominante nas vigas sob cargas concentradas, por exemplo nas regiões de apoio viga-pilar em que não há enrijecedores, [2]. Adicionalmente, [5] concluiu que a flambagem elástica dificilmente ocorre nos casos de FMA por cisalhamento, sendo que a maioria dos casos se encontra no regime de flambagem inelástico, [2].

A interação entre esses dois modos de falha, representada na Figura 4, pode ser observada principalmente em perfis de pequena esbeltez global, em fases construtivas ou nos casos em que o travamento lateral da estrutura não é feito corretamente, deixando livre o deslocamento. Essa interação é pouco explorada na literatura, por isso busca-se desenvolver uma curva de projeto para as vigas celulares submetidas à esforços que causam FLT e FMA, utilizando o Método da Resistência Direta (MRD), que surgiu inicialmente como alternativa à abordagem da largura efetiva para determinação da resistência de perfis de aço formado a frio, [6].

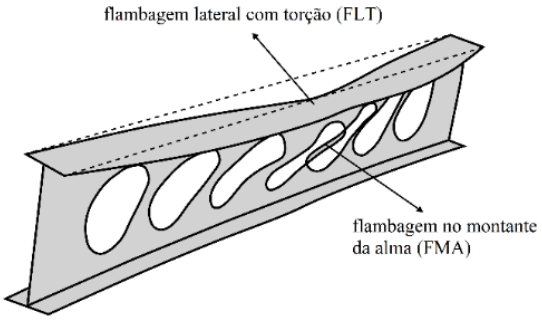

Figura 4. Interação entre modo de falha local e global em uma viga celular

Embora geralmente aplicado a perfis de aço formados a frio, como mostra o estudo feito por [7], pesquisas indicam a aplicabilidade do Método da Resistência Direta (MRD) também para perfis de aço com aberturas na alma sob flexão. Um exemplo disso é o estudo de [8], no qual investigaram a instabilidade de vigas casteladas devido à interação entre a flambagem local por compressão no "tê" da peça e a flambagem lateral por torção (FLT). Nesse estudo, foram propostas equações de dimensionamento pelo MRD, que levam em consideração as características plásticas da seção transversal do elemento e sua capacidade de carga máxima.

Existem inúmeros estudos que abordam a situação das vigas alveolares sob efeito de flambagem global e local, tanto do montante da alma, quanto do “tê” comprimido. [9] estudaram as vigas casteladas com ênfase na flambagem no montante da alma, concluindo que as regiões de extremidade são submetidas a maior força de cisalhamento. [10] também estudou as vigas alveolares sob FMA e concluiu que nas vigas casteladas curtas, a flambagem nos montantes de alma é um modo de colapso importante, e que ocorre, geralmente, em regime inelástico, mesmo nas vigas com alma esbelta. Da mesma forma, inúmeros outros autores estudaram o fenômeno da FLT em vigas alveolares, como é o caso de [3].

No entanto, quando se trata da interação entre esses dois modos de falha, percebe-se uma lacuna tanto na literatura quanto nas normas recomendadas, que fornecem curva de projeto que relacionam apenas a esbeltez global das vigas com o momento último de dimensionamento para FLT, não abrangendo o acoplamento entre instabilidade local e global, como é o caso do [11]. Por isso, propõe-se o estudo e modelagem de vigas sob carregamentos que gerem esses dois modos de falhas simultaneamente, a fim de determinar uma curva de projeto normalizada para esbeltez local-global da viga.

Utilizando o método dos elementos finitos, busca-se calibrar um modelo numérico e desenvolver um estudo paramétrico no software Abaqus com o objetivo de obter dados que permitam a determinação de uma curva de projeto para vigas celulares submetidas à interação de dois modos de falha. Pretende-se estabelecer uma proposta para o dimensionamento de vigas celulares de aço sujeitas a falha por interação entre a flambagem do montante da alma (FMA) e a flambagem lateral com torção (FLT), utilizando como base os princípios do Método da Resistência Direta (MRD).

Por fim, procura-se determinar os autovalores associados à ocorrência de FLT e FMA, para se determinar a capacidade resistente ou momento último dos perfis I de aço com abertura na alma. Com isso, busca-se realizar a otimização para o melhor ajuste de uma curva de projeto

aos dados para falha global e para falha local-global, ou seja, para as situações em que o elemento está submetido à carregamentos que geram flambagem lateral com torção e flambagem no montante da alma ao mesmo tempo.

2. REFERENCIAL TEÓRICO

Inúmeros autores têm estudado, desde muito tempo, sobre as formas de colapso em vigas alveolares e proposto equações para determinação da capacidade resistente desses elementos. [12] elaboraram gráficos para estimar a capacidade resistente de vigas casteladas, por meio da análise numérica, pelo Método dos Elementos Finitos. Também, realizaram ensaios experimentais com 12 vigas, as quais 10 sofreram falha por FMA.

[13] realizou uma análise experimental de 14 vigas casteladas, simulando-as numericamente com valores calibrados, a fim de se variar parâmetros como esbeltez da alma, resistência ao escoamento do aço e imperfeições iniciais, com o objetivo de entender como esses parâmetros podem influenciar na determinação da força cortante resistente nominal à FMA. Foi elaborada uma formulação para tal capacidade resistente e além disso, proposto quatro passos para sua determinação: cálculo da esbeltez do montante; cálculo dos índices de esbeltez limite (dependentes da imperfeição inicial e da resistência ao escoamento do aço); comparação da esbeltez do montante com os índices para determinação do fator de força cortante e por fim, a obtenção da força cortante resistente nominal.

[8] analisaram, por simulações, 197 vigas casteladas simplesmente apoiadas, a fim de determinar a capacidade resistente de elementos sujeitos à interação local-global, sendo, diferentemente do presente trabalho, a Flambagem do Tê Comprimido interagindo com a FLT. Pelo MRD, eles realizaram uma nova abordagem, comparada com os procedimentos padrão atuais. O estudo identificou distintos modos de falha, tais como flambagem global (FLT), flambagem local (enrijecimento em T), interação local-global e influenciados pelo escoamento. Essa interação complexa entre os modos de falha influenciou a capacidade de carga e o comportamento estrutural das vigas casteladas sob flexão. Os resultados mostram que a equação proposta prevê valores de resistência melhores em todos os casos, fornecendo informações valiosas para o projeto de vigas casteladas.

3. MÉTODO DE PESQUISA

A modelagem numérica das vigas celulares no software Abaqus foi feita em algumas etapas: determinação do material utilizado, definição das propriedades geométricas dos perfis, desenho do perfil no software, forma de travamento da estrutura, lançamento do carregamento, definição da malha e por fim as análises. Sendo que, anterior a todas essas, deve ser feita a calibração do modelo numérico, tendo como base o ensaio feito por [14] para validação dos modelos sob FMA e o ensaio de [3] para os modelos sob FLT.

Foi considerado o aço S355 e vigas celulares de seção transversal comercial, especificamente as vigas da série IPE, indicadas na Tabela 1. Ao todo, foram modeladas 120 vigas, com 20 variações de comprimento para cada um dos perfis, sendo o comprimento inicial (L_0) de cada uma delas, indicado também na Tabela 1.

Perfil	d	d_0	b_f	t_w	t_f	$b_f/2t_f$	h/t_w	L_0 [mm]
IPE 270	405	270	135	6.6	10.2	6.62	58.27	1000
IPE 330	495	330	160	7.5	11.5	6.96	62.93	1200
IPE 400	600	400	180	8.6	13.5	6.67	66.63	1700
IPE 500	750	500	200	10.2	16	6.25	70.39	2200
IPE 600	900	600	220	12	19	5.79	71.83	2700
IPE 750	1129.5	753	265	13.2	17	7.79	82.99	3200

Tabela 1. Perfis utilizados na análise

Para a simulação do material na fase elástica, foi considerado módulo de elasticidade de 200 GPa e coeficiente de Poisson de 0,3. Para a simulação do comportamento plástico na análise de pós-flambagem foi utilizado o modelo constitutivo de Earls, [15].

As imperfeições geométricas também foram aplicadas ao perfil, considerando a razão L/1000, para análise post-buckling, bem como as tensões residuais, presentes nas vigas devido ao seu processo de fabricação. Para simular estas, foi considerado o modelo de [3], indicado na Figura 5.

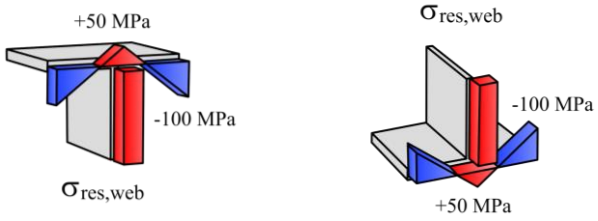

Figura 5. Distribuição das tensões residuais, [16]

Para a simulação da viga no Abaqus, foram utilizados elementos do tipo Shell, ou seja, de casca, como ilustrado na Figura 7.

Utilizou-se a aplicação de momento constante apara avaliar as hipóteses básicas do FLT, contudo como pretendia-se avaliar a instabilidade local por FMA fez-se necessário a utilização de carregamentos transversais para mobilizar tensões de cisalhamento na estrutura. A Figura 6 ilustra essa situação. Vale ressaltar que, para a realização das análises, todos os 6 perfis, com suas respectivas variações de comprimentos, foram simulados duas vezes: uma para cada disposição de carregamento.

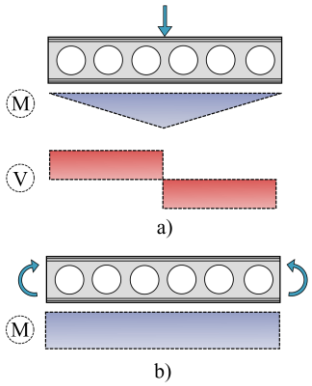

Figura 6. Carregamento e esforços atuantes na viga

Para que o deslocamento aconteça, fez-se necessário dispor das condições de contorno de forma que a viga fique com rotação em torno do eixo longitudinal travada e deslocamento livre na direção axial. Para malha, foi admitido 10mm seguindo validações feitas por [17]. A malha e as respectivas condições de contorno estão representadas na Figura 7.

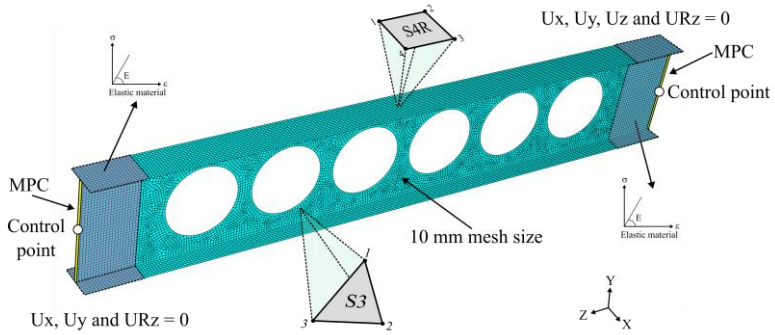

Figura 7. Definição da malha e condições de contorno

Finalizadas as etapas iniciais, a análise buckle foi feita, para as duas condições de carregamento previamente explicadas, computando valores de carga crítica global e local de todos os modelos, sendo estas indicadas pelos autovalores e as formas de flambagem, autovetores. Depois, realizou-se a análise post-buckling, em que se considera as imperfeições e tensões já citadas a pouco, a fim de computar os momentos últimos dos modelos e então relacioná-los com a esbeltez global dos perfis, calculada a partir da equação 1.

$$\lambda_G = \sqrt{M_p / M_{cr,global}} \tag{1}$$

Essa relação é feita pela normalização do momento último pelo momento de plastificação, plotando um gráfico em função da esbeltez global, desprezando, para o traçado do melhor ajuste, os modelos que geraram instabilidade local nos perfis. Assim, obteve-se a equação da curva, denominada de Momento Nominal Global, que serve de base para normalização do momento último, a fim de se construir um gráfico em função da esbeltez global-local dos perfis. Esta esbeltez de interação é calculada a partir da equação 2.

$$\lambda_{int} = \sqrt{M_{u,G} / M_{cr,local}} \tag{2}$$

O segundo gráfico, gerou uma curva que representa o Momento Nominal Global-Local, ou seja, dos perfis que falharam simultaneamente por FMA e FLT. Dessa forma, tem-se a redução da capacidade da estrutura em função da ocorrência do acoplamento entre instabilidade local e global.

4. RESULTADOS E DISCUSSÃO

4.1. Validação do Modelo

A validação do modelo no software Abaqus foi feita com base em ensaios e resultados experimentais, sendo estes já citados anteriormente. Na Tabela 2 encontra-se as vigas utilizadas para calibração do modelo numérico, tanto para FLT, quanto para FMA, bem como suas referências.

ID	Autor	Modo de falha
CS2_L3	[3]	FLT
A1	[14]	FMA

Tabela 2. Vigas utilizadas para validação do modelo

Para que a validação do modelo aconteça, reproduz-se no Abaqus as mesmas condições do ensaio realizado, sendo, para o primeiro caso, a viga com vínculo de garfo, simplesmente apoiada submetida a aplicação de uma carga concentrada. O resultado obtido numericamente, condiz com os resultados físicos, como se observa na Figura 9(a), em que a curva carga x deslocamento numérica, aproxima-se da experimental. Dessa forma, valida-se o modelo para FLT.

Já para a validação do modelo sob FMA, também se considerou vigas simplesmente apoiadas e condições de contorno indicadas na Figura 8. A tensão residual dos perfis foi implementada na parcela de imperfeição geométrica inicial, diferente para cada uma das vigas simuladas no caso em questão.

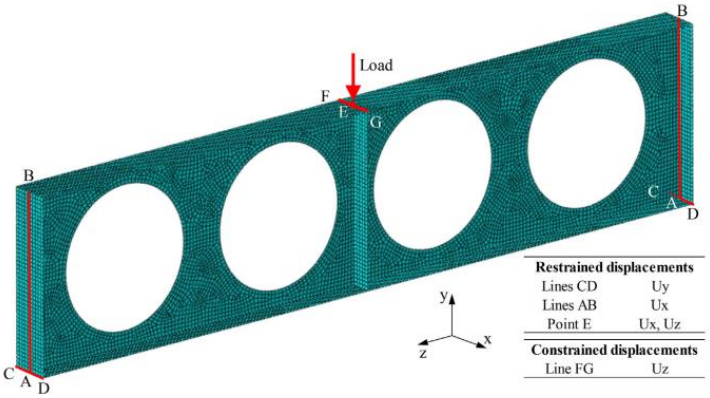

Figura 8. Condições de contorno proposta por [14] para validação do modelo

O resultado obtido, também se mostrou coerente, comparado aos resultados experimentais, como mostra a Figura 9(b).

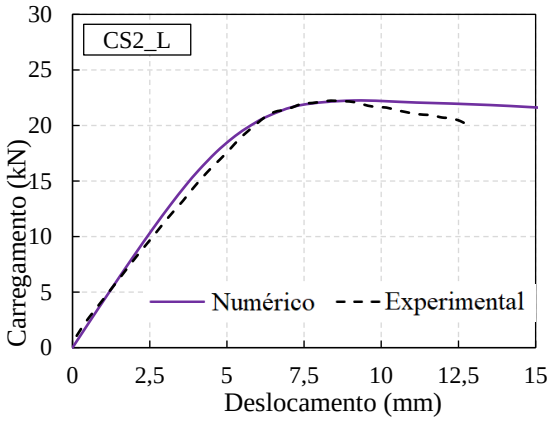

(a)

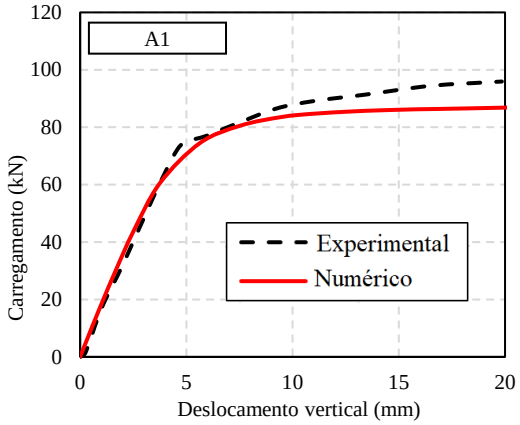

(b)

Figura 9. a) Validação para o caso em que ocorre FLT b) Validação para o caso em que ocorre FMA

4.2. Resultados

Tendo coletado o momento último global de todos os perfis analisados, foi possível construir o gráfico mostrado na Figura 10(a), plotado em função da esbeltez global, sendo o eixo das ordenadas a razão do momento último global pelo de plastificação. O momento último foi determinado pela curva carga vs. deslocamento, gerada na análise pós-flambagem, em todos os perfis e para as duas condições de carregamento. Observa-se que a maioria dos perfis, independentes do carregamento, exibiram um comportamento que se assemelha ao de uma curva bem definida.

Porém, alguns perfis de pequena esbeltez global não se enquadram no comportamento esperado da curva, evidente pelo quadrante inferior esquerdo do gráfico. Isto acontece porque as vigas sob carga concentrada e, portanto, sobre esforços de cisalhamento, apresentam falha por instabilidade local ou acoplamento por instabilidade global e local. Portanto, pode-se afirmar, num primeiro momento, que os pontos fora da curva, serão significativos para a análise da interação local-global.

Pelo Método da Resistência Direta, ajustou-se uma curva de dimensionamento para o Momento Nominal Global ($M_{u,G}$), que vai ser calculado de acordo com o valor da esbeltez global da viga, como sugerem as equações propostas. A curva ajustada, com coeficientes determinados pelo método dos mínimos quadrados, está representada no gráfico mostrado na Figura 10(b).

Fazendo-se a igualdade proposta na equação 3 e por meio do método dos mínimos quadrados, executado pela linguagem *Phyton* de programação, chega-se à proposta da equação 4 para vigas cujas estabilidade global está entre 0,2 e 1,2 e à proposta 5, para estabilidade global maior que 1,2.

$$M_{u,G} = M_p \quad \ldots \quad \lambda_G \leq 0.2 \tag{3}$$

$$M_{u,G} = M_p\left[\frac{1}{\phi_G + \sqrt{\phi_G - \lambda_G}}\right], \qquad para\ 0.2 < \lambda_G \leq 1.2 \tag{4}$$

$$sendo\ \phi_G = 0.5\left[1 + 0.29(\lambda_G - 0.2) + {\lambda_G}^2\right]$$

$$M_{u,G} = M_p\left[{\lambda_G}^{-2}\left(1 - 0.416{\lambda_G}^{-2.247}\right)\right], \qquad para\ \lambda_G > 1.2 \tag{5}$$

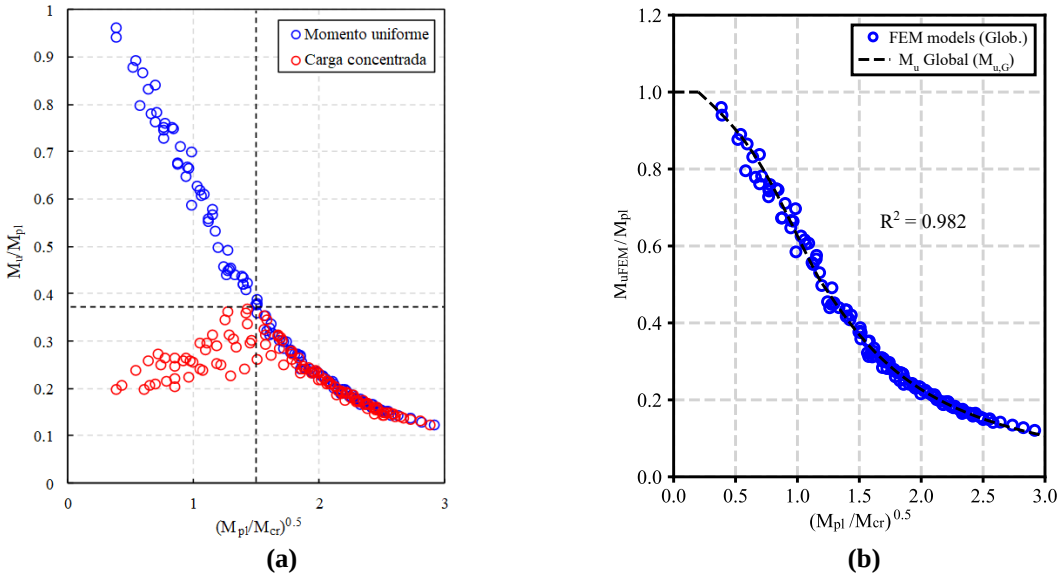

Figura 10. (a) Ajuste de curva para a falha global (b) Normalização do M_u em função da esbeltez global

Dessa forma, têm-se as equações que fornecem o valor do Momento Nominal Global ($M_{u,G}$), em função da esbeltez global, calculada pela equação 1, e em função do momento de plastificação da viga, que pode ser calculado, teoricamente, pela equação 6.

$$M_p = f_y.Z \tag{6}$$

Para que a parcela de perfis que falharam localmente também seja considerada, de modo a garantir a interação entre os dois modos de falha, normaliza-se o momento último global em função do Momento Nominal Global ($M_{u,G}$), produzindo um gráfico em função da esbeltez global-local, calculada pela equação 2. Assim, obtém-se o gráfico da Figura 11, que já representa os perfis que falharam devido a interação de FLT e FMA.

Semelhante ao primeiro gráfico, utiliza-se do MRD para determinar a equação da curva que melhor se ajusta ao gráfico, sendo essa representada como equação 7. Observa-se que o Momento Último de Interação ($M_{u,I}$) vale para perfis cuja esbeltez local-global é maior que 0.8. Dessa forma, observando-se a curva proposta no Gráfico 4.5, conclui-se que os modelos agrupados na faixa constante da curva, onde se observa $M_{uFEM}/M_{u,G} = 1$, são os perfis que falharam globalmente, e o restante, cuja $\lambda_{int} \geq 0.8$ são os que falharam pela interação local-global.

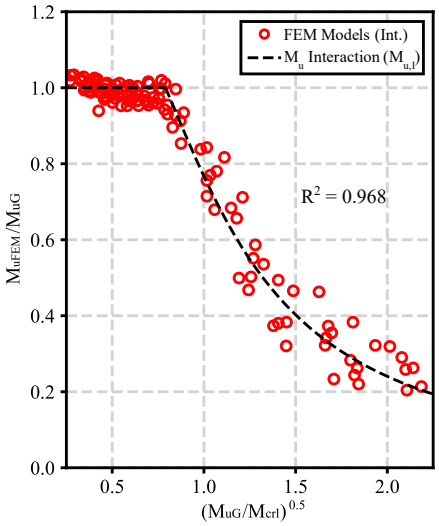

Figura 11. Ajuste de curva para os perfis que falharam por interação FLT e FMA

$$M_{u,I} = M_{u,G}\left[{\lambda_{int}}^{-1.942}\left(1 - 0.214{\lambda_{int}}^{-2.512}\right)\right], \qquad para\ \lambda_{int} \geq 0.8 \tag{7}$$

Sendo assim, a proposta de curva de dimensionamento para vigas celulares sujeitas a interação local-global é realizada, de modo com que fica sendo dependente do momento crítico global e local da viga, uma vez que $M_{u,I}$ depende da esbeltez local-global, que é dependente do momento crítico local. Esta grandeza pode ser calculada por fórmulas experimentais, como propõe inúmeras literaturas. Já o momento crítico global, pode ser encontrado facilmente pela equação 8, como calculado por [8].

$$M_{cr,global} = \frac{\pi}{L}\sqrt{GI_tEI_z + \frac{\pi^2}{L^2}EI_zEI_w} \tag{8}$$

AGRADECIMENTOS

Este estudo foi financiado em pelo Conselho Nacional de Desenvolvimento Científico e Tecnológico (CNPq) no âmbito do projeto nº 408498/2022-6.

REFERÊNCIAS

[1] C. H. VIEIRA. *Análise Numérica da Flambagem do Montante de Alma devida ao Cisalhamento em Vigas de Aço Celulares*, Dissertação (Mestrado em Engenharia de Estruturas), Universidade Federal de Minas Gerais. Belo Horizonte, (2014).

[2] D. KERDAL, D. A. NETHERCOT. *Failure modes for castellated beams*. Journal of Constructional Steel Research. v.4, p.295-315, (1984).

[3] D. SONCK, J. BELIS. *Lateral-torsional buckling resistance of cellular beams*. Journal of Constructional Steel Research. v.105, p.119-128, (2015).
[4] R. D. ZIEMIAN, *Guide to stability design criteria for metal structures*. Sixth Edition. New Jersey: John Wiley & Sons, Inc,1078p, (2010).
[5] R. DELESQUES, *Stabilité des montants de poutres ajourées*. Construction Métallique. 3:26-33; (1968)
[6] A. RUSCH, J. LINDNER. *Remarks to the Direct Strength Method.* Thin-Walled Structures. v.39, p.807-820, (2001)
[7]. J. P. MIYAZAKI, A. S. CARVALHO, C. H. MARTINS, A. ROSSI. *Evaluation of the interaction between distortional–global buckling in perforated cold-formed steel rack sections*. Structures. v.54, p.808-824, (2023).
[8] C. WEIDLICH, E. SOTELINO, D. CARDOSO. *An application of the direct strength method to the design of castellated beams subject to flexure*. Engineering Structures. v.243, (2021)
[9] R. REDWOOD, S. DEMIRDJIAN. *Castellated beam web buckling in shear*. Journal of Structural Engineering. v.124, n.10, p.1202-1207, (1998).
[10] W. B. VIEIRA. *Simulação numérica do comportamento estrutural de vigas casteladas de aço com ênfase na flambagem no montante de alma,* Dissertação (Mestrado em Engenharia Civil), Universidade Federal de Viçosa. Viçosa, (2011)
[11] EUROCODE 3. EN 1993-1-1 2005 – *Design of steel structures. Parte 1.1 General rules and rules for buildings*. CEN - European Committee for Standardization, (2005).
[12] W. J. ZAAROUR, R. G. REDWOOD. *Web Buckling in Thin Webbed Castellated Beams*. Journal of Structural Engineering. 860-866; (1996)
[13] W. B. VIEIRA. *Estudo numérico-experimental da flambagem do montante de alma em vigas casteladas de aço*, Tese (Doutorado em Engenharia Civil) – Universidade Federal de Viçosa, Viçosa, (2015)
[14] L. GRILO, R. H. FAKURY, A. SILVA, G. VERÍSSIMO. *Design procedure for the web-post buckling of steel cellular beams*. Journal of Constructional Steel Research. v.148, p.525-541, (2018).
[15] C. J. EARLS. *Effects of material property stratification and residual stresses on single angle flexural ductility*. Journal of Constructional Steel Research, n. 51, p.147-175, (1999)
[16] C. H. MARTINS,A. S. CARVALHO, A. ROSSI. *Avaliação numérica da Flambagem Lateral com Torção em vigas de aço em perfil I com aberturas sequenciais na alma em padrão senoidal.* XV Congresso Ibero-americano de Engenharia Mecânica, Madrid, (2022).
[17] A. S. CARVALHO, V. M. OLIVEIRA, A. ROSSI,A.; C. H. MARTINS; *Elastic lateral-torsional buckling behavior of steel I-beams with sinusoidal web openings*. Structures. v.47, p.23-36, (2023).

Congress on Numerical Methods in Engineering 2024
4-6 September 2024, University of Aveiro, Portugal

NUMERICAL SIMULATION OF LABORATORY COMBUSTORS: A COMPARISON OF TWO COMMERCIAL CODES

Bruno M. Pinto, Afonso Santoalha, Gonçalo P. Pacheco, Pedro J. Coelho and Miguel A. A. Mendes

IDMEC, Mechanical Engineering Department, Instituto Superior Técnico, Universidade de Lisboa, 1049-001 Lisboa, Portugal
email: pedro.coelho@tecnico.ulisboa.pt

Keywords: Computational fluid dynamics, Commercial codes, Laboratory combustor, Turbulence, Combustion, Radiation

Abstract *Commercial codes for the numerical simulation of fluid flows have been progressively become more sophisticated and user-friendly, including a wide variety of mathematical/physical models and numerical methods. Their robustness and accuracy has also been improved. Due to these features, they are nowadays widely used in research rather than only in the industry. In this context, the following question arises: to what extent can we be confident on the results computed using a commercial code? Moreover, how close are the results predicted by different codes? In the present work, a detailed comparison of two leading computational fluid dynamics (CFD) commercial codes (Ansys Fluent and Star-CCM+) is presented for the numerical simulation of a laboratory combustor. The calculations for both codes are performed using the same mesh, the same mathematical and physical models, the same discretization methods of the governing equations, and the same solution algorithm. Preliminary simulations are performed for an isothermal flow. Then, combustion is included and finally radiation is also considered. It is shown that despite the mathematical, physical and numerical methods are identical for both codes, there are differences between the predicted results, even for isothermal flow.*

1. INTRODUCTION

The mathematical and physical modelling of combustion chambers involves complex interacting physical phenomena, namely turbulence, chemical kinetics, convective and diffusive transport and heat transfer. These phenomena are governed by conservation equations that include terms that need to be modelled. The numerical solution of the governing equations is based on algorithms that are often complex. A few decades ago, the mathematical modelling and the numerical solution was only based on in-house codes written at universities and research laboratories. As more advanced models and more precise numerical methods were developed, commercial codes also appeared. The recognition by the industry of the potential of these codes in the development of better products has boosted the improvement of the commercial codes.

Nowadays, they are widely used, both in industrial applications and in research. This is demonstrated by the continuous increase of the number of references to such codes in citation databases. As an example, in the well-known Scopus database [1], the number of references to Ansys Fluent [2] in the article title, abstract or keywords increased monotonically from 78 in 2010 to 1791 in 2023, with a total of more than 12,000 references since 2010. A similar trend is observed with other popular computational fluid dynamics codes, such as Simcenter Star CCM+ [3], Ansys CFX and COMSOL. These codes largely remain like black boxes, since the source code is not available to the users. Even though they have been validated for a large amount of different problems, the validation is always an issue when a new problem needs to be solved. Hence, the confidence on the results computed using a commercial code is not as high as with an in-house code, because the full detail of the models and algorithms employed are not always available in the documentation of the software. In addition, the source code is not available and therefore the users have no access to the details of the computer programme.

A few works that report a comparison of two leading CFD commercial codes, Ansys Fluent and Star CCM+, have been previously published. Ni [4] used these two codes, as well as IESVE Microflo, to simulate an ambulance hall. While the same mesh was used in the simulations performed with the former two codes, a different one was used for the latter. Ansys Fluent is conclusively recommended for the modelling of complicated indoor airflows. Zou *et al*. [5] compared the performance of Ansys Fluent and Star CCM+ in the simulation of the indoor airflows. They used the same mathematical model, boundary conditions and mesh. They concluded that the two codes yielded almost the same results with similar computational requirements, although Ansys Fluent seemed a little better in some aspects and its user-defined functions were more user-friendly.

Visser *et al*. [6] reported a comparison of the predictions of three codes (Ansys Fluent, Star CCM+ and OpenFoam) for the simulation of a hybrid pool-type research nuclear reactor. There were several research groups involved in this work and each one used a different code. Similar qualitative predictions of the pressure, velocity and temperature fields were obtained. However, the local pressure drop over the core inlet grid was overpredicted by 15% or more and strong differences were found in the prediction of the pressure drop over the core inlet grid. A comparison of the geometry showed that there were differences between the models leading to the conclusion that the geometrical discrepancies in the CFD models of the reactor should be fixed in order to appropriately simulate the pressure losses.

Sondur *et al*. [7] presented a comparison of the same three codes for natural convection airflow in a square cavity for Rayleigh numbers of 10^6 and 10^7. The flow is laminar in this range of Ryleigh numbers. They considered seven different CFD algorithms, including both steady and transient solvers, and density-based and pressure-based solvers. The transient, density-based and pressure based commercial solvers were the most accurate, but required longer computational times.

Stiehl *et al*. [8] modelled turbulent combustion in a jet-in-crossflow axial combustion stage model of a gas turbine combustor at 5 bar. They used the same mesh, the SST k-ω turbulence model and the flamelet generated manifold combustion model. Significant differences between the two codes were found in the combustion model structure, tabulation

process, model initialization and numerical convergence. Although minor differences were found in the flow field and winward ignition location, major differences were observed in the lee-side flame ignition and overall reaction speed.
Among the previous works, only the latter one reports a comparison of Ansys Fluent and Star CCM+ for a reactive flow, and it does not consider thermal radiation. Moreover, that work was carried out for high pressure conditions. In the present work, the two codes are compared for the simulation of a laboratory combustor at atmospheric conditions. The primary objective is to assess how close are the predictions obtained by the two codes when the mesh, the mathematical model, the numerical methods and the solution algorithm are the same, whenever possible, i.e., when the two codes allow the selection of the same options. Non-reactive flow conditions, either isothermal or non-isothermal, are considered before combustion and, eventually, thermal radiation, are also considered.

2. MATHEMATICAL MODEL

2.1. Governing equations

The mathematical model is based on the numerical solution of the governing equations for mass, momentum, energy and mass fractions of chemical species, which may be written as follows for steady state conditions:

$$\frac{\partial \left(\rho u_j\right)}{\partial x_j} = 0 \tag{1}$$

$$\frac{\partial}{\partial x_j}\left(\rho u_j u_i\right) = -\frac{\partial p}{\partial x_i} + \frac{\partial \tau_{ij}}{\partial x_j} + \rho g_i \tag{2}$$

$$\frac{\partial \left(\rho u_j h\right)}{\partial x_j} = u_j \frac{\partial p}{\partial x_j} + \tau_{ij} \frac{\partial u_i}{\partial x_j} - \frac{\partial j_{q,j}}{\partial x_j} + \dot{q}_R''' \tag{3}$$

$$\frac{\partial \left(\rho u_j y_i\right)}{\partial x_j} = -\frac{\partial j_{i,j}}{\partial x_j} + \dot{\omega}_i \tag{4}$$

where u_j and x_j are the velocity component and the coordinate in the jth direction, respectively, h is the specific enthalpy (sum of sensible and chemical enthalpy), y_i the mass fraction of species i, p the pressure, ρ the density, g_i the component of the gravity vector in the ith direction, τ_{ij} the viscous stress tensor, $j_{q,j}$ the heat flux vector, $j_{i,j}$ the diffusion flux vector, $\dot{q}_R'''$ the radiative heat source and $\dot{\omega}_i$ the rate of mass production of species i per unit volume, i.e., the volumetric reaction rate.
The viscous stress tensor may be expressed as follows for a Newtonian fluid:

$$\tau_{ij} = \mu\left(\frac{\partial u_i}{\partial x_j} + \frac{\partial u_j}{\partial x_i}\right) - \frac{2}{3}\mu\frac{\partial u_k}{\partial x_k}\delta_{ij} \tag{5}$$

where μ stands for the dynamic viscosity and δ_{ij} is the Kronecker symbol. The diffusion flux vector is expressed by Fick's law when the Soret effect (diffusion flux due to the temperature gradient) and the diffusion due to the pressure gradient are negligible:

$$j_{i,j} = -\rho D_i^M \frac{\partial y_i}{\partial x_j} \tag{6}$$

where D_i^M is the average diffusion coefficient of species *i* in the mixture. Assuming that the Dufour effect (heat flux due to the gradient of species concentration) is negligible, the heat flux vector is due to heat conduction, expressed according to Fourier's law, and mass diffusion. Assuming further that the mass diffusion is given by Eq. (6) and the mixture behaves as an ideal gas, the heat flux vector may be written as

$$j_{q,j} = -\frac{\lambda}{c_p}\frac{\partial h}{\partial x_j} + \sum_{i=1}^{N}\left(1 - \frac{1}{\mathrm{Le}_i}\right)\frac{\lambda}{c_p}h_i\frac{\partial y_i}{\partial x_j} \tag{7}$$

where λ is the thermal conductivity, c_p the specific heat capacity and Le_i the Lewis number of species *i*.

The Reynolds decomposition, which expresses the instantaneous value of a fluctuating variable as the sum of an average value in time and a fluctuation around the average value, is commonly used in the simulation of turbulent flows. In the case of reacting flows, the Favre-average decomposition, also referred to as density-weighted decomposition, is more commonly used. The application of this decomposition to the governing equations yields:

$$\frac{\partial\left(\overline{\rho}\,\widetilde{u}_j\right)}{\partial x_j} = 0 \tag{8}$$

$$\frac{\partial}{\partial x_j}\left(\overline{\rho}\,\widetilde{u}_j\,\widetilde{u}_i\right) = -\frac{\partial\,\overline{p}}{\partial x_i} + \frac{\partial}{\partial x_j}\left[\mu\left(\frac{\partial\widetilde{u}_i}{\partial x_j} + \frac{\partial\widetilde{u}_j}{\partial x_i}\right) - \frac{2}{3}\mu\frac{\partial\widetilde{u}_k}{\partial x_k}\delta_{ij} - \overline{\rho}\,\widetilde{u_j''\,u_i''}\right] + \overline{\rho}\,g_i \tag{9}$$

$$\begin{aligned}\frac{\partial\left(\overline{\rho}\,\widetilde{u}_j\,\widetilde{h}\right)}{\partial x_j} &= \widetilde{u}_j\frac{\partial\,\overline{p}}{\partial x_j} + \overline{u_j''\frac{\partial p}{\partial x_j}} + \overline{\tau}_{ij}\frac{\partial\widetilde{u}_i}{\partial x_j} + \overline{\tau_{ij}\frac{\partial u_i''}{\partial x_j}} + \\ &+ \frac{\partial}{\partial x_j}\left[\overline{\frac{\lambda}{c_p}\frac{\partial h}{\partial x_j}} - \sum_{i=1}^{N}\left(1 - \frac{1}{\mathrm{Le}_i}\right)\overline{\frac{\lambda}{c_p}h_i\frac{\partial y_i}{\partial x_j}} - \overline{\rho}\,\widetilde{u_j''\,h''}\right] + \overline{\dot{q}_R'''}\end{aligned} \tag{10}$$

$$\frac{\partial\left(\overline{\rho}\,\widetilde{u}_j\,\widetilde{y}_i\right)}{\partial x_j}=\frac{\partial}{\partial x_j}\left(\overline{\rho\,D_i^M\,\frac{\partial y_i}{\partial x_j}}-\overline{\rho}\;\widetilde{u_j''\,y_i''}\right)+\overline{\dot{\omega}_i} \tag{11}$$

where the overbar denotes a time-averaged value and the tilde denotes a density-weighted average value, while the double prime identifies a fluctuation about the density-weighted averaged value. The second term on the right side of Eq. (10) is usually neglected. Similarly, the third and fourth terms on the right side of Eq. (10), which account for viscous dissipation, are negligible, except in high Mach number flows. Furthermore, the second term into the square brackets in Eq. (10) is also often neglected, assuming that the Lewis number is equal to unity for all species. The laminar diffusive fluxes of enthalpy and species may be modelled as:

$$\overline{\frac{\lambda}{c_p}\frac{\partial h}{\partial x_j}}=\frac{\lambda}{c_p}\frac{\partial\vec{\tilde{h}}}{\partial x_j} \tag{12}$$

$$\overline{\rho\,D_i^M\,\frac{\partial y_i}{\partial x_j}}=\overline{\rho}\;D_i^M\,\overline{\frac{\partial y_i}{\partial x_j}} \tag{13}$$

The Reynolds stresses, the enthalpy turbulent fluxes and the species turbulent fluxes (last term into parenthesis in Eqs. 9, 10 and 11, respectively) are calculated using a turbulence model. The mean reaction rate in Eq. (11) and the radiative heat source in Eq. (10) are modelled according to the combustion model and the radiation model, respectively. These models are summarized below.

2.2. Turbulence model

The standard k-ε model was used in the present work. According to this model, the Reynolds stresses and the turbulent scalar fluxes are approximated as follows:

$$-\overline{\rho}\;\widetilde{u_i''\,u_j''}=\mu_t\left(\frac{\partial\widetilde{u}_i}{\partial x_j}+\frac{\partial\widetilde{u}_j}{\partial x_i}-\frac{2}{3}\frac{\partial\widetilde{u}_k}{\partial x_k}\right)-\frac{2}{3}\,\overline{\rho}\;k\;\delta_{ij} \tag{14}$$

$$-\overline{\rho}\;\widetilde{u_i''\,\phi''}=\frac{\mu_t}{\sigma_\phi}\frac{\partial\widetilde{\phi}}{\partial x_j} \tag{15}$$

where ϕ is the scalar under consideration ($\widetilde{h}$ or $\widetilde{y}_i$) and σ_ϕ is the turbulent Prandtl or Schmidt number. The turbulent Prandtl number in the energy equation was set to 0.85 in both codes (this is the default value in Ansys Fluent, while that in Star CCM$^+$ is 0.9), while the Schmidt number in the species transport equations was set to 0.7 in both codes. The turbulent viscosity in Ansys Fluent is given by

$$\mu_t=C_\mu\,\overline{\rho}\,\frac{k^2}{\varepsilon} \tag{16}$$

where C_μ is a constant of the model. A slightly different definition is used in Star CCM+:

$$\mu_t = C_\mu \, \overline{\rho} \, k \, \max\left(\frac{k}{\varepsilon}, \sqrt{\frac{\nu}{\varepsilon}}\right) \tag{17}$$

However, the first term into parenthesis is typically greater than the second one, except in the near vicinity of a wall, and so this different definition is unlikely to lead to have an impact on the results, apart from the near-wall region. The k-ε model involves the solution of transport equations for the turbulent kinetic energy, k, and its dissipation rate, ε. The constants of the model are the same for the two codes (C_μ=0.09, C_1=1.44, C_2=1.92, σ_k=1.0 and σ_ε=1.3). In both cases, the standard wall functions were used to define the boundary conditions at the walls, with the von Karman constant set to κ=0.4187 and the roughness parameter to E=9.793. These are the default values in Ansys Fluent, but in Star CCM+ they are slightly different (κ=0.42 and E=9). In Ansys Fluent, the wall functions for the temperature include a contribution from viscous heating, while in Star CCM+ they do not. Moreover, ANSYS Fluent uses the logarithmic law of the wall only when the dimensionless distance from the wall, y^+, exceeds 11.2, and relies on the laminar stress-strain relationship if that condition is not satisfied. The Star CCM+ documentations does not refer to a threshold value to switch between the viscous sublayer region and the logarithmic layer.

2.3. Combustion model

The eddy dissipation concept (EDC) [9] was selected for combustion modelling. It requires the solution of the transport equations for the species mass fractions. The EDC model is based on the detailed description of dissipation of the turbulent eddies. The flow is divided into two regions, namely the region that contains the small scales of turbulence, called the region of fine structures of the turbulence, and the region surrounding it. The model assumes that chemical reactions occur only in the region of fine turbulence structures, where all the turbulent kinetic energy is dissipated into heat. The fine structures of turbulence are considered small chemical reactors and it is assumed that the reaction rate is equal to the rate of mass transfer of species between the fine turbulence structures and their surroundings.

The source term of the transport equation for the ith species, which represents the rate of mass production/consumption of that species per unit volume, $\overline{\dot{\omega}_i}$ [kg/m^3.s], is given by:

$$\overline{\dot{\omega}_i} = \frac{\rho \, \gamma^* \, \chi \left(y_i^* - y_i^o\right)}{\tau^*} = \frac{\rho \, \gamma^* \, \chi \left(y_i^* - \tilde{y}_i\right)}{\tau^* \left(1 - \gamma^* \chi\right)} \tag{18}$$

where γ^* is the ratio of the mass in the fine structures to the total mass, χ the reacting fraction of fine structures, y_i^* the fine-structure ith species mass fraction after reacting over the time scale τ^*, y_i^o the mass fraction of species i in the surroundings of the fine structures, and $\tilde{y}_i$ the mean mass fraction of species i. The time scale is defined as follows:

$$\tau^* = C_\tau \sqrt{\nu/\varepsilon} \tag{19}$$

where C_τ is a constant of the model, taken as 0.4083, and ν is the kinematic viscosity.
Different definitions of γ^* and χ have been proposed in the literature. In the original version of the EDC model [9], γ^* and χ were defined as

$$\gamma^* = \gamma_\lambda^3 \tag{20}$$

and

$$\chi = \frac{\tilde{y}_{pr}/(1+r)}{\gamma_\lambda\left(\tilde{y}_{pr}/(1+r)+\tilde{y}_{fu}\right)} \tag{21}$$

where $\tilde{y}_{pr}$ and $\tilde{y}_{fu}$ are the mean mass fractions of the products and fuel, respectively, and r is the stoichiometric oxygen to fuel mass ratio. In Eq. (20), γ_λ is the mass of fine-structure regions divided by total mass, which is computed as

$$\gamma_\lambda = C_\gamma \sqrt[4]{\nu\,\varepsilon/k^2} \tag{22}$$

The volume fraction constant, C_γ, is equal to 2.1377.
Later on, Magnussen [10] proposed a more complex expression for χ, but maintained the above definition of γ^*. More recently, a different definition of γ^* and χ was proposed [11]:

$$\gamma^* = \gamma_\lambda^2 \tag{23}$$

$$\chi = \frac{\tilde{y}_{pr}/(1+r)}{\tilde{y}_{pr}/(1+r)+\min\left(\tilde{y}_{fu},\tilde{y}_{oxygen}/r\right)} \tag{24}$$

A thorough discussion and comparison of these formulations along with a critical analysis of different values of the constants that have been proposed by several authors can be found in Ertesvåg [12] and He *et al.* [13].
Both Ansys Fluent and Star CCM+ use the definition of γ^* given by Eq. (20) and a constant value of unity for χ, as proposed by Gran and Magnussen [14]. An operator splitting algorithm is used in every iteration to determine the species mass fractions. In the first step, the fine-structure species mass fractions are calculated by solving a system of ordinary differential equations for a chemical reactor. While a perfectly stirred reactor is considered in the original formulation of the EDC model, a constant pressure reactor is employed in both Ansys Fluent and Star CCM+. A comparison of these two different reactors in the context of the EDC model is presented in Lewandowski and Ertesvåg [15]. The following equations are solved to determine the species mass fractions in the fine structures:

$$\frac{d\,y_i^*}{d\,t} = \frac{\dot{\omega}_i^*}{\rho} \tag{25}$$

The integration is performed at every control volume during a time period τ^* and with the initial condition $y_i(0) = \widetilde{y}_i$. The source term $\dot{\omega}_i^*$ in Eq. (25) is determined from the selected chemical kinetics mechanism. In Ansys Fluent, the system of ordinary differential equations given by Eq. (25), where *i* ranges from *i*=1 to *N* and *N* is the number of species in the reaction mechanism, is solved using a stiff chemistry solver. The *in situ* adaptive tabulation (ISAT) algorithm [16] is used to accelerate the chemistry calculations. In Star CCM+, the stiff CVODE ordinary differential equations solver [17] is used. The ISAT algorithm is available but it was not used since it originates a memory error. Instead, the clustering technique was used. This technique joins together control volumes with similar chemical compositions, integrates the reduced set of equations, and then interpolates the clusters back to the control volumes. In both codes, the computed values of the species mass fractions in the fine structures at $t=\tau^*$ are used in Eq. (18) to determine the mean reaction rates, which are required to solve the transport equations for the mean species mass fractions in the second step of the operator splitting algorithm.

2.4. Radiation model

Radiation in an emitting-absorbing medium is governed by the following equation:

$$\frac{d\, I_\nu(\mathbf{r},\mathbf{s})}{d\, s} = -\kappa_\nu(\mathbf{r}) I_\nu(\mathbf{r},\mathbf{s}) + \kappa_\nu(\mathbf{r}) I_{b\nu}(\mathbf{r}) \tag{26}$$

where I_ν is the spectral radiation intensity at location **r** and along **s** direction, $I_{b\nu}$ is the Planck function, κ_ν is the spectral absorption coefficient, *s* is the coordinate along the direction of propagation of radiation and subscripts ν and *b* denote wave number and black body, respectively. In the case of a grey medium, Eq. (26) is written as

$$\frac{d\, I(\mathbf{r},\mathbf{s})}{d\, s} = -\kappa(\mathbf{r}) I(\mathbf{r},\mathbf{s}) + \kappa(\mathbf{r}) I_b(\mathbf{r}) \tag{27}$$

where *I*, κ and I_b denote the total radiation intensity, absorption coefficient and blackbody radiation intensity, respectively.

The integration of Eq. (26) over all directions (solid angle of 4π) yields the radiative source term of the energy conservation equation:

$$\nabla \cdot \mathbf{q} = -\overline{\dot{q}_R'''} = \int_0^{+\infty} \kappa_\nu \left(4\pi\, I_{b\nu} - G_\nu\right) d\nu = \kappa\left(4\pi\, I_b - G\right) \tag{28}$$

where **q** is the total radiative heat flux vector, which is defined as

$$\mathbf{q} = \int_0^{+\infty} \mathbf{q}_\nu\, d\nu = \int_0^{+\infty} \int_0^{4\pi} I_\nu\, \mathbf{s}\, d\Omega\, d\nu \tag{29}$$

and *G* is the incident radiation given by

$$G = \int_0^{+\infty} \int_{4\pi} I_\nu\, d\Omega\, d\nu = \int_{4\pi} I\, d\Omega \tag{30}$$

Neither the manuals of Ansys Fluent or Star CCM+ provide details on how the spatial discretization of the term on the left hand side of Eqs. (26) or (27) is carried out. The two codes use different methods for the angular discretization. Ansys Fluent discretizes the solid angle of 4π into a finite number of discrete, nonoverlapping, solid angles defined by the intersection of lines of constant latitude and lines of constant longitude. Star CCM+ uses the level symmetric S_N quadrature satisfying sequential odd moments for $N<10$ and even moments for $N>10$.
The radiative properties of the medium are determined using the weighted-sum-of-grey gases (WSGG) model [18], which expresses the total emissivity of the medium as a weighted sum of the emissivities of fictitious grey gases. There are many versions of this model available in the literature, which propose different weighting coefficients and absorption coefficients of the fictitious grey gases. Most of them were developed for a mixture of carbon dioxide, water vapour and other transparent species, such as nitrogen. The version available in Ansys Fluent, which was proposed by Smith *et al.* [19], is outdated. Far more accurate versions that were obtained using recent spectroscopic data are available (see, e.g., [20]). Although it is not clear which version is used in Star CCM+, the references provided in the user guide, which are more than 40 years old, suggest that an obsolete version is also used. In addition, although the WSGG allows the medium to be modelled as non-grey, both codes rely on the assumption that the medium is grey. In fact, they solve Eq. (27) using an absorption coefficient obtained from the total emissivity according to Beer's law, and relying on an assumed path length, as discussed elsewhere [21]. However, this is a crude assumption that may lead to large errors in the evaluation of the radiative heat source (Eq. 28) of the energy conservation equation. Still, the impact on the accuracy of the results may be low whenever the importance of radiative heat transfer is not significant, as is often the case when the size of the physical domain is relatively small.

2.5. Numerical methods

The finite volume method is used in both codes to solve the governing equations. The convective fluxes of these equations are discretized using the second-order upwind scheme to calculate cell face values. The variable gradients in Ansys Fluent are calculated using the least-squares cell-based method. A standard gradient limiter proposed by Barth and Jespersen [22] is employed. In Star CCM+, the variable gradients are computed using a hybrid Gauss-least squares method and the gradient limiter proposed by Venkatakrishnan [23]. In both codes, the SIMPLE algorithm is employed for pressure-velocity coupling and the algebraic systems of discretized equations are solved using the algebraic multigrid linear solver. The calculations were performed using double precision for both codes. Under-relaxation factors of 0.7 and 0.3 were used for the momentum and pressure, respectively, 0.8 for the turbulent kinetic energy and its dissipation rate, and 1.0 for the energy and species mass fraction equations.
The two codes calculate the residuals in different ways. In Ansys Fluent, the residuals may be scaled and/or normalized. The residuals are scaled but they are not normalized by default. Either global or local scaling may be employed, the former being the default option. The globally scaled residuals of a variable ϕ at grid node P, ϕ_P, are defined as:

$$R_\phi = \frac{\sum_{cells} \left| a_P \phi_P - \sum_{nb} a_{nb} \phi_{nb} - b \right|}{\sum_{cells} |a_P \phi_P|} \tag{31}$$

where ϕ_{nb} is the value of ϕ at the neighbouring grid node, *nb*, and a_P and a_{nb} stand for the coefficients of grid nodes P and *nb* in the discretized equation for the control volume centred at grid node P. The source term of the discretized equation is denoted by *b*. The summations extend over all the control volumes in the mesh or all the neighbouring control volumes. In the case of the continuity equation (pressure correction equation), the scaled residual is defined as the ratio of the rate of mass creation in the control volume P at the iteration under consideration to the maximum rate of mass creation in the same control volume in the first five iterations. The residuals, either scaled or unscaled, may be normalized. The normalized residuals are defined as the ratio of the residual at the iteration under consideration to the maximum residual during the first *n* iterations, where *n* is set to 5 by default. Star CCM+ evaluates the root mean square of the residuals for all control volumes and reports, by default, a normalized value, where the normalization factor, denoted by R_{norm}, is also the maximum residual during the first *n* iterations (5, by default). Hence,

$$R_\phi = \frac{\sqrt{\frac{1}{n_{cells}} \sum_{cells} \left| a_P \phi_P - \sum_{nb} a_{nb} \phi_{nb} - b \right|^2}}{R_{norm}} \tag{32}$$

3. LABORATORY COMBUSTOR

The combustion chamber, depicted in Fig. 1, is a cylindrical structure measuring 150 mm in diameter and 300 mm in length [24]. It operates with methane as the fuel source. Positioned atop the combustion chamber is the burner, while the exhaust of the combusted gases is directed downwards through a convergent nozzle situated at the bottom, featuring a length of 50 mm and an inclination angle of 35º. Throughout the length of the combustion chamber, five ports are located, each boasting a diameter of 20 mm. These ports facilitate the insertion of probes for internal combustion chamber analysis. Equipped with electrical elements, the combustor enables preheating of its walls to temperatures reaching 900ºC. Monitoring and assessing temperature gradients within the combustor are facilitated by two thermocouples. The burner configuration comprises a central gas tube complemented by a conventional concentric annular tube for combustion air supply. To enhance efficiency, the combustion air undergoes preheating via an electrical system, capable of elevating inlet temperatures to 750ºC.

4. RESULTS AND DISCUSSION

The laboratory combustor described in section 3 was numerically simulated for steady-state conditions using Ansys Fluent, version 2023 R2, and Simcenter Star CCM+, version 2020.2. The comparison of the predicted results for four different cases is reported here. Firstly, a non-reactive isothermal flow was considered. Then, a non-reactive, non-isothermal flow was simulated. Combustion was included in the third case, which did not account for thermal radiation. Finally, in the last simulation, both combustion and thermal radiation were modelled. The primary objective is to assess the differences between the predictions of the two computational codes.

A two-dimensional axisymmetric, quadrilateral, structured mesh with 5040 control volumes was used, as depicted in Fig. 2. This mesh was generated in Ansys Fluent and then exported to Star CCM+. Therefore, the same mesh was used by both codes. The influence of grid refinement was formerly investigated by Rebola *et al.* [24] and it was found that a mesh with about the same number of control volumes used here yields numerically accurate results.

4.1. Isothermal flow

The simulation of a turbulent isothermal flow was performed by considering that air at ambient

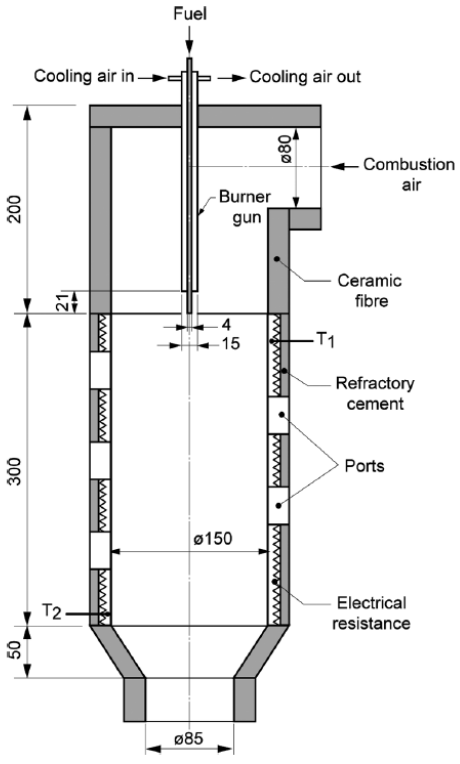

Figure 1. Schematic of the laboratory combustor.

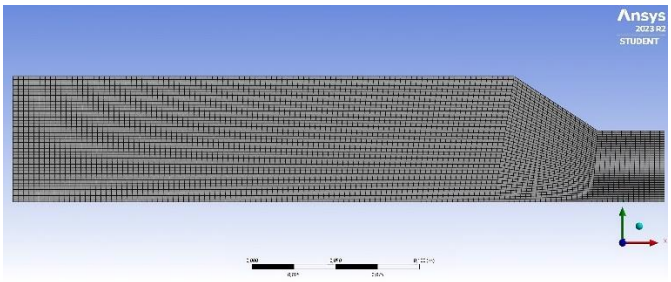

Figure 2. Structured quadrilateral mesh.

temperature is injected through the central tube, at a uniform velocity of u_{in}=24.4 m/s, and also through the concentric annulus, at a uniform velocity of u_{in}=102.1 m/s. The turbulent kinetic energy and its dissipation rate at the inlet are prescribed according to the following equations:

$$k_{in} = \frac{3}{2}\left(I\, u_{in}^2\right) \tag{33}$$

$$\varepsilon_{in} = \frac{C_\mu^{3/4}\, k_{in}^{3/2}}{l} \tag{34}$$

In these equations, I stands for the turbulence intensity and l is a turbulent length scale, taken as 0.07 D_h, where D_h is the hydraulic diameter. At the outlet, the pressure is atmospheric (0 Pa gauge pressure) and a pressure outlet boundary condition is used.

Both simulations were performed for 1500 iterations for all test cases. The residuals decrease by at least 9 orders of magnitude for both codes, demonstrating that the iterative error is small, and so is the round-off error. The discretization error could be estimated by refining the mesh but this will not be investigated here, since the primary concern is to assess how close are the results predicted by the two different codes. Figure 3 shows a comparison of the axial velocity contours predicted by the two codes. It reveals that even though they are rather similar, there are differences between them, which become more obvious in Fig. 4, which shows the axial velocity along the symmetry plane, as well as the difference between the axial velocity calculated using Ansys Fluent and that computed using Star CCM+. The largest discrepancy is observed in the vicinity of the inlet.

We recall that the mesh is the same, as well as the turbulence model and the boundary conditions, apart from little differences in the laws of the wall that were referred to above. These minor differences in the boundary conditions are unlikely to influence the velocity field in the centreline of the combustor. The numerical schemes are also similar, with just a difference in the numerical scheme used for the calculation of the variable gradients, as mentioned above, which could not be set identical in the two codes. Whether this difference or other subtle setup or coding details are responsible for the observed differences in the axial velocity is unclear.

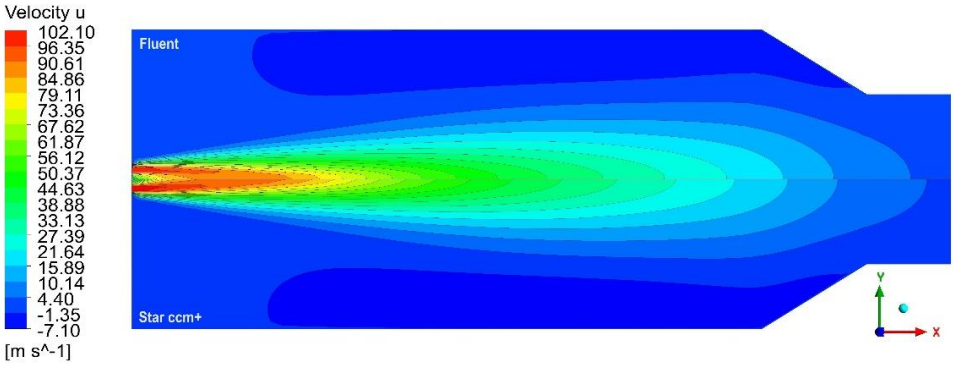

Figure 3. Predicted axial velocity contours for an isothermal flow (Ansys Fluent on the top, Star CCM+ on the bottom).

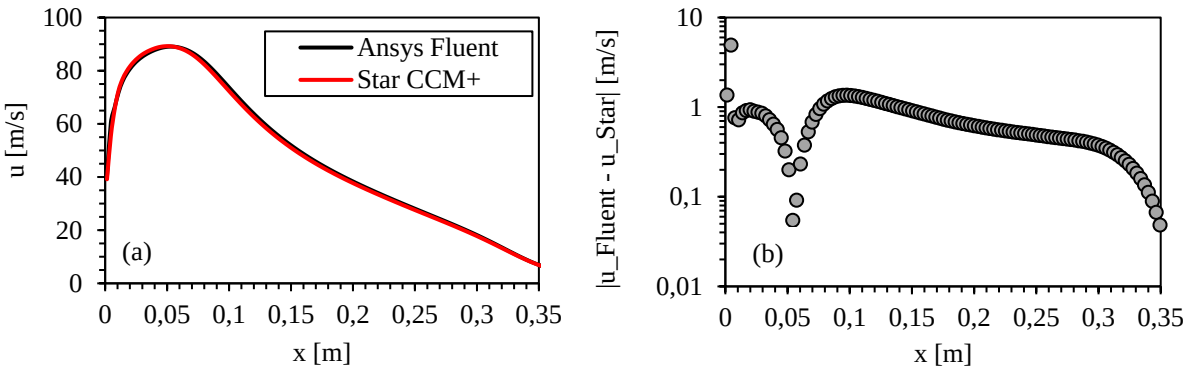

Figure 4. Predicted axial velocity (a) and absolute difference between the axial velocities computed by the two codes (b) along the centreline for an isothermal flow.

4.2. Non-isothermal, non-reactive flow

In the second teste case, the temperature of the air injected through the concentric annular tube is 1000 K, while the temperature of the air flowing in the central tube is maintained at ambient temperature. The inlet velocities remain unchanged, which means that the mass flow rate through the concentric annular tube is lower than in the first test case, due to the decrease of the density with the increase of temperature. The wall of the combustor is assumed to be adiabatic.

The energy equation is solved in addition to the equations for mass, momentum and turbulent quantities (k and ε). All the other physical model details, boundary conditions and numerical methods remain unchanged.

The evolution of the residuals reveals again that they decrease by at least 9 orders of magnitude in 1500 iterations for all the governing equations. Although the contours of the predicted axial velocity, which are shown in Fig. 5, are similar for the two codes, small differences are visible, as in the previous case. Likewise, the isotherms displayed in Fig. 6 for both codes exhibit differences. The radial temperature gradient predicted by Star CCM+ is slightly higher than that determined by Ansys Fluent in the mixing zone, which is zoomed in that figure. The temperature profiles along the centreline are shown in Fig. 7 along with the absolute value of the difference between the temperatures computed by the two codes. Although the profiles are visually rather similar, local differences in the range 10–50 K are observed in the vicinity of the burner, where mixing is more intense and the temperature gradient is largest. However, the differences decrease to values smaller than 1 K downstream of x=0.1 m.

4.3. Reactive flow without thermal radiation

A reactive flow is simulated in this section. Methane at ambient temperature is injected through the central tube, while air at 500ºC is introduced through the concentric annular tube. The inlet methane and air velocities are equal to 24.4 and 102.1 m/s, respectively, i.e., the velocities of the previous test cases were maintained. The mass flow rates are different

in comparison to the non-reactive flow cases, due to the different densities, yielding an excess air coefficient λ=2.0. The temperature of the walls is uniform and equal to 900ºC. The GRI-Mech - 1.2 reaction mechanism [25, 26] was used. This mechanism comprises 32 chemical species and 177 chemical reactions. Although it has been superseded by GRI-Mech 3.0, it was used in the present work since it is relatively detailed but comprises fewer species and reactions, and therefore it is less time consuming than GRI-Mech 3.0.
In this test case, the residuals do not decrease by more than 3 or 4 orders of magnitude during 1500 iterations, which is acceptable for convergence purposes. The predicted axial velocity and temperature contours are displayed in Figs. 8 and 9, respectively. Figure 10

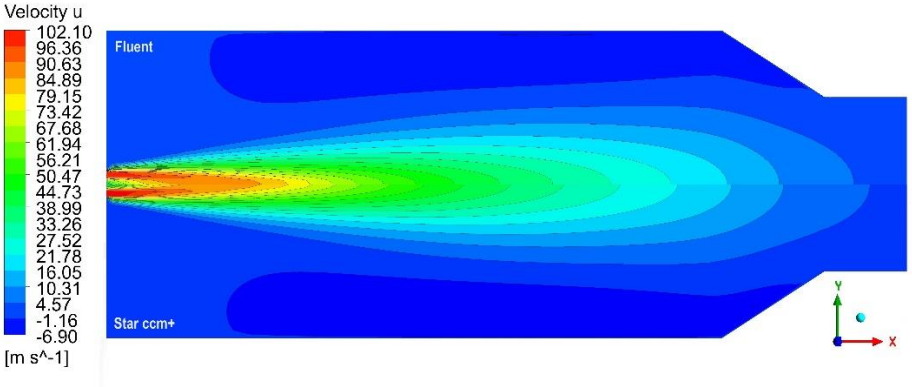

Figure 5. Predicted axial velocity contours for a non-isothermal, non-reactive flow (Ansys Fluent on the top, Star CCM+ on the bottom).

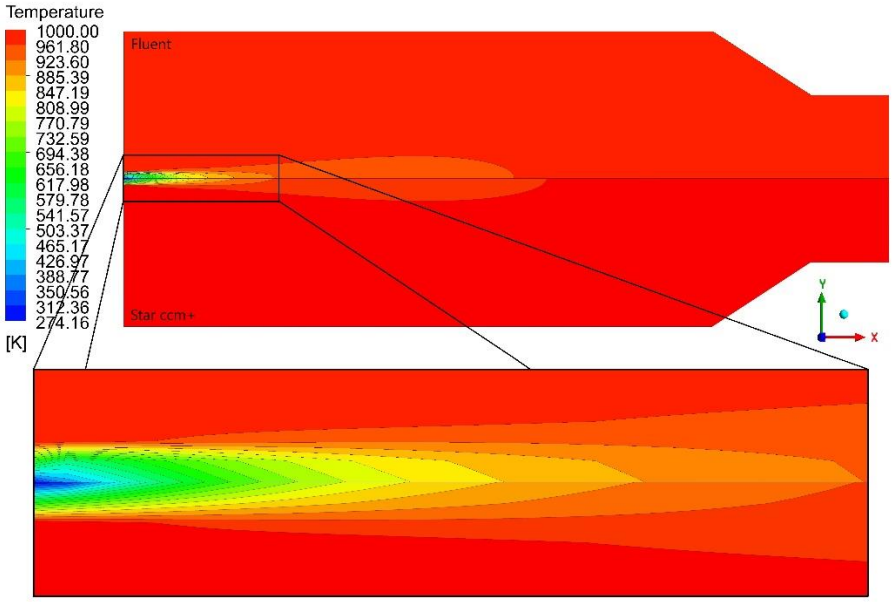

Figure 6. Predicted temperature contours for a non-isothermal, non-reactive flow (Ansys Fluent on the top, Star CCM+ on the bottom).

CMN Congress on Numerical Methods in Engineering 2024

U

APMTAC SEMNI universidade de aveiro